UNIVERSITÀ DEGLI STUDI DI PADOVA

DIPARTIMENTO DI GEOSCIENZE

FACULTÉ DES SCIENCES ET TECHNOLOGIES
Département Sciences de la Terre

Ph.D. course in Earth Sciences

Series XXXIII

Tectonic evolution of the north-central Patagonia: a thermochronological approach

Coordinator: Ch.ma Prof. Claudia Agnini

Supervisor: Ch.mo Prof. Massimiliano Zattin

Supervisor: Prof. Bruno Vendeville

Co-Supervisor: Dr. César Witt

Reviewer: Prof. Laura Giambiagi

Reviewer: Prof. Joseph Martinod

Ph.D. student: Marie C. Genge

Spécialité du doctorat :

Sciences de la Terre et de l'Univers

Thermochronologie

Evolution tectonique de la Patagonie Nord-Centrale par différentes approches de thermochronologie

Président du jury : Prof. Bernardo Cesare (Université de Padoue)
Examinateur : Prof. Matthias Bernet (Université de Grenoble-Alpes)
Examinateur : Prof. Jean-Yves Reynaud (Université de Lille)
Examinateur : Prof. Mario Tribaudino (Université de Parme)
Rapporteur : Prof. Laura Giambiagi (CONICET, Mendoza)
Rapporteur : Prof. Joseph Martinod (Université de Savoie Mont Blanc)
Directeur de thèse : Prof. Massimiliano Zattin (Université de Padoue)
Directeur de thèse : Prof. Bruno Vendeville (Université de Lille)
Co-directeur de thèse : Dr. César Witt (Université de Lille)

Thèse en cotutelle internationale présentée et soutenue par

Marie C. Genge, le 26 février 2021 à Lille

ABSTRACT

The change in plate kinematics, which may have affected slab dip, can deeply influence the interplate coupling and consequently the deformation of the overriding plate. The north-central Patagonia represents a unique region to study the impact of slab-dip changes as this area is characterized by alternating episodes of steep to flat-slab since the onset of subduction below the South American Plate. The alternation of the upper plate subsidence and exhumation events related with slab steepening and shallowing episodes, respectively, or with changes in kinematics has been widely studied in the recent years along the Andes. However, some topics remain highly debated, and especially the magnitude of the vertical movements through time and space. Low-temperature thermochronology systems, which are sensitive to events involving the upper first kilometers of the upper crust, represent an efficient approach for dating and quantifying significant episodes of burial and exhumation. This thesis investigates the thermal history of the north-central Patagonian broken foreland and the Cordillera. The latter area has been widely studied through bedrock thermochronology studies compared with data from the Patagonian foreland, where only few data are available. Thus, this work aims at improving our knowledge on the relationships between the surface cooling record and the geodynamic evolution.

Three apatites thermochronometers (U-Pb, fission tracks and (U-Th-Sm)/He) were used on bedrocks, Mesozoic and Cenozoic sandstones as well as on modern sediments. All samples were collected from the inner part of the north-central Patagonian Cordillera to the distal part of the broken foreland along the Atlantic coast. Compilation of these diverse thermochronology datasets, integrated by inverse thermal modeling and provenance analysis, is discussed here and compared with the different geodynamic processes proposed for Patagonia (e.g. convergence changes, slab dip variations). The new thermochronology records indicate that main unroofing of Patagonia (~3 – 4 km), Cordillera and broken foreland included, occurred during a slab-shallowing episode from late Early Cretaceous to early Paleogene, after a Jurassic – Early Cretaceous heating episode related to a significant burial below a thick sedimentary cover. This regional exhumation phase was followed by a period between the late Eocene and the early Miocene of foreland subsidence associated with slab rollback, characterized by a steady-state post-shortening low exhumation rates. During this period of relative quiescence, detrital analysis point to the Cordillera as a primary contributor of sediments for the entire foreland with a local input from the broken foreland reliefs. Finally, Miocene substantial exhumation is recognized into the Cordillera after a change of convergence rates and obliquity, especially along a dextral strike-slip fault zone active along the Cordillera. However, this exhumation phase is not detected regionally in the broken foreland. Since no regional sedimentary burial or relevant exhumation events affected the north-central Patagonian foreland, the few Oligo-Miocene ages identified along the foreland have been ascribed to the coeval intraplate magmatic processes.

RIASSUNTO

In un contesto di subduzione, il regime tettonico e la deformazione della placca superiore sono governati dalla dinamica della litosfera, avendo un impatto diretto sull'accoppiamento tra placche e talvolta sulla geometria della subduzione. La Patagonia centro-settentrionale (40-48° S) rappresenta un caso di studio ideale per gli studi sull'impatto che meccanismi profondi, come la variazione dell'angolo della placca in subduzione, hanno sul sollevamento topografico e la formazione del rilievo. Lungo le Ande sono stati effettuati diversi studi sull'alternanza di fasi di esumazione e subduzione indotte da processi geodinamici. Tuttavia, rimangono numerosi interrogativi sull'entità di questi movimenti verticali sia in termini temporali che spaziali. I sistemi di termocronologia a bassa temperatura sono molto sensibili ai movimenti verticali che interessano i primi chilometri della crosta. Questi sistemi rappresentano quindi un approccio efficace per localizzare, datare e quantificare i periodi più significativi di subduzione ed esumazione. L'obiettivo di questa tesi è quello di analizzare l'evoluzione termica e tettonica della catena andina e del suo avampaese nel settore della Patagonia centro-settentrionale. L'evoluzione topografica delle Ande a queste latitudini è state ampiamente studiata con analisi in situ, mentre esistono pochi dati di termocronologia nell'avampaese. Pertanto, questo studio mira a fornire una conoscenza più approfondita sulle relazioni tra i processi superficiali come l'erosione e la dinamica del mantello.

In questo lavoro sono stati utilizzati diversi termocronometri su apatite (U-Pb, tracce di fissione e (U-Th-Sm) / He) ottenuta da campioni di granita e di sedimenti recenti, Cenozoici e Mesozoici, tutti raccolti dalla Cordigliera della Patagonia alla costa atlantica. La compilazione di questo gruppo di dati, integrando modelli di inversione termica e analisi di provenienza, viene qui discussa e confrontata con i diversi processi geodinamici proposti per la Patagonia. Questi nuovi dati indicano che un importante episodio di esumazione di 3-4 km ha interessato tutta la Patagonia centro-settentrionale, Cordigliera e avampaese inclusi, durante una fase di subduzione a basso angolo dal tardo Cretaceo fino all'inizio del Paleogene. Questa fase è seguita da un periodo di subsidenza generalizzata tra tardo Eocene e il Miocene inferiore associata al "roll-back" della placca in subduzione. Questo periodo è caratterizzato da tassi di esumazione bassi e costanti lungo la Cordigliera. Le analisi su sedimenti dell'avampaese hanno dimostrato che la maggior parte di loro deriva dall'erosione della catena della Ande, con un contributo locale dei rilievi extraandini. Infine, dopo una variazione del tasso di convergenza e inclinazione della placca in subduzione, si è riconosciuta una fase di esumazione importante lungo la Cordigliera durante il Miocene, ed in particolare lungo una strutture tettonica trascorrente. Tuttavia, questa fase di esumazione non è stata rilevata nell'avampaese, dove la deformazione è stata quindi minore. Le poche età Oligo-Mioceniche ottenute nell'avampaese sono state qundi attribuite a processi magmatici e vulcanici intraplacca attivi durante la sedimentazione.

RESUME

Le régime tectonique des zones de subduction et la déformation de la plaque chevauchante sont régis par la convergence des plaques lithosphériques, ayant un impact direct sur le couplage intraplaque et parfois sur la géométrie de la plaque plongeante. La Patagonie centrale-nord (40-48°S) constitue une région remarquable pour étudier l'impact des mécanismes profonds, tel que l'horizontalisation de la plaque plongeante, ayant conduit à la surrection de la Cordillère Patagonienne et de son avant-pays. Diverses études sur l'alternance des phases d'exhumation et de subsidence en surface ont été menées le long des Andes. Pourtant, de nombreuses interrogations demeurent sur la magnitude de ces mouvements verticaux à travers le temps et l'espace. Les systèmes de thermochronologie basse-température sont sensibles aux mouvements verticaux impliquant les premiers kilomètres de la croûte supérieure. Ils représentent donc une approche efficace pour localiser, dater et quantifier les périodes de subsidence et d'exhumation les plus significatives. Cette thèse a pour objectif d'examiner les histoires thermiques de la Patagonie centrale-nord, de son avant-pays et de sa Cordillère. Les reliefs andins à ces latitudes ont été largement étudiés par des analyses in-situ, tandis que peu de données de thermochronologie existent dans l'avant-pays. Ainsi, cette étude vise à apporter des connaissances plus approfondies à propos des relations entre la dynamique mantellique et les processus de dénudation à la surface.

Trois thermochronomètres (l'U-Pb, les traces de fission et l'(U-Th-Sm)/He) ont été utilisés sur des apatites extraites d'échantillons provenant du substratum ainsi que de sédiments modernes, Cénozoïque et Mésozoïque, tous collectés dans la Cordillère Patagonienne et l'avant-pays, jusqu'à la côte Atlantique. La compilation de ces jeux de données, intégrant des modèles d'inversion thermique et des analyses de provenance, est discutée ici et comparée avec les différents processus géodynamiques proposés pour la Patagonie. Les nouveaux enregistrements de thermochronologie indiquent qu'un épisode d'exhumation majeure de 3 à 4 km a affecté l'intégralité de la Patagonie centrale-nord, Cordillère et avant-pays inclus, de la fin du Crétacé supérieur jusqu'au Paléogène, période correspondant à un épisode de subduction horizontale. Cette phase est suivie d'une période de subsidence de l'avant-pays entre l'Eocène tardif et le Miocène inférieur associé à la retraite du segment en subduction. Les analyses détritiques ont permis de mettre en évidence que, durant cette période, l'évolution de la Cordillère a été caractérisée par des taux d'exhumation post-déformation faibles et constants, et a été le principal contributeur sédimentaire de l'avant-pays proximal et distal. Une contribution locale des reliefs extra-andins a aussi été observée. Finalement, une phase d'exhumation considérable de la Cordillère est reconnue durant le Miocène, et particulièrement le long d'une zone de décrochement dextre active au sein de la Cordillère. Pourtant, cette phase d'exhumation, qui serait induite par un changement de taux de convergence et d'obliquité de la plaque de Nazca, n'est pas détectée régionalement dans l'avant-pays, ce qui signifie que la déformation y a été mineure. Comme aucun mouvement vertical notable n'a affecté l'avant-pays durant le Néogène, les rares âges Oligo-Miocène identifiés dans l'avant-pays ont été imputés à des processus magmatiques intraplaques.

ACKNOWLEDGMENTS

In the first place, my greatest thank you to my supervisor Massimiliano Zattin for his attentiveness, his patience and his continuous support to keep going through the analysis to the publication processes. He provided me a wide range of research experiences and freedom to organize my work. I could not imagine a better supervision. I would like to thank César Witt, my co-supervisor, for his willingness to join the project and his constant optimism that help me to keep motivation. Both of you allow me to start working in research on very interesting projects. I greatly appreciated these moments with you and your continual friendship. So, I am looking forward for many years of collaboration and pine-apple pizza. Bruno Vendeville, my co-supervisor is greatly thanked for his continuous sympathy and assistance since many years.

I am grateful to Stefano Mazzoli, Cécile Gautheron and Valerio Olivetti who were helpful mentors to me since the beginning of this project, through long discussions and collaboration. I have learned a lot from you and it will be a great benefit to me in the future. I feel fortunate for the time spent together on the field, accompanied by Marcelo and Jamie who shared their knowledges about Patagonia. I am also grateful to the members of my dissertation committee: Laura Giambiagi and Joseph Martinod.

I have grown into being a scientist at the Geology Department of Lille and Padua and sought many advises from people that shared their knowledges and help me over the years. J.-Y. Reynaud, F. Chanier, J. Ferrière, S. Clausen, L. Devaere, N. Tribovillard, F. Nestola, C. Agnini, A. d'Alpaos, M. Ghinassi and many more are all thanked for having available to discuss.

Silvia, Leo, Sandra, Elisa and Xia provided a nice working environment at the Department in Padua over my years here as well as all my peers and post-docs, who helped me in many ways. I sincerely appreciated all the nice moments together, with a special mention for the Chinese team, for all the unidentified food that you offered to me. Thanks to Monique, Marie-Christine, Sophie, Jessie and others who provided a friendly face over my time in the University of Lille. I would also like to thank the personal of the University of Paris-Saclay, Perugia and Rennes and the great people I met there as Claire, Thomas, Mustafa, Xavier, Maurizio, Maxime, Kerry, Nathan, and others, and particularly Alexis, for the unforgettable moments on the field, your knowledges, our fruitful collaboration and your perpetual kindness. This was a non-exhaustive list of some admirable persons I met and I am sorry for all the others who I can not mentioned. However, your friendship is forever appreciated.

Thanks to my friends over the world, my flatmates (especially Lisa), my family-izize and relatives – who are starting to understand what I am doing, more or less – for their continuous encouragements and interest about my professional pursuits. Finally, thank you Steven for your unending support and understanding every day.

CONTENTS

CHAPTER 1

INTRODUCTION

1.1 Overview

The influence of interactions between tectonics, climate and erosional processes in the mountain building have been a matter of considerable debate for the past decades (e.g. Roe et al., 2008; Whipple, 2009). Thermochronology methods are increasingly applied to obtain information about the cooling/exhumation history of rocks exposed at the surface in order to answer to a wide range of geological issues (e.g., Clinkscales et al., 2020; Lanari et al., 2020; Maydagán et al., 2020). The application of several complementary thermochronological techniques on bedrocks or detrital rocks (high- or low-temperature methods) presents various benefits to better understand geological processes and temporally constrain the geological history locally or regionally. Thus, thermochronometers have been widely used along the Andes to constrain timing and significance of diverse exhumation phases (e.g. Carrapa et al., 2009; Espurt et al., 2011; Gautheron et al., 2013b; Margirier et al., 2015; Stevens Goddard and Fosdick, 2019; Thomson et al., 2010, 2001; Villagómez and Spikings, 2013). The substantial along-strike segmentation along the orogeny resulted from a series of shortening pulses with different magnitude, style and timing since the late Early Cretaceous (e.g. Folguera et al., 2015; Horton, 2018a; Louterbach et al., 2018; Nie et al., 2012; Ramos, 2009; Roddaz et al., 2010). Therefore, this N-S extended belt and adjacent basins represent an ideal natural laboratory for examining surface processes and feedbacks on the erosion pattern. This thesis investigates the debated Meso-Cenozoic denudation history of the north-central Patagonian Cordillera and its broken foreland, with the objectives of using different thermochronology approaches on bedrocks, modern and ancient detrital apatites. Indeed, assessing past erosion rates through natural experiments requires indirect approaches enable to indicate timing of the exhumation of past reliefs. The timing and magnitude of exhumation episodes evidenced in this thesis are then discussed in order to evaluate the relationships between changes in geodynamics and erosional features at the surface.

1.2 Graphical introduction

The following cartoons have been extracted from the book “Sciences en bulles” (for *Fête de la Science 2019*, by *SNE – Sciences pour tous, Ministère de l’Enseignement Supérieur, de la Recherche et de l’Innovation, Ministère de la Culture, Université de Lorraine, Peb & Fox*) and translated. They introduce shortly the thermochronological method mostly applied in Patagonia for this thesis, a project chosen to represent the University of Lille in a French national project.

Rain, rivers and glaciers are constantly eroding mountains, forming sand at their foothills.

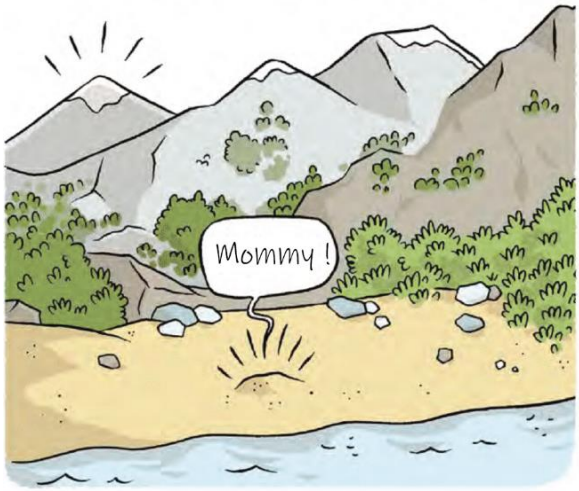

Sand represents a tool for studying the growth of the Andean Cordillera, which is relatively young: it wasn't there during the time of dinosaurs.

I have collected sandy samples in Patagonia. I am particularly interested to one of the diverse minerals inside: the apatites.

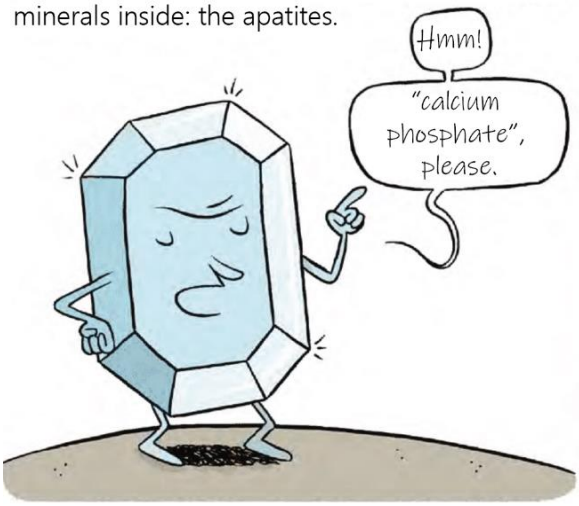

Appearing at considerable depth, apatites are going up slowly to the surface due to plate tectonics and erosion. When "going up", they come across an apatite damaging zone...

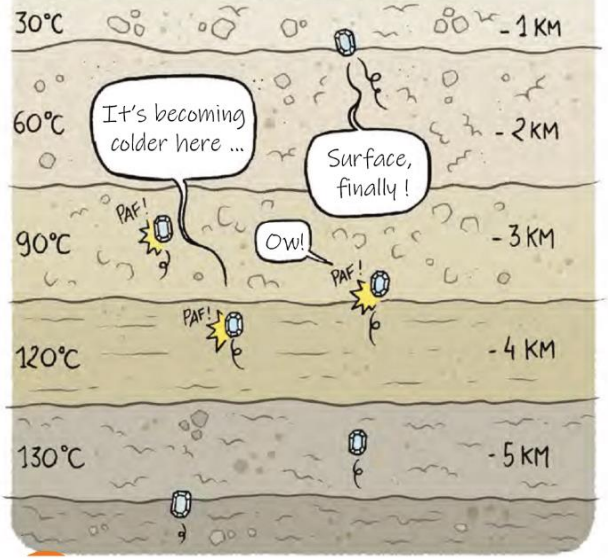

When apatite are crystallizing, they catch Uranium. Uranium is an heavy element, with many protons in the nucleus, making it unstable. I am interested by a reaction produced by Uranium: the spontaneous nuclear decay.

To be stable, atoms must have a nucleus respecting their own proton/neutron ratio.

This stability is unattainable for Uranium nucleus... however, it dreams too!

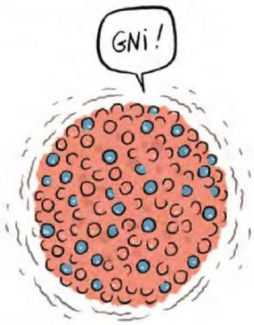

To attempt this achievement, it splits in two more stable nucleus, ejected in opposite directions.

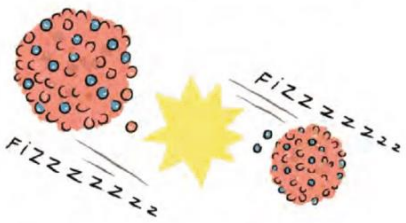

A straight array called "fission track" is thus created in the apatites.

The decay occurs regularly during the exhumation of the apatites. Fission tracks heal well at high temperatures but not completely between 120 and 60°C, allowing their observations under the microscope.

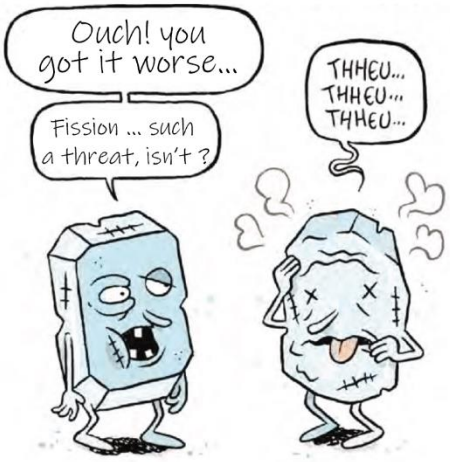

All these scars are a wealth of information to understand the moutain relief under study.

Two months of training are necessary to analyze and understand these marks of time!

Fission track length:
Longer tracks indicate a fast exhumation through 120 to 60°C (~2 - 4km). Moutains have been uplifted quickly.

Tracks couting:
By comparing uranium decayed with initial content, I can date the rock cooling age. I correlate then with ages calculated in the mountains to find a potential source.

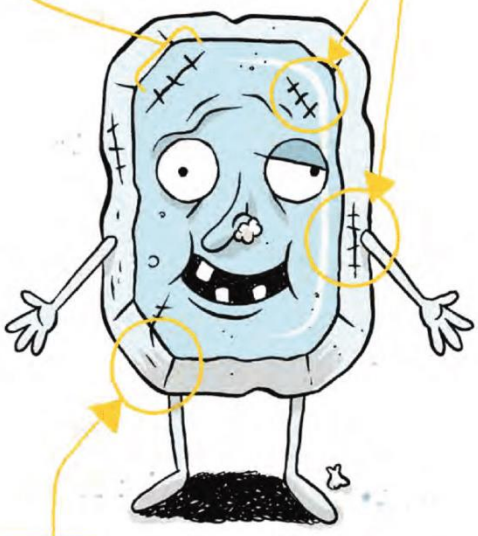

Shape of the grain:
Erosion transforms rocks into small grains. The latter will endure abrasion during transport. Round apatites suggest a longer transport.

Five hours are necessary at least to study each sample ...

1.3 Geological background

1.3.1 South America current geodynamic setting

The Andes are the longest active orogenic system in the world and were developed by several processes mainly associated with the subduction of various Pacific oceanic plates (Nazca and Antarctica plates nowadays) beneath the South American continental plate. The Andes are commonly subdivided in three regional morphostructural domains (Figure 1.1A), based on volcanic segmentation and major structural features (Gansser, 1973; Ramos, 1999): the Northern Andes (Venezuela to Ecuador, 12 °N – 4 °S), the Central Andes (Ecuador to North Chile, 4 °S – 46 °S), and the Southern Andes (South Chile, 46 °S – 55 °S). This nearly continuous belt presents spatial upper plate variations and shift of the volcanic arc through time. They are mostly related to kinematic changes (Maloney et al., 2013; Pardo-Casas and Molnar, 1987; Somoza, 1998) and geometric variations of the subduction along the margin (Figure 1.2A; Horton, 2018). Along the Andes, the slab dips to the east with an angle of ~ 30 ° (Figure 1.2C; Maksymowicz and Tassara, 2018). Three sub-horizontal segments have been recognized on the basis of the seismic events distribution (Espurt et al., 2008; Gutscher et al., 2000; Ramos and Folguera, 2009) and fit with gaps in volcanic arc activity in some parts of the chain (Figure 1.1A and Figure 1.2B). Furthermore, identification of such slab configurations in the past has been unraveled considering magmatic and tectonic cycle along the Andes (Figure 1.2A; Ramos and Folguera, 2009).

The Patagonian Andes extend from 35 °S to 55 °S and encompassed the southern Central Andes as well as the whole Southern Andes (Figure 1.1A). They correspond to a narrow, segmented and roughly linear belt with a lower average topography (with some summits reaching 3000 m of altitude), compared with the large and arched Central Andes that are characterized by a high average topography. Despite a relative morphological continuity, the north Patagonian Andes show a noticeable along-strike segmentation that influences magmatism and the style of deformation in the overriding plate (e.g. Coira et al., 1993; Gutscher, 2002; Ramos, 2009). The onset of subduction in this area occurred during the Paleozoic since the arc has been active since the Carboniferous (Oliveros et al., 2020, and references therein; Vasquez et al., 2011), and not during the Jurassic as previously proposed by Mpodozis and Ramos (1990, 2008). Then, the Cordillera grew by several pulses since late Early Cretaceous (e.g. Echaurren et al., 2016; Horton, 2018a, 2018b). The central Patagonia is the transitional zone between the North and the Austral Patagonia at ~ 46 °S (± 2 °), where the Chile Spreading Ridge (CSR) is currently subducted at the so-called Chile Triple Junction (CTJ) that separates the Nazca and the Antarctica Plates (Figure 1.3A; Scalabrino et al., 2009). The first CSR segment entered in subduction at ~ 15 Ma along the austral Patagonia (Lagabrielle et al., 2004; Scalabrino et al., 2009), then migrated northward to reach its current position (Figure 1.1B). The migration of the subducted ridge segments enabled the inception of a slab window, that extends nowadays under the whole Austral Patagonia (Figure 1.1B and Figure 1.2D; Breitsprecher and Thorkelson, 2009; Scalabrino et al., 2009). The development of this slab window has been enhanced by differences in velocity and orientation of the Nazca and the Antarctica low viscosity of the mantle induced by the slab window

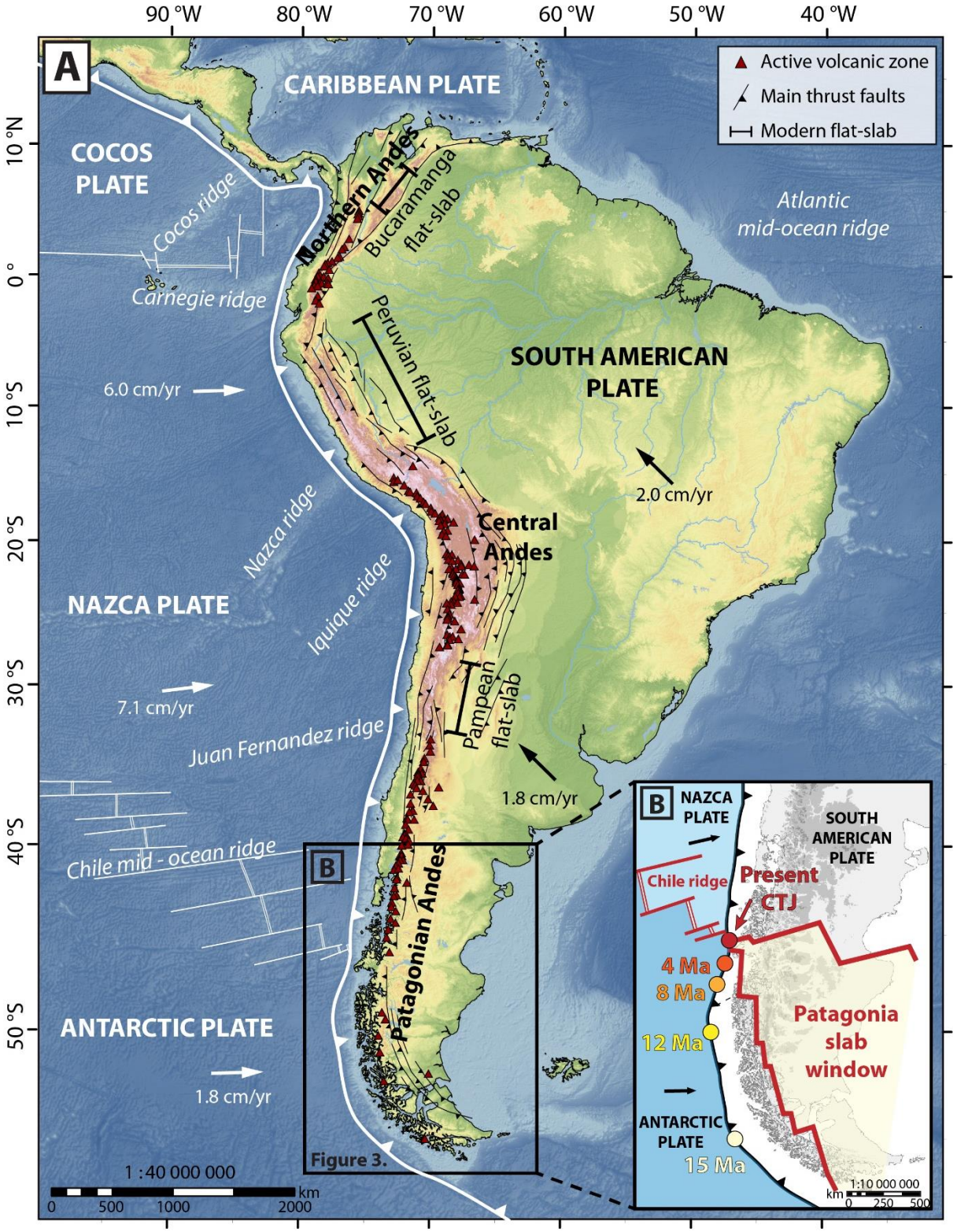

Figure 1.1 – Geodynamic setting of the Nazca-South American convergence system. (A) Digital Elevation Model (DEM from ESRI) of South America and bathymetric data (GEBCO 2014, ESRI) with present-day plate kinematics (according to global model NUVEL-1); major structural characteristics of the Cordillera, mainly thrust faults (Ramos, 1999); location of active volcanic zone (Gutscher et al., 2000), revealing the flat-slab segments (evidenced by earthquakes depth, shown in D and E, or tomography as presented by (Gutscher et al., 2000; Portner et al., 2017) and the slab window. Black square delimitates (B) and Figure 1.3. (B) Geodynamic setting of the active Chile Spreading Ridge beneath the South American Plate in a point called the Chile Triple Junction (CTJ) and the location of the current slab window located below the while Patagonia (Breitsprecher and Thorkelson, 2009). Migration of the CTJ is indicated by the colored circle migrating northward through time along the trench.

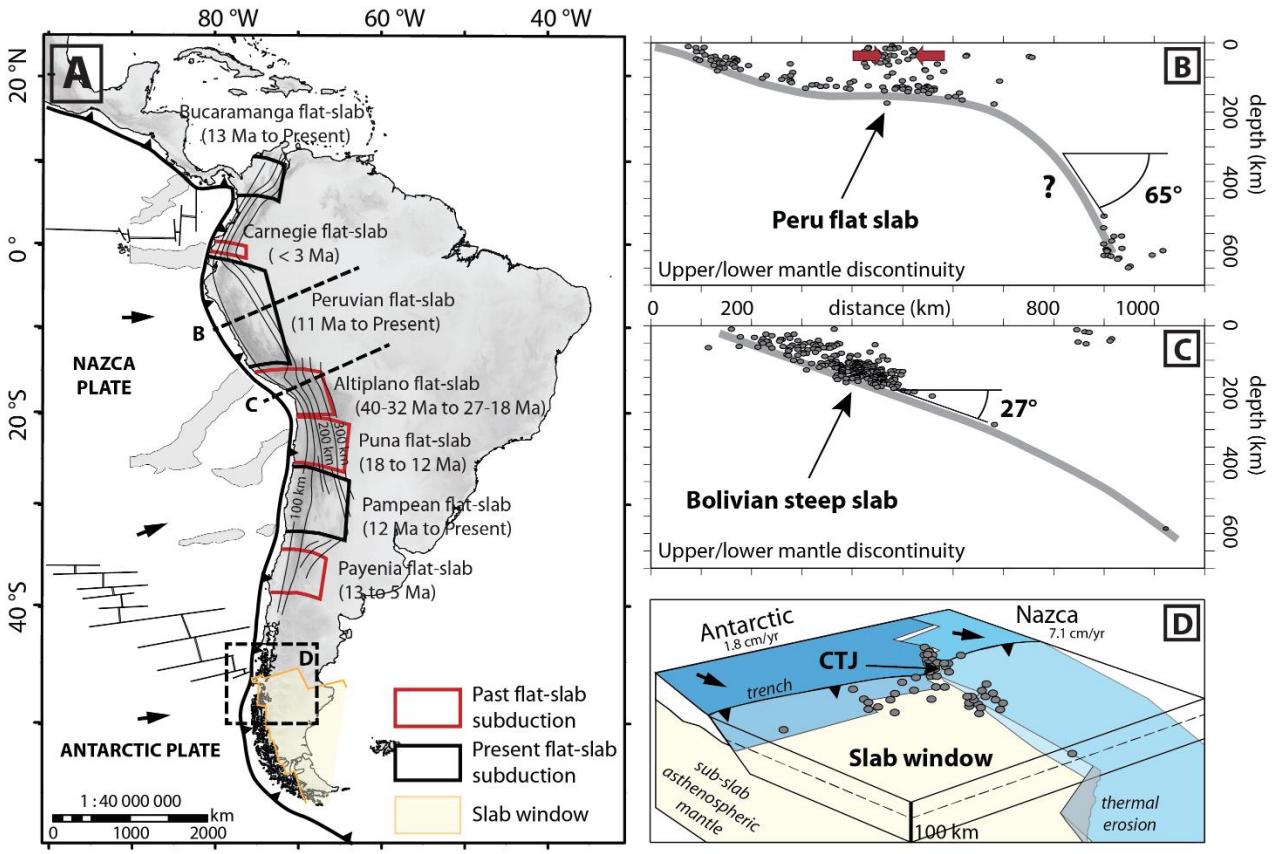

Figure 1.2 – Slab configuration along the South American Plate. (A) Cenozoic segments characterized by flat-slab geometries (Ramos and Folguera, 2009). (B) Profile of the Nazca slab beneath the South American plate from earthquake epicenter plotted (Gutscher et al., 2000) marked by a flat slab beneath Peru, and (C) by a ~ 30° dipping slab beneath northern Chile/Bolivia (profiles from Espurt et al., 2008). (D) Block diagram of modern Patagonia slab window projected towards the northwest (modified after Breitsprecher and Thorkelson, 2009) with earthquake epicenters plotted from USGS data.

below Patagonia favored high uplift rates and the migration of the deformation front, which extended through a wide fold and thrust belt, whereas north of the CTJ mild deformation involved the retro-arc basins (Figure 1.3 and 3D; Ramos, 2005).

The Patagonian Andes are also related to the Patagonian Broken Foreland system represented by a conspicuous NNW-trending intraplate belt, extended between 40 and 48 °S from the western North Patagonian Massif to the western Deseado Massif and across the San Bernardo Thrust Belt (San Bernardo FTB; Figure 1.3A; Gianni et al., 2015; Homovc et al., 1995; Peroni et al., 1995). These reliefs are separated by extensional basins, such as the transverse San Jorge (Gulf) Basin at the current latitude of the CTJ, or the Cañadon Asfalto Basin to the north (Figure 1.3B; Figari et al., 2015). The Rio Mayo Embayment is a retro-arc basin developed between the central Patagonian Andes and the broken foreland and linking westward with the San Jorge Basin (Miller and Marino, 2019; Navarrete et al., 2015).

1.3.2 North – central Patagonia geodynamic setting

North – central Patagonia has been affected since Jurassic times by variations of subduction kinematics (velocity, obliquity and orientation of the convergence) that strongly influenced magmatism and tectonic as reported in Figure 1.4 (Echaurren et al., 2016; Horton, 2018a; Mpodozis and Ramos, 2008). Nevertheless, the impact of the successive oceanic subduction episodes beneath Patagonia on the geodynamics of the overriding plate remains indirect and poorly constrained.

Significant subsidence affected the north-central Patagonia from the Early Jurassic to the Early Cretaceous (Mpodozis and Ramos, 2008). Toward the trench, the subsidence is evidenced by the opening of NNW-trending basins associated with the emplacement of the Subcordillera Plutonic Belt in a back-arc configuration (Page and Page, 1999; Rapela et al., 2005). Subsidence was triggered by a protracted slab

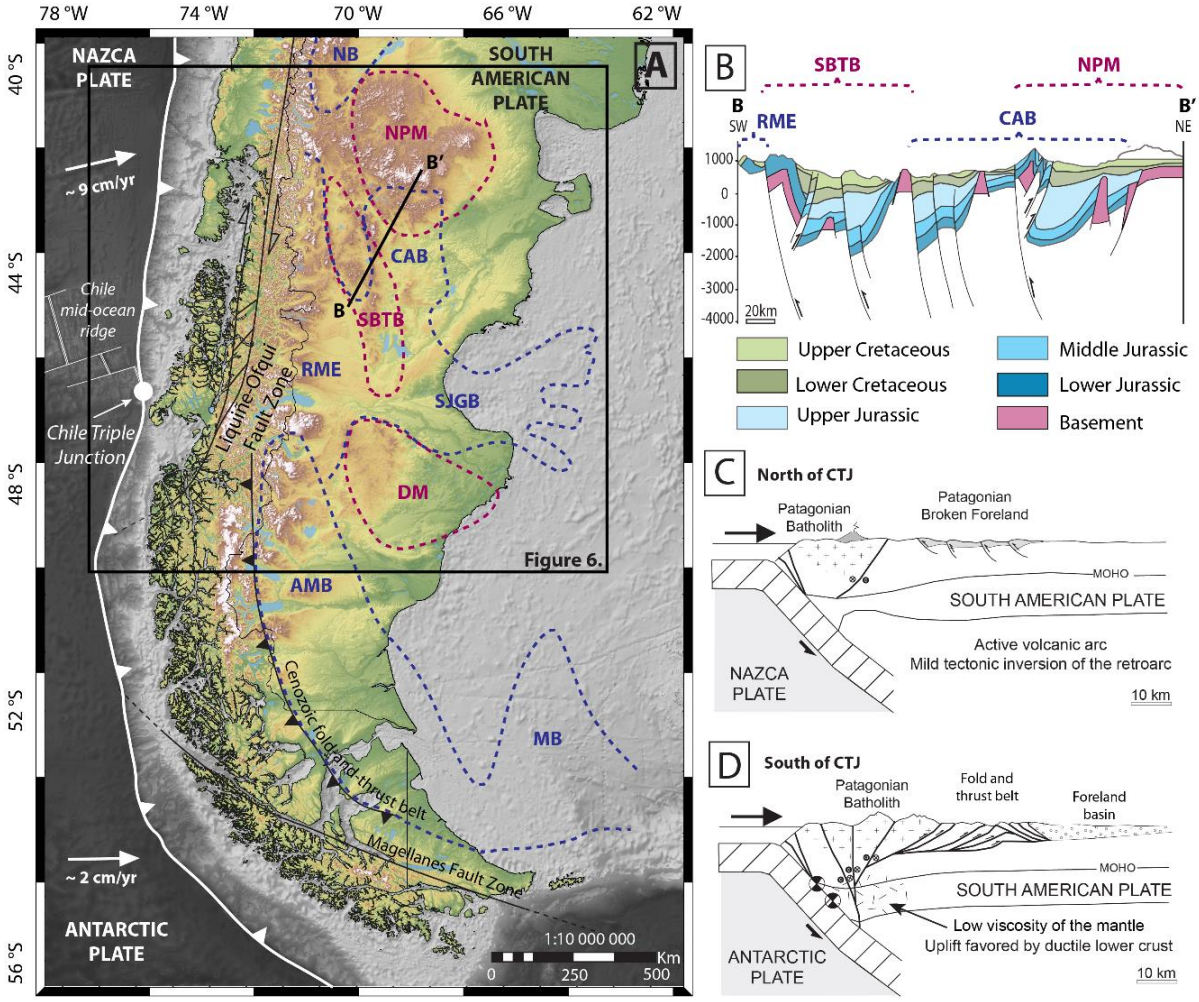

Figure 1.3 – (A) Plate tectonic setting in the Patagonian Andes with the indication of major tectonic features of Patagonia (modified from Navarrete et al., 2016). Blue surrounded areas represent foreland basins (AMB: Austral-Magallanes Basin, CAB: Cañadón Asfalto Basin, MB: Malvinas Basin, NB: Neuquén Basin, RME: Rio Mayo Embayment, SJGB: San Jorge Gulf Basin) and in purple the foreland reliefs (DM: Deseado Massif, NPM: North Patagonian Massif, SBTB: San Bernardo Thrust Belt). White arrows indicate current motions of oceanic plates relative to South America, according to global model NUVEL-1. (B) Schematic structural SW-NE cross-section (DD') across north Patagonia to show the inversion of the Jurassic – Early Cretaceous basins during Late Cretaceous (modified after Figari et al., 2015). (C) Present tectonic setting of the Patagonian Cordillera north of the Chile Triple Junction (CTJ) and (D) south of the CTJ (modified after Ramos, 2005).

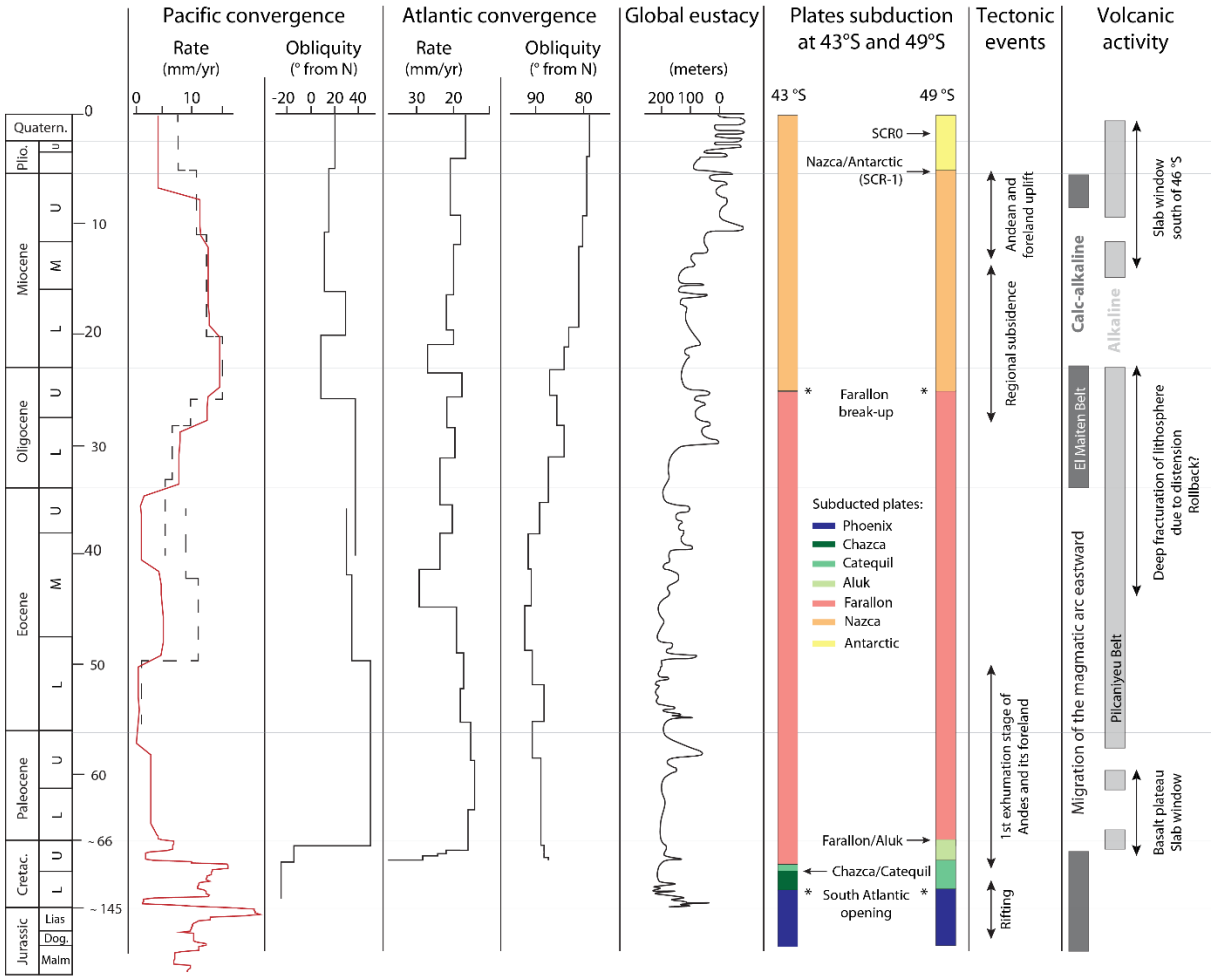

Figure 1.4 – Summary of plate kinematics affecting Patagonia: Pacific (Pardo-Casas and Molnar, 1987; Somoza, 1998) and Atlantic convergence variations (Nürnberg and Müller, 1991). Global eustacy curve from Haq et al. (1987). Plates and ridges subduction in North (43 °S) and Central-South Patagonia (49°S) from Maloney et al. (2013). SCR0 corresponds to the current Segment of the Chile Ridge while SCR-1 is related to the previous that has been already consumed by the subduction (Scalabrino et al., 2009). The tectonic events are summarized from Echaurren et al. (2016) and the volcanic activity (with the Pilcaniyeu and El Maíten Belts indicated) from (Butler et al., 2020).

rollback and the resulting slab steepening throughout this period (Figure 1.5A), coetaneous with a negative value of the trench-normal absolute velocity of the South American Plate (Maloney et al., 2013). Coevally to the east, the metamorphic basement experienced a broad rifting related to the break-up of Western Gondwana. This extensional regime generated NW-oriented strike half-grabens, the so-called Cañadón Asfalto Rift Basin (Figari et al., 2015) or the Neocomian Basin developed in the San Jorge Basin (Gianni et al., 2015a; Navarrete et al., 2015).

At the end of the Early Cretaceous (~ 120 Ma) the whole Patagonia recorded an earliest compressional stage. The deformation acted on a weakened continental lithosphere (due to crustal heterogeneities, mechanical and thermal weakening) and involved the formation of the initial fold-thrust belt and the Patagonian Broken Foreland (Cobbold and Rossello, 2003; Echaurren et al., 2016; Folguera and Ramos, 2011; Horton and Fuentes, 2016; Mpodozis and Ramos, 2008). For the latter, the noticeable inversion of the former basins was enhanced by the reactivation of the NNW-trending faults associated

with the deposition of synorogenic deposits (Gianni et al., 2015a; Navarrete et al., 2015). The formation of the Patagonian Broken Foreland, highlighted by growth strata, was controlled by NNW-trending former heterogeneities acting as anisotropies focalizing strain during compression ~500 km away from the trench (Gianni et al., 2015a; Homovc et al., 1995; Navarrete et al., 2015; Peroni et al., 1995). This late Early Cretaceous basin reorganization is also marked by the coeval exhumation of the Deseado Massif (Giacosa et al., 2010a) and the retroarc basin known as the Rio Mayo Embayment/Sub-basin (Aguirre-Urreta and Ramos, 1981) or Aysén Basin (Suarez et al., 2009). The latter is developed along the Andean piedmont and show deformation and regional angular unconformity between deposits of Aptian-Albian and Late Cretaceous ages (Folguera and Iannizzotto, 2004; Suarez et al., 2009). The onset of the regional shortening in north-central Patagonia during the late Early Cretaceous coincided with a change of the absolute motion of the South American Plate to the west (according to the model of Maloney et al., 2013) induced by the increase of the trench-normal plate convergence of the South American Plate and the acceleration of the South Atlantic seafloor global spreading (Eagles, 2007; Somoza, 1998). It is worth noting that high trenchward convergence rates of the overriding plate promote slab shallowing (Figure 1.5B; Heuret et al., 2007; Lallemand et al., 2005). As mechanical plate coupling variations are governed by subduction geometry changes, the shallowing of the slab beneath Patagonia (flattening during Late Cretaceous) favored a strong increase of the intraplate coupling resulting in an enhanced regional shortening (e.g. Gianni et al., 2018; Horton and Fuentes, 2016; Martinod et al., 2010).

Paradoxically, a second main stage of extensional tectonics occurred during Early Cretaceous. During the preceding first stage, sediments were restricted to deep half-grabens developed in variable orientations referred as Neocomian or Cañadón Asfalto Rift Basins, while this second phase generated wider depocenters along Patagonia known as the Chubutian Basin (Fitzgerald et al., 1990; Gianni et al., 2015a). The Chubutian Basin recovered unconformably the former depocenters and reached to up to 8000 m of thickness in the center of the San Jorge Gulf Basin (Barcat et al., 1989; Chelotti, 1997; Clavijo, 1986; Figari et al., 2002, 1999; Foix et al., 2012; Gianni et al., 2015a; Hechem et al., 1990; Paredes et al., 2013, 2018; Uliana et al., 1989). Another noticeable process at that time is the roughly N-S extension at ~ 46°S, responsible of the formation of the San Jorge Basin which cross-cuts the broken foreland at this latitude and involved the reactivation of structures mostly parallel to the maximum E-W horizontal stress active from late Early Cretaceous (Figari et al., 1999; Gianni et al., 2015a; Paredes et al., 2013; Ramos, 2015). Syn-extensional deposits are evidenced in the whole San Jorge Basin in the exception of the broken foreland area where structures are much more complexes due to the simultaneous activity of both compression and extension in this particular place of the foreland (Gianni et al., 2014, 2015a).

A second major compressional event occurred during Late Cretaceous times as evidenced by the regional angular unconformity that capped the Chubutian Basin in the foreland (e.g. Barcat et al., 1989; Ramos, 1981). This episode coincided with the main emplacement of the North Patagonian Batholith and is followed by an eastward migration of the magmatic arc (probably responsible of the closure of the Rio-Mayo Sub-basin; Suarez et al., 2009), related with the flattening of the slab (Figure 1.5C; Barcat et al., 1989; Folguera and Ramos, 2011; Gianni et al., 2018; Suarez et al., 2009). Between latest Cretaceous and

early Paleogene, the considerable within-plate volcanism provides surface evidences of the opening of a slab window following the subduction of the Farallon-Aluk ridge (Figure 1.5D; Aragón et al., 2011; Cande and Leslie, 1986; Echaurren et al., 2016; Maloney et al., 2013; Rapela et al., 1988; Suárez and De la Cruz, 2001). This setting may have consequence on the prolonged regional deformation that affected Patagonia as asthenospheric windows trigger mantle flow responsible of significant non-isostatic uplift on the overriding plate (Aragón et al., 2013; Guillaume et al., 2009). Slab flattening associated with increase of the intraplate coupling, and slab window producing non-isostatic uplift are frequently involved in kilometer-scale uplift (e.g. Ávila and Dávila, 2020; Bishop et al., 2018; Fan and Carrapa, 2014; Guillaume et al., 2009; Margirier et al., 2015).

Contractional events are still recorded in the foreland to the early Eocene (Gianni et al., 2017), characterized by a diminished shortening (Horton, 2018a; Horton et al., 2016; Horton and Fuentes, 2016). The following regional extension, recognized in the foreland from late Paleogene to early Neogene (Fernández Paz et al., 2020; Gianni et al., 2017; Muñoz, 1999), and the migration of the magmatic arc to the trench may have involved a slab steepening associated with pronounced slab roll-back and advanced intraplate decoupling (Figure 1.5E; Aragón et al., 2011; Iannelli et al., 2018; Muñoz, 1999; Ramos and Folguera, 2005; Rapela et al., 1988; Suárez and De la Cruz, 2001). This tectonic relaxation occurred after a proposed sharp reduction in average trench velocity (Maloney et al., 2013). The regional tectonic relaxation and the flexural response to the crustal thickening of the Cordillera allowed the marine flooding of the whole Patagonia from Oligocene to Early Miocene (Encinas et al., 2018). The location of the marine deposits evidences the existence of reliefs (the present Cordillera, the San Bernardo FTB and the Deseado Massif), acting as paleotopographic barriers during the Cenozoic (Figure 1.7B; Malumian and Nanez, 2011).

The break-up of the oceanic Farallon Plate into Nazca and Cocos Plate at ~23 Ma reorganized the plate convergence (Lonsdale, 2005). Therefore, increase of convergence rates is noticeable and convergence between the Nazca and the South American plates became oblique (Figure 1.4; Maloney et al., 2013). Since this time, higher convergence rate and a mostly orthogonal subduction affected the South American Plate at the latitudes of the north-central Patagonia (Maloney et al., 2013; Somoza, 1998). This new configuration may have allowed an increase of intraplate coupling not related with change of slab dip (Figure 1.5F). Middle Miocene to Pliocene exhumation of the Austral-Central Cordillera, clearly revealed by relict planar surfaces, is responsible of the actual deeply incised topography along Patagonian Andes (Scalabrino et al., 2009). It may have been enhanced by complex feedback between tectonic as the dextral Liquiñe-Ofqui Fault Zone extended from Central to Northern Patagonian Andes (Georgieva et al., 2016; Lagabrielle et al., 2007) and deeper dynamic processes, both triggered by the successive collisions of segments of the South Chile spreading ridge and subsequent outset of slab window (Guillaume et al., 2013), or by climate (Folguera et al., 2015; Thomson et al., 2010). Modest to substantial deformations controlled by former heterogeneities are also evidenced along the Patagonian Broken Foreland during the Neogene (Bilmes et al., 2013; Gianni et al., 2015a).

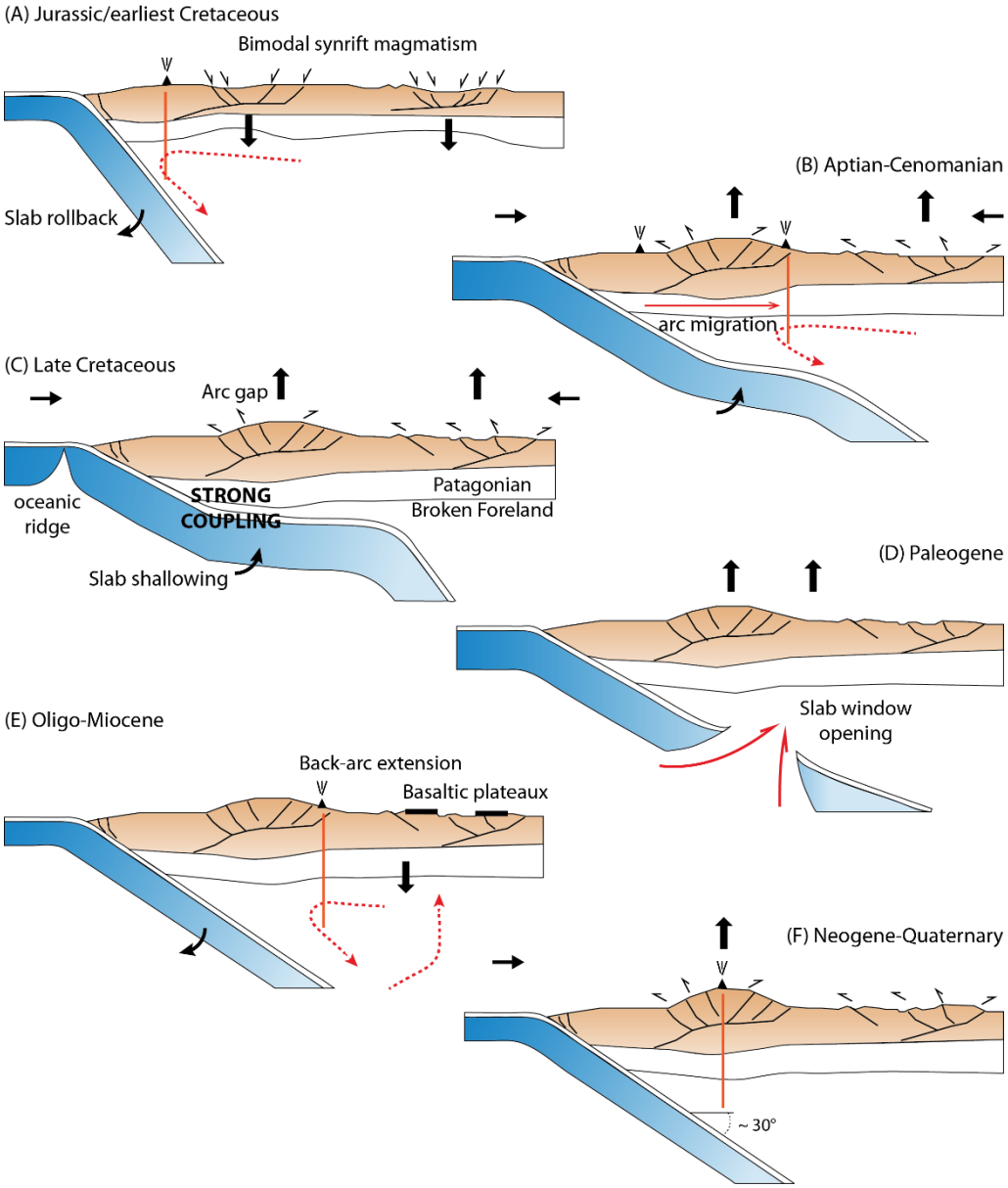

Figure 1.5 – Schematic representation of the tectonic evolution of the Patagonian fold and thrust belt and broken foreland from the Jurassic to the Present linking intraplate contraction and magmatic arc migration to changes in slab angle (modified after (Echaurren et al., 2016; Gianni et al., 2018). The slab window appearing during the Paleogene (D) affected first the north Patagonia and the central one as it migrated southward. See section above for details.

1.4 Stratigraphic setting

1.4.1 Patagonian Cordillera

Along the Andes, the Early Jurassic graben-like depocenters hosted the thick volcano-sedimentary Piltriquitrón Formation (Gabaldón, 1982; Suarez and Marquez, 2007) associated with some marine incursions. This formation overlies unconformably the Precambrian metamorphic basement represented by the Colohuincul Complex (Giacosa and Heredia, 2004; Lizuain, 1980; Lizuain Fuentes, 1983). It was then buried below the Middle-Late Jurassic volcanic Ibáñez-Lago La Plata Formations and the Early Cretaceous

sedimentary Coyhaique Group subdivided in the Toqui-Tres Lagunas, the Katterfeld and the Apeleg Formations (Figure 1.6; Suarez et al., 2009). This last group, deposited in the Rio Mayo Embayment, is characterized by an eastern provenance from the adjacent foreland areas (Bell et al., 1996) and is represented by shelf to open marine deposits interbedded with pyroclastic beds (Hervé et al., 2000; Olivero and Aguirre-Urreta, 2002; Suarez et al., 2009). An unconformably relationship is recognized between the Coyhaique Group and the Late Cretaceous Divisadero Group, the latest composed of synorogenic volcanic deposits (Echaurren et al., 2014).

South of the Rio Mayo Embayment (i.e. south of the General Carrera – Buenos Aires lake) the arc-related volcanic rocks that marked the initiation of the subduction of Pacific plates beneath the South American Plate are gathered in the El Quemado Complex (Iglesia Llanos et al., 2003; Ramos, 1982). There, Cretaceous formations are represented by continental deposits (Ramos, 1979). The Pueyrredón Group overlies the El Quemado Complex and is divided in three units defined as Springhill, Rio Mayer and Rio Belgrano Formations (Figure 1.6). The younger San Martin Group is composed of the Rio Tarde (correlated with the Apeleg Formation; Suarez et al., 2009) and the Cardiel Formations. During the Cenozoic, some sediments (defined below) are deposited along the Andean piedmont since the Eocene. During the Paleogene, retroarc volcanic plateau, represented by the Posadas Basalt for example, were erupted in Central and Austral Patagonia, while the gap of magmatism in the north Patagonian Cordillera is explained by the migration of the arc to the foreland (Folguera and Ramos, 2011; Ramos, 2005). The Paleogene volcanism, south of 44 °S, coincided in time and space with the region affected by the subduction of the Chasca-Catequil and Farallon-Aluk ridges (Maloney et al., 2013; Ramos, 2005). Intense magmatism along the entire Patagonian Cordillera commenced during Early Miocene as evidenced by Rb-Sr and U-Pb intrusion ages (Aragón et al., 2011; Pankhurst et al., 1999) and thermochronology ZFT and AFT ages (Thomson et al., 2001).

1.4.2 Patagonian Foreland

In Northern Patagonia, the pre-Jurassic basement of the foreland is composed of metamorphic rocks dated from Carboniferous to Triassic ages (Cushamen and Calcatapul Formations; Proserpio, 1978; Volkheimer, 1964) intruded by plutonic bodies as those represented by the Mamil Choique and the Lipetrén Formations (Duhart et al., 2002; Pankhurst et al., 2006; Ravazzoli and Sesana, 1977). In central Patagonia, pre-Jurassic units are recognized in the Deseado Massif (Guido et al., 2004). To the Atlantic coast, the Late Precambrian to Early Paleozoic basement is composed of low-grade metamorphic rocks intruded by granitoids (Rio Deseado Complex, La Modesta Formation, Río Lácteo Formation to the Cordillera; (Di Persia, 1962; Giacosa et al., 2002; Viera, 1976). All these rocks have been metamorphosed during the Pampean cycle in late Precambrian to Mid-Cambrian time (Guido et al., 2004). In north Patagonia, Carboniferous-Permian sedimentary units named the Tepuel Group rest unconformably on the metamorphic basement (Andreis and Cúneo, 1989). In central Patagonia, the Pre-Permian basement is

covered by Permian-Triassic thick sedimentary units (e.g. El Tranquilo Formation; Archangelsky, 1966; Arrondo, 1972; Di Persia, 1965).

The Patagonian foreland is then characterized by thick Early Jurassic to Early Cretaceous volcano-sedimentary successions hosted by the Cañadón Asfalto Rift Basin system: Las Leoneras Formation, Lonco Trapial Group, Cañadón Asfalto Formation and locally Cañadón Calcareo (Cúneo et al., 2013; Figari et al., 2015; Zaffarana and Somoza, 2012). These Jurassic sedimentary formations are associated with the Marifil Complex (Rapela and Pankhurst, 1993) developed in the eastern Patagonian Foreland (Figure 1.7A). To the southern Deseado Massif, the Chon Aike Magmatic Province emplaced coevally included various magmatic units as Roca Blanca, La Leona (solely to the east), or Bajo Pobre Formations, which have been overlain by the Bahia Laura Group (Guido et al., 2006; Pankhurst et al., 1998). These synextensional sequences are unconformably overlain by Neocomian deposits known as Bajo Grande Formation in the Deseado Massif (Giacosa et al., 2010a), and Las Heras Group in San Jorge Basin which gather various non-exposed formations as Pozo Anticlinal Aguada Bandera or Pozo Cerro Guadal appearing on seismic data (Lesta et al., 1980). An angular unconformity is recognized between these deposits and the late Early – Late Cretaceous Chubut Group (Figure 1.6; Codignotto et al., 1978; Lesta, 1968). This discontinuity has been documented with the first episode of the Andean uplift at these latitudes (Folguera and Iannizzotto, 2004; Ramos, 1981; Suarez et al., 2009).

The Chubut Group, representing the main hydrocarbon reservoirs in the Patagonian foreland, is widely documented. Deposition of the Chubut strata started during the Aptian with the pyroclastic Matasiete Formation, the fluvial Pozo D-129 Formation and the Baqueró Formation, which is their lateral equivalent in the Deseado massif. They are covered by the volcano-sedimentary Castillo Formation, which has been attributed to the Aptian-Albian (Hechem and Strelkov, 2002). The fluvial Bajo Barreal Formation (Cenomanian – Early Turonian) is a product of transitional or dissected magmatic arc, while the former Matasiete Formation presented clearly a source from a non-dissected magmatic arc (Olazábal et al., 2020). The upper layers of the Chubut Group are represented by the Laguna Palacios and the Lago Colhué-Huapi Formations (its basinward equivalent) with an interval age still discussed but possibly spanning from Late Cenomanian to Maastrichtian (Casal et al., 2015; Genise et al., 2007; Vallati et al., 2016). The continental successions of the Chubut Group are the oldest exposed rocks along the San Bernardo FTB (Figure 1.7A) and suggest a synorogenic character, evidence of the ongoing regional deformation in the foreland at deposition time (Barcat et al., 1989; Echaurren et al., 2016; Gianni et al., 2015a; Navarrete et al., 2015; Suarez et al., 2009). On the contrary, coeval strata in the eastern San Jorge Basin present a clear synextensional regime (Gianni et al., 2015b). The continental Chubut group is capped by a regional unconformity interpreted as the result of a major compressional event through the Cretaceous (Barcat et al., 1989; Echaurren et al., 2016; Feruglio, 1949; Proserpio, 1978; Ramos, 1981; Ramos et al., 2002) which can be related to tectonic inversion, especially in the San Jorge Basin, starting during the late Late Cretaceous (Allard et al., 2020; Foix et al., 2020; Paredes et al., 2018) or the late Early Cretaceous (Gianni et al., 2015a). Therefore, the development of the San Jorge Basin is still debated as period of extension and compression has been poorly constrained.

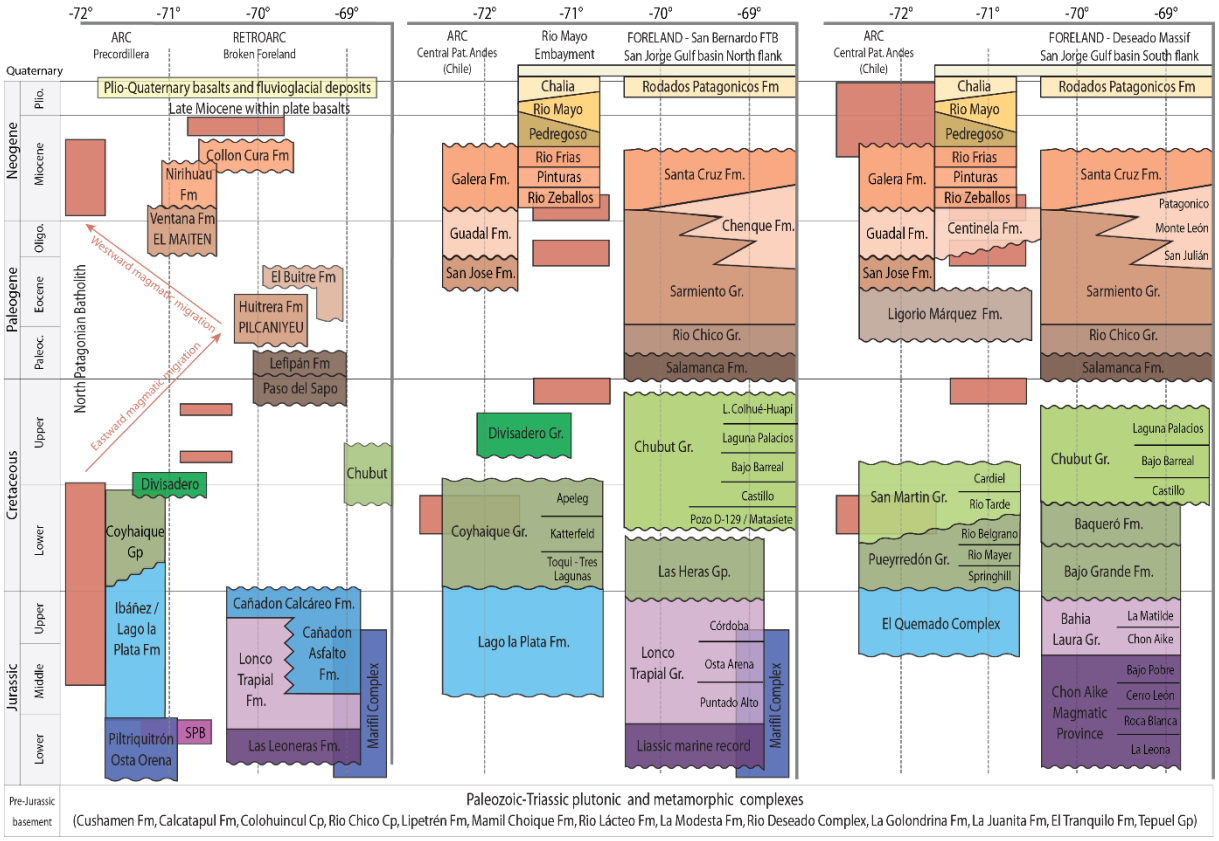

Figure 1.6 – Stratigraphic chart of the north Patagonia (at 42 °S), central Patagonia (at 46°S) and austral Patagonia (at 49 °S) Andes and foreland. Main magmatism episodes are indicated by salmon-pink rectangles. About (volcano-) sedimentary formations, same colors emphasize the coeval deposition of the different formations. See text for details. Modified from Echaurren et al. (2016) and Gianni et al. (2015b).

The Chubut Group is overlapped to the east by marine sediments associated with a Atlantic marine transgression occurring during the Maastrichtian – Danian. In the San Jorge Gulf Basin, this formation is known as Salamanca Formation. To the north Patagonia, it corresponds to the fluvial-estuarine Paso del Sapo and Lefipán Formations sustained by supply from the North Patagonian Massif (NPM; Lesta and Ferello, 1972). A fan of west-growing strata observed in all these deposits attested for their synorogenic character around the Patagonian Broken Foreland (Echaurren et al., 2016). The location of marine deposits indicates the presence of several topographic highs (Figure 1.7B). The gradational contact between the marine formations and the following continental formations suggested a progressive replacement. In the San Jorge Basin, the Late Paleocene – Early Eocene unit is known as the volcano-sedimentary Rio Chico Group and is strongly pyroclastic (Foix et al., 2013). This group display strong lateral variations mainly related with the diversity of fluvial architectures. Field observations and seismic data interpretation suggest synextensional deposition basinward, while synorogenic strata are evidenced close to the Patagonian Broken Foreland (San Bernardo FTB and western Deseado Massif), attesting respectively of the continuous subsidence of the San Jorge Basin, and of the foreland compression through the Paleogene (Gianni et al., 2017). To the NPM, the volcano-sedimentary layers deposited from the Paleogene to the Eocene are identified as the Huitrera Formation. They have been related to the retroarc Pilcaniyeu Belt associated with

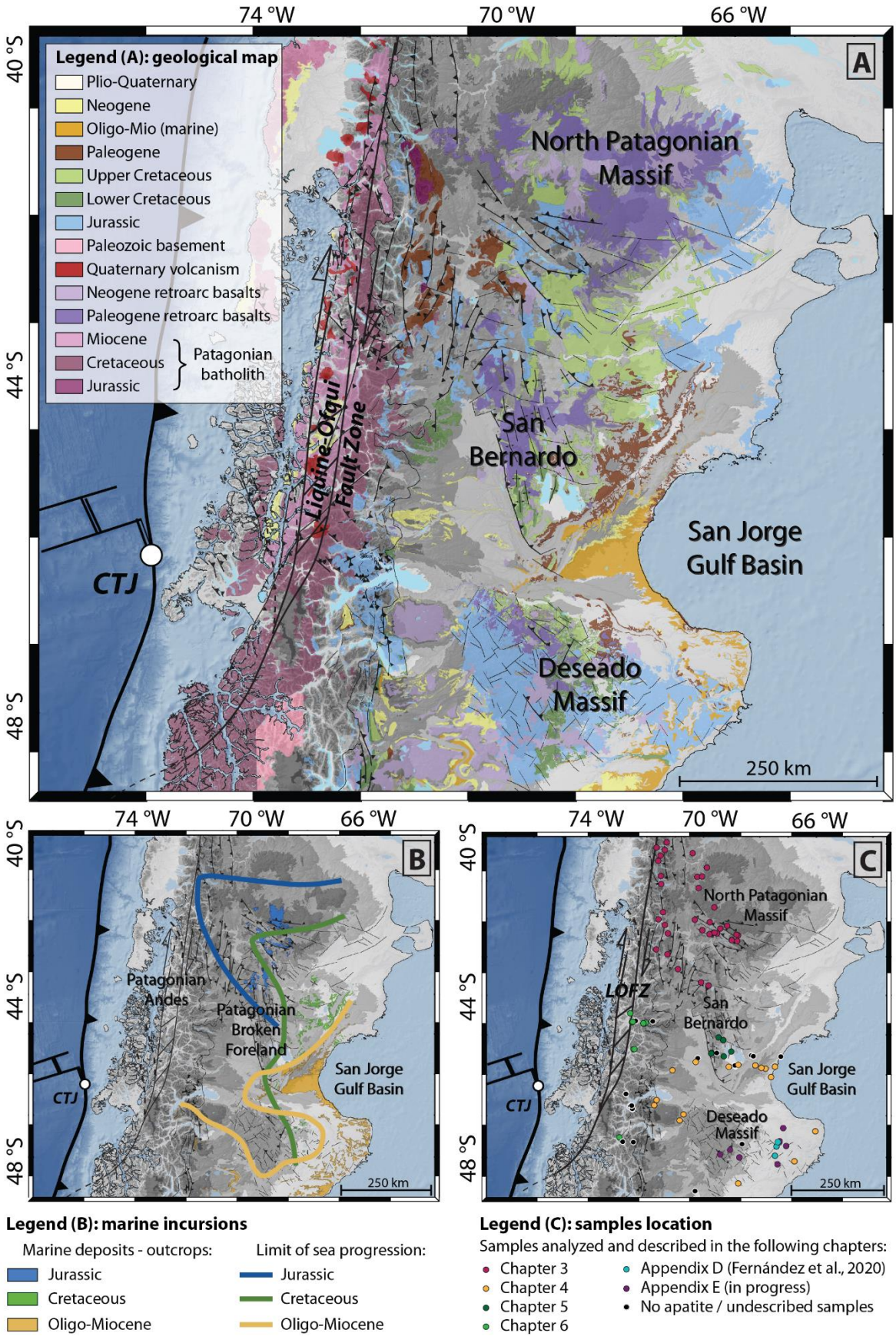

Figure 1.7 – (A) Geological map of the studied area in Patagonia between 40 and 49 °S. See section above for details about the formations. (B) Geological map of marine deposits with approximative limit of sea progression through time. (C) Map with the location of the samples analyzed in this study. The different colors used show in which chapter they are described.

bimodal volcanism (Figure 1.4; Aragón et al., 2011; Rapela et al., 1988). The Patagonian foreland is then affected by a regional relaxation from Late Eocene to Early Miocene (e.g. Echaurren et al., 2016; Horton et al., 2016) related to the intraplate magmatic events (e.g. Bruni et al., 2008) and the synextensional character of the continental formations: Sarmiento in San Jorge Basin, Ligorio Márquez along the Andes, Ventana close to the NPM (Bellosi, 2010; Orts et al., 2012). The last members of the Sarmiento Formation (San José Formation, equivalent in Chile) are laterally graded by the marine Chenque Formation, correlated with the Centinella Formation along the Andean piedmont and with the Guadal Formation in Chile. The equivalent of the Chenque Formation in the Deseado Massif is evidenced by three units: San Julián, Monte León and Patagonico Formations; Cuitiño et al., 2015b; Parras et al., 2012). Patagonia was largely flooded to the Andes from the Oligocene to the Early Miocene related to three episodes of Atlantic transgression through this period known as Juliense, Leonense and Superpatagoniense stages (Ameghino, 1906). Coevally in the north Patagonian Foreland, the development of a second retroarc belt named the El Maitén Belt, associated with the Ventana Formation, is developed to the west, compared to the Pilcaniyeu Belt. The tholeiitic affinity of the rocks from the El Maitén Belt may suggest similarity with the magmatic evolution of seafloor (Aragón et al., 2011; Rapela et al., 1988). On the other hand, the marine Chenque Formation is progressively overlain by the fluvial Santa Cruz formation (equivalent to the Galera Formation in Chile, and to Rio Frias, Rio Pinturas and Rio Zeballos along the Andean piedmont) evolving up to the Middle Miocene (Bellosi, 1998; Cuitiño et al., 2016; Suárez et al., 2000). This formation is associated with a new orogenic pulse along the Andes and a renewed contraction along the Patagonian Broken Foreland at ca. 16 Ma (Echaurren et al., 2016; Gianni et al., 2015a). Despite the evidences of synorogenic Cretaceous strata, some authors proposed that the Patagonian Broken Foreland was mainly deformed during this Miocene compression phase (e.g. Bilmes et al., 2013; Homovc et al., 1995; Peroni et al., 1995). This deformation is also recorded to the NPM by the Early and Middle Miocene Ñirihuau and Collón Curá Formations (Orts et al., 2012; J. M. Paredes et al., 2009; Ramos et al., 2011). Thus, timing and magnitude of deformation along the Patagonian Broken Foreland has been poorly constrained and few thermochronological studies, which can clarify these issues, exist along this intraplate belt (Fernández et al., 2020; Savignano et al., 2016). Along the Andean piedmont, especially in the Rio Mayo Embayment, the erosive regime related with the last Andean uplift phase supplied deposits forming the following sedimentary formations: Rio Frias, Pedregroso, Rio Mayo and Chalia Formations (Dal Molin and Franchi, 1996). In the foreland, deformation was sealed with mafic plateaus and Quaternary fluvio-glacial deposits as the Rodados Patagonicos Formation (Pliocene – Pleistocene) in the San Jorge Basin (Martínez and Kutschker, 2011).

1.5 Goals of the study

The aim of this thesis is to provide dating and magnitude of exhumation that affected the north-central Patagonia. Objectives are to identify and quantify the exhumation phases in the Patagonian Andes and the related intraplate belt at these latitudes, as well as to determine the sediment provenance history of

the foreland basin. Finally, this thesis intends to better understand the effects of geodynamic processes (changes of convergence or slab dip) on the tectonic and thermal evolution of the north-central Patagonian by providing an extensive thermochronology dataset including diverse methods to constrain main tectonic events in this area (40 to 48°S) in time and space. Sampling, analysis and data interpretation are detailed in different chapters (Figure 1.8).

This work has been done in the framework of a large project, which involves Italian, French and Argentinian researchers. The PhD thesis of Alexis Derycke (University of Paris-Saclay, France) focuses on U-Th-Sm/He thermochronology analysis on apatites and hematites from basement rocks of the Deseado Massif in order to decipher the significance of the exhumation events in this area, which is complementary with this thesis.

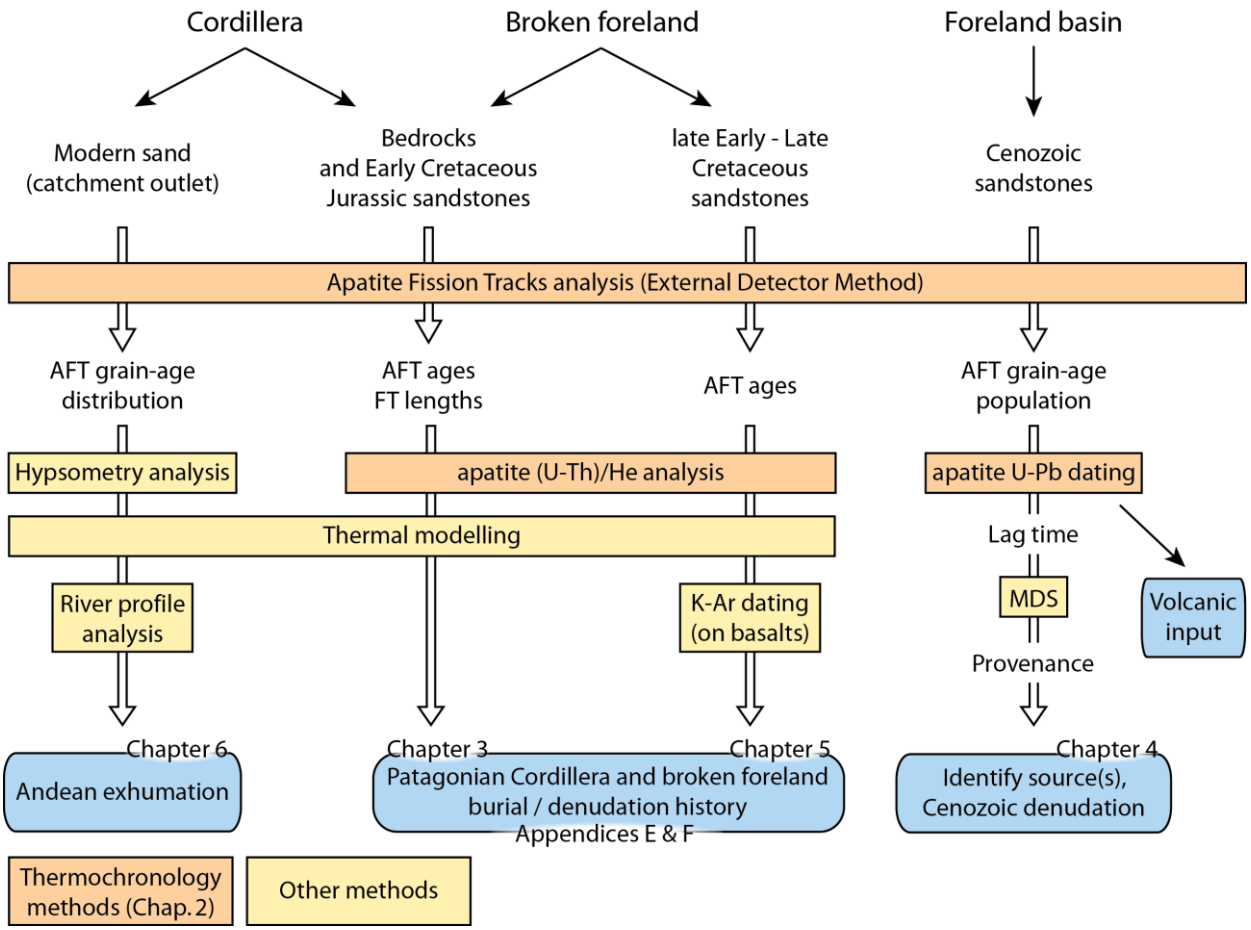

Figure 1.8 – Workflow followed in the thesis to study tectonic evolution and cooling history of the north-central Patagonia. All the thermochronology methods are described in Chapter 2 while others are explained in the following chapters.

1.6 Thesis outline

This thesis integrates one manuscript submitted for peer-review to a scientific journal, one chapter that will soon be submitted for peer-review, two chapters that will be submitted later as further analysis and/or discussions are needed, a general synthesis and three manuscripts in appendices.

Chapter 2 provides a synthesis of the background about thermochronometric methods used in this thesis (Figure 1.8).

Chapter 3 presents the application of apatite fission tracks and (U-Th-Sm)/He thermochronology between 40 and 44°S. This part of the work constitutes the achievement of the study initiated during the the PhD thesis of Elisa Savignano (Savignano, 2018). The aim was to quantify the exhumation of the Patagonian Precordillera and broken foreland at these latitudes and relate the surface unroofing with geodynamic processes.

Chapter 4 is focused on apatite U-Pb and fission-track ages extracted from detrital samples collected in the San Jorge Gulf Basin and surrounding areas (45° to 49° S) in order to better understand provenance and evolution of the source area(s) through the Cenozoic. Lag time is applied on apatite content to interpret the denudation of the source rocks.

Chapter 5 discusses the tectono-thermal history of the southern San Bernardo Fold and Thrust Belt, a complex intraplate belt for which tectonic evolution is still debated, from apatite fission tracks, (U-Th-Sm)/He ages and thermal modeling. Interestingly, this short chapter allows to explore the impact of moderate exhumation and volcanic activity on the low-temperature thermochronometer.

Chapter 6 is related to the central Patagonian Cordillera evolution based on detrital apatite fission track data obtained from modern outlet sample and inverse modeling following a recent method. This latter method allows to unravel the exhumation pattern along the central Patagonian Cordillera through a novel detrital thermochronology approach.

In Chapter 7 are summarized the main conclusions of the thesis from chapters 3 to 6. All the results are then discussed in a larger-scale context and perspectives are proposed.

In the appendices A, B, C and D are included supplementary materials for chapters 3, 4, 5 and 6.In other appendices, some works done during the thesis and not presented in the above mentioned chapters have been gathered in three manuscripts within the framework of other studies as they are relevant for the conclusions presented in the chapter 7: i) appendix E corresponds to a manuscript published in *Tectonophysics* (2020) as co-author and dealing with the structural analysis of La Paloma area (Deseado Massif, central Patagonia) associated with thermochronology analysis; ii) appendix F to a manuscript about the thermal history of the Deseado Massif, in preparation for *Journal of South American Earth Sciences* as co-author; and iii) appendix G to a paper published in *Tectonophysics* (2020) as first author about my Master thesis which focused on the tectonic evolution of the north-central Peruvian forearc through seismic analysis.

CHAPTER 2

MATERIALS AND METHODS

2.1 Sampling

The studied areas are located (i) in the Argentinian north Patagonia (between 40 and 44 °S), (ii) in the Argentinian central Patagonia (from 45 to 49 °S) and (iii) in the Chilean north-central Patagonia (from 44 to 48 °S). Fifty-nine samples have been collected and analyzed during this thesis (Figure 1.7C; the samples processed but without apatites have been excluded by the counting). Twenty-four samples from north Patagonia have been collected formerly for the thesis of E. Savignano (2018), mainly granitoids with some Paleozoic-Mesozoic sedimentary samples. She already analyzed these samples in the context of her PhD with the (U-Th-Sm)/He dating method described below. The same samples were thus analyzed in this study with the apatite fission tracks method. Samples from the Argentinian central Patagonia include a variety of sedimentary rocks spanning from Early Cretaceous to Pliocene. Thus, thirty samples have been collected for detrital thermochronology and three basalts for K-Ar analysis. In Chile, twenty-seven samples have been collected: two granites for apatite fission tracks dating, one from Pleistocene terrace for provenance analysis, six from sedimentary formations equivalent to the ones collected in Argentina., four from modern river sand for cosmogenic nuclides analysis, and thirteen from modern river sand for detrital thermochronology. Apatite fission tracks analysis of six basement samples collected in the central Patagonia (Deseado Massif) are still in progress. They are carried out within the framework of cooperation between the University of Padua and the University of Paris-Saclay where A. Derycke is doing his PhD about the tectonic evolution of the Deseado Massif by (U-Th-Sm)/He thermochronological studies on basement and iron oxydes. He analyzed some of our samples with the (U-Th-Sm)/He dating method on apatites. Samples information are presented in Table 2.1.

2.2 Apatites

Apatite, Ca5(PO4)3(OH, F, Cl), is amongst the most abundant phosphate minerals and is a common accessory phase in felsic through mafic igneous, all-grade metamorphic rocks and clastic sediments derived from them (Piccoli and Candela, 2002; Spear and Pyle, 2002). Apatite is often highly persistent during diagenesis and metamorphism while it is unstable during intense weathering. Apatite is more likely to be preserved after burial beyond the meteoric water sources (Morton and Hallsworth, 1999). Compared to chemically resistant minerals (zircon, rutile, tourmaline), apatite represents rather first-cycle detritus event if some refractory grains can resist through time (O'Sullivan et al., 2018). Furthermore, it has been demonstrated that abrasion and burial have almost no importance in the reduction of the diversity of heavy

mineral species in fluvial settings as they are reasonably physically resilient (e.g. Garzanti, 2017; Morton and Hallsworth, 2007; Morton and Smale, 1990). Therefore, the presence or absence of apatite in any given sediment can be mainly attributed to either the source fertility (abundance of apatite is very low in phosphorous-poor source rocks) or dissolution by acidic meteoric waters or prolonged alluvial storage.

Apatite is often used as geochronological or thermochronological tool owing to its ability to substitute Ca and halogens with rare earth elements as the actinides U and Th (Ayers and Watson, 1993; Nagasawa, 1970). Also, the incorporation of U into the apatite lattice enables the routine dating of individual apatite grains by the fission track, the (U-Th-Sm)/He and the U-Pb methods (Chew et al., 2011; Green et al., 1989; Wolf et al., 1996; see following sections). Furthermore, apatite has strong potential as provenance tool in basin analysis for paleotectonic reconstructions as different proxies can be employed combining the three mentioned methods (e.g. Carrapa et al., 2009; Zattin et al., 2012). Finally, differences in the abundance of the wide spectrum of incorporated elements can be used as a geological tracer recording both the age and the lithology of its source rock protolith (e.g. O'Sullivan et al., 2018).

2.3 Low-temperature thermochronometry

Low-T thermochronology measures the timing and rates at which rocks cool and approach the surface as a result of exhumation (e.g. Reiners and Brandon, 2006; Ring et al., 1999). It can be (in certain circumstances) related to the surface uplift (described as the vertical motion of a rock; England and Molnar, 1990) induced by tectonic and/or surficial processes as the erosion patterns (Figure 2.1A). It is important to notice that exhumation is defined as the movement of a rock with respect to the Earth's surface and occurs always by denudation, corresponding to the removal of rock by tectonism and/or erosion (Reiners and Brandon, 2006). The interaction and variations in space and time between these movements and the crustal thermal field result in specific thermal history studied by thermochronometry analysis (Figure 2.1B).

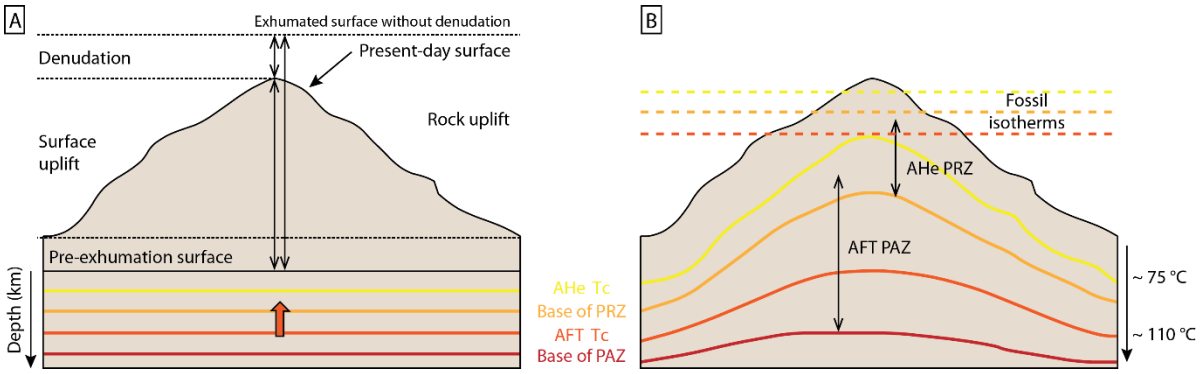

Figure 2.1 – Schematic representation of the denudation (blue arrow) and uplift (red arrow) concepts (A), of the PAZ/PRZ and Tc concepts with colored lines indicating present and past (dashed lines) isotherms (B) (modified from Vernon, 2008; Andreucci, 2013).

The thermochronometry methods are based on the radioactive decay of nuclides into a crystal and the accumulation of their products which correspond either to daughter nuclides or lattice damages. The

products are used to date the cooling age of a mineral directly related to their specific thermal sensitivity (Figure 2.2), represented by closure temperatures (Tc), of each radioactive system (thermochronometer) to switch from a closed to an open system (Dodson, 1973). Low-T thermochronology is concerning the thermochronometers with the lowest closure temperatures (generally comprised between ca. 30 °C and 550 °C) as the apatite fission track (AFT) and the apatite (U-Th-Sm)/He (AHe) described below. The closure temperature of a thermochronometer occurs through a range of temperatures where the retention of decay products progressively increases and register consequently the time-temperature history of the sample. This temperature window is called the Partial Annealing Zone (PAZ) for AFT system and the Partial Retention Zone (PRZ) for AHe system (Wagner, 1979). Thus, the thermochronometric age has a true temporal meaning in case of monotonic cooling, when the age corresponds to the cooling through the closure temperature. Thus, integrating different thermochronometers on various minerals or single grains (referred to as double- or triple-dating) allow better constraints to infer thermal histories of host rocks. This is particularly useful to detail complex histories affected by burial and reset. The latter term being a concept used to refer to rocks, after having been hold for a certain time at low temperature, buried sufficiently to reach temperature high enough to re-open a system. Therefore, the former products are partially or totally reset. In case of total reset, the thermal history record corresponds to the final cooling to the surface.

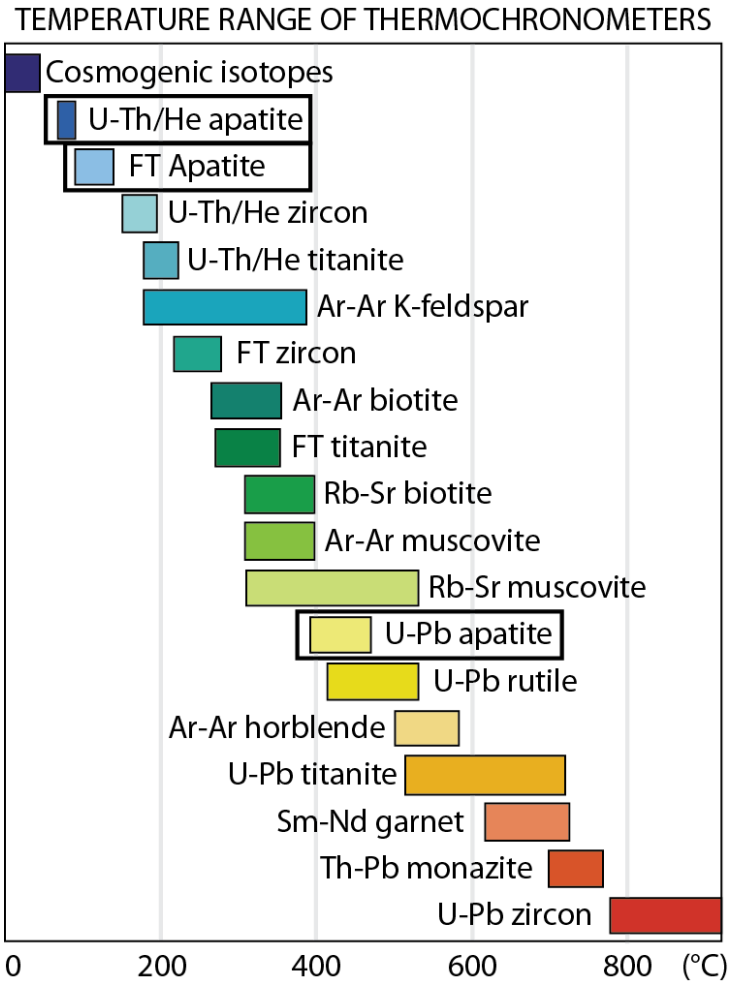

Figure 2.2 – Nominal closure temperatures of various geochronometers and thermochronometers. Systems are ordered by closure temperature on the Y-axis (Kronenberg et al., 2002). Black polygons show the thermochronometers used in this study.

TABLE 2.1. SAMPLE INFORMATION.

	Sample	Lat.	Long.	Elev. (m)	Formation	Lithology	Stratigraphic age	AFT	MTL	AHe	U-Pb	K-Ar
Samples collected in north Patagonia, Argentina (Savignano, 2016) AFT and AHe analysis already done, used for inverse modeling	G01	-42.1928	-69.1656	1134	Lipetren	granite	Triassic	x		x		
	G02	-42.2658	-69.4086	929	Mamil Choique	granite	Permian	x	x	x		
	G04	-42.3878	-69.5219	997	Mamil Choique	granite	Permian	x	x	x		
	G05	-42.3694	-69.6292	963	Cañadon Asfalto	conglomerate	Upper Jurassic	x		x		
	G06	-42.4444	-68.7803	1150	Cañadon Asfalto	arkose	Upper Jurassic	x		x		
	G07	-42.5597	-69.0039	1070	Mamil Choique	granite	Lower Permian	x	x	x		
	G08	-42.5639	-69.0042	1043	Mamil Choique	granite	Lower Permian	x	x	x		
	G09	-42.4131	-69.7822	995	Cañadon Asfalto	arkose	Upper Jurassic	x	x	x		
	G10	-42.0953	69.7749	1060	Mamil Choique	granite	Lower Permian			x		
	G11	-42.3114	-70.0367	999	Mamil Choique	dyke (granite)	Lower Permian			x		
	G12	-42.0353	-70.2992	976	Mamil Choique	granite	Lower Permian	x		x		
	G13	-42.3736	-69.6039	973	Cañadon Asfalto	sandstone	Upper Jurassic	x	x	x		
	G14	-42.4253	-68.8347	1177	Cañadon Asfalto	sandstone	Upper Jurassic	x		x		
	G15	-42.5861	-68.8128	1103	Mamil Choique	granite	Lower Permian	x		x		
	G17	-41.7119	-69.6192	1275	Mamil Choique	granite	Lower Permian	x	x	x		
	G18	-42.9306	-71.2606	617	Subcordilleran Plutonic Belt	granite	Lower Jurassic			x		
	G19	-42.8064	-71.6608	576	Pat. Batholith	granite	Upper Cretaceous			x		
	G20	-42.3847	-71.2453	663	Leleque	granite	Upper Jurassic			x		
	G21	-42.1672	-71.3572	616	Subcordilleran Plutonic Belt	granodiorite	Lower Jurassic	x		x		
	G22	-42.0303	-71.5761	275	Pat. Batholith	granite	Upper Cretaceous	x		x		
Samples collected in north Patagonia, Argentina (Savignano, 2016) AHe analysis already done	G24	-47.6439	-67.3292	141	La Leona	granite	Lower Jurassic	x	x	x		
	G25	-47.6183	-67.3464	140	La Leona	granite	Lower Jurassic	x	x	x		
	G26	-47.7358	-67.4267	176	La Leona	granite	Lower Jurassic	x		x		
	G28	-47.9556	-67.4794	116	Bajo Pobre	andesite	Mid. - Up. Jurassic	x		x		
	G30	-43.7439	-69.8186	670	Osta Arena	sandstone	Lower Jurassic	x	x	x		
	G31	-43.6650	-70.0839	825	Tepuel Group	sandstone	Carb.-Permian	x		x		
	G35	-43.3244	-70.8961	875	Rio Hielo	granitoid	Cretaceous	x	x	x		
	G37	-43.5250	-71.5181	473	Rio Hielo	granitoid	Cretaceous	x		x		
	G38	-41.8508	-71.4219	627	Colohuincul Cp	granodiorite	Lower Permian	x		x		
	G39	-41.5564	-71.4806	731	Pat. Batholith	granite	Cretaceous	x		x		
	G40	-40.3447	-71.5064	898	Colohuincul Cp	granodiorite	Lower Permian	x	x	x		
	G41	-41.1061	-71.4831	849	Pat. Batholith	granite	Cretaceous	x		x		
	G44	-41.2089	-70.1667	999	Pilcaniyeu plut.	granite	Lower Jurassic	x	x	x		
	G45	-40.9181	-70.2247	810	Mamil Choique	granodiorite	Ordovician	x				
	G46	-40.9017	-70.0461	1189	Mamil Choique	granodiorite	Ordovician	x				
	G47	-40.6692	-69.8833	1298	Mamil Choique	granodiorite	Ordovician	x	x			
	G48	-40.8936	-71.4950	805	Los Machis	granodiorite/tonalite	Upper Jurassic to Cretaceous	x		x		
	G49	-40.4853	-71.5894	903	Los Machis	granodiorite/tonalite	Upper Jurassic to Cretaceous	x		x		
	G50A	-40.1956	-71.3614	976	Colohuincul Cp	granodiorite	Devonian to Carb.	x		x		

	G51	-40.1289	-71.6456	791	Los Machis	tonalite	Upper Jurassic to Cretaceous	x		x		
	G53	-40.3683	-70.6619	645	Cushamen	granite	Devonian to Carb.	x	x			
	G54	-40.2822	-70.3803	986	Mamil Choique	granodiorite	Devonian to Carb.	x	x			
	G55	-41.3158	-65.6497	249	Mina Gonz. Cp ?	granite	Cambrian-Ordov.	x	x			
Samples collected in central Patagonia, Argentina (Genge, 2018)	MG1	-68.8806	-45.7784	395	Sarmiento	medium sandstone	Eocene	x				
	MG2	-68.8833	-45.7769	376	Rio Chico	conglomerates	upper Paleocene		No apatite			
	MG3	-68.7684	-45.7491	398	Sarmiento	sandstone	Eocene	x				
	MG4	-67.8128	-45.8422	367	Chenque	sandstone	Oligo-Miocene	x			x	
	MG5	-67.9561	-45.8297	610	Chenque	sandstone	Oligo-Miocene	x				
	MG6	-68.1723	-45.7721	613	Chenque	sandstone	Oligo-Miocene	x				
	MG7	-69.2818	-45.5345	283	Chubut Group	sandstone	Up. Cretaceous	x		x		
	MG8	-69.5332	-45.4704	635	Chubut Group	sandstone	Up. Cretaceous		No apatite			
	MG9	-69.7016	-45.4590	557	Chubut Group	sandstone	Low. Cretaceous	x		x		
	MG10	-70.1987	-45.5971	529	Rio Mayo	sandstone	up. Miocene -Pliocene		No apatite			
	MG11	-70.2658	-45.6747	484	Rio Mayo	sandstone	up. Miocene -Pliocene	x				
	MG12	-71.0792	-45.8858	733	Rio Mayo	sandstone	up. Miocene -Pliocene	x			x	
	MG13	-71.6418	-46.6084	325	Santa Cruz	sandstone	mid-Up. Miocene	x				
	MG14	-71.7229	-46.7390	709	Santa Cruz	sandstone	mid-Up. Miocene	x				
	MG15	-70.6897	-46.9614	693	Santa Cruz	sandstone	mid-Up. Miocene	x				
	MG16	-70.8325	-47.1046	700	Santa Cruz	fine sandstone	mid-Up. Miocene	x				
	MG17	-69.0178	-45.4174	373	Chubut Group	fine sandstone	Low. Cretaceous	x		x		
	MG18	-69.4250	-45.0682	739		basalt			Not good			
	MG19	-69.4609	-45.0694	643		basalt						x
	MG20	-69.3007	-45.1388	568	Chubut Group	medium sandstone	Low. Cretaceous	x		x	x	
	MG21	-69.7130	-45.4616	582		basalt						x
	MG22	-69.1036	-45.7973	300	Chubut Group	sandstone	Up. Cretaceous		No apatite			
	MG23	-69.0681	-45.8066	371	Chubut ?	fine sandstone	?		No apatite			
	MG24	-69.0668	-45.8004	376	Chubut ?	fine sandstone	?		No apatite			
Samples collected in central Patagonia, Chile (Genge, 2019)	MG25	-72.0815	-44.7204	290		sdt in modern river			No apatite			
	MG26	-72.1103	-44.7273	259		sdt in modern river			No apatite			
	MG27	-72.5112	-44.6843	45		sdt in modern river		x				
	MG28	-72.4870	-44.6772	35		sdt in modern river		x				
	MG29	-72.5742	-44.4614	23		sdt in modern river		x				
	MG30	-72.4426	-44.6369	357		dyke			No apatite			
	MG31	-72.3889	-44.6504	126		granite			No apatite			
	MG32	-72.0238	-44.6928			sdt in modern river		x				
	MG33	-71.8019	-44.6601		sandstone	fluvial terrace	Pleistocene	x				
	MG34	-72.1167	-44.7161	284		sdt in modern river		x				
	MG35	-72.4616	-45.3520	48		sdt in modern river		x				
	MG36	-72.4616	-45.3520			sdt in modern river		x				
	MG37	-72.7222	-46.4579	278		sdt in modern river			No apatite			
	MG38	-72.4698	-47.6203	577		sdt in modern river		x				
	MG39	-72.8401	-47.5981	53		sdt in modern river		x				
	MG40	-72.9532	-47.4986	80		sdt in modern river		x				
	MG41	-72.5718	-46.7829	507	Santa Cruz	sandstone	Miocene		No apatite			

	MG42	-72.5547	-46.7533	347	Guadal	sandstone	Oligo-Miocene		No apatite	
	MG43	-72.5064	-46.7985	593	San José	conglomerates	Eocene		No apatite	
	MG44	-72.4866	-46.8329	705	Santa Cruz	coarse-g. sandstone	Miocene		No apatite	
	MG45	-72.4951	-46.8204	631	Guadal	sandstone	Oligo-Miocene	x		
	MG46	-72.5135	-46.7408	342		sandstone	Pleistocene	x		
Samples collected in central Patagonia, Argentina (Genge, 2019)	MG47	-66.0674	-47.3632	108	Chenque	fine-g. sandstone	Oligo-Miocene	x		
	MG48	-67.7289	-49.1592	181	Chenque	fine-g. sandstone	Oligo-Miocene	x		
	MG49	-66.7981	-48.0737	116	Chenque	sandstone	Oligo-Miocene	x		x
	MG50	-68.7724	-48.5885	189	Chenque	sandstone	Oligo-Miocene	x		
	MG51	-70.2911	-48.7711	325	Santa Cruz / Chenque	sandstone	Miocene		No apatite	
	MG52	-69.0604	-47.7991	650	Bajo Grande	sandstone	Lower Cretaceous	x	x	
	MG53	-68.6408	-47.6750		Baquero (Chubut)	paleosoil	Cretaceous		No apatite	
	MG54	-67.6208	-46.0467	0	Chenque	sandstone	Oligo-Miocene	x		x
	MG55	-67.4823	-45.7994	36	Sarmiento	fine-g. sandstone	Eocene	x		
	MG57	-67.4825	-45.5919	15	Rio Chico	sandstone	Lower Eocene		No apatite	
	MG58	-68.2989	-45.5243	424	Rio Chico	sandstone	Upper Paleocene		No apatite	
	MG59	-68.2501	-45.5442	305	Salamanca	fine-g. sandstone	Lower Paleocene		No apatite	
Samples DES# - (Derycke, 2019) - AHe analysis done	#01	-67.3447	-47.6188	114	La Leona	granite	Triassic	x	x	
	#02	-67.0877	-47.7106	138	Rio Deseado Cp.	granitoide	Ordovicien	x	x	
	#05	-67.1791	-47.2927	68	Rio Deseado Cp.	granitoide	Paléozoique		x	
	#11	-67.3875	-48.1371	106	La Leona	granitoide	Paléozoique	x	x	
	#15	-68.7195	-47.9741	431	Bahia Laura	granitoïde	Lower Jurassic	x	x	
	#29	-69.3843	-47.9161	757	Bahia Laura	ignimbrite	Jurassic	x	x	

2.3.1 Apatite fission tracks thermochronometry

Fission track thermochronometry is based on the natural decay of ^{238}U into the crystal (e.g. Fleischer and Price, 1964; Hurford and Green, 1982; Price and Walker, 1963; Wagner, 1968) as the relative abundance of other radioactive isotopes is low (e.g. ^{234}U has a relative abundance of $5{,}44.10^{-5}$ % with respect to ^{238}U). Heavy and light fission fragments are expulsed in opposite directions by a combination of energy released by the spontaneous fission of ^{238}U and coulomb repulsion forces. These fragments provoke widespread dislocation of atoms in the surrounding crystal lattice induced by changes of electrostatic charge and ionization (Figure 2.3; Silk and Barnes, 1959). The fission track is indeed the linear damage zone (of ca. 16 µm length in apatite) formed by the displacement of atoms during the passage of the daughter nuclides through the lattice (Reiners and Brandon, 2006 and references therein). The AFT method rests on the quantification of the density of these tracks, whose accumulation is described by the decay equation. The decay equation has been modified with a much higher decay constant to include the effects of both spontaneous and α decay on the ^{238}U decay (equation (1), Tagami and O'Sullivan, 2005).

(1) $$N_s = \frac{\lambda_f}{\lambda_a} {}^{238}N(e^{\lambda_\alpha t} - 1)$$

N_s is the number of spontaneous fission tracks per unit volume; ^{238}N is the number of ^{238}U atoms per unit volume; λ_f and λ_α are the decay constants for spontaneous fission and α decay of ^{238}U ($\lambda_f = 8.5\ 10^{-17}$ yr^{-1} and $\lambda_\alpha = 1.5\ 10^{-10}$ yr^{-1}).

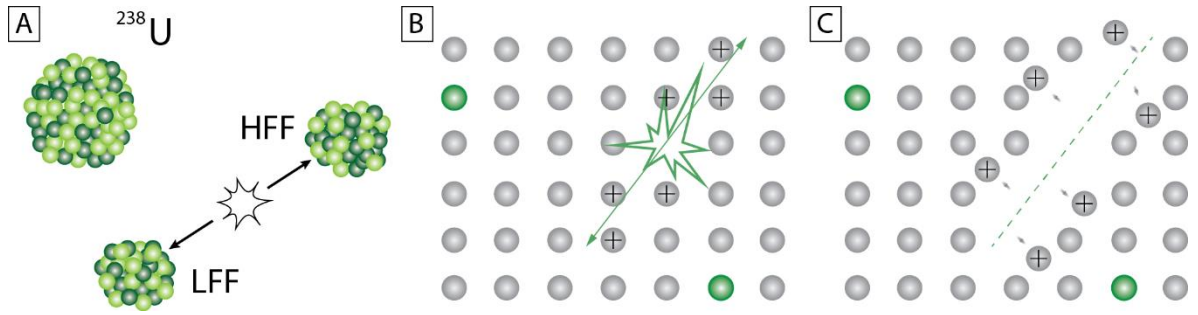

Figure 2.3 – The "Ion Explosion Spike" model for AFT formation (from Fleischer et al., 1975). The uranium nucleus splits in two nuclear fragments (A) (HFF and LFF are Heavy and Light Fission Fragments) pushed away from each other (B); along their track they tear off electrons from the atoms of the lattice and the positively charged atoms along the track dislocate from their lattice position due to repulsive electrostatic forces (C).

To infer single crystal age, parent and daughter products are measured indirectly by counting fission tracks with the External Detector Method (EDM) represented on Figure 2.5 (Gleadow, 1981; Hurford, 1990; Hurford and Green, 1983, 1982), and calculated following the equation (2):

(2) $$t_i = \frac{1}{\lambda_d} \ln\left(1 + \lambda_d \zeta\, g\, \rho_d \frac{\rho_{s,i}}{\rho_{i,i}}\right)$$

i refers to grain i; t_i is fission track age of grain i; λ_d is the total decay constant of ^{238}U; ζ is the zeta-calibration factor based on EDM of fission track age standards (usually calculated for IUGS age standards as Durango and Fish Canyon apatites; Hurford, 1990), depending on the microscope, the reactor and the operator; g is the geometry factor for spontaneous fission track registration, ρ_d the induced fission track density for a uranium standard corresponding to the sample position during neutron irradiation, $\rho_{s,i}$ is the spontaneous fission track density for grain i; $\rho_{i,i}$ is the induced fission track density for the grain i (Donelick et al., 2005).

The EDM comes to dominate the practice of AFT analysis over the variety of experimental methods developed as the EDM method provides information on individual grains, the first of any geochronological technique doing it routinely (Gleadow et al., 2019). Etching procedures of the grains are generally common or quite similar for each laboratory. The apatite grains for each sample are first mounted with epoxy resin

(previously separated by heavy liquids and magnetic separation techniques), then polished and chemically etched (20 seconds in 5.5M HNO3 at 20 °C) to reveal spontaneous fission tracks (Figure 2.5). Low-Uranium mica sheets are placed over the mount as external detector and then irradiated with low-energy thermal neutrons in a nuclear reactor. Neutron irradiation induces fission of ^{235}U and produces fission tracks in both apatites and mica sheet. Induced fission tracks can be measured on the mica surface after chemical etching (40 minutes in 40% HF at 20 °C) and not in the apatites mounted since the chemical etching of the minerals is done before the neutron irradiation (Figure 2.5). As ratio of ^{238}U / ^{235}U is constant, their content is then calculated from the density of spontaneous and induced fission tracks respectively counted on the mounted apatites and the mica monitor assembled in the same slide (Reiners and Brandon, 2006). Samples are analyzed by the operator with an optical microscope implemented with a sliding table and a dedicated software. The AFT age of a single apatite grain determined using the EDM method is given by the equation (2) and obtained through the software Trackey (Dunkl, 2002). To describe the age of an AFT age population, track densities are usually measured on 20 to 40 grains and visualized on radial plots. Age for a single population is therefore reported by the central age statistical parameter (Galbraith, 1988).

Fission tracks annealing is a process dependent of the temperature following the Arrhenius law, of the crystallographic orientation (higher annealing for tracks orthogonal to the C-axis), of the mineral composition and of the characteristics of the crystal (Barbarand et al., 2003; Carlson et al., 1999; Donelick et al., 1999; Green, 1985; Ketcham et al., 2007, 1999). Fission tracks annealing models have thus been developed using a completely empirical approach, looking at what form of the annealing relationship best fit the data statistically (Braun et al., 2006). The Dpar, i.e. the diameter of fission-track etched pits parallel to the apatite crystal C-axis, is a commonly proxy for track retentivity of single crystals (Ketcham et al., 1999). One way to quantify the effects of annealing is to measure the lengths of horizontal confined tracks (Figure 2.4; Gleadow et al., 1986) knowing that initial length of a fission track is ~ 16 µm in apatite (Carlson et al., 1999).

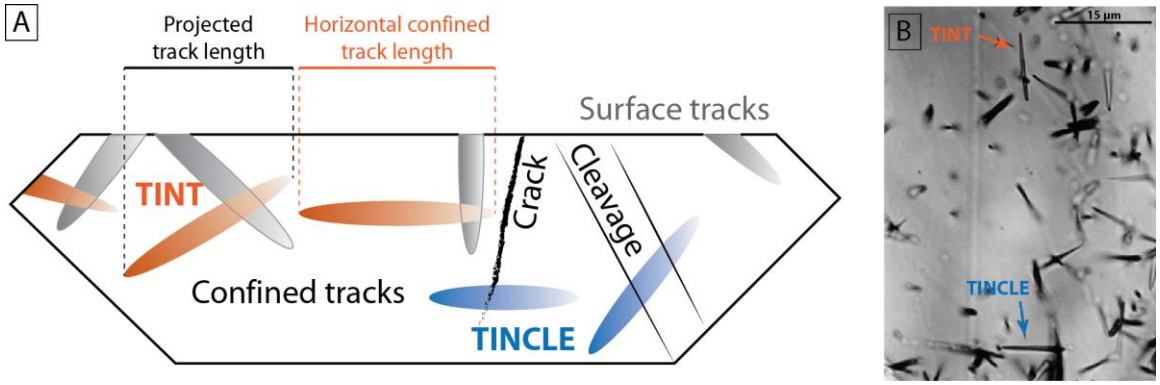

Figure 2.4 – (A) Schematic diagram of confined tracks in apatite. TINCLE is a confined track which intersects a crack or a cleavage. TINT is a confined track which intersects a surface track. Measurements of track lengths are done only on horizontal confined track length as the projected track length do not reflect the true length (from Hurford, 2019). (B) Photomicrograph of an apatite showing near horizontal confined tracks amongst surface track (TINT) and frack/cleavage (TINCLE) (picture from Kohn et al., 2019).

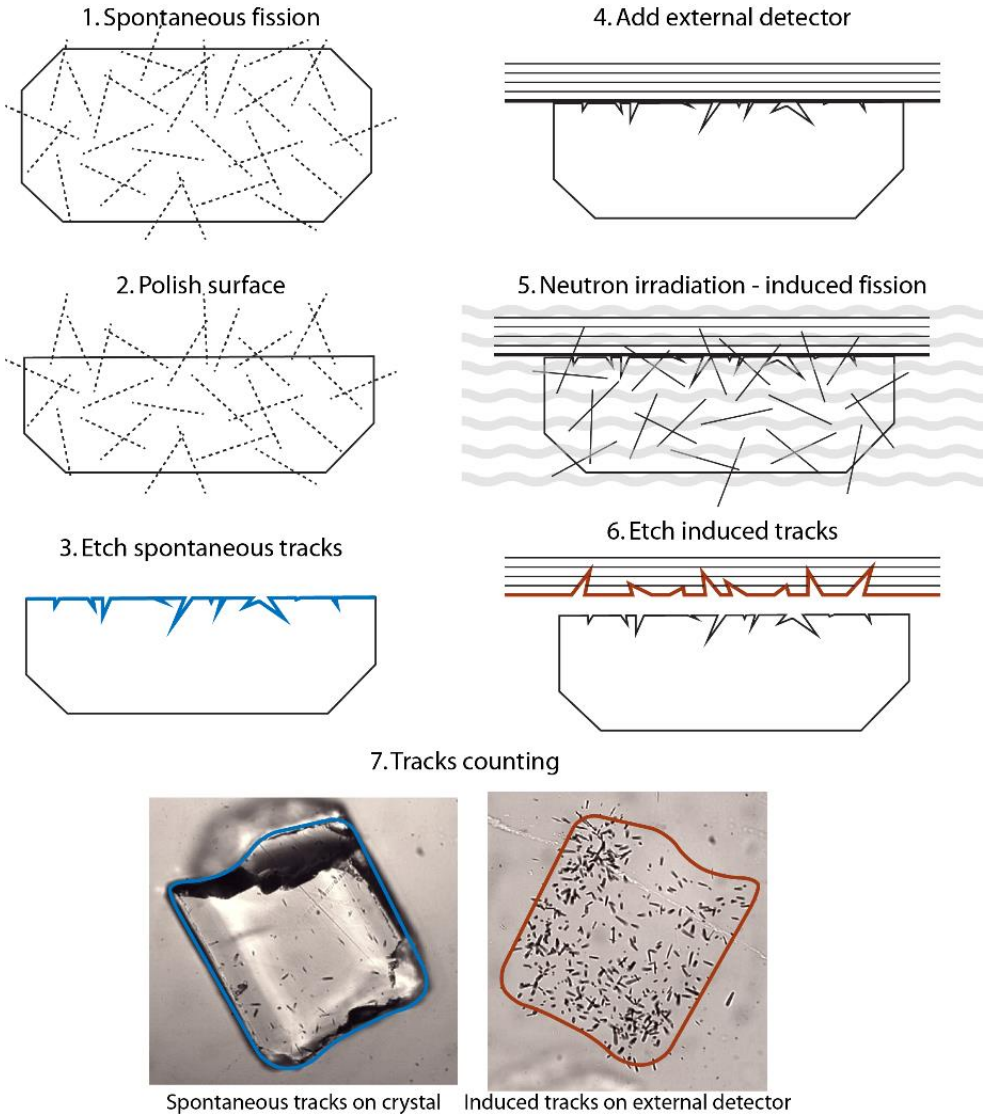

Figure 2.5 – Schematic procedure for AFT analysis with the EDM method (Tagami and O'Sullivan, 2005).

Their distribution, obtained by measuring a sufficient number of horizontal tracks (40 to 100), contains information on the thermal history experienced by the sample (Braun et al., 2006). The PAZ values depend on cooling rates and apatite chemistry and are generally comprised between 30 and 130 °C (Reiners and Brandon, 2006). Closure temperature vary between 80 and 120 °C but an apatite of average composition has a bulk closure temperature of ~ 116 °C (Fitzgerald and Gleadow, 1990; Ketcham et al., 2007, 1999). Tracks formed at higher temperatures than PAZ will anneal rapidly and not be preserved over geologic time while they will be close to their original length if crystals experience a rapid cooling (Figure 2.6). On the contrary, if samples reside in the PAZ for a significant time, fission tracks will shorten because the annealing processes produces an apparent AFT age younger than the real age (Wagner and Reimer, 1972). Sample can reside in PAZ during a long-term cooling or after burial. In the latter case, older tracks will be shorter than new tracks formed and it results in a bimodal distribution of track lengths. If burial is sufficient enough to reach temperatures higher than the PAZ, the fission tracks are reset and completely annealed (Figure 2.6).

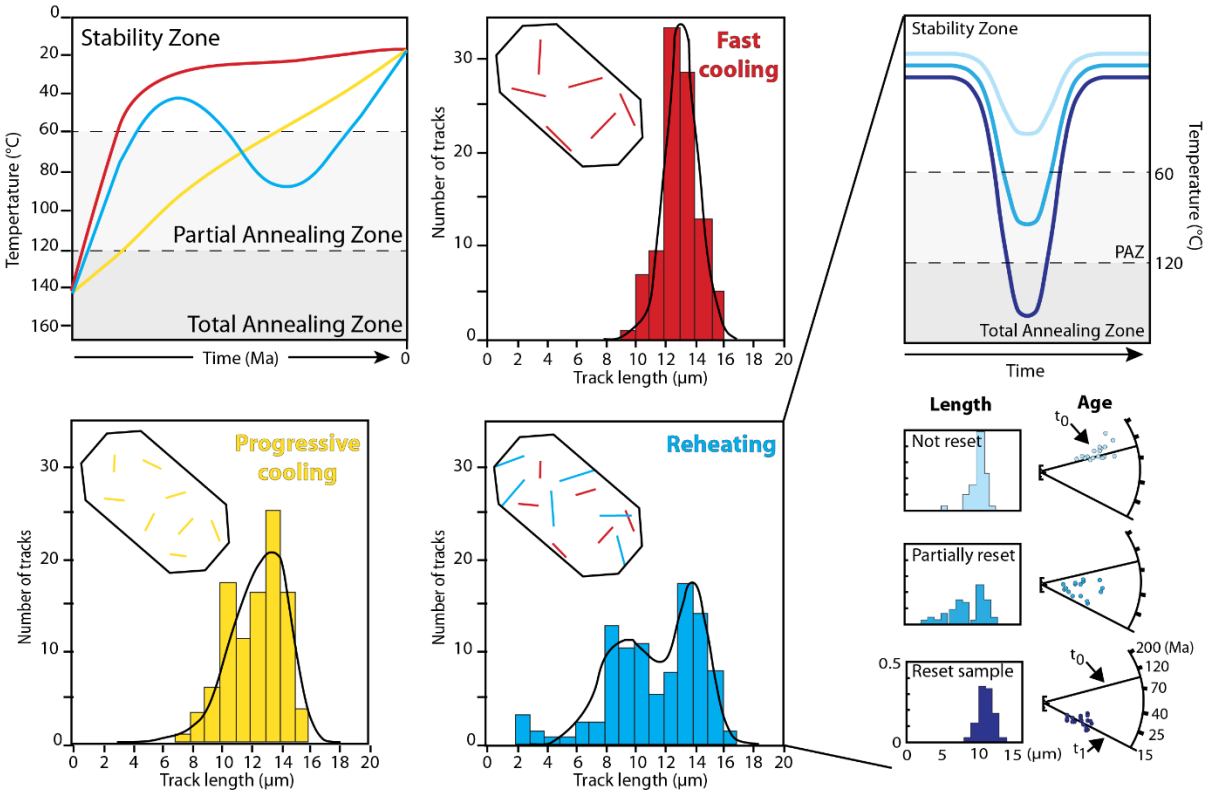

Figure 2.6 – Relationships between track length distribution and thermal history in case of fast cooling (red), progressive cooling (yellow) or different cases of reheating (blues) (modified after Dumitru, 1989; Tagami, 2005).

2.3.2 Apatite (U-Th-Sm)/He thermochronometry

(U-Th-Sm)/He thermochronometry is one of the most sensitive thermochronometer with a closure temperature of 75 ± 15 °C (Farley, 2000; Wolf et al., 1996). It is based on the production of He nuclei (corresponding to α particles) during the decay of Uranium, Thorium and Samarium. The decay equation is noting as following:

$$(3) \quad {}^{4}He = 8^{238}U(e^{\lambda_{238}t} - 1) + 7^{235}U(e^{\lambda_{235}t} - 1) + {}^{232}Th(e^{\lambda_{232}t} - 1) + {}^{147}Sm(e^{\lambda_{147}t} - 1)$$

where ^{4}He, ^{238}U, ^{235}U and ^{232}Th and ^{147}Sm are the present-day atoms, λ are their relevant decay constants and t is the accumulation time or Helium age (Farley and Stockli, 2002; Reiners et al., 2002). The coefficients preceding the Uranium and Thorium abundances account for the α multiple particles emitted within each decay series (Farley and Stockli, 2002). The ingrowth of helium with time can be written as a function of the concentration in U, Th and He as the ^{238}U / ^{235}U ratio has a constant value in the solar system (Steiger and Jäger, 1977). The He ingrowth equation assumes absence of ^{4}He, both initial and produced by sources extraneous to the crystal, and secular equilibrium among all daughters in the decay chain. These assumptions are valid for apatites without U-Th inclusions (e.g. zircons) or coating (e.g. oxides) as these latter mineral phases behaved as external sources of He and induced a bias in the results. Careful selection

of the grains (prismatic, inclusion free, intact, > 60 µm) is consequently required prior to analyze (Murray et al., 2014). Three to five grains from each sample are selected and packed in Nb tubes. A two-stage analytical procedure is commonly used to measure the concentration of ^{4}He, U, Th and Sm. In the first stage the crystal is degassed by twice heating using a diode laser to release totally the He contained (Fillon et al., 2013), then measured by gas-source mass spectrometry (during this study at the University of Paris-Saclay, IDES low-temperature thermochonology Laboratory, Orsay, France). In the second stage, after chemical dissolution of apatites in HNO3 5N (3 hours at 70 °C), U, Th and Sm concentrations are measured by quadrupole inductively coupled plasma mass spectrometry (in LSCE, University of Versailles, Gif-sur-Yvette, France, or Element XR from Thermo Scientific, Orsay, France). External age standards, in our case Limberg Tuff and/or Durango apatites, are used to calibrate the age.

When the AHe age is calculated, several factors must be considered: (i) the α-ejection, (ii) the diffusion behavior, (iii) the presence of zonation and (iv) the possible presence of U-rich inclusions. Data are consequently processed to test their significance and their meaning. The α-ejection takes into account the distance travelled by the α particles of ca. 20 µm during the decay process. The loss of α particles ejected out of the crystal leads to an underestimation of the age (Farley et al., 1996). The α-ejection correction factor is calculated as a function of the crystal size, assuming an idealized geometry of the crystal and homogeneous distribution of U and Th in apatites (Farley and Stockli, 2002). The diffusional behavior of He into the crystal impacts the temperature interval called Partial Retention Zone (PRZ), usually ranging between 20 – 60 °C (Ault et al., 2019; Reiners and Brandon, 2006), whereas the closure temperatures vary in the range 40 – 80 °C (Farley, 2000; Wolf et al., 1996). In order to constrain thermal histories, knowledges about the He diffusivity in the crystal are required, based on the relationships between the diffusivity and Arrhenius law:

$$\frac{D}{a^2} = \frac{D_0}{a^2} e^{\frac{-E_a}{RT}} \quad (4)$$

where D_0 is the frequency factor, that is diffusion at infinite temperature, E_a is the activation energy, T is the temperature, R is the gas law constant and a is the radius of the spherical diffusion domain corresponding, in most cases, to the grain volume (Farley, 2000; Reiners and Brandon, 2006). The diffusion parameter is obtained through step heating experiments and is used to estimate the PRZ and the closure temperature for He thermochronometers of analyzed grains for given cooling rates and size of grains (Reiners and Brandon, 2006). Several new diffusional models for He have been proposed, always based on the same equation, but accounting other complication as the radiation damages effect on He diffusivity (e.g. Flowers et al., 2009; Gautheron et al., 2009; Gautheron and Tassan-Got, 2010; Shuster and Farley, 2009). Both α-ejection and He diffusion kinetics are affected by a prolonged stay in the PRZ during a slow cooling. For such samples, AHe ages are representing a more complex thermal history (Reiners and Farley, 2001).

After the correction of the age, age reproducibility is first checked. Mean ages can be used for interpretation in case of well reproducible samples (Fitzgerald et al., 2006). In case of high dispersion, owing to differences in grain size, crystal defects, radiation damages or partially reset samples, single grain ages are preferably shown and biased ages are removed when they are identifiable.

2.3.3 Inverse modeling

With the central AFT ages, the track length distribution, the Dpar values and the single-grain AHe ages (including grains sizes and chemical characteristics), it is possible to determine the optimal thermal history (T-t paths) for single samples (Figure 2.7). A quantitative evaluation of the thermal history can be carried out through modeling procedures, which find a range of cooling paths compatible with the input data (Ketcham, 2005). Thermal history simulations can be conducted using the inverse modeling capabilities of the computer programs HeFTy (Ehlers et al., 2005) or QTQt (Gallagher, 2012) both generating possible T-t paths by a Monte Carlo algorithm. Hefty simulates random time-temperature (t-T) paths that satisfy the input data entered for each sample. Acceptable fit between model and data is given by the Goodness of Fit (GOF), which indicates the probability of failing the null hypothesis that the model and data are different. A modelled thermal history is considered good with a GOF > 0.5 for more than 100.000 random t-T paths simulated (Ketcham et al., 2009). The program QTQt allows inverting AFT annealing and AHe diffusion parameters with the Markov chain Monte Carlo method (Gallagher, 2012; Gallagher et al., 2009). It avoids also the over-interpretation of the data with a Bayesian transdimensional inversion approach which balances the complexity of the inferred thermal history models with the fit to the data (Gallagher, 2012). The inversion code incorporates kinetic models of He diffusion in apatite (Flowers et al., 2009; Gautheron et al., 2009) and AFT annealing multi-kinetic model (Ketcham et al., 2007). Thermal history simulations with QTQt are considered as robust when they are the product of 150.000 iterations (Gallagher, 2012).

2.4 Detrital apatite thermochronometry

Detrital thermochronometry is a branch of low- to intermediate temperature thermochronology which may constrain the cooling history of the source terrains of the sediments. The exhumation signal is transferred to the sedimentary basin during erosional processes with detrital apatite (or zircon) cooling ages. This record is more or less preserved during burial, depending of the amount of burial and consequent thermal conditions, as well as annealing. Apatites are regularly used as detrital chronometers in provenance studies as they are a common accessory component in clastic sedimentary rocks (Morton and Yaxley, 2007).

2.4.1 Ancient sandstones

Samples are generally collected through a stratigraphic succession. Indeed, the sedimentary rocks can provide information on the provenance and the exhumation of the source rocks, which is sometime impossible to investigate directly at the source rock location because of burial or substantial erosion. In detrital samples, a discrimination of the age populations is based on the distribution of the AFT grain ages. The χ-square statistical test is used to determine if counted grains belong to the same population of ages, by comparing the variance of the observed population with the variance predicted for the decay process

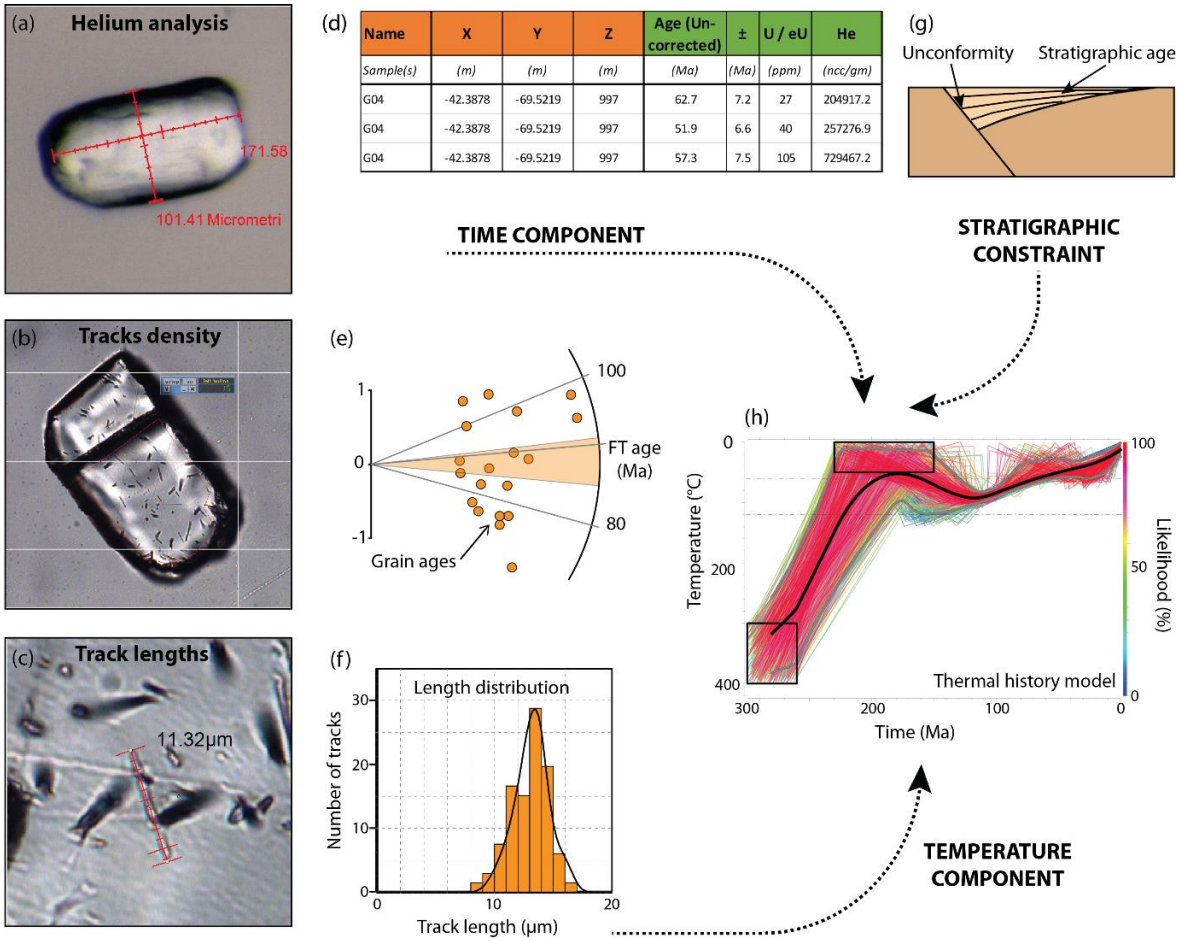

Name	X	Y	Z	Age (Un-corrected)	±	U / eU	He
Sample(s)	*(m)*	*(m)*	*(m)*	*(Ma)*	*(Ma)*	*(ppm)*	*(ncc/gm)*
G04	-42.3878	-69.5219	997	62.7	7.2	27	204917.2
G04	-42.3878	-69.5219	997	51.9	6.6	40	257276.9
G04	-42.3878	-69.5219	997	57.3	7.5	105	729467.2

Figure 2.7 – Analytical sequence required for the reconstruction of thermal histories from primary measurements of the number and the lengths of fission tracks in a mineral sample, together with the ^{238}U concentration and ^{4}He, from the sample G04 (described in this study). Image (a) shows good apatite grain selected for (U-Th-Sm)/He analysis. Image (b) includes a region of interest outlining the area to be counted and an internal grid to assist in counting. Image (c) shows a confined fission track and its measured length. In the center, a radial plot (e) shows the distribution all of grain ages, and a histogram the distribution of all lengths measured in a sample (f). The table (d) show some results obtained after (U-Th-Sm)/He analysis. These results can be thought of as primarily reflecting the time component, and the temperature component of the underlying thermal history. The thermal history reconstructed from such data, considering the diverse age constraints obtained from stratigraphy as unconformity or depositional age (g), is shown in the time-temperature plot (h) (modified from Gleadow et al., 2019).

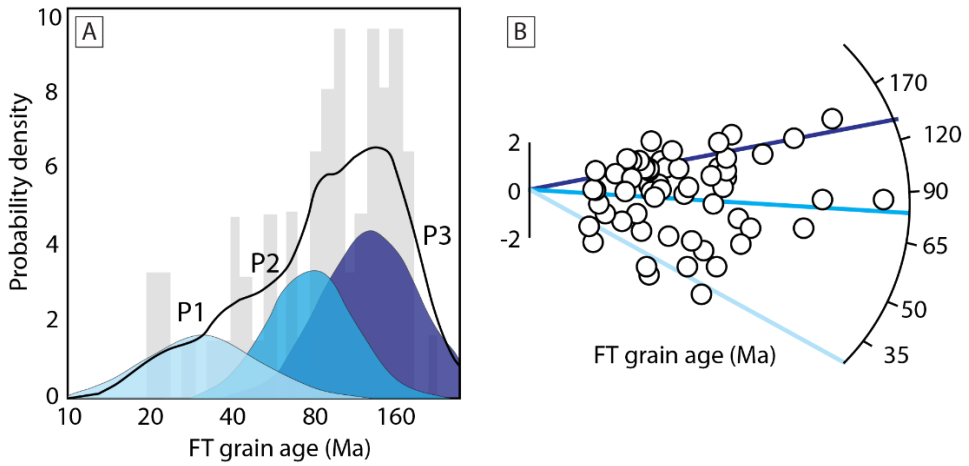

Figure 2.8 – Estimate of the components of a mixed grain age distribution made with BINOMFIT program (Brandon, 2002) (A) and associated radial plot (B) of sample MG33 (this study).

(Brandon, 2002; Galbraith, 1981). A probability (Pχ) of less than 5% is an evidence of asymmetric spread of single grain ages, and thus it indicates the presence of several age populations. The software BINOMFIT (by Brandon, 2002; summarized by Ehlers et al., 2005) is used to estimate the components in a mixed fission-track grain-age distribution (Figure 2.8) as it takes into consideration the binomial peak fitting algorithm of Galbraith and Laslett (1993). The ages obtained are compared with the depositional age to infer provenance (for not reset samples with AFT ages older than depositional ages) or basin exhumation story (for reset samples with AFT ages younger than depositional ages). Additionally, partially reset samples present a large dispersion with some grains younger or older than the depositional age. For considerable dataset, multidimensional scaling (MDS) can be applied with the software package `provenance` (Vermeesch et al., 2016) to visualize the level of similarity of individual samples of the dataset.

2.4.2 Lag time concept

The lag-time is the time elapsed from the closure of the thermochronometric system chosen, to the deposition of the grains in the depocenter after exhumation (Garver et al., 1999), with transport time considered as negligible (Heller and Paola, 1992) and deposition time reasonably well known (Figure 2.9A). Lag-time variations of sediments coming from the source provide then information on source evolution: a growing orogen would generate a lag-time decrease in the sediments, whereas a decaying orogen would induce a lag-time increase (Figure 2.9B). Change from slow to fast exhumation may cause variations of the isotherms affecting the geothermal gradient (Braun et al., 2016; Malusà and Fitzgerald, 2019; Rahl et al., 2007). These variations must be examined as they influence the lag-times (Figure 2.10). The flat isotherms are also influenced by the topography and tend to mimics the shape at the surface. Also long wavelength to the surface (e.g. deformation by folds) affected more the isotherms than short wavelength deformation (Figure 2.10).

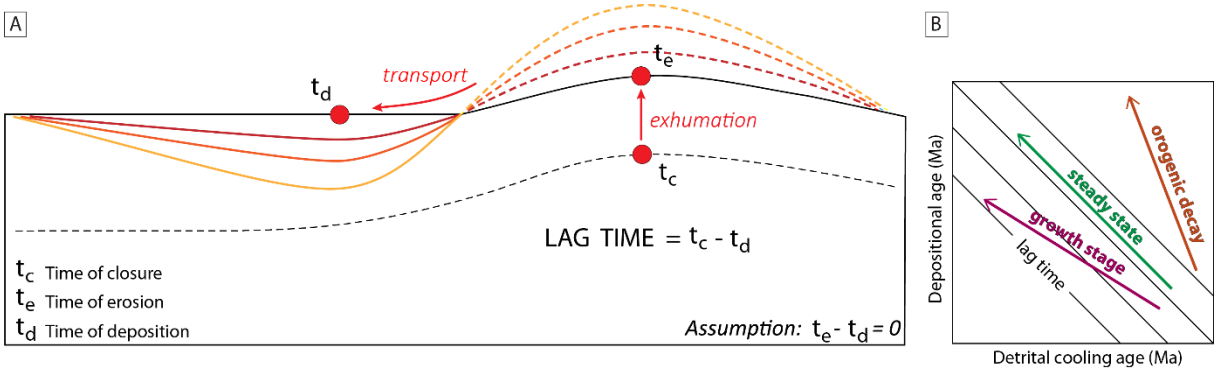

Figure 2.9 – (A) Schematic upper crustal cross-section of an orogen, showing the relationship between the progressive exhumation of a source region and deposition of the eroded exhumation record in an adjacent sedimentary basin (modified after Garver et al., 1999). A 'stratigraphy' of apatite fission-track ages develops within the basin, which is the inverse of the source-region exhumation age trend (modified from Lisker et al., 2009). (B) Expected distribution of thermochronometer ages for three separate scenarios: orogenic decay (or decreasing erosion rate), steady-state and orogenic growth (or increasing erosion rate). For the latter, ages will young faster than the stratigraphic age (modified from Rahl et al., 2007).

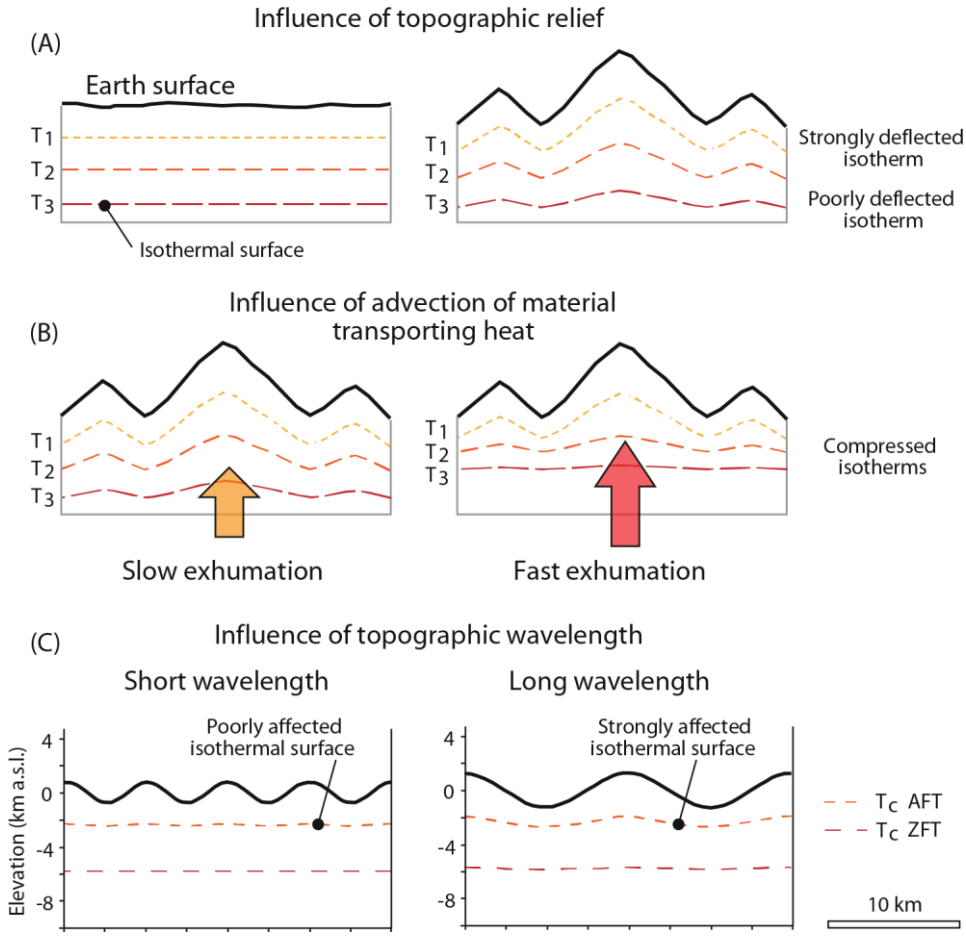

Figure 2.10 – (A) Isothermal surfaces mimic the shape of topography; (B) Heat advection during rapid exhumation determines the progressive elevation of isothermal surfaces and a transient increase in near-surface geothermal gradient; (C) Penetration of low-temperature isothermal surfaces beneath ridges is facilitated by longer topographic wavelength (from Malusà and Fitzgerald, 2019).

2.4.3 Modern sediments

Detrital thermochronology has been proposed as a method to quantify the distribution of catchment erosion (Stock and Dietrich, 2006; Vermeesch, 2007) and identify uniform and nonuniform erosion by comparing the measured detrital age distributions (probability density function, PDF) with the hypsometric curve of the catchment (Figure 2.11A; Brewer et al., 2003; Ehlers et al., 2015). Predicted PDF is formerly produced assuming uniform erosion from the convolution of the catchment hypsometry with linear age-elevation relationship from the catchment and consider therefore that every unit area of the catchment is delivering the amount of sediment. Measured PDF created using grain age data is then compared to the predicted one (which is mostly the equivalent of the hypsometric curve) to test the validity of several assumptions as the steady state erosion and topography (needed for the predicted age-elevation curve), the uniform modern erosion rates (can be modified by glacial erosion, Figure 2.11B), the sediment storage and mixing of the catchment. They are affected by inhomogeneous lithologies, structural geology or the presence or absence of vegetation. If the measured data do not match with the predicted one, it is difficult to assess which one of the assumptions were disregarded.

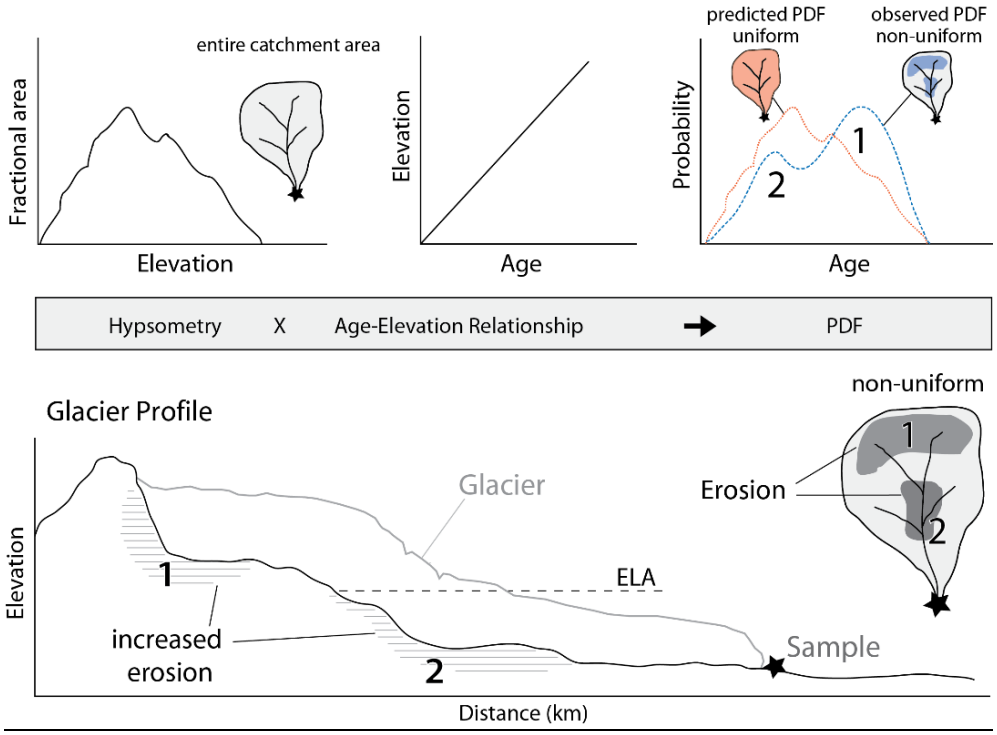

Figure 2.11 – (A) Schematic diagram illustrating how detrital thermochronometer data can be used to quantify the spatial distribution of erosion in a catchment. Simplified approach whereby the convolution of the catchment hypsometry and an age-elevation relationship are used to construct a predicted PDF. This approach assumes a uniform distribution of erosion over the catchment. If observed data are not uniform when compared with the predicted PDF, it means that erosion was not uniform. In this example, the peaks in measured ages (e.g., 1 and 2) are shifted to older and slightly younger ages when compared to the predicted PDF due to increased erosion at higher elevations. (B) Glacier profile, showing increased erosion at higher elevations and steps in the slope of the underlying bedrock (modified from Ehlers et al., 2015; Stock et al., 2006).

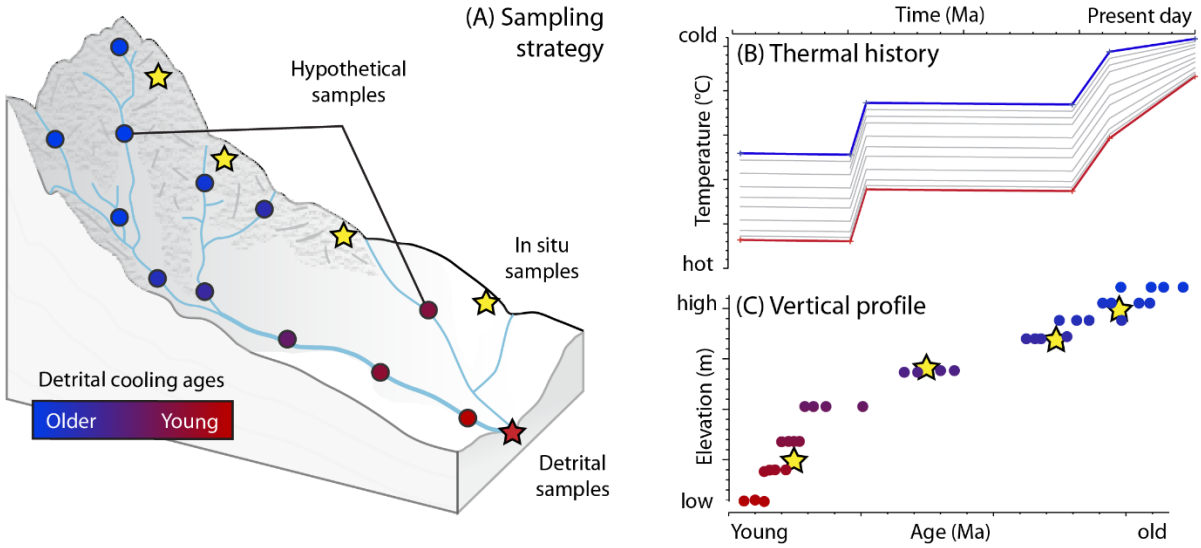

Figure 2.12 – Conceptual model to predict detrital distributions for thermochronological data (modified after Gallagher and Parra, 2020). (A) Comparison between typical in situ vertical profile, that may not cover the entire elevation range in catchment, and the modern detrital sample from the outlet for which a set of hypothetical dummy samples spanned over the total elevation range of the catchment. From a given specified thermal history (B) and the hypothetical samples, we can predict an age elevation profile (C) including kinetic parameters for FT (DPar). This allows to produce a set of AFT ages for the dummy samples at each elevation.

Recently, a new approach of inverse modelling has been proposed, relying on the assumption that thermal history was the same for the entire catchment studied (e.g. without fault activity across). This approach, based on the tendency of thermochronometer cooling ages to increase with elevation, allow to build hypothetical vertical profiles models (Figure 2.12; Gallagher and Parra, 2020). Despite the uncertainties of the results, the cooling age distribution of the detrital outlet sample and the hypsometry of the catchment used to predict thermal history offer reliable information about the catchment denudation. It may represent an alternative tool to study inaccessible areas were vertical profile sampling is unthinkable.

2.5 U-Pb dating

U-Pb dating of minerals by LA-ICP-MS is now a rapid, routine and effective dating tool with a precision better than 2% for apatites due to advance on data reduction and matrix-matched standards (Chew et al., 2014). It led to an increasing number of provenance studies employing the apatite U-Pb system in recent years (e.g. Carrapa et al., 2009; Mark et al., 2016; O'Sullivan et al., 2016; Zattin et al., 2012). Apatite U-Pb system has intermediate closure temperatures (375-550°C; Figure 2.2; Cochrane et al., 2014) and records lower temperature events than U-Pb zircon system. Nevertheless, the U-Pb apatite system is less precise and is generally employed to obtain first-order information, which is often sufficient to discriminate distinct sources. Indeed, apatite from igneous and high-grade metamorphic rocks typically contains sufficient U for U-Pb dating, while apatite from low-medium metamorphic terranes is often U-deficient and common Pb-enriched (Hsieh et al., 2008; O'Sullivan et al., 2016).

Nevertheless, this method is restrained by, for example, the grain size as an ablation spot of minimum 40 µm is required (O'Sullivan et al., 2018), so bigger grains are required. Limitations of the method concerned also low U abundance (do not yield favorable Pb*/Pbc ratios) and high initial common Pb incorporated during the crystallization of the grains (even with the common Pb-correction; Chew et al., 2014). Grains too young are therefore not reliable with this method.

Six isotopes (^{204,206,207,208}Pb, ^{232}Th and ^{238}U) are commonly analyzed for U-Pb geochronology studies. ^{43}Ca and ^{202}Hg are also measured as ^{43}Ca is used as an internal standard to correct variations in ablation volume and ^{202}Hg to monitor interference on the ^{204}Pb peak (Chew and Donelick, 2012). La-ICP-MS data are then reduced using the Iolite software, developed as a set of IgorPro, through the set VizualAge DRS (Petrus and Kamber, 2012). It expands from the original DRS by calculating ^{207}Pb/^{206}Pb ages and common Pb corrections for each time-slice of raw data. ^{207}Pb correction is applied on standard reference material (e.g. Madagascar and McClure mountain apatites, Thomson et al., 2012; Figure 2.13A and 2.13B) as this correction assumes that U-Pb (radiogenic component) data are concordant. ^{204}Pb correction can also be applied only for instruments able to measure ^{204}Pb precisely (MC-ICP-MS or ID-TIMS but not quadrupole ICP-MS), and ^{208}Pb correction is suited for U-Pb dating of accessory minerals as rutile. This correction is useful to solve the problem of elemental fractionation induced by the laser ablation and to correct common Pb on the standard, and by extension to unknown samples. Correction is then applied for all the samples and finally monitored on inverse (Tera-Wasserburg) concordia diagram (in IsoplotR;

Vermeesch, 2018) and different plots to verify the reliability of the age(s) obtained (Figure 2.13C, Figure 2.13D and Figure 2.13E). This late correction is applied first on the standard to verify if the lower intercept age obtained is accurate.

Additionally, lithological information can be obtained by the abundance of the REE, U/Th and Sr/Mn ratios and the magnitude of Eu and Ce anomalies (e.g. Belousova et al., 2002, 2001). The igneous type can be distinguished from one another geochemically (Hsieh et al., 2008) from the apatite trace-element geochemistry (e.g. "S-type" and "I-type" granitoid-derived apatite, basic apatite, and mantle-derived apatite).

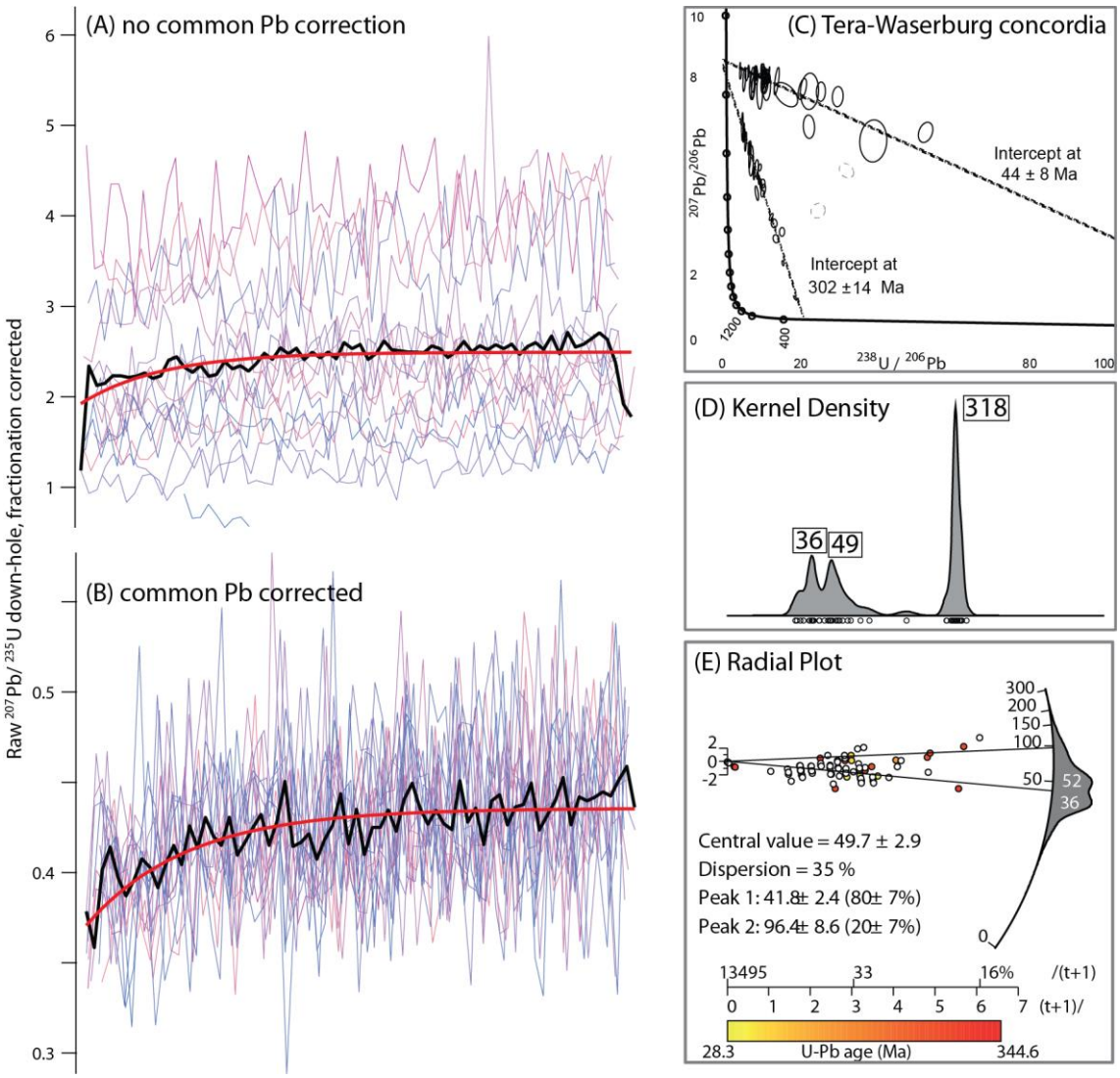

Figure 2.13 – (A) Time-resolved $^{207}Pb/^{235}U$ downhole signal collected from single-spot ablations of McClure Mountain apatite without any common Pb-correction and (B) a ^{207}Pb correction for common Pb (from Chew et al., 2014). Example of U-Pb analysis on apatite as a provenance tool (Mark et al., 2016) evidencing two populations in Tera-Wasserburg plot (C), Kernel Density plot (D) and Radial plot (E).

CHAPTER 3

THE ROLE OF SLAB GEOMETRY VARIATIONS IN THE EXHUMATION OF CORDILLERAN-TYPE OROGENS AND THEIR FORELAND: INSIGHTS FROM NORTHERN PATAGONIA

Marie C. Genge[1,2], Massimiliano Zattin[1], Elisa Savignano[1], Marta Franchini[3,4], Cécile Gautheron[5], Victor A. Ramos[6] and Stefano Mazzoli[7]

[1] Department of Geosciences, University of Padua, Italy

[2] Université de Lille, CNRS, Université du Littoral Côte d'Opale, UMR 8187, LOG, Laboratoire d'Océanologie et de Géosciences, F 59000 Lille, France

[3] Instituto de Investigación en Paleobiología y Geología, Universidad Nacional de Río Negro, Argentina

[4] Centro Patagónico de Estudios Metalogenéticos, Universidad Nacional del Comahue, Neuquén, Argentina

[5] GEOPS, Univ Paris Sud, CNRS, Université Paris-Saclay, Orsay, France

[6] Instituto de Estudios Andinos, UBA-CONICET, Buenos Aires, Argentina

[7] School of Science and Technology, Geology Division, University of Camerino, Italy

Declaration

This chapter is focused on the application of low-temperature thermochronology (apatite fission tracks and (U-Th-Sm)/He) between 40° and 44°S and aims to understand the contrasting exhumation pattern observed along the Patagonian Precordillera and the broken foreland. ES carried out all fieldwork, including sampling for low-temperature thermochronology dating methods, mineral separation, apatite picking, apatite (U-Th)/He dating and part of the AFT dating. MCG provided some AFT dating, the thermal models, all the figures and the original draft for this paper. MZ, SM and VAR made a careful review of the original draft. MZ acquired the funding for this work. SM managed the submission as corresponding author. MF participated on the field and discussions. CG supervised apatite (U-Th)/He dating and participated to discussions. This work has been presented during the 8th International Symposium on Andean Geodynamics (ISAG) in Quito, Ecuador (2019). The following version has been submitted for peer-review to the scientific journal Geological Society of America Bulletin as Genge M.C., Zattin M., Savignano E., Franchini M., Gautheron C., Ramos V.A. and Mazzoli S., The role of slab geometry variations in the exhumation of cordilleran-type orogens and their forelands: insights from northern Patagonia. The manuscript has been accepted with moderate revisions the 21st of November 2020.

Abstract

In cordilleran-type orogens, subduction geometry exerts a fundamental control on the tectonic behavior of the overriding plate. An integrated low-temperature, large thermochronological dataset is used in this study to investigate the burial and exhumation history of the overriding plate in northern Patagonia (40° – 45°S). Thermal inverse modeling allowed us to establish that a ~ 2.5 – 4 km thick section originally overlay the Jurassic – Early Cretaceous successions deposited in half-graben systems presently exposed in the foreland. Removal of the sedimentary cover started in the late Early Cretaceous. This was coeval with an increase of the convergence rate and a switch to a westward absolute motion of the South American Plate, accompanied by shallowing of the subducting slab. Unroofing was probably further enhanced by Late Cretaceous to early Paleogene opening of a slab window beneath the overriding plate. Following a tectonically quiescent period, renewed exhumation occurred in the orogen during relatively fast Neogene plate convergence. However, even the highly sensitive apatite (U-Th)/He thermochronometer does not record any coeval cooling in the foreland. The comparison between Late Cretaceous and Neogene exhumation patterns provides clear evidence of the fundamental role played by inter-plate coupling associated with shallow slab configurations in controlling plate-scale deformation. Our results, besides highlighting for the first time how the whole northern Patagonia was affected by an exhumation of several kilometers since the Late Cretaceous, provide unrivalled evidence of the link between deep geodynamic processes affecting the slab and the modes and timing of unroofing of different sectors of the overriding plate.

3.1 Introduction

Mechanical plate coupling is governed by subduction geometry, and particularly by slab dip. This latter is controlled by various parameters including: (i) upper plate absolute motion, (ii) subducting slab buoyancy, (iii) overriding plate temperature, and (iv) faulting of the oceanic lithosphere (Cerpa et al., 2018; Gutscher, 2002; Gutscher and Peacock, 2003; Lallemand et al., 2005; Rodríguez-González et al., 2012). Many authors also pointed out correlations in time and space between shallow slab segments and the subduction of buoyant oceanic features such as aseismic ridges or oceanic plateau (Gutscher et al., 2000; McGeary et al., 1985; Pilger and Rex, 1981). Upper plate compression is generally associated with strong interplate coupling during shallow to flat-slab subduction, while extension is correlated with weak interplate coupling during slab rollback. Therefore, plate coupling variations are believed to result in alternating phases of upper plate shortening and extension (Horton, 2018a; Lallemand et al., 2005), thereby regulating orogenic growth and foreland evolution (Martinod et al., 2010). Although a high degree of interplate coupling can also characterize steep subduction (depending on convergence rate), this is generally less effective with respect to that associated with shallow to flat-slab segments (Gutscher, 2002). At present, slab dip varies significantly along the Andean margin from the dominant dip angle of ~30° to flat-slab segments (Horton and Fuentes, 2016; Maksymowicz and Tassara, 2018; Ramos and Folguera, 2009). This

results in along-strike segmentation and coupling variations that influence magmatism and the style of recent to active deformation of the overriding plate (Coira et al., 1993; Ramos and Folguera, 2009; Yáñez and Cembrano, 2004).

The geological record of pulsed upper plate shortening episodes in Patagonia has been related with variable plate coupling associated with changes of plate convergence settings, particularly slab dip (Echaurren et al., 2016; Gianni et al., 2015; Horton, 2018; Orts et al., 2012). A late Early Cretaceous to early Paleogene and a middle Miocene to Pliocene orogenic stages have been recognized in the Patagonian Cordillera, Precordillera (Figure 3.1A) and the so-called broken foreland generated by the inversion of former graben/half graben systems (Echaurren et al., 2016). These latter were formed in the context of Early Jurassic to Early Cretaceous extension associated with a protracted slab rollback, which is coherent with the westward shift of arc magmatism (Ramos, 1999, 2010). Similar processes have been documented for the intervening late Eocene to early Miocene period, characterized by abundant magmatism toward the Cordillera and modest foreland subsidence (Folguera and Ramos, 2011; Horton, 2018a). Basin inversion emphasizes the role of inherited upper plate weaknesses in controlling the propagation of the deformation to the broken foreland during regional shortening episodes (Gianni et al., 2017). However, little is known about the amount of regional unroofing in the foreland of the Patagonian Andes, as thermochronological studies focused mainly on the growth of the Cordillera (Thomson et al., 2010a). In this study we present the results obtained by thermal inverse modeling of low-temperature thermochronology data collected in the Patagonian Precordillera and the broken foreland between 40° and 45°S (Figure 3.1B and Figure 3.1C) with the goal of evaluating the impact of slab geometry changes – and associated plate coupling variations – on the deformation of the overriding plate. Our results provide a new and unexpected picture of the large unroofing (in excess of 3 km considering an average geothermal gradient of ~ 34 ± 11 °C/km) experienced by the whole northern Patagonia – and not just the Cordillera – since the late Early Cretaceous.

3.2 Geological setting

The northern Patagonian margin is characterized by several morphotectonic units, including the Patagonian Precordillera and the broken foreland to the east (Figure 3.1A; Echaurren et al., 2016). The Precordillera is a retroarc thick-skinned fold-thrust belt (Giacosa and Heredia, 2004; Orts et al., 2012). On the other hand, the broken foreland got its name because it is structurally articulated and fragmented by a series of uplifted blocks (e.g. Bilmes et al., 2013). Regional deformation in northern Patagonia is characterized by the inversion of former sedimentary basins (Piltriquitrón Basin and Rio Mayo Basin along the Precordillera, Cañadón Asfalto Rift Basin to the foreland) developed on top of a low-grade metamorphic basement. The latter is constituted of Paleozoic-Triassic volcano-sedimentary successions (e.g. Cushamen, Calcatapul Formations; Volkheimer, 1964; Von Gosen and Loske, 2004) and coeval intrusions (e.g. Colohuincul Complex, Mamil Choique and Lipetrén Formations; Rapela et al., 1992; Ravazzoli and Sesana, 1977; Turner, 1965; Varela et al., 2005). The Cañadón Asfalto Rift Basin is mainly the product of extension induced by Gondwana break-up during the Early Jurassic and of the following Early Cretaceous sag stage

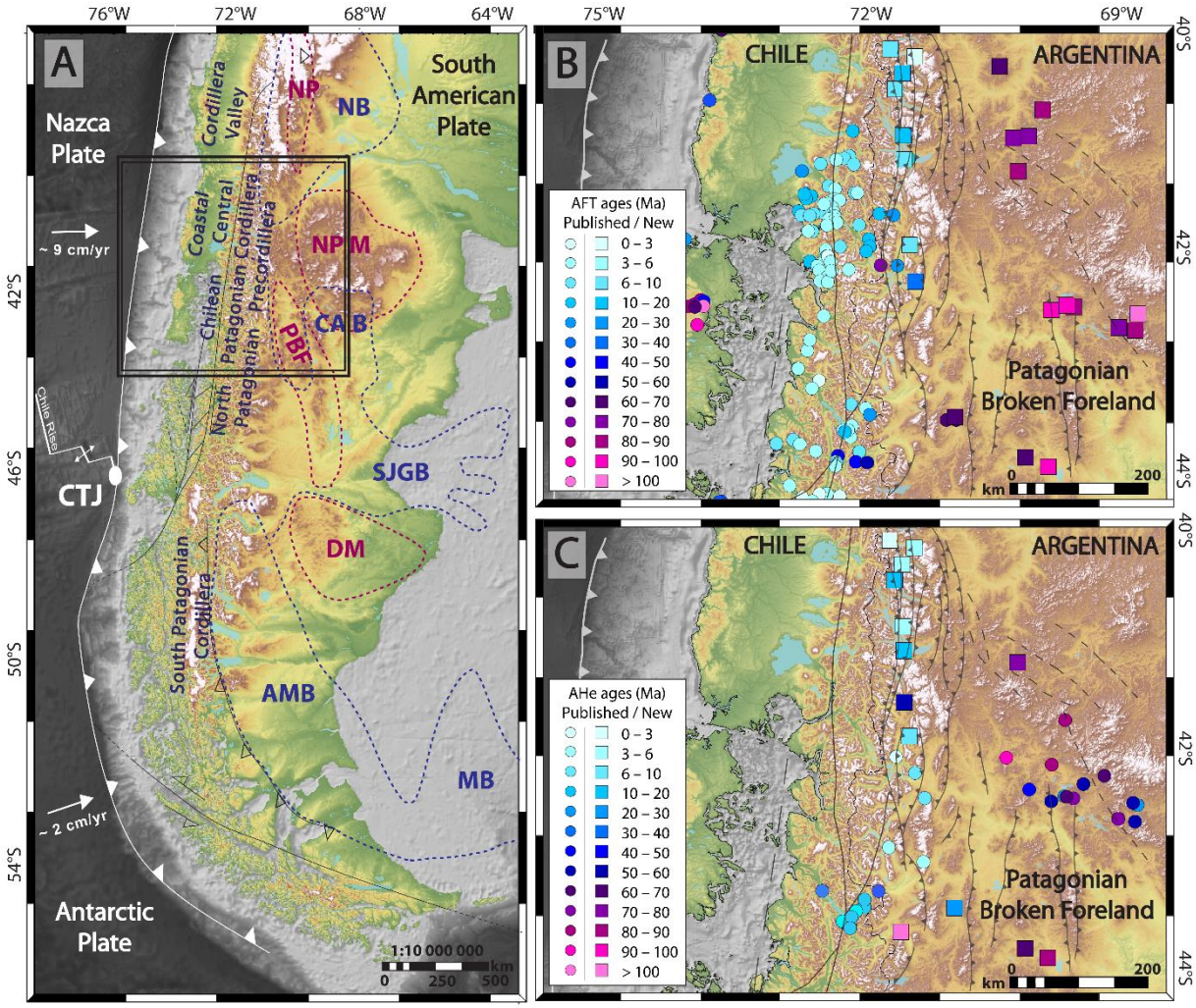

Figure 3.1 – A. Map view of major tectonic features of the Southern Andes showing (modified after Navarrete et al., 2016), showing location of diagrams B-C. Blue dashed lines outline foreland basins (AMB: Austral-Magallanes Basin, CAB: Cañadón Asfalto Basin, MB: Malvinas Basin, NB: Neuquén Basin, SJGB: San Jorge Gulf Basin), purple dashed lines outline foreland reliefs (DM: Deseado Massif, NPM: North Patagonian Massif, NP: Neuquén Precordillera, PBF: Patagonian Broken Foreland). White arrows indicate current motions of oceanic plates relative to South America, according to the global model NUVEL-1. B. Map view of main morphotectonic features between 40° and 45°S, with new and published (Thomson, 2002; Thomson et al., 2010a) AFT ages. C. New and published (Savignano et al., 2016; Thomson et al., 2010a) AHe ages.

(Figure 3.2; Figari et al., 2015; Mpodozis and Ramos, 2008). The sedimentary infill includes the marine Las Leoneras Formation, followed above by the continental Cañadon Asfalto and Cañadón Calcáreo Formations, laterally interbedded with the volcanic Lonco Trapial Formation (Cúneo et al., 2013; Zaffarana and Somoza, 2012). Few discordances observed in the basin succession are correlated with minor shortening events associated with changes in plate motion and volcanic activity (Figari et al., 2015; Maloney et al., 2013; Navarrete et al., 2016, 2018). Along the Precordillera, roughly coeval back-arc extension was triggered by a protracted slab rollback generated by low convergence rates and eastward motion of the South American Plate (Giacosa and Heredia, 2004; Horton, 2018a; Maloney et al., 2013; Seton et al., 2012; Suarez and Marquez, 2007). This resulted in steepening of the slab, as evidenced by the westward migration of the magmatic arc (Figure 3.2) marked by the Early Jurassic Sub-

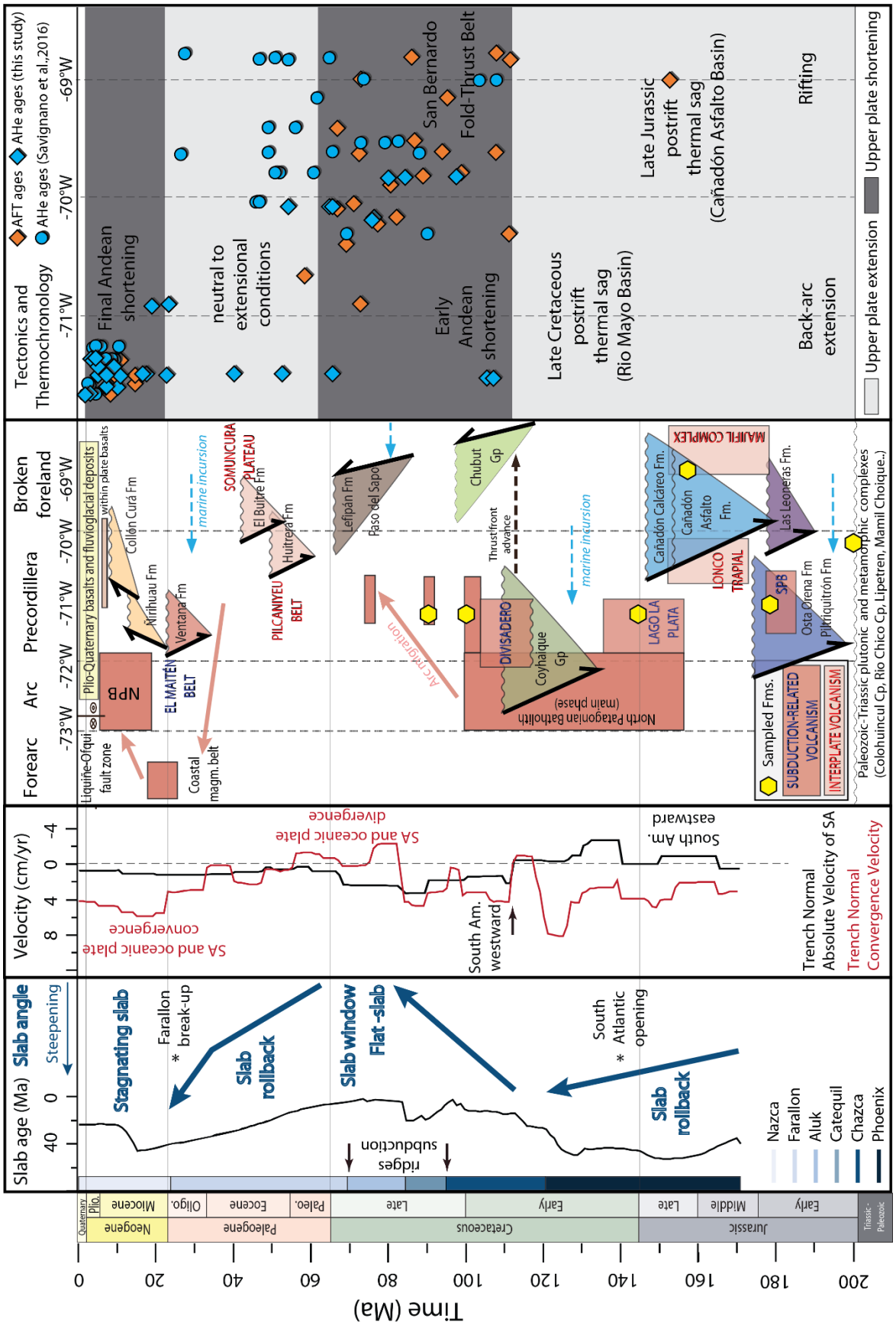

Figure 3.2 – Chronological table for northern Patagonia at around 43°S showing slab variations, plate convergence changes, time-space history of deformation, magmatism, basin development (Butler et al., 2020; Echaurren et al., 2016; Horton, 2018a; Maloney et al., 2013) and thermochronological data (AFT and AHe ages vs. longitudinal distribution) used in this study.

-cordillera Plutonic Belt (Gordon and Ort, 1993; Page and Page, 1999) and by the Late Jurassic – Early Cretaceous North Patagonian Batholith (Pankhurst et al., 2003; Suárez and De la Cruz, 2001). Coeval volcanism is recorded by the Middle – Late Jurassic Lago La Plata Formation (correlated with the Ibáñez Group in Chile; Folguera and Iannizzotto, 2004; Olivero, 1982) and the late Early Cretaceous Divisadero Group (Ramos, 1981; Suárez et al., 2009). These volcanic deposits overlie respectively the NNE-trending graben/half-graben systems of the Piltriquitrón Basin (filled by the Early – Middle Jurassic Osta Arena Formation, Piltriquitrón Formation and equivalent units; Gabaldón, 1982; Giacosa and Heredia, 2004; Suarez and Marquez, 2007), and the Late Jurassic – Early Cretaceous sedimentary successions of the Coyhaique Group hosted in the Rio Mayo Basin (Echaurren et al., 2017; Olivero, 1982; Skarmeta, 1976). As revealed by the regional unconformity observed in the upper volcanic succession of the Divisadero Group and on top of the Cañadón Asfalto Rift Basin deposits, extension was suddenly interrupted at ~ 120 Ma by a regional shortening episode (Folguera and Iannizzotto, 2004; Horton, 2018a; Suárez et al., 2009). This latter, acting on a mechanically and thermally weakened continental lithosphere, produced both the earliest stage of Andean uplift and deformation of the Patagonian broken foreland. The deformation, reaching areas ~ 500 km away from the trench (Navarrete et al., 2016), was dominated by fault reactivation and inversion of former depocenters (Gianni et al., 2015a). The initiation of regional shortening coincided with a change of absolute motion of the South American Plate, which became west directed (Figure 3.2; Maloney et al., 2013; Müller et al., 2016; Seton et al., 2012; Silver et al., 1998). Trenchward absolute motion of the overriding plate and increase of convergence rates (Eagles, 2007; Maloney et al., 2013; Müller et al., 2016) were accompanied by slab shallowing manifested in the upper crust by the eastward expansion of the magmatic arc during the Late Cretaceous (Haller et al., 2010; Aragón et al., 2013). This change in slab dip favored a strong increase of coupling between the subducting plates and the overriding plate (Horton and Fuentes, 2016). Growth strata in foreland basins have been detected in the continental Upper Cretaceous Chubut Group, Paso del Sapo Formations and in the marine Paleocene Lefipán Formations (Echaurren et al., 2016; Gianni et al., 2015a; Navarrete et al., 2016). It indicates that crustal shortening persisted throughout Late Cretaceous to Paleocene times (Echaurren et al., 2016; Horton, 2018a). Subduction of mid-ocean ridges may sustained this long-term and significant deformation, as the positive buoyancy of younger lithosphere tends to resist subduction (Cloos, 1993), and allow the opening of a slab window during latest Cretaceous (Echaurren et al., 2016). Slab window model, supported by seismic tomography (Aragón et al., 2011), is generally accompanied by an isostatic uplift of the overriding plate and a dynamic topography related with limited deformation of the retroarc (Aragón et al., 2013, 2011; Ávila and Dávila, 2020).

Growth strata in early Eocene deposits are observed north and south of the studied area (Charrier et al., 2007; Cobbold and Rossello, 2003; Gianni et al., 2017; Navarrete et al., 2016) where only syn-extensional strata have been recognized in the late Paleocene – Eocene Huitrera Formation associated with bimodal within-plate volcanism (Pilcaniyeu Belt; Figure 3.3; Echaurren et al., 2016; Iannelli et al., 2018; Mazzoni et al., 1991). Cessation of the contraction between 40° and 45°S during Paleocene may

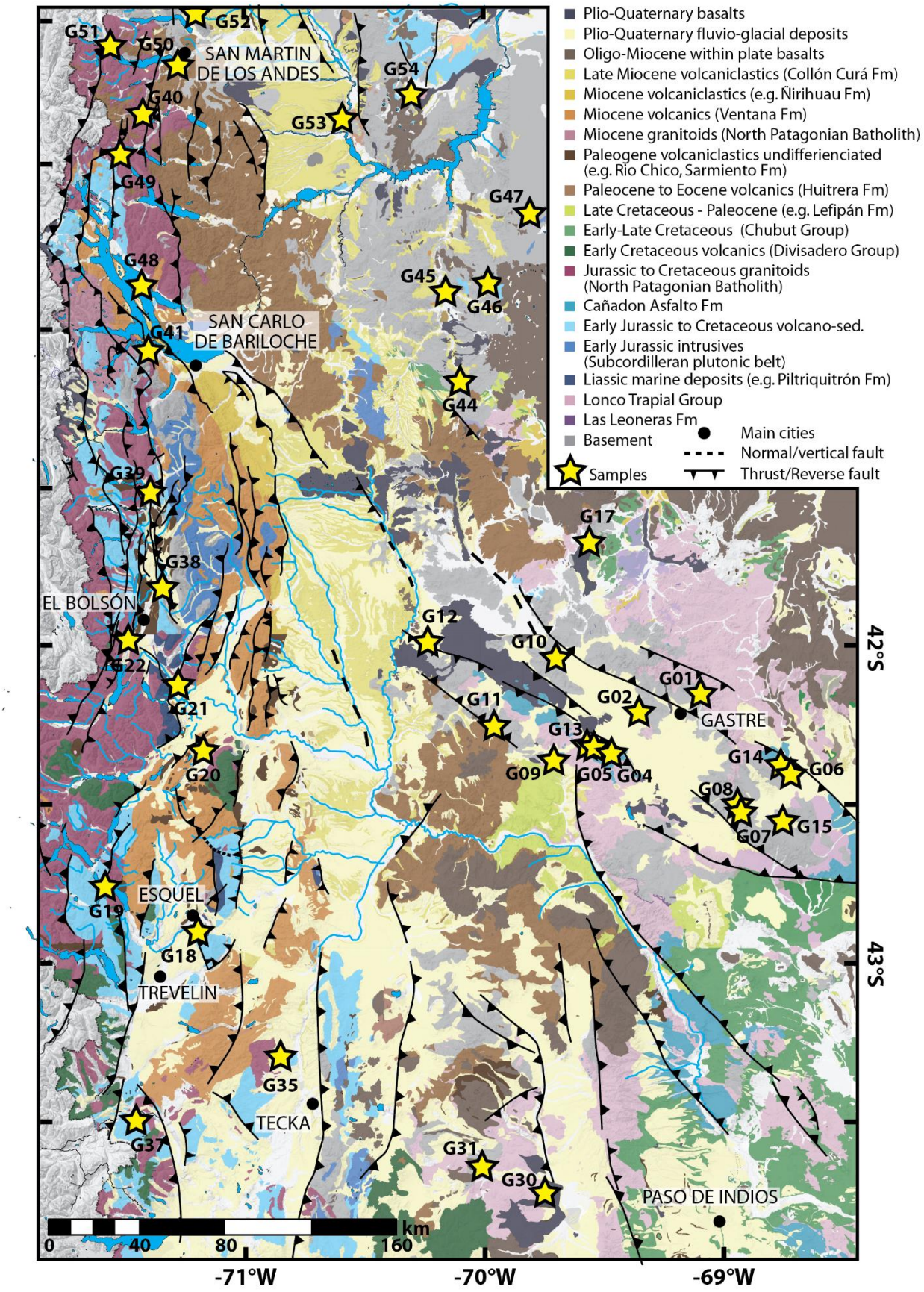

Figure 3.3 – Detailed geological map of the study area based on Anselmi et al., 2004; Ardolino et al., 2011; Cucchi et al., 2001, 1998; Escosteguy et al., 2013; Giacosa et al., 2001; González et al., 2000; Haller et al., 2010; Lizuaín et al., 2010; Lizuaín and Nieto, 2011; Orts et al., 2015; Remesal et al., 2001; Savignano et al., 2016; Silva Nieto et al., 2005.

be related with the resteepening of the subducting slab induced by a sharp reduction in average trench-ward velocity, an increase of slab pull forces after asthenospheric window development and/or the decreasing buoyancy of oceanic segments (Aragón et al., 2011; Echaurren et al., 2016; Horton, 2018a; Maloney et al., 2013; Suárez and De la Cruz, 2001). Pronounced slab rollback during late Paleogene generated decoupling of the subducting plate and intake of hot atmosphere (De Ignacio et al., 2001; Encinas et al., 2016). The steepening of the slab is revealed by pervasive magmatism close to the Precordillera (El Maitén Belt; Figure 3.3; Fernández Paz et al., 2018; Iannelli et al., 2018; Rapela et al., 1988) and a modest extensional setting (Ventana Formation) reported in the whole Patagonia (from Neuquén to Magallanes – Austral Basins; George et al., 2020; Horton et al., 2016; Orts et al., 2012). The Eocene – Miocene Somuncura Plateau and associated Formations (e.g. El Buitre Fm) represented magmatism in the distal retroarc zone. Several origins have been proposed (e.g. slab detachment, plume-like mantle upwelling) due to the complex geochemical signature of these volcanic plateaus (Aragón et al., 2013; De Ignacio et al., 2001; Kay et al., 2007).

Trench-normal absolute velocity of the South American Plate remained low to ~23 Ma, when the break-up of the oceanic Farallon Plate into Nazca and Cocos Plate reorganized the plate convergence (Lonsdale, 2005; Somoza, 1998). This new configuration allowed an increase of interplate coupling, not necessary linked with a change of slab dip (Cerpa et al., 2018; Schellart, 2020). Resumption of the upper plate shortening is recorded along the Precordillera and associated with the Miocene rejuvenation of the North Patagonian Batholith (Echaurren et al., 2016). Mild contractional deformation of the foreland has been proposed based on the growth strata documented in the early – middle Miocene foreland basins known as Ñirihuau and Collón Curá Basins (Figure 3.2; Echaurren et al., 2016; Orts et al., 2012; Ramos et al., 2011). Substantial Miocene deformation controlled by former heterogeneities is also suggested in the foreland (Bilmes et al., 2013; Gianni et al., 2015a).

3.3 Materials and methods

The low closure temperatures of apatite (U–Th)/He (AHe, ~ 65°C; e.g. Flowers et al., 2009; Gautheron et al., 2009) and apatite fission track (AFT, ~ 110°C; e.g. Ketcham et al., 2007) systems provide information on cooling histories and exhumation within the upper crust. In this study, we present thirty-three (U-Th)/He (AHe) and thirty-one apatite fission-track (AFT) new ages from samples collected from the Patagonian Precordillera and its broken foreland between 40° and 45°S. Fifteen of the new AFT ages (with track measurements) were obtained from the same samples that yielded further thirty-four single-grain AHe ages published by Savignano et al. (2016), thus achieving an extensive dataset (Figure 3.2). Geographic coordinates, elevation, formation (mainly metamorphic basement, Jurassic sedimentary rocks and Cretaceous granitoids), stratigraphic age and rock lithology of all samples are included in Table 3.1.

3.3.1 Apatite Fission Tracks (AFT)

We performed AFT analysis at the University of Padua (Italy). Apatite grains were mounted in epoxy resin, polished and etched at 5.5M HNO_3 during 20 seconds at 20°C to reveal spontaneous tracks. The samples were analyzed by applying the external detector method (Gleadow, 1981) using low-uranium muscovite foils, as external detector, to cover apatite mounts then irradiated at the Radiation Center of Oregon State University with a nominal fluence of 9×10^{15} neutrons/cm². After irradiation, we etched mica detectors for 40 minutes in 40% HF at 20°C to reveal induced tracks. We counted tracks and measured track length distribution using an Olympus optical microscope at a magnification of ×1250. We carried out age calculation and statistics with Trackkey software (Dunkl, 2002). We report AFT ages as central age with 1σ errors (Galbraith and Laslett, 1993), using a zeta calibration approach (Hurford and Green, 1983) with a zeta value of 345 ± 8 (samples G1-G22) and a zeta value of 346 ± 12 (samples G30-G55) for the CN5 dosimeter glass. Dpar measurements were used to characterize the chemical kinetic properties of the apatite crystals (Burtner et al., 1994). Both track density ratio and average track etch pit diameter (Dpar) is recorded for 20 grains per sample (Table1).

3.3.2 Apatite (U-Th-Sm)/He (AHe)

The first steps of AHe dating involved apatite picking at the University of Paris-Saclay (Orsay, France). Apatite grains were selected carefully according to their morphology, size (minimum width of 60 μm) and lack of visible inclusions or grain boundary phases (Murray et al., 2014), and then placed into a Niobium basket for He-extraction. From 1 to 3 grains were dated per sample, depending on sample apatite quality. The Niobium baskets were heated twice using a diode laser at 1030 ± 50°C for 5 min, allowing for total He degassing and to check the presence of He trapped in small inclusions (Fillon et al., 2013). The ^{4}He content was determined by comparison with a known amount of 3He spike added during analysis. After He extraction, Nb baskets were placed into single-used polypropylene vials. Apatite grains were dissolved for 3 hours at 70°C in a 50 μL HNO3 5N- solution containing a known content of 235U, 230Th, and 149Sm, and additional 50 μL HNO3 5N- and then filled with 0.9 mL of ultrapure MQ water. The final solution was measured for U, Th, and Sm concentrations by quadrupole inductively coupled plasma (ICP-quadrupole) mass spectrometry (CCT Thermo-Electron at LSCE, Gif/Yvette, France). The analysis was calibrated using external age standards, including Limberg Tuff and Durango apatites. A mean AHe age of 16.0 ± 1.4 Ma and 31.1 ± 2.1 Ma has been measured for the Limberg Tuff and yellow Durango apatite respectively, which are in agreement with published data (i.e., 16.8 ± 1.1 Ma and 31.0 ± 1.0 Ma; Kraml et al., 2006; McDowell et al., 2005). Single ages were corrected using the calculated ejection factor FT, determined using the Monte Carlo simulation technique of Ketcham et al. (2011); the equivalent-sphere radius was calculated using the procedure of Gautheron and Tassan-Got (2010). Single-grain apatite He ages and supporting data are presented in Table 2. The 1σ error on single-grain AHe ages should be considered as 9%, reflecting the sum of errors in the ejection-factor correction and age dispersion of the standards.

TABLE 3.1. SUMMARY OF SAMPLE INFORMATION AND APATITE FISSION TRACKS DATA

Samples†	Field*			Geology			AFT ages									AFT length			
	Latitude	Longitude	Elev. (m)	Lithology	Formation	Stratigraphic age	AFT (Ma)	σ	Ns	ρs	Ni	ρi	Nd	ρD	P(χ^2)	MTL (μm)	σ	n°	Dpar
G01	-42.1928	-69.1656	1134	granite	Lipetren	Triassic	96.3	6.4	400	5.90	822	12.12	4798	11.56	93.29				
G02	-42.2658	-69.4086	929	granite	Mamil Choique	Permian	68	5.2	268	5.15	775	14.89	4798	11.46	99.68	12.86	0.18	80	1.88
G04	-42.3878	-69.5219	997	granite	Mamil Choique	Permian	87.3	4.3	867	10.86	1938	24.27	4798	11.39	98.3	11.95	0.23	66	1.81
G05	-42.3694	-69.6292	963	conglomerate	Cañadon Asfalto	Upper Jurassic	108.2	11.2	155	4.15	282	7.55	8875	11.51	96.7				
G06	-42.4444	-68.7803	1150	arkose	Cañadon Asfalto	Upper Jurassic	109.2	7.8	352	3.23	625	5.73	8875	11.34	100				
G07	-42.5597	-69.0039	1070	granite	Mamil Choique	Lower Permian	154.4	6	2211	39.86	2832	51.05	4798	11.6	99.9	12.47	0.13	100	1.88
G08	-42.5639	-69.0042	1043	granite	Mamil Choique	Lower Permian	74.1	4	643	12.01	1670	31.20	4798	11.22	73.5	12.11	0.23	92	2.33
G09	-42.4131	-69.7822	995	arkose	Cañadon Asfalto	Upper Jurassic	99.9	5.6	602	5.81	1152	11.11	8875	11.17	91	12.02	0.27	56	2.39
G10	-42.0953	69.7749	1060	granite	Mamil Choique	Lower Permian													
G11	-42.3114	-70.0367	999	dyke (granite)	Mamil Choique	Lower Permian													
G12	-42.0353	-70.2992	976	granite	Mamil Choique	Lower Permian	112	6	710	11.24	1192	18.87	8875	11	88.66				
G13	-42.3736	-69.6039	973	sandstone	Cañadon Asfalto	Upper Jurassic	95	4.8	1475	15.71	2904	30.93	8875	10.94	63	11.73	0.19	61	1.90
G14	-42.4253	-68.8347	1177	sandstone	Cañadon Asfalto	Upper Jurassic	112.6	8.6	1184	13.84	2001	23.40	8875	10.89	92.78				
G15	-42.5861	-68.8128	1103	granite	Mamil Choique	Lower Permian	87.1	9	147	3.19	313	6.80	4798	10.83	99				
G17	-41.7119	-69.6192	1275	granite	Mamil Choique	Lower Permian	73.6	3.7	718	13.20	1794	32.99	8875	10.72	99.55	12.70	0.16	94	1.67
G18	-42.9306	-71.2606	617	granite	Subcordilleran Plutonic Belt	Lower Jurassic													
G19	-42.8064	-71.6608	576	granite	Patagonian Batholith	Upper Cretaceous													
G20	-42.3847	-71.2453	663	granite	Leleque	Upper Jurassic													
G21	-42.1672	-71.3572	616	granodiorite	Subcordilleran Plutonic Belt	Lower Jurassic	11.5	1.3	92	2.08	1464	33.06	4798	10.6	100				
G22	-42.0303	-71.5761	275	granite	Patagonian Batholith	Upper Cretaceous	14.8	1.3	162	3.14	1995	38.47	8875	10.55	36.74				

§

G30	-43.7439	-69.8186	670	sandstone	Osta Arena	Lower Jurassic	89.8	8.3	211	2.11	416	4.15	5000	10.3	100	12.61	0.15	65	1.39
G31	-43.6650	-70.0839	825	sandstone	Tepuel Group	Carboniferous to Permian	67.4	4.6	418	9.98	1078	25.74	5000	10.1	98.9				
G35	-43.3244	-70.8961	875	granitoid	Rio Hielo	Cretaceous	73.5	10.4	76	1.98	178	4.64	5000	10	99.98	12.14	0.2	25	1.33
G37	-43.5250	-71.5181	473	granitoid	Rio Hielo	Cretaceous													
G38	-41.8508	-71.4219	627	granodiorite	Complejo Colohuincul	Lower Permian	8.6	1	88	1.34	1743	26.57	5000	9.85	100				
G39	-41.5564	-71.4806	731	granite	Patagonian Batholith	Lower Cretaceous													
G40	-40.3447	-71.5064	898	granodiorite	Complejo Colohuincul	Lower Permian	14.2	1.7	86	1.14	1026	13.61	5000	9.77	99.95	13.87	0.09	60	1.34
G41	-41.1061	-71.4831	849	granite	Patagonian Batholith	Lower Cretaceous	9	1.1	73	2.03	1364	37.95	5000	9.69	99.37				
G44	-41.2089	-70.1667	999	granite	Plutonitas Pilcaniyeu	Lower Jurassic	83.5	5.6	489	4.84	968	9.58	5000	9.61	94.66	12.09	0.1	61	1.32
G45	-40.9181	-70.2247	810	granodiorite	Mamil Choique	Lower Permian	77.9	5.7	368	6.74	775	14.20	5000	9.54	97.69				
G46	-40.9017	-70.0461	1189	granodiorite	Mamil Choique	Lower Permian	71.6	5.1	382	5.76	869	13.10	5000	9.46	81.3				
G47	-40.6692	-69.8833	1298	granodiorite	Mamil Choique	Lower Permian	81.8	4.9	683	10.54	1349	20.81	5000	9.39	88.24	11.90	0.15	33	1.33
G48	-40.8936	-71.4950	805	granodiorite	Los Machis	Up. Jurassic to Cretaceous	14.5	1.2	188	2.79	2093	31.03	5000	9.31	99.85				
G49	-40.4853	-71.5894	903	granodiorite	Los Machis	Up. Jurassic to Cretaceous	6.9	0.9	60	1.07	1387	24.84	5000	9.23	100				
G50	-40.1956	-71.3614	976	granodiorite	Complejo Colohuincul	Lower Permian	4.9	0.6	66	1.12	2131	36.27	5000	9.15	100				
G51	-40.1289	-71.6456	791	tonalite	Los Machis	Up. Jurassic to Cretaceous	8.1	1.1	65	0.92	1242	17.56	5000	9	99.34				
G53	-40.3683	-70.6619	645	granite	Cushamen	Devonian to Carboniferous	59.3	4.2	392	6.66	1015	17.24	5000	8.92	99.98	12.66	0.11	86	1.29
G54	-40.2822	-70.3803	986	granodiorite	Mamil Choique	Lower Permian	69.6	4.6	486	8.69	1063	19.00	5000	8.85	100	12.83	0.13	100	1.28

* longitude and latitude coordinates are given in WGS84

† Zeta= 345 ± 8 § Zeta= 346 ± 12

N: number of apatite crystal counted; and ρ: track density (x 105 tracks/cm²); subscripts s, I and d denote spontaneous, induced and dosimeter, respectively; P(χ^2): probability of obtaining a Chi-square value for n degrees of freedom; Dpar: mean diameter of fission-track etch pit parallel to the c-axis.

TABLE 3.2. APATITE (U-TH)/HE SINGLE-GRAIN DATA.

Samples	Lat. (°S)	Long. (°W)	Elev. (m)	Weight (µg)	Rs (µm)	FT	^{4}He (ncc/g)	U (ppm)	Th (ppm)	Sm (ppm)	Th/U	eU (ppm)	AHe age (Ma)	Corrected age (Ma)	Error (Ma)
G01B	-42.1928	-69.1656	1134.00	1.70	38.00	0.64	481259.60	91	31	151	0.30	98	40.00	62.10	5.60
G02B	-42.2658	-69.4086	929.00	1.80	41.00	0.72	159254.40	18	59	82	3.30	32	40.60	56.50	5.10
G02C	-42.2658	-69.4086	929.00	0.90	35.00	0.66	70897.90	9	20	486	2.20	14	33.00	49.90	4.50
G04A	-42.3878	-69.5219	997.00	3.80	53.00	0.79	204917.20	21	22	66	1.00	27	62.70	79.90	7.20
G04B	-42.3878	-69.5219	997.00	1.40	41.00	0.71	257276.90	32	33	97	1.00	40	51.90	73.60	6.60
G04C	-42.3878	-69.5219	997.00	1.60	44.00	0.68	729467.20	83	96	17	1.20	105	57.30	83.80	7.50
G05C	-42.3694	-69.6292	963.00	1.80	46.00	0.75	116142.70	43	20	65	0.50	47	20.10	26.90	2.40
G06C	-42.4444	-68.7803	1150.00	3.50	55.00	0.78	70495.90	22	19	66	0.90	27	21.60	27.70	2.50
G07A	-42.5597	-69.0039	1070.00	2.60	52.00	0.73	1256944.80	134	3	152	0.00	135	76.50	104.60	9.40
G07C	-42.5597	-69.0039	1070.00	3.40	55.00	0.75	1587006.90	159	9	66	0.10	161	81.40	109.20	9.80
G08A	-42.5639	-69.0042	1043.00	1.90	39.00	0.69	113056.00	15	8	133	0.50	17	51.40	74.50	6.70
G09A	-42.4131	-69.7822	995.00	0.50	32.00	0.57	260075.30	33	89	933	2.70	54	35.10	61.40	5.50
G09B	-42.4131	-69.7822	995.00	0.90	33.00	0.63	124150.00	19	50	141	2.70	31	32.30	51.60	4.60
G09C	-42.4131	-69.7822	995.00	1.60	43.00	0.68	149903.50	19	67	58	3.40	36	34.60	51.10	4.60
G10B	-42.0953	69.7749	1060.00	8.80	77.00	0.85	172830.10	17	6	29	0.30	19	75.10	88.70	8.00
G10C	-42.0953	69.7749	1060.00	4.50	60.00	0.79	163455.50	18	7	83	0.40	19	67.60	85.20	7.70
G11B	-42.3114	-70.0367	999.00	1.30	38.00	0.69	89896.40	17	22	98	1.20	23	31.80	46.40	4.20
G11C	-42.3114	-70.0367	999.00	1.60	43.00	0.72	40621.00	8	3	114	0.40	9	34.10	47.50	4.30
G12A	-42.0353	-70.2992	976.00	3.90	53.00	0.78	170929.50	15	17	104	1.10	19	71.40	91.20	8.20
G12B	-42.0353	-70.2992	976.00	3.30	52.00	0.76	348509.60	50	13	159	0.30	53	53.30	70.20	6.30
G13B	-42.3736	-69.6039	973.00	3.90	58.00	0.80	239706.70	27	40	51	1.50	37	53.30	66.80	6.00
G13C	-42.3736	-69.6039	973.00	7.00	70.00	0.82	28134.20	3	15	79	4.40	7	30.00	36.40	3.30
G14A	-42.4253	-68.8347	1177.00	3.90	58.00	0.79	291854.30	35	83	61	2.40	56	43.30	55.00	4.90
G14C	-42.4253	-68.8347	1177.00	4.10	54.00	0.77	357806.40	64	74	89	1.20	82	36.10	46.90	4.20
G15B	-42.5861	-68.8128	1103.00	4.10	41.00	0.77	26296.80	3	11	52	4.30	5	39.20	51.00	4.60
G15C	-42.5861	-68.8128	1103.00	1.60	45.00	0.69	65107.30	5	23	135	4.30	11	44.90	65.40	5.90
G17C	-41.7119	-69.6192	1275.00	1.10	35.00	0.65	206061.00	25	13	126	0.50	28	58.10	88.90	8.00
G18B	-42.9306	-71.2606	617.00	2.50	47.00	0.73	42608.50	103	83	208	0.80	123	2.80	3.90	0.40
G19B	-42.8064	-71.6608	576.00	1.80	42.00	0.71	20037.80	26	95	249	3.60	49	3.30	4.60	0.40
G19C	-42.8064	-71.6608	576.00	1.30	39.00	0.69	11635.10	53	61	236	1.10	68	1.40	2.00	0.20
G20A	-42.3847	-71.2453	663.00	1.50	42.00	0.67	20451.30	11	50	164	4.70	23	7.20	10.60	1.00
G20B	-42.3847	-71.2453	663.00	0.90	36.00	0.68	12081.70	13	33	140	2.50	21	4.50	6.70	0.60
G20C	-42.3847	-71.2453	663.00	3.30	51.00	0.73	5681.20	6	24	85	3.80	12	3.70	5.00	0.50
G21A	-42.1672	-71.3572	616.00	0.90	20.00	0.61	41763.50	51	25	152	0.50	57	5.90	9.80	0.90
G21B	-42.1672	-71.3572	616.00	1.10	37.00	0.64	32364.80	38	30	237	0.80	45	5.80	9.10	0.80
G21C	-42.1672	-71.3572	616.00	1.90	44.00	0.73	16467.80	23	14	79	0.60	26	5.10	7.00	0.60
G22B	-42.0303	-71.5761	275.00	1.50	45.00	0.69	33055.70	84	185	70	2.20	129	2.10	3.10	0.30
G22C	-42.0303	-71.5761	275.00	2.00	46.00	0.73	19459.80	45	109	127	2.40	71	2.20	3.10	0.30
G30A	-43.7439	-69.8186	670.00	12.37	78.30	0.85	126233.00	4	39	76	9.10	14	73.40	85.90	0.70
G30B	-43.7439	-69.8186	670.00	3.58	55.60	0.78	145207.00	6	48	209	8.20	18	63.00	80.70	0.60
G30C	-43.7439	-69.8186	670.00	8.72	71.60	0.82	178090.00	6	50	107	9.20	18	81.20	98.80	0.80
G31A	-43.6650	-70.0839	825.00	5.46	59.00	0.79	0.00	8	21	131	2.50	14	52.30	66.40	5.30
G31C	-43.6650	-70.0839	825.00	2.95	43.20	0.68	0.00	11	45	102	4.30	21	45.20	66.40	5.30
G31D	-43.6650	-70.0839	825.00	5.25	56.40	0.75	0.00	5	32	91	6.40	13	41.40	55.20	4.40
G35A	-43.3244	-70.8961	875.00	4.23	46.70	0.72	22167.00	5	18	80	3.40	10	17.50	24.30	1.90
G35B	-43.3244	-70.8961	875.00	5.64	52.40	0.75	14432.00	4	14	51	3.20	8	15.10	20.10	1.60
G37A	-43.5250	-71.5181	473.00	0.54	27.80	0.56	141653.00	6	44	422	8.00	16	60.00	106.80	8.50
G37B	-43.5250	-71.5181	473.00	0.67	28.30	0.60	149258.00	9	31	343	3.50	17	64.40	107.80	8.60
G38A	-41.8508	-71.4219	627.00	1.62	37.40	0.68	27338.00	30	31	90	1.00	37	6.00	8.80	0.70
G38B	-41.8508	-71.4219	627.00	1.65	39.40	0.68	35968.00	35	49	92	1.40	46	6.40	9.40	0.80
G38C	-41.8508	-71.4219	627.00	2.77	50.50	0.72	16316.00	25	39	93	1.60	34	3.90	5.40	0.40
G39A	-41.5564	-71.4806	731.00	0.76	30.30	0.59	39981.00	6	12	242	2.10	9	31.60	53.70	0.30
G39B	-41.5564	-71.4806	731.00	0.76	26.20	0.59	35918.00	6	17	303	2.90	10	23.80	40.50	0.20
G39C	-41.5564	-71.4806	731.00	0.36	25.00	0.53	115956.00	15	31	601	2.00	23	35.30	66.20	0.40
G40A	-40.3447	-71.5064	898.00	0.92	33.70	0.64	13772.00	22	59	55	2.70	36	3.20	5.00	0.40
G40B	-40.3447	-71.5064	898.00	0.60	29.80	0.60	32916.00	23	62	95	2.60	38	7.00	11.80	0.90
G41A	-41.1061	-71.4831	849.00	0.85	31.40	0.65	103534.00	60	43	177	0.70	70	12.00	18.50	0.10
G41B	-41.1061	-71.4831	849.00	2.80	48.70	0.78	139480.00	52	47	143	0.90	63	18.00	23.20	0.20
G41C	-41.1061	-71.4831	849.00	0.60	28.60	0.57	133871.00	94	68	226	0.70	110	9.90	17.30	0.10
G44B	-41.2089	-70.1667	999.00	2.26	44.80	0.69	63247.00	9	1	95	0.10	9	53.10	77.10	6.20
G44C	-41.2089	-70.1667	999.00	3.63	50.40	0.72	303657.00	35	41	123	1.20	45	55.40	76.70	6.10
G48A	-40.8936	-71.4950	805.00	1.79	42.80	0.68	22054.00	34	57	177	1.70	48	3.70	5.50	0.40
G48B	-40.8936	-71.4950	805.00	2.91	50.30	0.75	23517.00	31	51	136	1.60	44	4.40	5.80	0.50
G48C	-40.8936	-71.4950	805.00	2.48	46.50	0.73	18720.00	19	38	130	1.90	28	5.30	7.30	0.60
G49A	-40.4853	-71.5894	903.00	0.74	32.90	0.59	37522.00	35	55	143	1.60	49	6.30	10.70	0.90
G49B	-40.4853	-71.5894	903.00	1.60	39.00	0.65	23932.00	23	58	134	2.60	37	5.30	8.20	0.70
G50A	-40.1956	-71.3614	976.00	0.93	32.60	0.62	23618.00	73	9	245	0.10	75	2.50	4.10	0.30
G50B	-40.1956	-71.3614	976.00	2.48	48.90	0.72	18111.00	44	7	145	0.10	45	3.20	4.50	0.40
G50C	-40.1956	-71.3614	976.00	1.41	41.00	0.66	45107.00	106	31	284	0.30	114	3.20	4.80	0.40
G51A	-40.1289	-71.6456	791.00	2.26	45.90	0.73	6474.00	15	19	58	1.20	20	2.70	3.60	0.00
G51B	-40.1289	-71.6456	791.00	3.73	53.00	0.76	2563.00	10	13	37	1.30	13	1.60	2.10	0.00

Note: Rs: sphere equivalent radius of hexagonal crystal with the same surface/volume ratio; FT: geometric correction factor for age calculation; eU: effective uranium concentration.

3.3.3 Time-temperature modeling

In this work we used the QTQt software (version PC 5.7.0) to model thirty samples including those, previously never modeled, from Savignano et al. (2016). The program allows inverting AFT annealing and AHe diffusion parameters with the Markov chain Monte Carlo method (Gallagher, 2012; Gallagher et al., 2009). The inversion code incorporates kinetic models of He diffusion in apatite (Flowers et al., 2009; Gautheron et al., 2009) and AFT annealing multi-kinetic model (Ketcham et al., 2007). The modeling procedure is detailed in Gallagher (2012). The input parameters used to model each profile are: (i) central AFT ages, (ii) track length distribution, (iii) Dpar values, and (iv) single-grain AHe ages, with grain size and chemical characteristics. Chemical composition ranges of the analyzed apatites were taken into consideration during both AFT and AHe modeling, by imposing the mean measured Dpar values for the sample, following Gautheron et al. (2013). Thermal history constraints included: (i) age and emplacement depth of intrusive bodies such as the Permian Mamil Choique formation (t = 275 ± 25 Ma, T = 350 ± 50°C), the Lower Jurassic Subcordilleran Batholith and equivalents (t = 190 ± 20 Ma, T = 350 ± 50°C), the Upper Jurassic to Lower Cretaceous North Patagonian Batholith (t = 135 ± 35 Ma, T = 350 ± 50°C), and Upper Cretaceous shallow intrusions (t = 80 ± 20 Ma and T = 100 ± 20°C); (ii) depositional age of sedimentary rocks such as the Osta Arena Formation (Lower Jurassic) and Cañadon Asfalto Formation (Upper Jurassic); (iii) age of the unconformity (Early Jurassic) on top of the basement; and (iv) present day temperature (10 ± 10 °C for all the rocks). Thermal history simulation results were obtained taking into account the influence of α-recoil damage, grain size and apatite kinetic properties.

3.4 Results

A homogeneous single grain AFT population (χ^2 test passed) was detected in all the samples, whereas significant intra-sample variability was observed in only two cases among the AHe data despite the large variety of rock types and U-Th-Sm composition (in both these latter samples, apatites derive from Paleozoic rocks from the foreland). No particular relationships occur between age, eU (eU = [U] + 0.235[Th] + 0.0047[Sm]) and grain radius. Obtained AFT ages are in all instances older than AHe ages, as expected given the closure temperatures. The regional picture is characterized by a marked thermochronological age difference between the Precordillera and the foreland (Figure 3.1B, Figure 3.1C and Figure 3.4). In fact, the samples from the Precordillera show consistent middle Miocene to Pliocene cooling ages. In contrast, AFT and AHe ages in the broken foreland range from 154.4 ± 6.0 Ma to 59.3 ± 4.2 Ma, and from 109.2 ± 9.8 Ma to 26.9 ± 2.4 Ma, respectively. Both AFT and AHe ages are always younger than depositional age of the sampled sedimentary rocks. This testifies that all samples were affected by a significant heating able to almost completely reset both AFT and AHe systems. It is noteworthy that the samples from the broken foreland display short fission track lengths (Table 3.1), thus suggesting a long residence in the so-called Partial Annealing Zone (~60 – 120°C; Green et al., 1989).

Cretaceous granitoids collected in the Precordillera register Late Neogene AFT and AHe records excepted for three samples with older AFT or/and AHe ages.

Temperatures were then extracted from the best-fit models (Figure 3.4; see Data Repository, Figures DR1a and DR1b) at different times and then plotted in the map of Figure 3.5. During Early Jurassic times, most of samples were at shallow depths (at temperatures comprised between 40 and 80°C) whereas some granitoids were emplaced along the so-called Subcordillera Plutonic Belt (red dots in Figure 3.5A). Between Early and early Late Cretaceous maximum burial temperatures, exceeding or very close to the total reset limit for fission tracks in apatite (i.e. ~120°C; Green et al., 1989) were reached all across the foreland. Soon later, exhumation of the foreland samples started at very slow rates. From the Late Cretaceous, a clear differentiation occurred between the foreland and the orogen. Samples from the latter still lay at greater depth (except for a few intrusions, away from the basins and therefore not affected by any burial, that were already close to the surface). The foreland area remained quite stable for the following 70 m.y., whereas the Precordillera was affected by rapid cooling during late Miocene – Pliocene times.

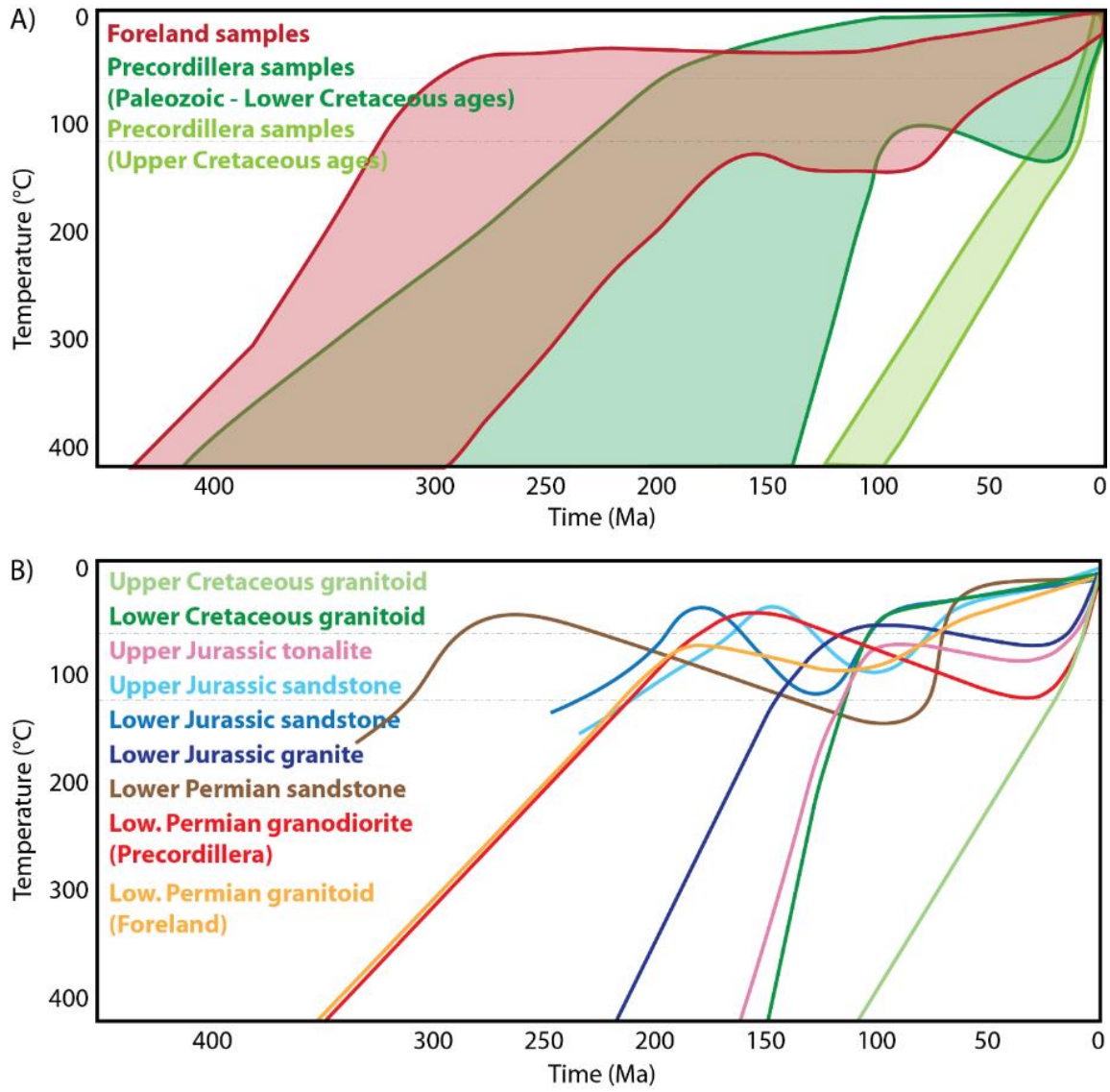

Figure 3.4 – Best-fit time-temperature models for all samples considering: (A) their location (Precordillera or broken foreland), or (B) their age and lithology.

3.5 Discussion

Best-fit thermal histories derived from the inverse modeling for samples collected in the foreland show maximum burial at temperatures higher than 110°C (Figure 3.4Figure 3.5Figure 3.6). Despite a precise estimation of paleo-geothermal gradients is not possible, these data demonstrate a regional burial of 3-4 km across the foreland (taking into account variations around an average geothermal gradient of ~ 30 °C/km). This significant burial may be explained by the thickness of the Jurassic-Early Cretaceous sedimentary succession deposited in the half-graben systems forming the Cañadón Asfalto Rift Basin (Figari et al., 2015; Zaffarana and Somoza, 2012). The samples from the Precordillera were collected close to the thick successions deposited in Piltriquitrón and Rio Mayo Basins (Cesari, 1977; Ghiorzi, 1979) for which basin subsidence was related to back-arc extension triggered by ongoing slab roll-back and slab steepening (Figure 3.6B; Horton, 2018a). Also for these samples, an exhumation of 2.5 to 4 km may be envisaged.

Regional exhumation recorded by our data is consistent with the unconformity recognized between the Jurassic – Early Cretaceous succession and the synorogenic Late Cretaceous deposits (Gianni et al., 2015a). This regional exhumation was favored by the strong increase of coupling between the subducting plates and the overriding plate (Horton and Fuentes, 2016), which also resulted in regional uplift (Figure 3.6C; e.g. Mescua et al., 2013). Strong coupling is related to slab shallowing induced by the change of absolute motion of the South American Plate, which became west directed (Maloney et al., 2013). Overriding plate kinematics exert a first-order control on slab dip evolution (Cerpa et al., 2018). This is dominant over oceanic subducting plate convergence as demonstrated in the Central Andes, where an increase of deformation occurred during stages of convergence rate decrease (Oncken et al., 2006; Silver et al., 1998). Slab shallowing is recognized to produce significant foreland uplift, as observed along the present day flat-slab in central Chile (Ramos et al., 2002) and Peru (Bishop et al., 2018). Examples in the geological record include the Late Cretaceous to early Eocene low-angle subduction in the Laramide orogen (USA; Fan and Carrapa, 2014; Jordán et al., 1983) and Paleocene low-angle subduction in Alaska (Finzel et al., 2011). In northern Patagonia, exhumation of the overriding plate during the Late Cretaceous may have been further enhanced by the subduction of mid- ocean ridges, further triggering shallow subduction and possibly also opening of a slab window (Aragón et al., 2011). This latter may have added a further component of foreland uplift (Figure 3.6; Ávila and Dávila, 2020; Guillaume et al., 2009). The integrated uplift and coeval erosion may account for the cooling ages recorded over the whole northern Patagonia, and particularly in the broken foreland. Although a significant spread of cooling ages characterizes the foreland samples, almost all of them record exhumation during upper plate shortening, around the Late Cretaceous deformation peak and through the early Paleocene (Figure 3.6D). Actually, few single grain ages from the Gastre-Navidad area yielded AHe ages spanning through the early Eocene and the Oligocene (Savignano et al., 2016). However, discrepancy among replicates makes a reliable evaluation of thermal history not possible.

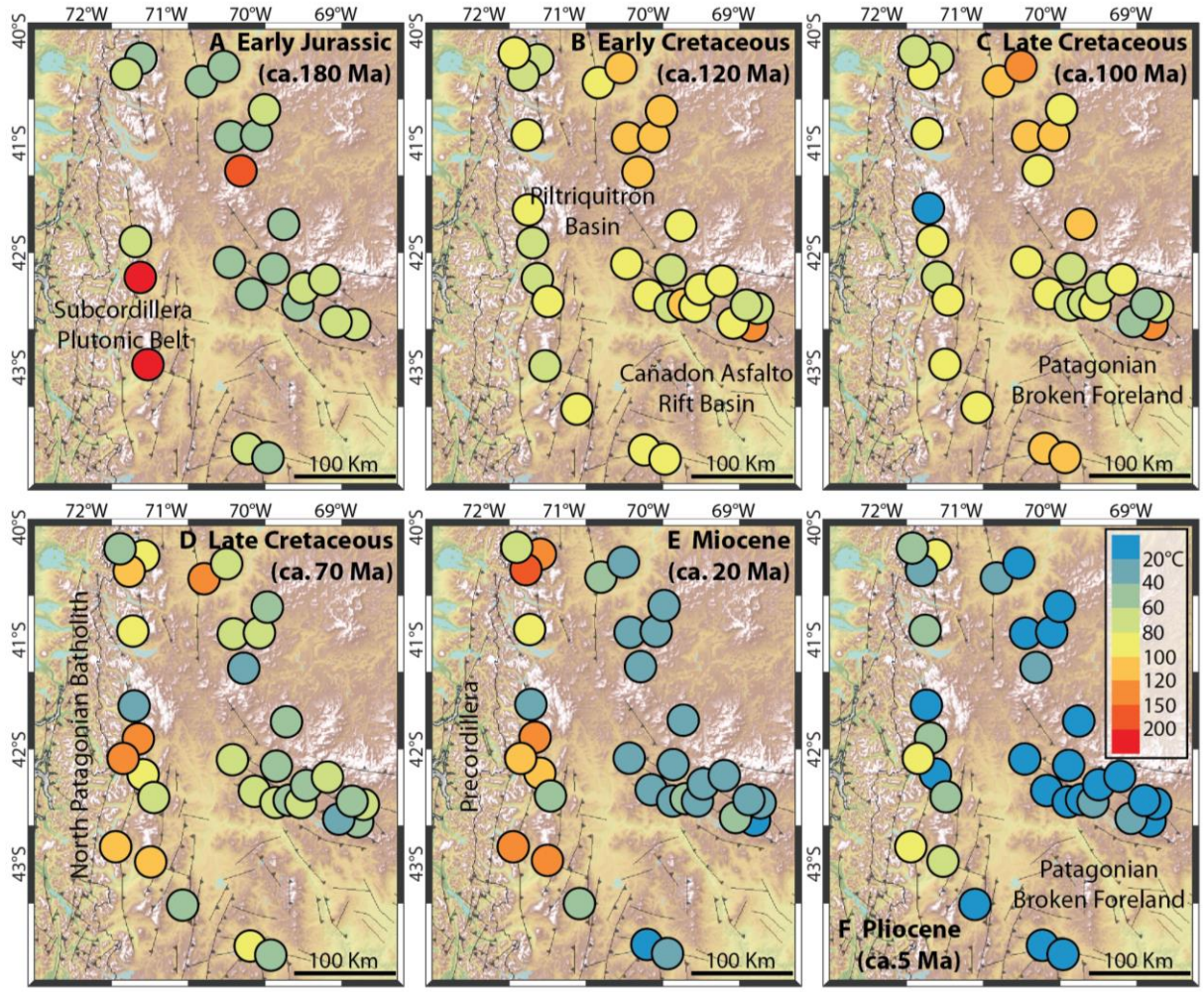

Figure 3.5 – Reconstructed Early Jurassic to Pliocene (A-F) paleotemperature evolution for the samples collected in northern Patagonia.

The lack of late Eocene – early Miocene exhumation both in the foreland and the mountain range is a clear signal of tectonic quiescence – or even local subsidence – which we relate to plate decoupling due to the onset of slab rollback and re-steepening of the subduction geometry (Figure 3.6E). This was induced by a sharp reduction in average trenchward velocity and/or by subduction of the former oceanic segment of the Farallon plate and related decreasing buoyancy (Aragón et al., 2011; Maloney et al., 2013). Coeval retroarc magmatism was widespread (Pilcaniyeu Belt, El Maitén Belt and Somuncura Plateau; De Ignacio et al., 2001; Echaurren et al., 2016; Iannelli et al., 2018). Cooling ages and thermal histories derived from thermal modeling indicate distinct evolution patterns for the Andean chain and the broken foreland during the Neogene. Indeed, middle Miocene – Pliocene exhumation is solely recorded by our data in the Precordillera, although the cooling pattern is not homogenous throughout the investigated area. In fact, a few samples collected from sub-volcanic bodies show a rapid cooling soon after emplacement at shallow depths during the Cretaceous (Adriasola et al., 2006). Other samples were affected at the same time by minor heating, maybe related with the intrusion of the North Patagonia Batholith. While Late Cretaceous – Paleocene regional shortening was related to flat-slab subduction, Neogene deformation occurred without major changes in the subduction geometry (Echaurren et al., 2019). Plate coupling

increase at this time was rather controlled by plate reorganization due to higher convergence rates and a mostly orthogonal subduction induced by the break-up of the Farallon Plate at ~23 Ma (Lonsdale, 2005; Somoza, 1998). On the other hand, our data do not record any significant Neogene exhumation in the broken foreland. Although substantial middle Miocene – Pliocene shortening was suggested also in this sector (Bilmes et al., 2013), the lack of any thermochronology signal since the Paleogene confirms that Neogene deformation was minor (Savignano et al., 2016) and anyway unable to produce significant vertical movements. Based on inverse modeling, we propose that the thermal history of the foreland over the last 70 m.y. was characterized by regional cooling not affected by any particular thermal and/or important deformation event (with the exception of few local areas characterized by some heating related with volcanic activity). Available low-temperature thermochronological data from the southern Andean foreland at 47° – 49°S (Deseado Massif; Fernández et al., 2020) suggest that such a nearly steady-state, slow cooling may have characterized the whole Patagonian foreland since the Late Cretaceous.

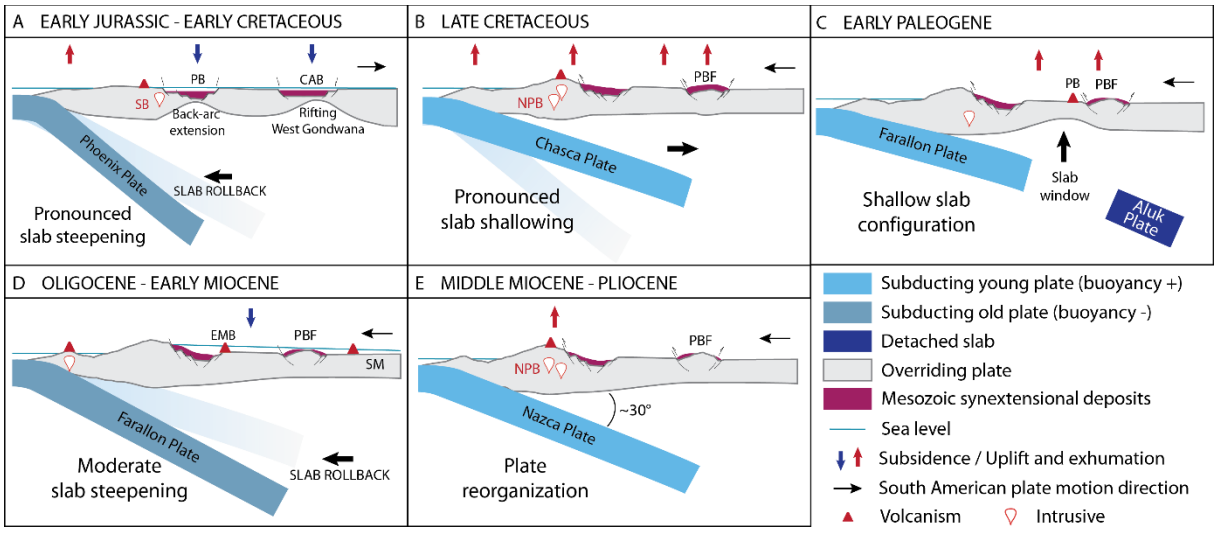

Figure 3.6 – Cartoons showing interpreted geodynamic evolution and migrations of the magmatism revealing slab geometry variations. (A) Regional subsidence linked with pronounced slab rollback and Gondwana rifting during Jurassic – Early Cretaceous times (PB: Piltriquitrón Basin, CAB: Cañadon Asfalto Basin, SB: Subcordilleran Batholith). (B) Late Cretaceous shallowing of the subducting slab and increase of plate coupling, triggering tectonic inversion of former basins (PBF: Patagonian Broken Foreland, NPB: North Patagonian Batholith). (C) Paleogene opening of a slab window, enhancing uplift (PB: Pilcaniyeu Belt). (D) Arc retreating (EMB: El Maitén Belt), distal retroarc volcanism (SM: Somuncura plateau) and retroarc quiescence during the late Paleogene to Early Miocene time frame. (E) Increased interplate coupling induced by plate reorganization, triggering exhumation of the Precordillera (and possibly modest deformation of the broken foreland).

3.6 Conclusions

AFT and AHe data, as well as temperature-time history modeling, suggest spatio-temporal variations of exhumation associated with alternating phases of plate-scale regional shortening and tectonic quiescence in Patagonia. Kilometer-scale subsidence during the Jurassic resulted from protracted slab rollback and a rifting phase in the eastern retro-arc. Exhumation of the Precordillera and the broken foreland related to slab shallowing started during the late Early Cretaceous to the Paleocene and was

enhanced by the inversion of former grabens. Thermochronological data in the foreland show minor subsidence from late Eocene to early Miocene. Marked contrast is observed between the broken foreland samples, already at low temperature during Paleogene, and the Precordilleran granite samples, affected by a late reheating phase possibly linked with Miocene arc magmatism. Middle Miocene – Pliocene exhumation is then exclusively recorded in the Andean chain, whereas coeval deformation in the broken foreland was rather limited and anyway insufficient to produce noticeable exhumation. Besides allowing us to define the articulated exhumation pattern characterizing the Andean orogen and its foreland between 40° and 45°S, altogether our results unravel with unprecedented resolution the significant magnitude of Jurassic to Early Cretaceous burial and Late Cretaceous to present unroofing of northern Patagonia.

3.7 Acknowledgments

Funding for this work was provided by the University of Padova (Progetto di Ateneo 2015, CPDA158355) and the Universidad Nacional de Río Negro (PICT-FONCyT 2013-2916, PIP-CONICET 330, U.N. Comahue). S. Boesso, R. Pinna, and L. Bordier are thanked for sample preparation and for their assistance during the analyses.

CHAPTER 4

TRACING THERMAL HISTORY OF THE CENTRAL PATAGONIAN ANDES AND ITS BROKEN FORELAND WITH DETRITAL MULTI-DATING OF FORELAND BASIN DEPOSITS

Marie C. Genge[1,2], Massimiliano Zattin[1], César Witt[2], Alexis Derycke[3], Cécile Gautheron[3], Stefano Mazzoli[4], Marcelo Marquez[5], Maurizio Petrelli[6], Nathan Cogné[7]

[1] Dipartimento di Geoscienze, Università degli Studi di Padova, via G. Gradenigo 6, 35131 Padova, Italy

[2] Univ. Lille, CNRS, Univ. Littoral Côte d'Opale, UMR 8187, LOG, Laboratoire d'Océanologie et de Géosciences, F 59000 Lille, France

[3] Université Paris-Saclay, CNRS, GEOPS, 91405, Orsay, France

[4] School of Science and Technology, Geology Division, University of Camerino, Italy

[5] Servicio Geológico Minero-Argentino, Delegación Patagonia, Barrio Don Bosco km 8, Comodoro Rivadavia, Argentina

[6] Department of Physics and Geology, University of Perugia, Perugia, Italy

[7] Univ Rennes, CNRS, Géosciences Rennes, UMR 6118, 35000, Rennes, France

Declaration

This chapter is focused on the application of both detrital apatite U-Pb and fission tracks thermochronology in the central Patagonian foreland (44 – 48°S) in order to quantify denudation of source area(s) through provenance analysis. It results from two fieldworks carried out across the southern Chubut and northern Santa Cruz provinces (Argentina). This area has been chosen because the San Jorge Basin recorded Cenozoic successions which are exposed along the basin borders. MCG, MZ, CW, AD, CG, SM and MM carried out at least one of the two fieldworks, including sampling for thermochronology dating methods. MCG provided all apatite fission tracks dating, all the figures and the original draft for this paper. MP and MCG achieved the apatite U-Pb data, which have been interpreted by NC, MP and MCG. MZ and CW made a careful review of the original draft and acquired fundings for this work. The following chapter corresponds to the version of the manuscript almost ready to be submitted to Basin Research. Few analyses are still needed before submission to improve the lag-time constraints, as well as the review of the co-authors.

4.1 Abstract

Detrital thermochronology in a wide foreland basin documents erosion of diverse sediment source areas along an adjacent orogen through time. This study presents new detrital apatite thermochronology data (U-Pb and fission tracks) from the central Patagonian foreland (44°S – 48 °S) that identify at first a persistent volcanic input through Oligocene to late Miocene. The apatite U-Pb dating was effective to discriminate AFT ages related to exhumation of the source and to the volcanic input, which can easily overtake the exhumation signal along the Patagonian Andes. This belt is characterized by several orogenic events and has been continuously exhumed since the late Early Cretaceous. Lag time, calculated from the youngest AFT component (~30 Ma), indicates that the entire central Patagonian Cordillera was in steady-state erosion at ca. 30 Ma until the resumption of shortening during the late Neogene. Moreover, our new detrital thermochronological data emphasize a signal of low rate post-orogenic erosional processes (0.1 – 0.4 km/Ma) with a significant unroofing of 2 – 4 km between the Oligocene and the late Miocene. Uniform denudation occurred therefore during a period of relative quiescence, which is following the active tectonics that marked the late Early Cretaceous – middle Eocene period. AFT ages, generally older in the north-eastern central Patagonian foreland, are consistent with a sediment contribution from the erosion of the intraplate belt at these latitudes from the late Eocene to the Miocene. This study constrains the timing and rates of the post-orogenic cooling along the central Patagonian Andes, thus contributing new insights on a period of tectonic quiescence poorly studied.

4.2 Introduction

The modern Andean retroarc foreland basin system represents an elongated trough on the eastern side of the Andean Cordillera (e.g. DeCelles and Giles, 1996; Jordan et al., 1983). The Andean foreland basins record the inception of topographic growth and exhumation phases of the belt from the Northern Andes to the Patagonian Andes (e.g. DeCelles and Horton, 2003; Folguera et al., 2015; Horton, 2018b; Louterbach et al., 2018; Nie et al., 2012; Parra et al., 2012; Roddaz et al., 2010; Romans et al., 2010). It is now accepted that deformation along the Patagonian Andes resulted from fluctuations in slab dynamics, mostly from flat to steep subductions (e.g. Horton, 2018a). Indeed, flat or shallow subduction resulted in a significant coupling between plates evidenced by the shortening along the Andes and coeval growth of an intraplate belt called in Patagonia the 'Patagonian Broken Foreland' (Savignano et al., 2016). These processes may have strongly influenced the vertical rock motion along the chain and caused tectonic deformations that may have exerted strong changes in the sourcing to the foreland area.

A significant amount of data derives from detrital thermochronological tools that have been applied on sandstones from Andean foreland basins (e.g. Bande et al., 2012; Folguera et al., 2015; Leonard et al., 2020; Spikings et al., 2010). However, such studies are lacking for the central Patagonia where Early Cretaceous to upper Miocene sedimentary records exposed around the San Jorge Basin may provide information about the long-term exhumation of the southern segment of the Andes, previously studied

mainly by in-situ analysis (Georgieva et al., 2016, 2019; Guillaume et al., 2013; Thomson et al., 2001; Thomson, 2002; Thomson et al., 2010a), as well as the Patagonian Broken Foreland (Fernández et al., 2020; Savignano et al., 2016). These in-situ thermochronology studies, based on apatite fission tracks

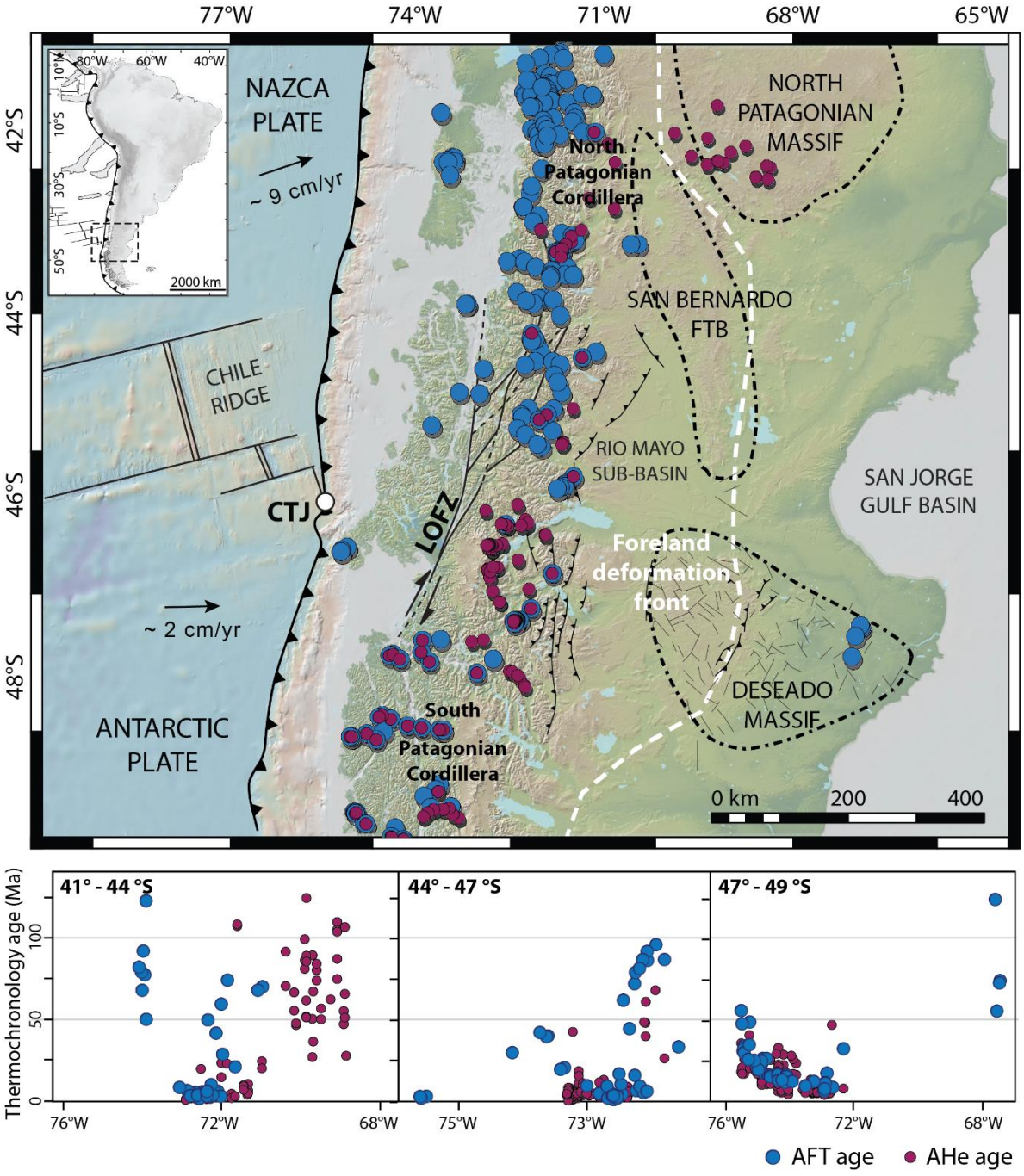

Figure 4.1 – Published apatite (U-Th)/He (AHe) and apatite fission-track (AFT) plotted on a simplified topography and tectonic map of the Patagonia (41 – 50°S; Fernández et al., 2020; Georgieva et al., 2016; Guillaume et al., 2013; Savignano et al., 2016; Thomson et al., 2010, 2001). Areas surrounded by dotted black lines outline the intraplate reliefs belonging to the Patagonian Broken Foreland. White circle indicates the present position of the Chile Triple Junction (Breitsprecher and Thorkelson, 2009). Compilation of thermochronology data from all tectonic domains of the Patagonia plotted by latitudes: north Patagonia (41 – 44°S), central Patagonia (44 – 47°S) and austral Patagonia (47 – 49°S).

(AFT) and (U-Th-Sm)/He (AHe) dating, evidenced Miocene ages along the Cordillera, with few Oligocene and Cretaceous ages in the western and the eastern Patagonian Andes around 46°S, whereas only Cretaceous – early Paleogene ages have been recognized in the Deseado Massif and close to the North Patagonian Massif (Figure 4.1).

Among the different methodologies, single-grain geochronological techniques are particularly powerful to identify source areas. Nevertheless, a major limitation is given by the substantial Andean volcanic input in this area, recognized in the considerable tuffaceous content along the entire stratigraphic column (Allard et al., 2020; Foix et al., 2020; José M. Paredes et al., 2009; Umazano et al., 2009). A key-tool is represented by multi-dating on a single-phase as high-temperature method reveals crystallization age whereas low-temperature ages are related to cooling at shallow depths. The use of multiple chronometers along the South American foreland is prevalent on individual detrital zircon grains (Gianni et al., 2017; Leonard et al., 2020; Romans et al., 2010; Ruiz et al., 2004; Saylor et al., 2011; among others), whereas the less resistant and less abundant detrital apatite grains are often disregarded (Carrapa et al., 2009).

This work is based on U-Pb and fission tracks dating of detrital apatites which were collected from Cretaceous to upper Miocene sedimentary successions exposed in the San Jorge Basin, around the San Bernardo Fold and Thrust Belt (FTB) and the Deseado Massif, which are the main topographic features of the central Patagonian foreland (Figure 4.2). The San Jorge Basin is a deep E-W elongated depocenter resulting from a long-lived subsidence characterized by a complex structural pattern (Gianni et al., 2015a). This basin interacts with the NNW-trending contractional structures of the San Bernardo FTB. Both extensional and compressional styles in the San Bernardo FTB are mainly triggered by the reactivation of inherited structures developed during a late Early Cretaceous – early Paleogene shortening event (Gianni et al., 2015b; Navarrete et al., 2018).

Our data demonstrate that sediments, volcanic input apart, derived both from distant (i.e. the Cordillera) and local (i.e. the San Bernardo FTB) sources. Furthermore, these sediments allow to obtain first order constraints for the reconstruction of the topographic growth and shed light into the geodynamics of the entire system.

4.3 Regional geological setting

The current geodynamic configuration of central Patagonia is governed by the subduction of the Nazca and Antarctic plates beneath the South American plate (Figure 4.1 and Figure 4.2). The central Patagonia (44 – 48 °S) corresponds to the transitional zone between the north and the austral Patagonia. This region is coincident with the Chile Triple Junction at 46°30’ S, where the Chilean mid-oceanic ridge segment, which separates the Nazca and the Antarctic oceanic plates, is currently being subducted beneath the South American plate (e.g. Cande and Leslie, 1986). The northward migration of the Chilean mid-oceanic ridge (from 54°S to 46°S) during the past 14 Ma resulted in the opening of a slab window extended below the whole Austral Patagonia (e.g. Breitsprecher and Thorkelson, 2009; Scalabrino et al., 2009).

Compared to other sectors of the Andean Cordillera, the central Patagonian Andes are characterized by lower elevations, narrow width and reduced crustal thickness (Mpodozis and Ramos, 2008; Orts et al., 2012). The foreland at these latitudes is represented by the San Jorge Basin (Figure 4.1), which is a broadly E-W elongated off-shore and on-shore intraplate basin limited to the south by the igneous-metamorphic province known as the Deseado Massif (e.g. Giacosa et al., 2010). This basin is bordered to the north by the sedimentary successions deposited in the Cañadón Asfalto Basin (Figari et al., 2015), which is derived from the breakup of the Gondwana paleocontinent through the entire Jurassic and the Early Cretaceous (Fitzgerald et al., 1990; Mpodozis and Ramos, 2008). Inversion of the Cañadón Asfalto Basin, occurred episodically since late Early Cretaceous and resulted in the development of the NNW-SSE-trending broken (deformed) foreland, named the San Bernardo FTB, dividing the eastern San Jorge Basin from the Rio-Mayo Sub-basin (Figari et al., 1999; Homovc et al., 1995; Navarrete et al., 2015; Peroni et al., 1995). Thermochronological data obtained in the Precordillera and the foreland at ~42°S

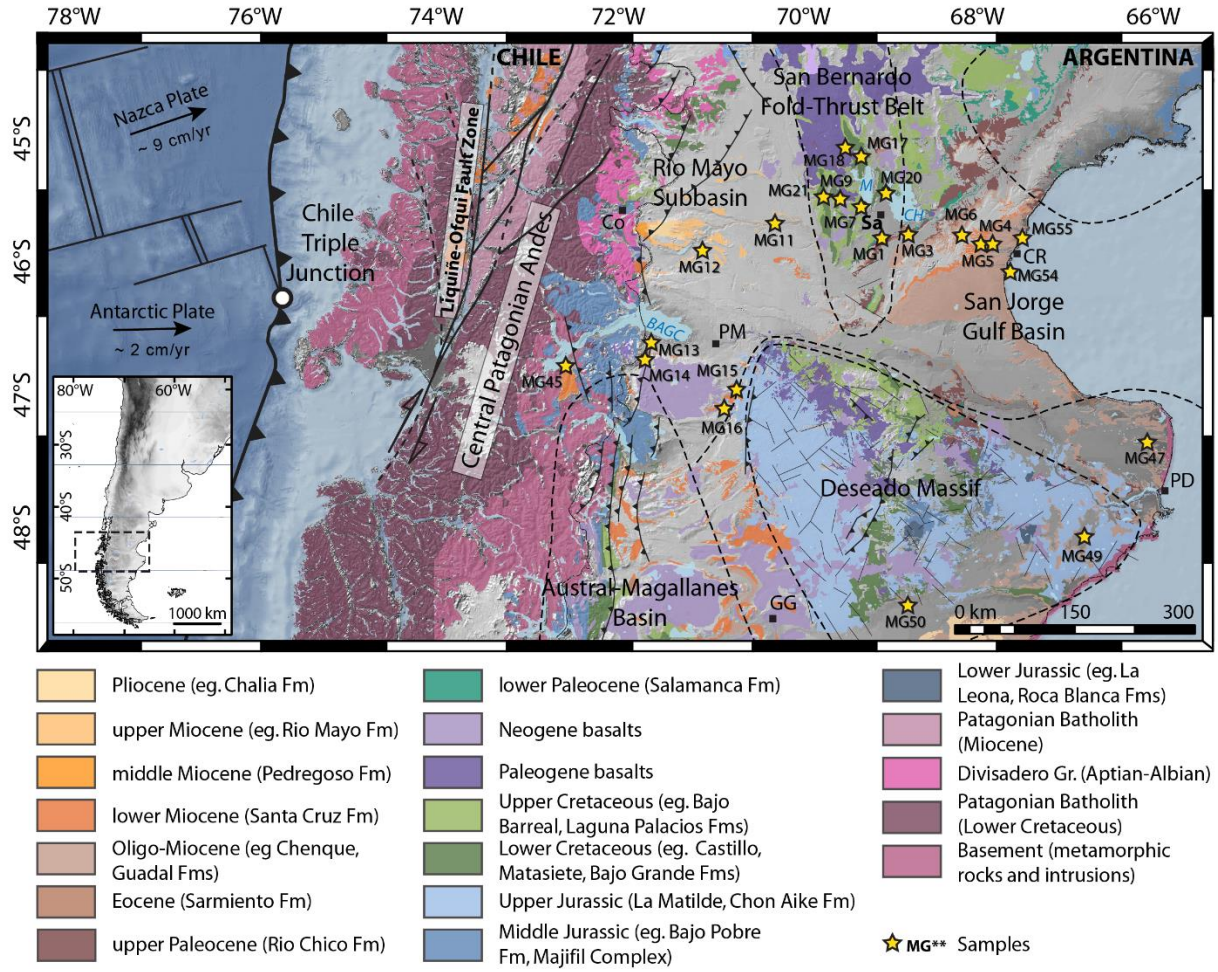

Figure 4.2 – Geological map of the Central Patagonian Andes. Black squares correspond to main localities. Co: Coyhaique. CR: Comodora Rivadavia. GG: Gobernadore Gregores. PD: Puerto Deseado. PM: Perito Moreno. Sa: Sarmiento. In blue BAGC: Buenos Aires – General Carrera lake, M: Musters lake, CH: Colhué-Huapi lake. Yellow stars indicate sample location. Geological units are described in the legend (Anselmi et al., 2004b; Ardolino et al., 2003; Cobos et al., 2003; Dal Molin, 1998; Escosteguy et al., 2003; Giacosa et al., 2001a; Giacosa and Genini, 1998; Lizuain et al., 1995; Panza et al., 2018, 2003, 2001a, 2001b, 1998, 1994; Panza and Márquez, 1994; Pezzuchi, 2018; Sciutto et al., 2008, 2000).

(Figure 4.1) suggest that this intraplate belt was mostly developed during a period with shallow-slab subduction (from late Early Cretaceous to early Paleogene) related to arc and chain broadening processes including coupling between the foreland and the orogen (Savignano et al., 2016).

The major unconformity observed regionally on top of the Jurassic – Early Cretaceous deposits is related to the late Early Cretaceous to early Paleogene E-W shortening associated with a slab shallowing in the region (Horton, 2018a; Navarrete et al., 2016, 2018) that progressed to a flat-slab during Late Cretaceous (Gianni et al., 2018). This change of slab dip is originated from the increase of convergence rates and the switch of the absolute velocity of the South American plate to the west (Figure 4.3; Maloney et al., 2013). This E-W shortening affected the whole central Patagonia as evidenced by the synorogenic character of the late Early – Late Cretaceous Chubut Group, generally characterized by a high proportion of volcaniclastic supply and mainly exposed across the San Bernardo FTB (Figure 4.2; e.g. Allard et al., 2020; Clavijo, 1986; Gianni et al., 2015a; Homovc et al., 1995; Lesta and Ferello, 1972; Navarrete et al., 2015; Tunik et al., 2004; Umazano et al., 2012). The E-W main stress also controlled the coeval N-S extension of the San Jorge Basin, with the reactivation of structures mostly parallel to the maximum horizontal stress (Foix et al., 2012; Gianni et al., 2015b; Ramos, 2014).

The continental Chubut Group is locally covered by transitional to unconformable marine successions of the Danian – Paleocene Salamanca Formation (Bellosi et al., 2000; Clyde et al., 2014; Lesta and Ferello, 1972; Navarrete et al., 2015). Deposition of these sediments is related to an Atlantic marine transgression given by a global highstand (Haq et al., 1987), combined with regional tilting linked to the Andean uplift (Nullo and Combina, 2011) and/or with dynamic subsidence focused at the edges of a flat-slab segment (Gianni et al., 2018). Subsequent regression is recorded by the continental Rio Chico Group (late Paleocene – middle Eocene) deposited conformably above the Salamanca Formation (Feruglio, 1949; Foix et al., 2013; Gianni et al., 2017; Krause and Bellosi, 2006; Navarrete et al., 2015; Raigemborn et al., 2010). The Rio Chico Group subsequently evolves to the overlying middle Eocene – early Miocene continental Sarmiento Formation, extensively composed of tuffaceous deposits accumulated under low subsidence rates (Bellosi, 2010; Feruglio, 1949; Figari et al., 2002, 1999; Legarreta and Uliana, 1994; Ré et al., 2010). The upper section of the Sarmiento Formation is laterally interfingered with late Oligocene – middle Miocene marine deposits (Figure 4.3; Barreda and Bellosi, 2014; Bellosi, 2010; Bellosi et al., 2002; Paredes et al., 2015).

Several marine transgressions from the Atlantic Ocean flooded most of the foreland and reached the present Patagonian Andes during the Miocene (Bechis et al., 2014; Encinas et al., 2019, 2018; Malumian and Nanez, 2011; Ramos, 1982). The marine deposits are gathered into different units depending mostly on their location and their age: i) the Chenque Formation in the San Jorge Basin assigned to 86Sr/87Sr ages of 19.6 to 15.3 Ma (Cuitiño et al., 2015b) is limited to the west by the San Bernardo FTB; ii) the late Oligocene San Julián Formation and the early Miocene Monte León Formation (22.12 – 17.91 Ma) surrounding the Deseado Massif (Parras et al., 2012); iii) the Guadal Formation (Centinella Formation in Argentina), or El Chacay Formation to the south, representing the westernmost deposits of this Atlantic transgression (~19 Ma; Cuitiño et al., 2015a). All these ages have been obtained

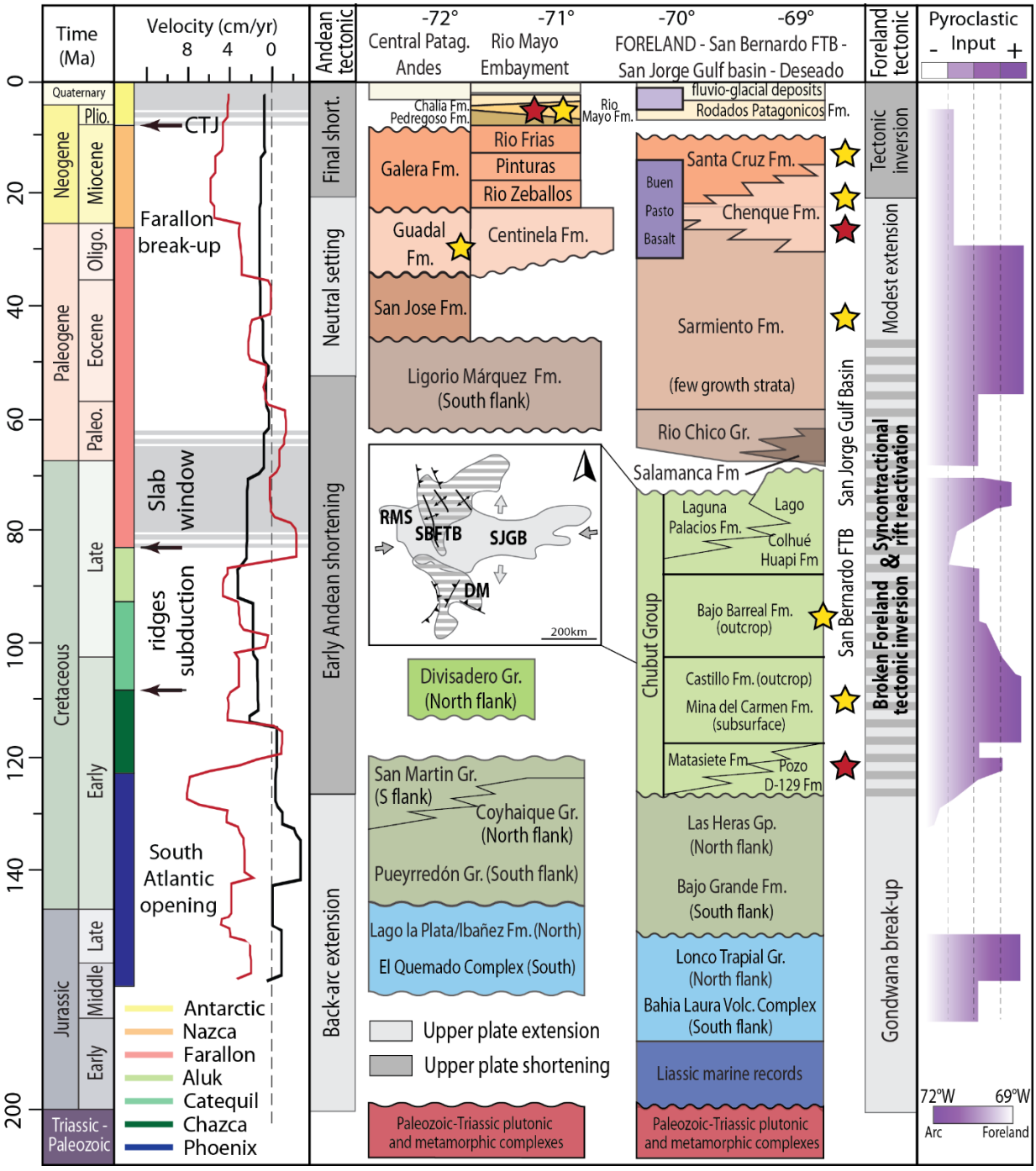

Figure 4.3 – Chronological table for the central Patagonia between 45 and 48°S depicting plate convergence variations (Maloney et al., 2013), slab window events (CTJ for Chile Triple Junction; (Breitsprecher and Thorkelson, 2009; Maloney et al., 2013), stratigraphic log indicating diverse formations found north and south of the San Jorge Gulf Basin (e.g. Gianni et al., 2015a), deformation mode along the Andean Cordillera and its foreland (e.g. Horton, 2018b) and volcanic input variations considering formations and distance from the magmatic arc (Foix et al., 2020 and references therein). The central panel is a sketch of the complex tectonic setting in the area during Late Cretaceous (Gianni et al., 2015a); DM: Deseado Massif, RMS: Rio Mayo Sub-basin, SBFTB: San Bernardo Fold and Thrust Belt, SJGB: San Jorge Gulf Basin. Stars indicate the different formations sampled in this study: yellow stars for samples analyzed only with AFT method and red stars for samples analyzed both with AFT and apatite U-Pb dating methods.

from 87Sr/86Sr chronostratigraphy from skeletal material as oysters' valves (Cuitiño et al., 2015b, 2015a; Parras et al., 2012). These marine deposits grade transitionally to synorogenic early – middle Miocene fluvial and aeolian deposits of the Santa Cruz Formation (Barreda and Bellosi, 2014; Cuitiño et al., 2016, 2015a; Lesta et al., 1980). The sedimentary succession is closed by late Miocene to Pleistocene fluvio-glacial and alluvial units (i.e. Rio Mayo Formation; Dal Molin and Franchi, 1996; De Iuliis et al., 2008). Arc volcanism was coeval to sedimentary deposition into the foreland through the Eocene, part of the Oligocene and the entire Neogene (Butler et al., 2020 and references therein; Suárez et al., 2015).

4.4 Material and methods

Twenty-three samples were collected from sedimentary outcrops in the Cordillera, the proximal foreland and the distal foreland including four samples from the Chubut Group exposed in the southern San Bernardo FTB (Table 1; Figure 4.4A). Cenozoic samples represent different sedimentary successions spanning from middle Eocene to upper Miocene: the Sarmiento Formation, the Chenque Formation (Figure 4.4B, Figure 4.4C and Figure 4.4D), the Santa Cruz Formation (Figure 4.4E) and the Rio Mayo Formation (Figure 4.4F). These samples give the chance to investigate the evolution of the chain during a ~40 m.y. period. Detrital apatite fission tracks (AFT) thermochronology was applied to all the sandstones whereas apatite U-Pb geochronology was limited to five selected samples from different sedimentary formations. All detrital samples were processed to extract apatite crystals by standard mineral separation techniques given by crushing, magnetic separator and heavy liquids (sodium metatungstate and methylene iodide with a density of 2.89 $g.mL^{-1}$).

4.4.1 Apatite Fission Tracks

Spontaneous fission decay of 238U in apatite lead to the accumulation of linear damage trails in the crystal lattice (e.g. Hurford and Green, 1982; Gleadow et al., 1986; Reiners and Brandon, 2006). These trails are erased above ~120 °C and retained below ~60 °C, defining the range of temperature for the Partial Annealing Zone (PAZ; Green et al., 1989). All the samples were dated by the external detector method at the University of Padua (Italy) using a Zeta calibration factor for Fish Canyon and Durango age standards (Gleadow, 1981; Hurford, 1990). Apatites extracted from the detrital samples were mounted in epoxy, polished and etched in a 5M HNO3 solution at 20°C for 20s to reveal spontaneous fission tracks. Apatite mount were then covered by U-poor mica sheet as external detector and irradiated at the Radiation Center of Oregon State University with a nominal fluence of 9×1015 neutrons/cm². Induced tracks on the mica detectors appeared after etching in 40% HF at 20°C for 40 minutes. Ages were obtained after fission tracks counting and statistical processing with the Trackkey software (Dunkl, 2002; Table 2). Only 10 to 67 grains per sample were analyzed due to the paucity of apatites in the samples (Table 2).

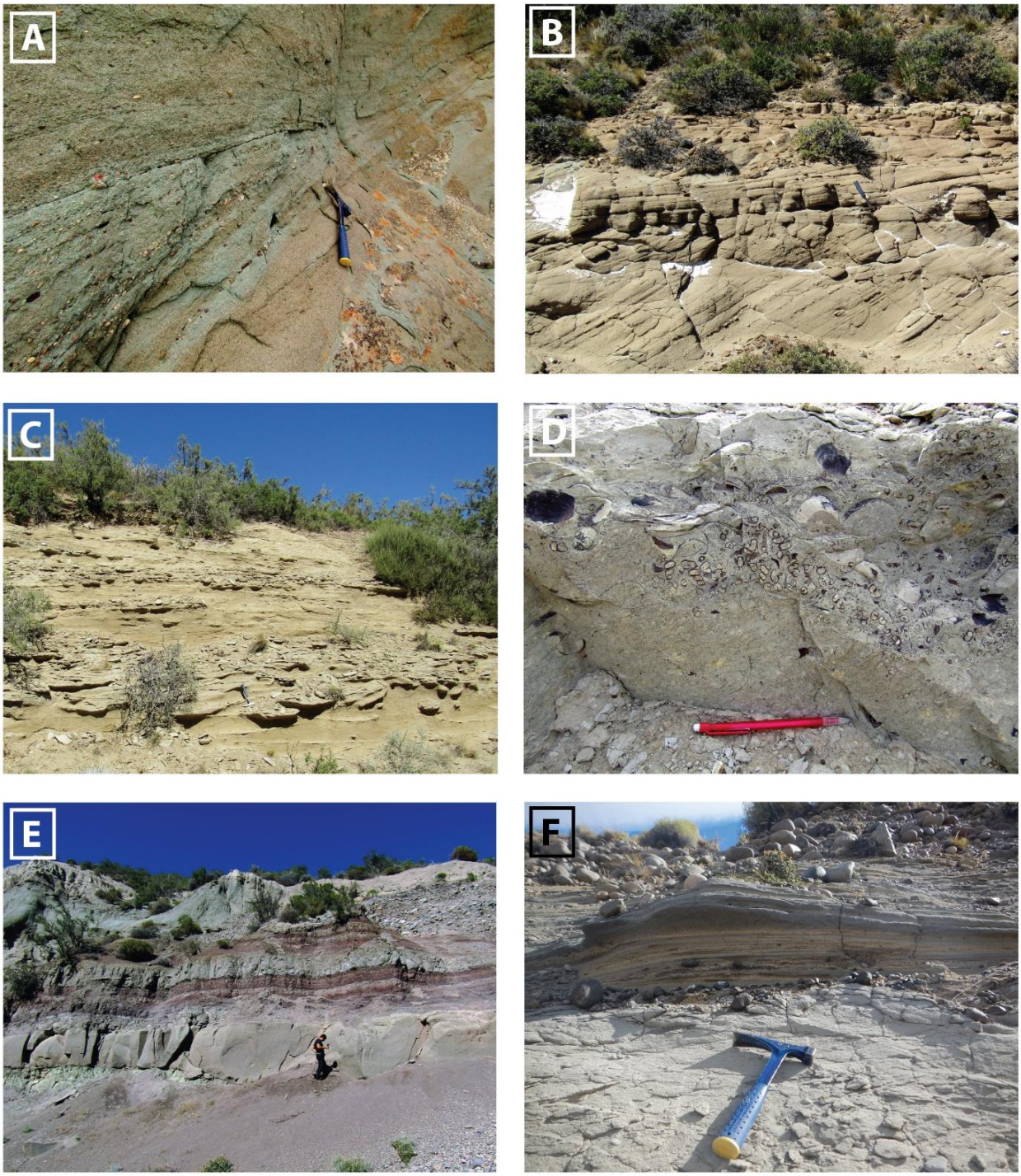

Figure 4.4 - Pictures of sedimentary formations sampled for this study: Cretaceous deposits of the Chubut Group (A), Oligo-Miocene marine deposits of the Chenque Formation and equivalents (B, C and D), Miocene strata of the Santa Cruz Formation (E), late Miocene Rio Mayo Formation (F).

4.4.2 Apatite U-Pb dating

Along the Andes, the exhumation signal may be easily overtaken by the significant volcanic input, which is recognized in the detrital record by the presence of considerable tuffs in the entire region (Figure 4.3). In order to distinguish detrital AFT ages related to exhumation from those related to rapid magmatic cooling, apatite grains belonging to the youngest cluster were dated by apatite U-Pb chronology. Indeed,

as the closure temperature of this thermochronometer is around 450 – 550 °C (Cherniak et al., 1991), an U-Pb age overlapping the AFT cooling age is indicative for magmatic cooling. However, U-Pb dating on apatite is more challenging than in zircons as the amount of uranium is generally lower and the content of common Pb higher. Therefore, apatite grains are discordant in the U-Pb system and a ^{207}Pb-based correction is needed using a known initial ^{207}Pb/^{206}Pb ratio (e.g. Chew et al., 2014).

TABLE 1. SUMMARY OF SAMPLE INFORMATION

Samples	Field (WGS84)			Geology		
	Longitude	Latitude	Elev. (m)	Lithology	Formation	Stratigraphic age
MG1	-68.8806	-45.7784	395	medium sandstone	Sarmiento	Eocene
MG3	-68.7684	-45.7491	398	sandstone	Sarmiento	Eocene
MG4	-67.8128	-45.8422	367	medium sandstone	Chenque	Oligo-Miocene
MG5	-67.9561	-45.8297	610	medium sandstone	Chenque	Oligo-Miocene
MG6	-68.1723	-45.7721	613	medium sandstone	Chenque	Oligo-Miocene
MG7	-69.2818	-45.5345	283	medium sandstone	Chubut Group	Cenomanian
MG9	-69.7016	-45.4590	557	medium sandstone	Chubut Group	Aptian - Albian
MG11	-70.2658	-45.6747	484	sandstone	Rio Mayo	Upper Miocene to Pliocene
MG12	-71.0792	-45.8858	733	sandstone	Rio Mayo	Upper Miocene to Pliocene
MG13	-71.6418	-46.6084	325	medium sandstone	Santa Cruz	Medium to Upper Miocene
MG14	-71.7229	-46.7390	709	medium sandstone	Santa Cruz	Medium to Upper Miocene
MG15	-70.6897	-46.9614	693	medium sandstone	Santa Cruz	Medium to Upper Miocene
MG16	-70.8325	-47.1046	700	finesandstone	Santa Cruz	Medium to Upper Miocene
MG17	-69.0178	-45.4174	373	fine sandstone	Chubut Group	Aptian
MG20	-69.3007	-45.1388	568	medium sandstone	Chubut Group	Aptian - Albian
MG45	-72.4951	-46.8204	631	sandstone	Guadal	Oligo-Miocene
MG47	-66.0674	-47.3632	108	fine grained sandstone	Chenque	Oligo-Miocene
MG49	-66.7981	-48.0737	116	sandstone	Chenque	Oligo-Miocene
MG50	-68.7724	-48.5885	189	fine grained sandstone	Chenque	Oligo-Miocene
MG54	-67.6208	-46.0467	0	sandstone	Chenque	Oligo-Miocene
MG55	-67.4823	-45.7994	36	fine grained sandstone	Sarmiento	Eocene

Fifty-three apatite grains belonging to the AFT P1 component, described below, from four samples (MG4, MG12, MG49 and MG54) and from one Cretaceous sample (MG20) were analyzed at the University of Perugia (Italy) with a quadrupole inductively coupled plasma mass spectrometry (LA-ICP-MS quad). Considering the generally small size of the apatites, one ablation spot of 30 µm diameter laser per crystal was sufficient, except for few bigger grains for which two ablations have been done. Fission track mounts used for AFT thermochronology analysis were prepared for U-Pb analysis together with standard mounts of Madagascar (to correct elemental mass fractionation) and of McClure Mountains apatites (to correct ion counter gain and instrument drift during the session). Repeated measurements on these standards (Thomson et al., 2012) were made following the VizualAge scheme (IOLITE) for data reduction (Petrus and Kamber, 2012). This allows correcting the presence of variable common Pb in the standard material while further analyses are needed to correct the common Pb in unknown detrital apatites as using an iterative approach based on ^{207}Pb correction (Chew et al., 2011) or plotting the data on a Tera-

Wasserburg diagram. In the latter, cogenetic apatite grains from a single source defined a linear array that allows to visualize initial $^{207}Pb/^{206}Pb$ ratio from the discordia intercept. Final data reduction and calculation of concordia ages, isochron ages, radial plot and Kernel density plots were done using IsoplotR (Vermeesch, 2018).

4.5 Results

4.5.1 AFT data

As clearly visible in the radial plots by comparison of single-grain ages with depositional age (Figure 4.5), all the Cretaceous samples have been partially reset (MG7, MG9, MG17 and MG20) with depositional ages generally slightly older than the AFT ages. Only the sample MG20 seems less affected by the reset and displays a central age similar to the deposition age. Thus, the four Cretaceous samples do not give any indication about provenance. Despite the low closure temperature of the AFT thermochronometer and the period of extension recognized in this area during the Oligocene – early Miocene (Bechis et al., 2014; Echaurren et al., 2016; Fernández Paz et al., 2020, 2018), Cenozoic sediments have never been fully reset (Figure 4.5). It means that samples were not subjected to any substantial post-depositional heating as subsidence was not significant enough through the Cenozoic, and that data can be interpreted in terms of lag times.

On the contrary, the AFT ages in Cenozoic deposits vary widely (from ~20 Ma to ~180 Ma), especially for the middle Eocene – early Miocene deposits of the Sarmiento Formation, and are all older than depositional age, suggesting that apatites were never fully reset by burial or heating. Analyses were subjected to χ^2 test in order to identify statistically spread of single-grain dates and detect the presence of multiple age components. For samples which did not pass the test, grain-age distributions were decomposed by using the binomial peak fitting with the BINOMFIT software (Brandon, 2002). Most of the Oligocene – upper Miocene samples show an age component (here named P1) that roughly ranges between 20 and 40 Ma (Table 2). The second age component here detected (named P2) corresponds to Paleocene – middle Eocene ages (ca. between 44 and 60 Ma). Surprisingly, most of the Oligo-Miocene samples present a single population corresponding to either P1 or P2 components, as indicated by a chi-square probability $P(\chi)^2 > 5\%$. Components P1 and P2 were both recognized in only two samples, i.e. MG49 and MG12. On sample MG54, beyond the P1 component, an older component with Late Cretaceous ages (P3) has been detected. Cretaceous ages have been identified also in the three middle Eocene – early Miocene samples from the Sarmiento Formation. The oldest component (P4) yields Lower Cretaceous – Jurassic ages and has been detected in only two Eocene samples, collected directly south of the San Bernardo FTB.

TABLE 2. SUMMARY OF APATITE FISSION TRACKS DATA

Samples†	Field				Fission tracks data									< 40 Ma			40 - 65 Ma			65 - 100 Ma			> 100 Ma		
	Longitude	Latitude	Elev. (m)	n	C. age	σ	Ns	ρs	Ni	ρi	Nd	ρD	Disp. (%)	P(χ²)	P1	σ	%	P2	σ	%	P3	σ	%	P4	σ	%
MG1	-68.8806	-45.7784	395	36	81.4	6.8	307	1.6	832	4.3	5000	13.0	18	42							77.6	7.0	95	181.0	75.3	5
MG3	-68.7684	-45.7491	398	41	79.7	8.3	520	2.7	833	6.1	5000	10.1	65	0							66.4	6.4	84	178.5	15.2	16
MG4	-67.8128	-45.8422	367	40	33.1	2.4	296	1.2	1623	6.6	5000	10.5	0	100	33.1	2.4	100									
MG5	-67.9561	-45.8297	610	12	33.6	6.1	37	1.0	215	6.1	5000	11.3	0	80	33.6	6.1	100									
MG6	-68.1723	-45.7721	613	17	51.7	7.5	62	0.7	275	3.1	5000	13.3	0	100				51.7	5.5	100						
MG7	-69.2818	-45.5345	283	20	88.5	11.4	97	1.4	209	2.9	5000	11.1	0	100												
MG9	-69.7016	-45.4590	557	10	92.6	12.5	88	2.5	178	5.1	5000	10.9	0	100												
MG11	-70.2658	-45.6747	484	16	44.4	4.3	162	1.6	728	7.1	5000	12.2	8	92				44.4	4.3	100						
MG12	-71.0792	-45.8858	733	57	32.6	3.2	256	1.1	2056	9.1	5000	13.2	44	0	20.1	2.1	62	60.9	8.7	38						
MG13	-71.6418	-46.6084	325	34	31.4	3.6	166	0.7	851	0.5	5000	10.2	0	100	31.4	3.6	100									
MG14	-71.7229	-46.7390	709	21	31.1	3.1	115	1.0	652	5.6	5000	10.2	5	85	31.1	3.1	100									
MG15	-70.6897	-46.9614	693	53	38.9	3.5	172	0.8	970	4.5	5000	12.7	2	92	38.1	3.6	100									
MG16	-70.8325	-47.1046	700	21	35.6	5.4	56	0.6	267	3.0	5000	9.8	2	84	35.6	5.4	100									
MG17	-69.0178	-45.4174	373	11	96.7	13.8	83	1.1	143	2.0	5000	9.7	0	100												
MG20	-69.3007	-45.1388	568	53	128.0	8.7	483	2.6	847	4.6	5000	13.1	0	100												
MG45	-72.4951	-46.8204	631	54	26.5	2.2	207	1.1	1493	7.9	5000	9.9	10	97	26.5	2.2	100									
MG47	-66.0674	-47.3632	108	54	55.4	3.9	362	1.5	1126	4.8	5000	10.0	0	100				55.4	3.9	100						
MG49	-66.7981	-48.0737	116	67	43.5	3.2	502	2.6	2022	10.3	5000	10.3	25	26	31.4	3.8	50	56.8	5.3	50						
MG50	-68.7724	-48.5885	189	39	39.8	3.6	176	1.7	1006	9.5	5000	13.2	0	100	39.8	3.6	100									
MG54	-67.6208	-46.0467	0	52	43.4	3.7	507	2.2	2755	11.9	5000	12.9	40	0	28.9	2.7	62				71.2	7.7	38			
MG55	-67.4823	-45.7994	36	22	91.5	7.3	303	4.6	592	9.0	5000	10.4	0	100							91.5	7.3	100			

† Zeta= 346 ± 12 using dosimeter glass CN5

N: number of apatite crystal counted; and ρ: track density (x 10^5 tracks/cm²); subscripts s, I and d denote spontaneous, induced and dosimeter, respectively; P(χ²): probability of obtaining a Chi-square value for n degrees of freedom, samples with a probability P(χ²) < 5% and/or dispersion > 15% have been analysed with the binomial peak-fitting method.

TABLE 3. APATITE ISOTOPIC AND AGE DATA AFTER COMMON PB-CORRECTION.

Samples	$^{207}Pb/^{235}U$	± 2σ	$^{207}Pb/^{235}U$	± 2σ	$^{238}U/^{206}Pb$	± 2σ	$^{207}Pb/^{206}Pb$	± 2σ	$^{206}Pb/^{238}Pb$ age	± 2σ	$^{207}Pb/^{235}U$ age	± 2σ	U (ppm)	Th (ppm)	Pb (ppm)	U/Th	**^{207}Pb corr. age**	**± 2σ**	**S&K value (5th it.)**
McClure_1	3.270	0.240	0.106	0.007	9.479	0.647	0.220	0.015	646.0	42.0	1470.0	55.0	15.39	32.64	3.02	0.442	**531**	**44**	
McClure_2	2.710	0.130	0.101	0.007	9.881	0.654	0.190	0.010	621.0	39.0	1324.0	35.0	33.50	91.80	7.13	0.326	**526**	**41**	
McClure_3	3.910	0.480	0.110	0.009	9.132	0.709	0.252	0.020	669.0	49.0	1597.0	85.0	14.76	57.80	4.43	0.297	**518**	**40**	
McClure_4	4.890	0.370	0.124	0.010	8.084	0.621	0.305	0.023	751.0	54.0	1796.0	63.0	9.19	20.50	2.49	0.567	**535**	**57**	
McClure_5	2.190	0.140	0.097	0.007	10.320	0.724	0.162	0.012	596.0	40.0	1188.0	45.0	17.50	40.50	3.11	0.506	**522**	**46**	
MG54_1	1.690	0.110	0.033	0.002	30.769	1.609	0.389	0.026	206.0	10.0	1006.0	42.0	55.50	16.51	3.35	3.510	**118.6**	**9.2**	**0.8433**
MG54_2	10.100	1.600	0.090	0.014	11.111	1.728	0.880	0.160	548.0	80.0	2350.0	150.0	1.48	4.56	0.52	0.329	**-34.4**	**118.6**	**0.8334**
MG54_3	19.100	1.800	0.171	0.016	5.848	0.547	0.803	0.076	1010.0	86.0	3013.0	91.0	2.44	8.18	1.69	0.319	**49.7**	**105.8**	**0.8388**
MG54_4	0.587	0.044	0.021	0.001	48.638	2.366	0.207	0.012	131.2	6.5	469.0	26.0	74.30	105.20	2.48	0.727	**105.2**	**5.5**	**0.8424**
MG54_5	2.190	0.260	0.036	0.003	27.933	2.419	0.416	0.030	226.0	19.0	1154.0	73.0	36.50	9.60	2.99	4.150	**122.9**	**13.7**	**0.8436**
MG54_6	2.800	0.280	0.030	0.003	33.113	2.851	0.701	0.098	191.0	16.0	1340.0	72.0	6.54	25.94	0.90	0.266	**33.6**	**24.2**	**0.8378**
MG54_7	7.390	0.550	0.077	0.005	13.072	0.803	0.704	0.045	475.0	28.0	2121.0	55.0	9.29	27.10	2.75	0.364	**84.6**	**28.5**	**0.8411**
MG54_8	9.330	0.630	0.076	0.005	13.210	0.873	0.915	0.072	470.0	30.0	2347.0	64.0	3.89	13.78	1.44	0.294	**-51.4**	**45.4**	**0.8324**
MG54_9	3.610	0.260	0.048	0.003	20.661	1.153	0.545	0.032	305.0	17.0	1537.0	58.0	18.80	27.00	2.85	0.734	**116.0**	**14.1**	**0.8431**
MG54_10	5.990	0.500	0.068	0.005	14.684	1.057	0.662	0.039	424.0	29.0	1977.0	74.0	12.17	26.30	2.93	0.536	**98.8**	**22.7**	**0.8420**
MG54_11	7.100	0.380	0.077	0.005	12.937	0.803	0.662	0.031	480.0	29.0	2125.0	48.0	10.20	34.49	3.11	0.307	**112.5**	**20.8**	**0.8429**
MG54_12	9.300	0.700	0.084	0.008	11.848	1.165	0.835	0.063	520.0	49.0	2350.0	72.0	5.03	17.07	1.88	0.304	**0.4**	**43.8**	**0.8356**
MG4_1	6.880	0.590	0.059	0.005	16.978	1.384	0.816	0.076	369.0	29.0	2079.0	79.0	4.82	10.87	1.13	0.393	**9.7**	**36.7**	**0.8362**
MG4_2	34.500	2.400	0.275	0.025	3.636	0.331	0.862	0.075	1557.0	120.0	3608.0	68.0	1.41	4.54	1.47	0.266	**-69.7**	**171.9**	**0.8312**
MG4_3	22.930	0.940	0.198	0.015	5.063	0.385	0.843	0.047	1159.0	80.0	3227.0	40.0	4.13	6.72	3.08	0.513	**-13.3**	**77.2**	**0.8348**
MG4_4	10.970	0.820	0.097	0.008	10.288	0.815	0.765	0.040	597.0	45.0	2514.0	69.0	8.37	12.22	3.15	0.565	**58.6**	**32.3**	**0.8394**
MG4_5	15.410	0.560	0.133	0.010	7.508	0.558	0.820	0.042	805.0	56.0	2858.0	36.0	6.08	9.21	3.08	0.531	**18.2**	**46.4**	**0.8368**
MG4_6	16.300	1.200	0.148	0.012	6.743	0.546	0.798	0.068	890.0	65.0	2870.0	66.0	3.53	10.33	1.93	0.261	**49.0**	**82.2**	**0.8388**
MG4_7	21.500	1.200	0.183	0.017	5.464	0.508	0.858	0.053	1077.0	92.0	3143.0	53.0	3.06	9.84	2.15	0.232	**-37.1**	**80.9**	**0.8333**
MG4_8	20.000	1.100	0.167	0.014	5.981	0.501	0.857	0.064	994.0	75.0	3073.0	55.0	2.76	5.78	1.78	0.345	**-32.1**	**88.7**	**0.8336**
MG4_9	21.040	0.960	0.179	0.015	5.587	0.468	0.836	0.048	1067.0	83.0	3143.0	48.0	2.88	6.03	2.03	0.343	**-0.6**	**71.2**	**0.8356**
MG4_10	18.600	1.000	0.160	0.013	6.254	0.508	0.836	0.051	954.0	72.0	3005.0	53.0	3.17	6.64	1.91	0.339	**-0.5**	**67.5**	**0.8356**

MG4_11	26.500	1.600	0.250	0.018	4.000	0.288	0.766	0.037	1435.0	94.0	3356.0	58.0	5.25	1.62	4.38	2.340	**159.9**	**75.7**	**0.8461**
MG4_12	5.390	0.230	0.060	0.004	16.807	1.215	0.654	0.028	372.0	26.0	1893.0	38.0	22.92	98.30	4.82	0.162	**90.0**	**15.2**	**0.8414**
MG12_13	30.700	1.600	0.260	0.021	3.846	0.311	0.836	0.061	1484.0	110.0	3506.0	47.0	2.14	3.91	2.10	0.379	**-0.9**	**130.7**	**0.8356**
MG12_14	1.420	0.100	0.027	0.002	36.496	2.531	0.373	0.025	174.3	12.0	899.0	40.0	31.40	37.50	1.75	0.558	**103.5**	**9.0**	**0.8423**
MG12_15	15.840	0.540	0.133	0.010	7.536	0.568	0.854	0.041	802.0	57.0	2866.0	34.0	7.22	14.38	3.65	0.348	**-21.5**	**45.6**	**0.8343**
MG12_16	25.600	1.300	0.207	0.016	4.822	0.372	0.880	0.030	1229.0	83.0	3332.0	50.0	7.00	18.62	5.62	0.257	**-85.2**	**54.2**	**0.8303**
MG12_17	72.900	3.800	0.616	0.047	1.623	0.124	0.848	0.036	3080.0	190.0	4354.0	50.0	1.94	5.55	4.64	0.247	**-90.0**	**189.2**	**0.8303**
MG12_18	17.400	1.200	0.150	0.011	6.684	0.492	0.843	0.051	897.0	59.0	2961.0	69.0	3.57	10.85	2.02	0.233	**-9.8**	**63.3**	**0.8350**
MG12_19	29.300	1.600	0.252	0.019	3.968	0.299	0.862	0.048	1443.0	100.0	3475.0	55.0	3.65	12.55	3.50	0.218	**-63.0**	**101.6**	**0.8317**
MG12_20	16.480	0.890	0.141	0.012	7.077	0.601	0.902	0.067	850.0	69.0	2916.0	54.0	2.85	8.33	1.55	0.263	**-83.6**	**79.6**	**0.8303**
MG12_21	10.040	0.920	0.085	0.007	11.820	0.964	0.880	0.110	523.0	41.0	2437.0	87.0	2.81	7.60	0.98	0.297	**-32.2**	**76.7**	**0.8336**
MG12_22	11.300	0.600	0.098	0.008	10.163	0.785	0.852	0.043	604.0	45.0	2542.0	49.0	5.86	21.22	2.24	0.234	**-13.9**	**35.3**	**0.8347**
MG12_23	13.720	0.590	0.118	0.009	8.511	0.666	0.853	0.045	715.0	53.0	2721.0	41.0	7.62	13.61	3.28	0.499	**-17.8**	**44.1**	**0.8345**
MG20_24	21.400	1.300	0.203	0.015	4.936	0.365	0.758	0.044	1187.0	81.0	3139.0	57.0	3.29	11.44	2.39	0.467	**140.8**	**72.7**	**0.8448**
MG20_25	17.800	1.200	0.173	0.017	5.780	0.568	0.755	0.058	1027.0	92.0	2961.0	66.0	3.66	14.20	2.27	0.452	**123.1**	**81.6**	**0.8436**
MG20_27	14.300	0.530	0.146	0.011	6.868	0.519	0.740	0.032	875.0	62.0	2773.0	36.0	9.24	51.40	4.95	0.403	**121.0**	**39.2**	**0.8435**
MG49_29	15.000	1.200	0.134	0.012	7.491	0.673	0.806	0.067	815.0	72.0	2813.0	82.0	2.73	9.46	1.50	0.699	**34.5**	**73.1**	**0.8378**
MG49_30	7.860	0.680	0.074	0.009	13.459	1.612	0.800	0.086	461.0	53.0	2204.0	77.0	5.41	20.99	1.43	0.650	**22.4**	**52.2**	**0.8371**
MG49_31	6.510	0.940	0.067	0.011	14.925	2.450	0.728	0.096	417.0	62.0	1980.0	120.0	3.36	9.83	0.80	0.894	**60.5**	**53.0**	**0.8395**
MG49_32	8.610	0.380	0.077	0.006	13.021	1.051	0.848	0.027	477.0	37.0	2291.0	39.0	43.70	11.12	12.49	10.420	**-8.1**	**17.8**	**0.8351**
MG49_33	3.980	0.240	0.036	0.003	27.933	2.263	0.839	0.056	227.0	18.0	1636.0	44.0	11.58	50.10	1.61	0.610	**-1.0**	**16.6**	**0.8356**
MG49_34	5.950	0.430	0.052	0.005	19.084	1.712	0.873	0.061	329.0	29.0	1972.0	64.0	11.90	30.50	2.21	0.993	**-16.5**	**26.5**	**0.8346**
MG49_35	7.660	0.620	0.077	0.009	12.937	1.523	0.767	0.060	478.0	54.0	2177.0	71.0	4.24	13.03	1.27	0.823	**44.9**	**38.2**	**0.8385**
MG49_36	2.400	0.130	0.038	0.003	26.455	1.960	0.462	0.019	239.0	17.0	1234.0	40.0	41.25	78.10	3.92	1.291	**115.8**	**10.4**	**0.8431**
MG49_37	9.490	0.570	0.100	0.007	10.040	0.726	0.698	0.034	612.0	42.0	2368.0	55.0	11.68	49.30	4.12	0.514	**116.2**	**28.8**	**0.8431**
MG49_38	9.600	1.100	0.092	0.013	10.870	1.536	0.825	0.092	568.0	76.0	2400.0	120.0	3.87	13.32	1.40	0.613	**8.4**	**69.3**	**0.8362**
MG49_39	6.660	0.350	0.077	0.007	13.021	1.102	0.655	0.040	476.0	39.0	2055.0	46.0	14.12	36.60	3.62	0.738	**116.1**	**26.7**	**0.8431**
MG49_40	4.920	0.380	0.059	0.005	16.835	1.474	0.620	0.027	372.0	31.0	1789.0	63.0	32.40	32.40	5.67	1.824	**106.4**	**16.1**	**0.8425**
MG49_41	2.720	0.220	0.028	0.003	36.232	3.282	0.723	0.060	176.0	15.0	1322.0	58.0	25.10	42.30	2.48	1.015	**25.7**	**13.7**	**0.8373**
MG49_42	12.200	0.890	0.109	0.010	9.141	0.794	0.828	0.056	668.0	55.0	2613.0	65.0	4.21	12.55	1.86	0.521	**7.2**	**50.5**	**0.8361**
MG49_43	12.400	1.100	0.106	0.010	9.425	0.862	0.866	0.088	649.0	56.0	2623.0	81.0	4.43	13.63	1.84	0.474	**-28.0**	**77.0**	**0.8338**

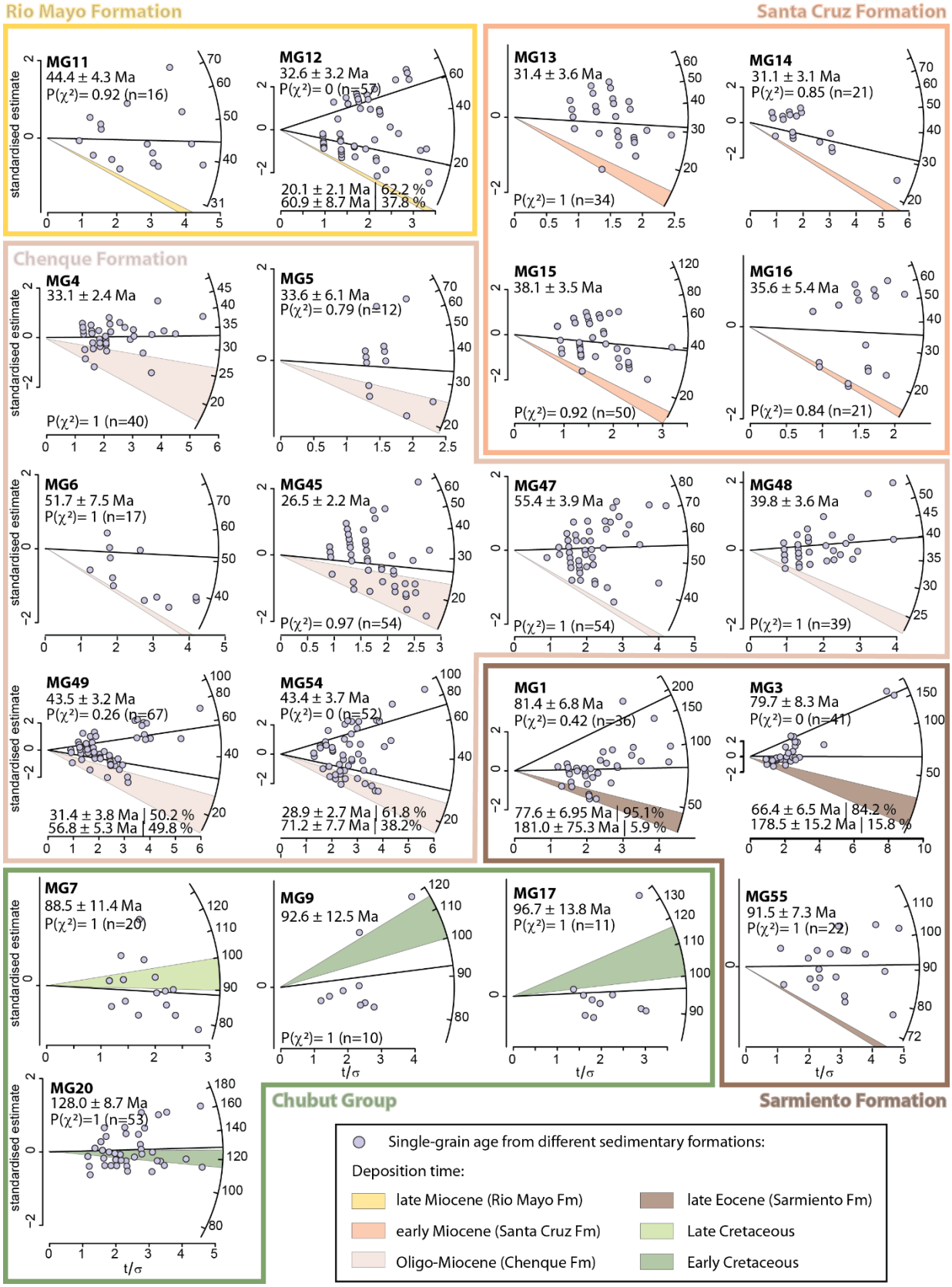

Figure 4.5 – Radial plots of single-grain AFT ages arranged according to the different sedimentary formations sampled for this study. Cretaceous samples from the Chubut Group clearly evidence a partial annealing of AFT data while Cenozoic samples show that no late heating affected those samples. Ages of deposition from Cuitiño et al., 2016, 2015b, 2015a; De Iuliis et al., 2008; Parras et al., 2012.

4.5.2 Apatite U-Pb data

Large uncertainties can result from low radiogenic Pb content in young grains or low-U content. As a first step, we excluded grains with 2σ errors > 25% (as in Mark et al., 2016; Zattin et al., 2012) and ^{207}Pb corrected ages with negative values. Seventeen grains produced ages that range from 84.6 ± 28.5 Ma to 159.9 ±75.7 Ma (Table 3). These ages give a peak at 109.64 ± 3.21 Ma on the radial plot and ~114 Ma on the Kernel density plot (Figure 4.6). The ^{238}U/^{206}Pb and ^{207}Pb/^{206}Pb ratios for those grains form a linear array on the Tera-Wasserburg plot intercepting the ^{207}Pb/^{206}Pb axis at 0.8362 ± 0.0242 and giving an age of 107.92 ± 6.11 Ma which is coherent with the ages obtained from the radial plot and the Kernel density plot (Figure 4.6). We consider that this population around ~110 Ma is robust. This population is present in all the samples, from the Cretaceous to the upper Miocene sandstones.

Surprisingly, previously rejected grains (i.e. 2σ errors > 25%) plotted on a Tera-Wasserburg diagram display a mostly linear array (Figure 4.6). MSWD for these data is comprised between 1 and 2 indicating a single population and a peak age at 21.8 ± 13.3 Ma. Negative values obtained for ^{207}Pb corrected age were rejected to plot this population on radial and Kernel density plots giving a mean age of 32.58 ± 16.23 Ma and ~24 Ma respectively (Figure 4.6). The age of this peak is debatable but clearly indicates the existence of a younger population with ages similar to AFT P1 component, most likely related to a volcanic input.

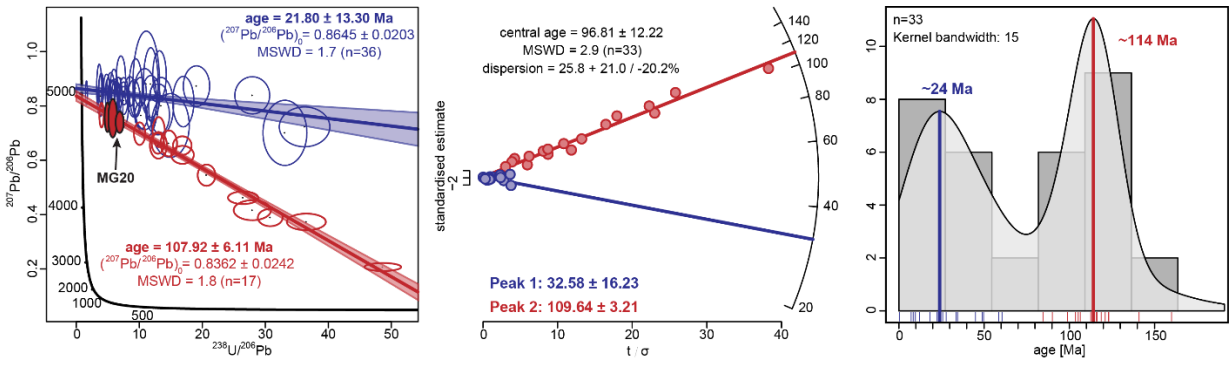

Figure 4.6 – Apatite U-Pb results. In red all the data with a robust Cretaceous age, in blue with the younger population detected. From left to right are the Tera-Wasserburg plot, the radial plot and the Kernel density plot.

4.6 Discussion

4.6.1 Volcanic content

In detrital thermochronology studies, the youngest cooling age population (here P1) is usually paired with the sedimentation age to measure the lag time in order to obtain information about the exhumation history of the source rock, assuming that the age of grains is not related to a volcanic input (Bernet et al., 2001; Garver et al., 1999). The combined application of U-Pb and AFT analysis allows to

discriminate the presence of syn-depositional volcanic apatites. In the case of volcanism, the single-grain U-Pb and AFT ages obtained should be very similar to the depositional age as cooling is almost instantaneous.

A significant volcanic content can be actually recognized in all the samples as supported by the numerous volcanic clasts observed in thin sections analysis (Figure 4.7) and the euhedral morphologies of some apatites, especially for the Cretaceous samples. The petrography of Cretaceous rocks from this region has been extensively interpreted (e.g. Foix et al., 2020; Olazábal et al., 2020) and related to volcanic arc with a decreasing signal in the distal foreland.

Our results from double dating confirm that a volcanic input was active during deposition of the Oligo-Miocene sedimentary strata (i.e. U-Pb ages overlap within error with P1; Figure 4.6). This volcanic input is consistent with literature that describes an arc volcanic activity through the late Paleogene and the Neogene (Butler et al., 2020; Suárez et al., 2015) and within-plate volcanism during the late Oligocene (Bruni et al., 2008b; Gianni et al., 2015a), after the acceleration in plate convergence rate during middle Eocene, Oligocene and early Miocene (Figure 4.3; Maloney et al., 2013).

4.6.2 Provenance of Oligo-Miocene deposits

Beyond the syn-depositional volcanism, double dating allowed to identified a source rock that crystallized at ca. 110 Ma and was then exhumed between about 20 and 40 Ma. However, an unambiguous identification of the source area is extremely difficult, also because the apatite U-Pb signal is remarkably uniform. We therefore used the multi-dimensional scaling (MDS) method to add some constraints on the interpretation of the dataset. This is a dimension reducing technique which analyzed objectively the level of similarity of individual data (Borg and Groenen, 2005) and has been adapted for provenance studies (Vermeesch, 2013). The method is based on pairwise dissimilarities between samples translated into a scatter plot representing a way to visualize similar samples plotted close together (Vermeesch et al., 2016). Here we choose a distributional dataset including single-grain AFT data and related analytical uncertainties with the Sircombe-Hazelton distance. The results display short distances for all the Oligo-Miocene samples excepted for two samples collected close to the Cordillera in the Santa Cruz Formation (MG13 and MG14) (Figure 4.8A). This analysis shows therefore that Oligo-Miocene samples may have had the same source(s) while the deposits from the Sarmiento Formation are clearly different and probably derive from a different source. The 'Shepard plot' (Figure 4.8B) displays a linear array which illustrates the good fit of our data in this non-metric configuration.

Similarity of the Oligo-Miocene data, with the only exception of sample MG45, is also shown by the lag time plot realized for the P1 component (Figure 4.9), in which lag time is ranging from 10 to 20 m.y. The proximity of the data plotted on the lag time demonstrates a similar source for those samples.

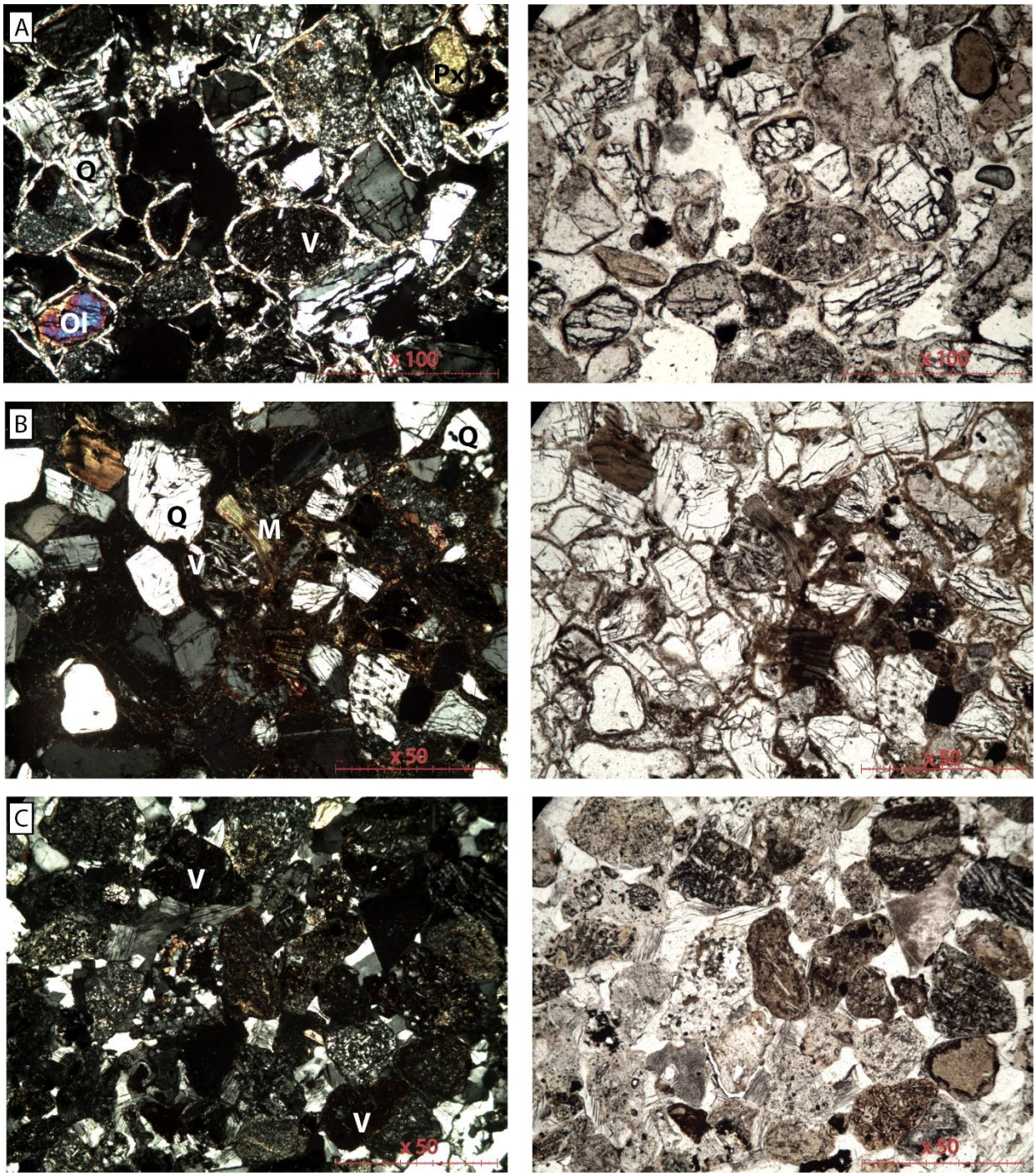

Figure 4.7 - Thin sections photomicrographs to illustrate the high volcanic content in all the formations (V: basic to acidic volcanic lithic grain). Metamorphic, plutonic and sediments clasts are rare (Q: monocrystalline quartz with patches and healed fractures typic of plutonic rocks). A. Sample MG1 (Eocene) with V, Q, Ol: olivine, Px: pyroxene (mainly augite). B. MG9 (Albian) with V, Q, M: micas (mainly deformed biotites). C. MG14 (lower Miocene) with altered V.

To summarize, the uniformity of the detrital AFT thermochronology results across the foreland (Figure 4.10A), the consistency of apatite U-Pb ages, the results shown by the MDS statistics and the lag time plot suggest a similar source for the Oligo-Miocene deposits across this broad study area, despite the changes in sedimentation style and depositional environments. Remarkably, detrital AFT ages belonging to P1 population are very similar to in-situ samples dated in the western and eastern Patagonian Cordillera

(Figure 4.1; Thomson et al., 2010, 2001), whereas much older ages have been recognized in the Deseado Massif (Derycke et al., 2019; Fernández et al., 2020). In addition, paleoflow indicators (e.g. Guillaume et al., 2009) point to the Cordillera as a primary contributor of sediment for the San Jorge Basin during early Miocene. Therefore, we interpret the apatites younger than 40 Ma as deriving from exhumation of the Cordillera that took place during contemporaneous volcanism (Figure 4.10C).

Although less represented but widespread detected in this large area, the component P2 suggests an active source exhuming during Paleocene – middle Eocene. The P2 component is not recorded in the sandstones of the Santa Cruz Formation (~46°S) but is present in the two samples of the upper Miocene – Pliocene Rio Mayo Formation, collected in the Rio Mayo Sub-basin, in two samples around the Deseado Massif and in one sample from the distal San Jorge Basin (Figure 4.10A). More in detail, the Rio Mayo Sub-basin is directly bordered to the west by the Cretaceous Patagonian Batholith for which few Paleocene – middle Eocene and late Eocene – early Miocene bedrock AFT ages have been dated (Thomson et al., 2010a). A direct connection between a western source and the Rio Mayo basin can be therefore inferred (Figure 4.10C). This sector of the Cordillera was probably representing a major source also for sediments that deposited close to the present-day Atlantic coast during the early Miocene, as indicated by sample MG6 and the reconstructions of the drainage made by Guillaume et al. (2009). Indeed, a recent thermochronology study in the Deseado Massif shows few Paleocene – middle Eocene AFT ages (Fernández et al., 2020), suggesting that the Deseado Massif is a potential source for the P2 component in the surrounding areas. However, detrital data obtained all around the Deseado Massif lack the Cretaceous AFT ages that are dominant in the bedrock analysis (Fernández et al., 2020). Therefore, despite the proximity with the surrounding basins, we infer that the Deseado Massif was not actively eroding during Oligo-Miocene.

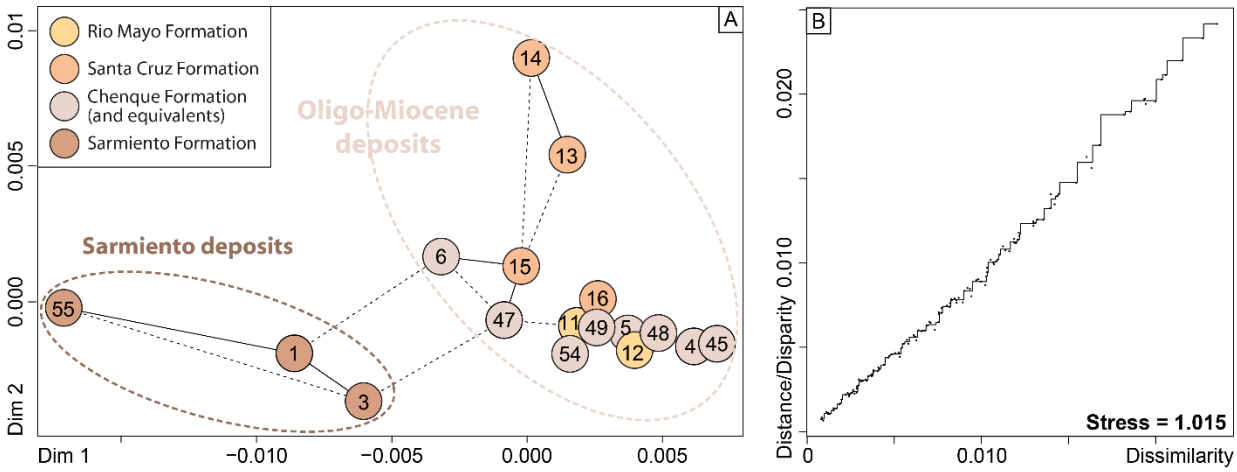

Figure 4.8 – A. MDS diagram for no reset samples indicates a clear difference between deposits from the Sarmiento Formation and younger Oligo-Miocene deposits. The Sircombe-Hazelton distance was used to take in account the analytical uncertainties in the analysis. B. Goodness of fit of the MDS plot (Shepard plot).

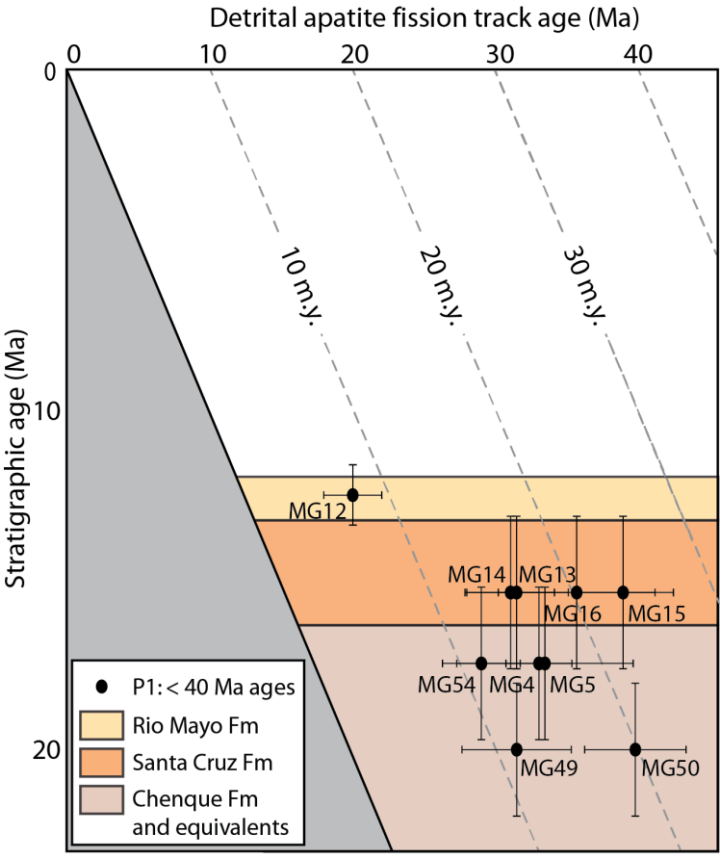

Figure 4.9 – Lag time plot for AFT ages younger than 40 Ma (P1). Dashed grey lines represent lag time lines. Error bar for apatite FT ages are ± 1σ (Table 2). Error for depositional age of each sample is given for the Chenque Formation (Cuitiño et al., 2015b), the Monte Léon Formation (Parras et al., 2012), the Santa Cruz Formation (Cuitiño et al., 2016) and the Rio Mayo Formation (De Iuliis et al., 2008), and detailed in the Geological setting section.

To summarize, the recognition of P1 and P2 in all the Oligo-Miocene deposits supports the idea of a direct sediment routing pathway from the magmatic arc to the distal foreland through late Oligocene to the Miocene.

4.6.3 Provenance of sediments in the north-eastern San Jorge Basin

Although detrital data demonstrate that the Deseado Massif was not the primary source of sediments during the Oligo-Miocene, AFT Cretaceous or older ages (P3 and P4) have been detected all around the San Bernardo FTB (Figure 4.10A), mostly in the middle Eocene – early Miocene samples from the Sarmiento Formation (MG1, MG3 and MG55) and in one Oligo-Miocene sample from marine deposits (MG54).

Deposits from the Sarmiento Formation, exposed along the southern and eastern margin of the San Bernardo FTB, show therefore a different provenance signature than Oligo-Miocene deposits, as well evidenced by the MDS diagram (Figure 4.8A). All of them yield apatites belonging to P3 component, matching well the ages found in Cretaceous samples, thus suggesting that Eocene deposits may derive from the erosion of the Chubut than AFT ages found in partial reset Cretaceous samples but precision in detrital data is lower due to a poor amount of counted grains and the occurrence of local partial reset. In any case, the occurrence of P3 ages testify the exposure of San Bernardo FTB during the Eocene – early Miocene. The reappearance of the Cretaceous ages in one sample collected in Oligo-Miocene marine deposits (MG54) may indicate recycling of Sarmiento Formation or drainage reorganization with directly sourced remnants of the Cretaceous units exposed along the San Bernardo FTB.

The existence of the oldest component P4 in two samples (MG1 and MG3) is coherent with the partial reset AFT ages recorded in the Cretaceous deposits of the San Bernardo FTB. Despite the larger error for this component, we can refer these ages to basement clasts from the Rio Chico High, a Paleozoic basement igneous-metamorphic complex presently buried under Jurassic and Cretaceous units (Cortiñas,

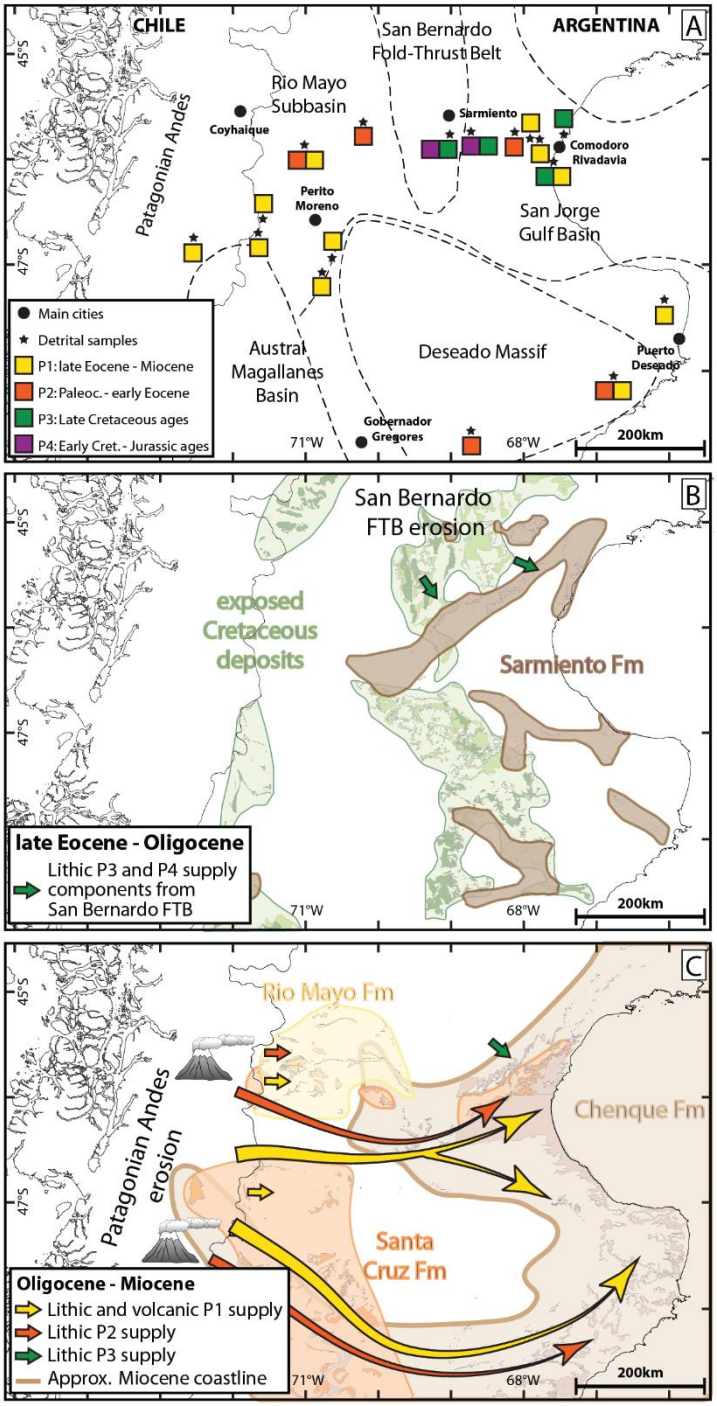

Figure 4.10 – A. AFT populations obtained for each sample. B. Sarmiento Formation looks mostly constituted of reworked clasts from the surrounding Cretaceous layers as evidenced by the components P3 and P4. C. Chenque (and equivalents), Santa Cruz and Rio Mayo Formations are mostly composed of P1 and P2 peaks representing the ages of the central Patagonian Andes exhumation, coeval with volcanism for the P1 component. P3 peak recorded in one sample may be explained by reworking of surrounding Chubut Group or Sarmiento Formation.

1996; Navarrete et al., 2016; Renda et al., 2019), or from the Early Cretaceous Las Heras Group (Figure 4.10B; Clavijo, 1986), recognized in the deposits of the Chubut Group (Foix et al., 2020).

The sandstones deposited prior to the Oligo-Miocene marine incursion in the north-eastern San Jorge basin are thus mainly made by clasts from the surrounding Cretaceous rocks exposed in the San Bernardo FTB. Erosion of this belt was significantly reduced in late Oligocene – early Miocene as older AFT ages are poorly recognized in the surrounding marine Oligo-Miocene deposits.

4.6.4 Andean denudation through the Cenozoic

The first Andean shortening event started during the late Early Cretaceous and persisted to the middle Eocene as evidenced by angular unconformities recognized between Aptian and Albian deposits (Giacosa et al., 2010b), and growth-strata observed in coeval deposits both along the Cordillera and the broken foreland (Gianni et al., 2017; Navarrete et al., 2016).

The deformation period is followed by a neutral tectonic regime across the retroarc region (Horton et al., 2016; Horton and Fuentes, 2016) coeval with a regional extensional setting reported through the whole Patagonian foreland and associated to a pronounced slab roll-back and a

particularly low trench normal absolute velocity (Maloney et al., 2013; Muñoz, 1999; Orts et al., 2012, p. 201; Ramos and Folguera, 2005). During times of relative tectonic quiescence, eustatic sea-level changes may govern the deposition of sediments. Thus, extension was prevalent in the central Patagonian foreland from the late Eocene to the early Miocene, during marine flooding occurring over a large area (e.g. Bechis et al., 2014; Encinas et al., 2018). Marine deposits are also identified along the western and the eastern areas of the Patagonian Cordillera, with fossil records indicating Pacific and Atlantic origin respectively (Encinas et al., 2018). Although these deposits are geographically close, the lack of an extended transient connection between the Pacific and the Atlantic in the Patagonia Andes evidences the persistence of existing reliefs acting as an orographic barrier during the marine incursion from the late Oligocene to the early Miocene (Frassinetti and Covacevich, 1999; Mpodozis and Ramos, 1990; Ramos, 1982). Furthermore, the wide distribution of Oligo-Miocene deposits to the distal foreland evidenced a significant bypass and, in consequence, the absence of a topographic barrier as a pronounced forebulge. This is typical for broken foreland as deformation is controlled there by former heterogeneities of the upper crust rather than a flexural uplift (DeCelles and Giles, 1996). Moreover, few AFT ages in the central Patagonian Cordillera show that this area was governed by denudation processes at ca. 30 Ma (Thomson et al., 2010b, 2001). This result is also coherent with data from the eastern front adjacent to the Neuquén and the Magallanes retroarc basin, north and south of the study area respectively (e.g. Bande et al., 2012; Folguera et al., 2015; Leonard et al., 2020).

Our data provide further information about the evolution of the Cordillera during the Oligo-Miocene. In fact, as described above, lag time derived for P1 component allow to quantify the denudation in the last 30 Ma. Although quite scattered, lag time trend appears relatively constant and generally comprised between 10 and 20 m.y. (Figure 4.9). This trend is consistent with a nearly steady-state exhumation (as defined by Garver et al., 1999) from Oligocene to Miocene. Considering an average geothermal gradient of 34 ± 11°C/km through the Cenozoic for the central Patagonia (Adriasola et al., 2006; Hamza and Muñoz, 1996; Muñoz, 1999; Thomson, 2002), the lag time indicates that ~2 – 4 km of overburden has been removed from the Cordillera in 10 – 20 m.y. We can therefore document that the Cordillera exhumed with exhumation rates of 0.1 – 0.4 km/Ma between 40 to 20 Ma. As last shortening event occurred during middle Eocene (Gianni et al., 2017), we conclude that the Cordillera was in nearly exhumational steady-state (as defined by Willett and Brandon, 2002) through the Oligocene. Our oldest Oligo-Miocene sample (MG45), is actually showing a much shorter lag time that may be related to the transition from an orogenic constructional state with higher erosion rates.

Afterward, a new orogenic exhumation episode started during the middle – late Miocene, coinciding with an increase of the plate convergence rates and a shift from a mostly orthogonal to oblique subduction (Gianni et al., 2017; Maloney et al., 2013; Orts et al., 2012; Pardo-Casas and Molnar, 1987; Ramos, 2005; Thomson, 2002).

4.7 Conclusion

Detrital thermochronology in the central Patagonian foreland basin is dominated by a persistent volcanic signal but, nevertheless, it provides valuable provenance information on source denudation history. Our findings highlight that the adjacent Cordillera was the primary source of sediment for the distal foreland since ca. 50 Ma and persisted until Miocene time. The lag time relationships indicate that the chain was broadly in a steady erosional state during Oligocene and Miocene, coeval with a regional extensional setting in the foreland. This phase started after the cessation of an early significant shortening episode along the Patagonian Andes, here recorded by our detrital Paleocene – middle Eocene AFT age populations. Therefore, the identified Oligo-Miocene steady-state erosion, previously unrecognized, may be a signal of low rate (0.1 – 0.4 km/Ma) erosional processes over the entire width of the Cordillera with a noticeable unroofing of 2 – 4 km in 10 – 20 m.y. Additionally, our AFT ages suggest: 1) a waning of sediment contribution from the Deseado Massif, supporting that this area was definitely stable since at least the Oligocene, and 2) an active erosion of the San Bernardo FTB during the Eocene – Oligocene.

4.8 Acknowledgements

Funding for this work was provided by the University of Padova (Progetto di Ateneo 2015, CPDA158355) and the INSU (Institut National des Sciences de l'Univers, France) through a Telus-Syster scholarship. S. Boesso and L. di Tauro are thanked for sample preparation. We thank Valerio Olivetti for helpful discussions that helped to construct this manuscript.

CHAPTER 5

TECTONO-THERMAL HISTORY OF THE SAN BERNARDO FOLD AND THRUST BELT FROM LOW-TEMPERATURE THERMOCHRONOLOGY

Marie C. Genge[1,2], Alexis Derycke[3], Cécile Gautheron[3], Massimiliano Zattin[1], César Witt[2], Stefano Mazzoli[4], Xavier Quidelleur[3]

[1] Dipartimento di Geoscienze, Università degli Studi di Padova, via G. Gradenigo 6, 35131 Padova, Italy
[2] Univ. Lille, CNRS, Univ. Littoral Côte d'Opale, UMR 8187, LOG, Laboratoire d'Océanologie et de Géosciences, F 59000 Lille, France
[3] Université Paris-Saclay, CNRS, GEOPS, 91405, Orsay, France
[4] School of Science and Technology, Geology Division, University of Camerino, Italy

Declaration

This chapter is targeted to explore the tectono-thermal history of the San Bernardo Fold and Thrust Belt through low-temperature thermochronology (fission tracks and (U-Th-Sm)/He) and thermal modeling carried out for the first time in this area. This area has been chosen as the successive contraction episodes and widespread intraplate volcanism allowed to explore the effect of tectonic and magmatism on the low-temperature thermochronometers. All co-authors carried out fieldwork, including sampling for thermochronology dating methods and structural observations. MCG provided all apatite fission tracks dating, thermal models, all the figures and the original draft for this paper. CG, MZ and CW made a careful review of the original draft and acquired fundings for this work. AD provided apatite (U-Th-Sm)/He data and gave helpful comment to improve the manuscript and the modeling. XQ provided the K-Ar ages. The following chapter corresponds to the version of the manuscript submitted to a Special Issue of *Journal of South American Earth Sciences*.

5.1 Abstract

First low-temperature thermochronology data across the San Bernardo fold and thrust belt (FTB) in central Patagonia (44 – 46 °S) provide information on the thermal history of this intraplate belt. Apatite (U-Th-Sm)/He (AHe), fission tracks (AFT) ages and inverse thermal modeling indicate that the sedimentary rocks presently at the surface of the southwestern San Bernardo FTB have experienced a broadly similar thermal history: i) cooling at the deposition time during the Cretaceous, ii) thermal quiescence from Cretaceous to Oligocene, and iii) a significant thermal event which totally reset the AHe data and partially the AFT data. Although former thermochronology studies in surrounding areas do not evidence any Neogene thermal event, our regionally consistent ages and thermal modeling most likely indicate a large-scale thermal event through late Oligocene and early Miocene. It is coeval with a widespread intraplate volcanic event leading to massive basal emplacement in central Patagonia. As sedimentary burial was not significant in this area through the Cenozoic, we propose that the late Oligocene – early Miocene heating episode might have been caused by coeval intraplate volcanic processes associated with a high heat flow, which have been strong enough to significantly affect the low-temperature thermochronometers regionally. The subsequent slow cooling phase may have been related with the termination of this intraplate volcanic phase and with a modest exhumation related to a mild deformation episode of the broken foreland during the middle Miocene.

5.2 Introduction

Intraplate belts are enigmatic features, developed far from the orogen due to the reactivation of upper plate weaknesses mostly perpendicular to the main compressional stress during orogenic shortening as the Iberian Chain (Guimerá and Alvaro, 1990; Guimerà Rosso, 2018), the Yinshan fold-and-thrust belt (Davis et al., 1998; Lin et al., 2013), the Laramide (Blackstone, 1980; Yonkee and Weil, 2015) and the Arabia-Eurasia collision zone (Cavazza et al., 2019). The external part of the Patagonian Andes is also related with a conspicuous NNW-trending intraplate belt named the Patagonian Broken Foreland and extended between 40 and 48 °S (Gianni et al., 2015a; Homovc et al., 1995; Peroni et al., 1995). This work aims to understand the thermal evolution of the central segment of the Patagonian Broken Foreland, called the San Bernardo Fold and Thrust Belt (FTB) (Figure 5.1A). This intraplate belt, characterized by wide asymmetrical anticlines associated with WNW – ESE striking normal faults and NNE – SSW inverted normal faults, was built by several contraction episodes. The earliest compressive stage is recorded during the late Early Cretaceous and may have been sustained until the middle Eocene as evidenced by the synorogenic character of the Cretaceous – middle Eocene sedimentary formations exposed across the San Bernardo FTB (Barcat et al., 1989; Gianni et al., 2017; Navarrete et al., 2015; Suarez et al., 2009). Neogene and Quaternary deformation episodes are also recognized for the intraplate belt (Gianni et al., 2015a). The topographic growth of the San Bernardo FTB is directly related to the inversion of former depocenters enhanced by the reactivation of NNW-trending faults (Homovc et al., 1995; Navarrete et al.,

2015; Peroni et al., 1995). These structural inheritances acted as anisotropies focalizing strain during compression ~500 km away from the trench (Navarrete et al., 2015). To unravel the significance of these deformational stages, still debated, we analyzed low-temperature thermochronology from the syntectonic Cretaceous deposits exposed across the southwestern San Bernardo FTB. Low-temperature thermochronological ages can record the signal of diverse thermal events which may be related to significant sedimentary burial (Brandon et al., 1998), magmatism (Calk and Naeser, 1973; Roy et al., 2004), faulting (Ehlers et al., 2001), or exhumation (Malusà et al., 2005; Willett et al., 2003). The southwestern San Bernardo FTB represents a valuable natural laboratory to study the effect of burial, denudation and volcanism. Indeed, three main intraplate magmatism events occurred during the late Eocene, from the late Oligocene to the early Miocene and during the Pliocene, which are related with periods of tectonic quiescence across the study area (Bruni et al., 2008; Gianni et al., 2015). In this work, we will mostly focus on apatite fission tracks (AFT) and (U-Th-Sm)/He (AHe) data. The latter allow to identify an Oligo – Miocene thermal event, whose interpretation could be either related to tectonic and associated denudation, or volcanism heating in this area.

5.3 Geological setting

The San Bernardo FTB represents an intraplate belt that disrupts the central Patagonian foreland at ~45°S. This NNW-SSE trending broken foreland was initiated through several contraction episodes that reactivated inherited faults and former depocenters (Homovc et al., 1995). Many half-graben systems were developed across this area through the Jurassic and the Early Cretaceous (Figari et al., 2015). Indeed, the magmatic-metamorphic basement was buried below thick Jurassic to Early Cretaceous volcano-sedimentary sequences deposited in these half-graben systems (Allard et al., 2020 and references therein). These deposits are topped by a regional unconformity underlain by the late Early – Late Cretaceous Chubut Group, mainly exposed across the southern San Bernardo FTB. Initial sedimentation of the continental Chubut Group is represented by the Aptian Matasiete Formation, interfingered to the east with the Pozo D-129 Formation (e.g. Sciutto, 1981; Carignano et al., 2017; Paredes et al., 2007). Both units are overlain by the Aptian – Albian Castillo Formation (e.g. Lesta and Ferello, 1972; Tunik et al., 2015; Suarez et al., 2009), which is topped (locally unconformably) by the fluvial members of the Bajo Barreal Formation assigned to Cenomanian – Maastrichtian (e.g. Hechem et al., 1990; Umazano et al., 2009). Thereby, the Laguna Palacios Formation and the Lago Colhué Huapi Formation (restricted to the western domain) represent the last fluvial infill of the Chubut Group (e.g. Genise et al., 2007; Casal et al., 2015; Vallati et al., 2016). They are unconformably covered by Paleogene successions stratigraphically arranged as follows: Danian – early Paleocene marine Salamanca Formation restricted to the east due to the existence of topographic barriers at deposition time (e.g. Lesta et al., 1980; Legarreta and Uliana, 1994); late Paleocene – middle Eocene continental Rio Chico Formation (e.g. Foix et al., 2013); and middle Eocene – early Miocene tuffaceous Sarmiento Formation (e.g. Bellosi, 2010; Ré et al., 2010). Neogene marine deposits recognized in the foreland basin (e.g. Chenque Formation) were not deposited across the

southwestern San Bernardo FTB as this area represented already a topographic barrier during the Oligocene (Barreda and Bellosi, 2014; Sciutto et al., 2008).

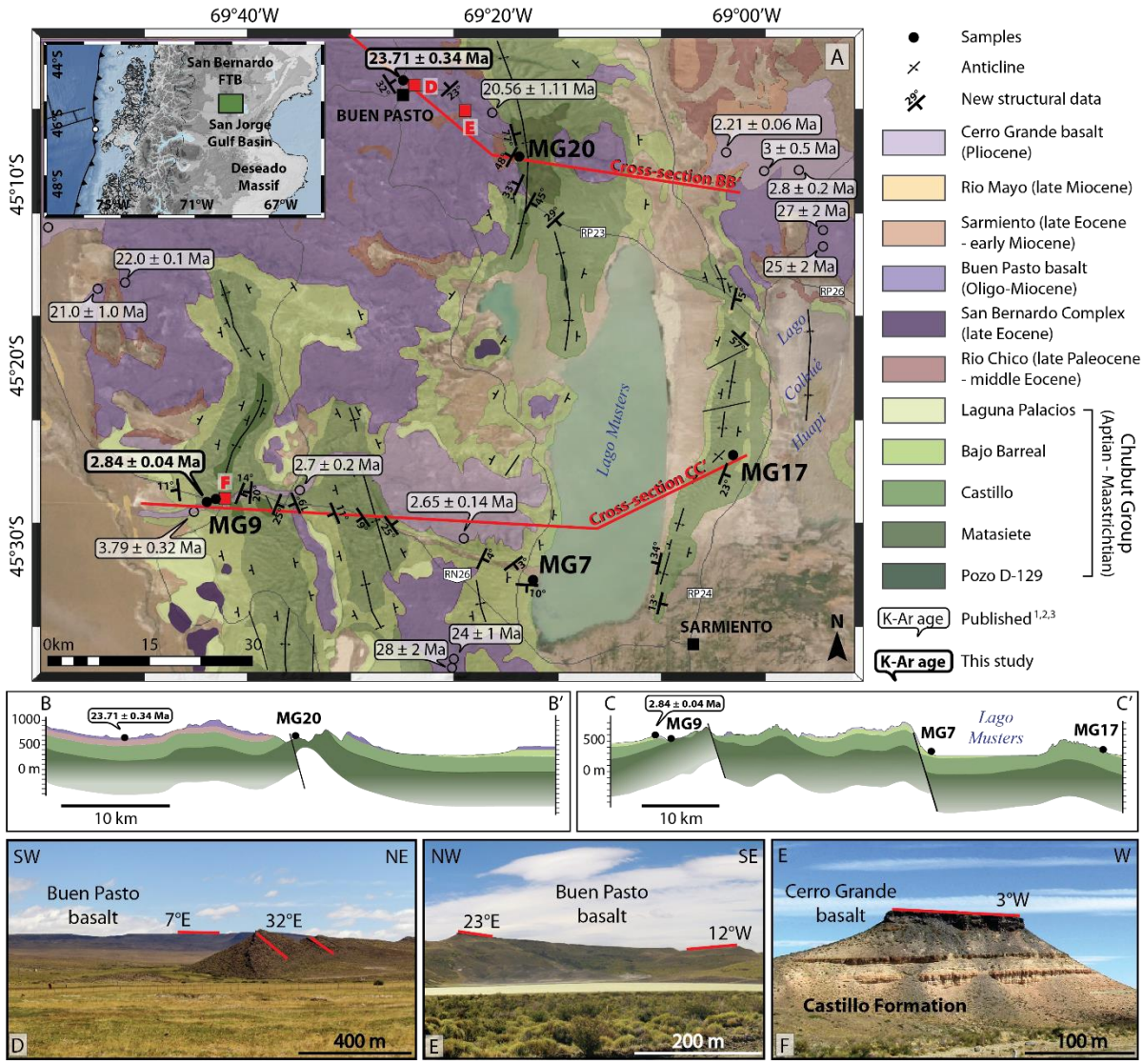

Figure 5.1 – Geological map of the southern San Bernardo Fold-Thrust Belt showing K-Ar ages ([1]Sinito, 1980; [2]Linares *et al.*, 1989; [3]Bruni *et al.*, 2008; this study) on basalt units. Geological units from Pezzuchi (2018) and Sciutto *et al.* (2008). Principal structures from Homovc *et al.* (1995). Cross-sections (B and C) inspired from new structural data, seismic analysis (Allard et al., 2020; Gianni et al., 2015a) and existing cross-sections (Pezzuchi, 2018). Stratigraphic thickness of Chubut unit from Allard *et al.* (2020). Samples indicated on cross-sections correspond to projection of the real location of sampling sites (15 kilometers maximum with sample MG7). Red squares correspond to places were pictures of tilted Oligo–Miocene Buen Pasto basalts (D and E) and Pliocene Cerro Grande basalts (F) have been taken.

In the study area, the description of sediments belonging to the upper Chubut Group, the Salamanca and the Rio Chico Formations, evidence a late Early – Late Cretaceous and a Paleocene – middle Eocene deformation episodes acting in the intraplate belt (Gianni et al., 2017, 2015a; Navarrete et al., 2015), while these formations appear mostly related to a syn-rift stage into the adjacent San Jorge Basin (Gianni et al., 2015a; Paredes et al., 2018, 2013) and into the lower Chubut Group units (Allard et al., 2020 and references therein). These Late Cretaceous – Paleogene contractional events are followed

by a period of tectonic quiescence characterized by intraplate volcanism and modest foreland subsidence resulting from crustal thinning (Bruni et al., 2008; Encinas et al., 2018) which is related to slab rollback (Echaurren et al., 2016; Rapela and Kay, 1988) after a reduction in average trench velocity (Maloney et al., 2013). Intraplate late Oligocene – early Miocene basalts, called the Buen Pasto Formation, whose origin is still debated (e.g. mantle plume, Kay et al., 2007; asthenospheric upwelling, Bruni et al., 2008; delamination, Remesal et al., 2012), cap vast portions of the southern San Bernardo FTB, sometimes forming plateaus (Figure 5.1A). These basalts are also associated with moderate extensional processes as evidence by coeval activity of minor normal faults (Gianni et al., 2017; Bruni et al., 2008). The Plio–Pleistocene Cerro Grande basalts lie unconformably above all the underlying formations and remain mostly undeformed (Bruni et al., 2008), unlike the Buen Pasto basaltic cover. Indeed, the latter has been affected by narrow NNW-trending folds with a maximum tilting of ~35° (Figure 5.1A) which indicate deformation processes across the broken foreland through the Miocene (Barcat et al., 1989; Homovc et al., 1995; Peroni et al., 1995).

5.4 Material and methods

Four Cretaceous tuffaceous sandstones were collected for apatite fission tracks and (U-Th-Sm)/He analysis in the southwestern San Bernardo FTB (MG7, MG9, MG17 and MG20; Figure 5.1A) in diverse formations of the Chubut Group, i.e. the Aptian Matasiete Formation, the Aptian – Albian Castillo Formation and the Cenomanian – Maastrichtian Bajo Grande Formation (Figure 5.2A). Geographic location and stratigraphic age of the detrital samples are detailed in Table 1. In addition, two basalts were collected in this area for K-Ar dating: a tilted basalt MG18 (69.4250 °W, 45.0682 °S, 739 m) sampled in the Buen Pasto basalts and a basaltic dike MG21 (69.7130 °W, 45.4616 °S, 582 m) associated to the Cerro Grande basalts.

5.4.1 Apatite fission tracks

The apatite fission tracks (AFT) dating depends of the accumulation of linear damage in the apatite lattice due to the spontaneous fission decay of ^{238}U into the crystal. The partial annealing zone (PAZ) corresponds to the interval (~120 – 60°C) above which tracks are retained in the lattice (Green et al., 1989). AFT have been counted in this study with the external detector method on the four Cretaceous detrital samples (Figure 5.2A). Apatite grains were separated from crushed rock samples at the University of Padua (Italy) using standard magnetic and heavy-liquid separation technique (Na-polytungstate with a density of 2.8 g/cm^3). Apatite grains were then mounted in epoxy resin, polished and etched at 5.5M HNO3 during 20 seconds at 20°C to reveal spontaneous tracks. The mounts were covered by low-uranium muscovite foils, as external detector (Gleadow, 1981), and irradiated at the Radiation Center of Oregon State University with a nominal fluence of 9×10^{15} neutrons/cm^2. After irradiation, mica detectors were etched for 40 minutes in 40% HF at 20°C to reveal induced tracks. We counted tracks and measured track

length distribution using an Olympus optical microscope at a magnification of ×1250. Age calculation and statistics were carried out with the Trackkey software (Dunkl, 2002). We report AFT ages as central age with 1σ errors (Galbraith and Laslett, 1993), using a zeta calibration approach (Hurford and Green, 1983) with a zeta value of 346 ± 12 for the CN5 dosimeter glass.

5.4.2 Apatite (U-Th-Sm)/He

The (U-Th-Sm)/He thermochronology method is based on the production, ejection and accumulation in the crystal of ^{4}He gas produced by the decay of radioactive elements (^{238}U, ^{235}U, ^{232}Th, ^{147}Sm). As He is a gas, the accumulation in the crystal is thermo-dependent and will be function of the time-temperature path, crystal size and diffusion coefficient that is strongly modified by the amount of radiation damage (Farley, 2000; Gautheron et al., 2009; Flowers et al., 2009). The partial retention zone (PRZ) is the interval above which He diffusivity is sufficiently low to retain He within the crystal. For apatite, the PRZ ranges approximately from 40 to 120°C depending on the thermal history and damage amount (Ault et al., 2019 and references therein). We performed (U-Th-Sm)/He analysis at the University of Paris-Saclay (Orsay, France) on ten single grains from samples MG7, MG17 and MG20. After a careful selection (morphology, size, lack of visible inclusions, grain boundary phase), 2 to 4 apatite grains per sample were placed into platinum baskets and heated twice by a diode laser (1030 ± 50°C for 5 min) for He-extraction. The ^{4}He gas is mixed with a known ^{3}He spike, purified and analyzed with a Prisma quadrupole mass spectrometer. These grains were then dissolved in a nitric acid solution (3 hours at 70°C in 50 µL HNO_3 5N containing a known content of ^{42}Ca, ^{235}U, ^{232}Th, and ^{149}Sm followed by the addition of 0.9 mL ultrapure MQ water), before to be analyzed with high resolution ICP mass spectrometry (Element XR from Thermo Scientific). Durango apatite fragments analyzed similarly were used for calibration. Single ages were corrected using the calculated ejection factor F_T, determined using the Monte Carlo simulation technique of Ketcham et al. (2011); the equivalent-sphere radius (Rs) was calculated using the procedure of (Gautheron and Tassan-Got, 2010). The 1σ error on single-grain AHe ages should be considered as 9%, reflecting the sum of errors in the ejection-factor correction and age dispersion of the standards.

5.4.3 K-Ar dating

In order to constrain the timing of the late deformation phase in this area (e.g. Bruni et al., 2008), a tilted basalt (MG18) and an undeformed basaltic dike related to the basaltic plateau (MG21) were collected in the San Bernardo FTB for K-Ar dating into the Oligo-Miocene Buen Pasto formation, and in the Pliocene Cerro Grande basalts, respectively. The K-Ar dating technique, which relies on the measurement of radiogenic argon (^{40}Ar*) content produced from the radioactive decay of ^{40}K, has been applied here to the groundmass. As it is the last mineral phase to crystallize, this technique provides ages

of the lava emplacement. Effectively, any inherited ^{40}Ar carried by early crystallizing minerals, such as olivine, pyroxene, or plagioclase, is not a concern here (e.g. Samper et al., 2008). Furthermore, this phase is enriched in incompatible elements including potassium, and it was in isotopic equilibrium with the atmosphere during cooling to surface temperature. From both samples, groundmass was separated within a 125-250 μm size fraction, determined from thin section analyses. Following manual crushing and sieving, heavy liquids (diiodomethane) were used to extract groundmass within a narrow density range in order to remove any undetected weathered fraction. Both potassium and argon measurements were carried out twice in the GEOPS laboratory (Paris-Saclay University, France) by using the unspiked K-Ar Cassignol-Gillot technique (e.g. Gillot et al., 2006). Decay constants and isotopic ratios of Steiger and Jäger (1977) have been used. The full description of analytical procedures, standards, age calculation and uncertainty calculation are given in Bablon et al. (2018).

5.5 Results

5.5.1 Partially reset AFT ages

Despite the low number of counted grains (10 to 53), Cretaceous samples yield consistent late Early – Late Cretaceous AFT ages between 128.0 ± 8.7 Ma and 88.5 ± 11.4 Ma. The chi-square probability (> 5%) indicates a single population for all the samples. Looking at the radial plot for single-grain AFT ages (Figure 5.2C), a significant number of grains are younger than the depositional age and few grains are older, which evidences a moderate partial reset of the AFT ages. For the samples MG7, MG9 and MG17, the central AFT ages are fairly younger than the depositional age whereas the sample MG20 is somewhat older (Table 1; Figure 5.2A). However, taking in account the uncertainty for these values (Figure 5.2A), the overall picture shows AFT ages quite similar to the depositional ages. Noticeable also, most of the apatite grains in the samples are euhedral. Therefore, the apatite crystals are mainly considered as volcanic and the ages obtained could be related to coeval arc volcanism during the deposition of the Chubut deposits (Foix et al., 2020). Then, the apatite grains have been moderately affected by a thermal event as evidenced by the modest partial reset of the AFT data.

5.5.2 Totally reset AHe ages

AHe samples yield single grain ages between 15.9 ± 1.3 Ma and 28.7 ± 2.3 Ma with low effective Uranium (eU) content that range from 5 to 40 ppm and relatively high Th/U ratio (5 to 12) (Table 2). The AHe ages are significantly younger than the depositional age (Figure 5.2A) and indicate a post-depositional resetting. Although no correlation appears between AHe dates and eU content, correlation is recognized to some extent between AHe dates and Rs size (Figure 5.2B).

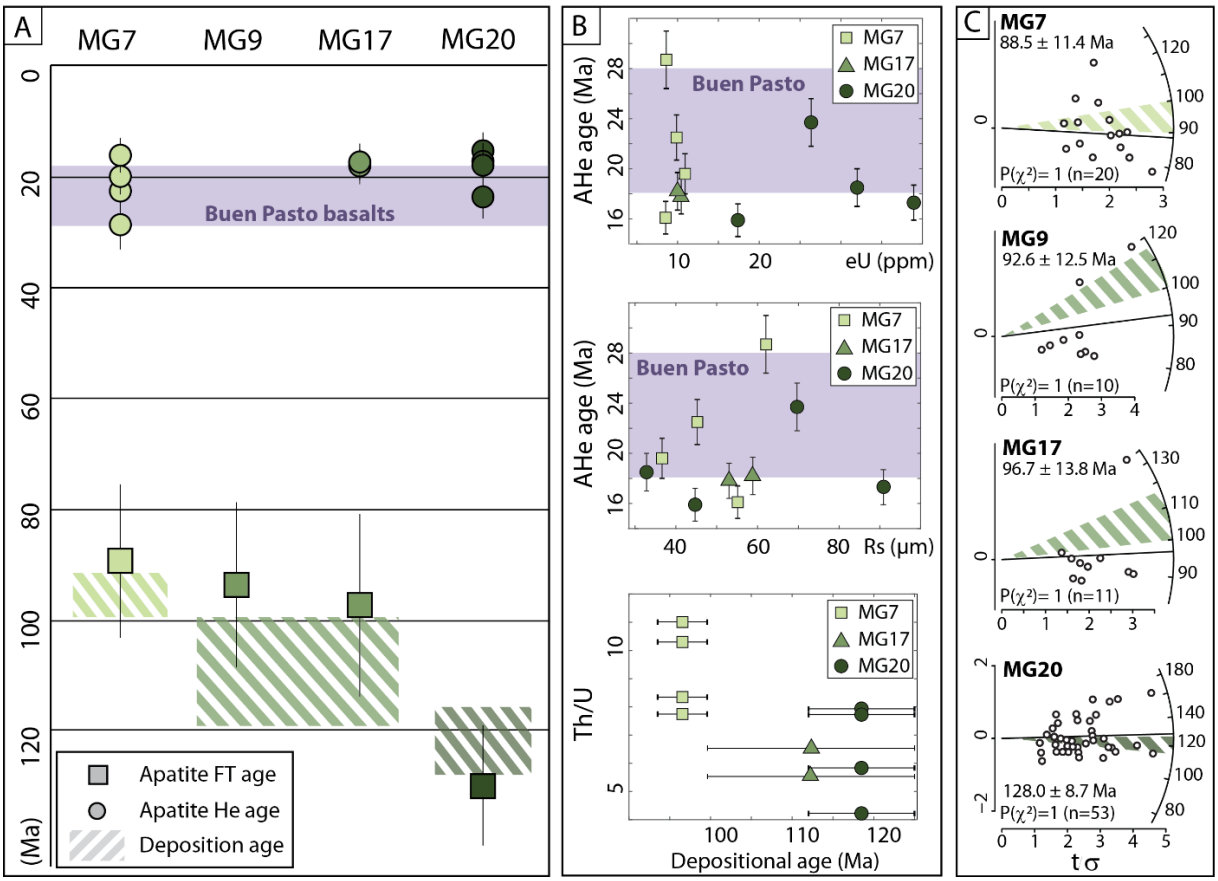

Figure 5.2 – A. Comparison of apatite FT and (U-Th-Sm)/He ages with deposition ages for the samples collected in the Chubut Group. B. Diagrams representing AHe data (eU/AHe age, Rs/AHe age and depositional age / Th/U). The effective Uranium content being eU=U+0.234×Th+0.0046×Sm. C. Radial plots with IsoplotR (Vermeesch, 2018) for single-grain AFT ages which evidence partial reset of the data.

5.5.3 Thermal history

With the aim of evaluating the thermal history of the San Bernardo FTB, T-t histories for samples MG7, MG17 and MG20 have been realized through inverse modelling with the QTQt software (v. 5.7.1; Gallagher, 2012). The QTQt software allows inverting AFT annealing and AHe diffusion parameters with the Markov Chain Monte Carlo method (Gallagher, 2012; Gallagher et al., 2009) for single samples. He diffusion model incorporating the impact of radiation damage in apatite from Flowers et al. (2009), rather than the He diffusion model from Gautheron et al. (2009), has been used because of the relatively low eU content and thus damage content. Beyond the He diffusion model, AFT annealing kinetic model by Ketcham et al. (2007) has been considered. The modeling procedure is detailed in Gallagher (2012). The input parameters used to model each sample are the single-grain AFT and AHe ages, as well as the grains sizes and the chemical characteristics for AHe data. Main constraints were the depositional age of each sample (at 20 ± 10°C) and a present-day temperature at 10 ± 10°C. A high-temperature constraint has been added closely before the deposition age as the high Th/U ratio (Table 2) and the euhedral shape of the apatite grains suggests a volcanic (not recycled) origin for those apatite crystals. The thermal history results (Figure 5.3) are strongly impacted by the total reset of the AHe data that impose a minimum

temperature of ~60 °C during the Oligo – Miocene. Therefore, the models demonstrate the presence of a significant heating phase through the late Paleogene, closely followed by a cooling event starting from early Miocene (Figure 5.3). Predicted values obtained for AHe and AFT ages are mostly consistent with observed ages.

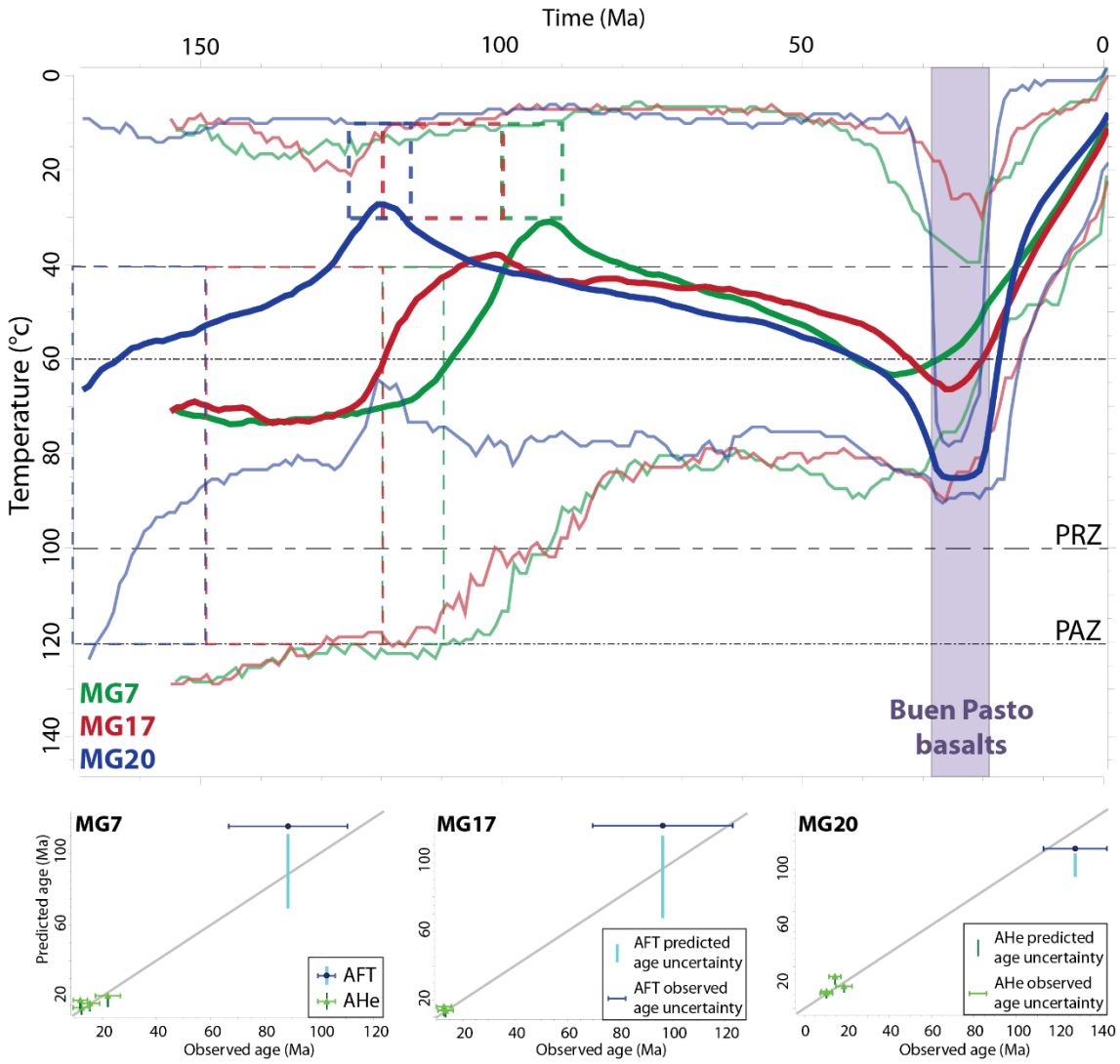

Figure 5.3 – Inverse modeling evidencing late Oligocene heating and early Miocene cooling for all the samples. Each line represents the best-fit model (in bold) and the uncertainties. Dotted rectangles show the constraints used for the models as the deposition time (in bold) or the initial high temperatures. Below, observed vs predicted ages plots for all the samples.

5.5.4 K-Ar ages

The tilted basalt and the basaltic dike yield ages of 23.71 ± 0.34 and 2.84 ± 0.04 Ma, respectively. Age results are given at the 1σ confidence level and details are given in Table 3. These ages are in agreement with former studies, which reported ages between 28 and 18 Ma for the Buen Pasto basalts and younger than 4 Ma for Cerro Grande basalts (Sinito, 1980; Linares *et al.*, 1989; Bruni *et al.*, 2008). Thus,

TABLE 1. SUMMARY OF SAMPLE INFORMATION AND APATITE FISSION TRACKS DATA

Samples†	Field*			Geology		Fission tracks data								
	Longitude	Latitude	Elev. (m)	Formation	Stratigr. age	n	**C. age**	**σ**	Ns	ρs	Ni	ρi	Nd	ρD	P(χ^2)
MG7	-69.2818	-45.5345	283	Bajo Barreal	Cenomanian	20	**88.5**	**11.4**	97	1.4	209	2.9	5000	11.1	100
MG9	-69.7016	-45.4590	557	Castillo	Aptian-Albian	10	**92.6**	**12.5**	88	2.5	178	5.1	5000	10.9	100
MG17	-69.0178	-45.4174	373	Castillo	Aptian-Albian	11	**96.7**	**13.8**	83	1.1	143	2.0	5000	9.7	100
MG20	-69.3007	-45.1388	568	Matasiete	Aptian	53	**128.0**	**8.7**	483	2.6	847	4.6	5000	13.1	100

* longitude and latitude coordinates are given in WGS84

† Zeta= 346 ± 12

N: number of apatite crystal counted; and ρ: track density (x 105 tracks/cm²); subscripts s, I and d denote spontaneous, induced and dosimeter, respectively; P(χ^2): probability of obtaining a Chi-square value for n degrees of freedom.

TABLE 2. APATITE (U-TH)/HE SINGLE-GRAIN DATA.

Sample	Longitude	Latitude	Elevation (m)	weight (μg)	Rs (μm)	FT	^{4}He (ncc/g)	U (ppm)	Th (ppm)	Sm (ppm)	eU (ppm)	Th/U	AHe age (Ma)	**Corrected AHe age**	**± 1σ (Ma)**
MG7B	-69.2818	-45.5345	283	2.3	62.1	0.77	22362	2.3	25.4	265.4	9	11.0	22.12	**28.7**	**2.3**
MG7C	-69.2818	-45.5345	283	1.0	45.2	0.69	18043	2.8	28.8	217.4	10	10.3	15.49	**22.5**	**1.8**
MG7D	-69.2818	-45.5345	283	1.1	36.6	0.63	15984	3.7	29.0	252.3	11	7.7	12.42	**19.6**	**1.6**
MG7E	-69.2818	-45.5345	283	2.2	55.1	0.74	11913	2.7	22.9	358.2	9	8.3	11.96	**16.1**	**1.3**
MG17A	-69.0178	-45.4174	373	4.1	58.9	0.74	8915	2.4	13.0	134.1	6	5.5	13.52	**18.2**	**1.5**
MG17C	-69.0178	-45.4174	373	3.9	53.0	0.72	15715	3.9	25.8	380.5	10	6.5	12.84	**17.8**	**1.4**
MG20A	-69.3007	-45.1388	568	1.7	44.7	0.66	21273	5.8	46.1	647.3	17	7.9	10.45	**15.9**	**1.3**
MG20B	-69.3007	-45.1388	568	9.1	90.9	0.83	67143	16.2	94.3	179.6	39	5.8	14.43	**17.3**	**1.4**
MG20D	-69.3007	-45.1388	568	0.9	32.8	0.56	39320	11.0	85.2	687.9	32	7.7	10.39	**18.5**	**1.5**
MG20G	-69.3007	-45.1388	568	5.4	69.7	0.79	58989	13.0	55.0	175.7	26	4.2	18.72	**23.7**	**1.9**

Note: Rs: sphere equivalent radius of hexagonal crystal with the same surface/volume ratio; FT: geometric correction factor for age calculation; eU: effective uranium concentration.

our results further support earlier observations that the area was affected by two intraplate volcanic events from the late Oligocene to the early Miocene, and later, through the Pliocene. Overall, the Oligo-Miocene Buen Pasto basalts display ages between 28 and 18 Ma, but only ages older than 20.5 Ma have been previously reported (Bruni et al., 2008a) close to the sampled areas. The youngest K-Ar ages (< 20 Ma) have been obtained about 20 km to the north and to the east of our study area (Bruni *et al.*, 2008). As erosion of this Oligo-Miocene basaltic cover is clearly visible on cross-sections (Figure 5.1B and 5.1C) , the upper layers of the basaltic cover with ages younger than 20 Ma may have been removed or altered. Therefore, as demonstrated by the geometry of the basalts sampled, and the K-Ar ages obtained here, a tectonic phase occurred between the deposition of these Oligo-Miocene and Pliocene basaltic layers.

TABLE 3. K-AR AGES

Sample	experiment no.	weight fused (g)	K (wt.%)	^{40}Ar* (%)	^{40}Ar* E+12 (at/g)	Age ± 1σ (Ma)	Weighted mean age ± 1σ (Ma)
MG18	5654	0.50052	1.188	62.9	29.348	23.50 ± 0.33	
(Buen Pasto)	5668	0.40044	1.188	64.9	29.862	23.91 ± 0.34	23.71 ± 0.34
MG21	5655	0.49925	1.790	46.7	5.3165	2.84 ± 0.04	
(Cerro Grande)	5667	1.40480	1.790	56.9	5.3209	2.84 ± 0.04	2.84 ± 0.04

5.6 Discussion

Consistent totally reset Oligo – Miocene AHe ages and partially reset AFT ages have been obtained in all the samples. Thermal models (Figure 5.3) are coherent with a period of thermal quiescence between the Cretaceous and the Oligocene. This period is followed by a significant heating event during the early Miocene with peak temperatures reached at ca. 25 ± 2 Ma, mostly coincident with the K-Ar ages in the area (Figure 5.1A). We discuss here the causes for this heating event, which could be due either to a sedimentary load, basaltic load and / or to magmatic heating effects. We will also discuss the tectonic implications in the post-heating phase recorded into the San Bernardo FTB during the Miocene.

5.6.1 Burial heating below sediments

Deposition of the Chubut deposits in the southwestern San Bernardo is directly controlled by fault activity and the development of folds (Gianni et al., 2015a). Seismic data in the southwestern San Bernardo FTB show that synorogenic Cretaceous deposits were locally buried below few hundred meters of Paleogene deposits, especially between anticlines (Rio Chico Formation; Gianni *et al.*, 2015), which are not sufficient to reset the low-temperature thermochronometers, even the AHe one locally. In areas where no Paleogene deposits have been recognized, Oligo-Miocene basalts (Buen Pasto Formation) lie directly on top of the Chubut Group strata (Allard et al., 2020; Gianni et al., 2015a; Navarrete et al., 2016,

2015). This unconformity indicates that underlying formations were at the surface prior the emplacement of these basalts, which is inconsistent with a significant burial below a Paleogene cover. Although the removal of Paleogene sediments cannot be a priori excluded, the lack of significant Paleogene sedimentary burial is supported by the thermal models which show a period of relative thermal quiescence between the Cretaceous and the Oligocene (Figure 5.3).

Thus, considering that at least 1 km of sediments are necessary to reset totally the AHe (with a closure temperature of ~ 65°C; e.g. Flowers et al., 2009; Gautheron et al., 2009) and partially the AFT thermochronometers, using an average thermal gradient of 30°C/km, we exclude burial as main cause for heating.

5.6.2 Impact of late Oligocene – early Miocene volcanic activity

Thermal models show that maximum temperature of 60 – 80°C was attained at 20 – 30 Ma, which is roughly coeval with the emplacement of the Buen Pasto basalts (Figures 2A, 2B and 3). Given the absence of a significant Cenozoic sedimentary burial in the area, we propose that the heating phase observed could be related to diverse Oligo – Miocene volcanic processes as: 1) an increase of the geothermal gradient due to heat flow anomaly, 2) a top-down heating by thermal advection after basalts emplacement, and 3) the burial exerted by the volcanic deposits.

Rocks near the surface cannot be significantly affected by a deep heat flow anomaly (Gautier et al., 2002). Indeed, in areas affected by magmatism, the increase of the geothermal gradient resulting from magma ascent is modest toward the surface. This kind of process could give relevant effects on high-temperature thermochronometers but not to AFT or AHe systems.

Otherwise, instantaneous heating events near the surface are associated with a downward thermal heating below the basalts (Fayon and Whitney, 2007; Hu et al., 2020). For basaltic floods of 50 m with a temperature of 1000 °C, heating may affect instantly the first 250 meters of rocks beneath the basalts (Fayon and Whitney, 2007) and can affect the AFT thermochronometer (Hu et al., 2020). It is noteworthy to consider that multiple heating events occurred in the study area from ~28 Ma to at least ~18 Ma, according to the K-Ar ages obtained on the basaltic cover across the San Bernardo FTB (this work; Bruni *et al.*, 2008; Sinito, 1980; Linares *et al.*, 1989). Therefore, it is very likely that Cretaceous rocks located near the surface during Oligo-Miocene experienced short-term high temperatures events from 28 to 18 Ma due to downward thermal diffusion. Thermal diffusion of such processes may, however, not explain the few AHe ages younger than 18 Ma obtained in this study since cooling may occur instantly at the end of the volcanic event. As 18 Ma is the presumed age of the cessation of this Oligo-Miocene intraplate volcanic activity (Bruni *et al.*, 2008), other processes are necessary to explain these younger AHe ages: i) the basaltic cover may have reached a sufficient thickness to maintain the samples below the closure temperature of the AHe system after 18 Ma; or ii) the intraplate volcanic activity may have continued to ~16 Ma, as constrained by younger AHe ages obtained here.

As previously suggested, minor displacements along normal faults evidenced extensional processes through the Oligo-Miocene in the southwestern San Bernardo FTB, associated with the Buen Pasto basalts (Gianni et al., 2017). Therefore, although there is an absence of constraint about the thickness of the original basaltic cover (and hence of its erosion; Figure 5.1), a modest burial of the Cretaceous strata produced by the basaltic cover cannot be ignored as the Oligo-Miocene intraplate volcanism lasted for at least ~10 Ma and covered vast areas of the foreland. Considering an average geothermal gradient of ~30 °C/km and a closure temperature of ~ 65°C for the AHe system (e.g. Flowers et al., 2009; Gautheron et al., 2009), a basaltic cover thickness of at least one kilometer above the entire San Bernardo FTB would have been necessary to maintain sufficient temperatures (> 65 °C) after the cessation of volcanic activity at ~18 Ma. Then, a comparable erosion of the basaltic cover would have been required in order to achieve current basalt thicknesses. Even a modest erosion may have been sufficient to erode intensively the Oligo-Miocene basalts of the Buen Pasto Formation as this silicate rocks is easily weathered (Margirier et al., 2019; Meybeck, 1987) especially during a climatic optimum, here through the late middle Miocene (Zachos et al., 2001). Nevertheless, the scenario involving a basaltic cover thickness of one kilometer minimum is not suitable with: 1) the thickness of the basaltic layers in the whole central Patagonia as they often display only tens of meters (Figures 1D and 1E), and 2) the geological record as the Neogene sedimentary units in surrounding depocenters which do not show any significant basalt sourcing (Anselmi et al., 2004b; Pezzuchi, 2018; Sciutto et al., 2008) and are subjected to felsic sources coming from the main Cordillera (Genge, 2021).

Considering that basaltic cover thickness alone was not sufficient to maintain high temperatures in the sediments below, we propose that the younger AHe ages obtained are related to the persistence of the volcanic activity up to ~16 Ma. As a portion of the basaltic cover has been eroded on top, the timing of the cessation of the volcanic activity so far defined at ~18 Ma, which corresponds actually to the youngest age obtained by K-Ar dating across the San Bernardo FTB (Bruni *et al.*, 2008), may have been underestimated as the topmost basaltic layers have been removed. It is noteworthy that, the Oligo-Miocene volcanic products were extruded through several extensional faults and fissures (Gianni et al., 2017) and accompanied by the emplacement of sills and dikes over the San Bernardo FTB (Plazibat et al., 2019) that caused the entire area to be affected by high heat flow from Oligocene to early Miocene.
The Oligo-Miocene volcanic activity was much more significant than the Pliocene intraplate volcanism as no Pliocene thermal perturbation has been evidenced by our data. In other words, the intraplate Pliocene volcanic event did not trigger any significant heating by downward thermal diffusion able to reset our thermochronology data. This difference may be explained by thinner basaltic layers, which are thus related to a minor impact of the downward thermal heating, and/or minor circulation of fluids through faults and fissures across the San Bernardo FTB.

5.6.3 Miocene cooling and associated exhumation

As suggested in the previous sections, a cooling episode from c. 20 Ma to present is then observed, at the end of the Oligo-Miocene intraplate volcanic event. The correlation between the AHe ages and apatite crystal size (Rs) (Figure 5.2B), as well as the thermal models (Figure 5.3), indicate that the samples cooled down at moderate rates. The thermal models show that maximum cooling rate (~ 4°C/Ma) is observed for the sample MG20, considering a peak temperature of 80°C at ca. 20 Ma (Figure 5.3). For the sample MG20, cooling occurred instantly at the presumed end of the magmatic episode (~ 18 Ma), which is consistent with the cessation of the volcanic event. Nevertheless, the cooling rate obtained is not compatible with a post-magmatic cooling, which is usually much faster.

Giving the ages obtained by K-Ar dating on the tilted basalt and the undeformed basalt, 23.71 ± 0.34 and 2.84 ± 0.04 Ma, respectively, deformation phase occurred between the early Miocene and Pliocene. Growth strata observed in surrounding sedimentary records and reactivation of inherited normal faults pointed to the existence of a distinct tectonic event during the middle Miocene in the study area (e.g. Gianni *et al.*, 2017), which, according to Maloney *et al.* (2013), could be related to the change of convergence of the Nazca plate. This deformation event was also evidenced in the northern (Gastre Basin; Bilmes *et al.*, 2013) and the southern Patagonian Broken Foreland (Deseado Massif; Giacosa *et al.*, 2010), although low-temperature in-situ thermochronology studies in these areas suggest minor vertical displacements (Fernández et al., 2020; Savignano et al., 2016). Considering field observations (see bedding attitudes on Figure 5.1) and thermochronology results in surrounding areas, it is proposed here that the role of tectonism during the Miocene is also negligible along the southwestern San Bernardo FTB, and, thus, only modest deformation occurred in this area from early Miocene to present.

Therefore, we consider that the obtained Miocene cooling ages result from the cessation of the magmatic activity, accompanied by a slow decrease of the heat flow, whereas the role of deformation as a triggering source of enhanced exhumation was probably very minor. We thus conclude that, as previously proposed for other parts of the Patagonian Broken Foreland, main deformation of the southern San Bernardo FTB occurred from the Cretaceous to the early Paleogene, while Miocene deformation was modest, especially in terms of vertical displacements. Indeed, we can estimate the exhumation of the area lower than 1 km, as it did not significantly affect the low-temperature thermochronometer.

5.7 Conclusions

AFT and AHe thermochronology have been applied for the first time to the San Bernardo FTB to constrain the tectono-thermal evolution of this intraplate belt. The main results from dating and thermal modeling highlight a period of thermal quiescence from the Cretaceous to the Oligocene, while a thermal episode affected all the region. According to the thermal models and the ages of the Buen Pasto basalts, the Oligo-Miocene heating phase recorded by our data must be regarded as a magmatic signal induced mainly by the thermal downward advection from the basaltic layers, that affected thermochronometers

from rocks near the surface. The emplacement of dikes, sills and the circulation of hot fluids along faults and fissures during this long-term volcanic phase may allowed to maintain a high heat flow in the area. Our thermochronological data most likely resulted from the long-term activity of the Oligo-Miocene intraplate volcanism rather than to a significant tectonic activity during the Neogene.

5.8 Acknowledgements

This work was funded by the University of Padova (Progetto di Ateneo 2015, CPDA158355), the Tellus Program of CNRS/ INSU and the CESSUR Program of CNRS / INSU for the AHe analysis. A. Hildenbrand is kindly thanked for K-Ar analysis (Orsay, France). Thanks to R. Pinna-Jamme and F. Haurine for their technical support in AHe analysis. V. Olivetti (University of Padua) and M. Marquez (SEGEMAR, Comodoro Rivadavia) are thanked for their constructive comments.

CHAPTER 6

TECTONIC EVOLUTION FROM SEDIMENTS: DETRITAL COOLING AGES DISTRIBUTION IN MODERN RIVER CATCHMENTS FROM CENTRAL PATAGONIAN ANDES

Marie C. Genge[1,2], Massimiliano Zattin[1], Valerio Olivetti[1], Kerry Gallagher[3], Jamie Buscher[4,5]

[1] Dipartimento di Geoscienze, Università degli Studi di Padova, via G. Gradenigo 6, 35131 Padova, Italy

[2] Univ. Lille, CNRS, Univ. Littoral Côte d'Opale, UMR 8187, LOG, Laboratoire d'Océanologie et de Géosciences, F 59000 Lille, France

[3] Géosciences Rennes/OSUR, University of Rennes, Rennes, 35042, Rennes, France

[4] Department of Geology, FCFM, Universidad de Chile, Plaza Ercilla 803, Santiago, Chile

[5] Andean Geothermal Centre of Excellence (CEGA), FCFM, Universidad de Chile, Plaza Ercilla, Santiago, 803, Chile

Declaration

This chapter aims to infer thermal histories and the evolution of catchment erosion within the central Patagonian Andes based on detrital apatite fission tracks age distribution, hypsometric curves and geomorphic data, without any vertical profiles. This chapter is also written in order to validate tectonic scenario proposed and better understand the impact of different features (as faults) on the AFT age distribution. MCG, MZ, VO and JB carried out fieldwork, including sampling for thermochronology dating methods. MCG provided all apatite fission tracks dating, thermal models, river profiles, all the figures and the original draft for this paper. MZ made a careful review of the original draft and acquired fundings for this work. This work is still in preparation as further analysis (vertical bedrock profile?) and discussions with VO (for geomorphology and impact of glaciations) and KG (for thermal modeling) are needed to improve the interpretation of the results.

6.1 Abstract

Detrital thermochronological data has been recognized as a reliable proxy to assess spatial variation and long-term evolution of catchment erosion. Based on the distribution of detrital cooling ages and the hypsometry of the catchment, a recent approach infers hypothetical vertical profile and subsequent thermal history of a single catchment. Assuming a similar history across the catchment, cooling ages increase with elevation. Thus, the study of an outlet detrital sample provides an integrated signal of rock cooling from all the sediment source areas in a catchment, including areas inaccessible for bedrock dating. In Patagonian Andes, because the access to the highest elevations is usually arduous due to the steep slopes, few vertical profiles have been carried out. In this study, we investigate the thermal histories of 8 catchments of the north-central Patagonian Andes by analyzing the apatite fission tracks age distribution of modern river sand collected at the outlet of the catchment. Only small catchments (< 400 km²), with a significant elevation ratio (~1500 m) and a unique lithology (Cretaceous granitoids of the Patagonian Batholith) were selected. Results are in good agreement with published bedrock data suggesting that some areas, affected by the activity of the Liquiñe-Ofqui Fault, recorded a recent late Miocene cooling. However, significant variations in cooling age distribution are observed between close catchments (some sharing watershed limit). We related these discrepancies to local sediment storage and focused erosion identified on river profiles. Therefore, this study show how significant are the impact of glacier and fault activity on the cooling age distribution across a single catchment. Despite the relative unprecise information obtained, we demonstrate that this approach linked with geomorphologic study allows to obtain a respectable and quick overview of the regional evolution of a mountain range.

6.2 Introduction

The Patagonian Andes building is the result of alternating phases of compressional and extensional deformation since late Early Cretaceous which are related mainly to deep geodynamic evolution (e.g. slab flattening, slab window opening; Guillaume et al., 2013; Horton, 2018a), but with still poorly known inference due to climate (Thomson et al., 2010a). Current knowledges about the thermal evolution of the central Patagonian Cordillera are based on an extensive in-situ thermochronology dataset (Figure 6.1B; Georgieva et al., 2019, 2016; Guillaume et al., 2013; Thomson, 2002; Thomson et al., 2010, 2001). However, given the large extent of the study area (44° to 48°S) and the diverse processes affecting denudation of this range, uneven data are not sufficient to interpret regional trends. Detrital thermochronology on samples collected at the outlet of modern rivers represents a novel approach to infer the evolution of catchment erosion in inaccessible areas. Associated to hypsometry measurements extracted from digital elevation model (DEM) (Brewer et al., 2003; Ehlers et al., 2015) and predicted cooling age distribution (Gallagher and Parra, 2020; Stock et al., 2006), this approach allows to quantify the distribution of catchment erosion (Stock and Dietrich, 2006; Vermeesch, 2007), to identify catchments

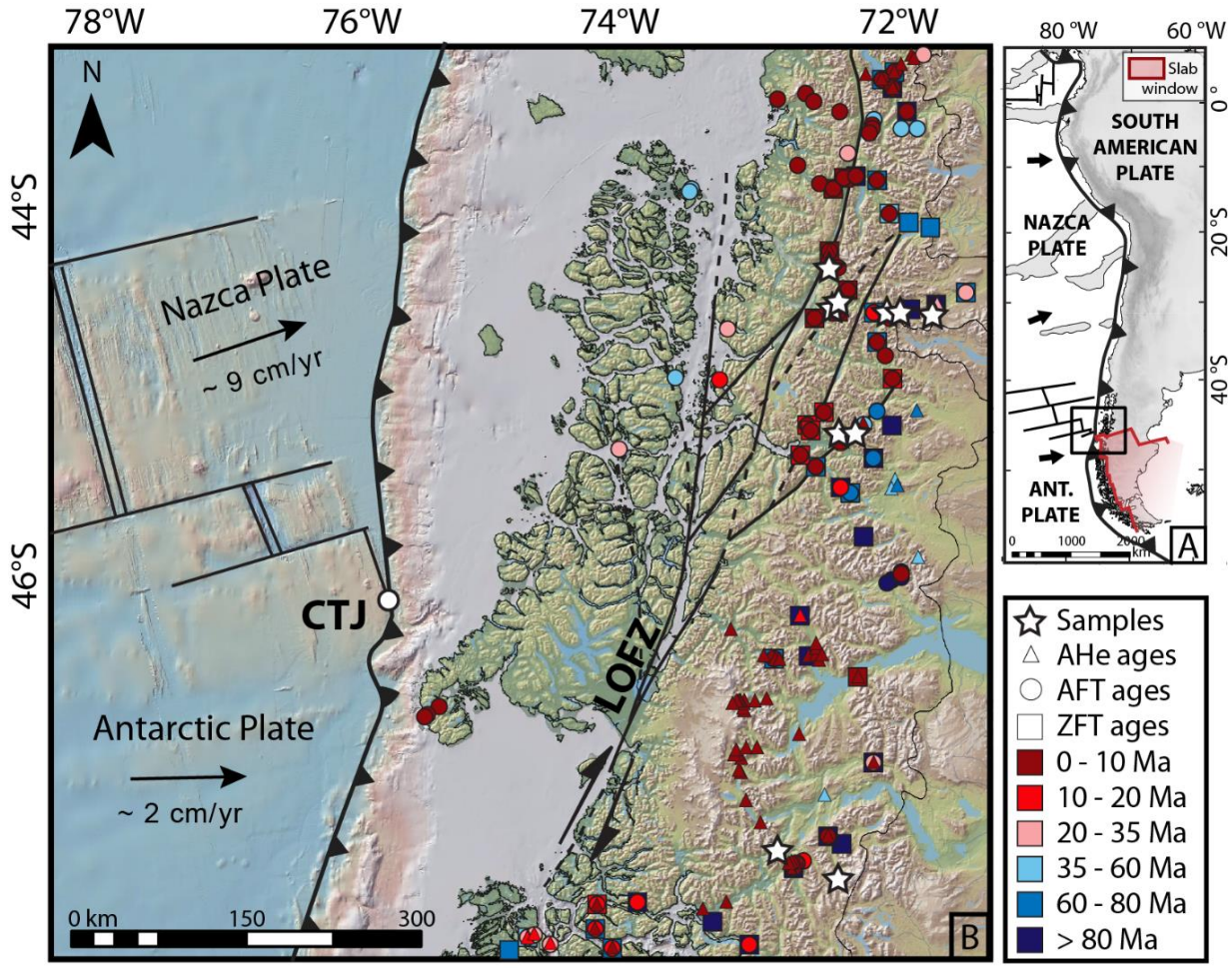

Figure 6.1. Map of South America with red area delimiting the current slab window extended below the austral Patagonia and location of map B. B. Structural map of the central Patagonian Andes (44 – 48 °S) which evidences the position of the Liquiñe-Ofqui Fault Zone (LOFZ). Location of detrital (white stars) samples, with zircon and apatite fission tracks (ZFT and AFT, respectively) and apatite (U-Th-Sm)/He (AHe) ages (from Guillaume et al., 2013; Thomson, 2002; Thomson et al., 2010, 2001).

with a nonuniform erosion and to infer thermal histories directly from detrital inverse modeling (Gallagher and Parra, 2020). Indeed, in the case of uniform erosion, each location of the DEM is delivering the same amount of sediment (Stock et al., 2006). Assuming that thermochronometer cooling ages are increasing with elevation, a comparison of the predicted data with the measured probability density function (PDF) evidences the uniformity of the erosion and the significance of the delivery from higher or lower elevations, even if the exact source for single grain detrital data remains unknown. In this study, apatite fission tracks (AFT) and hypsometry data from 10 catchments were used as input into the QTQt software (Gallagher, 2012) to obtain the predicted PDF in order to unravel the exhumation pattern along the Cordillera. The studied catchments were selected in key areas: i) on both side of a dextral strike-slip fault zone (Liquiñe-Ofqui fault zone); ii) along the Precordillera where in-situ thermochronological data yield Cretaceous – Paleogene ages; iii) in a catchment where modern glacier cover large areas; and iv) south of the Chile Triple Junction (46° – 48°S) to observe the effect of the slab window opened below the austral Patagonia on the overriding plate (Figure 6.1A). Furthermore, changes in erosion rates can be also indicated by geomorphic markers as the steepness variations of river profiles delimited by knickpoints

(Gailleton et al., 2019). Therefore, as few attentions were dedicated to the river systems along the central Patagonian Cordillera, longitudinal river profiles have been analyzed through the 10 selected catchments with the aim to reveal patterns of erosion. Thus, for the first time in this area, detrital thermochronology associated with hypsometric data and longitudinal stream profiles analysis were conducted to understand the variability of the denudation and the different causes of these variations through the central Patagonian Cordillera. The results highlight the significant impact of local features on the cooling age distribution obtained at the outlet of the catchment.

6.3 Geological setting

The central Patagonia (44 – 48 °S) coincides with the Chile Triple Junction (CTJ) that joins the Nazca, Antarctic and South American plates at ~46 °S (Figures 1A and 1B). The differences in direction and velocity between the oceanic plates convergence – N80 orientation at 84 mm/year for the Nazca plate and E-W direction at 20 mm/year for the Antarctic plate (DeMets et al., 1990; Gripp and Gordon, 1990) – resulted in the northward migration of the CTJ since ~15 Ma, and generated the opening of a slab window currently extended below the entire austral Patagonia (Figure 6.1A; Breitsprecher and Thorkelson, 2009; Gorring and Kay, 2001). North of the CTJ, topography along the Cordillera is reduced and uniform with an average of 2000 m, while high topography reaching locally 5000 m is recognized south of the CTJ (Georgieva et al., 2016) and may have been affected by the successive ridge collisions (Lagabrielle et al., 2007; Scalabrino et al., 2011, 2009). The oblique subduction of the Nazca plate, north of the CTJ, led to tectonic partitioning in the Cordillera evidenced by the Liquiñe-Ofqui Fault Zone (LOFZ; Figure 6.1B; Cembrano et al., 2002, 1996; Hervé, 1994; Rosenau et al., 2006). This ~ 1000 km intra-arc dextral strike-slip fault system is often associated with earthquakes, volcanic activity, middle Miocene – Pliocene cooling and related exhumation (e.g. Adriasola et al., 2006; Buscher et al., 2016; Lange et al., 2008; Thomson, 2002).

Subduction of Pacific plates below the South American plate started during the Paleozoic, and possibly since the Carboniferous (e.g. Oliveros et al., 2020, and references therein). The Patagonian Andes underwent then several ridges subduction and plate configuration shifts through time (Maloney et al., 2013). The variation of kinematics, occasionally associated with slab dip changes, is linked with alternating stages of upper crust shortening and extension as a consequence of mechanical plate coupling variations (Horton and Fuentes, 2016; Ramos and Ghiglione, 2008). Thus, two main shortening pulses are recognized from the late Early Cretaceous to the early Paleogene, and from the middle Miocene to the Pliocene (e.g. Echaurren et al., 2016; Gianni et al., 2017; Horton, 2018a; Lagabrielle et al., 2004). Low-temperature thermochronology studies show that topographic evolution of the central Patagonian Cordillera was governed by complex feedbacks between these deep geodynamic processes (Georgieva et al., 2019; Guillaume et al., 2013) with climate (Thomson et al., 2010a; Willett et al., 2020) and upper crustal tectonics (Georgieva et al., 2016). Few vertical profiles in the area evidence dynamic uplift

processes, which are more important south of the CTJ as this area has been affected by the slab window and associated lithospheric heating (Guillaume et al., 2013).

Deformation episodes involved plutons related with the Patagonian Batholith (Giacosa and Heredia, 2004). The granitic suites emplaced progressively since the Jurassic, broadly coincident with the Andean shortening episodes (Adriasola et al., 2006; Butler et al., 2020; Herve et al., 2007; Pankhurst et al., 1999; Rolando et al., 2002). The alternation of steep and flat-slab in this region is evidenced by the migration of the magmatic arc toward the forearc and the foreland respectively (Aragón et al., 2013; Folguera and Ramos, 2011; Pankhurst et al., 2003). Cessation of the magmatic arc activity is recognized between ~70 and 55 Ma (Butler et al., 2020) while enhanced arc magmatic activity occurred during the Late Cretaceous and the Miocene along the entire Patagonian Cordillera. Thus, the calk-alkaline series of the Patagonian batholith corresponds to one of the largest cordilleran plutonic complexes related to subduction processes around the world (Pankhurst et al., 1999). The emplacement of these large plutons is coeval with a significant bimodal activity represented by the Late Jurassic Ibañez Formation and the Lower Cretaceous Divisadero Formation (Pankhurst et al., 2003). South of the CTJ, the presence of isolated upper Miocene plutons is common east of the Patagonian Batholith (Ramírez de Arellano et al., 2012; Ramos, 2002), involving deformation of the surrounded areas coeval with their emplacement (Skarmeta and Castelli, 1997). Such plutons are observed around the Cerro San Lorenzo which has been dated at 6.2-6.6 Ma (Welkner et al., 2002 and references therein), which is roughly coincident with the collision of the ridge at this latitude (e.g. Breitsprecher and Thorkelson, 2009).

6.4 Material and methods

Ten small catchments (<400 km²), with a significant elevation ratio (~1500 m minimum) and a unique lithology (Cretaceous granitoids of the Patagonian Batholith) were selected for this study. Modern sands have been collected at the outlet of these ten catchments (Figure 6.1B). To simplify, watersheds are called here with the same name than the samples collected at their outlet. Samples MG27 and MG28 have been selected to compare two close watersheds, sharing one ridgeline (Figure 6.2B). An active glacier is present in the watershed MG29 (Figure 6.2A). Samples MG32, MG34 and CN4 have been collected toward the eastern border of the Cordillera (Figure 6.2C). They are located in a key area as young and old AFT cooling ages have been detected to the west and to the east of the samples, respectively. Samples MG35 and MG36 were collected at the outlet of catchments located on both side of a fault (Figure 6.3A) evidenced by the work of Thomson (2002). As demonstrated by the in-situ thermochronology data existing along the surrounding valleys, recent Miocene activity is supposed for the areas located to the western side of the fault. MG38 and MG40 are the only samples located south of the CTJ (Figure 6.3B) and, thus, they are possibly affected by the slab window opening and subsequent dynamic topography.

As position of the faults related to the LOFZ are not well constrained from the satellite view and existing thermochronological in-situ data, a granite was sampled (MG31; Figure 6.2B) in an area with few data in order to extend the AFT dataset in this particular sampling area. A detrital sandstone (MG33)

was collected in the Pleistocene fluvial terrace bordering the Rio Cisnes, close to the sample CN4 (Figure 6.2C), to provide information about the source areas and their contribution in this large watershed. Indeed, as the topography indicate low reliefs toward the east and higher relief south of the sampling site, detrital thermochronology on this sample would allow to better constrain the impact of the relief on the cooling age distribution.

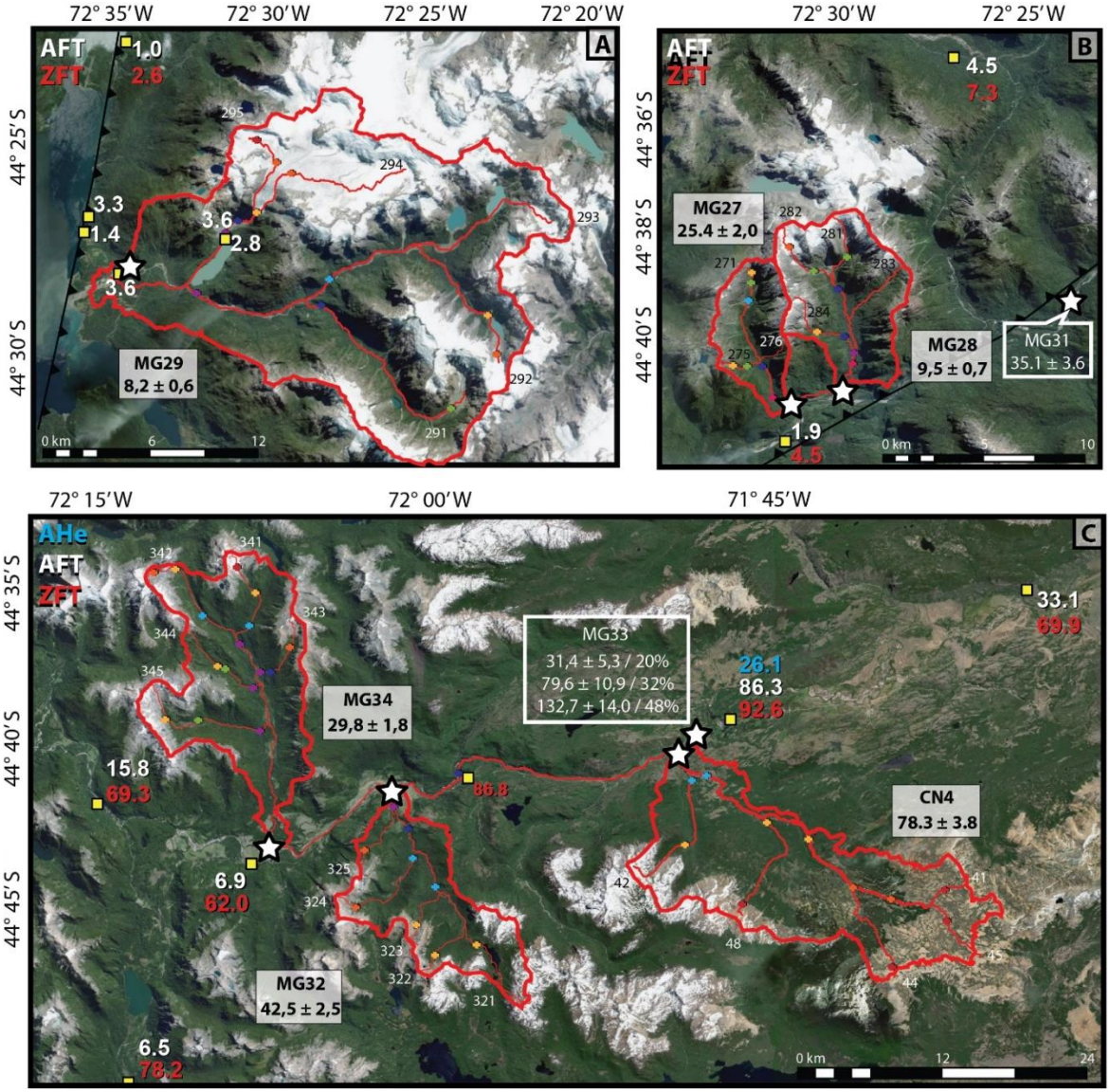

Figure 6.2. Satellite view of the studied areas with available in-situ (from Thomson et al., 2001, 2010; Thomson, 2002; Guillaume et al., 2013; this study) and detrital (this study) thermochronology data, contour of the studied watersheds with geomorphic data. A. Catchment MG29 with a modern glacier. B. Catchments MG27 and MG28 with sample MG31 in an area possibly affected by a fault related to the LOFZ. C. Catchments CN4, MG32 and MG34 with sample MG33. Clear distinction appear from in-situ thermochronology data with Miocene ages for apatites thermochronometers toward the inner part of the Cordillera and older ages toward the eastern foreland.

6.4.1 Apatite fission tracks

Detrital apatite fission tracks (AFT) was applied to all the samples with a minimum of 61 grains used for counting, which is sufficient to approximate the likely current distribution of ages (Brewer et al.,

2003). Apatite crystals were extracted from modern sands by standard mineral separation (crushing, magnetic and heavy liquids separation) and mounted in epoxy at the University of Padua (Italy). Spontaneous fission decay of ^{238}U in apatite lead to the accumulation of linear damage trails in the crystal

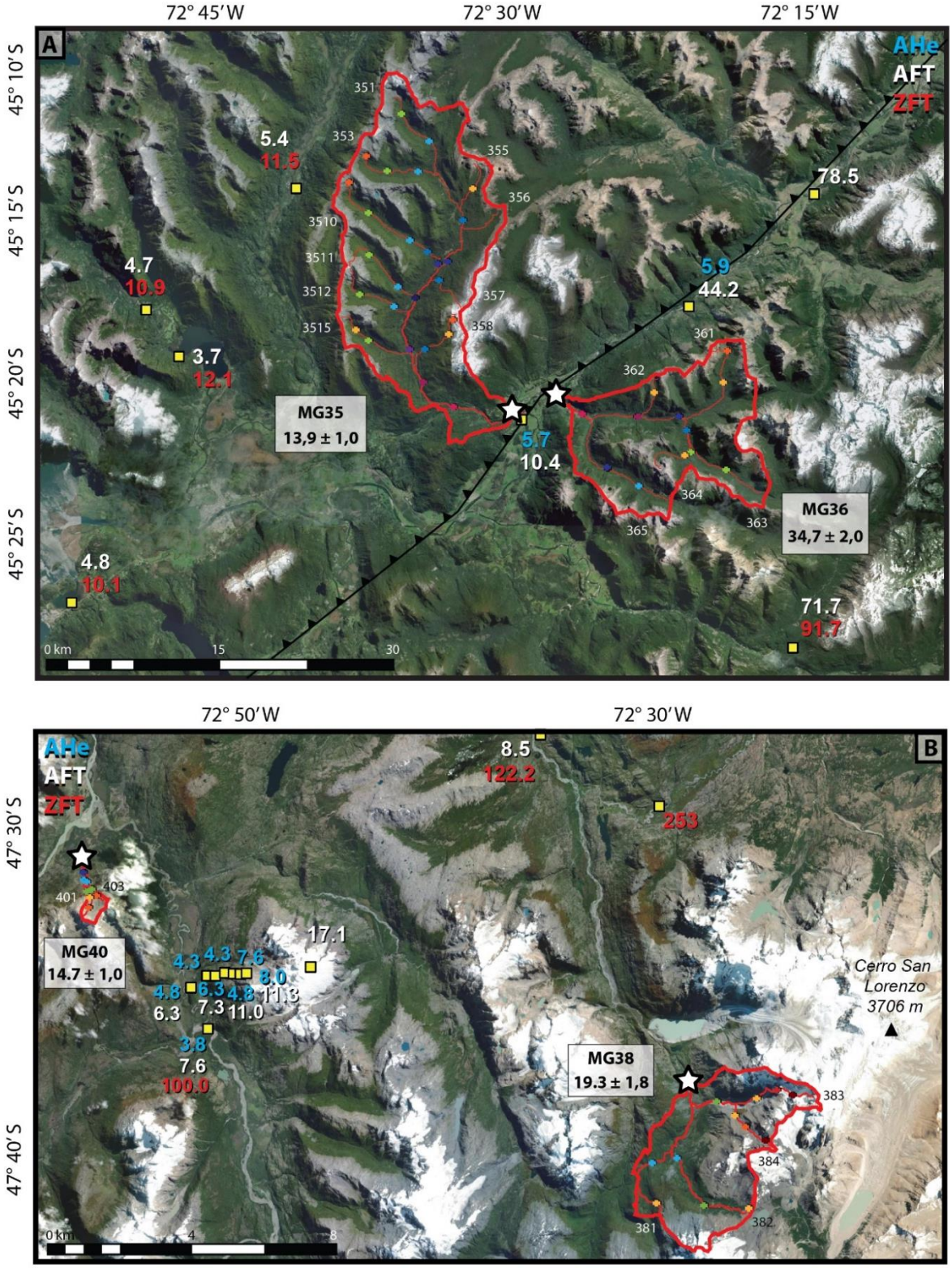

Figure 6.3. Satellite view of the studied areas with available in-situ (from Thomson et al., 2001, 2010; Thomson, 2002; Guillaume et al., 2013) and detrital (this study) thermochronology data, contour of the studied watersheds with geomorphic data. A. Catchments MG35 and MG36 separated by a fault related to the LOFZ. B. Catchments MG38 close to the Cerro San Lorenzo summit and MG40, located on both sides of an existing vertical profile.

lattice (e.g. Gleadow et al., 1986; Hurford and Green, 1982) that can be revealed after etching of the latter polished apatite mount in a 5M HNO_3 solution at 20°C for 20s. The samples were all analyzed by applying the external detector method (Gleadow, 1981) using low-uranium muscovite foils, as external detector, to cover apatite mounts. Induced tracks were obtained after irradiation of the samples with a nominal fluence of 9×10^{15} neutrons/cm² (Radiation Center of Oregon State University) and etching of the mica sheet in a 40% HF solution at 20°C for 40 minutes. We carried out age calculation using a zeta calibration approach (346 ± 12 for the CN5 dosimeter glass) and statistics with IsoplotR (Vermeesch, 2018).

6.4.2 Hypsometry data

The hypsometry statistics was extracted from the fields of integer DEMs delimiting the studied catchments by using the raster data-model of ArcGIS, as explained in Pérez-Peña et al. (2009a). These data are necessary for the thermal modeling to obtain more confident results than with detrital data alone. For the thermal modeling, we used the QTQt software (version 5.7.1; Gallagher, 2012) to model hypothetical vertical profiles based on AFT age distribution and hypsometry data.

We investigated hypsometric curves through the percent hypsometric method to obtain geomorphologic information about the maturity of each studied watershed. Indeed, the relative area plotted with the relative elevation displays a curve with variable sinuosity distinctive for youth, mature and older stages. A convex shape curve may predict unstable and younger geomorphology, possibly actively uplifted, while concave curves indicate a denuded or mature stage (Pérez-Peña et al., 2009b). Hypsometric integrals (HI), calculated from mean, minimum and maximum elevation (equation from Özkaymak and Sözbilir, 2012) and verified with the Hypsometric Integral Toolbox (Matos and Dilts, 2019), are greater than 0.60 for unstable or young basins and less than 0.30 for older stage of basins. Intermediate values represent a mature or equilibrium stage which indicate the watershed is still under development. Thus, the HI values provide relevant information about the development stage of the watershed and can be used as indicators of the geomorphic evolution of drainage basins.

6.4.3 River longitudinal profile analysis

We achieved river longitudinal profile analysis over the studied catchments using Aster global DEMs, released by the USGS (spatial resolution 30 m), to obtain further information on catchment erosion. River profiles display often diverse segments with particular steepness (k_s) and concavity indices (θ) which are separated by knickpoints characterizing by their equilibrium (Whipple, 2004). When two segments hold different concavity index, the knickpoint in the middle reflects an abrupt change in channel slope and, consequently, in uplift rate. The latter rate can be related with tectonic activity as knickpoints tend to migrate headward in the case of increasing rate (Kirby and Whipple, 2012). Thus, relationship between k_s and rock uplift is generally accepted (e.g. Dietrich et al., 2003; Snyder et al., 2000; Wobus et

al., 2006). Extreme values for θ are associated with downstream increase or decrease and consequently to the formation of knickpoints. Indeed, spatial and temporal information on tectonics and uplift may be extracted through the analysis of θ, k_s and knickpoints, as any perturbation of the steady state may be related to abrupt changes in reliefs and, therefore, on channel slopes (Kirby and Whipple, 2001).

We carried out the morphometric analysis to investigate river profiles using a dedicated MATLAB script on hydrographic network defined in ArcGIS (StreamProfiler; Snyder et al., 2000; Wobus et al., 2006). This software allows to extract stream profiles and calculate θ and k_s. Smoothing window of 250 m and a contour interval of 12 m have been applied to river profiles for which we removed spikes. We chose a reference concavity value of $\theta_{ref} = 0.45$ within the theoretical range 0.3 – 0.6 (Sólyom and Tucker, 2004; Whipple and Tucker, 1999; Wickert and Schildgen, 2019) to normalize the steepness index values (k_{sn}) as θ and k_s are autocorrelated (Sklar and Dietrich, 1998). Knickpoints were then defined manually at abrupt and minor changes as main and secondary knickpoints, respectively. This script allows to separate stream profiles into different segments with their own θ and k_s. The StreamProfiler tool generates then automatically the θ and k_s into log-log diagrams of slope versus area data and a map of k_{sn} (corresponding to the k_s values normalized) for all the rivers.

6.5 Results

6.5.1 AFT results

For the granite sample (MG31), we obtained an age of 35.1 ± 3.6 Ma. AFT results for modern detrital samples yield central ages between 8.2 ± 0.6 Ma and 78.1 ± 4.0 Ma (Table 1). The obtained youngest single-grain cooling ages are fairly consistent with the existing bedrocks thermochronology data (Guillaume et al., 2013; Thomson et al., 2010a, 2001). Young central ages have been detected in the inner part of the Cordillera with the samples MG28, MG29 and MG35, collected close to the LOFZ, and samples MG38 and MG40 collected south of the CTJ. Older central ages have been obtained in samples collected toward the east (MG32, MG34, CN4 and MG36) and in catchments not affected by faults or glaciers (MG27). The probability density function (PDF) (Vermeesch, 2007 and references therein) of all detrital ages has been realized for each sample with RadialPlotter (Vermeesch, 2009) as well as the binning of these data into histograms (Figure 6.4).

All the modern detrital samples and the granite yield a χ^2 probability higher than 5%, indicating a single population, whereas it is null for the sample MG33 (Table 1). Therefore, grain-age distribution were decomposed for this sample with the BINOMFIT software (Brandon, 2002) which is using the binomial peak fitting to identify the different age components. Three age components were clearly identified in this sample: the component P1 corresponding to 31.4 ± 5.3 Ma (~20% of the grains) and the component P2 equal to 79.6 ± 11.0 Ma (around 32%), corresponding exactly to the Late Cretaceous and Paleogene ages from the literature (Thomson et al., 2010a, 2001) located few kilometers upstream to the east, whereas the oldest component P3 representing about 48% of the grains with an age of 132.7 ± 14.0

Ma displays a clear provenance from the adjacent southern reliefs as demonstrated by the results obtained for the sample CN4 (Table 2).

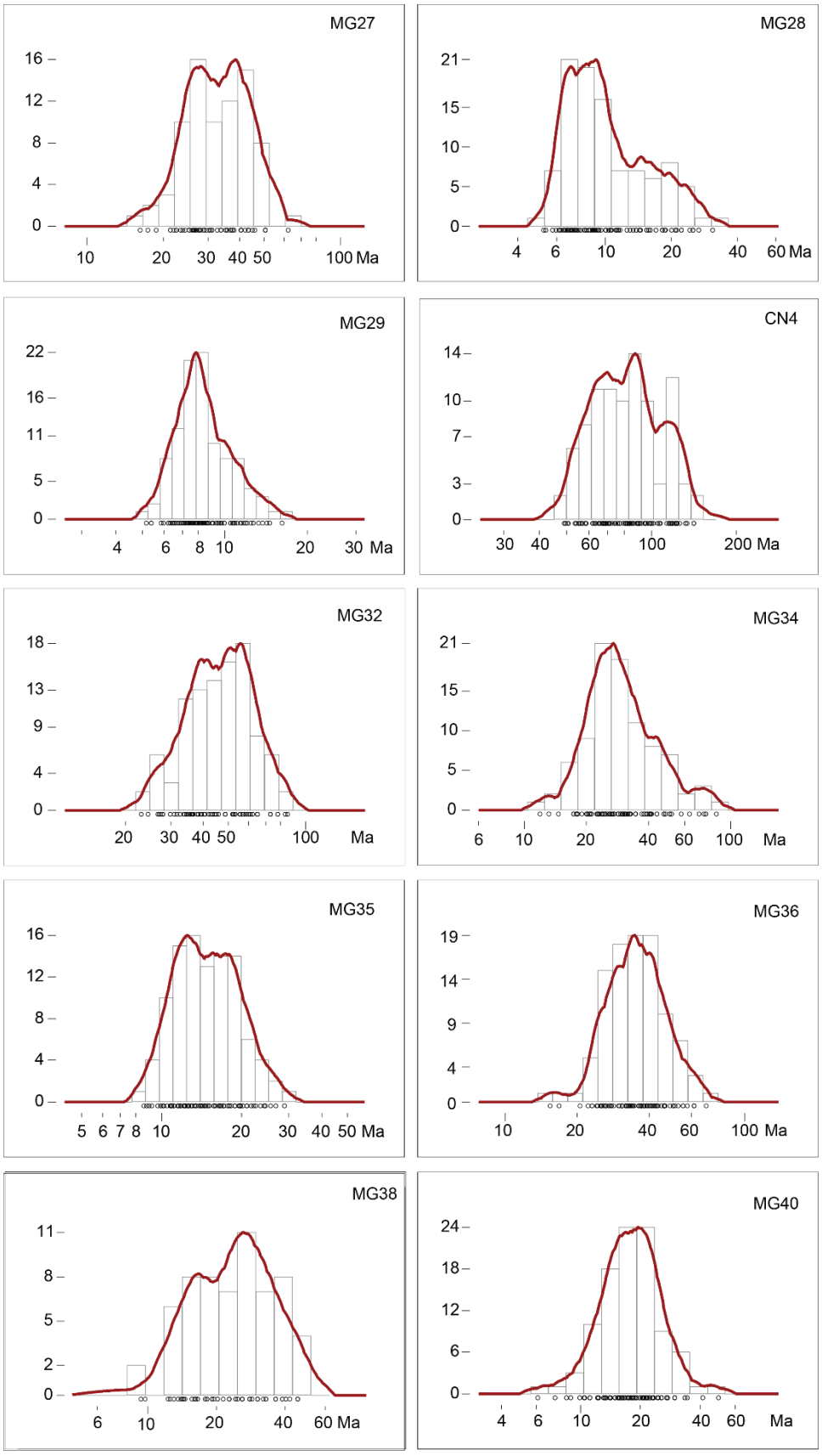

Figure 6.4. Histogram (bars) Probability Density Function (PDF) of the single-grain AFT ages (black circles) obtained for all the samples. Observation show that ages are more or less dispersed for each sample and that most of them present only one main age peak.

Table 1. Apatite fission tracks data

Samples	Field †			Fission tracks data §									
	Longitude	Latitude	El. (m)	N	C. age	σ	Ns	ρs	Ni	ρi	Nd	ρD	P(χ^2)
MG27*	-72.5112	-44.6843	45	78	25.4	2.0	238	1.6	1891	12.4	5000	11.7	100
MG28*	-72.4870	-44.6772	35	100	9.5	0.7	306	0.9	6447	19.7	5000	11.6	100
MG29*	-72.5742	-44.4614	23	101	8.2	0.6	309	1.3	7498	31.7	8875	11.5	100
MG31	-72.3889	-44.6504	126	14	35.1	3.6	126	3.2	700	17.7	5000	11.3	100
CN4*	-71.8128	-44.6665	576	92	78.1	4.0	1206	3.8	3519	11.2	5000	13.2	64
MG32*	-72.0238	-44.6928	334	100	42.5	2.5	551	2.6	2526	11.9	5000	11.3	100
MG33	-71.8019	-44.6601	576	61	88.1	7.5	711	4.7	1669	11.0	5000	11.1	0
MG34*	-72.1167	-44.7161	284	90	29.8	1.8	529	2.3	3377	14.8	5000	11.0	97
MG35*	-72.4616	-45.3520	48	100	13.9	1.0	308	1.2	4162	16.6	5000	10.9	100
MG36*	-72.4616	-45.3520	60	100	34.7	2.0	590	2.9	3141	15.7	5000	10.7	100
MG38*	-72.4698	-47.6203	577	61	19.3	1.8	159	1.0	1497	9.1	5000	10.5	100
MG40*	-72.9532	-47.4986	80	100	14.7	1.0	321	1.3	3883	15.3	5000	10.3	100

* modern detrital samples

† longitude and latitude coordinates are given in WGS84

§ Zeta= 346 ± 12

N: number of apatite crystal counted; and ρ: track density (x 10^5 tracks/cm²); subscripts s, I and d denote spontaneous, induced and dosimeter, respectively; P(χ^2): probability of obtaining a Chi-square value for n degrees of freedom; Dpar: mean diameter of fission-track etch pit parallel to the c-axis.

6.5.2 Hypsometric curves and integral values

The hypsometric table and curves are shown in Table 2 and Figure 6.5, respectively. The hypsometric integral values vary mostly from 0.42 to 0.57 except for the sample MG38 with a value of 0.27 and the sample MG40 with a value reaching 0.77. This is coherent with the shape of the hypsometric curves which differs significantly for the samples MG38 and MG40. For the sample MG40, the shape of the hypsometric curve presents a clear convex shape that we relate to a youthful stage of development and less eroded relief, whereas MG38 displays a concave shape related with an older development and a stable landscape. For the remaining eight watersheds, similar shapes of the curve and values of the integral indicate a similar erosional status despite the different cooling history highlighted by the AFT data. Average hypsometric integral value (~0.50) and intermediate shape obtained for these samples highlight the mature stage reached by these watersheds. The hypsometric curve for the watershed MG29 exhibits a more concave surface demonstrating that the development of this watershed is relatively mature. The HI value and the concave hypsometric curve for the catchments MG29 and MG38 may also be related to the glacial landscape displayed by these areas, as demonstrated by modern glacier into or adjacent to these watersheds, rather than old development stage of the topography.

These results are consistent with the size of the studied watersheds, all located in regions of homogeneous rock. Indeed, previous works evidence that hypsometric curve in small catchments with a unique lithology is generally convex and dominated by hillslope processes, whereas they are more

concave and with decreasing HI value for larger catchments (e.g. Hurtrez et al., 1999; Willgoose and Hancock, 1998).

Table 2. Hypsometry data.

Samples	Field			Hypsometry			
	Longitude	Latitude	Elevation (m)	Drainage area (km²)	Maximum elev. (m)	Mean elev. (m)	HI
MG27	-72.5112	-44.6843	45	22	1587	928.37	0.57
MG28	-72.4870	-44.6772	35	42	1711	942.26	0.54
MG29	-72.5742	-44.4614	23	356	2167	1102.13	0.50
CN4	-71.8128	-44.6665	576	265	1886	1187.64	0.47
MG32	-72.0238	-44.6928	334	121	1734	1045.90	0.51
MG34	-72.1167	-44.7161	284	191	1884	949.93	0.42
MG35	-72.4616	-45.3520	48	291	1772	995.56	0.55
MG36	-72.4616	-45.3520	60	162	1894	1003.05	0.51
MG38	-72.4698	-47.6203	577	149	3301	1313.84	0.27
MG40	-72.9532	-47.4986	80	5	1726	1341.03	0.77

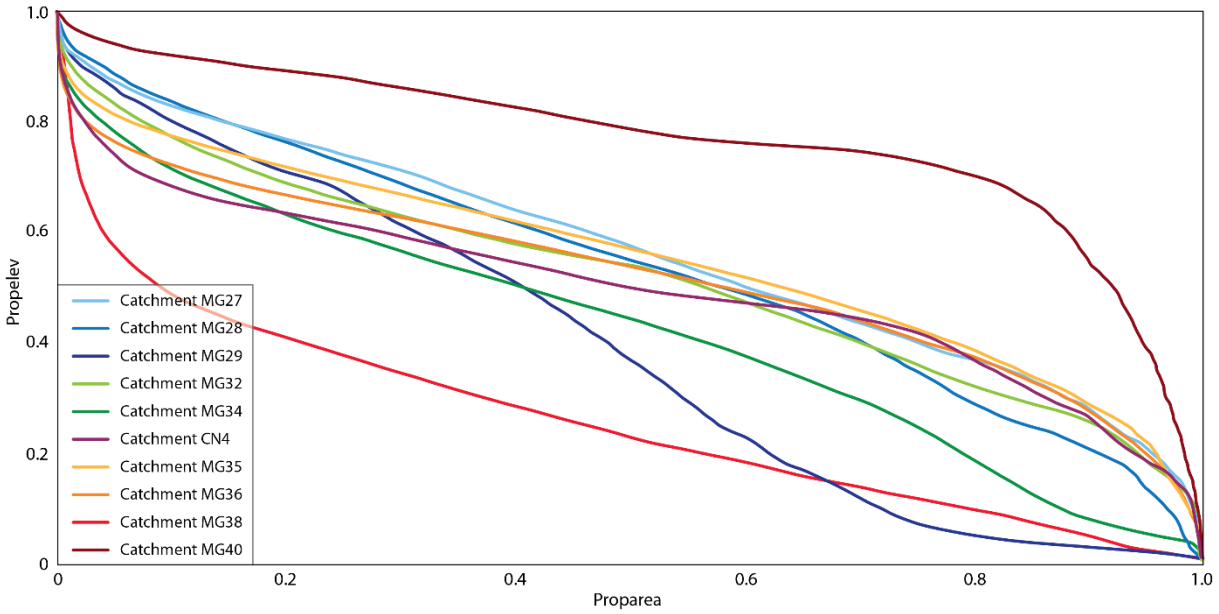

Figure 6.5. Hypsometric curves of the watersheds with convex shape indicating a system recently deformed and concave shape corresponding to old deformation stage.

6.5.3 PDF vs hypsometry

In the case of uniform erosion, sediment delivery is homogeneous through the catchment and therefore, the PDF has approximately the same shape than the hypsometric curve (Stock et al., 2006). Taking in account this assumption, the superimposition of the elevation distribution (Figure 6.6) and the

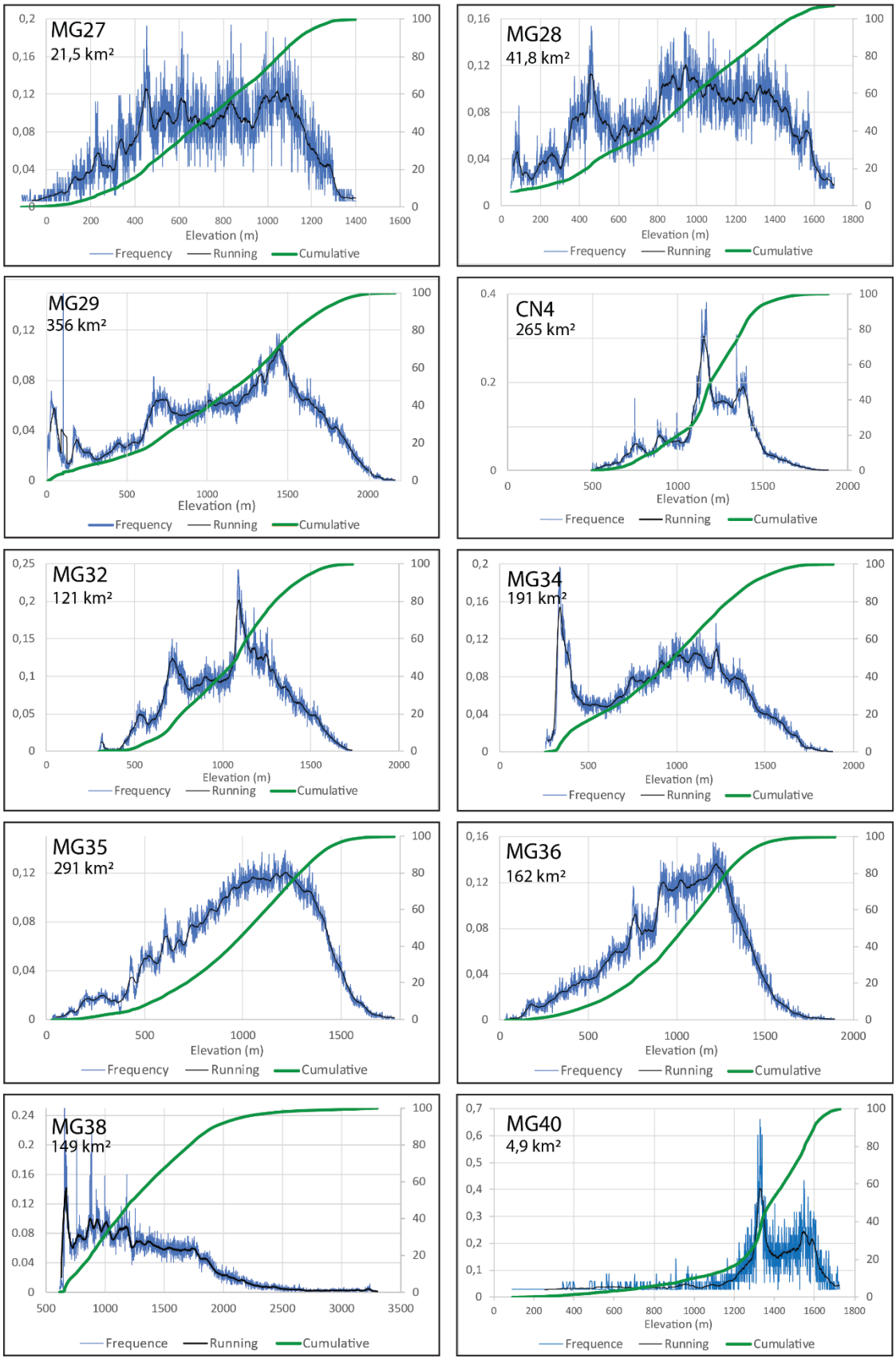

Figure 6.6. Present day distribution of elevation (ASTER 30 m), or hypsometry, in the selected catchments. The black line is a running mean, and the green line is the cumulative distribution of elevation.

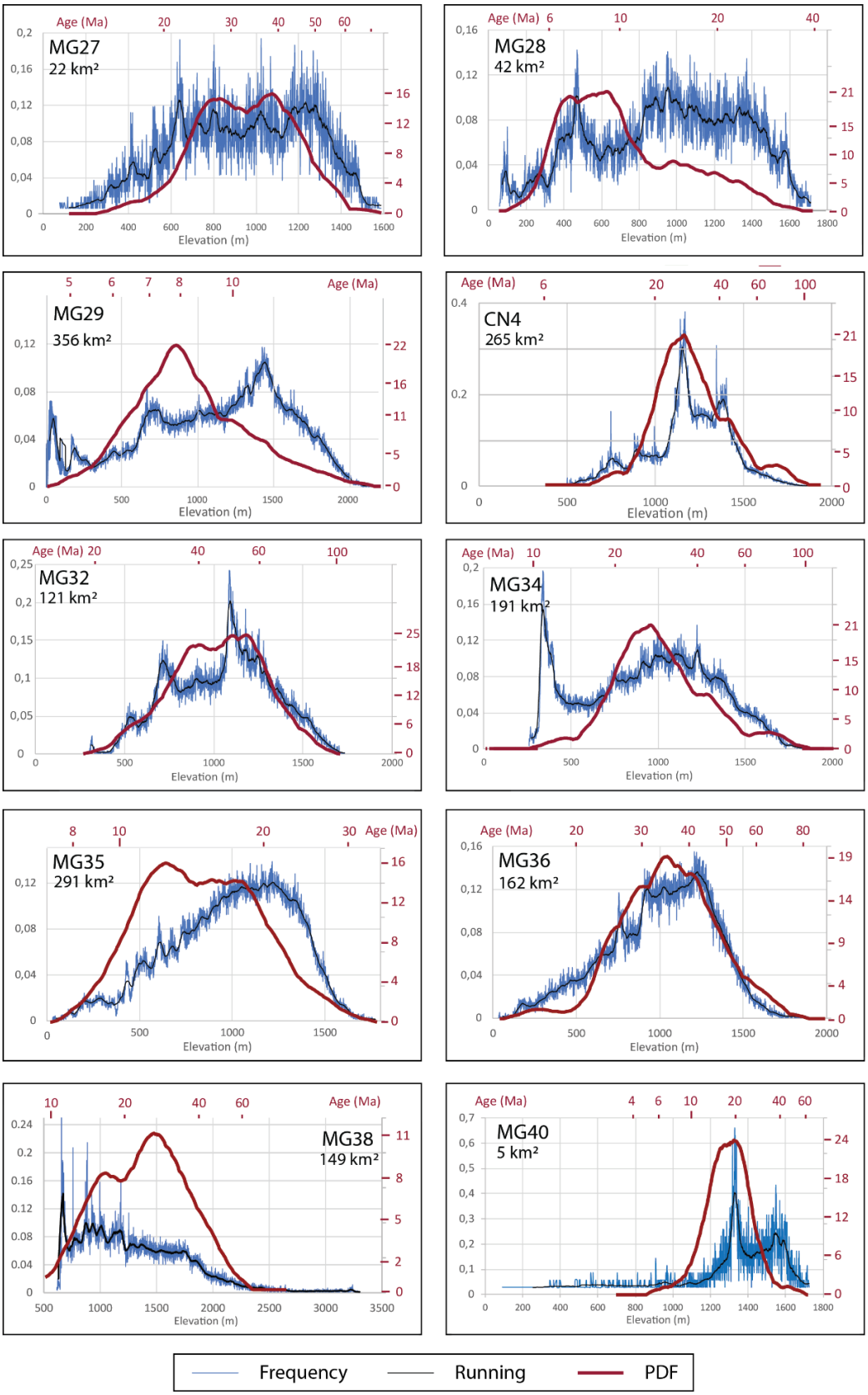

Figure 6.7. Comparison of Figures 4 and 5 with elevation (in blue and black) and PDF (in red) data to evidence watersheds with a uniform erosion (graphs with elevation and PDF peak superimposed) or not (mismatch between the elevation and the PDF peaks). Here, some samples show a good match between the peaks (e.g. MG32) and some others are displaced (e.g. MG35).

PDF (Figure 6.4) allows to see easily that erosion of some catchments is uniform while erosion is more localized in other catchments (Figure 6.7). For MG27, CN4, MG32 and MG36, PDF and elevation distribution curves shape are quite similar and stack well on each other (Figure 6.7). This means that erosion in these four latter catchments is mostly uniform from the top to the outlet, where the samples have been collected. For the catchments MG28, MG29, MG34, MG35 and MG40, the PDF peak is more or less located toward the lower elevations, which is directly related with peaks of lower elevations for some catchments (e.g. MG28 and MG34). Indeed, as we consider that cooling ages are getting older with the highest elevations, if lower elevations are more eroded, PDF is displaced to younger cooling ages. This is more evident for samples MG28 and MG40 as their PDF fit clearly with a peak of lower elevations. Thus, erosion in these catchments is more focused around these elevations. Looking at the PDF peak for sample MG38, which seems located toward higher elevation, and the data for the sample MG35, it is more difficult to explain why the curves are not similar. However, we can conclude that erosion is not uniform across these two watersheds too.

6.5.4 Thermal modeling

We model thermal histories with the QTQt software (v. 5.7.1; Gallagher, 2012) from modern detrital data following the protocol used in Gallagher and Parra (2020). Thus, input data used in this study are a detrital data set (apatite fission tracks only) and the present-day distribution of the elevation into the catchment. Minimum and maximum elevations used as input are similar to those of the hypsometric curve and allow to define the temperature offset parameter. Dummy files with diverse elevations are generated automatically by QTQt to predict vertical profiles, similarly to a sampling. Constraints used were a general prior temperature of 110 ± 110°C and a geothermal gradient of 30 ± 30°C/km with the temperature offset allowed to vary over time.

As the models are only constrained by the AFT ages and the hypsometry, age-elevation relations obtained are mostly linear, with different steepness (Figure 6.8). The steepest age-elevation profile is quite similar for the catchments MG28, MG29 and MG40 (Figure 6.10A). Intermediate steepness defines the age-elevation profiles of the catchments MG27, MG32, MG34, MG35, MG36 and MG38 while the catchment CN4 is characterized by the less steep slope (Figure 6.10A). Similarly, the T-t paths present similar faster cooling trend at low temperatures for catchments MG27 and MG28, MG35 and MG40, and slower cooling for MG27, MG34, MG36 and MG38, and finally MG32 and CN4 display the most progressive cooling (Figure 6.9 Figure 6.10B). However, none of these T-t paths evidences any significant cooling during the Miocene while a substantial exhumation is recognized during this period in central Patagonia.

Prediction plots (Figure 6.11), also obtained from the QTQt software after inverse modeling, allow to observe if predicted single-grain AFT distribution match or not with the observed one, the latter

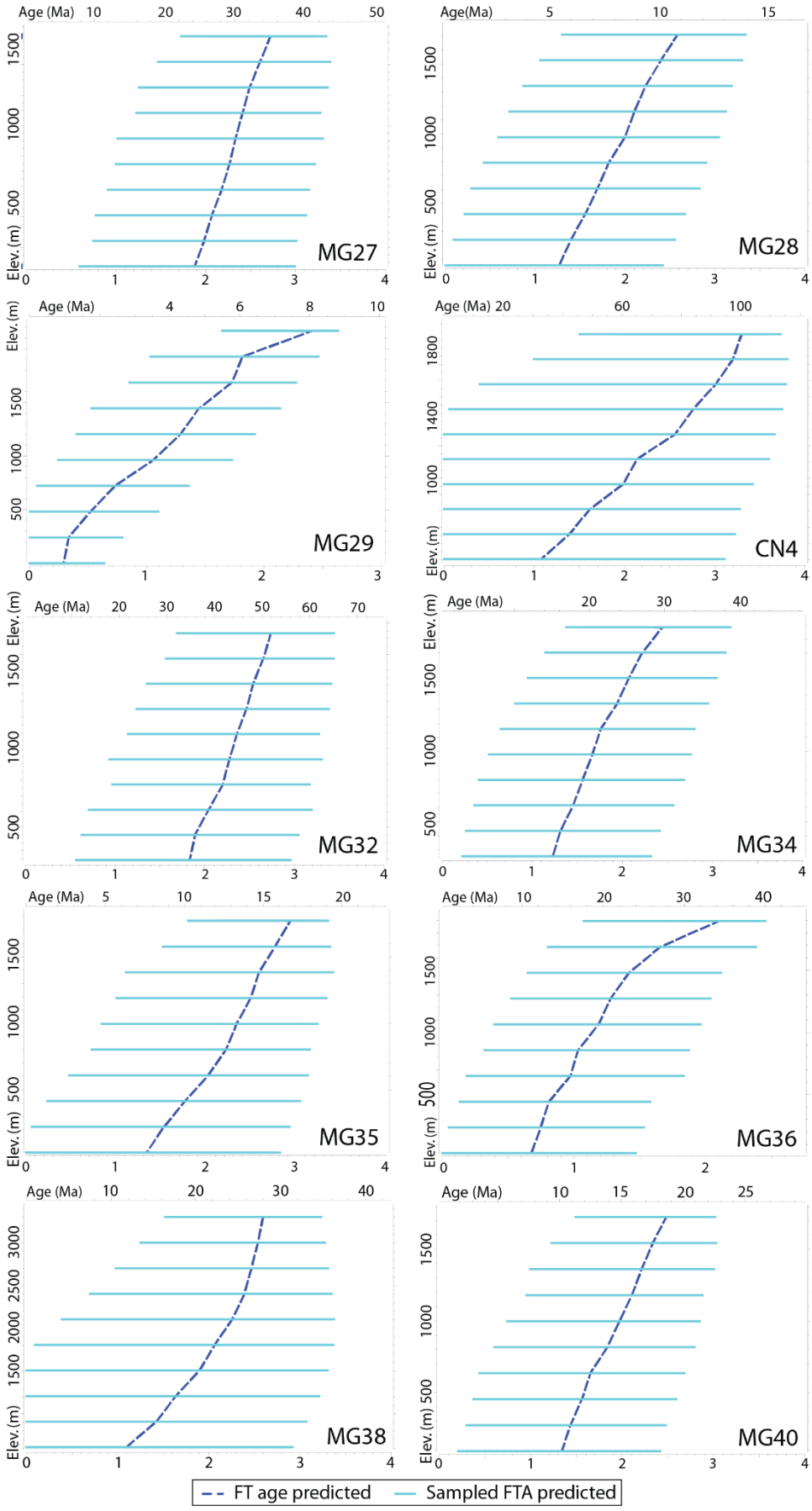

Figure 6.8. Age-elevation plot for the samples obtained by inverse modeling with the QTQt software. For most of the samples, the age-elevation relation observed is linear.

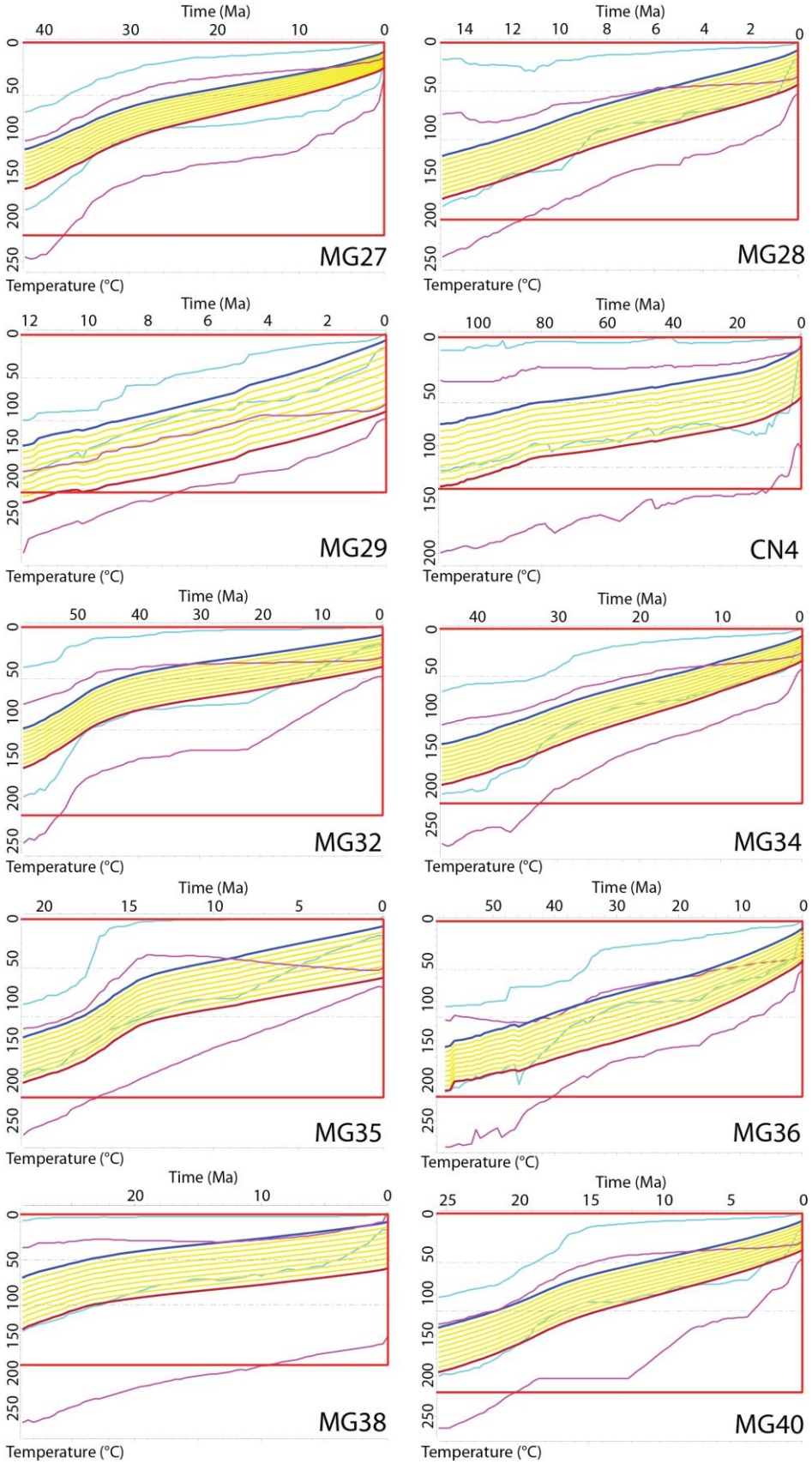

Figure 6.9. Inferred thermal history (QTQt software) from the detrital sample at the outlet of the selected catchments. The blue and red lines indicate the thermal histories for the uppermost and lowermost elevation bedrock samples with a 95% credible range defined by light blue and pink lines, respectively. The yellow lines are the thermal histories for dummy samples and the red box is the prior distribution for time-temperature points.

corresponding to the PDF. MG27, CN4, MG32 and MG36 show a pretty good match between the predicted and observed distributions (Figure 6.11). It means that age-elevation relation for these samples are mostly linear and, consequently, that erosion in these catchments is mainly uniform. Contrarily, significative mismatch is observed in the prediction plots for samples MG28, MG34, MG35 and MG38, where predicted single-grain AFT distributions are systematically displaced toward younger ages (Figure 6.11). Finally, minor mismatch is observed for samples MG29 and MG40.

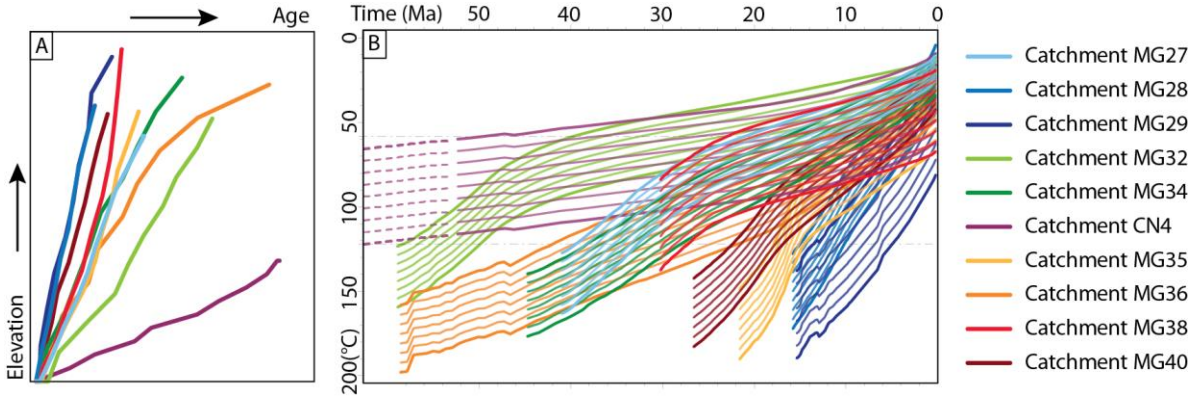

Figure 6.10. Superposition of age-elevation (A) and T-t paths (B) for all the samples. Each parallel line on the graph B represent the uppermost and lowermost elevation bedrock samples and each intermediary dummy files.

6.5.5 River profiles

We extracted the longitudinal profile of 51 rivers draining the ten studied watersheds, all reported in Figure 6.12. Results evidence that catchments are quite deeply incised but few significant knickpoints have been observed. Nevertheless, the presence of many knickpoints evidence that streams are not in equilibrium conditions and that diverse events affecting the morphology of the streams occurred through time. As watersheds have been selected for their unique lithology, these knickpoints are not related to any changes in rock type but to changes in denudation rates or effect of glaciers. The catchment MG29 presents a high variability in the river longitudinal profiles which is related to the presence of a glacier and lakes (Figure 6.12).

Singular relations between the watersheds were evidence from the θ and k_{sn} values (Table 3). In all the catchments, highest elevations are systematically concave with low θ (< 0.4) and lowest k_{sn} values of the streams, excepted for 10 rivers in watersheds MG29, MG35 and MG38. These upland landscapes are separated from lower stream segments by variable knickpoints more or less developed at different altitude. No particular trend has been observed with knickpoints analysis (Table 4) but the existence of uneven knickpoints evidence that distinct tectonic perturbations affected the different watersheds. In addition, as the steepness index (k_{sn}) is a function of rock uplift rate, the global increase of the k_{sn} values in lower channel segments of the watersheds may be correlated to an irregular increase of the uplift rates

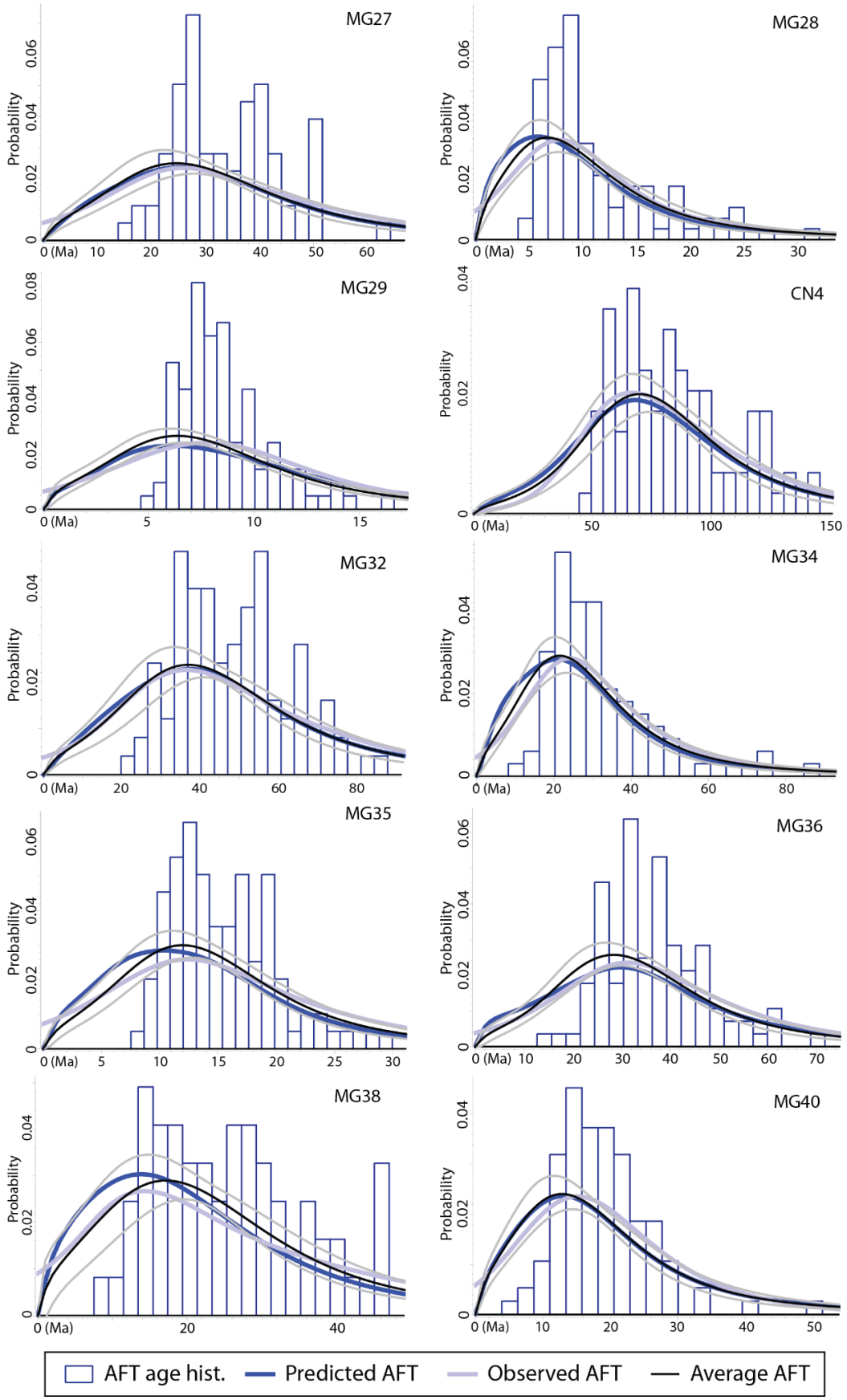

Figure 6.11. Prediction plot of detrital AFT age using the thermal history obtained by inverse modeling with the QTQt software. Histogram and light blue line represent the observed detrital AFT ages while the predicted distribution for thermal history is represented by the darker blue line. The black line is the average of the predicted detrital distributions for all accepted thermal histories.

through time. The concavity index θ comprises a wide range of value: low values < 0.4, moderate value between 0.4 and 0.7, and high value > 0.7 (May and Lisle, 2012). High values are particularly omnipresent in diverse segments of streams located in watersheds MG29, CN4, MG36 and MG38 which result from a temporal decline in rock uplift in these areas. For watersheds MG32 and MG34, high and moderate values are prevalent and corresponds to decreasing uplift rates. Low values are often detected toward high elevations and frequent in many segments belonging to the watersheds MG35 and MG40. These low values are commonly related to actively uplifting channels with debris flow and steep drainage generally associated to well-developed knickpoints.

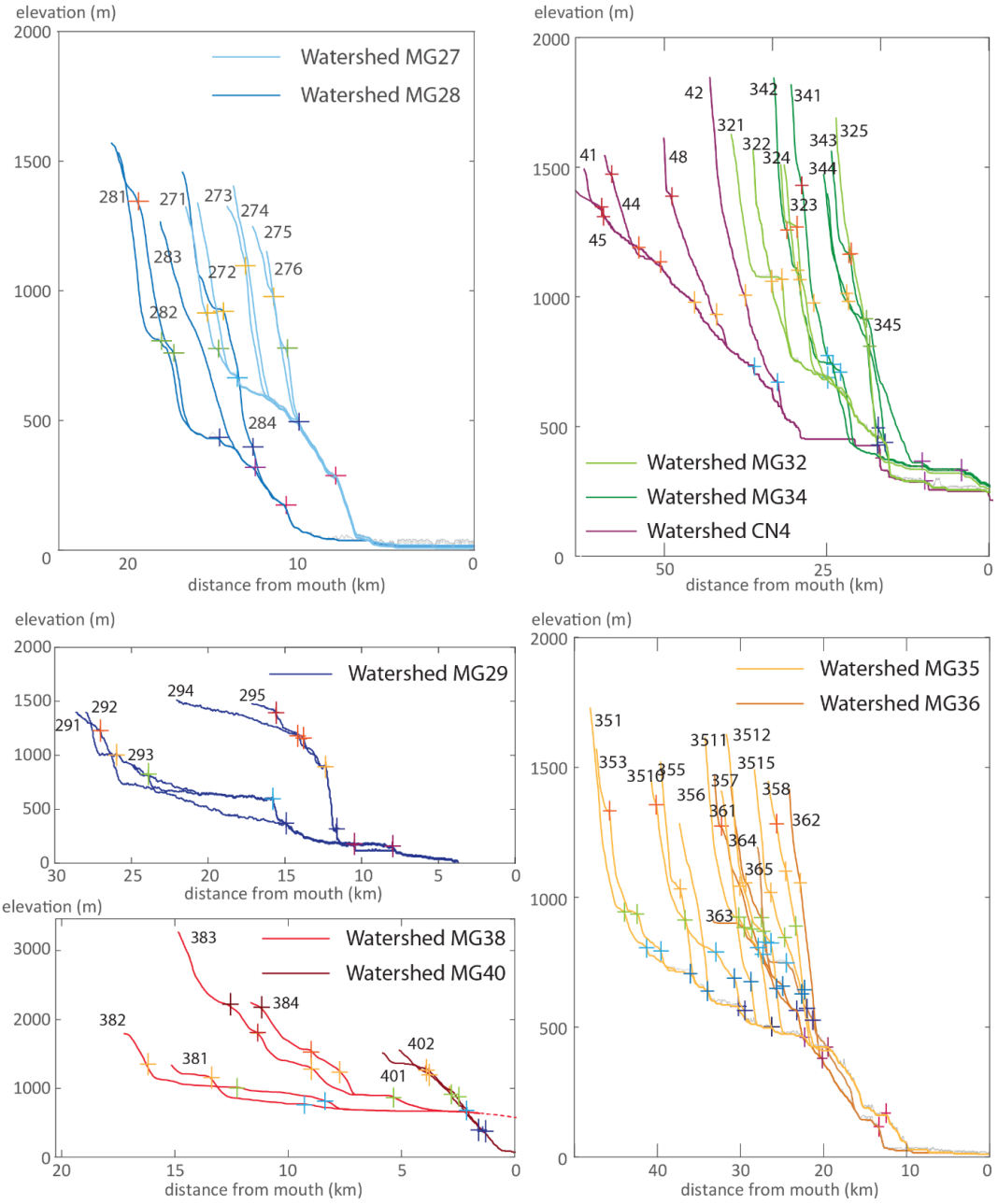

Figure 6.12. Longitudinal stream / river profiles realized for main rivers of each catchment. Colored crosses represent knickpoints at diverse elevations. Numbers correspond to the selected rivers which are display on the satellite views (Figures 2 and 3).

TABLE 1. Concavity and steepness indices, minimum and maximum areas

*	n°	Segm.	Teta	error	ksn	error	MinA	MaxA
MG27	5	1	0.47	0.1	158.09	165.51	0.98	20.11
		2	1.12	0.71	114.48	128.88	0.34	0.98
		3	-0.09	0.22	42.77	48.39	0.01	0.34
	6	1	0.24	0.03	91.09	95.78	0.01	20.09
MG28	1	1	-1.12	1.21	157.83	170.02	19.5	37.09
		2	2.4	0.83	230.71	265.3	5.05	19.5
		3	0.18	0.12	108.25	116.08	0.01	5.26
	2	1	0.83	0.2	125.64	135.35	4.34	37.09
		2	0.64	0.33	234.41	243.28	0.84	4.34
		3	0.05	0.22	41.41	46.26	0.02	0.84
	3	1	2.94	1.5	192.86	210.38	28.39	37.09
		2	0.12	0.05	109.87	117.88	0.01	28.38
	4	1	0.66	0.22	137.62	151.82	3.79	37.09
		2	1.76	1.73	287.93	301.57	2.69	3.79
		3	0.34	0.11	69.35	72.79	0.01	2.69
MG29	1	1	4.18	3.62	111.57	141.57	164.94	247.23
		2	1.73	1.13	105.78	146.9	48.83	164.46
		3	0.6	0.82	69.64	73.41	15.06	48.72
		4	4.75	3.35	164.47	219.04	7.3	12.87
		5	0.3	0.05	105.81	110.23	0.01	7.3
	2	1	4.18	3.62	111.57	141.57	164.94	247.23
		2	4.13	0.97	207.38	254.96	86.3	164.94
		3	0.96	0.34	76.7	83.62	6.93	86.32
		4	1.09	0.76	206.33	237.47	0.89	7.64
		5	0.38	0.17	31.35	33.91	0.01	0.86
	3	1	6.08	4.42	95.91	118.45	164.95	247.57
		2	3.71	0.97	165.9	201.77	86.35	164.95
		3	0.75	0.24	85.53	97.91	3.72	86.35
		4	0.45	0.07	79.22	82.01	0.01	2.84
	4	1	1.23	0.8	62.2	72.83	50.2	247.66
		2	33.37	7.22	1836	1979	46.82	50.17
		3	3.98	3.67	334.27	426.3	34.09	43.82
		4	13.06	7.75	265.15	336.54	31.17	34.09
		5	0.58	0.18	47.99	51.01	7.76	31.17
		6	0.45	0.21	28.57	31.52	0.02	0.68
	5	1	1.55	0.67	59.2	69.81	50.27	247.66
		2	34.14	7.05	1825.79	1972.89	43.82	50.24
		3	0.33	0.59	177.99	221.49	6.74	43.82
		4	9.95	1.66	174.75	218.48	5.51	6.74
		5	1.65	0.69	89.76	101.96	2.28	5.41
		6	0.49	0.14	22.22	23.54	0.02	2.28
CN4	1	1	1.79	4.48	180.4	209.18	146.1	186.08
		2	-0.31	4.94	203.08	236.68	146.12	184.61
		3	1.79	4.47	180.4	209.18	143.11	186.08
		4	29.93	65.56	142.05	173.74	140.15	146.11
		5	18.15	88.26	162.38	200.64	140.01	143.82
		6	1.67	1.12	109.18	115.59	89.38	140.15
		7	2.11	2.13	89.2	100.32	64.95	89.37
		8	0.16	0.89	48.11	52.92	27.27	64.87
		9	0.52	0.22	40.06	41.61	3.7	27.22
		10	0.39	0.14	22.79	24.03	0.04	4.05
	2	1	0.78	0.43	270.68	331.31	35.74	187.62
		2	0.71	0.29	135.53	141.21	7.7	35.68

TABLE 2. Information about knickpoints selected manually

*	n°	Knick.	elev. (m)
MG27	5	1	986
		2	787
		3	261
	6	1	279
MG28	1	1	794
		2	446
		3	172
	2	1	1356
		2	760
		3	185
	3	1	864
		2	327
		3	189
	4	1	922
		2	390
		3	163
MG29	1	1	807
		2	630
		3	336
		4	132
	2	1	1338
		2	973
		3	537
		4	148
	3	1	1234
		2	462
		3	104
	4	1	1705
		2	1171
		3	1021
		4	812
		5	141
	5	1	1415
		2	1145
		3	954
		4	812
		5	140
CN4	1	1	1186
		2	1084
		3	964
		4	730
	2	1	1560
		2	996
		3	666
	4	1	1462
		2	1127
		3	970
		4	730
	5	1	1327
		2	1158
		3	1081
		4	958
		5	715

		3	0.38	0.14	91.58	93.93	0.79	7.83
		4	0.81	0.18	89.76	94.51	0.31	0.76
		5	0.17	0.07	39.18	41.82	0.06	0.27
	4	1	2.05	5.02	170.9	198.83	146.15	186.09
		2	14.84	46.28	138.59	161.98	140.15	146.15
		3	1.76	1.2	109.93	115.64	89.43	140.01
		4	-0.06	1.05	94.5	102.32	29.57	89.43
		5	0.55	0.15	38.89	39.84	0.48	29.58
		6	0.64	1.08	15.77	21.16	0.05	0.48
	5	1	0.45	4.31	204.23	230.44	146.11	185.67
		2	14.85	46.28	138.59	161.98	140.15	146.15
		3	2.65	2.24	90.71	102.06	95.18	140.15
		4	36.38	21.03	122.99	134.71	89.44	95.14
		5	2.13	1.8	86.81	95.69	64.95	89.44
		6	0.35	5.09	49.54	59.48	27.52	64.79
		7	0.68	1.17	50.91	55.45	12.67	27.46
		8	0.01	0.27	8.71	12.47	0.08	12.67
	8	1	0.45	4.31	204.23	230.44	146.12	186.07
		2	29.93	65.56	142.05	173.74	140.01	146.12
		3	1.01	0.43	106.22	125.84	28.8	140.15
		4	1.71	4.31	102.3	116.97	21.28	28.1
		5	0.17	0.12	64.07	65.89	1.21	21.23
		6	0.88	0.12	39.49	48.94	0.03	1.21
MG32	1	1	0.42	1.01	111.25	116.95	59.21	117.27
		2	3.14	0.71	136.78	169.41	20.63	60.15
		3	0.19	0.13	50.14	55.3	0.02	20.62
	2	1	0.42	1.01	111.25	116.95	59.42	117.77
		2	0.86	0.16	89.57	95.07	2.92	60.04
		3	0.3	0.08	55.95	58.99	0.02	2.93
	3	1	0.53	0.07	110.27	113.09	2.04	117.77
		2	0.56	0.21	26.83	32.46	0.01	2.06
	4	1	0.96	0.48	99.05	108.88	26.81	117.27
		2	1.28	0.26	82.99	93.63	3.1	26.75
		3	0.19	0.12	51.92	54.86	0.02	3.09
	5	1	0.62	0.25	185.2	205.28	4.54	117.27
		2	0.82	0.34	87.85	92.44	1.76	4.54
		3	0.44	0.18	40.22	43.95	0.02	1.75
MG34	1	0	0.55	0.13	57.43	61.69	23.39	8019.53
		1	1.2	0.39	91.92	103.5	7.28	23.32
		2	0.66	0.16	160.94	168.81	0.82	7.28
		3	0.3	0.14	49.67	52.79	0.01	0.82
	2	0	0.5	0.11	59.27	63.4	17.18	8019
		1	1.63	0.49	104.27	116.25	4.03	17.18
		2	0.7	1.52	89.4	110.41	1.65	4.03
		3	0.37	0.12	95.98	99.52	0.01	1.65
	3	1	0.55	0.06	102.11	110.28	3.79	8019.53
		2	0.33	0.06	68.09	71.08	0.01	3.77
	4	1	0.24	0.22	58.92	66.23	14.11	8019.52
		2	-3.03	0.81	183.34	200.49	7.85	17.77
		3	0.48	0.07	47.85	48.84	0.01	8.89
		4	-0.65	0.24	21.81	29.26	0.01	0.07
	5	1	0.54	0.08	90.39	96.22	18.76	8019.53
		2	0.42	0.09	76.13	78.45	0.02	18.67
MG35	5	1	-16.13	157.85	263.27	295.19	153.34	155.21
		2	-3.97	18.47	270.57	291.73	138.82	152.06
		3	11.63	101.43	160.12	669.63	117.67	138.89
		4	2.33	1.45	59.79	74.91	54.76	117.67
		5	0.67	0.17	144.51	157.72	1.89	54.75
		6	0.26	0.16	87.99	93.44	0.01	1.86

	8	1	1372
		2	953
		3	730
MG32	1	1	1071
		2	691
		3	410
	2	1	1064
		2	692
		3	410
	3	1	1268
		2	419
	4	1	1070
		2	597
		3	410
	5	1	1136
		2	851
		3	410
MG34	1	1	1391
		2	880
		3	641
	2	1	1245
		2	1090
		3	727
	3	1	1118
	4	1	870
	5	1	874
MG35	5	1	1031
		2	554
		3	430
		4	370
		5	264
		6	167
	6	1	554
		2	429
		3	167
	7	1	674
		2	501
		3	430
		4	157
	8	1	1281
		2	1073
		3	831
		4	571
		5	408
		6	160
	9	1	1269
		2	640
		3	160
	10	1	1354
		2	924
		3	788
		4	700
		5	563
		6	501
		7	429
		8	167
	11	1	805
		2	429
		3	157

	6	1	-16.13	157.85	263.27	295.19	152.06	155.21
		2	-3.98	18.47	270.57	291.73	138.82	151.96
		3	11.63	101.43	160.12	669.63	117.67	138.89
		4	6.05	47.22	29.78	146.85	99.61	117.67
		5	2.13	3.19	91.99	120.69	54.77	99.6
		6	0.15	0.12	91.48	100.46	0.02	54.76
	7	1	-16.13	157.85	263.27	295.19	152.06	155.21
		2	-3.98	18.47	270.57	291.73	138.82	151.96
		3	11.63	101.43	160.12	669.63	117.67	138.89
		4	6.05	47.22	29.78	146.85	99.61	117.67
		5	0.55	0.24	227.92	254.14	3.55	99.61
		6	0.08	0.08	103.07	110.84	0.01	3.54
	8	1	-16.13	157.85	263.27	295.19	152.06	155.21
		2	-3.98	18.47	270.57	291.73	138.82	151.96
		3	-0.08	0.41	60.39	92.44	5.69	142.07
		4	4.16	1.53	151.48	183.93	3.75	138.95
		5	0.96	0.76	260.14	273.98	2.54	3.75
		6	0.16	0.38	142.83	144.56	1.34	2.53
		7	0.73	0.24	77.05	80.78	0.39	1.29
	9	1	-16.13	157.85	263.27	295.19	152.06	155.21
		2	0.46	0.07	191.01	198.36	0.88	153.34
		3	0.23	0.11	69.83	71.82	0.01	0.11
	10	1	-3.98	18.47	270.57	291.73	138.82	151.96
		2	11.63	101.43	160.12	669.63	117.67	138.89
		3	6.05	47.22	29.78	146.85	99.61	117.67
		4	1.74	0.48	71.27	117.12	22.88	99.61
		5	27.23	38.86	296.51	357.99	21.97	22.89
		6	-0.36	1.37	103.11	109.81	12.85	21.97
		7	1.66	0.97	51.78	61.78	5.07	12.87
		8	0.53	0.12	97.03	99.71	0.25	5.09
		9	0.59	0.16	26.57	28.56	0.01	0.25
	11	1	-16.13	157.85	263.27	295.19	152.06	155.21
		2	-3.98	18.47	270.57	291.73	138.82	151.96
		3	11.63	101.43	160.12	669.63	117.67	138.89
		4	0.71	0.21	333.22	350.27	9.35	117.53
		5	0.31	1.59	74.46	80.86	5.59	9.35
		6	0.35	0.06	82.99	85.88	0.01	5.59
	15	1	-16.13	157.85	263.27	295.19	152.06	155.21
		2	-3.98	18.47	270.57	291.73	138.82	151.96
		3	-0.4	0.16	125.23	133.49	1.44	138.82
		4	0.03	0.11	68.92	75.61	0.01	1.44
MG36	1	1	2.04	0.89	162.96	169.36	44.86	87.06
		2	0.8	0.25	118.33	123.57	6.13	44.86
		3	0.31	0.29	89.76	95.09	1.07	6.13
		4	0.54	0.13	36.3	39.85	0.02	1.07
	2	1	0.46	0.05	199.36	202.78	0.59	87.03
		2	0.33	0.04	58.92	60.31	0.01	0.55
	5	1	1.16	0.58	148.72	196.4	22.32	81.05
		2	1.26	1.29	118.45	122.7	13.99	22.32
		3	1.31	6.94	121.04	152.47	9.51	13.99
		4	-3.71	2.23	119.03	139.5	4.99	10.04
		5	0.29	0.21	78.61	83.57	0.01	4.99
	3	1	2.02	0.97	166.06	172.15	44.86	87.03
		2	11.04	32.35	182.81	215.97	20.53	44.71
		3	0.09	0.63	81.27	86.56	0.01	20.53
	4	1	2.02	0.97	166.06	172.15	44.86	87.03
		2	11.04	32.35	182.81	215.97	20.53	44.71
		3	0.99	0.37	208.85	234.47	4.87	20.53
		4	0.45	0.98	72.85	78	2.09	4.87

	12	1	779
		2	429
		3	167
	13	1	1277
		2	1077
		3	416
		4	160
	14	1	868
		2	742
		3	504
	15	1	1017
		2	429
		3	167
MG36	1	1	1210
		2	863
		3	505
		4	131
	2	1	1054
		2	159
		3	147
	3	1	676
		2	568
		3	159
		4	117
	4	1	900
		2	826
		3	671
		4	547
		5	105
	5	1	741
		2	526
		3	253
		4	115
		5	1311
MG38	1	1	1127
		2	729
		3	864
	2	1	1302
		2	1035
		3	974
		4	714
	3	1	2182
		2	1934
		3	1765
		4	1297
		5	849
	4	1	1511
		2	1233
		3	873
MG40	2	1	1159
		2	746
		3	579
	3	1	1575
		2	1091
		3	1256
		4	903

		5	0.21	0.1	62.39	67.01	0.01	2.12
MG38	1	1	0.99	0.52	26.23	35.74	7.08	95.88
		2	0.95	1.37	27.33	31.11	2.75	6.97
		3	1.91	0.27	134.18	150.99	0.88	2.78
		4	-42	16	147.75	171.68	0.85	0.89
		5	0.54	0.17	15.65	18.08	0.1	0.87
	2	1	4.64	3.53	19.03	44.18	33.42	97.78
		2	-19.34	6.08	289.48	325.03	31.08	33.4
		3	5.36	13.54	100.41	120.68	29.38	31.09
		4	4.69	2.81	47.84	20.59	13.93	29.4
		5	0.52	0.73	21.66	25.64	2.47	13.77
		6	-3.1	3.96	55.78	74.68	0.69	1.69
		7	1.55	0.39	68.69	78.23	0.09	0.58
		8	-0.77	0.26	58.91	61.87	0.02	0.07
	3	1	1.78	0.93	145.41	176.4	26.72	98.25
		2	1.66	0.51	174.51	209.34	7.49	26.59
		3	-2.44	1.18	307.82	351.02	5.78	7.49
		4	3.86	0.77	144.05	164.49	3.76	5.78
		5	-103.82	31.64	474.21	513.18	3.73	3.78
		6	2.94	0.53	236.87	267.97	2.58	3.73
		7	-22.37	6.45	197.12	216.59	2.39	2.58
		8	0.42	0.09	163.37	168.32	0.03	2.47
	4	1	1.81	0.91	152.42	183.67	26.71	98.22
		2	2.1	0.45	115.24	186.59	5.05	26.59
		3	-4.45	1.79	406.48	432.78	4.07	5.05
		4	1.38	1.91	175.97	184.29	3.24	4.07
		5	0.78	0.12	112.76	117.65	0.2	3.24
		6	-0.58	0.21	42.91	53.29	0.01	0.2
MG40	1	1	-0.07	0.13	279.79	287.63	1.61	3.34
		2	-19.39	6.52	315.41	333.63	1.53	1.53
		3	-0.22	0.11	169.85	185.81	0.31	1.45
		4	0.28	0.09	62.79	64.42	0.02	0.32
	2	1	0.21	0.14	292.59	295.92	1.52	3.36
		2	5.34	7.81	198.03	207.86	1.44	1.52
		3	-6.99	6.85	218.25	236.48	1.32	1.44
		4	-10.78	17.5	64.09	82.07	1.11	1.32
		5	0.59	0.13	54.96	57.98	0.02	1.11

* catchment name

6.6 Discussion

Results obtained from modern sediments collected at the outlet of some catchments located along the Cordillera are in good agreement with published bedrock data (Figures 1B, 2 and 3). Previous studies north of the CTJ suggest that some areas, affected by the activity of the LOFZ at these latitudes, recorded a recent late Miocene cooling, while other areas display older ages (Thomson, 2002). The work of Guillaume et al. (2013), south of the CTJ, also evidences spatiotemporal variations of dynamic topography for the last 16 m.y., which is consistent with the results obtained in this study.

The upper knickpoints delimit sudden change in channel slope and steepness index from the steep upper slopes to less abrupt slopes. This is bounded downstream by few knickpoints representing a progressive incision to the valley in response to change in uplift rate or fault activity into the watersheds (Kirby and Whipple, 2001; Stock and Montgomery, 1999; Wobus et al., 2006), or the effect of glaciers.

Analysis of geomorphic data demonstrated that uplift and erosion affected unequally the mountain range even in adjacent catchments with a similar size and lithology. Indeed, they present different evolution of the streams, whereas knickpoints and steepness should have been similar in the case of homogeneous denudation related to a regional uplift.

6.6.1 Impact of the Liquiñe-Ofqui Fault Zone

The results show that there is a good correlation between the elevation profile and the PDF for samples MG27, CN4, MG32 and MG36, as well as between observed and predicted AFT ages on the prediction plot (Figure 6.11). This indicates that these four watersheds are uniformly eroded. Furthermore, concavity and steepness indexes as well as river longitudinal profiles do not evidence any particular knickpoint and segment which can be related to changes of erosion rate. These results are also coherent with the high to moderate concavity index defined for these watersheds that doesn't indicate any recent stage of development. We can conclude that these watersheds reach an equilibrium thermal steady state. Unlike these samples, a significant mismatch is observed between the data for the samples MG28, MG34 and MG35. Predicted cooling age distribution peaks obtained by inverse modeling are systematically younger than the PDF (or observed cooling age distribution) peaks. This signifies that central ages of these watersheds are underestimated, and that unknown spatial variations of erosion rates or recent deformation increase in the catchment area occurred, causing a nonuniform erosion across the catchments. The watersheds MG28 and MG34 may have been affected by the topography as a lower elevation peak is recognized in these catchments (Figure 6.7). Nevertheless, noticeable variations between concavity and steepness indexes of some segments separated by knickpoints have been identified from the geomorphic data, which are indicative of different uplift rates affecting these segments. Watersheds explored are too far from each other to recognize a systematic pattern through the area delimiting a boundary between areas with similar uplift rates (Wobus et al., 2006). Thus, the changes in denudation pattern can be related with differential erosion rates directly related with the recent fault activity of the LOFZ as these catchments are located close to faults identified or presumed by in-situ thermochronology (Thomson, 2002; Thomson et al., 2010a, 2001). These studies evidence that the LOFZ is active since the late Miocene and associated with faulted block structures which led to differential uplift across the central Patagonian Andes. Therefore, the poor match observed for those samples possibly affected by the fault activity may result from inhomogeneous erosion rates within the catchments. This is particularly clear for the catchments MG27 and MG28 where AFT results display distinct detrital signals while the watersheds are sharing a water line. Such difference may occur only in the case of restricted features able to impact locally the denudation processes and, therefore, the cooling history. In this case, the pattern of cooling ages reflects a local complexity here associated with a peak of lower elevations and nonuniform denudation due to fault activity across the watershed which allow more significant delivery of grains presenting younger ages. The presence of a recently active fault in this area is definitely evidenced by the new in-situ AFT cooling age (MG31) that yield a Paleogene age while Pliocene age has been identified

to the northwest in former study (Thomson, 2002; Thomson et al., 2010a, 2001). The impact of faults activity is also noticed for the watershed MG35, located right west of a previously identified fault (Thomson, 2002), whereas impact of topography is probably dominant for the watershed MG34 where no fault was recognized in surrounding areas. Nevertheless, faults related to the LOFZ are difficult to recognize either on the field or the satellite view but their presence is testified by significant variations of in-situ cooling ages from Cretaceous to late Miocene from east to west, respectively. These variations have been recognized in the sector of the Rio Cisnes, where samples CN4, MG32 and MG34 were collected (Figure 6.2B). Thus, impact of possible fault activity or local exhumation of a faulted block can not be disregarded. Cooling ages distribution for samples MG28, MG34 and MG35 are consequently biased towards young ages due to particular topography of the watersheds and plausible fault activity, which induced a focused erosion of uplifted areas (Brewer et al., 2003). Therefore, a regional and uniform uplift is not appropriated to explain the thermochronology and geomorphic results north of the CTJ. Uplift governed by faults activity or independent faulted blocks vertical movements is more appropriate to explain the results obtained in this study. This is also consistent with previous works proposing a focus enhanced denudation due to the vertical motion of several faulted blocks (Thomson, 2002).

6.6.2 Storage of grains

Potential sources of mismatch between the predicted and observed data, or hypsometry and PDF, include also sediment storage in the system. Indeed, a significant storage can bring to long-term imbalances in sediment supply to the outlet. The presence of a glacier and lakes noticeable in the northern and southeastern areas, respectively, of the watershed MG29 can be related to sediment storage. Here, the elevation profile and the predicted data mismatch with the observed PDF data. Unlike the hypothesis of fault activity across the catchments inducing focused erosion, we propose that mismatch observed between the data may be directly related to irregular erosion across the catchment which is enhanced by sediment storage promoted by glaciers or induced by the presence of lakes. Large areas cover by the ice can not deliver sediments, which represent a significant fraction of sediments not represented in the outlet modern detrital sample. Furthermore, the remaining topography after ice-cover removal (e.g. cirques and lateral moraines) can also trap sediments and delay their delivery to the outlet. Thus, post-glacial topography may significantly affect the distribution of cooling ages through sediment storage. In both cases, recent past and modern glaciers result in nonuniform erosion through the catchment due to sediment storage. Focused erosion of particular elevations related to glacial abrasion may also affect the denudation (Ehlers et al., 2015).

6.6.3 Disruption due to slab window

The watershed MG40 represents the only watershed which endured a youth stage of erosion, as demonstrated by the convex hypsometric curve, which indicate a recent stage of deformation. This is

coherent with the young ages obtained with in-situ thermochronology along valleys and close vertical profiles (Guillaume et al., 2013; Thomson et al., 2010a). The PDF peak mimics exactly the youngest elevation distribution peak. Furthermore, the river network for the catchment MG40 is poorly developed and has an elongated shape, which is consistent with early stage of development that we relate to a recent significant uplift.

On the contrary, the watershed MG38 is characterized by a great concave shape hypsometry, a nonuniform erosion as evidenced by the mismatch between predicted and observed data, a well-developed river network within a large catchment, and an older central cooling age peak. These significant differences may be related to the presence of a notable high topography (> 3000 m) while lower summits characterized the catchment MG40 (< 1800 m). Indeed, high erosion rates are predicted at high elevations due to higher debris flows which are carrying these rocks from the areas fractured by glacier and frosting (e.g. Fox et al., 2015; Sanders et al., 2012; Stoffel et al., 2005).

Despite the difference of topography, cooling ages distribution for samples MG38 and MG40 present similar minimum and maximum single-grain ages. The young single-grain cooling ages recognized in these two watersheds can be related to the recent subduction of the Chilean mid-oceanic ridges below the South American Plate at these latitudes which is responsible of the opening of a slab window below the austral Patagonia. Superficial uplift triggered by slab window is a process well accepted (e.g. Ávila and Dávila, 2020 and references therein). However, we notice a significant difference between the cooling age distribution obtained for these two watersheds (with single-grain ages from ca. 6 to 50 Ma) and the vertical profile realized in the same sector where highest elevations have been characterized by a cooling age of 17.1 Ma (Thomson et al., 2010a). Thus, detrital AFT data show ages older than expected. It means that, despite a regional uplift generated by the opening of a slab window, denudation is not homogeneous across the Patagonian Andes as for watersheds studied north of the CTJ. Unlike the narrow distribution of cooling ages for catchments affected by the LOFZ north of the CTJ with oldest single-grain ages around ~30 Ma, the PDFs obtained for samples MG38 and MG40 display a wider distribution of cooling ages (to ~50 Ma) that we relate with a progressive and regional uplift, rather than sudden events linked to fault activity. This slower cooling is also evidence by the inverse modeling (Figure 6.9, Figure 6.10B). This result is consistent with previous study about the dynamic topography above the austral Patagonian slab window (e.g. Ávila and Dávila, 2020; Guillaume et al., 2013).

6.6.4 Central Patagonian Andes denudation

Our graphical representation between predicted and observed data, obtained by inverse modeling of the detrital data, enables to visualize the mismatch between the data and evaluate the uniformity of the denudation across the catchments. Data reflect that cooling distribution signal is easily disturbed by some local complexities responsible for a focused erosion (e.g. fault activity, steep slopes) or storage of grains (e.g. glaciers). Thus, north of the CTJ, data evidence that erosion is nearly

uniform in areas not affected by any faults whereas the active faults related to the LOFZ has a strong impact on the local denudation processes and sediment delivery as demonstrated by the faster cooling and the steeper age-elevation profiles (Figure 6.10). On the contrary, slab window opening is responsible for the recent and regional uplift observed south of the CTJ which appears more progressive as demonstrated by the inverse modeling.

Our results may indicate that catchments underwent differential uplift. This is consistent with the river profiles analysis as knickpoints should be generated at the same elevation approximately for catchments affected by a similar event, while here no relation between the numerous knickpoints have been observed. These spatial variations in erosion rates are add up to other assumptions known to affect a little the detrital cooling ages as: the variable concentration of specific mineral, the sorting of grain-size fractions due to drainage, the presence of partial annealing zone within the catchment inducing a non-linear age-elevation relationship (Ehlers et al., 2015 and references therein). Despite these numerous factors of inaccuracy, this study evidences that detrital thermochronology on modern outlet sample is a reliable tool to infer spatial pattern of catchment erosion without vertical profile bedrock data and to constrain thermal history of the catchment through the distribution of the thermochronology data and the inverse modeling. Nevertheless, modelling processes for a watershed can be easily complexified by local features as faults, steepness variations or modern glaciers, which cause variable erosion rates within the catchments. Therefore, combining multiple detrital sampling with the recent inverse modeling approach and geomorphologic study bring valuable information about the long-term thermal history experienced by bedrocks samples into the catchments of the central Patagonian Andes and about the uniformity of denudation processes affected by faults and glaciers, whereas local vertical age profiles are commonly used for these predictions (e.g. Brewer et al., 2003; Malusà and Fitzgerald, 2019; Stock et al., 2006).

6.7 Conclusion

Detrital AFT data and hypsometric data, as well as temperature-time history modeling, suggest significant variations of denudation across the catchments of the central Patagonian Andes related to the activity of faults, the presence of glaciers ant the effects of deep geodynamic processes as the asthenospheric slab window. About the latter, opened south of the Chile Triple Junction, progressive cooling has been observed with a quite young central cooling age which may correspond to the dynamic topography support recognized in this sector. To the north, catchments affected by the activity of Liquiñe-Ofqui Fault Zone present a rapid cooling in recent times with a nonuniform denudation while other catchments, mainly located to the east, display the slowest cooling and uniform erosion that we can relate to a thermal steady-state. Thus, catchments underwent a differential uplift along the central Patagonian Andes which is enhanced by focused erosion and

storage of sediments locally associated to diverse factors identified with the hypsometry and the geomorphic data.

Therefore, our results highlight the relevance of combining detrital sampling and hypsometry to constrain denudation and thermal histories regionally as well as the impact of numerous climatic, tectonic or deeper mechanical factors.

6.8 Acknowledgments

Funding for this work was provided by the University of Padova (Progetto di Ateneo 2015, CPDA158355). S. Boesso and L. di Tauro are thanked for samples preparation.

CHAPTER 7

GENERAL DISCUSSION AND CONCLUSIONS

The principal aim of this thesis was to address the Meso-Cenozoic thermal history of the north-central Patagonian Andes and its broken foreland (40 – 48°S) to better understand the relationships between the denudation processes and the geodynamic evolution. The primary regional focus of this investigation was the north Patagonia (40 – 44°S) and its eastern broken foreland as basement and Jurassic sedimentary units are widely exposed. Therefore, the north Patagonian foreland has a great potential to record thermal phases associated either with burial or exhumation. Indeed, the north Patagonian foreland may have been affected by a significant exhumation during the Cretaceous or the Miocene that has been potentially recorded by low-temperature thermochronometers. The central Patagonian foreland depocenters (44 – 48 °S) and intraplate belt were then explored through detrital apatite double-dating (fission-tracks and U-Pb analysis) as the Cretaceous – Cenozoic cover gives the opportunity to investigate the source-to-sink evolution in the last 60 m.y. A particular emphasis was given to the San Bernardo Fold and Thrust Belt (FTB) where Cretaceous deposits are locally exposed and may record the signature of possible Cenozoic tectonic activity. Lastly, modern detrital samples were collected at the outlet of catchments located along the central Patagonian Andes in order to examine the denudation pattern. As sampling along vertical profiles is particularly complicated in this region, detrital data from modern rivers may be particularly helpful in the quantification of denudation rates.

7.1 Cretaceous – Paleogene unroofing of the Patagonian Andes and its foreland

The thermochronological data presented in chapters 3, 4 and 5, and appendices E and F, support the idea that a late Early Cretaceous – middle Eocene shortening phase affected significantly both the Cordillera and the entire broken foreland (Figure 7.1A; Horton, 2018a; Savignano et al., 2016). The deformation of the overriding plate is affected by plate kinematics, which exert a first-order control on plate coupling. Particularly, the change of convergence direction of the overriding plate is a dominant process as demonstrated in the Central Andes (~ 19°S), where an increase of deformation occurred despite the decrease of convergence rate (Oncken et al., 2006). Into the north-central Patagonian foreland, this deformation active from the late Early Cretaceous to the middle Eocene is characterized by the inversion of inherited structures such as Mesozoic rift-related normal faults (half-graben systems) developed with various directions (Figari et al., 2015). The faults oriented mostly perpendicularly to the compressional stress were preferentially reactivated during the Cretaceous shortening and transmitted deformation far from the orogen due to the upper crustal weaknesses (Gianni et al., 2015a). The reactivation of inherited faults and inversion of former basins in the broken foreland may complexify significantly the evolution

of the foreland as it has been observed for example along the Iberian Chain, the Yinshan fold-and-thrust belt and the Arabia-Eurasia collision zone (Cavazza et al., 2019; Guimerà Rosso, 2018; Yonkee and Weil, 2015). Thus, the uneven reactivation of former structures obscured the tectonic signal as in the north-central Patagonian foreland. Since the AFT thermochronometer records cooling below the ~110°C isotherm, corresponding roughly to the upper 3 – 4 km of the crust for an average geothermal gradient of ~30°C/Ma, the relationships between surface processes, tectonics and geodynamic evolution were explored in this study. Furthermore, the surface processes, that may significantly impact the cooling age patterns, were also investigated through the AHe system which records cooling below the interval 40 – 100 °C, corresponding approximately to the upper 1 – 3 km of the crust. As a general pattern, the AHe data mimic the AFT cooling ages except for few younger AHe ages identified in the foreland, especially in the southern San Bernardo FTB (chapter 5). These AHe data may have been strongly affected by heating related to the widespread intraplate volcanism active during the Oligo-Miocene (e.g. Buen Pasto Formation in the central Patagonian foreland, Somuncura Plateau in the north Patagonian foreland, El Maitén Belt close to the north Patagonian Precordillera). Despite the complexity of the broken foreland history, the overall picture given by the thermochronological ages suggests that the main episode of mountain building along the north-central Patagonian Cordillera and its broken foreland belt occurred from the late Early Cretaceous to the early Paleogene, which is coeval with a slab shallowing episode (Figure 7.1D). The onset of this regional deformation was likely triggered by a significant increase of interplate coupling induced by slab shallowing which has been provoked by the change of absolute motion of the South American Plate to the west during late Early Cretaceous (Horton, 2018a; Maloney et al., 2013). Thus, this study provides new insights for the impact of geodynamic processes on the denudation at the surface with valuable values for unroofing magnitude and denudation rates.

7.2 Persistent denudation during a phase of tectonic quiescence

The lack of late Eocene – early Miocene shortening across the whole north-central Patagonia points to a tectonic quiescence period that initiated after a sharp reduction in average trenchward velocity (Maloney et al., 2013) which may be responsible for plate decoupling. The increase of subsidence in the foreland from the late Eocene to the early Miocene, allowing significant marine incursions toward the inner parts of the Cordillera (Encinas et al., 2018), was probably related to slab rollback and steepening of the subducting slab. Nevertheless, as demonstrated by the persistent ~30 Ma AFT population recorded in the entire foreland and the older AFT components identified only around the San Bernardo FTB, denudation was still affecting the central Patagonian Cordillera and its broken foreland through this period (Figure 7.1A; chapter 4). Lag time estimates on the youngest component allow to identify very slow denudation rates (Figure 7.1C). This is supported by in-situ thermochronological analysis in the Cordillera that shows some ~30 Ma AFT ages (Thomson et al., 2010a, 2001) and detrital analysis of modern river sediments along the Cordillera (chapter 6), where similar AFT central ages have been commonly identified. We suggest that this denudation at ca. 30 Ma was related to post-shortening denudation

processes after the establishment of more or less high reliefs along the Patagonian Cordillera. The lag time obtained evidences a significant unroofing of 2 – 4 km of the central Patagonian Cordillera between the Oligocene and the late Miocene. The denudation of the Cordillera is well testified by the derived detritus that were transported all across the foreland. The wide distribution of the similar deposits identified in this study evidences the absence of a relevant topographic barrier related to the flexure of the lithospheric plate in response to orogenic loading (forebulge; DeCelles and Giles, 1996). As the forebulge is missing during tectonic unloading cycle (Catuneanu et al., 1997), the absence of forebulge in the central Patagonia during late Eocene to early Miocene is consistent with the quiescence stage recognized.

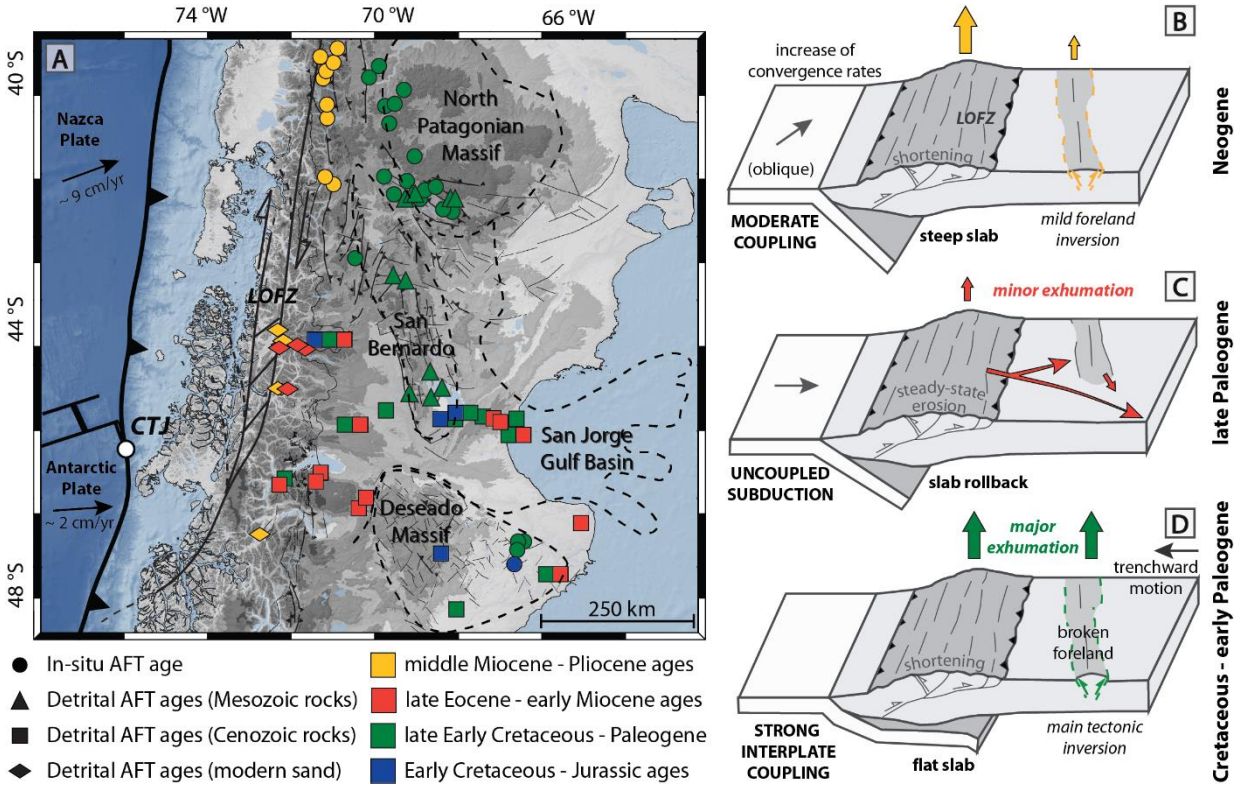

Figure 7.1 – A. Topographic map of the north-central Patagonia with all the AFT results obtained for all the samples analyzed. Following sketches were modified from Savignano et al., 2016. B. Exhumation focused along the Cordillera during late Neogene due to the increase of convergence rates and obliquity associated with a moderate increase of the coupling. C. Steady-state erosion of the reliefs during a tectonic quiescence phase. D. Main deformation of Patagonia during Cretaceous – Paleogene due to strong interplate coupling related to shallow slab episode. B, C and D have been modified from Savignano et al., 2016.

7.3 Significance of the late shortening episode

Thermochronometric ages from the north Patagonian Precordillera, corresponding to reliefs east of the main range (chapter 3), and from the inner part of the central Patagonian Cordillera (chapter 6) document fast cooling since the Miocene which may be related with a significant exhumation of the north-central Patagonian Cordillera (Figure 7.1A). This stage is not recorded in the foreland, even by the low-

temperature AHe thermochronometer, as the few Oligo-Miocene AHe ages in the foreland (chapters 3 and 5) are associated to Oligo-Miocene volcanic processes. The Miocene compressive stage often described for the broken foreland (Bilmes et al., 2013; Gianni et al., 2015a; Homovc et al., 1995) must have been negligible in terms of vertical displacements and exhumation. On the other hand, we relate the substantial Miocene exhumation clearly defined along the Patagonian Cordillera with the renewal of shortening. This phase may have been controlled by the reorganization of plate kinematics after the break-up of the Farallon Plate ~23 Ma, which caused the convergence to become oblique (Figure 7.1B; Lonsdale, 2005; Maloney et al., 2013). Thrusts and faults activity had a significant impact on the denudation of the north-central Patagonian Cordillera as demonstrated by the thermochronological data from modern outlet samples collected around the Liquiñe-Ofqui Fault Zone (chapter 6). Indeed, catchments explored on both side of this strike-slip fault zone indicate clearly that the catchment affected by these faults display a younger AFT cooling ages that we related to a recent Miocene exhumation. South of the Liquiñe-Ofqui Fault Zone, this recent exhumation, also recorded by our detrital data, is most likely associated with the opening of a slab window below the South American Plate, as evidenced by (e.g.) Guillaume et al. (2013).

7.4 Perspectives

7.4.1 Critical wedge theory in Patagonia

The episodic propagation of the deformational front to the foreland and the continuous exhumation of the Cordillera through time bring us to consider the north-central Patagonia tectonic evolution in the framework of the critical wedge theory (Davis et al., 1983). The critical wedge theory was successfully applied to the study of mountain belt in order to understand the relationships between exhumation and kinematic processes (e.g. Davis et al., 1983; DeCelles and Mitra 1995). Indeed, the critical wedge theory relies on the prediction of changes of mass distribution, which are controlled by the spatiotemporal variations of exhumation, on the kinematic history of the orogenic wedge. Thus, critical taper theory predicts that front of the orogenic wedge propagates toward the foreland when the taper developed reach a critical angle, whereas continuous internal deformation occurs through folding and thrusting during subcritical state (when the taper value is less than the critical value) to increase the taper and recover a critical taper (Gray and Mitra, 1999). The exhumation of the orogenic wedge may be considered as a response to changes of taper state (Davis et al., 1983), that may be caused by active tectonics or enhanced erosion.

Studies applying the critical wedge theory in Patagonia indicate that the orogenic Patagonian wedge underwent through critical stage during the Cretaceous (Ghiglione and Ramos, 2005). Lag-time analysis performed in this thesis show that ~2 km of exhumation has been observed in the central Patagonian Cordillera from the late Eocene to early Miocene (chapter 4), which is consistent with a period of tectonic quiescence along the margin (Horton and Fuentes, 2016). Referring to the critical wedge

theory, lag time is constant upsection for steady-state exhumation while a decreasing lag time upsection characterize increasing exhumation (e.g. Carrapa et al., 2009). Thus, a precise lag-time is needed to recognized such trends. U-Pb dating on zircons extracted from the Cenozoic sandstones collected in the central Patagonian foreland will be carried out to obtain more precise constraints about the deposition ages of the deposits sampled. These analyses would clarify the lag time and understand if it records a critical wedge state (no deformation) dominated by the erosion of former reliefs, or a subcritical state inducing an enhanced internal deformation.

7.4.2 Deseado Massif thermal history: the role of mantle processes

The PhD thesis of Alexis Derycke (University of Paris-Saclay, France) focuses on U-Th-Sm/He thermochronology analysis on apatites and hematites from basement rocks of the Deseado Massif. This study aims to constrain the thermal history of the Deseado Massif in order to decipher the significance of the exhumation events including considerations about the potential thermal impact of mantle processes. Indeed, deformation stages in the Deseado Massif are poorly constrained as few surface markers have been preserved in this area. The second target of this study is to better understand how mantle processes may affect the surface evolution and thermal history. AFT analysis realized at the University of Padova, as part of the collaboration between the projects, brought critical data to better constrain the thermal history of this area and the whole Patagonian Broken Foreland. Better knowledges about the denudation of the Deseado Massif may also help clarifying sediment delivery to the adjacent foreland basin (e.g. San Jorge Basin).

7.4.3 Double dating with apatite fission tracks and U-Pb dating

In provenance studies, the use of a multi-dating approach on a single-phase with high (U-Pb) and low-temperature (fission tracks and / or (U-Th-Sm)/He) thermochronometers is advantageous to reveal the crystallization age and the cooling/exhumation age of the grains, respectively. Although much progress has been made during the past decade, zircon thermochronometers are prevalent in multi-dating studies whereas apatite thermochronometers are still often neglected. The main cause is the lower amount of U content and the higher common Pb content, which result in the discordance of the apatite grains in the U-Pb system. Thus, double dating achieved in the chapter 4 is not routinary, while results were suitable to distinguish clearly apatite cooling ages related to rapid volcanic cooling and longer exhumation cooling. The chapter 4 evidences the potential of this approach, especially in areas where the exhumation signal may be overtaken by the volcanic input. Recent works also propose to use apatite trace elements to reveal specific provenance (e.g. O'Sullivan et al., 2020). Thus, this thesis participates to the growing interest for apatite multi-dating in provenance studies, which may become a conventional method in a very near future.

7.4.4 Thermal modeling on modern outlet samples

Finally, the thermal modeling applied in the chapter 6 on modern sandstones represents a novel approach to investigate mountain range denudation pattern and thermal history. This thesis demonstrates the ability of this recent approach to catch denudation variability through inaccessible areas, therefore giving some hints about erosional processes and the role of tectonics. If further developed, it may become a routine analysis in detrital thermochronology studies.

7.5 Companion projects

Basin evolution is controlled by diverse factors as the development of reliefs, which can restrict bypass to the basin. Forebulges and intraplate belts represent the main topographic barriers developed in foreland, which prevent the bypass of sediments to the entire foreland, whereas outer forearc high characterized the structural highs uplifted in the forearc regions. The outer forearc high controls directly the formation of forearc basin by restricting a depocenter landward and the bypass to the trench. Although the inception of an outer forearc high in accretionary margin (such as the Nankai margin in Japan or the New Zealand) is well established, the presence of structural high in erosional margin, as the Peruvian segment, is less understood. However, similar structures appear in erosional margins near the slope-break. Additional study of seismic data from the north-central Peruvian forearc was performed during this thesis in order to constrain the long-term evolution of a structural high developed along this erosional margin (appendix G; Genge et al., 2020) and provide farther knowledges about the relationships between uplift and subsidence in forearc setting.

References

Adriasola, A.C., Thomson, S.N., Brix, M.R., Hervé, F., Stöckhert, B., 2006. Postmagmatic cooling and late Cenozoic denudation of the North Patagonian Batholith in the Los Lagos region of Chile, 41-42 15′ S. International Journal of Earth Sciences 95, 504–528.

Aguirre-Urreta, M.B., Ramos, V.A., 1981. Crustáceos decápodos del Cretácico inferior de la Cuenca Austral, provincia de Santa Cruz, Argentina. Comité Sudamericano del Jurásico y Cretácico: cuencas sedimentarias del Jurásico y Cretácico de América del Sur 2, 599–623.

Allard, J.O., Foix, N., Bueti, S.A., Sánchez, F.M., Ferreira, M.L., Atencio, M., 2020. Comparative structural analysis of inverted structures in the San Bernardo fold belt (Golfo San Jorge basin, Argentina): Inversion controls and tecto-sedimentary context of the Chubut Group. Journal of South American Earth Sciences 97, 102405.

Ameghino, F., 1906. Las formaciones sedimentarias del Cretáceo superior y del Terciario de Patagonia, con un paralelo entre sus faunas mastológicas y las del Antiguo Continente, in: Anales Del Museo Nacional de Historia Natural de Buenos Aires. pp. 1–568.

Andreis, R.R., Cúneo, R., 1989. Late Paleozoic high-constructive deltaic sequences from northwestern Patagonia, Argentine Republic. Journal of South American earth sciences 2, 19–34.

Anselmi, G., Gamba, M.T., Panza, J.L.A., 2004a. Hoja Geológica 4369-IV Los Altares. Servicio Geológico Minero Argentino. Instituto de Geología y Recursos Minerales.

Anselmi, G., Panza, J.L.A., Cortés, J.M., Ragona, D., 2004b. Hoja Geológica 4569-II El Sombrero. Servicio Geológico Minero Argentino. Instituto de Geología y Recursos Minerales.

Aragón, E., D'Eramo, F., Castro, A., Pinotti, L., Brunelli, D., Rabbia, O., Rivalenti, G., Varela, R., Spakman, W., Demartis, M., 2011. Tectono-magmatic response to major convergence changes in the North Patagonian suprasubduction system; the Paleogene subduction–transcurrent plate margin transition. Tectonophysics 509, 218–237.

Aragón, E., Pinotti, L., Fernando, D., Castro, A., Rabbia, O., Coniglio, J., Demartis, M., Hernando, I., Cavarozzi, C.E., Aguilera, Y.E., 2013. The Farallon-Aluk ridge collision with South America: Implications for the geochemical changes of slab window magmas from fore-to back-arc. Geoscience Frontiers 4, 377–388.

Archangelsky, S., 1966. Estudio de la Formación Baqueró. Cretácico Inferior de Santa Cruz, Argentina. Revista del Museo de La Plata 5, 63–171.

Ardolino, A., Lizuain, A., Salani, F., Pezzuchi, H., 2011. Mapa geológico preliminar de la Hoja 4369-II. Gan Gan, provincia del Chubut. Programa Nacional de Cartas Geol ógicas de la República Argentina, escala 1.

Ardolino, A.A., Panza, J.L.A., Ylláñez, E.D., Parisi, C., Franchi, M., 2003. Hoja Geológica 4566-I Garayalde. Servicio Geológico Minero Argentino. Instituto de Geología y Recursos Minerales.

Arrondo, O.G., 1972. Estudio geológico y paleontológico en la zona de la estancia La Juanita y alrededores, Provincia de Santa Cruz, Argentina. Revista del Museo de La Plata 7, 1–194.

Ault, A.K., Gautheron, C., King, G.E., 2019. Innovations in (U–Th)/He, fission track, and trapped charge thermochronometry with applications to earthquakes, weathering, surface-mantle connections, and the growth and decay of mountains. Tectonics 38, 3705–3739.

Ávila, P., Dávila, F.M., 2020. Lithospheric thinning and dynamic uplift effects during slab window formation, southern Patagonia (45˚-55˚ S). Journal of Geodynamics 133, 101689.

Ayers, J.C., Watson, E.B., 1993. Apatite/fluid partitioning of rare-earth elements and strontium: Experimental results at 1.0 GPa and 1000 C and application to models of fluid-rock interaction. Chemical Geology 110, 299–314.

Bablon, M., Quidelleur, X., Samaniego, P., Le Pennec, J.-L., Lahitte, P., Liorzou, C., Bustillos, J.E., Hidalgo, S., 2018. Eruptive chronology of Tungurahua volcano (Ecuador) revisited based on new K-Ar ages and geomorphological reconstructions. Journal of Volcanology and Geothermal Research 357, 378–398.

Bande, A., Horton, B.K., Ramírez, J.C., Mora, A., Parra, M., Stockli, D.F., 2012. Clastic deposition, provenance, and sequence of Andean thrusting in the frontal Eastern Cordillera and Llanos foreland basin of Colombia. Bulletin 124, 59–76.

Barbarand, J., Carter, A., Wood, I., Hurford, T., 2003. Compositional and structural control of fission-track annealing in apatite. Chemical Geology 198, 107–137.

Barcat, C., Cortiñas, J.S., Nevistic, V.A., Zucchi, H.E., 1989. Cuenca Golfo San Jorge. Cuencas Sedimentarias Argentinas 6, 319–345.
Barreda, V., Bellosi, E., 2014. Ecosistemas terrestres del Mioceno Temprano de la Patagonia central, Argentina: primeros avances. Revista del Museo Argentino de Ciencias Naturales nueva serie 5, 125–134.
Bechis, F., Encinas, A., Concheyro, A., Litvak, V.D., Aguirre-Urreta, B., Ramos, V.A., 2014. New age constraints for the Cenozoic marine transgressions of northwestern Patagonia, Argentina (41–43 S): Paleogeographic and tectonic implications. Journal of South American Earth Sciences 52, 72–93.
Bell, M., De La Cruz, R., Suárez, M., Townsend, M., 1996. The evolution of the Aysen Basin, an early Cretaceous epicontinental interior seaway in southernmost South America, in: 3rd International Symposium of Andean Geodynamics, Saint Malo, France. p. 292.
Bellosi, E.S., 2010. Loessic and fluvial sedimentation in Sarmiento Formation pyroclastics, middle Cenozoic of central Patagonia. The Paleontology of Gran Barranca: Evolution and Environmental Change through the Middle Cenozoic of Patagonia. Cambridge University Press, Cambridge 278–292.
Bellosi, E.S., 1998. Depósitos progradantes de la Formación Santa Cruz. Mioceno de la Cuenca de San Jorge. 7ª Reunión Argentina de Sedimentología. Actas de Resúmenes 110–111.
Belousova, E.A., Griffin, W.L., O'Reilly, S.Y., Fisher, N.I., 2002. Apatite as an indicator mineral for mineral exploration: trace-element compositions and their relationship to host rock type. Journal of Geochemical Exploration 76, 45–69.
Belousova, E.A., Walters, S., Griffin, W.L., O'reilly, S.Y., 2001. Trace-element signatures of apatites in granitoids from the Mt Isa Inlier, northwestern Queensland. Australian Journal of Earth Sciences 48, 603–619.
Bernet, M., Zattin, M., Garver, J.I., Brandon, M.T., Vance, J.A., 2001. Steady-state exhumation of the European Alps. Geology 29, 35–38.
Bétard, F., Peulvast, J.-P., Rabassa, J., Aguilera, E.Y., 2014. Meso-Cenozoic Paleotopographies and Paleolandscapes in the Deseado Massif (Santa Cruz Province, Argentina), in: Gondwana Landscapes in Southern South America. Springer, pp. 477–501.
Bilmes, A., D'Elia, L., Franzese, J.R., Veiga, G.D., Hernández, M., 2013. Miocene block uplift and basin formation in the Patagonian foreland: the Gastre Basin, Argentina. Tectonophysics 601, 98–111.
Bishop, B.T., Beck, S.L., Zandt, G., Wagner, L.S., Long, M.D., Tavera, H., 2018. Foreland uplift during flat subduction: Insights from the Peruvian Andes and Fitzcarrald Arch. Tectonophysics 731, 73–84.
Blackstone, D.L., 1980. Foreland deformation; compression as a cause. Rocky Mountain Geology 18, 83–100.
Borg, I., Groenen, P.J., 2005. Modern multidimensional scaling: Theory and applications. Springer Science & Business Media.
Brandon, M.T., 2002. Decomposition of mixed grain age distributions using Binomfit. On track 24, 13–18.
Brandon, M.T., Roden-Tice, M.K., Garver, J.I., 1998. Late Cenozoic exhumation of the Cascadia accretionary wedge in the Olympic Mountains, northwest Washington State. Geological Society of America Bulletin 110, 985–1009.
Braun, J., Stippich, C., Glasmacher, U.A., 2016. The effect of variability in rock thermal conductivity on exhumation rate estimates from thermochronological data. Tectonophysics 690, 288–297.
Braun, J., Van Der Beek, P., Batt, G., 2006. Quantitative thermochronology: numerical methods for the interpretation of thermochronological data. Cambridge University Press.
Breitsprecher, K., Thorkelson, D.J., 2009. Neogene kinematic history of Nazca–Antarctic–Phoenix slab windows beneath Patagonia and the Antarctic Peninsula. Tectonophysics 464, 10–20.
Brewer, I.D., Burbank, D.W., Hodges, K.V., 2003. Modelling detrital cooling-age populations: insights from two Himalayan catchments. Basin Research 15, 305–320.
Bruni, S., D'ORAZIO, M., Haller, M.J., Innocenti, F., Manetti, P., PECskay, Z., Tonarini, S., 2008a. Time-evolution of magma sources in a continental back-arc setting: the Cenozoic basalts from Sierra de San Bernardo (Patagonia, Chubut, Argentina). Geological Magazine 145, 714–732.
Bruni, S., D'ORAZIO, M., Haller, M.J., Innocenti, F., Manetti, P., Pecskay, Z., Tonarini, S., 2008b. Time-evolution of magma sources in a continental back-arc setting: the Cenozoic basalts from Sierra de San Bernardo (Patagonia, Chubut, Argentina). Geological Magazine 145, 714–732.

Burtner, R.L., Nigrini, A., Donelick, R.A., 1994. Thermochronology of Lower Cretaceous source rocks in the Idaho-Wyoming thrust belt. AAPG bulletin 78, 1613–1636.

Buscher, J., Morata, D., Arancibia, G., Cembrano, J.M., 2016. Deciphering the Role of Tectonic and Climatic Processes on the Landscape Development of the Patagonian Andes Along the Liquiñe-Ofqui Fault System, Chile. AGUFM 2016, EP11B–0998.

Butler, K.L., Horton, B.K., Echaurren, A., Folguera, A., Fuentes, F., 2020. Cretaceous-Cenozoic growth of the Patagonian broken foreland basin, Argentina: Chronostratigraphic framework and provenance variations during transitions in Andean subduction dynamics. Journal of South American Earth Sciences 97, 102242.

Calk, L.C., Naeser, C.W., 1973. The thermal effect of a basalt intrusion on fission tracks in quartz monzonite. The Journal of Geology 81, 189–198.

Cande, S.C., Leslie, R.B., 1986. Late Cenozoic tectonics of the southern Chile trench. Journal of Geophysical Research: Solid Earth 91, 471–496.

Carignano, A.P., Paredes, J.M., Olazábal, S.X., Valle, M.N., 2017. Ostracoda (Crustacea) from the Pozo D-129 formation (upper Barremian?–Aptian), Golfo san Jorge basin, Patagonia, Argentina: taxonomic descriptions, palaeoenvironments and palaeogeographical implications. Cretaceous Research 78, 206–220.

Carlson, W.D., Donelick, R.A., Ketcham, R.A., 1999. Variability of apatite fission-track annealing kinetics: I. Experimental results. American mineralogist 84, 1213–1223.

Carrapa, B., DeCelles, P.G., Reiners, P.W., Gehrels, G.E., Sudo, M., 2009. Apatite triple dating and white mica 40Ar/39Ar thermochronology of syntectonic detritus in the Central Andes: A multiphase tectonothermal history. Geology 37, 407–410.

Casal, G.A., Allard, J.O., Foix, N., 2015. Análisis estratigráfico y paleontológico del Cretácico Superior en la Cuenca del Golfo San Jorge: nueva unidad litoestratigráfica para el Grupo Chubut. Revista de la Asociación Geológica Argentina 72, 77–95.

Catuneanu, O., Beaumont, C., Waschbusch, P., 1997. Interplay of static loads and subduction dynamics in foreland basins: Reciprocal stratigraphies and the "missing" peripheral bulge. Geology 25, 1087–1090.

Cavazza, W., Albino, I., Galoyan, G., Zattin, M., Catto, S., 2019. Continental accretion and incremental deformation in the thermochronologic evolution of the Lesser Caucasus. Geoscience Frontiers 10, 2189–2202.

Cembrano, J., Hervé, F., Lavenu, A., 1996. The Liquiñe Ofqui fault zone: a long-lived intra-arc fault system in southern Chile. Tectonophysics 259, 55–66.

Cembrano, J., Lavenu, A., Reynolds, P., Arancibia, G., López, G., Sanhueza, A., 2002. Late Cenozoic transpressional ductile deformation north of the Nazca–South America–Antarctica triple junction. Tectonophysics 354, 289–314.

Cerpa, N.G., Guillaume, B., Martinod, J., 2018. The interplay between overriding plate kinematics, slab dip and tectonics. Geophysical Journal International 215, 1789–1802.

Cesari, O., 1977. Informe de ensayo inicial del pozo YPF. Ch. PRM. es-1. Sección: Consideraciones estratigráficas. Unpublished report of YPF.

Charrier, R., Pinto, L., Rodríguez, M.P., 2007. Tectonostratigraphic evolution of the Andean Orogen in Chile, in: The Geology of Chile. pp. 21–114.

Chelotti, L., 1997. Evolución tectónica de la Cuenca del Golfo San Jorge en el Cretácico y Terciario; algunas observaciones desde la interpretación sísmica. Boletín de Informaciones Petroleras 49, 62–82.

Chew, D.M., Donelick, R.A., 2012. Combined apatite fission track and U-Pb dating by LA-ICP-MS and its application in apatite provenance analysis. Quantitative Mineralogy and Microanalysis of Sediments and Sedimentary Rocks: Mineralogical Association of Canada, Short Course 42, 219–247.

Chew, D.M., Petrus, J.A., Kamber, B.S., 2014. U–Pb LA–ICPMS dating using accessory mineral standards with variable common Pb. Chemical Geology 363, 185–199.

Chew, D.M., Sylvester, P.J., Tubrett, M.N., 2011. U–Pb and Th–Pb dating of apatite by LA-ICPMS. Chemical Geology 280, 200–216.

Clavijo, R., 1986. Estratigrafía del Cretácico Inferior en el sector occidental de la Cuenca del Golfo San Jorge. Boletín de Informaciones Petroleras 9, 15–32.

Clinkscales, C., Kapp, P., Wang, H., 2020. Exhumation history of the north-central Shanxi Rift, North China, revealed by low-temperature thermochronology. Earth and Planetary Science Letters 536, 116146.
Cloos, M., 1993. Lithospheric buoyancy and collisional orogenesis: Subduction of oceanic plateaus, continental margins, island arcs, spreading ridges, and seamounts. Geological Society of America Bulletin 105, 715–737.
Cobbold, P.R., Rossello, E.A., 2003. Aptian to recent compressional deformation, foothills of the Neuquén Basin, Argentina. Marine and Petroleum Geology 20, 429–443.
Cobos, J.C., Panza, J.L.A., Zubía, M.A., Figari, E.G., Cardinali, G., Lucero, M., Borderas, M., 2003. Hoja Geológica 4769-I El Pluma. Servicio Geológico Minero Argentino. Instituto de Geología y Recursos Minerales.
Cochrane, R., Spikings, R.A., Chew, D., Wotzlaw, J.-F., Chiaradia, M., Tyrrell, S., Schaltegger, U., Van der Lelij, R., 2014. High temperature (> 350 C) thermochronology and mechanisms of Pb loss in apatite. Geochimica et Cosmochimica Acta 127, 39–56.
Codignotto, J., Nullo, F., Panza, J., Proserpio, C., 1978. Estratigrafía del Grupo Chubut entre Paso de Indios y Las Plumas, provincia del Chubut, Argentina, in: VII Congreso Geologico Argentino, Neuquén (9–15 Abril 1978), Actas. pp. 471–480.
Coira, B., Kay, S.M., Viramonte, J., 1993. Upper Cenozoic magmatic evolution of the Argentine Puna—A model for changing subduction geometry. International Geology Review 35, 677–720.
Cortiñas, J.S., 1996. La cuenca de Somuncurá-Cañadón Asfalto: sus límites, ciclos evolutivos del relleno sedimentario y posibilidades exploratorias, in: XIII Congreso Geológico Argentino y III Congreso de Exploración de Hidrocarburos, Buenos Aires, Actas. pp. 147–163.
Creer, K.M., Mitchell, J.G., Abou Deeb, J., 1972. Palaeomagnetism and radiometric age of the Jurassic Chon Aike Formation from Santa Cruz province, Argentina: implications for the opening of the South Atlantic. Earth and Planetary Science Letters 14, 131–138.
Cucchi, R.J., Busteros, A.G., Lema, H.A., Dalponte, M.R., Espejo, P.M., Franchi, M., 2001. Hoja Geológica 4169-II Los Menucos. Servicio Geológico Minero Argentino. Instituto de Geología y Recursos Minerales.
Cucchi, R.J., Espejo, P.M., González, R., 1998. Hoja Geológica 4169-I Piedra del Águila.
Cuitiño, J.I., Fernicola, J.C., Kohn, M.J., Trayler, R., Naipauer, M., Bargo, M.S., Kay, R.F., Vizcaíno, S.F., 2016. U-Pb geochronology of the Santa Cruz Formation (early Miocene) at the Río Bote and Río Santa Cruz (southernmost Patagonia, Argentina): Implications for the correlation of fossil vertebrate localities. Journal of South American Earth Sciences 70, 198–210.
Cuitiño, J.I., Santos, R.V., Muruaga, P.J.A., Scasso, R.A., 2015a. Sr-stratigraphy and sedimentary evolution of early Miocene marine foreland deposits in the northern Austral (Magallanes) Basin, Argentina. Andean Geology 42, 364–385.
Cuitiño, J.I., Scasso, R.A., Santos, R.V., Mancini, L.H., 2015b. Sr ages for the Chenque Formation in the Comodoro Rivadavia región (Golfo San Jorge basin, Argentina): stratigraphic implications. Latin American journal of sedimentology and basin analysis 22, 3–12.
Cúneo, R., Ramezani, J., Scasso, R., Pol, D., Escapa, I., Zavattieri, A.M., Bowring, S.A., 2013. High-precision U–Pb geochronology and a new chronostratigraphy for the Cañadón Asfalto Basin, Chubut, central Patagonia: Implications for terrestrial faunal and floral evolution in Jurassic. Gondwana Research 24, 1267–1275.
Dal Molin, C., Franchi, M., 1996. Reinterpretación estratigráfica de las sedimentitas terciarias del sudoeste de Chubut, in: XIII Congreso Geológico Argentino y III Congreso de Exploración de Hidrocarburos, Actas. pp. 473–478.
Dal Molin, C.N., 1998. Hoja Geológica 4572-IV Alto Río Senguerr.
Davis, D., Suppe, J., Dahlen, F.A., 1983. Mechanics of fold-and-thrust belts and accretionary wedges. Journal of Geophysical Research: Solid Earth 88, 1153–1172.
Davis, G.A., Cong, W., Yadong, Z., Jinjiang, Z., Changhou, Z., Gehrels, G.E., 1998. The enigmatic Yinshan fold-and-thrust belt of northern China: New views on its intraplate contractional styles. Geology 26, 43–46.
De Giusto, J.M., Di Persia, C.A., Pezzi, E., 1980. Nesocratón del Deseado. Geología Regional Argentina 2, 1389–1430.
De Ignacio, C., López, I., Oyarzun, R., Márquez, A., 2001. The northern Patagonia Somuncura plateau basalts: a product of slab-induced, shallow asthenospheric upwelling? Terra Nova 13, 117–121.

De Iuliis, G., Kay, R., F Vizcaíno, S., 2008. Fossil mammals of the late Miocene (11.6-5.3 million years ago) Santa Cruz Formation (SCF), Santa Cruz (Patagonia), Argentina.
DeCelles, P.G., Giles, K.A., 1996. Foreland basin systems. Basin research 8, 105–123.
DeCelles, P.G., Horton, B.K., 2003. Early to middle Tertiary foreland basin development and the history of Andean crustal shortening in Bolivia. Geological Society of America Bulletin 115, 58–77.
DeMets, C., Gordon, R.G., Argus, D.F., Stein, S., 1990. Current plate motions. Geophysical journal international 101, 425–478.
Derycke, A., Gautheron, C., Genge, M.C., Zattin, M., Mazzoli, S., Witt, C., Marquez, M., 2019. Southern Patagonian foreland (~ 44 - 48° S) evolution: insight from low-temperature thermochronological approach, in: 8th International Symposium on Andean Geodynamics (ISAG). Quito.
Di Persia, C.A., 1965. Presencia de sedimentos triásicos en el ambiente del Deseado. Actas de la 2 das. J. Geol. Argentinas 3, 147–155.
Di Persia, C.A., 1962. Acerca del descubrimiento del Precámbrico en la Patagonia Extraandina (provincia de Santa Cruz). 1eras. Jornadas Geológicas Argentinas, San Juan. Buenos Aires 2, 65–68.
Dietrich, W.E., Bellugi, D.G., Sklar, L.S., Stock, J.D., Heimsath, A.M., Roering, J.J., 2003. Geomorphic transport laws for predicting landscape form and dynamics. Geophysical Monograph-American Geophysical Union 135, 103–132.
Dodson, M.H., 1973. Closure temperature in cooling geochronological and petrological systems. Contributions to Mineralogy and Petrology 40, 259–274.
Donelick, R.A., Ketcham, R.A., Carlson, W.D., 1999. Variability of apatite fission-track annealing kinetics: II. Crystallographic orientation effects. American Mineralogist 84, 1224–1234.
Donelick, R.A., O'Sullivan, P.B., Ketcham, R.A., 2005. Apatite fission-track analysis. Reviews in Mineralogy and Geochemistry 58, 49–94.
Duhart, P., Haller, M., Hervé, F., 2002. Diamictitas como parte del protolito de las metamorfitas de la Formación Cushamen en Río Chico, provincias de Río Negro y Chubut, Argentina, in: Congreso Geológico Argentino. pp. 97–100.
Dumitru, T.A., 1989. Constraints on uplift in the Franciscan subduction complex from apatite fission track analysis. Tectonics 8, 197–220.
Dunkl, I., 2002. TRACKKEY: a Windows program for calculation and graphical presentation of fission track data. Computers & Geosciences 28, 3–12.
Eagles, G., 2007. New angles on South Atlantic opening. Geophysical Journal International 168, 353–361.
Echaurren, A., Folguera, A., Gianni, G., Orts, D., Tassara, A., Encinas, A., Giménez, M., Valencia, V., 2016. Tectonic evolution of the North Patagonian Andes (41–44 S) through recognition of syntectonic strata. Tectonophysics 677, 99–114.
Echaurren, A., Henkel, M., Rusconi, F., Tobal, J., Sagripanti, L., Ramos, M., Orts, D., Folguera, A., 2014. Geología y fases de deformación en la Cordillera Patagónica, norte de Chubut (Parque Nacional Los Alerces), in: XIX Congreso Geológico Argentino, Actas Electrónicas, Córdoba.
Echaurren, A., Lucía, F.P., Navarrete, C., Verónica, O., Encinas, A., Mario, G., Lince-Klinger, F., Andrés, F., 2019. Tectonic controls on the building of the North Patagonian fold-thrust belt (~ 43° S), in: Andean Tectonics. Elsevier, pp. 609–650.
Echaurren, A., Oliveros, V., Folguera, A., Ibarra, F., Creixell, C., Lucassen, F., 2017. Early Andean tectonomagmatic stages in north Patagonia: insights from field and geochemical data. Journal of the Geological Society 174, 405–421.
Echeveste, H., Fernández, R.R., Bellieni, G., Tessone, M.O.R., Llambías, E.J., Schalamuk, I.B.A., Piccirillo, E.M., De Min, A., 2001. Relaciones entre las Formaciones Bajo Pobre y Chon Aike [Jurásico Medio a Superior] en el área Estancia El Fénix-Cerro Huemul, zona centro-occidental del Macizo del Deseado, provincia de Santa Cruz. Revista de la Asociación Geológica Argentina 56.
Ehlers, T.A., Armstrong, P.A., Chapman, D.S., 2001. Normal fault thermal regimes and the interpretation of low-temperature thermochronometers. Physics of the Earth and Planetary Interiors 126, 179–194.
Ehlers, T.A., Chaudhri, T., Kumar, S., Fuller, C.W., Willett, S.D., Ketcham, R.A., Brandon, M.T., Belton, D.X., Kohn, B.P., Gleadow, A.J., 2005. Computational tools for low-temperature thermochronometer interpretation. Reviews in Mineralogy and Geochemistry 58, 589–622.

Ehlers, T.A., Szameitat, A., Enkelmann, E., Yanites, B.J., Woodsworth, G.J., 2015. Identifying spatial variations in glacial catchment erosion with detrital thermochronology. Journal of Geophysical Research: Earth Surface 120, 1023–1039.

Encinas, A., Folguera, A., Bechis, F., Finger, K.L., Zambrano, P., Pérez, F., Bernabé, P., Tapia, F., Riffo, R., Buatois, L., 2018. The late Oligocene–early Miocene marine transgression of Patagonia, in: The Evolution of the Chilean-Argentinean Andes. Springer, pp. 443–474.

Encinas, A., Folguera, A., Oliveros, V., Del Mauro, L.D.G., Tapia, F., Riffo, R., Hervé, F., Finger, K.L., Valencia, V.A., Gianni, G., 2016. Late Oligocene–early Miocene submarine volcanism and deep-marine sedimentation in an extensional basin of southern Chile: Implications for the tectonic development of the North Patagonian Andes. GSA Bulletin 128, 807–823.

England, P., Molnar, P., 1990. Surface uplift, uplift of rocks, and exhumation of rocks. Geology 18, 1173–1177.

Escosteguy, L.D., Dal Molin, C.N., Franchi, M., Geuna, S.E., Lapido, O.R., 2003. Hoja Geológica 4772-II Lago Buenos Aires. Servicio Geológico Minero Argentino. Instituto de Geología y Recursos Minerales.

Escosteguy, L.D., Geuna, S.E., Franchi, M., González Díaz, E.F., Dal Molin, C.N., Etcheverría, M.P., Cegarra, M.I., Wilson, C., González, R., 2013. Hoja Geológica 4172-II San Martín de los Andes. Servicio Geológico Minero Argentino. Instituto de Geología y Recursos Minerales.

Espurt, N., Barbarand, J., Roddaz, M., Brusset, S., Baby, P., Saillard, M., Hermoza, W., 2011. A scenario for late Neogene Andean shortening transfer in the Camisea Subandean zone (Peru, 12 S): Implications for growth of the northern Andean Plateau. Bulletin 123, 2050–2068.

Espurt, N., Funiciello, F., Martinod, J., Guillaume, B., Regard, V., Faccenna, C., Brusset, S., 2008. Flat subduction dynamics and deformation of the South American plate: Insights from analog modeling. Tectonics 27.

Fan, M., Carrapa, B., 2014. Late Cretaceous–early Eocene Laramide uplift, exhumation, and basin subsidence in Wyoming: Crustal responses to flat slab subduction. Tectonics 33, 509–529.

Farley, K.A., 2000. Helium diffusion from apatite: General behavior as illustrated by Durango fluorapatite. Journal of Geophysical Research: Solid Earth 105, 2903–2914.

Farley, K.A., Stockli, D.F., 2002. (U-Th)/He dating of phosphates: Apatite, monazite, and xenotime. Reviews in mineralogy and geochemistry 48, 559–577.

Farley, K.A., Wolf, R.A., Silver, L.T., 1996. The effects of long alpha-stopping distances on (U Th)/He ages. Geochimica et cosmochimica acta 60, 4223–4229.

Fayon, A.K., Whitney, D.L., 2007. Interpretation of tectonic versus magmatic processes for resetting apatite fission track ages in the Niğde Massif, Turkey. Tectonophysics 434, 1–13.

Fernández, M.L., Mazzoli, S., Zattin, M., Savignano, E., Genge, M.C., Tavani, S., Garrone, A., Franchini, M., 2020. Structural controls on Jurassic gold mineralization, and Cretaceous-Tertiary exhumation in the foreland of the southern Patagonian Andes: New constraints from La Paloma area, Deseado Massif, Argentina. Tectonophysics 775, 228302.

Fernández Paz, L., Iannelli, S.B., Echaurren, A., Ramos, M., Bechis, F., Litvak, V.D., Encinas, A., Kasemann, S., Lucassen, F., Folguera, A., 2020. The late Eocene–early Miocene El Maitén Belt evolution: Magmatic response to the changing subduction zone geodynamics. Journal of South American Earth Sciences 102713.

Fernández Paz, L., Litvak, V.D., Echaurren, A., Iannelli, S.B., Encinas, A., Folguera, A., Valencia, V., 2018. Late Eocene volcanism in North Patagonia (42 30′–43 S): arc resumption after a stage of within-plate magmatism. Journal of Geodynamics 113, 13–31.

Feruglio, E., 1949. Descripción geológica de la Patagonia. Casa Editora" Coni".

Figari, C.E., Scasso, R.A., Cúneo, N.R., Escapa, I.H., 2015. Estratigrafía y evolución geológica de la Cuenca de Cañadón Asfalto, Provincia del Chubut, Argentina. Latin American Journal of Sedimentology and Basin Analysis 22, 135–169.

Figari, E., Strelkov, E., Cid de La Paz, M.S., Celaya, J., Laffitte, G., Villar, H., 2002. Cuenca del Golfo San Jorge: Síntesis estructural, estratigráfica y geoquímica, in: Geología y Recursos Naturales de Santa Cruz. Relatorio Del XV Congreso Geológico Argentino. El Calafate. pp. 571–601.

Figari, E.G., Strelkov, E., Laffitte, G., Cid de La Paz, M.S., Courtade, S.F., Celaya, J., Vottero, A., Lafourcade, P., Martinez, R., Villar, H.J., 1999. Los sistemas petroleros de la Cuenca del Golfo San Jorge: síntesis estructural, estratigráfica y geoquímica, in: 4 Congreso de Exploración y Desarrollo de Hidrocarburos. pp. 197–237.

Fillon, C., Gautheron, C., van der Beek, P., 2013. Oligocene–Miocene burial and exhumation of the Southern Pyrenean foreland quantified by low-temperature thermochronology. Journal of the Geological Society 170, 67–77.
Finzel, E.S., Trop, J.M., Ridgway, K.D., Enkelmann, E., 2011. Upper plate proxies for flat-slab subduction processes in southern Alaska. Earth and Planetary Science Letters 303, 348–360.
Fitzgerald, M.G., Mitchum Jr, R.M., Uliana, M.A., Biddle, K.T., 1990. Evolution of the san Jorge basin, Argentina. AAPG bulletin 74, 879–920.
Fitzgerald, P.G., Baldwin, S.L., Webb, L.E., O'Sullivan, P.B., 2006. Interpretation of (U–Th)/He single grain ages from slowly cooled crustal terranes: a case study from the Transantarctic Mountains of southern Victoria Land. Chemical Geology 225, 91–120.
Fitzgerald, P.G., Gleadow, A.J., 1990. New approaches in fission track geochronology as a tectonic tool: Examples from the Transantarctic Mountains. International Journal of Radiation Applications and Instrumentation. Part D. Nuclear Tracks and Radiation Measurements 17, 351–357.
Fleischer, R.L., Price, P.B., 1964. Decay constant for spontaneous fission of U 238. Physical Review 133, B63.
Flowers, R.M., Ketcham, R.A., Shuster, D.L., Farley, K.A., 2009. Apatite (U–Th)/He thermochronometry using a radiation damage accumulation and annealing model. Geochimica et Cosmochimica acta 73, 2347–2365.
Foix, N., Allard, J.O., Ferreira, M.L., Atencio, M., 2020. Spatio-temporal variations in the Mesozoic sedimentary record, Golfo San Jorge Basin (Patagonia, Argentina): Andean vs. cratonic sources. Journal of South American Earth Sciences 98, 102464.
Foix, N., Paredes, J.M., Giacosa, R.E., 2013. Fluvial architecture variations linked to changes in accommodation space: Río Chico Formation (late Paleocene), Golfo San Jorge basin, Argentina. Sedimentary Geology 294, 342–355.
Foix, N., Paredes, J.M., Giacosa, R.E., 2012. Upper Cretaceous-Paleocene extensional phase in the Golfo San Jorge basin (Argentina): Growth-fault model, paleoseismicity and paleostress analysis. Journal of South American Earth Sciences 33, 110–118.
Folguera, A., Bottesi, G., Duddy, I., Martín-González, F., Orts, D., Sagripanti, L., Vera, E.R., Ramos, V.A., 2015. Exhumation of the Neuquén Basin in the southern Central Andes (Malargüe fold and thrust belt) from field data and low-temperature thermochronology. Journal of South American Earth Sciences 64, 381–398.
Folguera, A., Iannizzotto, N.F., 2004. The lagos La Plata and Fontana fold-and-thrust belt: long-lived orogenesis at the edge of western Patagonia. Journal of South American Earth Sciences 16, 541–566.
Folguera, A., Ramos, V.A., 2011. Repeated eastward shifts of arc magmatism in the Southern Andes: a revision to the long-term pattern of Andean uplift and magmatism. Journal of South American Earth Sciences 32, 531–546.
Folguera, Alicia, Zárate, M., Tedesco, A., Dávila, F., Ramos, V.A., 2015. Evolution of the Neogene Andean foreland basins of the Southern Pampas and northern Patagonia (34°–41° S), Argentina. Journal of South American Earth Sciences 64, 452–466.
Fox, M., Leith, K., Bodin, T., Balco, G., Shuster, D.L., 2015. Rate of fluvial incision in the Central Alps constrained through joint inversion of detrital 10Be and thermochronometric data. Earth and Planetary Science Letters 411, 27–36.
Frassinetti, D., Covacevich, V., 1999. Invertebrados fósiles marinos de la Formación Guadal (Oligoceno superior-Mioceno inferior) en Pampa Castillo, región de Aisen, Chile. Servicio Nacional de Geología y Minería.
Gabaldón, V., 1982. Estratigrafía y sedimentología del Liásico del noroeste del Chubut, Argentina.
Gailleton, B., Mudd, S.M., Clubb, F.J., Peifer, D., Hurst, M.D., 2019. A segmentation approach for the reproducible extraction and quantification of knickpoints from river long profiles. Earth surface dynamics. 7, 211–230.
Galbraith, R.F., 1988. Graphical display of estimates having differing standard errors. Technometrics 30, 271–281.
Galbraith, R.F., 1981. On statistical models for fission track counts. Journal of the International Association for Mathematical Geology 13, 471–478.
Galbraith, R.F., Laslett, G.M., 1993. Statistical models for mixed fission track ages. Nuclear tracks and radiation measurements 21, 459–470.

Gallagher, K., 2012. Transdimensional inverse thermal history modeling for quantitative thermochronology. Journal of Geophysical Research: Solid Earth 117.
Gallagher, K., Charvin, K., Nielsen, S., Sambridge, M., Stephenson, J., 2009. Markov chain Monte Carlo (MCMC) sampling methods to determine optimal models, model resolution and model choice for Earth Science problems. Marine and Petroleum Geology 26, 525–535.
Gallagher, K., Parra, M., 2020. A new approach to thermal history modelling with detrital low temperature thermochronological data. Earth and Planetary Science Letters 529, 115872.
Gansser, A., 1973. Facts and theories on the Andes: twenty-sixth William Smith Lecture. Journal of the Geological Society 129, 93–131.
Garver, J.I., Brandon, M.T., Roden-Tice, M., Kamp, P.J., 1999. Exhumation history of orogenic highlands determined by detrital fission-track thermochronology. Geological Society, London, Special Publications 154, 283–304.
Garzanti, E., 2017. The Maturity Myth In Sedimentology and Provenance AnalysisE. GARZANTITHE MATURITY MYTH IN SEDIMENTARY PETROLOGY. Journal of Sedimentary Research 87, 353–365.
Gautheron, C., Barbarand, J., Ketcham, R.A., Tassan-Got, L., van der Beek, P., Pagel, M., Pinna-Jamme, R., Couffignal, F., Fialin, M., 2013a. Chemical influence on α-recoil damage annealing in apatite: Implications for (U–Th)/He dating. Chemical Geology 351, 257–267.
Gautheron, C., Espurt, N., Barbarand, J., Roddaz, M., Baby, P., Brusset, S., Tassan-Got, L., Douville, E., 2013b. Direct dating of thick-and thin-skin thrusts in the Peruvian Subandean zone through apatite (U–Th)/He and fission track thermochronometry. Basin Research 25, 419–435.
Gautheron, C., Tassan-Got, L., 2010. A Monte Carlo approach to diffusion applied to noble gas/helium thermochronology. Chemical Geology 273, 212–224.
Gautheron, C., Tassan-Got, L., Barbarand, J., Pagel, M., 2009. Effect of alpha-damage annealing on apatite (U–Th)/He thermochronology. Chemical Geology 266, 157–170.
Gautier, P., Bozkurt, E., Hallot, E., Dirik, K., 2002. Dating the exhumation of a metamorphic dome: geological evidence for pre-Eocene unroofing of the Nigde Massif (Central Anatolia, Turkey). Geological Magazine 139, 559–576.
Genge, M.C., 2021. Tectonic evolution of the north-central Patagonia: a thermochronological approach.
Genise, J.F., Melchor, R.N., Bellosi, E.S., González, M.G., Krause, M., 2007. New insect pupation chambers (Pupichnia) from the Upper Cretaceous of Patagonia, Argentina. Cretaceous Research 28, 545–559.
George, S.W., Davis, S.N., Fernández, R.A., Manríquez, L.M., Leppe, M.A., Horton, B.K., Clarke, J.A., 2020. Chronology of deposition and unconformity development across the Cretaceous–Paleogene boundary, Magallanes-Austral Basin, Patagonian Andes. Journal of South American Earth Sciences 97, 102237.
Georgieva, V., Gallagher, K., Sobczyk, A., Sobel, E.R., Schildgen, T.F., Ehlers, T.A., Strecker, M.R., 2019. Effects of slab-window, alkaline volcanism, and glaciation on thermochronometer cooling histories, Patagonian Andes. Earth and Planetary Science Letters 511, 164–176.
Georgieva, V., Melnick, D., Schildgen, T.F., Ehlers, T.A., Lagabrielle, Y., Enkelmann, E., Strecker, M.R., 2016. Tectonic control on rock uplift, exhumation, and topography above an oceanic ridge collision: Southern Patagonian Andes (47° S), Chile. Tectonics 35, 1317–1341.
Ghiglione, M.C., Ramos, V.A., 2005. Progression of deformation and sedimentation in the southernmost Andes. Tectonophysics 405, 25–46.
Ghiorzi, A., 1979. Informe final de pozo YPF. Ch. Ca. es-1. Section: Geología. Unpublished report of YPF.
Giacosa, R., Zubia, M., Sánchez, M., Allard, J., 2010a. Meso-Cenozoic tectonics of the southern Patagonian foreland: Structural evolution and implications for Au–Ag veins in the eastern Deseado Region (Santa Cruz, Argentina). Journal of South American Earth Sciences 30, 134–150.
Giacosa, R., Zubia, M., Sánchez, M., Allard, J., 2010b. Meso-Cenozoic tectonics of the southern Patagonian foreland: Structural evolution and implications for Au–Ag veins in the eastern Deseado Region (Santa Cruz, Argentina). Journal of South American Earth Sciences 30, 134–150.
Giacosa, R.E., Franchi, M., Genini, A., Panza, J.L.A., 2001a. Hojas Geológicas 4772-III Lago Belgrano y 4772-IV Lago Posadas. Servicio Geológico Minero Argentino. Instituto de Geología y Recursos Minerales.

Giacosa, R.E., Genini, A., 1998. Hoja Geológica 4766-III/IV Puerto Deseado.
Giacosa, R.E., Heredia Carballo, N., Zubía, M.A., González, R., Faroux, A.J., Césari, O., Franchi, M., 2001b. Hoja geológica 4172-IV San Carlos de Bariloche. Servicio Geológico Minero Argentino. Instituto de Geología y Recursos Minerales.
Giacosa, R.E., Heredia, N., 2004. Estructura de los Andes Nordpatagónicos en los cordones Piltriquitrón y Serrucho y en el valle de El Bolsón (41º 30-42 º 00 S), Río Negro. Revista de la Asociación Geológica Argentina 59, 91–102.
Giacosa, R.E., Márquez, M.M., Panza, J.L., 2002. Basamento paleozoico inferior del Macizo del Deseado, in: Geología y Recursos Naturales de Santa Cruz. Relatorio 15º Congreso Geológico Argentino. pp. 33–44.
Gianni, G., Navarrete, C., Orts, D., Tobal, J., Folguera, A., Giménez, M., 2014. Cuenca de Chubut: su relación con el antepaís fragmentado y el impactogeno andino, in: 19 Congreso Geológico Argentino, Córdoba, Argentina, Actas Electrónicas.
Gianni, G.M., Echaurren, A., Folguera, A., Likerman, J., Encinas, A., Garcia, H.P.A., Dal Molin, C., Valencia, V.A., 2017. Cenozoic intraplate tectonics in Central Patagonia: Record of main Andean phases in a weak upper plate. Tectonophysics 721, 151–166.
Gianni, G.M., Navarrete, C., Liendo, I., Díaz, M., Giménez, M.E., Encinas, A., Folguera, A., 2018. Cretaceous intraplate contraction in southern Patagonia: a far-field response to changing subduction dynamics? Tectonics 37, 2915–2937.
Gianni, G.M., Navarrete, C., Orts, D., Tobal, J., Folguera, A., Giménez, M., 2015a. Patagonian broken foreland and related synorogenic rifting: The origin of the Chubut Group Basin. Tectonophysics 649, 81–99.
Gianni, G.M., Navarrete, C.G., Folguera, A., 2015b. Synorogenic foreland rifts and transtensional basins: A review of Andean imprints on the evolution of the San Jorge Gulf, Salta Group and Taubaté Basins. Journal of South American Earth Sciences 64, 288–306.
Gillot, P.-Y., Hildenbrand, A., Lefèvre, J.-C., Albore-Livadie, C., 2008. The K/Ar dating method: principle, analytical techniques, and application to Holocene volcanic eruptions in southern Italy.
Gleadow, A., Kohn, B., Seiler, C., 2019. The Future of Fission-Track Thermochronology, in: Fission-Track Thermochronology and Its Application to Geology. Springer, pp. 77–92.
Gleadow, A.J., Duddy, I.R., Green, P.F., Hegarty, K.A., 1986. Fission track lengths in the apatite annealing zone and the interpretation of mixed ages. Earth and planetary science letters 78, 245–254.
Gleadow, A.J.W., 1981. Fission-track dating methods: what are the real alternatives? Nuclear Tracks 5, 3–14.
González, P., Coluccia, A., Franchi, M., Caba, R., Dalponte, M.R., 2000. Hoja Geológica 4169-III Ingeniero Jacobacci.
Gordon, A., Ort, M.H., 1993. Edad y correlación del plutonismo subcordillerano en las provincias de Río Negro y Chubut (41-42 30'LS), in: Congreso Geológico Argentino. pp. 120–127.
Gorring, M.L., Kay, S.M., 2001. Mantle processes and sources of Neogene slab window magmas from southern Patagonia, Argentina. Journal of petrology 42, 1067–1094.
Gray, M.B., Mitra, G., 1999. Ramifications of four-dimensional progressive deformation in contractional mountain belts. Journal of Structural Geology 21, 1151–1160.
Green, P.F., 1985. Comparison of zeta calibration baselines for fission-track dating of apatite, zircon and sphene. Chemical Geology: Isotope Geoscience section 58, 1–22.
Green, P.F., Duddy, I.R., Laslett, G.M., Hegarty, K.A., Gleadow, A.W., Lovering, J.F., 1989. Thermal annealing of fission tracks in apatite 4. Quantitative modelling techniques and extension to geological timescales. Chemical Geology: Isotope Geoscience Section 79, 155–182.
Gripp, A.E., Gordon, R.G., 1990. Current plate velocities relative to the hotspots incorporating the NUVEL-1 global plate motion model. Geophysical Research Letters 17, 1109–1112.
Guido, D.M., Escayola, M.P., de Barrio, R.E., Schalamuk, B.I., Franz, G., 2006. La Formación Bajo Pobre (Jurásico) en el este del Macizo del Deseado, Patagonia: vinculación con el Grupo Bahía Laura.
Guido, D.M., Escayola, M.P., Schalamuk, I.B., 2004. The basement of the Deseado Massif at Bahía Laura, Patagonia, Argentina: a proposal for its evolution. Journal of South American Earth Sciences 16, 567–577.
Guillaume, B., Gautheron, C., Simon-Labric, T., Martinod, J., Roddaz, M., Douville, E., 2013. Dynamic topography control on Patagonian relief evolution as inferred from low temperature thermochronology. Earth and Planetary Science Letters 364, 157–167.

Guillaume, B., Martinod, J., Husson, L., Roddaz, M., Riquelme, R., 2009. Neogene uplift of central eastern Patagonia: Dynamic response to active spreading ridge subduction? Tectonics 28.
Guimerá, J., Alvaro, M., 1990. Structure et évolution de la compression alpine dans la Chaîne Ibérique et la Chaîne côtière catalane (Espagne). Bulletin de la Société géologique de France 6, 339–348.
Guimerà Rosso, J.J., 2018. Structure of an intraplate fold-and-thrust belt: The Iberian Chain. A synthesis. Geologica acta 16, 0427–438.
Gutscher, M.-A., 2002. Andean subduction styles and their effect on thermal structure and interplate coupling. Journal of South American Earth Sciences 15, 3–10.
Gutscher, M.-A., Peacock, S.M., 2003. Thermal models of flat subduction and the rupture zone of great subduction earthquakes. Journal of Geophysical Research: Solid Earth 108, ESE–2.
Gutscher, M.-A., Spakman, W., Bijwaard, H., Engdahl, E.R., 2000. Geodynamics of flat subduction: Seismicity and tomographic constraints from the Andean margin. Tectonics 19, 814–833.
Haller, M.J.F., Lech, R.R., Martínez, O., Meister, C.M., Poma, S., Viera, R.L.M., 2010. Hoja Geológica 4372-III/IV Trevelin. Servicio Geológico Minero Argentino. Instituto de Geología y Recursos Minerales.
Hamza, V.M., Muñoz, M., 1996. Heat flow map of South America. Geothermics 25, 599–646.
Haq, B.U., Hardenbol, J.A.N., Vail, P.R., 1987. Chronology of fluctuating sea levels since the Triassic. Science 235, 1156–1167.
Hechem, J.J., Homovc, J.F., Figari, E.G., 1990. Estratigrafía del Chubutiano (Cretácico) en la Sierra de San Bernardo, cuenca del Golfo San Jorge, Argentina, in: 11 Congreso Geológico Argentino. p. 173e176.
Hechem, J.J., Strelkov, E., 2002. Secuencia sedimentaria mesozoica del Golfo San Jorge, in: Geología y Recursos Naturales de Santa Cruz. Relatorio Del XV Congreso Geológico Argentino. Asociación Geológica Argentina Buenos aires, pp. 129–147.
Heller, P.L., Paola, C., 1992. The large-scale dynamics of grain-size variation in alluvial basins, 2: Application to syntectonic conglomerate. Basin Research 4, 91–102.
Hervé, F., 1994. The southern Andes between 39 and 44 S latitude: The geological signature of a transpressive tectonic regime related to a magmatic arc, in: Tectonics of the Southern Central Andes. Springer, pp. 243–248.
Hervé, F., Demant, A., Ramos, V.A., Pankhurst, R.J., Suárez, M., 2000. The Southern Andes (2000) Tectonic Evolution of South America. Cordani, U. G, Milani, E. J, Filho, AT y Campos, D. A, eds, Rio de Janeiro 605–634.
Herve, F., Pankhurst, R.J., Fanning, C.M., Calderón, M., Yaxley, G.M., 2007. The South Patagonian batholith: 150 my of granite magmatism on a plate margin. Lithos 97, 373–394.
Heuret, A., Funiciello, F., Faccenna, C., Lallemand, S., 2007. Plate kinematics, slab shape and back-arc stress: A comparison between laboratory models and current subduction zones. Earth and Planetary Science Letters 256, 473–483.
Homovc, J.F., Conforto, G.A., Lafourcade, P.A., Chelotti, L.A., 1995. Fold belt in the San Jorge Basin, Argentina: an example of tectonic inversion. Geological Society, London, Special Publications 88, 235–248.
Homovc, J.F., Constantini, L., 2001. Hydrocarbon exploration potential within intraplate shear-related depocenters: Deseado and San Julian basins, southern Argentina. AAPG bulletin 85, 1795–1816.
Horton, B.K., 2018a. Tectonic regimes of the central and southern Andes: Responses to variations in plate coupling during subduction. Tectonics 37, 402–429.
Horton, B.K., 2018b. Sedimentary record of Andean mountain building. Earth-Science Reviews 178, 279–309.
Horton, B.K., Fuentes, F., 2016. Sedimentary record of plate coupling and decoupling during growth of the Andes. Geology 44, 647–650.
Horton, B.K., Fuentes, F., Boll, A., Starck, D., Ramirez, S.G., Stockli, D.F., 2016. Andean stratigraphic record of the transition from backarc extension to orogenic shortening: A case study from the northern Neuquén Basin, Argentina. Journal of South American Earth Sciences 71, 17–40.
Hsieh, P.-S., Chen, C.-H., Yang, H.-J., Lee, C.-Y., 2008. Petrogenesis of the Nanling Mountains granites from South China: constraints from systematic apatite geochemistry and whole-rock geochemical and Sr–Nd isotope compositions. Journal of Asian Earth Sciences 33, 428–451.
Hu, D., Tian, Y., Hu, J., Rao, S., Wang, Y., Zhang, C., Hu, S., 2020. Thermal imprints of late Permian Emeishan basalt effusion: Evidence from zircon fission-track thermochronology. Lithos 352, 105224.

Hurford, A.J., 2019. An historical perspective on fission-track thermochronology, in: Fission-Track Thermochronology and Its Application to Geology. Springer, pp. 3–23.
Hurford, A.J., 1990. Standardization of fission track dating calibration: Recommendation by the Fission Track Working Group of the IUGS Subcommission on Geochronology. Chemical Geology: Isotope Geoscience Section 80, 171–178.
Hurford, A.J., Green, P.F., 1983. The zeta age calibration of fission-track dating. Chemical Geology 41, 285–317.
Hurford, A.J., Green, P.F., 1982. A users' guide to fission track dating calibration. Earth and Planetary Science Letters 59, 343–354.
Hurtrez, J.-E., Sol, C., Lucazeau, F., 1999. Effect of drainage area on hypsometry from an analysis of small-scale drainage basins in the Siwalik Hills (Central Nepal). Earth Surface Processes and Landforms: The Journal of the British Geomorphological Research Group 24, 799–808.
Iannelli, S.B., Paz, L.F., Litvak, V.D., Jones, R.E., Ramos, M.E., Folguera, A., Ramos, V.A., 2018. Paleogene arc-related volcanism in the southern central Andes and north Patagonia (39–41 S), in: The Evolution of the Chilean-Argentinean Andes. Springer, pp. 343–359.
Iglesia Llanos, M.P., Lanza, R., Riccardi, A.C., Geuna, S., Laurenzi, M.A., Ruffini, R., 2003. Palaeomagnetic study of the El Quemado complex and Marifil formation, Patagonian Jurassic igneous province, Argentina. Geophysical Journal International 154, 599–617.
Jordan, T.E., Isacks, B., Ramos, V.A., Allmendinger, R.W., 1983. Mountain building in the Central Andes. Episodes 3, 20–26.
Jordán, T.E., Isacks, B.L., Allmendinger, R.W., Brewer, J.A., Ramos, V.A., Ando, C.J., 1983. Andean tectonics related to geometry of subducted Nazca plate. Geological Society of America Bulletin 94, 341–361.
Jovic, S.M., Liñan, P., Guido, D.M., Paéz, G.N., Ruiz, R., Schalamuk, I.B., 2009. Metals distribution and correlations in polymetallic veins from Pingüino Indium-bearing deposit, Deseado Massif, Patagonia, Argentina, in: 24th International Applied Geochemistry Symposium, Fredericton, New Brunswick, Canadá. pp. 501–504.
Kay, S.M., Ardolino, A.A., Gorring, M.L., Ramos, V.A., 2007. The Somuncura Large Igneous Province in Patagonia: interaction of a transient mantle thermal anomaly with a subducting slab. Journal of Petrology 48, 43–77.
Ketcham, R.A., 2005. Forward and inverse modeling of low-temperature thermochronometry data. Reviews in mineralogy and geochemistry 58, 275–314.
Ketcham, R.A., Carter, A., Donelick, R.A., Barbarand, J., Hurford, A.J., 2007. Improved modeling of fission-track annealing in apatite. American Mineralogist 92, 799–810.
Ketcham, R.A., Donelick, R.A., Balestrieri, M.L., Zattin, M., 2009. Reproducibility of apatite fission-track length data and thermal history reconstruction. Earth and Planetary Science Letters 284, 504–515.
Ketcham, R.A., Donelick, R.A., Carlson, W.D., 1999. Variability of apatite fission-track annealing kinetics: III. Extrapolation to geological time scales. American Mineralogist 84, 1235–1255.
Ketcham, R.A., Gautheron, C., Tassan-Got, L., 2011. Accounting for long alpha-particle stopping distances in (U–Th–Sm)/He geochronology: Refinement of the baseline case. Geochimica et Cosmochimica Acta 75, 7779–7791.
Kirby, E., Whipple, K., 2001. Quantifying differential rock-uplift rates via stream profile analysis. Geology 29, 415–418.
Kirby, E., Whipple, K.X., 2012. Expression of active tectonics in erosional landscapes. Journal of Structural Geology 44, 54–75.
Kohn, B., Chung, L., Gleadow, A., 2019. Fission-track analysis: field collection, sample preparation and data acquisition, in: Fission-Track Thermochronology and Its Application to Geology. Springer, pp. 25–48.
Kraml, M., Pik, R., Rahn, M., Selbekk, R., Carignan, J., Keller, J., 2006. A new multi-mineral age reference material for 40Ar/39Ar,(U-Th)/He and fission track dating methods: The Limberg t3 tuff. Geostandards and Geoanalytical Research 30, 73–86.
Kronenberg, A., Brandon, M.T., Fletcher, R., Karlstrom, K., Rushmer, T., Simpson, C., Yin, A., 2002. Beyond Plate Tectonics: Rheology and Orogenesis of the Continents, in: New Departures in Structural Geology and Tectonics—A White Paper Resulting from a Workshop Held at Denver Colorado.

Lagabrielle, Y., Suárez, M., Malavieille, J., Morata, D., Espinoza, F., Maury, R.C., Scalabrino, B., Barbero, L., Cruz, R. de la, Rossello, E., 2007. Pliocene extensional tectonics in the Eastern Central Patagonian Cordillera: geochronological constraints and new field evidence. Terra Nova 19, 413–424.

Lagabrielle, Y., Suárez, M., Rossello, E.A., Hérail, G., Martinod, J., Régnier, M., de la Cruz, R., 2004. Neogene to Quaternary tectonic evolution of the Patagonian Andes at the latitude of the Chile Triple Junction. Tectonophysics 385, 211–241.

Lallemand, S., Heuret, A., Boutelier, D., 2005. On the relationships between slab dip, back-arc stress, upper plate absolute motion, and crustal nature in subduction zones. Geochemistry, Geophysics, Geosystems 6.

Lanari, R., Fellin, M. v, Faccenna, C., Balestrieri, M.L., Pazzaglia, F.J., Youbi, N., Maden, C., 2020. Exhumation and Surface Evolution of the Western High Atlas and Surrounding Regions as Constrained by Low-Temperature Thermochronology. Tectonics 39, e2019TC005562.

Lange, D., Cembrano, J., Rietbrock, A., Haberland, C., Dahm, T., Bataille, K., 2008. First seismic record for intra-arc strike-slip tectonics along the Liquiñe-Ofqui fault zone at the obliquely convergent plate margin of the southern Andes. Tectonophysics 455, 14–24.

Legarreta, L., Uliana, M.A., 1994. Asociaciones de fósiles y hiatos en el Supracretácico-Neógeno de Patagonia: una perspectiva estratigráfico-secuencial. Ameghiniana 31, 257–281.

Leonard, J.S., Fosdick, J.C., VanderLeest, R.A., 2020. Erosional and Tectonic Evolution of a Retroarc Orogenic Wedge as Revealed by Sedimentary Provenance: Case of the Oligocene–Miocene Patagonian Andes. Frontiers in Earth Science 7, 353.

Lesta, P., Ferello, R., 1972. Región extraandina de Chubut y norte de Santa Cruz. Geología Regional Argentina 2, 602–687.

Lesta, P., Ferello, R., Chebli, G., 1980. Chubut extraandino, in: Simposio Geología Regional Argentina. Academia Nacional de Ciencias de Córdoba. pp. 1307–1387.

Lesta, P.J., 1968. Estratigrafía de la cuenca del Golfo San Jorge. Jornadas Geológicas Argentinas, 3 Actas 1, 251–289.

Lin, W., Faure, M., Chen, Y., Ji, W., Wang, F., Wu, L., Charles, N., Wang, J., Wang, Q., 2013. Late Mesozoic compressional to extensional tectonics in the Yiwulüshan massif, NE China and its bearing on the evolution of the Yinshan–Yanshan orogenic belt: Part I: Structural analyses and geochronological constraints. Gondwana Research 23, 54–77.

Linares, E., González, R.R., Argentina, A.G., 1989. Catálogo de edades radimétricas de la República Argentina, años 1957-1987. Asociación Geológica Argentina.

Lisker, F., Ventura, B., Glasmacher, U.A., 2009. Apatite thermochronology in modern geology. Geological Society, London, Special Publications 324, 1–23.

Lizuain, A., 1980. Las formaciones suprapaleozoicas y jurásicas de la Cordillera Patagónica, provincias de Río Negro y Chubut. Revista de la Asociación Geológica Argentina 35, 174–182.

Lizuaín, A., Nieto, D.S., 2011. Hoja 4369-I, Gastre. Escala.

Lizuain, A., Ragona, D., Folguera, A., 1995. Mapa Geológico de la Provincia del Chubut, República Argentina. Secretaría de Minería, Dirección Nacional del Servicio Geológico, Escala 1.

Lizuaín, A., Viera, R.L.M., Franchi, M., 2010. Hoja Geológica 4372-I y II Esquel. Servicio Geológico Minero Argentino. Instituto de Geología y Recursos Minerales.

Lizuain Fuentes, A., 1983. Geología de la cordillera patagónica entre las localidades de Lago Puelo y Leleque, Provincia del Chubut (PhD Thesis). Universidad de Buenos Aires. Facultad de Ciencias Exactas y Naturales.

Lonsdale, P., 2005. Creation of the Cocos and Nazca plates by fission of the Farallon plate. Tectonophysics 404, 237–264.

Louterbach, M., Roddaz, M., Antoine, P.-O., Marivaux, L., Adnet, S., Bailleul, J., Dantas, E., Santos, R.V., Chemale Jr, F., Baby, P., 2018. Provenance record of late Maastrichtian–late Palaeocene Andean Mountain building in the Amazonian retroarc foreland basin (Madre de Dios basin, Peru). Terra Nova 30, 17–23.

Maksymowicz, A., Tassara, A., 2018. The Geometry of the Continental Wedge and Its Relation to the Rheology and Seismicity of the Chilean Interplate Boundary, in: The Evolution of the Chilean-Argentinean Andes. Springer, pp. 31–58.

Maloney, K.T., Clarke, G.L., Klepeis, K.A., Quevedo, L., 2013. The Late Jurassic to present evolution of the Andean margin: Drivers and the geological record. Tectonics 32, 1049–1065.

Malumian, N., Nanez, C., 2011. The Late Cretaceous–Cenozoic transgressions in Patagonia and the Fuegian Andes: foraminifera, palaeoecology, and palaeogeography. Biological Journal of the Linnean Society 103, 269–288.
Malusà, M.G., Fitzgerald, P.G., 2019. From cooling to exhumation: setting the reference frame for the interpretation of thermochronologic data, in: Fission-Track Thermochronology and Its Application to Geology. Springer, pp. 147–164.
Malusà, M.G., Polino, R., Zattin, M., Bigazzi, G., Martin, S., Piana, F., 2005. Miocene to Present differential exhumation in the Western Alps: Insights from fission track thermochronology. Tectonics 24.
Margirier, A., Braun, J., Gautheron, C., Carcaillet, J., Schwartz, S., Jamme, R.P., Stanley, J., 2019. Climate control on Early Cenozoic denudation of the Namibian margin as deduced from new thermochronological constraints. Earth and Planetary Science Letters 527, 115779.
Margirier, A., Robert, X., Audin, L., Gautheron, C., Bernet, M., Hall, S., Simon-Labric, T., 2015. Slab flattening, magmatism, and surface uplift in the Cordillera Occidental (northern Peru). Geology 43, 1031–1034.
Mark, C., Cogné, N., Chew, D., 2016. Tracking exhumation and drainage divide migration of the Western Alps: A test of the apatite U-Pb thermochronometer as a detrital provenance tool. Bulletin 128, 1439–1460.
Martínez, O.A., Kutschker, A., 2011. The 'Rodados Patagónicos'(Patagonian shingle formation) of eastern Patagonia: environmental conditions of gravel sedimentation. Biological Journal of the Linnean Society 103, 336–345.
Martinod, J., Husson, L., Roperch, P., Guillaume, B., Espurt, N., 2010. Horizontal subduction zones, convergence velocity and the building of the Andes. Earth and Planetary Science Letters 299, 299–309.
Matos, A., Dilts, T.E., 2019. Hypsometric Integral Toolbox for ArcGIS®. University of Nevada Reno.
May, C.L., Lisle, T.E., 2012. River profile controls on channel morphology, debris flow disturbance, and the spatial extent of salmonids in steep mountain streams. Journal of Geophysical Research: Earth Surface 117.
Maydagán, L., Zattin, M., Mpodozis, C., Selby, D., Franchini, M., Dimieri, L., 2020. Apatite (U–Th)/He thermochronology and Re–Os ages in the Altar region, Central Andes (31° 30′ S), Main Cordillera of San Juan, Argentina: implications of rapid exhumation in the porphyry Cu (Au) metal endowment and regional tectonics. Mineralium Deposita 1–20.
Mazzoni, M.M., Kawashita, K., Harrison, S., Aragón, E., 1991. Edades radimétricas eocenas en el borde occidental del Macizo Norpatagónico. Revista de la Asociación Geológica Argentina 46, 150–158.
McDowell, F.W., McIntosh, W.C., Farley, K.A., 2005. A precise 40Ar–39Ar reference age for the Durango apatite (U–Th)/He and fission-track dating standard. Chemical Geology 214, 249–263.
McGeary, S., Nur, A., Ben-Avraham, Z., 1985. Spatial gaps in arc volcanism: The effect of collision or subduction of oceanic plateaus. Tectonophysics 119, 195–221.
Mescua, J.F., Giambiagi, L.B., Ramos, V.A., 2013. Late Cretaceous uplift in the Malargüe fold-and-thrust belt (35° S), southern Central Andes of Argentina and Chile. Andean Geology 40, 102–116.
Meybeck, M., 1987. Global chemical weathering of surficial rocks estimated from river dissolved loads. American journal of science 287, 401–428.
Miller, M., Marino, J., 2019. New insights from the Neocomian basins in the West of Chubut and Santa Cruz provinces, Argentina. Journal of South American Earth Sciences 96, 102255.
Morton, A., Yaxley, G., 2007. Detrital apatite geochemistry and its application in provenance studies. Special Papers-Geological Society of America 420, 319.
Morton, A.C., Hallsworth, C., 2007. Stability of detrital heavy minerals during burial diagenesis. Developments in Sedimentology 58, 215–245.
Morton, A.C., Hallsworth, C.R., 1999. Processes controlling the composition of heavy mineral assemblages in sandstones. Sedimentary geology 124, 3–29.
Morton, A.C., Smale, D., 1990. The effects of transport and weathering on heavy minerals from the Cascade River, New Zealand. Sedimentary Geology 68, 117–123.
Mpodozis, C., Ramos, V., 1990. The Andes of Chile and Argentina.
Mpodozis, C., Ramos, V.A., 2008. Tectónica jurásica en Argentina y Chile: extensión, subducción oblicua, rifting, deriva y colisiones? Revista de la Asociación geológica Argentina 63, 481–497.

Müller, R.D., Seton, M., Zahirovic, S., Williams, S.E., Matthews, K.J., Wright, N.M., Shephard, G.E., Maloney, K.T., Barnett-Moore, N., Hosseinpour, M., 2016. Ocean basin evolution and global-scale plate reorganization events since Pangea breakup. Annual Review of Earth and Planetary Sciences 44, 107–138.

Muñoz, M., 1999. Tectonophysics of the Andes region: relationships with heat flow and the thermal structure, in: International Symposium on Andean Geodynamics. pp. 532–534.

Murray, K.E., Orme, D.A., Reiners, P.W., 2014. Effects of U–Th-rich grain boundary phases on apatite helium ages. Chemical Geology 390, 135–151.

Nagasawa, H., 1970. Rare earth concentrations in zircons and apatites and their host dacites and granites. Earth and Planetary Science Letters 9, 359–364.

Navarrete, César, Gianni, G., Christiansen, R., Kamerbeek, Y., Periale, S., Folguera, A., 2019. Jurassic intraplate contraction of southern Patagonia: the El Tranquilo anticline area, Deseado Massif. Journal of South American Earth Sciences 94, 102224.

Navarrete, C., Gianni, G., Echaurren, A., Kingler, F.L., Folguera, A., 2016. Episodic Jurassic to lower Cretaceous intraplate compression in Central Patagonia during Gondwana breakup. Journal of Geodynamics 102, 185–201.

Navarrete, C., Gianni, G., Encinas, A., Márquez, M., Kamerbeek, Y., Valle, M., Folguera, A., 2019. Triassic to Middle Jurassic geodynamic evolution of southwestern Gondwana: From a large flat-slab to mantle plume suction in a rollback subduction setting. Earth-science reviews 194, 125–159.

Navarrete, C.R., Gianni, G.M., Echaurren, A., Folguera, A., 2018. Lower jurassic to early paleogene intraplate contraction in central Patagonia, in: The Evolution of the Chilean-Argentinean Andes. Springer, pp. 245–271.

Navarrete, C.R., Gianni, G.M., Folguera, A., 2015. Tectonic inversion events in the western San Jorge Gulf Basin from seismic, borehole and field data. Journal of South American Earth Sciences 64, 486–497.

Nie, J., Horton, B.K., Saylor, J.E., Mora, A., Mange, M., Garzione, C.N., Basu, A., Moreno, C.J., Caballero, V., Parra, M., 2012. Integrated provenance analysis of a convergent retroarc foreland system: U–Pb ages, heavy minerals, Nd isotopes, and sandstone compositions of the Middle Magdalena Valley basin, northern Andes, Colombia. Earth-Science Reviews 110, 111–126.

Nürnberg, D., Müller, R.D., 1991. The tectonic evolution of the South Atlantic from Late Jurassic to present. Tectonophysics 191, 27–53.

Olazábal, S.X., Tunik, M.A., Paredes, J.M., 2020. Sandstone petrography and provenance of the Chubut Group (Cretaceous) in the Cañadón Matasiete (Golfo San Jorge Basin, central Patagonia): Implications for basin evolution and alluvial organization. Journal of South American Earth Sciences 98, 102463.

Olivero, E.B., 1982. Estratigrafía de la cuenca sur del< Lago Fontana> (PhD Thesis). Universidad de Buenos Aires. Facultad de Ciencias Exactas y Naturales.

Olivero, E.B., Aguirre-Urreta, M.B., 2002. Sucesión de amonoideos de la Formación Katterfeld (Valanginiano–Hauteriviano) en su área tipo, Lago Fontana, Chubut, in: Congreso Geológico Argentino No. 15, Actas I. pp. 485–90.

Oliveros, V., Vásquez, P., Creixell, C., Lucassen, F., Ducea, M.N., Ciocca, I., González, J., Espinoza, M., Salazar, E., Coloma, F., 2020. Lithospheric evolution of the Pre-and Early Andean convergent margin, Chile. Gondwana Research 80, 202–227.

Oncken, O., Chong, G., Franz, G., Giese, P., Götze, H.-J., Ramos, V.A., Strecker, M.R., Wigger, P., 2006. The Andes: active subduction orogeny. Springer Science & Business Media.

Orts, D.L., Folguera, A., Encinas, A., Ramos, M., Tobal, J., Ramos, V.A., 2012. Tectonic development of the North Patagonian Andes and their related Miocene foreland basin (41° 30′-43° S). Tectonics 31.

Orts, D.L., Folguera, A., Giménez, M., Ruiz, F., Vera, E.A.R., Klinger, F.L., 2015. Cenozoic building and deformational processes in the North Patagonian Andes. Journal of Geodynamics 86, 26–41.

O'Sullivan, G.J., Chew, D.M., Morton, A.C., Mark, C., Henrichs, I.A., 2018. An integrated apatite geochronology and geochemistry tool for sedimentary provenance analysis. Geochemistry, Geophysics, Geosystems 19, 1309–1326.

O'Sullivan, G.J., Chew, D.M., Samson, S.D., 2016. Detecting magma-poor orogens in the detrital record. Geology 44, 871–874.

Özkaymak, Ç., Sözbilir, H., 2012. Tectonic geomorphology of the Spildağı high ranges, western Anatolia. Geomorphology 173, 128–140.
Page, S., Page, R., 1999. Las diabasas y gabros del Jurasico de la Precordillera del Chubut. Geologíca Argentina. Servicio Geológico Minero Argentino, Instituto de Geología y Recursos Minerales, Anales 29, 489–495.
Pankhurst, R.J., Hervé, F., Fanning, M., Suárez, M., 2003. Coeval plutonic and volcanic activity in the Patagonian Andes: the Patagonian Batholith and the Ibáñez and Divisadero formations, Aysén, southern Chile, in: Congreso Geológico Chileno.
Pankhurst, R.J., Leat, P.T., Sruoga, P., Rapela, C.W., Márquez, M., Storey, B.C., Riley, T.R., 1998. The Chon Aike province of Patagonia and related rocks in West Antarctica: a silicic large igneous province. Journal of volcanology and geothermal research 81, 113–136.
Pankhurst, R.J., Rapela, C.W., Fanning, C.M., Márquez, M., 2006. Gondwanide continental collision and the origin of Patagonia. Earth-Science Reviews 76, 235–257.
Pankhurst, R.J., Riley, T.R., Fanning, C.M., Kelley, S.P., 2000. Episodic silicic volcanism in Patagonia and the Antarctic Peninsula: chronology of magmatism associated with the break-up of Gondwana. Journal of Petrology 41, 605–625.
Pankhurst, R.J., Weaver, S.D., Hervé, F., Larrondo, P., 1999. Mesozoic-Cenozoic evolution of the North Patagonian batholith in Aysen, southern Chile. Journal of the Geological Society 156, 673–694.
Panza, J.L.A., Cobos, J.C., Zubía, M.A., Franchi, M., 2001a. Hoja Geológica 4769-III Destacamento La María. Servicio Geológico Minero Argentino. Instituto de Geología y Recursos Minerales.
Panza, J.L.A., Genini, A., Franchi, M., 2001b. Hoja Geológica 4769-IV Monumento Natural Bosques Petrificados. Servicio Geológico Minero Argentino. Instituto de Geología y Recursos Minerales.
Panza, J.L.A., Marín, G., Zubía, M.A., 1998. Hoja Geológica 4969-I Gobernador Gregores.
Panza, J.L.A., Márquez, M.J., 1994. Hoja Geológica 4966-I/II Bahía Laura.
Panza, J.L.A., Sacomani, L.E., Cobos, J.C., Asato, C.G., Candaosa, N.G., Chavez, S.B., Gambadé Álvarez, M.L., Olmos, M.I., Tavitian Serrano, A.F., 2003. Mapa geológico de la provincia de Santa Cruz.
Panza, J.L.A., Sacomani, L.E., Giacosa, R.E., Franchi, M., 2018. Hoja Geológica 4972-II Lago Cardiel.
Panza, J.L.A., Zubía, M.A., Godeas, M.C., 1994. Hoja Geológica 4969-II Tres Cerros.
Pardo-Casas, F., Molnar, P., 1987. Relative motion of the Nazca (Farallon) and South American plates since Late Cretaceous time. Tectonics 6, 233–248.
Paredes, J.M., Aguiar, M., Ansa, A., Giordano, S., Ledesma, M., Tejada, S., 2018. Inherited discontinuities and fault kinematics of a multiphase, non-colinear extensional setting: Subsurface observations from the South Flank of the Golfo San Jorge basin, Patagonia. Journal of South American Earth Sciences 81, 87–107.
Paredes, J.M., Foix, N., Piñol, F.C., Nillni, A., Allard, J.O., Marquillas, R.A., 2007. Volcanic and climatic controls on fluvial style in a high-energy system: the Lower Cretaceous Matasiete Formation, Golfo San Jorge basin, Argentina. Sedimentary Geology 202, 96–123.
Paredes, J. M., Giacosa, R.E., Heredia, N., 2009. Sedimentary evolution of Neogene continental deposits (Ñirihuau Formation) along the Ñirihuau River, North Patagonian Andes of Argentina. Journal of South American Earth Sciences 28, 74–88.
Paredes, José M., Ibañez, L.M., Moyan, M.S., Aceñolaza, G.F., 2009. Sedimentary evolution of the Golfo San Jorge basin, central Patagonia, Argentina, in: Argentinean Fluvial Basins: Ancient and Present Day Examples: Tucumán, Argentina, Excursion Guide Book, 9 International Conference on Fluvial Sedimentology. pp. 187–275.
Paredes, J.M., Plazibat, S., Crovetto, C., Stein, J., Cayo, E., Schiuma, A., 2013. Fault kinematics and depocenter evolution of oil-bearing, continental successions of the Mina del Carmen Formation (Albian) in the Golfo San Jorge basin, Argentina. Journal of South American Earth Sciences 46, 63–79.
Parra, M., Mora, A., Lopez, C., Ernesto Rojas, L., Horton, B.K., 2012. Detecting earliest shortening and deformation advance in thrust belt hinterlands: Example from the Colombian Andes. Geology 40, 175–178.
Parras, A., Dix, G.R., Griffin, M., 2012. Sr-isotope chronostratigraphy of Paleogene–Neogene marine deposits: Austral Basin, southern Patagonia (Argentina). Journal of South American Earth Sciences 37, 122–135.

Pérez-Peña, Azañón, J.M., Booth-Rea, G., Azor, A., Delgado, J., 2009. Differentiating geology and tectonics using a spatial autocorrelation technique for the hypsometric integral. Journal of Geophysical Research: Earth Surface 114.
Pérez-Peña, J.V., Azañón, J.M., Azor, A., 2009. CalHypso: An ArcGIS extension to calculate hypsometric curves and their statistical moments. Applications to drainage basin analysis in SE Spain. Computers & Geosciences 35, 1214–1223.
Peroni, G.O., Hegedus, A.G., Cerdan, J., Legarreta, L., Uliana, M.A., Laffitte, G., 1995. Hydrocarbon accumulation in an inverted segment of the Andean Foreland: San Bernardo belt, Central Patagonia.
Petrus, J.A., Kamber, B.S., 2012. VizualAge: A novel approach to laser ablation ICP-MS U-Pb geochronology data reduction. Geostandards and Geoanalytical Research 36, 247–270.
Pezzuchi, H.D., 2018. Hoja Geológica 4569-III Sarmiento.
Piccoli, P.M., Candela, P.A., 2002. Apatite in igneous systems. Reviews in Mineralogy and Geochemistry 48, 255–292.
Pilger, J.R., Rex, H., 1981. Plate reconstructions, aseismic ridges, and low-angle subduction beneath the Andes. Geological Society of America Bulletin 92, 448–456.
Plazibat, S., Rasgido, A., Paredes, J.M., 2019. Subsurface characterization of Cenozoic igneous activity at Cerro Dragón area (Golfo San Jorge Basin, central Patagonia): Implications for basin evolution and hydrocarbon prospectivity. Journal of South American Earth Sciences 96, 102389.
Portner, D.E., Beck, S., Zandt, G., Scire, A., 2017. The nature of subslab slow velocity anomalies beneath South America. Geophysical Research Letters 44, 4747–4755.
Price, P.B., Walker, R.M., 1963. Fossil tracks of charged particles in mica and the age of minerals. Journal of Geophysical Research 68, 4847–4862.
Proserpio, C.A., 1978. DESCRIPCION GEOLOGICA DE LA HOJA 42 D, GASTRE, PROVINCIA DEL CHUBUT.
Rahl, J.M., Ehlers, T.A., van der Pluijm, B.A., 2007. Quantifying transient erosion of orogens with detrital thermochronology from syntectonic basin deposits. Earth and Planetary Science Letters 256, 147–161.
Ramírez de Arellano, C., Putlitz, B., Müntener, O., Ovtcharova, M., 2012. High precision U/Pb zircon dating of the Chaltén Plutonic Complex (Cerro Fitz Roy, Patagonia) and its relationship to arc migration in the southernmost Andes. Tectonics 31.
Ramos, M.E., Orts, D.L., Calatayud, F., Pazos, P.J., Folguera Telichevsky, A., Ramos, V.A., 2011. Estructura, Estratigrafía y evolución tectónica de la cuenca de Ñirihuau en las nacientes del río Cushamen, Chubut.
Ramos, V., 1999. Plate tectonic setting of the Andean Cordillera. Episodes 22, 183–190.
Ramos, V.A., 2015. Evolución de la cuenca golfo San Jorge: su estructuración y régimen tectónico. Revista de la Asociación Geológica Argentina 72, 12–20.
Ramos, V.A., 2014. Evolution of the Golfo San Jorge Basin: structure and tectonic regime. Revista de la Asociacion Geologica Argentina 72, 263–282.
Ramos, V.A., 2010. The tectonic regime along the Andes: Present-day and Mesozoic regimes. Geological Journal 45, 2–25.
Ramos, V.A., 2009. Anatomy and global context of the Andes: Main geologic features and the Andean orogenic cycle. Memoir of the Geological Society of America 204, 31–65.
Ramos, V.A., 2005. Seismic ridge subduction and topography: Foreland deformation in the Patagonian Andes. Tectonophysics 399, 73–86.
Ramos, V.A., 2002. Evolución tectónica. Geología y recursos naturales de Santa Cruz 165–174.
Ramos, V.A., 1982. Descripción geológica de las Hojas 53 a Monte San Lorenzo y 53 b, Monte Belgrano, Provincia de Santa Cruz. Servicio Geológico Nacional (inéd.), Buenos Aires.
Ramos, V.A., 1981. Descripción Geológica de la Hoja 47 Ab-" Lago Fontana", Provincia Del Chubut: Carta Geológico-económica de la República Argentina, Escala 1: 200.000. Servicio Geológico Nacional.
Ramos, V.A., 1979. Tectónica de la región del río y lago Belgrano, Cordillera Patagónica, Argentina. Actas II Congr. Geol. Chileno 1, 1B–32.
Ramos, V.A., Cristallini, E.O., Pérez, D.J., 2002. The Pampean flat-slab of the Central Andes. Journal of South American earth sciences 15, 59–78.
Ramos, V.A., Folguera, A., 2009. Andean flat-slab subduction through time. Geological Society, London, Special Publications 327, 31–54.

Ramos, V.A., Folguera, A., 2005. Tectonic evolution of the Andes of Neuquén: constraints derived from the magmatic arc and foreland deformation. Geological Society, London, Special Publications 252, 15–35.
Ramos, V.A., Ghiglione, M.C., 2008. Tectonic evolution of the Patagonian Andes. Developments in quaternary sciences 11, 57–71.
Rapela, C.W., Kay, S.M., 1988. Late Paleozoic to Recent magmatic evolution of northern Patagonia. Episodes 11, 175–182.
Rapela, C.W., Pankhurst, R.J., 1993. El volcanismo riolítico del noreste de la Patagonia: Un evento meso-jurásico de corta duración y origen profundo, in: Acts Del XII Congreso Geológico Argentino, Mendoza. pp. 170–188.
Rapela, C.W., Pankhurst, R.J., Fanning, C.M., Herve, F., 2005. Pacific subduction coeval with the Karoo mantle plume: the Early Jurasssic Subcordilleran belt of northwestern Patagonia. Geological Society, London, Special Publications 246, 217–239.
Rapela, C.W., Pankhurst, R.J., Harrison, S.M., 1992. Triassic "Gondwana" granites of the Gastre district, north Patagonian massif. Earth and Environmental Science Transactions of The Royal Society of Edinburgh 83, 291–304.
Rapela, C.W., Spalletti, L.A., Merodio, J.C., Aragón, E., 1988. Temporal evolution and spatial variation of early Tertiary volcanism in the Patagonian Andes (40 S–42 30′ S). Journal of South American Earth Sciences 1, 75–88.
Ravazzoli, I.A., Sesana, F.L., 1977. Descripción geológica de la Hoja 41c, Río Chico, provincia de Río Negro.
Ré, G.H., Bellosi, E.S., Heizler, M., Vilas, J.F., Madden, R.H., Carlini, A.A., Kay, R.F., Vucetich, M.G., 2010. A geochronology for the Sarmiento Formation at Gran Barranca. Cambridge University Press Cambridge.
Reiners, P.W., Brandon, M.T., 2006. Using thermochronology to understand orogenic erosion. Annu. Rev. Earth Planet. Sci. 34, 419–466.
Reiners, P.W., Farley, K.A., 2001. Influence of crystal size on apatite (U-Th)/He thermochronology: an example from the Bighorn Mountains, Wyoming. Earth and Planetary Science Letters 188, 413–420.
Reiners, P.W., Farley, K.A., Hickes, H.J., 2002. He diffusion and (U–Th)/He thermochronometry of zircon: initial results from Fish Canyon Tuff and Gold Butte. Tectonophysics 349, 297–308.
Remesal, M., Salani, F., Franchi, M., Ardolino, A.A., Dalponte, M.R., Espejo, P.M., Lizuaín, A., 2001. Hoja Geológica 4169 IV Maquinchao.
Remesal, M.B., Salani, F.M., Cerredo, M.E., 2012. Petrología del complejo volcánico Barril Niyeu (Mioceno inferior), Patagonia Argentina. Revista mexicana de ciencias geológicas 29, 463–477.
Renda, E.M., Alvarez, D., Prezzi, C., Oriolo, S., Vizán, H., 2019. Inherited basement structures and their influence in foreland evolution: A case study in Central Patagonia, Argentina. Tectonophysics 772, 228232.
Riley, T.R., Knight, K.B., 2001. Age of pre-break-up Gondwana magmatism. Antarctic Science 13, 99–110.
Ring, U., Brandon, M.T., Willett, S.D., Lister, G.S., 1999. Exhumation processes. Geological Society, London, Special Publications 154, 1–27.
Roddaz, M., Hermoza, W., Mora, A., Baby, P., Parra, M., Christophoul, F., Brusset, S., Espurt, N., 2010. Cenozoic sedimentary evolution of the Amazonian foreland basin system. Amazonia, landscape and species evolution: a look into the past. Blackwell-Wiley, Hoboken 61–88.
Rodríguez-González, J., Negredo, A.M., Billen, M.I., 2012. The role of the overriding plate thermal state on slab dip variability and on the occurrence of flat subduction. Geochemistry, Geophysics, Geosystems 13.
Roe, G.H., Whipple, K.X., Fletcher, J.K., 2008. Feedbacks among climate, erosion, and tectonics in a critical wedge orogen. American Journal of Science 308, 815–842.
Rolando, A.P., Hartmann, L.A., Santos, J.O.S., Fernandez, R.R., Etcheverry, R.O., Schalamuk, I.A., McNaughton, N.J., 2002. SHRIMP zircon U–Pb evidence for extended Mesozoic magmatism in the Patagonian Batholith and assimilation of Archean crustal components. Journal of South American Earth Sciences 15, 267–283.
Romans, B.W., Fildani, A., Graham, S.A., Hubbard, S.M., Covault, J.A., 2010. Importance of predecessor basin history on sedimentary fill of a retroarc foreland basin: provenance analysis of the Cretaceous Magallanes basin, Chile (50–52 S). Basin Research 22, 640–658.

Rosenau, M., Melnick, D., Echtler, H., 2006. Kinematic constraints on intra-arc shear and strain partitioning in the southern Andes between 38 S and 42 S latitude. Tectonics 25.
Roy, M., Kelley, S., Pazzaglia, F., Cather, S., House, M., 2004. Middle Tertiary buoyancy modification and its relationship to rock exhumation, cooling, and subsequent extension at the eastern margin of the Colorado Plateau. Geology 32, 925–928.
Ruiz, G.M.H., Seward, D., Winkler, W., 2004. Detrital thermochronology–a new perspective on hinterland tectonics, an example from the Andean Amazon Basin, Ecuador. Basin Research 16, 413–430.
Samper, A., Quidelleur, X., Boudon, G., Le Friant, A., Komorowski, J.C., 2008. Radiometric dating of three large volume flank collapses in the Lesser Antilles Arc. Journal of Volcanology and Geothermal Research 176, 485–492.
Sanders, J.W., Cuffey, K.M., Moore, J.R., MacGregor, K.R., Kavanaugh, J.L., 2012. Periglacial weathering and headwall erosion in cirque glacier bergschrunds. Geology 40, 779–782.
Savignano, E., 2018. Apatite (U-Th)/He and Fission Track thermochronometry in the Northern Patagonian Andes: New insights into the exhumation history of the thrust belt foreland sector.
Savignano, E., Mazzoli, S., Arce, M., Franchini, M., Gautheron, C., Paolini, M., Zattin, M., 2016. (Un) Coupled thrust belt-foreland deformation in the northern Patagonian Andes: New insights from the Esquel-Gastre sector (41° 30′–43° S). Tectonics 35, 2636–2656.
Saylor, J.E., Horton, B.K., Nie, J., Corredor, J., Mora, A., 2011. Evaluating foreland basin partitioning in the northern Andes using Cenozoic fill of the Floresta basin, Eastern Cordillera, Colombia. Basin Research 23, 377–402.
Scalabrino, B., Ritz, J.-F., Lagabrielle, Y., 2011. Relief inversion triggered by subduction of an active spreading ridge: evidence from glacial morphology in Central Patagonia. Terra Nova 23, 63–69.
Scalabrino, B., Ritz, J.F., Lagabrielle, Y., 2009. Using glacial morphology to constrain the impact of the Chile active spreading ridge subduction in Central Patagonia, in: EGU General Assembly Conference Abstracts. p. 8518.
Schellart, W.P., 2020. Control of subduction zone age and size on flat slab subduction. Frontiers in Earth Science 8, 1–18.
Sciutto, J.C., 1981. Geología del codo del río Senguerr, Chubut, Argentina, in: CONGRESO GEOLÓGICO ARGENTINO. pp. 203–219.
Sciutto, J.C., César, O., Escribano, V., Pezzuchi, H.D., 2000. Hoja Geológica 4566-III Comodoro Rivadavia. Servicio Geológico Minero Argentino. Instituto de Geología y Recursos Minerales.
Sciutto, J.C., César, O., Lantanos, N., Ardolino, A.A., 2008. Hoja Geológica 4569-IV Escalante. Servicio Geológico Minero Argentino. Instituto de Geología y Recursos Minerales.
Seton, M., Müller, R.D., Zahirovic, S., Gaina, C., Torsvik, T., Shephard, G., Talsma, A., Gurnis, M., Turner, M., Maus, S., 2012. Global continental and ocean basin reconstructions since 200 Ma. Earth-Science Reviews 113, 212–270.
Shuster, D.L., Farley, K.A., 2009. The influence of artificial radiation damage and thermal annealing on helium diffusion kinetics in apatite. Geochimica et cosmochimica acta 73, 183–196.
Silk, E.C.H., Barnes, R.S., 1959. Examination of fission fragment tracks with an electron microscope. Philosophical Magazine 4, 970–972.
Silva Nieto, D.G., Márquez, M.J., Ardolino, A.A., Franchi, M., 2005. Hoja Geológica 4369-III Paso de Indios. Servicio Geológico Minero Argentino. Instituto de Geología y Recursos Minerales.
Silver, P.G., Russo, R.M., Lithgow-Bertelloni, C., 1998. Coupling of South American and African plate motion and plate deformation. Science 279, 60–63.
Sinito, A.M., 1980. Edades geológicas, radimétricas y magnéticas de algunas vulcanitas cenozoicas de las provincias de Santa Cruz y Chubut. Rev. Asoc. Geol. Argent 35, 332–339.
Skarmeta, J., 1976. Evolución tectónica y paleogeográfica de los Andes Patagónicos de Aisén durante el Neocomiano, in: I Congreso Geológico Chileno (Santiago). pp. 1–56.
Skarmeta, J.J., Castelli, J.C., 1997. Intrusión sintectónica del granito de las Torres del Paine, Andes Patagónicos de Chile. Andean Geology 24, 55–74.
Sklar, L., Dietrich, W.E., 1998. River longitudinal profiles and bedrock incision models: Stream power and the influence of sediment supply. Geophysical Monograph-American Geophysical Union 107, 237–260.
Smith, G.A., Lowe, D.R., 1991. Lahars: Volcano hydrologic-events and deposition in the debris flow—hyperconcentrated flow continuum.

Snyder, N.P., Whipple, K.X., Tucker, G.E., Merritts, D.J., 2000. Landscape response to tectonic forcing: Digital elevation model analysis of stream profiles in the Mendocino triple junction region, northern California. Geological Society of America Bulletin 112, 1250–1263.
Sólyom, P.B., Tucker, G.E., 2004. Effect of limited storm duration on landscape evolution, drainage basin geometry, and hydrograph shapes. Journal of Geophysical Research: Earth Surface 109.
Somoza, R., 1998. Updated azca (Farallon)—South America relative motions during the last 40 My: implications for mountain building in the central Andean region. Journal of South American Earth Sciences 11, 211–215.
Spear, F.S., Pyle, J.M., 2002. Apatite, monazite, and xenotime in metamorphic rocks. Reviews in Mineralogy and Geochemistry 48, 293–335.
Spikings, R.A., Crowhurst, P.V., Winkler, W., Villagomez, D., 2010. Syn-and post-accretionary cooling history of the Ecuadorian Andes constrained by their in-situ and detrital thermochronometric record. Journal of South American Earth Sciences 30, 121–133.
Steiger, R.H., Jäger, E., 1977. Subcommission on geochronology: convention on the use of decay constants in geo-and cosmochronology. Earth and planetary science letters 36, 359–362.
Stevens Goddard, A.L., Fosdick, J.C., 2019. Multichronometer thermochronologic modeling of migrating spreading ridge subduction in southern Patagonia. Geology 47, 555–558.
Stock, G.M., Ehlers, T.A., Farley, K.A., 2006. Where does sediment come from? Quantifying catchment erosion with detrital apatite (U-Th)/He thermochronometry. Geology 34, 725–728.
Stock, J.D., Dietrich, W.E., 2006. Erosion of steepland valleys by debris flows. Geological Society of America Bulletin 118, 1125–1148.
Stock, J.D., Montgomery, D.R., 1999. Geologic constraints on bedrock river incision using the stream power law. Journal of Geophysical Research: Solid Earth 104, 4983–4993.
Stoffel, M., Lièvre, I., Conus, D., Grichting, M.A., Raetzo, H., Gärtner, H.W., Monbaron, M., 2005. 400 years of debris-flow activity and triggering weather conditions: Ritigraben, Valais, Switzerland. Arctic, Antarctic, and Alpine Research 37, 387–395.
Suárez, M., De la Cruz, R., 2001. Jurassic to Miocene K–Ar dates from eastern central Patagonian Cordillera plutons, Chile (45–48 S). Geological Magazine 138, 53–66.
Suarez, M., De La Cruz, R., Aguirre-Urreta, B., Fanning, M., 2009. Relationship between volcanism and marine sedimentation in northern Austral (Aisén) Basin, central Patagonia: Stratigraphic, U–Pb SHRIMP and paleontologic evidence. Journal of South American Earth Sciences 27, 309–325.
Suárez, M., De La Cruz, R., Etchart, H., Márquez, M., Fanning, M., 2015. Síntesis de la Cronología Magmática Meso-Cenozoica de Patagonia Central, Aysén, Chile: edades U-Pb SHRIMP, in: XIV Congreso Geológico Chileno, ST-4. pp. 789–792.
Suárez, M., De la Cruz, R., Troncoso, A., 2000. Tropical/subtropical upper Paleocene–lower Eocene fluvial deposits in eastern central Patagonia, Chile (46 45′ S). Journal of South American Earth Sciences 13, 527–536.
Suarez, M., Marquez, M., 2007. A Toarcian retro-arc basin of Central Patagonia (Chubut), Argentina: Middle Jurassic closure, arc migration and tectonic setting. Andean Geology 34, 63–79.
Suárez, M., Márquez, M., De La Cruz, R., Fanning, M., 2009. Aptian-Albian subaerial volcanic rocks in central Patagonia: Divisadero and Chubut Groups, in: XII Congreso Geológico Chileno. pp. 1–4.
Tagami, T., 2005. Zircon fission-track thermochronology and applications to fault studies. Reviews in Mineralogy and Geochemistry 58, 95–122.
Tagami, T., O'Sullivan, P.B., 2005. Fundamentals of fission-track thermochronology. Reviews in Mineralogy and Geochemistry 58, 19–47.
Thomson, S.N., 2002. Late Cenozoic geomorphic and tectonic evolution of the Patagonian Andes between latitudes 42 S and 46 S: An appraisal based on fission-track results from the transpressional intra-arc Liquiñe-Ofqui fault zone. Geological Society of America Bulletin 114, 1159–1173.
Thomson, S.N., Brandon, M.T., Tomkin, J.H., Reiners, P.W., Vásquez, C., Wilson, N.J., 2010a. Glaciation as a destructive and constructive control on mountain building. Nature 467, 313.
Thomson, S.N., Brandon, M.T., Tomkin, J.H., Reiners, P.W., Vásquez, C., Wilson, N.J., 2010b. Glaciation as a destructive and constructive control on mountain building. Nature 467, 313.
Thomson, S.N., Gehrels, G.E., Ruiz, J., Buchwaldt, R., 2012. Routine low-damage apatite U-Pb dating using laser ablation–multicollector–ICPMS. Geochemistry, Geophysics, Geosystems 13.
Thomson, S.N., Herve, F., Stockhert, B., Brix, M.R., Adriasola, A., 2001. Late cenozoic tectonic and geomorphic evolution of the Patagonian Andes between 42 ${$sup o$}$ S and 52 ${$sup o$}$ S, southern Chile assessed using fission-track thermochronology.

Tunik, M.A., Paredes, J.M., Fernández, M.I., Foix, N., Allard, J.O., 2015. Análisis petrográfico de areniscas de la formación castillo (Albiano) en la faja plegada de San Bernardo, cuenca golfo San Jorge, Argentina.

Tunik, M.A., Vietto, M.E., Sciutto, J.C., Estrada, E., 2004. Procedencia de areniscas del Grupo Chubut en el área central de la Sierra de San Bernardo. Análisis preliminar. Revista de la Asociación Geológica Argentina 59, 601–606.

Turner, J.C., 1965. Estratigrafía de Aluminé y adyacencias, provincia de Neuquén. Revista de la Asociación Geológica Argentina 20, 153–184.

Uliana, M.A., Biddle, K.T., Cerdan, J., 1989. Mesozoic Extension and the Formation of Argentine Sedimentary Basins: Chapter 39: Analogs.

Umazano, A.M., Bellosi, E.S., Visconti, G., Jalfin, G.A., Melchor, R.N., 2009. Sedimentary record of a Late Cretaceous volcanic arc in central Patagonia: petrography, geochemistry and provenance of fluvial volcaniclastic deposits of the Bajo Barreal Formation, San Jorge Basin, Argentina. Cretaceous Research 30, 749–766.

Umazano, A.M., Bellosi, E.S., Visconti, G., Melchor, R.N., 2012. Detecting allocyclic signals in volcaniclastic fluvial successions: Facies, architecture and stacking pattern from the Cretaceous of central Patagonia, Argentina. Journal of South American Earth Sciences 40, 94–115.

Vallati, P., Casal, G., Foix, N., Allard, J., Tomas, A.D.S., Calo, M., 2016. First report of a Maastrichtian palynoflora from the Golfo san Jorge Basin, central Patagonia, Argentina. Ameghiniana 53, 495–505.

Varela, R., Basei, M.A., Cingolani, C.A., Siga Jr, O., Passarelli, C.R., 2005. El basamento cristalino de los Andes norpatagónicos en Argentina: geocronología e interpretación tectónica. Revista geológica de Chile 32, 167–187.

Vasquez, P., Glodny, J., Franz, G., Frei, D., Romer, R.L., 2011. Early Mesozoic Plutonism of the Cordillera de la Costa (34–37 S), Chile: constraints on the onset of the Andean Orogeny. The Journal of Geology 119, 159–184.

Vermeesch, P., 2018. IsoplotR: A free and open toolbox for geochronology. Geoscience Frontiers 9, 1479–1493.

Vermeesch, P., 2013. Multi-sample comparison of detrital age distributions. Chemical Geology 341, 140–146.

Vermeesch, P., 2009. RadialPlotter: A Java application for fission track, luminescence and other radial plots. Radiation Measurements 44, 409–410.

Vermeesch, P., 2007. Quantitative geomorphology of the White Mountains (California) using detrital apatite fission track thermochronology. Journal of Geophysical Research: Earth Surface 112.

Vermeesch, P., Resentini, A., Garzanti, E., 2016. An R package for statistical provenance analysis. Sedimentary Geology 336, 14–25.

Viera, R., 1976. PRESENCIA DE SEDIMENTITAS PERMICAS EN CONTACTO CON ROCAS DEL" COMPLEJO METAMORFICO" DE LA PATAGONIA EXTRAANDINA, ESTANCIA DOS HERMANOS, PROVINCIA DE SANTA CRUZ.

Villagómez, D., Spikings, R., 2013. Thermochronology and tectonics of the Central and Western Cordilleras of Colombia: Early Cretaceous–Tertiary evolution of the northern Andes. Lithos 160, 228–249.

Volkheimer, W., 1964. Estratigrafía de la zona extraandina del departamento de Cushamen (Chubut) entre los paralelos 42 y 42 30'y los meridianos 70 y 71. Revista de la Asociación Geológica Argentina 19, 85–107.

Von Gosen, W., Loske, W., 2004. Tectonic history of the Calcatapul Formation, Chubut province, Argentina, and the "Gastre fault system." Journal of South American Earth Sciences 18, 73–88.

Wagner, G.A., 1979. Correction and interpretation of fission track ages, in: Lectures in Isotope Geology. Springer, pp. 170–177.

Wagner, G.A., 1968. Fission track dating of apatites. Earth and Planetary Science Letters 4, 411–415.

Wagner, G.A., Reimer, G.M., 1972. Fission track tectonics: the tectonic interpretation of fission track apatite ages. Earth and Planetary Science Letters 14, 263–268.

Welkner, D., Godoy, E., Bernhardt, H.-J., 2002. Peralkaline rocks in the Late Cretaceous Del Salto Pluton, Eastern Patagonian Andes, Aisén, Chile (47° 35'S). Revista geológica de Chile 29, 3–15.

Whipple, K.X., 2009. The influence of climate on the tectonic evolution of mountain belts. Nature geoscience 2, 97–104.

Whipple, K.X., 2004. Bedrock rivers and the geomorphology of active orogens. Annu. Rev. Earth Planet. Sci. 32, 151–185.
Whipple, K.X., Tucker, G.E., 1999. Dynamics of the stream-power river incision model: Implications for height limits of mountain ranges, landscape response timescales, and research needs. Journal of Geophysical Research: Solid Earth 104, 17661–17674.
Wickert, A.D., Schildgen, T.F., 2019. Long-profile evolution of transport-limited gravel-bed rivers.
Willett, C.D., Ma, K.F., Brandon, M.T., Hourigan, J.K., Christeleit, E.C., Shuster, D.L., 2020. Transient glacial incision in the Patagonian Andes from~ 6 Ma to present. Science advances 6, eaay1641.
Willett, S.D., Brandon, M.T., 2002. On steady states in mountain belts. Geology 30, 175–178.
Willett, S.D., Fisher, D., Fuller, C., En-Chao, Y., Chia-Yu, L., 2003. Erosion rates and orogenic-wedge kinematics in Taiwan inferred from fission-track thermochronometry. Geology 31, 945–948.
Willgoose, G., Hancock, G., 1998. Revisiting the hypsometric curve as an indicator of form and process in transport-limited catchment. Earth Surface Processes and Landforms: The Journal of the British Geomorphological Group 23, 611–623.
Wobus, C., Whipple, K.X., Kirby, E., Snyder, N., Johnson, J., Spyropolou, K., Crosby, B., Sheehan, D., 2006. Tectonics from topography: Procedures, promise, and pitfalls. Special papers-geological society of america 398, 55.
Wobus, C.W., Whipple, K.X., Hodges, K.V., 2006. Neotectonics of the central Nepalese Himalaya: Constraints from geomorphology, detrital 40Ar/39Ar thermochronology, and thermal modeling. Tectonics 25.
Wolf, R.A., Farley, K.A., Silver, L.T., 1996. Helium diffusion and low-temperature thermochronometry of apatite. Geochimica et Cosmochimica Acta 60, 4231–4240.
Yáñez, G., Cembrano, J., 2004. Role of viscous plate coupling in the late Tertiary Andean tectonics. Journal of Geophysical Research: Solid Earth 109.
Yonkee, W.A., Weil, A.B., 2015. Tectonic evolution of the Sevier and Laramide belts within the North American Cordillera orogenic system. Earth-Science Reviews 150, 531–593.
Zachos, J., Pagani, M., Sloan, L., Thomas, E., Billups, K., 2001. Trends, rhythms, and aberrations in global climate 65 Ma to present. science 292, 686–693.
Zaffarana, C.B., Somoza, R., 2012. Palaeomagnetism and 40Ar/39Ar dating from Lower Jurassic rocks in Gastre, central Patagonia: further data to explore tectonomagmatic events associated with the break-up of Gondwana. Journal of the Geological Society 169, 371–379.
Zattin, M., Andreucci, B., Thomson, S.N., Reiners, P.W., Talarico, F.M., 2012. New constraints on the provenance of the ANDRILL AND-2A succession (western Ross Sea, Antarctica) from apatite triple dating. Geochemistry, Geophysics, Geosystems 13.

APPENDIX A
Supplementary material for chapter 3

Supplementary material for "**The role of slab geometry variations in the exhumation of cordilleran-type orogens and their forelands: insights from northern Patagonia**"

Thermal histories modeling

The data repository contains input files for inverse thermal modeling of the results presented in Figures 1a and 1b.

Figure 1a: Thermal history results from QTQt (samples G1 to G22).
Figure 1b: Thermal history results from QTQt (samples G30 to G54).

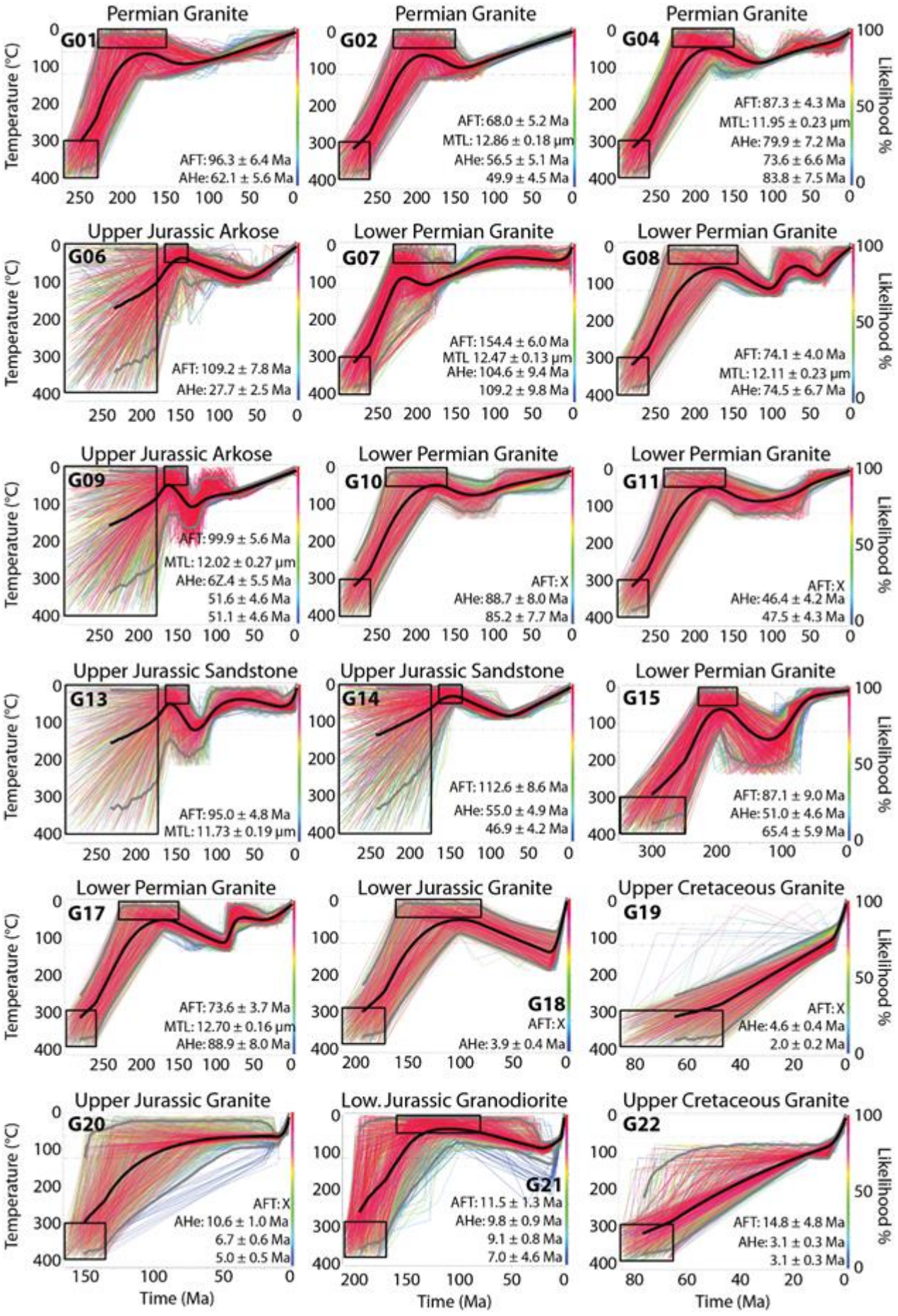

Figure 1a: Thermal history results from QTQt (samples G01 to G22).

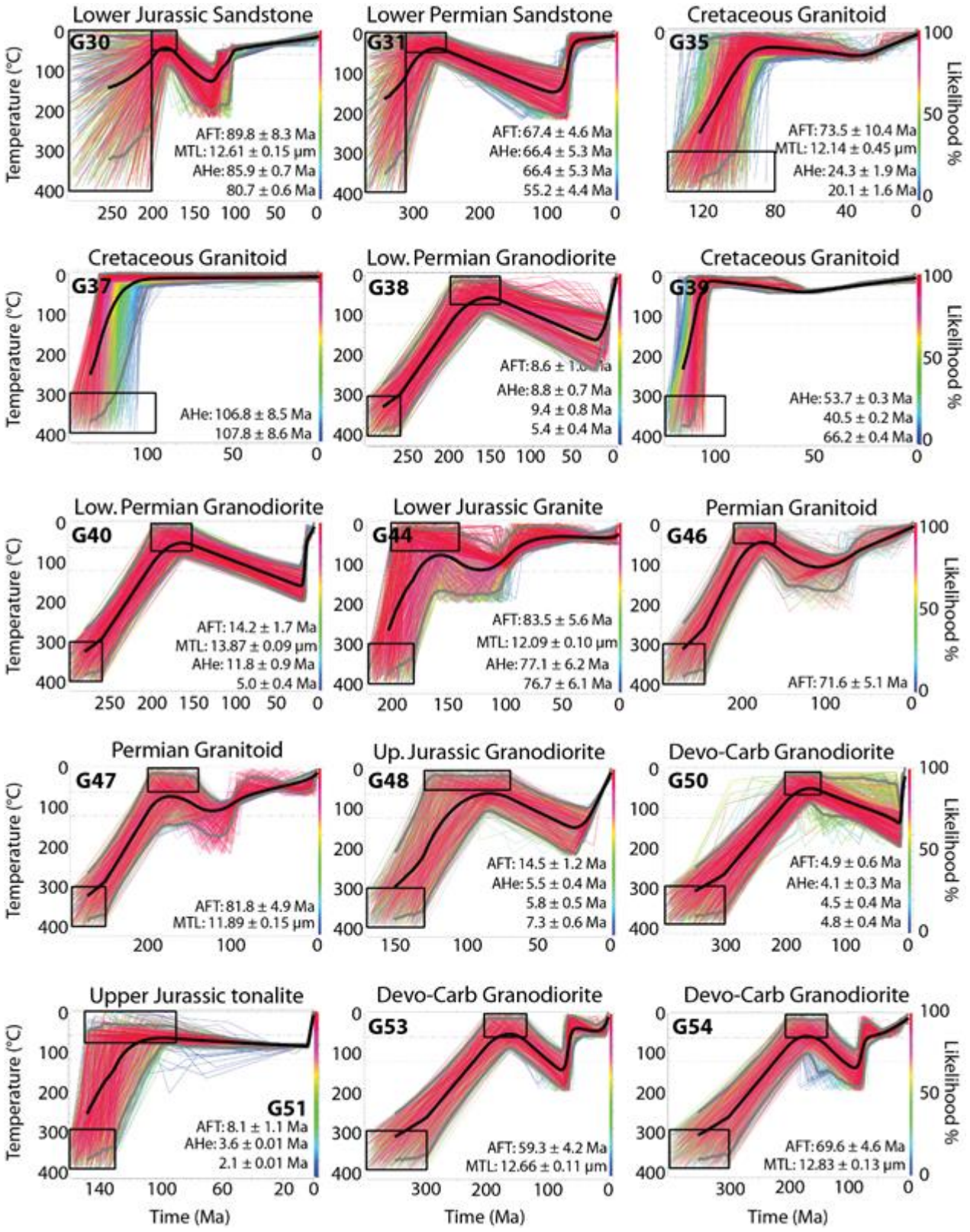

Figure 1b: Thermal history results from QTQt (from samples G30 to G54).

G10
-42.1 69.77 0
0 0 0 0 0 0
105
0 1.5 0.5
0 16.3
0
0
1
0 0
0 0
0 0
2
2
172830.1 19 0 0 75.1 8 77 0 0
A 19.8 0.00060714 122300 2 2 0
163455.5 19 0 0 67.6 7.7 60 0 0
A 19.8 0.00060714 122300 2 2 0

G11
-42.31 -70.04 0
0 0 0 0 0 0
105
0 1.5 0.5
0 16.3
0
0
1
0 0
0 0
0 0
2
2
89896.4 23 0 0 31.8 4.2 38 0 0
A 19.8 0.00060714 122300 2 2 0
40621 9 0 0 34.1 4.3 43 0 0
A 19.8 0.00060714 122300 2 2 0

G18
-42.93 -71.26 0
0 0 0 0 0 0
105
0 1.5 0.5
0 16.3
0
0
1
0 0
0 0
0 0
1
2
42608.5 123 0 0 2.8 0.4 47 0 0
A 19.8 0.00060714 122300 2 2 0

G19
-42.81 -71.66 0
0 0 0 0 0 0
105
0 1.5 0.5
0 16.3
0
0
1
0 0
0 0
0 0
2
2
20037.8 49 0 0 3.3 0.4 42 0 0
A 19.8 0.00060714 122300 2 2 0
11635.1 68 0 0 1.4 0.2 39 0 0
A 19.8 0.00060714 122300 2 2 0

G20
-42.38 -71.25 0
0 0 0 0 0 0
105
0 1.5 0.5
0 16.3
0
0
1
0 0
0 0
0 0
3
2
20451.3 23 0 0 7.2 1 42 0 0
A 19.8 0.00060714 122300 2 2 0
12081.7 21 0 0 4.5 0.6 36 0 0
A 19.8 0.00060714 122300 2 2 0
5681.2 12 0 0 3.7 0.5 51 0 0
A 19.8 0.00060714 122300 2 2 0

G37
-43.52 -71.52 0
0 0 0 0 0 0
105
0 1.5 0.5
0 16.3
0
0
1
0 0
0 0
0 0
2
2
141653 16.4 0 0 60 8.5 27.8 0 0
A 19.8 0.00060714 122300 2 2 0
149258 16.6 0 0 64.4 8.6 28.3 0 0
A 19.8 0.00060714 122300 2 2 0

G39
-41.56 -71.48 0
0 0 0 0 0 0
105
0 1.5 0.5
0 16.3
0
0
1
0 0
0 0
0 0
3
2
39981 8.7 0 0 31.6 0.3 30.3 0 0
A 19.8 0.00060714 122300 2 2 0
35918 10.2 0 0 23.8 0.2 26.2 0 0
A 19.8 0.00060714 122300 2 2 0
115956 22.6 0 0 35.3 0.4 25 0 0
A 19.8 0.00060714 122300 2 2 0

G46
0 0 0
0 0 20 346.11 9460005000
105
0 1.358000 0.000000
1 16.3
0
0
1
71.57 4.51
0.00 0
0.000 0
13 26 1.358
4 15 1.358
15 31 1.358
33 48 1.358

G38
-41.85 -71.42 0
0 0 0 0 0 0
105
0 1.5 0.5
0 16.3
0
0
1
0 0
0 0
0 0
2
2
27338 37.1 0 0 6 0.7 37.4 0 0
A 19.8 0.00060714 122300 2 2 0

G31
-43.66 -70.08 0
0 0 0 0 0 0
105
0 1.5 0.5
0 16.3
0
0
1
0 0
0 0
0 0
3
2
0 13.5 0 0 52.3 5.3 59 0 0
A 19.8 0.00060714 122300 2 2 0

G01
-42.19 -69.17 0
0 0 0 0 0 0
105
0 1.5 0.5
0 16.3
0
0
1
0 0
0 0
0 0
1
2
481259.6 98 0 0 40 5.6 38 0 0
A 19.8 0.00060714 122300 2 2 0

G15
-42.59 -68.81 0
0 0 0 0 0 0
105
0 1.5 0.5
0 16.3
0
0
1
0 0
0 0
0 0
2
2
26296.8 5 0 0 39.2 4.6 41 0 0
A 19.8 0.00060714 122300 2 2 0

G48
-40.89 -71.5 0
0 0 0 0 0 0
105
0 1.5 0.5
0 16.3
0
0
1
0 0
0 0
0 0
3
2
22054 47.8 0 0 3.7 0.4 42.8 0 0
A 19.8 0.00060714 122300 2 2 0

G22
-42.03 -71.58 0
0 0 0 0 0 0
105
0 1.5 0.5
0 16.3
0
0
1
0 0
0 0
0 0
2
2
33055.7 129 0 0 2.1 0.3 45 0 0
A 19.8 0.00060714 122300 2 2 0

19 55 1.358
16 33 1.358
17 27 1.358
8 24 1.358
17 35 1.358
38 93 1.358
27 79 1.358
12 37 1.358
7 26 1.358
12 22 1.358
31 68 1.358
15 27 1.358
32 85 1.358
21 45 1.358
26 57 1.358
19 36 1.358

16316 33.9 0 0 3.9 0.4 50.5 0 0
A 19.8 0.00060714 122300 2 2 0

G38
Zeta: Traditional
zeta sig zeta rho-d (N/cm?) Nd
346.11 11.81 0.985E+06 5000
Ns Ni Dpar
3 69 1.358
4 93 1.358
2 34 1.358
8 117 1.358
7 146 1.358
6 103 1.358
5 101 1.358
3 55 1.358
2 37 1.358
3 58 1.358
4 68 1.358
4 73 1.358
3 64 1.358
4 76 1.358
3 58 1.358
3 52 1.358
4 97 1.358
9 216 1.358
7 139 1.358
4 87 1.358

0 21.3 0 0 45.2 5.3 43.2 0 0
A 19.8 0.00060714 122300 2 2 0

0 12.6 0 0 41.4 4.4 56.4 0 0
A 19.8 0.00060714 122300 2 2 0

G31
Zeta: Traditional
zeta sig zeta rho-d (N/cm?) Nd
346.11 11.81 1.01E+06 5000
Ns Ni Dpar
5 9 1.3285
16 39 1.3285
9 17 1.3285
18 42 1.3285
20 45 1.3285
18 43 1.3285
19 40 1.3285
18 44 1.3285
17 45 1.3285
18 42 1.3285
12 23 1.3285
23 60 1.3285
32 107 1.3285
48 105 1.3285
19 68 1.3285
24 71 1.3285
13 39 1.3285
38 104 1.3285
17 45 1.3285
34 90 1.3285

G01

0 0 0

0 0 21 344.99 1.156e+06 4798

105
0 1.617143 0.139145
1 16.3
0
0
1
96.31 6.03
0.00 0
0.000 0
16 24 1.79
5 15 1.78
8 25 1.47
13 23 1.65
82 164 1.72
25 51 1.79
53 91 1.69
7 21 1.74
18 40 1.82
21 34 1.65
33 54 1.44
11 20 1.74
17 42 1.46
6 11 1.68
8 22 1.66
16 49 1.47
9 25 1.53
17 34 1.45
13 26 1.56
5 18 1.41
17 33 1.46

65107.3 11 0 0 44.9 5.9 45 0 0
A 19.8 0.00060714 122300 2 2 0

OSU10A_G15A.apa

0 0 0

0 0 20 344.99 1.083e+06 4798
105
0 1.783500 0.211443
1 16.3
0
0
1
87.14 8.80
0.00 0
0.000 0
4 9 2.03
8 30 1.89
18 24 1.52
7 16 1.69
3 11 2.01
13 23 1.69
7 16 1.85
8 20 2.08
6 14 1.45
4 9 1.55
10 17 1.67
7 15 2.13
7 15 1.56
5 8 1.74
6 12 1.63
5 12 1.85
6 9 1.62
7 20 1.72
9 15 1.84
7 18 2.15

23517 43.5 0 0 4.4 0.5 50.3 0 0
A 19.8 0.00060714 122300 2 2 0

18720 28.4 0 0 5.3 0.6 46.5 0 0
A 19.8 0.00060714 122300 2 2 0

G48
0 0 0
105
0 0 20 346.11 977000 5000
105
0 1.338000 0.000000
0
1 16.3
0
1
14.16 1.60
0.00 0
0.000 0
4 41 1.338
3 45 1.338
2 37 1.338
5 62 1.338
2 22 1.338
6 72 1.338
4 52 1.338
4 63 1.338
4 47 1.338
6 56 1.338
6 43 1.338
5 44 1.338
8 86 1.338
4 59 1.338
5 59 1.338
4 39 1.338
5 47 1.338
2 41 1.338

19459.8 71 0 0 2.2 0.3 46 0 0
A 19.8 0.00060714 122300 2 2 0

G22
0 0 0
0 0 21 344.99 1.055e+06 5000
105
0 2.711429 0.208837
1 16.3
0
0
1
14.76 1.23
0.00 0
0.000 0
4 58 2.46
9 61 2.46
7 135 2.46
10 159 2.6
8 50 2.9
6 117 2.93
10 74 2.38
9 82 2.97
5 98 2.75
12 142 2.69
4 75 2.9
12 107 2.96
5 70 2.4
3 69 2.65
5 78 2.53
8 74 2.95
6 82 2.67
7 101 3.01
10 116 2.71
9 150 2.68

G21	G51	G50	G14	G06	G47	G35
-42.17 -71.36 0	-40.13 -71.65 0	-40.2 -71.36 0	-42.43 -68.83 0	-42.44 -68.78 0	0 0 0	-43.32 -70.9 0
0 0 0 0 0 0	0 0 0 0 0 0	0 0 0 0 0 0	0 0 0 0 0 0	0 0 0 0 0 0	0 33 20 346.11 939000 5000	0 0 0 0 0 0
105	105	105	105	105	105	105
0 1.5 0.5	0 1.5 0.5	0 1.5 0.5	0 1.5 0.5	0 1.5 0.5	0 1.332 0.035	0 1.5 0.5
0 16.3	0 16.3	0 16.3	0 16.3	0 16.3	1 16.3	0 16.3
0	0	0	0	0	-1	0
0	0	0	0	0	0	0
1	1	1	1	1	1	1
0 0	0 0	0 0	0 0	0 0	81.75 4.01	0 0
0 0	0 0	0 0	0 0	0 0	11.90 1.19	0 0
0 0	0 0	0 0	0 0	0 0	1.268 0.1268	0 0
2	2	4	2	1	21 64 1.3025	2
2	2	2	2	2	32 48 1.2925	2
41763.5 57 0 0 5.9 0.9 20 0 0	6474 19.7 0 0 2.7 0 45.9 0 0	23618 75.3 0 0 2.5 0.3 32.6 0 0	291854.3 56 0 0 43.3 4.9 58 0 0	70495.9 27 0 0 21.6 2.5 55 0 0	35 70 1.265	22167 9.9 0 0 17.5 1.9 46.7 0 0
A 19.8 0.00060714 122300 2 2 0	A 19.8 0.00060714 122300 2 2 0	A 19.8 0.00060714 122300 2 2 0	A 19.8 0.00060714 122300 2 2 0	A 19.8 0.00060714 122300 2 2 0	65 146 1.345	A 19.8 0.00060714 122300 2 2 0
32364.8 45 0 0 5.8 0.8 37 0 0	2563 12.8 0 0 1.6 0 53 0 0	18111 45.2 0 0 3.2 0.4 48.9 0 0	357806.4 82 0 0 36.1 4.2 54 0 0		35 71 1.3	14432 7.6 0 0 15.1 1.6 52.4 0 0
A 19.8 0.00060714 122300 2 2 0	A 19.8 0.00060714 122300 2 2 0	A 19.8 0.00060714 122300 2 2 0	A 19.8 0.00060714 122300 2 2 0	OSU10A_G06.apa	46 105 1.2675	A 19.8 0.00060714 122300 2 2 0
		45107 114 0 0 3.2 0.4 41 0 0		0 0 0	25 54 1.3475	
OSU10A_G21.apa	G51	A 19.8 0.00060714 122300 2 2 0	G14	0 0 36 344.99 1.134e+06 8875	23 55 1.315	G35
0 0 0	0 0 0	39855 100.8 0 0 3.2 0.4 51.7 0 0	0 0 0	105	66 107 1.3575	0 0 0
0 0 20 344.99 1.06e+06 4798	0 0 20 346.11 900000 5000	A 19.8 0.00060714 122300 2 2 0	0 0 27 344.99 1.089e+06 4798	0 2.753889 0.280706	35 56 1.4	0 25 20 346.11 1e+06 5000
105	105		105	1 16.3	37 58 1.2875	105
0 2.355000 0.441725	0 1.353000 0.000000	G50	0 1.679259 0.115955	0	36 74 1.24	0 1.329 0.032
1 16.3	1 16.3	0 0 0	1 16.3	0	41 84 1.44	1 16.3
0	0	0 0 19 346.11 915000 5000	0	1	20 43 1.405	-1
0	0	105	0	109.24 7.37	9 22 1.3375	0
1	1	0 1.322500 0.000000	1	0.00 0	12 27 1.3475	1
11.48 1.24	8.15 1.04	1 16.3	112.56 8.30	0.000 0	24 51 1.3175	87.18 7.47
0.00 0	0.00 0	0	0.00 0	17 39 2.51	55 96 1.345	12.14 1.214
0.000 0	0.000 0	0	0.000 0	10 18 2.65	41 74 1.2775	1.579 0.1579
7 111 2.79	4 114 1.353	1	39 45 1.7	9 12 3.41	25 44 1.4475	7 13 1.3725
3 55 1.86	3 55 1.353	4.93 0.63	32 102 1.77	20 29 2.82	10.91 21.19 1.3322	9 18 1.4
4 87 2.25	2 38 1.353	0.00 0	69 74 2.12	9 15 3.2	8.5 65.25 1.3322	7 14 1.39333333333333
3 49 2	7 70 1.353	0.000 0	17 32 1.62	5 13 2.9	12.07 56.55 1.3322	18 36 1.3725
3 49 2.5	2 46 1.353	7 175 1.3225	17 28 1.75	8 9 3.2	10.58 16.5 1.3322	8 15 1.37333333333333
3 54 1.48	1 14 1.353	2 58 1.3225	25 17 1.77	5 9 3.06	10.33 74.94 1.3322	5 11 1.33
5 57 2.58	1 12 1.353	8 209 1.3225	41 60 1.71	10 11 2.76	12.08 45.7 1.3322	8 17 1.3425
9 122 2.56	4 85 1.353	4 112 1.3225	50 96 1.69	13 16 2.91	10.82 65.74 1.3322	16 31 1.33
7 101 2.69	8 94 1.353	2 67 1.3225	41 43 1.55	11 18 2.94	12.87 52.42 1.3322	8 16 1.375
3 51 1.18	4 67 1.353	2 61 1.3225	13 20 1.69	7 18 2.96	12.88 49.61 1.3322	23 45 1.275

6 115 2.43
3 52 2.44
5 74 2.3
5 80 2.22
5 75 2.8
4 45 2.54
5 75 2.4
4 53 2.43
4 74 2.98
4 85 2.67

2 47 1.353
7 138 1.353
5 84 1.353
2 41 1.353
2 52 1.353
1 22 1.353
6 171 1.353
1 19 1.353
1 28 1.353
2 45 1.353

5 185 1.3225
1 34 1.3225
4 137 1.3225
2 42 1.3225
4 157 1.3225
3 125 1.3225
6 229 1.3225
3 115 1.3225
2 64 1.3225
2 59 1.3225
1 21 1.3225
2 73 1.3225
3 100 1.3225

102 195 1.56
63 73 1.55
3 5 1.63
50 137 1.72
21 41 1.72
65 96 1.71
51 90 1.72
59 80 1.59
124 181 1.6
37 62 1.75
37 83 1.55
23 83 1.69
45 61 1.56
26 78 1.55
44 112 1.63
29 52 1.72
61 55 1.72

20 41 2.68
7 18 2.25
11 19 2.53
6 15 2.5
6 12 2.41
5 10 2.98
12 16 2.78
13 30 2.32
4 7 2.85
12 21 2.91
8 13 2.23
25 43 2.64
8 19 2.85
6 11 2.75
6 9 2.43
5 8 2.61
14 24 2.57
6 13 2.81
15 25 2.73
12 20 3.09
3 5 2.91
9 11 2.55
10 16 3.06
5 12 2.38

12.52 53.85 1.3322
11.26 36.97 1.3322
11.92 52.99 1.3322
10.5 26.3 1.3322
12.12 54.73 1.3322
12.63 67.64 1.3322
10.64 41.99 1.3322
11.23 32.88 1.3322
11.45 65.67 1.3322
12.46 66.47 1.3322
11.73 11.0 1.3322
12.04 71.67 1.3322
11.22 58.39 1.3322
13.56 18.37 1.3322
12.37 72.81 1.3322
11.28 66.34 1.3322
12.17 46.59 1.3322
14.33 37.06 1.3322
10.97 10.02 1.3322
12.09 18.52 1.3322
13.63 9.33 1.3322
15.1 79.98 1.3322
13.05 19.23 1.3322
11.3 22.65 1.3322

9 18 1.2275
12 22 1.35
7 16 1.285
10 21 1.25
11 21 1.2575
4 7 1.3289
8 18 1.3289
9 17 1.3289
9 18 1.3289
23 42 1.3289
15.24 38.6 1.3289
12.31 10.41 1.3289
10.57 12.57 1.3289
12.51 79.09 1.3289
10.73 12.6 1.3289
11.52 4.09 1.3289
14.11 82.93 1.3289
11.19 9.69 1.3289
12.75 6.32 1.3289
12.16 50.21 1.3289
11.48 10.72 1.3289
10.6 5.89 1.3289
14.9 25.42 1.3289
11.49 69.7 1.3289
11.41 7.76 1.3289
12.35 65.11 1.3289
10.82 38.98 1.3289
10.09 21.24 1.3289
11.34 5.01 1.3289
15.33 8.43 1.3289
11.41 58.19 1.3289
12.95 72.83 1.3289
10.26 68.75 1.3289
11.28 6.77 1.3289
14.67 9.53 1.3289

G13	G40	G44	G53	G04	G17
0 0 0	-40.34 -71.51 0	-41.21 -70.17 0	0 0 0	-42.39 -69.52 0	0 0 0
0 61 34 344.99 1.094e+06 8875	0 0 0 0 0 0	0 0 0 0 0 0	0 86 20 346.11 892000 5000	0 0 0 0 0 0	0 93 21 344.99 1.072e+06 8875
105	105	105	105	105	105
0 1.903 0.197	0 1.5 0.5	0 1.5 0.5	0 1.287 0.028	0 1.5 0.5	0 1.661 0.143
1 16.3	0 16.3	0 16.3	1 16.3	0 16.3	1 16.3
-1	0	0	-1	0	-1
0	0	0	0	0	0
1	1	1	1	1	1
94.96 4.29	0 0	0 0	59.34 3.63	0 0	73.59 3.34
11.73 1.173	0 0	0 0	12.67 1.267	0 0	12.76 1.276
1.447 0.1447	0 0	0 0	1.142 0.1142	0 0	1.429 0.1429
40 77 1.9	2	2	16 46 1.29	3	35 102 1.79
52 84 1.9	2	2	17 57 1.2475	2	59 167 1.59
126 218 1.9	13772 35.9 0 0 3.2 0.4 33.7 0 0	63247 9.1 0 0 53.1 6.2 44.8 0 0	20 52 1.2875	204917.2 27 0 0 62.7 7.2 53 0 0	38 92 1.57
33 42 1.9	A 19.8 0.00060714 122300 2 2 0	A 19.8 0.00060714 122300 2 2 0	22 52 1.2175	A 19.8 0.00060714 122300 2 2 0	38 72 1.66
97 144 1.9	32916 38.2 0 0 7 0.9 29.8 0 0	303657 44.6 0 0 55.4 6.1 50.4 0 0	21 61 1.2025	257276.9 40 0 0 51.9 6.6 41 0 0	32 73 1.71
48 60 1.9	A 19.8 0.00060714 122300 2 2 0	A 19.8 0.00060714 122300 2 2 0	16 35 1.2075	A 19.8 0.00060714 122300 2 2 0	19 58 1.63
20 42 1.9			16 44 1.2375	729467.2 105 0 0 57.3 7.5 44 0 0	28 61 1.53
55 113 1.9	G40	G44	31 74 1.3825	A 19.8 0.00060714 122300 2 2 0	26 56 1.65
40 79 1.9	0 0 0	0 0 0	17 38 1.2375		20 54 1.64
52 110 1.9	0 60 20 346.11 977000 5000	0 61 20 346.11 960000 5000	10 23 1.3925	G04	30 68 1.77
32 81 1.9	105	105	17 36 1.3525	0 0 0	41 88 1.53
33 64 1.9	0 1.338 0.039	0 1.323 0.030	18 50 1.2175	0 66 20 344.99 1.139e+06 4798	42 118 1.64
30 45 1.9	1 16.3	1 16.3	13 41 1.255	105	25 57 1.6
61 157 1.9	-1	-1	5 16 1.345	0 1.708 0.126	28 72 1.7
27 75 1.9	0	0	33 82 1.3225	1 16.3	39 100 1.77
36 45 1.9	1	1	13 35 1.2575	-1	48 120 1.79
18 37 1.9	14.16 1.60	83.38 4.77	24 53 1.2525	0	29 80 1.72
74 175 1.9	13.87 1.387	12.09 1.209	29 71 1.3225	1	52 136 1.65
110 196 1.9	0.725 0.0725	1.075 0.1075	32 83 1.42	87.30 3.78	24 68 1.66
40 60 1.9	4 41 1.4475	28 48 1.3225	22 66 1.2875	11.95 1.195	31 78 1.67
29 94 1.9	3 45 1.4625	27 47 1.3075	15.74 4.86 1.28675	1.873 0.1873	34 74 1.66
16 46 1.9	2 37 1.3575	32 56 1.2475	12.67 46.69 1.28675	20 44 1.7	11.11 69 1.476
25 85 1.9	5 62 1.3225	34 51 1.29	11.42 48.95 1.28675	30 71 1.77	11.72 76 1.416
26 48 1.9	2 22 1.4075	26 56 1.24	10.71 87.14 1.28675	37 68 2.12	9.83 83 1.416
24 49 1.9	6 72 1.2375	36 72 1.3775	10.46 38.85 1.28675	20 44 1.62	13.03 86 1.573
17 68 1.9	4 52 1.3225	41 68 1.22	15.12 28.07 1.28675	105 209 1.75	10.61 66 1.573
11 26 1.9	4 63 1.26	23 58 1.35	11.68 53.68 1.28675	20 46 1.77	14.13 40 1.426
3 5 1.9	4 47 1.3225	33 79 1.25	13.85 73.02 1.28675	25 63 1.71	15.36 27 1.426
37 65 1.9	6 56 1.195	9 17 1.3525	11.43 64.09 1.28675	110 228 1.69	12.58 5 1.426

100 218 1.9
6 8 1.9
24 39 1.9
75 137 1.9
58 112 1.9
11.53 75 1.983
7.76 45 1.983
9.88 34 1.983
11.42 85 1.89
11.02 83 1.89
10.34 54 1.89
7.86 82 1.89
14.02 36 1.89
11.57 56 1.89
10.77 72 1.89
9.42 20 1.89
13.52 23 1.89
11.5 89 2.19
10.7 79 2.19
10.5 58 2.19
13.15 84 2.19
11.3 70 2.19
13.12 83 2.19
10.69 61 2.19
11.07 39 2.19
11.99 58 1.843
10.56 52 1.843
12.94 83 1.843
11.09 53 1.763
12.46 46 1.85
14.16 64 1.85
13.67 85 1.946
10.8 60 1.946
11.6 61 1.886
11.9 50 1.886
11.34 83 2.00
12.5 59 1.91
12.44 49 1.91
10.82 41 1.91
14.31 38 1.91
14.24 50 2.036
12.86 70 2.036
13.44 63 2.036
13.33 64 1.92
10.69 72 1.87
13.73 25 1.87
11.12 67 2.07
6 43 1.315
5 44 1.27
8 86 1.3925
4 59 1.345
5 59 1.46
4 39 1.34
5 47 1.2775
2 41 1.2275
3 44 1.4125
4 67 1.3825
14.73 81.61 1.337875
14.06 18.22 1.337875
14.76 12.94 1.337875
15.02 83.62 1.337875
13.15 52.08 1.337875
14.98 58.55 1.337875
13.58 42.38 1.337875
13.2 15.79 1.337875
14.59 43.28 1.337875
13.89 65.3 1.337875
13.66 72.65 1.337875
14.97 51.89 1.337875
13.84 64.42 1.337875
14.44 31.72 1.337875
13.46 75.77 1.337875
13.34 77.96 1.337875
14.08 27.15 1.337875
13.97 38.18 1.337875
14.91 77.63 1.337875
14.61 68.48 1.337875
14.17 40.69 1.337875
14.91 61.82 1.337875
14.65 36.42 1.337875
15.11 60.14 1.337875
12.44 14.72 1.337875
13.25 16.06 1.337875
14.38 63.29 1.337875
13.42 48.34 1.337875
13.07 55.57 1.337875
12.68 72.23 1.337875
12.56 8.62 1.337875
13.05 22.37 1.337875
12.97 56.88 1.337875
14.36 35.5 1.337875
13.97 70.39 1.337875
14.56 35.5 1.337875
12.03 41.69 1.337875
11 30 1.315
39 64 1.3375
33 63 1.2975
13 29 1.405
14 27 1.245
20 47 1.3975
16 50 1.43
29 54 1.3125
10 21 1.385
15 31 1.3675
12.04 40.55 1.3225
13.12 48.2 1.3225
11.58 59.11 1.3225
13.81 69.44 1.3225
10.42 16.94 1.3225
12.56 44.57 1.3225
11.27 43.68 1.3225
11.62 5.85 1.3225
12.42 67.56 1.3225
10.1 67.19 1.3225
11.34 85.63 1.3225
12.11 61.65 1.3225
12.02 66.07 1.3225
10.24 46.21 1.3225
11.1 47.75 1.3225
13.22 9.53 1.3225
13.52 52.37 1.3225
11.98 75.02 1.3225
13.13 47.85 1.3225
13.01 52.7 1.3225
12.22 82.52 1.3225
11.32 63.3 1.3225
11.44 63.17 1.3225
13.82 62.61 1.3225
12.56 23.4 1.3225
12.09 51.84 1.3225
12.43 66.0 1.3225
11.02 59.73 1.3225
12.94 57.54 1.3225
11.6 45.14 1.3225
11.48 31.95 1.3225
12.32 56.61 1.3225
11.82 66.49 1.3225
11.46 47.16 1.3225
11.15 17.59 1.3225
12.28 48.91 1.3225
11.52 36.08 1.3225
13.24 11.29 1.28675
12.24 80.74 1.28675
11.87 26.29 1.28675
12.07 7.7 1.28675
13.52 67.7 1.28675
11.66 59.63 1.28675
13.76 84.61 1.28675
11.05 59.31 1.28675
13.13 72.25 1.28675
11.02 38.19 1.28675
14.13 56.74 1.28675
14.12 69.31 1.28675
14.22 69.72 1.28675
12.00 71.77 1.28675
11.91 39.02 1.28675
13.73 68.13 1.28675
14.2 27.1 1.28675
12.57 35.04 1.28675
12.61 41.27 1.28675
12.33 86.88 1.28675
12.72 82.44 1.28675
12.54 74.08 1.28675
12.97 50.9 1.28675
11.22 62.24 1.28675
13.61 15.69 1.28675
14.41 85.22 1.28675
11.94 20.06 1.28675
12.35 39.54 1.28675
12.3 8.26 1.28675
12.97 67.85 1.28675
13.12 10.29 1.28675
12.12 22.62 1.28675
13.52 56.55 1.28675
11.98 12.11 1.28675
12.67 6.09 1.28675
12.24 40.61 1.28675
11.1 66.21 1.28675
12.09 15.67 1.28675
11.61 60.86 1.28675
12.35 65.29 1.28675
13.7 60.84 1.28675
12.3 69.74 1.28675
12.56 18.18 1.28675
14.83 58.64 1.28675
11.27 28.04 1.28675
12.65 34.45 1.28675
11.15 79.72 1.28675
28 72 1.55
35 79 1.69
40 102 1.56
40 104 1.55
47 133 1.63
23 41 1.72
56 111 1.72
24 47 1.71
63 139 1.72
46 108 1.59
52 113 1.6
46 116 1.75
8.58 58.48 1.603
9.13 47.63 1.603
14.55 31.66 1.573
9.88 34.4 1.92
7.68 29.31 1.92
9.18 46.49 1.423
10.63 55.72 1.423
11.8 8.48 1.633
12.3 38.33 1.633
8.06 9.43 1.633
12.31 51.62 1.633
11.47 75.00 1.49
10.9 50.00 1.61
9.27 28.0 1.87
13.49 5.0 1.87
12.75 53.0 1.87
13.07 79.0 1.87
11.52 72.0 1.74
15.34 89.0 1.72
11.43 23.0 1.8
11.5 51.0 1.536
14.83 50.0 1.536
13.93 21.0 1.766
13.8 17.0 1.676
11.75 5.0 1.546
12.8 80.5 1.696
12.94 80.5 1.603
10.24 64.0 1.603
12.43 82.0 1.753
11.52 77.0 1.636
14.71 21.0 1.703
11.67 35.0 1.703
13.72 59.0 1.72
9.44 79.0 1.713
11.11 25.0 1.713
12.01 87 1.583
12.19 66 1.583
10.76 83 1.646
13.15 11 1.766
13.16 53 1.583
13.27 52 1.76
11.11 77 1.496
12.95 50 1.636
11.59 78 1.596
15.94 23 1.606
12.73 77 1.75
13.72 46 1.74
12.26 51 1.74
13.72 65 1.616
11.15 47 1.616
10.86 40 1.806
12.51 43 1.513
13.52 53 1.66
12.38 59 1.75
12.5 53 1.75
11.76 61 2.00
12.63 49 1.443
11.84 15 1.663
12.66 14 1.736
11.95 25 1.716
11.39 84 1.74
13.34 55 1.686
12.36 71 1.813
12.09 24 1.71
12.89 9 1.84
13.06 89 1.84
13.88 64 1.84
11.3 62 1.606
12.43 60 1.606
10.95 9 1.673
13.44 31 1.683
15.47 34 1.65
13.2 37 1.65
12.47 53 1.646
12.69 69 2.1
10.79 70 2.1
12.36 58 1.766
10.03 62 1.606
12.9 30 1.823
13.37 33 1.743
15.2 37 1.723
13.8 45 1.493

12.45 52 1.94
12.92 44 2.103
10.67 19 2.103
10.21 60 2.103
11.96 83 1.973
12.29 71 1.179
10.92 76 1.179
10.7 70 1.179
12.99 86 1.179
12.03 58 1.179
10.06 70 1.87
12.01 56 1.87
13.06 51 1.87
10.73 79 1.993
12.13 53 1.993
10.79 74 1.993
12.97 67 1.993
9.84 69 2.016
13.53 89 1.85

14.25 12.27 1.337875
13.62 84.78 1.337875
12.63 78.57 1.337875
13.55 37.89 1.337875
13.92 16.14 1.337875
14.38 23.51 1.337875
13.56 56.94 1.337875
13.58 31.31 1.337875
14.28 86.8 1.337875
14.6 39.91 1.337875
13.77 40.44 1.337875
13.42 53.61 1.337875
13.55 66.04 1.337875
14.22 66.29 1.337875
13.05 30.65 1.337875
13.15 72.81 1.337875
14.61 37.47 1.337875
13.53 46.82 1.337875
13.21 12.2 1.337875
14.13 52.24 1.337875
14.32 41.65 1.337875
14.03 74.39 1.337875
13.74 68.63 1.337875

11.25 75.1 1.3225
10.39 40.34 1.3225
11.17 7.25 1.3225
13.23 20.45 1.3225
12.79 47.1 1.3225
11.77 80.31 1.3225
13.67 60.72 1.3225
14.03 87.97 1.3225
11.36 44.19 1.3225
13.98 51.24 1.3225
11.11 33.09 1.3225
14.54 25.98 1.3225
12.13 18.32 1.3225
12.23 15.19 1.3225
12.35 63.72 1.3225
11.4 31.9 1.3225
10.73 34.45 1.3225
12.07 32.88 1.3225
13.09 40.94 1.3225
14.08 14.23 1.3225
12.37 22.39 1.3225
10.12 1.45 1.3225
10.5 81.85 1.3225
12.97 34.52 1.3225

12.74 67.27 1.28675
13.79 18.05 1.28675
12.51 40.87 1.28675
12.52 10.5 1.28675
14.78 86.68 1.28675
11.96 88.43 1.28675
11.69 7.5 1.28675
12.81 20.66 1.28675
12.05 37.4 1.28675
12.45 62.53 1.28675
11.39 45.43 1.28675
14.54 44.88 1.28675
10.61 80.74 1.28675
11.67 51.91 1.28675
14.81 54.44 1.28675
11.38 64.1 1.28675
12.92 34.94 1.28675
12.63 41.26 1.28675
13.9 14.97 1.28675
12.19 4.15 1.28675
14.01 43.55 1.28675
12.8 18.79 1.28675
11.81 42.9 1.28675
14.53 75.54 1.28675
13.99 51.62 1.28675
13.52 35.9 1.28675
12.2 76.25 1.28675
12.89 81.05 1.28675
11.23 61.00 1.28675
12.79 42.68 1.28675

13.36 83.0 1.713
15.11 52.0 1.846
12.5 73.0 1.79
12.23 62.0 1.79
14.66 38.0 1.79
9.03 15.0 1.62
11.8 19.0 1.62
12.87 18.0 1.62
13.14 24.0 1.62
10.1 27.0 1.62
12.98 31.0 1.563
11.15 42.0 1.563
12.95 61.0 1.78
12.03 70.0 1.723
11.57 69.0 1.723
11.82 81.0 1.847
11.94 1.0 1.756
12.5 27.0 1.756
16.68 16.0 1.91
10.34 43.0 1.91
13.5 65.0 1.91
10.9 84.0 1.91
13.54 36.0 1.91
9.68 54.0 1.91
10.84 36.0 1.81
13.93 19.0 1.81
13.36 54.0 1.736
11.68 42.0 1.736
10.11 23.0 1.643
9.56 46.0 1.643
13.2 31.0 1.643

10.89 36 1.826
12.27 52 1.626
13.62 32 1.43
14.47 30 1.67
11.39 59 1.63
10.87 82 1.513
13.55 46 1.61
12.3 59 1.78
13.2 31 1.863
15.14 71 1.566
13.89 72 1.566
11.21 17 1.43
14.81 63 1.743
12.59 66 1.743
11.04 71 1.846
14.2 75 1.74
14.98 77 1.68
11.6 29 1.74
12.7 85 1.816
12.89 87 1.716
14.04 15 1.743
12.31 84 1.743
16.63 89 1.58
13.94 49 1.756
10.14 74 1.69
11.44 47 1.24
13.86 57 1.24
16.15 33 1.446
12.97 58 1.58
10.65 54 1.68
14.75 64 1.68
11.47 75 1.45
14.24 9 1.536
12.79 50 1.706
14.02 85 1.836
13.38 83 1.793
13.7 15 1.86
12.09 66 1.543

G02	G09	G54	G30	G08	G07
-42.27 -69.41 0	-42.41 -69.78 0	0 0 0	-43.74 -69.82 0	-42.56 -69 0	-42.56 -69 0
0 0 0 0 0 0	0 0 0 0 0 0	0 100 20 346.11 885000 5000	0 0 0 0 0 0	0 0 0 0 0 0	0 0 0 0 0 0
105	105	105	105	105	105
0 1.5 0.5	0 1.5 0.5	0 1.275 0.016	0 1.5 0.5	0 1.5 0.5	0 1.5 0.5
0 16.3	0 16.3	1 16.3	0 16.3	0 16.3	0 16.3
0	0	-1	0	0	0
0	0	0	0	0	0
1	1	1	1	1	1
0 0	0 0	69.64 3.94	0 0	0 0	0 0
0 0	0 0	12.83 1.283	0 0	0 0	0 0
0 0	0 0	1.349 0.1349	0 0	0 0	0 0
2	3	27 58 1.22	2	1	2
2	2	38 86 1.2125	2	2	2
159254.4 32 0 0 40.6 5.1 41 0 0	260075.3 54 0 0 35.1 5.5 32 0 0	28 62 1.2975	126233 13.8 0 0 73.4 0.7 78.3 0 0	113056 17 0 0 51.4 6.7 39 0 0	1256944.8 135 0 0 76.5 9.4 52 0 0
A 19.8 0.00060714 122300 2 2 0	A 19.8 0.00060714 122300 2 2 0	12 29 1.2925	A 19.8 0.00060714 122300 2 2 0	A 19.8 0.00060714 122300 2 2 0	A 19.8 0.00060714 122300 2 2 0
70897.9 14 0 0 33 4.5 35 0 0	124150 31 0 0 32.3 4.6 33 0 0	30 57 1.26	145207 17.6 0 0 63 0.6 55.6 0 0		1587006.9 161 0 0 81.4 9.8 55 0 0
A 19.8 0.00060714 122300 2 2 0	A 19.8 0.00060714 122300 2 2 0	17 42 1.2725	A 19.8 0.00060714 122300 2 2 0	G08	A 19.8 0.00060714 122300 2 2 0
	149903.5 36 0 0 34.6 4.6 43 0 0	17 38 1.2225		0 0 0	
G02	A 19.8 0.00060714 122300 2 2 0	24 57 1.27	G30	0 92 20 344.99 1.122e+06 4798	G07
0 0 0		29 76 1.3525	0 0 0	105	0 0 0
0 80 16 344.99 1.151e+06 4798	G09	31 70 1.2225	0 65 40 346.11 1.03e+06 5000	0 2.311 0.253	0 100 34 344.99 1.16e+06 4798
105	0 0 0	15 36 1.2775	105	1 16.3	105
0 1.886 0.180	0 56 40 344.99 1.117e+06 8875	7 19 1.32	0 1.316 0.132	-1	0 1.937 0.282
1 16.3	105	18 39 1.2675	1 16.3	0	1 16.3
-1	0 2.135 0.236	31 58 1.3225	-1	1	-1
0	1 16.3	28 60 1.2675	0	74.09 3.60	0
1	-1	40 74 1.3325	1	12.11 1.211	1
108.21 10.93	0	16 34 1.2725	93.18 5.73	2.226 0.2226	152.17 4.54
12.88 1.288	1	15 28 1.3025	12.61 1.261	46 108 2.21	12.47 1.247
1.638 0.1638	99.91 5.14	46 102 1.255	1.225 0.1225	27 60 2.52	1.301 0.1301
3 6 2.02	12.02 1.202	17 38 1.2625	7 13 1.33	32 88 2.55	104 129 1.7
3 3 2.64	2.016 0.2016	13.15 18.73 1.275125	9 18 1.29	16 39 2.16	55 75 1.95
2 3 2.19	12 34 2.27	11.95 74.85 1.275125	7 14 1.33	16 52 2.09	136 189 1.76
3 5 1.83	8 13 2.05	10.49 21.02 1.275125	18 36 1.3	14 63 2.3	144 179 1.62
1 1 1.87	10 18 2.18	11.86 79.69 1.275125	8 15 1.36	45 114 2.48	102 131 1.77
6 14 1.78	28 64 2.41	12.3 82.04 1.275125	5 11 1.39	25 74 2.54	190 205 1.91
1 2 1.9	10 11 2.57	11.14 14.78 1.275125	8 17 1.35	19 60 2.4	77 90 1.51
24 34 1.6	13 23 2.36	13.51 41.36 1.275125	16 31 1.24	14 25 2.54	85 107 1.78

1 2 1.64
9 23 1.74
13 16 2.5
1 3 2.21
21 44 2.03
39 59 1.98
3 8 1.87
25 59 1.83
10.31 57.21 2.026
12.37 73.11 1.863
11.82 48.03 1.77
11.86 76 1.9
11.00 28.28 1.75
14.88 39.24 1.846
12.34 48.26 1.9
13.24 85.84 1.74
12.66 23.2 1.763
14.05 84.54 1.896
13.98 62.03 1.773
12.27 68.2 1.773
13.89 69.19 1.94
13.81 67.91 1.94
7.75 70.18 1.603
12.48 28.51 1.72
13.00 86.05 1.646
13.21 35.81 1.596
12.95 44.59 2.006
14.7 72 1.616
14.19 56.49 1.896
12.79 52.98 1.896
11.95 73.12 1.913
12.6 45.12 1.52
14.3 38.3 1.926
14.24 87.73 1.796
10.78 72.59 1.796
11.68 87.68 1.703
11.59 33.63 1.703
12.26 56.65 2.15
12.83 43.8 1.966
14.74 62.4 1.806
13.41 94.81 1.806
11.67 79.39 1.933
13.51 86.67 2.02
10.82 47.44 1.87
12.91 54.33 1.916
13.6 3.39 1.916
14.6 20.85 1.916
35 50 2.06
9 21 1.85
8 16 2.06
16 24 2.02
7 13 1.88
12 18 2.28
18 42 1.86
12 19 2.13
21 48 2.14
16 30 2.07
14 19 1.9
23 43 1.96
18 23 2.13
17 23 1.98
14 39 1.96
19 37 1.8
6 19 1.92
20 55 1.94
20 31 2.32
17 19 1.82
27 67 1.8
12 25 1.94
10 24 1.86
15 32 1.76
19 36 2.15
13 24 2.71
9 11 2.14
14 28 1.77
12 25 1.77
10 15 1.69
14 33 2.08
22 27 2.15
13 38 1.99
9 15 1.87
11.63 45.0 1.736
12.29 54.0 2.493
12.54 32.0 2.493
12.62 11.0 2.493
10.18 36.0 1.94
12.19 64.0 2.42
13.74 27.0 2.42
11.43 68.0 2.42
14.02 36.0 2.42
12.27 77.0 2.42
9.0 89.0 2.42
9.41 55.0 2.42
14.93 84.0 2.42
13.02 25.26 1.275125
11.3 14.1 1.275125
12.59 10.66 1.275125
14.18 68.37 1.275125
13.48 66.96 1.275125
13.85 51.96 1.275125
11.72 14.48 1.275125
14.46 30.71 1.275125
14.47 77.97 1.275125
11.39 74.86 1.275125
13.92 41.37 1.275125
13.51 35.82 1.275125
11.45 68.85 1.275125
12.84 35.51 1.275125
11.4 61.24 1.275125
11.16 32.28 1.275125
11.07 12.57 1.275125
13.62 64.21 1.275125
10.52 82.03 1.275125
10.26 12.87 1.275125
13.1 8.39 1.275125
12.25 73.18 1.275125
11.2 60.41 1.275125
12.6 15.95 1.275125
11.24 56.26 1.275125
13.04 24.72 1.275125
15.41 57.37 1.275125
13.66 19.96 1.275125
11.09 54.04 1.275125
14.22 57.63 1.275125
14.64 58.29 1.275125
12.25 50.74 1.275125
12.45 22.33 1.275125
13.88 82.6 1.275125
14.43 57.21 1.275125
13.19 37.26 1.275125
12.53 38.04 1.275125
15.21 42.41 1.275125
14.31 5.56 1.275125
11.86 74.32 1.275125
13.15 83.89 1.275125
12.09 6.52 1.275125
11.49 13.95 1.275125
13.69 10.77 1.275125
15.08 17.99 1.275125
12.14 77.68 1.275125
12.27 39.69 1.275125
8 16 1.31
23 45 1.37
9 18 1.31
12 22 1.27
7 16 1.33
10 21 1.3
11 21 1.48
4 7 1.27
8 18 1.32
9 17 1.41
9 18 1.25
23 42 1.37
11 23 Dpar
10 24 1.3285
9 18 1.3285
12 18 1.3285
18 28 1.3285
12 18 1.3285
12 22 1.3285
8 20 1.3285
9 16 1.3285
11 24 1.3285
11 21 1.3285
16 27 1.3285
16 30 1.3285
5 10 1.3285
10 19 1.3285
12 20 1.3285
7 12 1.3285
6 10 1.3285
10 16 1.3285
10 17 1.3285
14.42 69.57 1.3285
13.92 30.18 1.3285
13.83 77.67 1.3285
12.41 76.25 1.3285
12.03 46.37 1.3285
13.57 67.11 1.3285
11.73 63.65 1.3285
14.26 56.63 1.3285
11.77 32.67 1.3285
14.39 64.58 1.3285
12.69 32.43 1.3285
13.35 19.23 1.3285
12.75 84.05 1.3285
12.41 46.87 1.3285
11.58 6.66 1.3285
44 134 2.17
23 71 1.9
51 112 2.2
46 119 2.04
46 132 1.88
51 137 2.05
10 36 1.88
23 50 2.7
65 131 2.08
30 65 2.02
14.07 79 2.503
9.31 80 1.667
10.44 82 1.667
10.67 74 1.667
7.73 56 1.667
13.24 54 2.31
14.91 89 2.31
14.6 68 2.31
11.22 51 2.49
12.46 85 2.49
9.29 17 2.49
11.19 75 2.49
15.83 76 2.016
14.4 41 1.893
15.26 26 1.893
13.61 76 2.323
13.74 87 2.323
14.28 76 2.323
14.12 52 1.856
15.38 37 1.856
11.17 61 2.596
8.23 77 2.596
13.09 36 2.173
13.77 3 2.173
13.6 25 2.486
10.63 78 2.486
12.75 80 2.73
16.61 35 2.613
12.6 83 2.613
15.58 65 2.26
9.21 63 2.223
9.49 70 2.526
12.48 51 2.526
13.81 36 2.526
12.18 63 2.13
13.97 44 2.263
14.18 56 2.346
54 78 1.95
208 267 1.71
101 140 1.83
146 178 1.64
124 147 1.53
99 112 1.5
138 177 1.62
267 333 1.72
67 92 1.71
73 123 1.85
97 143 1.79
89 114 1.52
118 151 1.79
25 43 2.64
8 19 2.85
6 11 2.75
6 9 2.43
5 8 2.61
14 24 2.57
6 13 2.81
15 25 2.73
12 20 3.09
3 5 2.91
9 11 2.55
10 16 3.06
5 12 2.38
12.53 52.55 1.77
12.37 88.42 1.77
12.06 79.81 1.77
12.29 77.47 1.77
10.63 36.49 1.77
13.18 74.13 1.873
12.16 74.89 1.873
13.18 81.41 1.873
11.61 67.83 1.873
13.58 71.19 1.716
10.86 22.8 1.716
11.11 44.45 1.716
12.41 12.71 1.716
10.84 71.92 1.69
13.3 40.25 1.69
11.88 86.55 1.69
14.49 85.42 1.793
11.41 60.05 1.793
13.14 11.55 1.793
12.62 14.44 1.793
13.78 42.0 1.896

13.34 13.35 1.976
13.73 40.95 1.976
13.19 45.48 1.976
13.77 66.02 1.976
14.48 26.48 1.863
12.46 54.6 1.71
11.56 81.13 1.826
14.5 20.04 1.946
15.46 27.18 1.946
12.88 60.82 2.166
12.87 33.02 2.05
13.55 56.77 1.873
13.25 85.94 1.846
11.39 32.85 1.846
12.65 53.6 1.846
10.1 44.2 1.843
13.93 17.38 1.983
15.19 67.48 1.89
14.08 36.4 1.786
11.07 59.47 1.786
15.57 44.32 2.16
14.64 62.39 1.953
9.01 42.27 1.786
11.87 59.37 1.163
15.76 46.75 1.86
14.95 39.14 1.836
8.34 62.95 1.92
15.24 85.4 1.91
14.5 77.14 1.91
13.73 78.12 2.06
14.32 58.84 1.89
13.62 87.09 1.89
10.61 75.78 2.023
10.94 35.26 2.186
14.12 63.22 2.013
11.21 52.78 1.97
11.22 11.22 1.796
10.8 34.37 1.796
14.11 71.43 1.94
11.61 84.16 1.91
13.6 73.37 1.85
9.02 58.0 2.42
14.04 81.0 1.95
9.35 46.0 1.95
14.38 81.0 1.953
13.6 69.0 2.37
10.57 83.0 2.193
12.49 56.0 2.193
8.56 69.0 2.31
13.08 74.0 2.31
9.66 42.0 2.31
9.91 56.0 2.31
10.86 44.0 1.793
10.81 75.0 1.793
13.29 50.0 1.92
14.48 53.0 1.92
13.16 89.0 2.013
10.33 78.0 2.013
11.05 59.0 2.013
11.47 69.0 2.84
14.32 82.0 1.786
13.69 23.0 1.786
10.15 1.0 2.103
12.57 1.0 2.103
10.35 28.0 2.103
10.57 61.0 2.103
13.94 35.0 2.37
9.24 78.0 2.376
13.8 47.0 2.376
13.26 67.0 2.356
13.79 58.0 2.356
9.77 32.0 2.356
11.94 16.0 2.356
10.38 69.0 2.356
14.88 58.0 2.356
11.94 51.0 2.356
14.73 62.0 1.943
15.73 41.0 1.943
8.09 75.0 1.943
11.81 41.0 1.943
12.18 85.0 1.943
16.68 14.0 2.32
9.61 55.0 2.32
13.38 72.0 2.32
15.14 10.91 1.275125
14.64 57.97 1.275125
13.44 34.57 1.275125
13.53 29.04 1.275125
12.58 9.07 1.275125
15.95 79.72 1.275125
13.66 83.17 1.275125
11.36 66.63 1.275125
10.74 67.99 1.275125
13.17 68.65 1.275125
13.5 19.31 1.275125
12.01 10.41 1.275125
15.02 17.35 1.275125
13.24 19.69 1.275125
12.27 59.01 1.275125
11.46 47.88 1.275125
13.6 19.69 1.275125
14.98 26.73 1.275125
13.61 45.21 1.275125
14.1 82.72 1.275125
13.86 58.56 1.275125
13.85 12.89 1.275125
13.63 87.01 1.275125
12.11 15.12 1.275125
12.23 16.00 1.275125
15.76 64.58 1.275125
10.73 11.9 1.275125
13.52 29.46 1.275125
12.2 11.92 1.275125
12.89 56.69 1.275125
10.79 61.00 1.275125
11.87 86.45 1.275125
13.69 32.45 1.275125
11.12 55.68 1.275125
13.12 35.9 1.275125
10.72 76.25 1.275125
14.11 81.05 1.275125
12.38 17.82 1.275125
10.21 58.99 1.275125
11.71 6.02 1.275125
12.53 84.54 1.275125
13.07 80.01 1.275125
12.12 70.44 1.275125
12.97 47.61 1.275125
14.59 42.98 1.275125
12.09 64.12 1.275125
12.82 63.1 1.3285
13.67 25.16 1.3285
12.39 65.63 1.3285
13.24 25.25 1.3285
10.35 87.87 1.3285
15.9 19.06 1.3285
12.67 13.7 1.3285
12.91 29.96 1.3285
11.59 5.85 1.3285
15.14 4.21 1.3285
11.84 34.06 1.3285
12.17 67.77 1.3285
11.32 81.46 1.3285
10.77 42.43 1.3285
12.37 89.62 1.3285
11.27 16.8 1.3285
11.77 58.24 1.3285
12.06 6.25 1.3285
11.48 69.02 1.3285
14.17 38.23 1.3285
12.72 32.26 1.3285
11.95 48.07 1.3285
13.82 69.02 1.3285
12.14 51.04 1.3285
13.31 70.07 1.3285
11.55 43.59 1.3285
13.62 88.87 1.3285
11.74 59.58 1.3285
11.02 32.82 1.3285
13.13 41.48 1.3285
13.81 3.37 1.3285
11.11 62.74 1.3285
11.56 79.52 1.3285
13.75 74.78 1.3285
13.47 55.46 1.3285
11.76 15.44 1.3285
13.89 2.31 1.3285
12.16 21.14 1.3285
12.9 34.23 1.3285
13.46 76.01 1.3285
10.17 28.45 1.3285
10.77 64.36 1.3285
12.51 68.04 1.3285
15.41 3.4 1.3285
13.54 58.99 1.3285
12.33 18.44 1.3285
12.71 39.92 1.3285
14.48 80 2.346
10.55 16 2.466
13.87 75 2.466
9.89 11 2.346
9.5 67 2.346
12.63 56 2.346
10.1 89 2.346
8.84 53 2.346
9.15 62 2.736
8.04 62 2.736
9.57 34 2.736
11.39 63 2.736
11.43 81 2.26
9.64 31 2.26
8.41 78 2.26
14.39 15 2.453
14.44 67 2.453
10.37 60 2.396
11.58 84 2.396
10.08 40 2.473
9.16 62 2.473
16.15 58 2.086
13.37 54 2.25
10.59 62 2.25
11.08 43 2.25
13.36 56 2.233
14.81 30 2.233
9.05 44 2.233
10.48 61 2.233
14 87 2.2
11.19 49 2.2
9.74 46 2.66
9.8 62 2.553
8.37 71 2.553
15.05 30 2.803
12.61 87 2.803
9.71 51 1.99
13.4 58 1.99
14.45 25 2.3
10.3 79 2.07
10.6 56 2.513
11.92 43 2.513
13.67 38 2.446
11.6 67 2.196
9.71 71 2.196
11.9 26 2.196
12.41 0 2.196
13.76 37.0 1.896
10.91 65.0 1.896
13.67 82.0 1.896
10.93 57.0 1.896
12.0 55.0 1.896
10.81 89.0 1.896
13.78 73.0 1.896
15.33 88.0 1.896
13.56 13.0 1.896
14.83 34.0 1.863
13.47 58.0 1.863
9.04 77.0 1.863
14.27 89.0 1.863
13.11 83.0 2.136
12.8 62.0 2.136
12.94 83.0 2.136
12.71 71.0 1.903
13.6 17.0 1.903
12.82 39.0 1.903
15.38 85.0 1.903
12.18 81.0 1.903
11.68 35.0 1.903
7.41 12.0 1.903
10.18 21.0 1.946
11.09 72.0 1.946
13.44 85.0 1.946
13.24 74.0 1.946
12.83 57.0 1.946
13.36 63.0 1.946
13.25 33.0 1.946
12.56 72.0 1.946
12.78 70.0 1.946
12.3 88.0 1.946
11.91 41.0 1.946
12.01 76.0 1.906
12.82 65.0 1.906
12.16 38.0 1.906
13.42 35.0 1.906
13.68 68.0 1.906
12.16 64.0 1.84
11.15 53.0 1.84
12.24 83.0 1.84
13.2 51.0 1.84
12.74 44.0 1.84
13.94 40.0 1.98
11.41 84.0 1.98
13.13 74.0 1.98

12.05 47.25 1.3285
10.81 68.96 1.3285
11.37 76.04 1.3285

14.2 42.79 2.196
12.73 62 2.263
13.04 85 2.263
12.94 65 2.263
12.36 47 2.263
15.44 12 2.263
15.5 17 2.62
11.8 35 2.62

11.36 69.0 1.98
15.28 20.0 1.98
11.4 65.0 1.98
12.72 50.0 1.98
14.04 22.0 1.633
11.95 35.0 1.633
12.12 63.0 1.633
14.06 21.0 1.633
11.86 79.0 1.633
12.56 53.0 2.023
12.65 60.0 2.023
12.156 63.0 2.023
13.44 74.0 2.023
11.25 21.0 1.58
11.62 74.0 1.58
12.3 74.0 1.923
13.11 89.0 1.923
11.46 67.0 1.923
9.86 39.0 2.006
11.65 55.0 2.006
12.73 62.0 2.006
10.78 82.0 2.006
11.36 68.0 2.01
10.97 54.0 2.01
12.87 64.0 2.01
13.02 48.0 2.01
12.81 49.0 1.856
14.4 41.0 1.856
11.2 73.0 1.856
11.45 52.0 1.856
13.95 78.0 1.856
13.58 55.0 1.856

APPENDIX B
Supplementary material for chapter 4

Supplementary material for "**Tracing thermal history of the central Patagonian Andes and its broken foreland with detrital multi-dating of foreland basin deposits**"

MDS data

The data repository contains input files for multidimensional scaling.

Table 1. AFT ages
Table 2. AFT age uncertainties

TABLE 1. AFT AGES FOR CENOZOIC DETRITAL SAMPLES

MG1	MG3	MG4	MG5	MG6	MG11	MG12	MG13	MG14	MG15	MG16	MG45	MG47	MG48	MG49	MG54	MG55
37.39	187.91	37.92	38.99	65.43	52.57	69.79	47.96	25.17	43.81	21.89	48.86	57.43	37.96	34.57	60.6	102.03
41.53	112.12	33.72	24.92	65.43	57.32	22.76	43.98	25.84	24.37	16.97	34.24	40.59	28.49	25.82	68.33	84.14
95.7	54.39	36.24	41.77	91.41	43.75	21.68	26.1	58.57	65.6	22.13	34.24	71.71	32.55	62.01	52.31	107.09
51.71	49.75	36.24	24.4	76.27	30.97	18.98	27.81	24.28	31.32	56.4	14.29	68.85	22.8	53.25	31.07	78.26
74.56	43.55	36.24	20.55	76.27	42.94	23.55	25.17	27.81	36.53	63.41	15.59	82.24	32.55	48.43	78.07	89.37
44.84	21.81	26.86	19.53	50.95	38.86	24.74	43.98	54.09	72.85	21.21	53.43	73.74	50.56	27.9	69.39	118.88
111.52	58	31.8	44.97	65.43	66.83	19.52	58.57	65.86	51.51	53.44	13.03	44.99	35.97	53.25	37.1	89.37
246.66	47.49	31.52	36.56	41.71	36.09	45.45	12.6	19.58	33.72	56.4	34.24	36.98	45.53	70.91	17.6	78.26
83.4	63.25	38.14	43.31	57.29	33.69	70.87	70.22	35.86	36.53	72.42	56.97	57.43	57.97	36.59	76.09	85.82
40.77	51.2	31.25	83.27	44.11	75.92	69.31	43.98	58.57	26.32	56.4	23.37	51.71	52.5	42.3	55.57	98.54
59.28	63.25	33.56	35.46	45.87	42.09	22.76	58.57	27.68	23.09	15.43	42.78	61.51	41.4	53.25	52.18	82.54
87.44	195.69	47.77	74.78	44.88	32.4	26.77	35.21	87.66	38.11	56.4	28.55	66.95	37.96	50.73	22.86	113.53
40.05	52.22	24.73		41.71	53.98	11.51	43.98	58.57	43.81	65.03	15.36	50.7	39.27	37.03	87.35	103.22
79.34	62.62	38.82		50.95	39.92	20.7	58.57	31.07	48.66	14.76	13.32	74.81	39.61	70.91	31.26	77.03
39.58	53.56	28.63		65.43	36.76	19.52	35.21	58.57	72.85	56.4	12.25	32.37	32.55	71.86	54.07	95.86
95.7	52.22	33.23		45.87	69.99	14.24	35.21	58.57	26.32	15.43	61.51	62.19	41.82	33.86	92.07	75.91
81.97	121.2	22.67		91.41		32.5	24.3	87.66	24.83	56.4	14.29	67.36	36.94	37.42	35.78	82.54
86.34	58	28.33				17.52	25.17	50.24	24.37	56.4	21.42	79.38	28.49	50.73	36.24	97.43
63.96	65.21	38.14				16.27	39.11	58.57	26.86	61.5	15.83	43.12	44.06	16.18	44.49	99.22
69.92	173.69	22.12				14.09	28.67	28.75	28	56.4	18.05	49.26	35.05	44.41	59.26	89.37
108.16	63.77	34.85				47.01	43.98	67.54	81.9	29.92	13.54	35.71	32.55	39.49	37.1	71.59
100.45	132.29	33.72				15.19	65.86		93.51		20.78	51.71	28.49	44.41	93.76	98.24
150.24	43.55	16.01				64.83	39.11		72.85		32.11	43.12	56.86	17.8	46.34	
53.34	58	41.8				16.27	25.17		72.85		19.93	49.26	57.61	30.93	36.59	
65.83	55.94	45.27				42.62	20.14		81.9		24.48	39.81	42.69	59.14	48.35	
94.04	65.21	28.63				14.7	39.11		72.85		19.78	51.71	28.49	44.41	100.68	
111.52	58	36.24				45.45	43.98		22.79		38.04	47.02	29.73	53.25	18.97	
78.92	21.81	24.73				49.39	43.98		79.43		18.46	43.12	33.34	58.13	23.46	
67.14	138.33	36.24				17.19	20.14		24.37		23.37	54.42	45.53	29.64	30.37	

79.85	80.17	27.09
83.82	37.89	47.23
79.85	186.62	29.24
71.19	206.4	29.01
81.29	86.81	17.28
74.56	63.25	40.25
89.37	43.55	51.71
	30.77	36.24
	38.72	41.4
	24.92	25.19
	43.55	45.27
	43.55	

28.89	25.17
11.99	39.11
19.38	22.03
25.29	25.17
14.54	29.35
53.44	58.57
14.7	20.73
75.57	50.24
70.87	58.57
83.08	58.57
63.04	63.87
84.96	17.63
75.57	65.86
68.05	16.03
90.58	58.57
13.4	58.57
77.92	87.66
75.57	16.03
82.4	70.22
75.57	16.03
68.05	17.63
69.79	58.57
13.4	52.74
14.7	58.57
16.75	58.57
15.82	87.66
15.71	58.57
12.66	19.58
	17.63
	58.57
	58.57
	58.57
	58.57
	58.57
	87.66
	70.22
	87.66
	58.57
	54.09
	58.57
	58.57
	58.57
	58.57
	50.24

72.85
87.32
19.95
25.8
39.84
24.37
72.85
28.85
77.11
87.32
79.43
78.02
72.85
35.35
34.61
29.24
14.64
72.85
72.85
72.85
65.6

48.86	64.57	35.97	72.72	55.57
31.14	44.99	26.82	48.43	21.67
56.97	38.34	34.17	31.61	63.47
38.04	43.12	29.73	37.03	19.22
16.67	39.81	39.8	63.35	30.03
19.78	43.12	35.44	41	26.89
28.55	73.74	32.55	27.07	44.49
34.24	64.57	45.53	47.36	24.22
34.24	36.33	36.74	59.14	92.35
28.55	85.95	35.05	59.14	42.2
28.55	34.52		48.43	21.85
25.96	32.37		50.52	21.43
31.14	68.85		50.73	25.71
24.48	85.95		35.55	22.94
24.48	53.85		44.41	47.83
17.14	71.71		44.41	21.74
26.36	45.98		32.92	52.93
42.78	57.43		73.84	75.23
27.53	50.7		53.25	94.97
28.55	56.26		25.41	40.99
48.86	55.14		44.41	100.68
22.85	62.62		41	23.05
42.78	73.74		20.18	27
20.9	60.79		48.75	
16.81	73.74		70.91	
85.27			15.09	
89.73			34.04	
			30.36	
			71.59	
			63.59	
			37.42	
			41.8	
			50.73	
			59.14	
			28.3	
			27.67	
			31.75	
			22.76	

TABLE 2. AFT AGE UNCERTAINTIES FOR CENOZOIC DETRITAL SAMPLES

MG1	MG3	MG4	MG5	MG6	MG11	MG12	MG13	MG14	MG15	MG16	MG45	MG47	MG48	MG49	MG54	MG55
18.11	78.73	13.97	30.24	37.17	33.99	39.99	31.29	15.56	27.75	11.66	27.76	46.94	29.03	14.34	39.53	45.38
20.28	43.57	9.26	10.84	37.17	37.4	7.25	28.43	8.4	18.19	17.81	37.53	22.61	30.24	9.26	39.15	36.21
66.14	27.94	12.04	26.62	76.56	10.62	16.07	14.02	47.87	43.25	13.61	37.53	17.27	34.82	11.22	16.9	26.37
33.18	39.93	16.26	18.32	62.34	14.88	11.42	17.31	4.47	23.7	65.16	10.53	33.36	23.93	35.11	13.59	35.58
49.78	48.71	22.96	15.3	62.34	14.99	7.19	13.48	17.31	39.48	43	7.3	30.3	34.82	31.6	21.02	20.59
28.41	13.38	14.43	10.26	39.87	8.75	11.69	28.43	30.99	84.16	13.01	27.44	25.59	39.57	10.66	25.27	108.61
41.39	30.02	10.97	28.85	52.51	29.11	11.76	47.87	44.65	28.69	25.1	5.54	20.69	22.38	35.11	28.37	38.84
82.85	30.98	17.12	23.04	22.73	11.36	35.25	9.23	20.66	25.65	46.1	26.55	16.69	28.84	59.38	7.49	25.24
19.79	26.21	21.03	33.89	64.08	18.19	36.41	58.81	11.94	27.93	50.05	32.96	38.34	18.14	15.25	25.61	30.3
31.38	26.11	15.18	57.54	21.6	21.67	24.01	24.64	39.11	16.11	46.1	14.41	34.09	33.68	21.11	35.93	30.9
22.33	26.21	16.39	27.29	35.57	46.13	23.89	39.11	9.04	17.19	16.13	27.66	32.13	31.86	35.11	12.24	40.85
34.53	25.78	12.45	39.45	16.44	24.64	20.04	22.3	107.41	20.69	37.66	30.85	21.23	41.03	40.72	6.98	39.04
19.5	34.43	15.25		18.58	14.03	5.29	49.2	67.67	27.75	34.31	6.57	25.86	19.07	18.25	28.78	21.66
28	24.45	24.74		39.87	13.21	15.31	67.67	19.49	26.96	10.9	4.91	20.23	15.24	42.03	11.86	16.79
17.59	30.68	17.82		37.17	12.09	11.76	22.3	67.67	42.14	65.16	8.98	20.4	15.61	22.16	20.2	25.58
29.75	34.43	10.97		16.83	57.21	14.69	38.59	30.32	11.41	11.41	24.02	20.25	15.25	18.52	21.35	24.37
29.05	59.89	17.03		76.56		13.19	12.99	107.41	10.74	65.16	14.88	26.6	16.31	20.63	12.92	40.85
24.86	38.72	13.66				18.19	26.92	40.32	11.53	32.63	11.39	39.29	21.39	40.72	14.83	49.58
29.7	31.31	7.13				16.85	30.61	67.67	11.66	35.98	6.78	48.24	19.72	16.91	34.5	32.16
35.92	21.79	6.1				5.95	11.73	11.02	12.18	46.1	7.77	39.53	26.65	49.68	33.42	38.84
33.19	22.6	8.61				21.16	24.64	35.63	55.53	18.77	8.13	16.07	34.82	30.9	13.43	59.96
23.57	48.97	7.6				15.69	44.65		64.62		11.03	34.09	30.24	49.68	33.9	37.05
39.29	34.46	9.66				36.83	21.67		48.64		20.24	21.62	28.51	10.8	22.85	
26.62	38.72	18.99				16.85	19.05		59.54		9.45	22.87	14.95	16.79	11.48	
33.58	1.67	29.27				19.03	10.66		55.53		15.14	25.54	26.9	34.22	23.92	
39.78	21.53	17.82				4.41	30.61		84.16		12.08	34.09	21.39	28.71	54.43	
45.71	31.31	28.1				20.39	34.81		8.51		29.77	30.68	18.28	13.4	9.91	
37.59	38.72	15.25				24.44	28.43		46.47		7.38	10.9	14.63	15.51	10.1	
44.27	23.15	16.26				5.18	10.66		25.71		14.41	25.56	49.9	10.18	8.43	
41.71	53.81	8.12				10.9	26.92		59.54		39.22	43.78	22.38	21.75	35.93	
56.83	19.99	21.72				8.71	30.61		73.13		23.96	20.69	20.07	13	8.62	
41.71	18.74	14.13				10.12	13.51		20.85		46.56	21.24	12.28	12.18	25.55	
31	75.01	15.66				26.67	15.56		19.31		29.77	27.88	18.28	18.25	8.98	
47.56	88.69	12.81				8.68	14.22		12.59		6.63	25.54	10.27	33.09	9.3	
43.13	35.58	31.5				29.76	67.67		18.19		12.08	24.16	14.46	26.31	10.8	
74.84	37	41.5				10.74	15.52		84.16		17.83	50.96	24.64	11.03	34.5	
	19.3	22.96				43.72	40.32		13.77		21.69	43.78	28.84	26.71	8.11	
	30.3	16.3				36.41	47.87		36.73		37.53	14.2	12.59	48.34	16.74	
	18.86	12.06				29.45	67.67		73.13		30.85	52.73	26.65	39.49	13.97	
	48.71	35.83				31.95	37.37		46.47		30.85	18.95		31.6	10.27	
	34.46					57.6	18.5		40.75		12.49	11.82		9.86	5.85	
						35.73	44.65		84.16		23.96	40.81		40.72	11.12	
						44.87	16.75		17.09		26.18	30.55		38.97	6.49	
						75.86	39.11		15.26		9.93	27.66		35.15	11.92	
						9.76	67.67		22.04		9.01	27.12		35.15	5.75	
						27.39	107.41		10.7		20.04	25.93		16.08	26.41	

29.22	16.75	59.54	33.85	46.94	19.84	19.66
48.21	58.81	84.16	9.94	25.86	35.11	38
43.72	16.75	42.14	17.83	16.33	19.23	16.93
44.87	18.5	43.25	39.22	22.49	28.71	38.58
39.99	67.67		17.22	36.64	18.63	14.01
13.8	34.77		33.85	29.51	6.46	14.33
10.74	67.67		9.93	28.95	14.82	
7.78	67.67		7.9	25.59	59.38	
7.34	107.41		39.6		7.05	
11.5	67.67		35.21		12.45	
13.01	11.94				12.47	
	8.29				18.7	
	67.67				17.16	
	67.67				20.63	
	67.67				23.28	
	67.67				40.72	
	47.87				39.49	
	107.41				11.56	
	58.81				11.29	
	107.41				15.46	
	67.67				7.34	
	30.99					
	67.67					
	33.89					
	67.67					
	47.87					
	40.32					

APPENDIX C
Supplementary material for chapter 5

Supplementary material for "**Tectonothermal history of the San Bernardo Fold and Thrust Belt from low-temperature thermochronology**"

Thermal histories modeling

The data repository contains input files for inverse thermal modeling of the results presented in Figure 1.

Figure 1: Thermal history results from QTQt (samples MG7, MG17 and MG20).

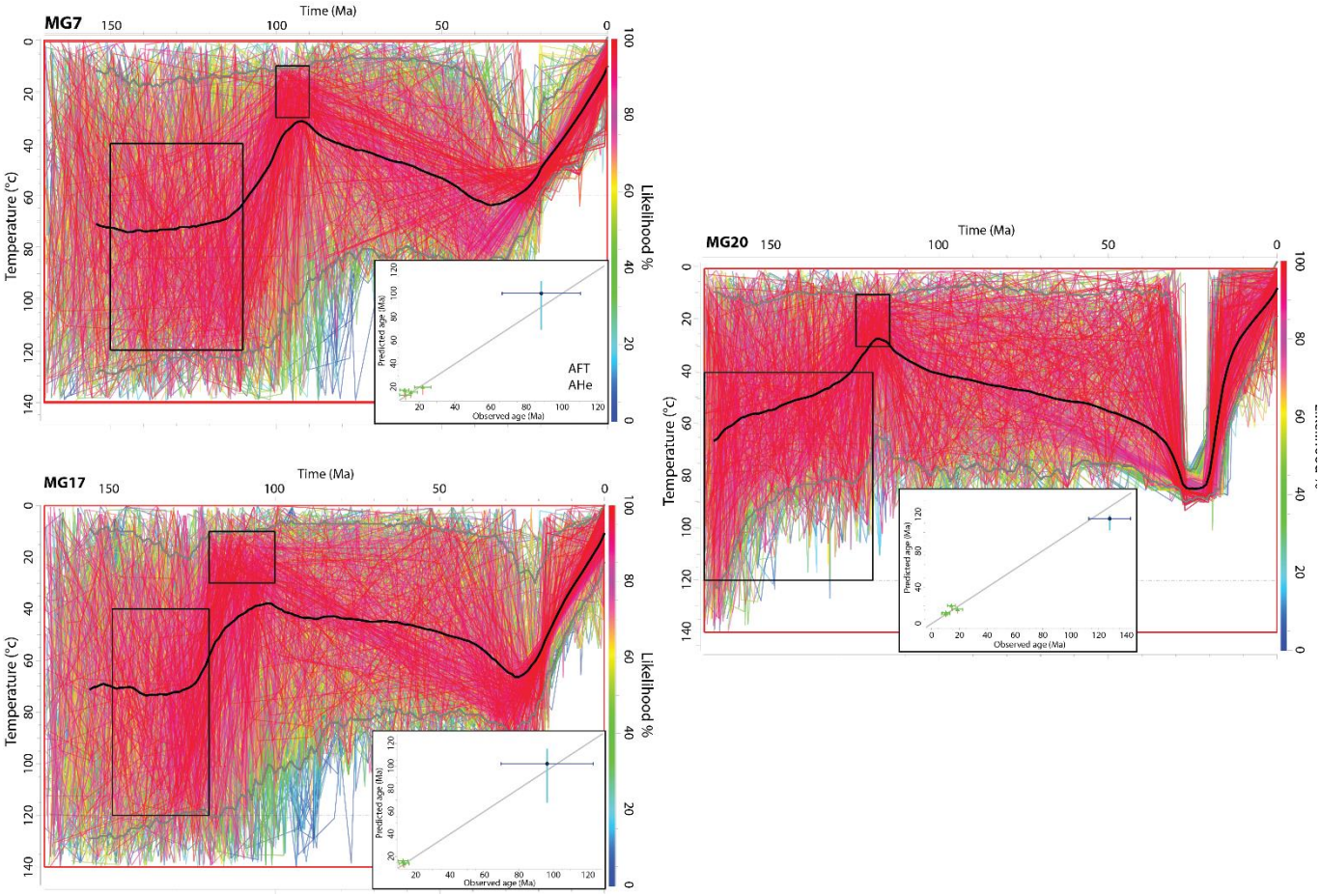

Figure 1. Thermal history results from QTQt with related observed/predicted ages plot.

MG7
-69.28 -45.53 0
0 0 0 0 0 0
105
0 1.5 0.5
0 16.3
0
0
1
0 0
0 0
0 0
4
2
22361.9 8.61 0 0 22.12 2.29 62.07 0 0
A 19.8 0.00060714 122300 2 2 0
18042.58 9.87 0 0 15.49 1.8 45.23 0 0
A 19.8 0.00060714 122300 2 2 0
15984.49 10.9 0 0 12.42 1.56 36.6 0 0
A 19.8 0.00060714 122300 2 2 0
11912.6 8.52 0 0 11.96 1.29 55.15 0 0
A 19.8 0.00060714 122300 2 2 0

MG7
0 0 0
0 0 20 346.11 1.11e+06 5000
105
0 1.625000 0.137898
1 16.3
0
0
1
88.54 10.95
0.00 0
0.000 0
5 7 1.79
8 19 1.78
3 6 1.47
3 5 1.65
5 9 1.72
3 7 1.79
2 5 1.69
7 15 1.74
3 6 1.82
7 16 1.65
2 4 1.44
2 4 1.74
11 27 1.46
6 12 1.68
6 13 1.66
8 19 1.47
2 4 1.53
4 10 1.45
8 17 1.56
2 4 1.41

MG17
-69.02 -45.42 0
0 0 0 0 0 0
105
0 1.5 0.5
0 16.3
0
0
1
0 0
0 0
0 0
2
2
8914.7 5.58 0 0 13.52 1.46 58.85 0 0
A 19.8 0.00060714 122300 2 2 0
15714.7 10.43 0 0 12.84 1.43 53.02 0 0
A 19.8 0.00060714 122300 2 2 0

MG17
0 0 0
0 0 11 346.11 967000 5000
105
0 1.685455 0.127386
1 16.3
0
0
1
96.41 13.37
0.00 0
0.000 0
13 24 1.79
14 26 1.78
15 18 1.47
8 14 1.65
4 7 1.72
3 5 1.79
4 8 1.69
6 11 1.74
5 10 1.82
6 11 1.65
5 9 1.44

MG20
-69.3 -45.14 0
0 0 0 0 0 0
105
0 1.5 0.5
0 16.3
0
0
1
0 0
0 0
0 0
4
2
21272.6 17.38 0 0 10.45 1.27 44.72 0 0
A 19.8 0.00060714 122300 2 2 0
67142.5 38.95 0 0 14.43 1.39 90.87 0 0
A 19.8 0.00060714 122300 2 2 0
39320.5 32 0 0 10.39 1.48 32.8 0 0
A 19.8 0.00060714 122300 2 2 0
58989.4 26.36 0 0 18.72 1.9 69.7 0 0
A 19.8 0.00060714 122300 2 2 0

MG20
0 0 0
0 0 53 346.11 1.31e+06 5000
105
0 1.540189 0.116841
1 16.3
0
0
1
128.00 7.52
0.00 0
0.000 0
8 16 1.79
5 11 1.78
2 5 1.47
2 6 1.65
8 17 1.72
4 7 1.79
3 5 1.69
14 30 1.74
4 9 1.82
6 13 1.65
12 20 1.44
5 7 1.74
5 11 1.46
2 4 1.68
6 11 1.66
8 18 1.47
4 8 1.53
14 20 1.45
4 7 1.56
4 6 1.41
12 21 1.53
9 12 1.45
6 12 1.56
9 13 1.41
4 7 1.53
5 6 1.45
10 19 1.56
19 25 1.41
36 49 1.53
4 7 1.45
12 18 1.56
3 5 1.41
6 12 1.53
7 13 1.45
4 6 1.56
4 7 1.41
15 27 1.53
17 33 1.53
18 36 1.45
16 31 1.56
4 7 1.41
5 9 1.53
12 22 1.45
6 12 1.56
22 29 1.41
32 63 1.53
4 7 1.45
7 14 1.56
26 49 1.41
14 17 1.53
2 4 1.45
7 13 1.56
6 11 1.41

APPENDIX D
Supplementary material for chapter 6

Supplementary material for "**Predict thermal history of mountain range from detrital cooling ages distribution in catchments: insights from north-central Patagonian Andes**"

Thermal histories modeling

The data repository contains input files for inverse thermal modeling of the results presented in Figures 8, 9, 10 and 11 (Chapter 6). These input data correspond to detrital fission tracks data and hypsometry data used to create the dummy files.

11 1 D		11 1 D		11 1 D		11 1 D		11 1 D	
0	75	0	55	0	1	0	504	0	290
0.1	501	0.1	401	0.1	363	0.1	874	0.1	673
0.2	634	0.2	536	0.2	667	0.2	1016	0.2	765
0.3	734	0.3	727	0.3	835	0.3	1118	0.3	878
0.4	834	0.4	865	0.4	1014	0.4	1158	0.4	984
0.5	945	0.5	968	0.5	1177	0.5	1197	0.5	1080
0.6	1044	0.6	1077	0.6	1320	0.6	1259	0.6	1134
0.7	1152	0.7	1198	0.7	1432	0.7	1324	0.7	1209
0.8	1238	0.8	1322	0.8	1543	0.8	1383	0.8	1292
0.9	1329	0.9	1444	0.9	1700	0.9	1451	0.9	1414
1	1587	1	1711	1	2167	1	1886	1	1734

Random Detrital Sample27	Random Detrital Sample28	Random Detrital Sample29	Random Detrital SampleCN4	Random Detrital Sample32
0.0 0.0 0.0	0.0 0.0 0.0	0.0 0.0 0.0	0.0 0.0 0.0	0.0 0.0 0.0
0 0 78 346.11 1170000.00 5000.00	0 0 100 346.11 1160000.00 5000.00	0 0 101 346.11 1150000.00 8875.00	0 0 92 346.11 1320000.00 5000.00	0 0 100 346.11 1130000.00 5000.00
105	105	105	105	105
0 2.00 0.50	0 2.00 0.50	0 2.00 0.50	0 2.00 0.50	0 2.00 0.50
1 16.30	1 16.30	1 16.30	1 16.30	1 16.30
0	0	0	0	0
0	0	0	0	0
1	1	1	1	1
25.400000 2.00000	9.500000 0.700000	8.200000 0.600000	78.100000 4.000000	42.500000 2.500000
0.000000 0.000000	0.000000 0.000000	0.000000 0.000000	0.000000 0.000000	0.000000 0.000000
0.000000 0.000000	0.000000 0.000000	0.000000 0.000000	0.000000 0.000000	0.000000 0.000000
2 11	6 137	10 240	23 58	9 59
3 12	5 100	3 91	12 28	6 37
4 32	1 30	2 56	13 31	12 87
2 14	1 25	4 84	17 52	2 7
1 6	4 92	1 31	15 47	10 51
8 61	3 85	2 64	31 113	4 14
1 25	1 27	7 210	18 53	4 15
5 42	4 91	3 92	16 68	2 11
4 20	5 119	2 51	8 15	5 20
1 4	5 86	2 59	9 27	5 29
3 28	2 38	3 82	16 56	5 22
3 20	1 13	2 74	15 54	2 5
3 39	4 58	1 29	10 39	3 9
1 6	3 69	6 137	14 59	2 10
2 14	2 30	9 192	15 29	2 7
3 22	2 38	4 136	17 57	5 25
7 63	4 43	7 183	16 65	3 9
2 23	2 25	3 71	8 24	4 15
2 15	5 48	4 97	16 59	7 39
1 5	2 52	2 53	14 46	9 52
5 54	2 19	2 68	10 24	3 8
5 45	4 30	1 19	15 43	4 14
3 35	1 18	2 49	11 29	3 7
9 108	4 94	3 37	18 45	4 13
3 26	2 38	3 70	14 38	10 54
1 13	3 54	3 79	12 23	2 9
1 15	2 65	1 28	16 54	4 16
4 34	2 26	2 42	21 57	3 8
2 16	1 31	1 21	14 45	4 15
3 22	2 29	2 37	13 24	4 14
2 15	2 55	1 19	16 34	3 15
2 16	3 87	1 20	10 16	3 15
5 24	4 119	2 40	13 32	8 25
4 22	1 9	4 67	13 22	6 18
9 68	5 59	3 83	34 93	5 22
4 29	2 31	2 41	14 56	4 17
2 17	2 16	2 32	7 12	4 12
4 13	2 18	2 29	24 78	3 13
4 27	3 115	3 80	21 47	6 21
3 23	9 157	4 88	16 66	8 36
1 8	2 61	2 54	10 34	3 22
1 10	4 33	5 104	17 79	6 24
7 83	2 28	3 47	17 48	7 16
5 54	1 10	5 107	17 66	4 15
3 24	2 16	2 37	8 28	3 10

3 24
4 33
4 41
1 7
3 32
1 8
2 19
4 44
2 17
2 13
3 14
5 57
4 16
3 12
5 31
3 14
1 6
2 8
4 22
5 36
1 7
3 22
1 5
1 4
2 9
3 14
3 23
2 16
1 5
1 7
3 20
3 27
3 15

2 13
9 125
2 46
2 57
1 11
6 166
4 118
3 89
1 31
7 174
4 98
2 43
6 113
2 46
1 31
2 57
2 45
3 33
2 45
1 21
3 68
2 22
5 97
5 163
2 64
1 23
2 70
2 53
2 58
7 151
4 89
2 75
1 20
2 35
8 191
2 43
2 60
3 32
2 44
2 65
3 84
1 14
4 118
6 120
5 112
1 16
3 75
3 101
2 40
8 142
3 39
7 89
2 50
5 156
3 82

2 48
1 32
3 71
1 14
8 194
2 50
4 101
1 37
2 55
4 96
2 77
3 51
5 131
5 119
6 159
3 57
3 87
4 96
3 52
2 63
4 99
2 33
2 48
1 22
3 69
1 31
1 26
3 55
10 265
2 64
1 30
1 23
3 41
5 128
5 132
2 52
6 133
3 85
2 41
1 15
3 86
6 123
4 72
4 98
1 27
3 79
3 76
2 35
1 32
3 73
3 56
4 93
4 109
1 31
3 100
4 96

19 43
19 56
20 39
12 30
9 35
13 35
4 8
34 140
5 17
25 113
22 56
9 24
32 89
21 82
10 46
13 52
13 45
9 19
11 21
27 50
29 57
36 66
17 47
25 54
18 49
6 11
21 40
28 86
7 16
8 20
8 21
17 39
7 18
15 48
5 16
22 73
15 50
8 36
13 33
15 24
15 42
6 14
16 38
7 23
15 27
7 28
17 61

2 8
11 51
3 17
8 43
2 16
3 11
22 109
4 12
7 26
3 11
2 10
6 22
5 27
25 80
6 29
4 13
7 28
4 14
3 8
4 18
7 38
5 16
5 22
4 18
3 21
5 17
4 18
8 48
15 72
6 38
3 8
9 41
7 24
1 4
6 32
3 10
6 31
10 85
3 11
5 15
7 49
7 50
2 9
5 27
14 81
12 60
4 14
2 6
6 24
14 48
6 30
3 13
2 14
4 10
2 7

11 1 D		11 1 D		11 1 D		11 1 D		11 1 D	
0	255	0	25	0	30	0	611	0	90
0.1	390	0.1	539	0.1	552	0.1	750	0.1	985
0.2	562	0.2	710	0.2	733	0.2	878	0.2	1238
0.3	741	0.3	836	0.3	856	0.3	989	0.3	1311
0.4	870	0.4	940	0.4	952	0.4	1109	0.4	1335
0.5	980	0.5	1030	0.5	1037	0.5	1230	0.5	1378
0.6	1080	0.6	1117	0.6	1123	0.6	1381	0.6	1441
0.7	1180	0.7	1203	0.7	1203	0.7	1544	0.7	1500
0.8	1288	0.8	1288	0.8	1278	0.8	1771	0.8	1549
0.9	1423	0.9	1387	0.9	1381	0.9	1926	0.9	1596
1	1884	1	1772	1	1894	1	3301	1	1726

Random Detrital Sample34	Random Detrital Sample35	Random Detrital Sample36	Random Detrital Sample38	Random Detrital Sample40
0.0 0.0 0.0	0.0 0.0 0.0	0.0 0.0 0.0	0.0 0.0 0.0	0.0 0.0 0.0
0 0 90 346.11 1100000.00 5000.00	0 0 100 346.11 1090000.00 5000.00	0 0 100 346.11 1070000.00 5000.00	0 0 61 346.11 1050000.00 5000.00	0 0 98 346.11 1030000.00 5000.00
105	105	105	105	105
0 2.00 0.50	0 2.00 0.50	0 2.00 0.50	0 2.00 0.50	0 2.00 0.50
1 16.30	1 16.30	1 16.30	1 16.30	1 16.30
0	0	0	0	0
0	0	0	0	0
1	1	1	1	1
29.800000 1.800000	13.900000 1.000000	34.700000 2.000000	19.300000 1.800000	17.500000 1.100000
0.000000 0.000000	0.000000 0.000000	0.000000 0.000000	0.000000 0.000000	0.000000 0.000000
0.000000 0.000000	0.000000 0.000000	0.000000 0.000000	0.000000 0.000000	0.000000 0.000000
17 56	2 26	3 22	2 10	3 25
5 23	3 34	6 29	2 8	6 46
15 55	3 46	4 20	1 7	5 30
10 27	4 38	5 27	3 18	4 26
9 23	2 32	6 20	6 36	3 23
9 20	3 36	19 108	2 11	10 111
3 13	2 19	2 8	10 112	4 31
3 15	1 11	1 12	5 64	1 21
5 29	1 19	9 44	4 58	3 88
4 20	1 16	3 25	5 51	11 119
4 15	4 34	9 40	3 19	5 63
2 6	6 82	15 76	2 14	3 21
8 51	6 77	2 14	3 30	2 22
6 46	6 93	3 15	2 15	3 36
2 11	3 34	10 32	2 26	3 13
12 47	5 59	3 13	2 13	7 58
6 15	1 7	9 37	2 25	3 25
5 35	3 31	25 99	2 13	4 35
10 47	2 22	9 34	2 15	3 34
4 22	5 73	16 87	1 7	8 75
3 30	2 30	4 17	3 30	2 14
3 20	2 13	7 39	3 21	6 59
7 64	3 38	6 29	1 5	3 31
8 75	2 26	9 41	3 38	3 18
1 8	5 71	17 95	1 8	5 63
4 15	3 26	11 55	1 7	3 41
6 26	1 11	1 6	1 4	1 10
10 40	3 23	7 39	2 16	5 60
4 33	4 31	2 22	2 26	3 28
3 32	2 19	3 11	6 89	8 137
6 46	3 22	12 81	2 17	4 53
10 67	3 25	9 52	3 14	4 40
7 41	4 52	3 14	1 8	2 32
2 21	2 21	2 10	2 18	3 29
8 37	2 31	9 63	2 8	3 38
2 14	2 25	8 46	2 13	4 29
8 47	2 29	5 31	2 28	2 34
4 32	2 32	8 39	3 34	4 51
5 45	3 40	5 29	2 19	6 61
5 30	2 30	8 41	2 9	4 39
7 41	4 70	3 14	3 22	4 33
11 68	1 8	6 27	1 5	4 36
19 93	5 48	7 35	2 9	3 18
8 66	1 11	3 18	1 6	7 84
5 24	3 28	6 34	3 13	4 31

3 19
3 12
5 42
12 108
6 40
8 56
7 41
8 49
2 29
3 14
5 40
9 64
9 57
14 117
9 56
10 73
5 46
4 44
3 23
2 19
1 16
3 22
8 76
2 15
3 27
4 31
5 36
5 32
2 14
1 8
6 39
8 68
7 56
8 64
2 26
2 11
8 41
6 38
3 32
2 8
4 42
2 22
3 24
3 18
9 71

2 23
1 9
16 238
2 19
2 20
4 45
2 21
3 32
1 14
3 34
2 23
3 63
8 106
2 34
2 21
3 51
2 28
5 78
4 65
3 52
2 36
3 56
2 20
2 39
4 58
6 92
4 40
10 164
2 18
2 27
4 70
3 42
2 24
2 44
1 11
3 49
4 86
2 24
2 37
3 36
1 15
3 57
2 41
5 48
7 119
6 84
2 25
4 69
1 15
4 54
3 52
2 22
3 29
1 16
2 18

7 51
1 5
2 12
9 48
8 41
12 86
5 23
4 16
6 33
7 43
6 20
2 14
3 18
3 20
5 38
2 13
6 41
1 9
6 43
2 14
6 46
7 42
11 73
2 12
1 8
8 59
1 6
4 19
5 18
5 20
4 19
22 121
2 8
3 12
5 29
3 22
5 20
6 24
2 10
5 22
7 30
7 49
4 18
3 9
2 16
14 84
5 15
3 13
3 8
3 11
4 12
1 6
4 14
3 13
3 15

5 67
2 11
2 19
2 13
1 11
6 56
2 22
3 24
2 39
1 9
1 4
1 6
7 131
3 17
3 14
3 35

5 58
3 44
6 88
2 23
6 68
3 24
3 22
2 23
3 25
4 54
2 32
6 31
6 32
2 16
4 24
5 41
3 34
4 39
2 29
5 18
2 16
1 12
9 121
3 31
4 35
3 32
2 13
2 24
4 54
4 32
2 36
7 54
3 27
5 33
3 44
1 9
3 33
3 38
9 63
2 32
6 56
2 19
2 22
2 29
2 17
1 20
1 24
7 60
3 32
1 7
3 27
12 104
3 31

APPENDIX E

STRUCTURAL CONTROLS ON JURASSIC GOLD MINERALIZATION, AND CRETACEOUS-TERTIARY EXHUMATION IN THE FORELAND OF THE SOUTHERN PATAGONIAN ANDES: NEW CONSTRAINTS FROM LA PALOMA AREA, DESEADO MASSIF, ARGENTINA.

María Lis Fernández[a], Stefano Mazzoli[b], Massimiliano Zattin[c], Elisa Savignano[c], **Marie Catherine Genge**[c], Stefano Tavani[d], Alejandro Garrone[e], Marta Franchini[a]

[a] CONICET - Centro Patagónico de Estudios Metalogenéticos, Departamento de Geología y Petróleo, Facultad de Ingeniería, Universidad Nacional del Comahue, Buenos Aires 1400, Neuquén, Argentina

[b] School of Science and Technology, Geology Division, University of Camerino (MC), Via Gentile III Da Varano, 62032 Camerino, (MC), Italy

[c] Dipartimento di Geoscienze, Università degli Studi di Padova, via G. Gradenigo 6, 35131 Padova, Italy

[d] Dipartimento di Scienze della Terra, dell'Ambiente e delle Risorse (DiSTAR), Università degli Studi di Napoli Federico II, Complesso di Monte S. Angelo, Via Cinthia, 21 - Edificio L, 80126 Napoli, Italy

[e] Minera Don Nicolás S.A., Estancia El Condor, Ruta Nacional Nro. 3 km 2080, Provincia de Santa Cruz, Argentina

This chapter describes newly discovered fault structures reactivated and associated with the formation of Au-Ag epithermal deposits in the Deseado Massif (La Paloma area). Based on field observation and apatite fission tracks data, it discusses the relation between the late reactivation of these faults with a late Early Cretaceous shortening event followed by a steady-state cooling of the Deseado Massif. MLF, SM and ES carried out the field structural analysis. MLF and AG carried out background geological mining investigations. MF integrated and supervised the ore geology part of the study. ST integrated the structural part of the study, also with diagrams. MZ, ES and MCG carried out the thermochronological work. MLF and SM wrote the paper, with the contribution of MZ for the thermochronological study. This paper has been published as: Fernández, M. L., Mazzoli, S., Zattin, M., Savignano, E., Genge, M. C., Tavani, S., Garrone A. and Franchini, M. (2020). Structural controls on Jurassic gold mineralization, and Cretaceous-Tertiary exhumation in the foreland of the southern Patagonian Andes: New constraints from La Paloma area, Deseado Massif, Argentina. Tectonophysics, 775, 228302. doi: 10.1016/j.tecto.2019.228302.

Tectonophysics 775 (2020) 228302

Contents lists available at ScienceDirect

Tectonophysics

journal homepage: www.elsevier.com/locate/tecto

Structural controls on Jurassic gold mineralization, and Cretaceous-Tertiary exhumation in the foreland of the southern Patagonian Andes: New constraints from La Paloma area, Deseado Massif, Argentina

María Lis Fernández[a], Stefano Mazzoli[b,*], Massimiliano Zattin[c], Elisa Savignano[c], Marie Catherine Genge[c], Stefano Tavani[d], Alejandro Garrone[e], Marta Franchini[a]

[a] CONICET - Centro Patagónico de Estudios Metalogenéticos, Departamento de Geología y Petróleo, Facultad de Ingeniería, Universidad Nacional del Comahue, Buenos Aires 1400, Neuquén, Argentina
[b] School of Science and Technology, Geology Division, University of Camerino (MC), Via Gentile III Da Varano, 62032 Camerino, (MC), Italy
[c] Dipartimento di Geoscienze, Università degli Studi di Padova, via G. Gradenigo 6, 35131 Padova, Italy
[d] Dipartimento di Scienze della Terra, dell'Ambiente e delle Risorse (DiSTAR), Università degli Studi di Napoli Federico II, Complesso di Monte S. Angelo, Via Cinthia, 21 - Edificio L, 80126 Napoli, Italy
[e] Minera Don Nicolás S.A., Estancia El Condor, Ruta Nacional Nro. 3 km 2080, Provincia de Santa Cruz, Argentina

ARTICLE INFO

Keywords:
Structural analysis
Multiple Inversion Method
Ore geology
Au-Ag epithermal veins
Low-temperature thermochronometry
Patagonia

ABSTRACT

Fluid-rock interaction occurring within high-permeability conduits represented by fault-fracture meshes is well known to control the development of hydrothermal ore deposits. In this study we document the fundamental role of four sets of precursor joints, reactivated as dilational faults displaying variable normal dip-slip and strike-slip components of motion, in the formation of epithermal Au-Ag deposits of economic interest. Paleostress analysis unravels how all the resulting four sets of hybrid extension-shear fractures are kinematically compatible with an extensional stress field characterized by multiple permutations between the σ_3 and the σ_2 axes. Such permutations are interpreted to be associated with dominantly normal fault reactivation of suitably oriented early joint sets as a result of continued regional extension, and by orthogonal stretching produced by differential downthrow of the hanging-wall blocks of laterally-terminating Jurassic normal faults.

Later fault reactivation appears to be associated with far field propagation of Andean stresses, marked by superposed strike-slip and reverse fault slip components recording roughly E-W horizontal compression. This late fault reactivation could be related with a late Early Cretaceous shortening event known to have affected the studied sector of the Deseado Massif. The subsequent tectonic evolution of the study area occurred within the general framework of a slow Cretaceous to Tertiary exhumation recorded by apatite fission track cooling ages. Our new thermochronometric results, recording steady-state cooling at a rate of c. 1 °C/Ma during the last 90 Ma, shed new light onto the post-Jurassic geodynamic evolution of the foreland of the southern Patagonian Andes.

1. Introduction

Worldwide evidences of fluid interaction with fault-fracture meshes developed at shallow crustal depths (< 1 ± 3 km) in areas of extensional tectonics are abundant (Sibson, 2000). Fault-fracture meshes are interpreted as important high-permeability conduits for large volume fluid flux and for bonanza grade ore formation (Henley, 1985; Sibson, 1987; Henley and Etheridge, 1995; Sibson, 1996; Henley and Berger, 2000; Berger et al., 2003; Begbie et al., 2007). At the deposit scale, location and geometry of the ore shoots are controlled by fault zone architecture, wall-rock competence and permeability contrasts, and fluid pressure during hydrothermal activity (Cox et al., 2001; Cox, 2005).

In this paper, we present detailed structural data obtained from surface field measurements in the exposed fault-fracture systems at La Paloma (47°42′30″ S, 67°46′23″ W), a Au-Ag and base metal epithermal deposit of the Don Nicolás district, located in the northeast of the Deseado Massif, in the south of the extra-Andean Patagonia (Fig. 1). The regional tectonic regime during the Jurassic in the Deseado Massif was characterized by bulk NE-SW directed horizontal extension and led to the formation of dilatational and hybrid fault-fracture networks that host Au-Ag epithermal veins (Giacosa et al., 2010). As shown in this

* Corresponding author.
E-mail address: stefano.mazzoli@unicam.it (S. Mazzoli).

https://doi.org/10.1016/j.tecto.2019.228302
Received 7 April 2019; Received in revised form 21 November 2019; Accepted 26 November 2019
Available online 29 November 2019
0040-1951/

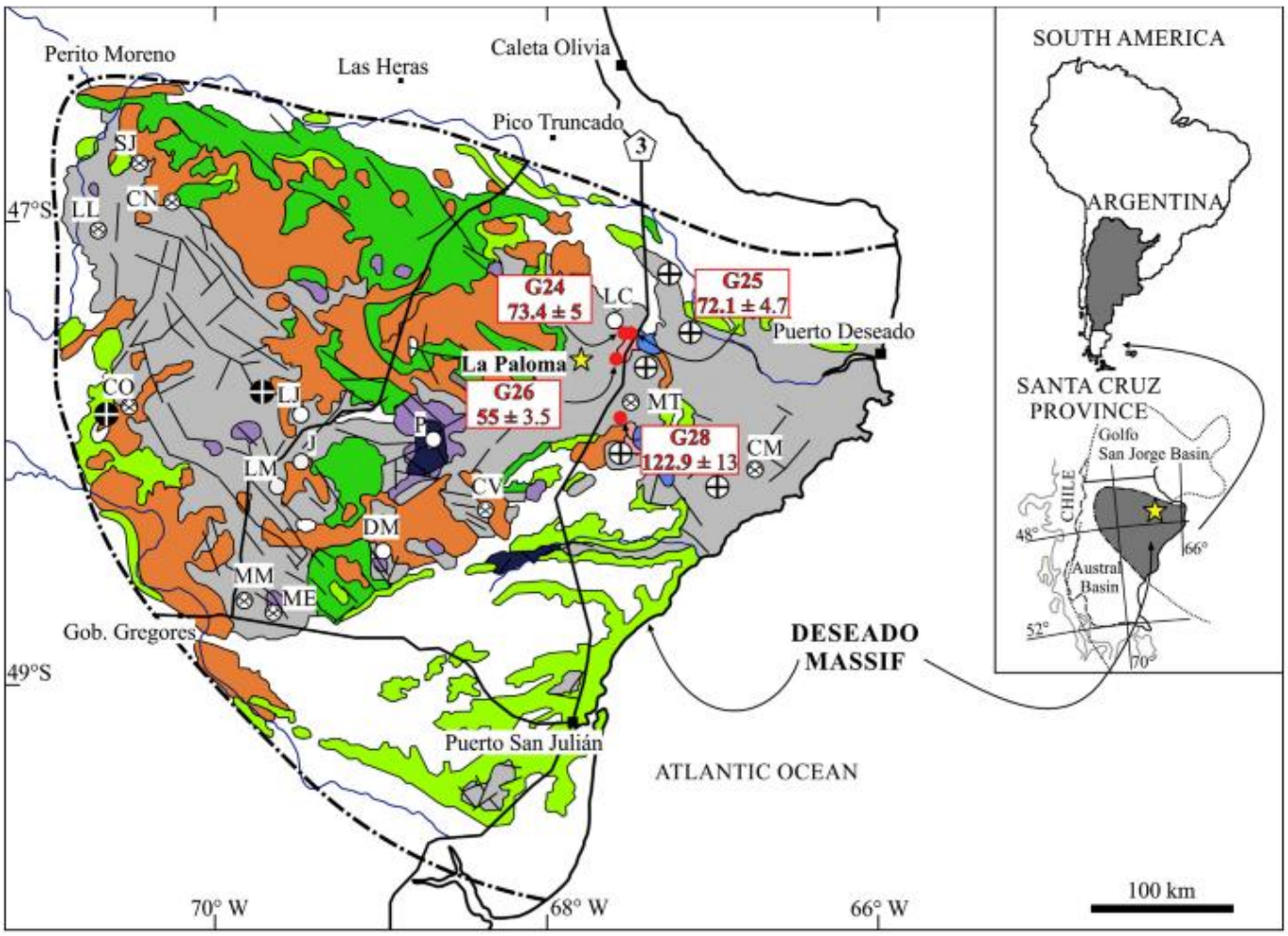

REFERENCES

- La Paloma District
- Non operative mine
- Operative mine
- Advanced exploration
- Route 3
- Main faults
- AFT Age data
- Quaternary deposits
- Plateau basalts (Tertiary-Quaternary)
- Marine and continental sedimentary rocks (Tertiary)
- Bajo Grande - Baqueró Fms. (Upper Jurassic-Cretaceous)
- Chon Aike - La Matilde Fms. (Middle-Upper Jurassic)
- Bajo Pobre Formation (Middle-Upper Jurassic)
- Roca Blanca Formation (Lower Jurassic)
- La Leona Formation (Lower Jurassic)
- La Golondrina - La Juanita - El Tranquilo Fms. (Permian-Triassic)
- La Modesta Formation (Upper Precambrian-Paleozoic)
- Rio Deseado Complex (Upper Precambrian-Paleozoic)

Fig. 1. Regional geologic map of the Deseado Massif, showing location of the study area, Au-Ag mines and epithermal deposits in advanced exploration (modified from Guido et al., 2004; Ramos, 2002). Abbreviations: CM: Cerro Moro, CN: Cerro Negro, CO: Cap Oeste, CV: Cerro Vanguardia, DM: Dorado-Monserrat, J: Joaquín, LC: Las Calandrias, LJ: La Josefina, LL: Lomada de Leiva, LM: La Manchuria, LP: La Paloma, ME: Manantial Espejo, MM: Mina Marta, MT: Martinetas, SJ: San José. Apatite fission track cooling ages obtained in this study are also shown (AFT age data).

paper, the complex vein network that hosts the epithermal mineralization at La Paloma is characterized by a strong structural control. However, no previous detailed scientific study was carried out to understand the connection between hydrothermal mineralization and structural evolution. The implications of the results of our structural analysis may contribute to the prediction of the fracture network geometry and properties in the subsurface that will guide future brownfield exploration activities. More in general, we discuss the relationships between the structural pattern and the fault-fracture sets hosting the epithermal Au-Ag quartz vein systems, considering the influence of the structures inherited from host rocks. This represents a major change of perspective in a field dominated by structural models that generally try to link kinematically the pattern of mineralized veins to coeval major fault activity (e.g. Ramos, 2002; Echavarría et al., 2005; Giacosa et al., 2010; Páez et al., 2016), thereby neglecting the complexity of fracture attitude and geometry that may characterize early (i.e. cooling) joint systems in magmatic rocks. We also consider vein thickness, textures, and ore shoot geometries to constrain dominant components of motion in structural pathways that focused fluid flow and facilitated ore deposition. The subsequent Cretaceous to Tertiary tectonic evolution of

Table 1
Apatite fission track data.

Sample number	Formation (age)	Coordinates	Elevation (m a.s.l.)	No. of crystals	Spontaneous		Induced		$P(\chi)^2$	Dosimeter		Age (Ma) ± 1σ	Mean confined track length (μm) ± std. err.	Std. dev.	No. of tracks measured	Mean Dpar (μm)
					ρ_s	N_s	ρ_i	N_i		ρ_d	N_d					
G24	La Leona (Lower Jur.)	47.643889 S, 67.329167 W	141	26	9.30	425	2.35	1076	100.0	1.06	5367	72.1 ± 4.9	12.27 ± 0.18	1.55	72	1.01
G25	La Leona (Lower Jur.)	47.618333 S, 67.346389 W	143	20	6.44	468	1.66	1207	100.0	1.05	5328	70.1 ± 4.6	10.69 ± 0.35	1.52	19	0.98
G26	La Leona (Lower Jur.)	47.735833 S, 67.426667 W	179	20	6.41	466	2.17	1578	100.0	1.05	5290	53.4 ± 3.4	n.d.	n.d.	n.d	0.99
G28	Baio Pobre (Mid-Upper J.)	47.955556 S, 67.479444 W	137	25	2.64	168	3.98	253	91.1	1.04	5251	118.4 ± 12.6	n.d.	n.d.	n.d	1.03

Central ages calculated using dosimeter glass CN5 and ζ-CN5 = 346.11 ± 11.81. ρ_s: spontaneous track densities ($\times 10^5$ cm^{-2}) measured in internal mineral surfaces; N_s: total number of spontaneous tracks; ρi and ρ_d: induced and dosimeter track densities ($\times 10^6$ cm^{-2}) on external mica detectors (g = 0.5); N_i and N_d: total numbers of tracks; $P(\chi^2)$: probability of obtaining χ^2-value for ν degrees of freedom (where ν = number of crystals-1); a probability > 5% is indicative of an homogenous population.

the study area is analysed with the aid of low-temperature thermochronology, by means of apatite fission track analysis.

2. Regional geological setting

The Deseado Massif is located north of the Santa Cruz province, between 46° and 49°S latitude, in the extra-Andean Patagonia (Fig. 1). It is characterized by a flat topographic relief and hosts numerous Jurassic epithermal Au-Ag veins (Schalamuk et al., 1997, 1999). Its geology is mainly represented by the Middle to Upper Jurassic Bahía Laura Volcanic Complex (BLVC) (Feruglio, 1949; Guido, 2004; Sruoga et al., 2008) which overlays (i) a metamorphic basement of Neo-proterozoic to Late Paleozoic (Carboniferous) age (Di Persia, 1962; Viera and Pezzuchi, 1976), and (ii) Late Permian *syn*-rift and Triassic sag basin successions intruded by granitoids of the La Leona Formation (Arrondo, 1972). These granitoids yielded Rb/Sr ages of 202 ± 2 Ma and 203 ± 2 Ma (Pankhurst et al., 1993) and have been interpreted as the southeasternnmost outcrops of the Batholith of Central Patagonia (Rapela and Pankhurst, 1996; Rapela et al., 2005).

The Jurassic BLVC is made of volcanic rocks with bimodal characteristics, chemically dominated by rhyolite with andesite and basaltic andesite (Pankhurst et al., 1998; Feraud et al., 1999). Such widespread volcanism resulted from an extensional tectonic regime related to intracontinental rifting, which affected Southern Gondwana during the Jurassic (Giacosa et al., 2010). In details, the volcanic rocks filled major WNW-ESE trending grabens and half grabens (Homovc and Constantini, 2001), consistently with a NE-SW directed extension (Giacosa et al., 2010). The volcanic succession comprises the Bajo Pobre, Cerro León, Chon Aike and La Matilde formations, with multiple interfingering (Echeveste et al., 2001; Guido, 2004) that support the idea of coetaneous and cogenetic relationships between them (Guido et al., 2006). The Bajo Pobre Formation (Lesta and Ferello, 1972; 40Ar/39Ar in plagioclase of 177 ± 4 Ma; Guido et al., 2006; Rb/Sr in whole rock of 173 ± 8 Ma; Tessone et al., 1999) consists of calc-alkaline andesite and basaltic-andesite lavas flows and volcaniclastic deposits. The andesitic and basaltic subvolcanic rocks of the Cerro León Formation (Panza, 1982; Ar/Ar in whole rock of 180.1 ± 1.5 Ma, Guido et al., 2004) represent the intrusive equivalents of the Bajo Pobre Formation (De Barrio et al., 1999; Jovic et al., 2008) emplaced in the early *syn*-rift stage (Giacosa et al., 2010). The Chon Aike Formation (Sruoga and Palma, 1984; K-Ar between 140 and 160 Ma, Spalletti et al., 1982; Rb/Sr in whole rock of 162 ± 11 Ma and 168 ± 2 Ma, De Barrio, 1993 and Pankhurst et al., 1993a, respectively) consists of rhyolitic and dacitic ignimbrites with epiclastic deposits, ash-fall tuffs and intercalated lava flows cut by dikes (Pankhurst et al., 1998). The lacustrine fossiliferous tuffs and tuffaceous sediments of the La Matilde Formation represent the reworking of the pyroclastic material (Pankhurst et al., 1998) during the late-rift stage (Giacosa et al., 2010). During the Late Jurassic period of volcanism, the development of large hydrothermal fluid cells resulted in several veins that host Au/Ag and polymetallic epithermal deposits in the Deseado Massif (Schalamuk et al., 1997; Schalamuk et al., 1999; Guido et al., 2005; Jovic et al., 2011; López et al., 2015).

The Jurassic formations are overlain by alluvial and lacustrine deposits of the Bajo Grande Formation (of pre-Upper Barreamian age; Hechem and Homovc, 1988; Panza, 1998; Giacosa et al., 2010). The Baqueró Formation (Archangelsky, 1967; Archangelsky and Cuneo, 1984) rests unconformably on top of the Bajo Grande Formation and consists of Cretaceous (Upper Barremian to Lower Albian; Archangelsky, 1967; Cladera et al., 1999) continental deposits. The unconformity is related with a shortening event that affected the massif (Homovc and Constantini, 2001). Cenozoic marine and continental sedimentary rocks and extensive basaltic flows partially cover the Jurassic and Cretaceous units (Gorring et al., 1997; Panza and Franchi, 2002) (see Fig. 2).

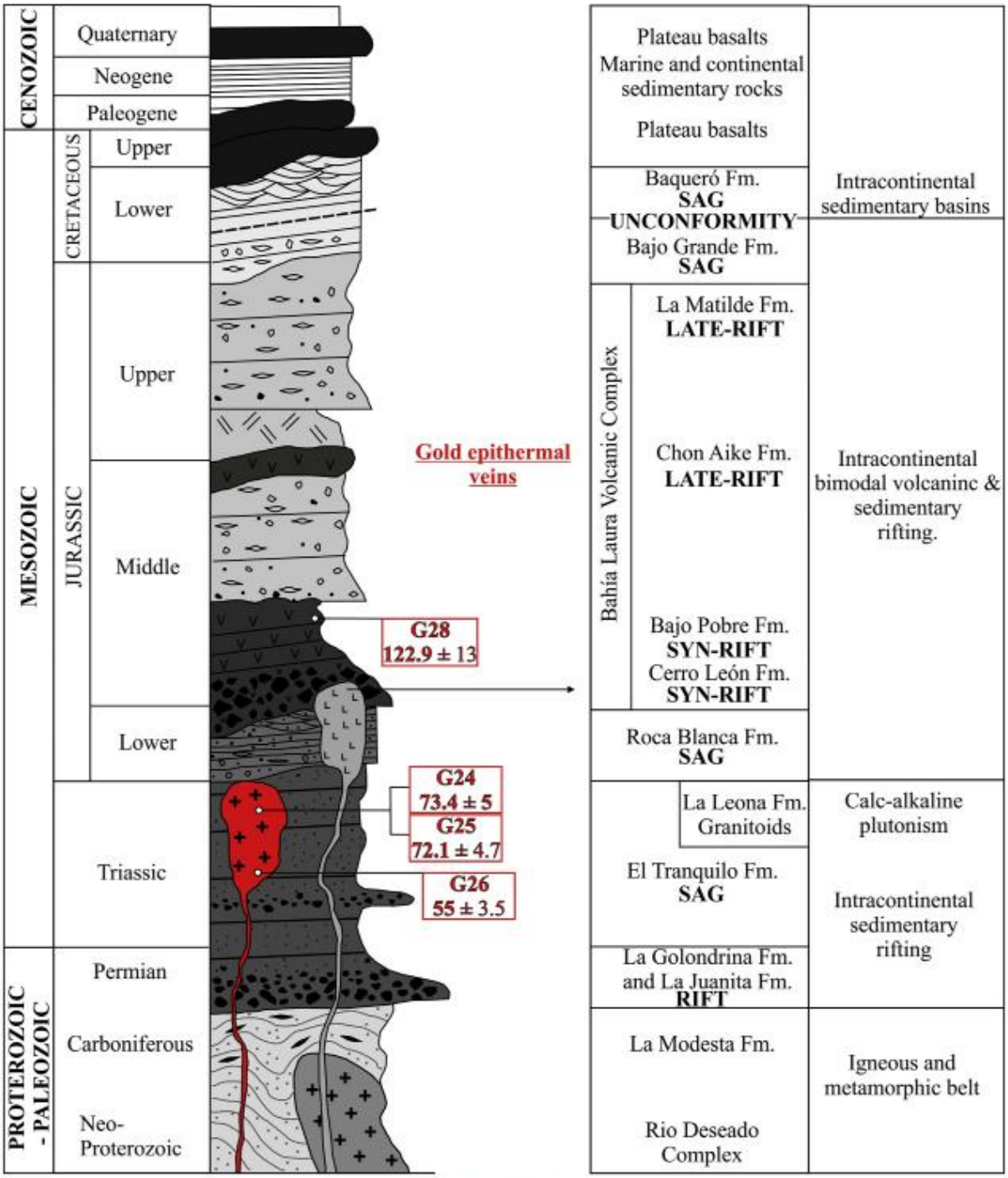

Fig. 2. Chronostratigraphic column for the Deseado Massif (modified from Jovic, 2010), showing location of AFT samples (left) and different types of magmatism related to major tectonic events in the eastern Deseado Massif (modified from Giacosa et al., 2010; right).

3. Ore geology of the Deseado Massif

The Deseado Massif is a major site of gold and silver production. It hosts eight operating mines, some of which constitute world-class deposits (Cerro Vanguardia, Manantial Espejo, Mina Martha, San José, Cap Oeste, Cerro Negro, Don Nicolás and Cerro Moro), and several projects in different exploration stages (Schalamuk et al., 1997, 1999; Echeveste, 2005; Fernández et al., 2008; Wallier, 2009; Jovic et al., 2011; Moreira and Fernandez, 2015; López et al., 2015; Permuy Vidal et al., 2016). These deposits are mainly of low sulfidation style (Guido and Schalamuk, 2003; Echavarría et al., 2005; Fernández et al., 2008), although some have been classified as intermediate sulfidation style (González Guillot et al., 2004; Guido et al., 2005; Jovic et al., 2011; Páez, 2012; Permuy Vidal, 2014). According to Echavarría et al. (2005), Giacosa et al. (2010), and Páez et al. (2016), ore deposits are regionally controlled by dominant NW striking, rift-related faults and minor NE to E-W striking structures, although local variations are common and structural trends may significantly differ from those described by the latter authors (as it occurs in our study area; Fig. 3).

Located in the northeastern part of the Deseado Massif (Fig. 1), the La Paloma deposit consists of five major vein systems and covers an area of ~2200 ha. The Sulfuro vein system is the largest one, with a

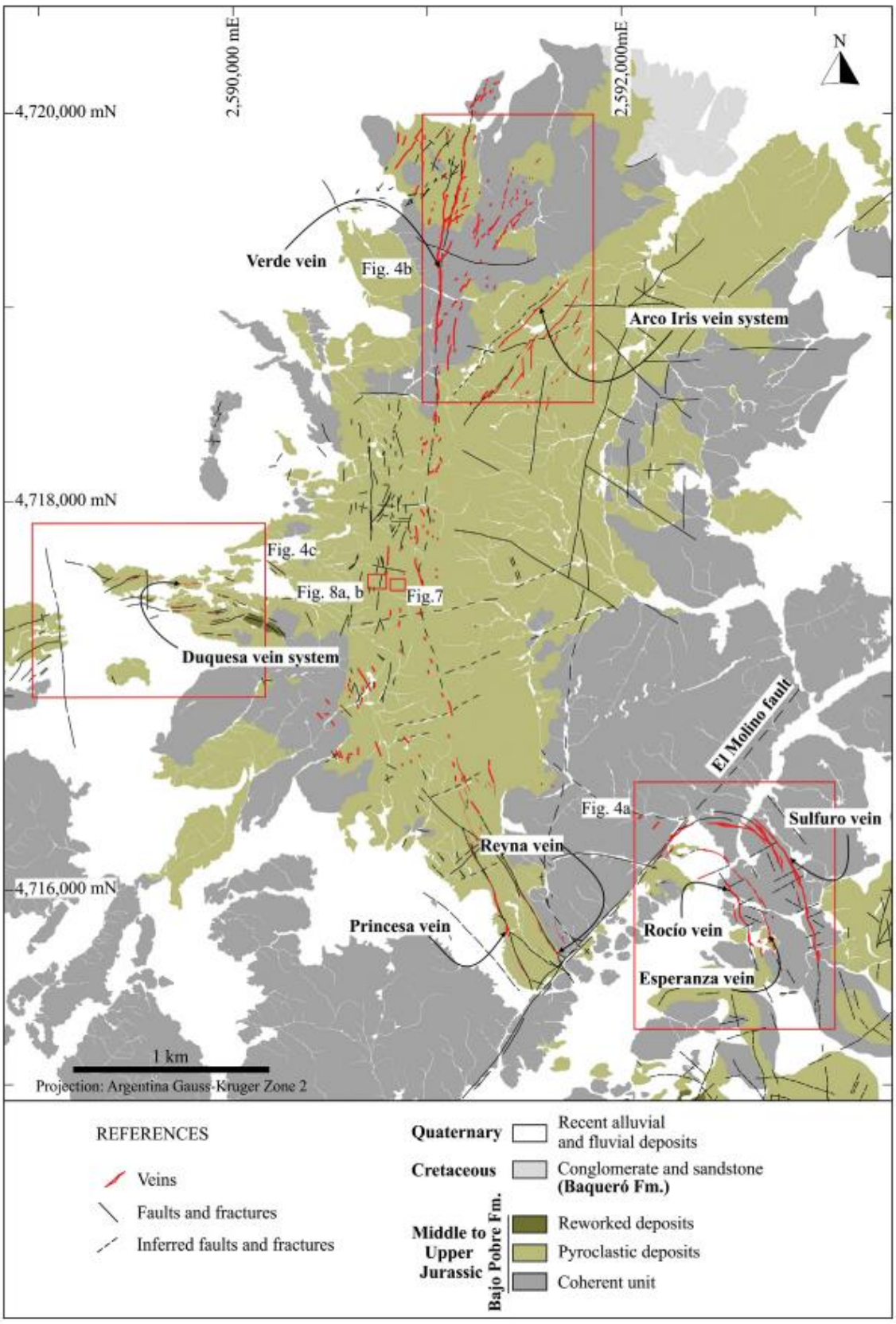

Fig. 3. Simplified geological map of La Paloma, showing mineralized fracture-fault network (red lines width is proportional to outcrop vein thicknes. (For interpretation of the references to colour in this figure legend, the reader is referred to the web version of this article.)

measured mineral resource of 260.566 Oz of gold and 637.590 Oz of silver, and an average grade of 5.55 g/t Au and 13.58 g/t Ag (Garrone, Unpublished). La Paloma was discovered by Polimet S.A company in the early 1990s. Between 1996 and 2013, exploration activities were conducted by several companies (Newcrest, Yamana Resources, Minas Buenaventura; RYSA, Hidefield and IRL) and in 2014 the property was bought by the CIMINAS mining company. The exploration activities carried out over > 20 years included surface sampling, trenching and limited drilling, both core and percussion (RC) (~472 holes for 53,900 m). Mining operations started in 2018 at the Sulfuro Vein in La Paloma and currently brownfield exploration is being conducted by the company to increase the mine resources.

4. Geological setting of the study area

Jurassic volcanic rocks of the Bajo Pobre Formation are dominant at La Paloma and host the epithermal veins. Three main units (coherent, pyroclastic and reworked) were mapped by us in the study area (Fig. 3). The coherent unit, represented by andesite and basaltic-andesite lava flows, autobreccias, and minor subvolcanic intrusions, is the most widespread. The pyroclastic unit is intercalated within the lava flows and shows lateral facies and thickness changes along the district. This unit includes intercalations of pyroclastic surge and flow deposits. The former consists of alternations of homogeneous, normal and reversed graded lapilli tuff layers with parallel and low-angle cross-stratification, with accretionary lapilli and local impact structures. The flow deposits include massive and thick beds, poorly welded to unwelded polimictic lapillitic-breccias. Lithoclasts are andesitic in composition, with variable colours and textures, and include andesite blocks up to 50 cm in diameter at the base of the sequence.

The reworked pyroclastic unit is either sitting above or locally intercalated within the volcanic rocks and is represented by two main deposits. The first consists of block-size fragments of andesitic composition in a sandstone-size matrix of similar composition with diffuse stratification (primarily interpreted as debris-flow deposits). The second one comprises homogeneous laminated and fine-grained reworked material. These deposits are areally restricted and poorly preserved, except where they show intense silicification. Sparse outcrops of silicic volcanic rocks of the Chon Aike Formation occur southeast of La Paloma and comprise rhyolitic domes, lava flows and dykes. In the northern part of the area, continental sedimentary rocks of the Cretaceous Baqueró Formation complete the local geologic record. Modern alluvial to colluvial sediments partially cover the whole sequence.

5. Characteristics of the La Paloma deposit

The La Paloma deposit is a large and well-preserved epithermal vein field with > 12 km of cumulative vein strike length (Fig. 3). Vein systems have a strong footprint at surface that is typically manifested as morphologically prominent, resistantive features in the landscape surrounded by strong argillic alteration and oxidation halos. The mineralization consists of numerous Au-Ag with base metal epithermal quartz veins, stockworks and hydrothermal breccias that can be grouped into five mineralized trends according to their general orientation and location: (i) Sulfuro-Esperanza-Rocio, (ii) Princesa & Reyna, (iii) Verde, (iv) Arco Iris-Esperanza, and (v) Duquesa vein systems; Figs. 3, 4).

The main NNW to NW trending veins form the Sulfuro Vein corridor. This comprises one major structure (Sulfuro vein), which is the main ore body within the district, and two subparallel mineralized structures called Esperanza and Rocío (Fig. 4a). The Princesa & Reyna veins, located ~1 km west of the Sulfuro vein (Fig. 3), are subparallel, NNW to NW striking mineralized structures with dip angles of 70–80°, showing both NE and SW dip directions. Towards the north, the Reyna and Princesa veins join into a single system continuing with a N-S strike. The Verde trend represents the northern continuation of the Princesa vein (Figs. 3, 4b). It shows a N-S strike, locally switching to NNE. Dip angles are in the range of 80°–90°, with an east dip direction in the southern and central portions and a westward dip direction in the northern portion. The Duquesa vein system includes all the ENE to E-W trending veins and consists of several subparallel vein segments steeply dipping (70–90°) to the N (Fig. 4c). The NE strike trend is represented by the Arco Iris vein system, which crops out in the northern part of the district with dip angles of 60° to 80° to the NW (Fig. 4b).

In summary, the mineralization occurs within a complex vein network dominated by NNW to NW striking veins (e.g. Sulfuro Vein Corridor; Princesa & Reyna and Verde trends), by ENE to E-W striking structures (e.g. Duquesa trend) and also NE striking veins (e.g. Arco Iris Trend). The El Molino fault separates the Sulfuro Vein corridor from the further vein systems located towards the north (Fig. 3).

The main vein characteristics (textures, ore and gangue minerals) of each trend are briefly described below, with particular emphasis on the Sulfuro vein.

NNW to NW striking faults include several metres wide and a few kilometres long structures. The major veins, which are hosted within andesite lavas and pyroclastic rocks, are associated with these faults and show variable levels of exposure. The Sulfuro Vein corridor, located in the southern part of the La Paloma district (Fig. 3), constitutes a 1000 m long and up to 600 m wide block occupied by several segments of mineralized lodes between 0.3 and 6 m thick. To the north, this trend turns to a WNW and then to an ENE orientation that confers it an arcuate shape. In the Sulfuro vein the mineralization has been defined for 850 m along strike and to a depth of 230 m, with an average width of 2.9 m, reaching a maximum of 6 m. The major lodes consist of multiple phases of vein deposition and show dominant quartz vein breccias textures composed of angular vein quartz and/or wall-rock fragments in a quartz and/or sulfide-bearing cement (Fig. 5a–c). The general vein filling sequence can be subdivided into a main stage characterized by quartz including molybdenite-rich bands (S1), a second massive sulfide-bearing stage (S2), and a late stage characterized by fluorite, carbonates (calcite, dolomite with minor siderite), gypsum and cavities filled by clay minerals (S3). The latter stage is less important in terms of mineral volumes and involves the formation of narrow veinlets that mark the last event in the vein deposition sequence (Fig. 5a, b). Quartz is a major component of the vein fill and occurs as microcrystalline to coarse-grained, massive to colloform and crustiform banded veins and as vein breccia cement (Fig. 5). Precious metal mineralization is typically microscopic and associated with specific bands of very fine grained molybdenite (Fig. 5), and with massive sulfides mainly represented by pyrite, sphalerite, galena and chalcopyrite (Fig. 5a, c). The rest of the NNW to NW striking veins (e.g. Princesa & Reyna and Verde trends) have only been tested by shallow core drilling and historical trenches. They are characterized by weak Au and base metal contents (up to 3 g/t Au) (Grant et al., 2012). Shallow level features of these veins are similar to those described for the Sulfuro Vein corridor, suggesting that mineralization could extend far below the depths already tested by core drilling.

ENE to E-W striking structures, represented by the Duquesa trend, are hosted by pyroclastic deposits and reworked volcanic rocks. They consist of disrupted outcrops of individual thin veins of few centimetres up to 1 m thick, sheeted veinlets and/or stockwork zones that extend for almost 700 m along vein strike. Fills of individual veins consist of single phases deposited symmetrically on both vein walls with crustiform textures, mainly represented by massive and comb quartz, carbonates and fluorite. They are characterized by low gold grades (up to 1–3 g/t Au), with no base metal content in surface samples (Fig. 5d, e).

In contrast, NE striking faults (e.g. Arco Iris trend and El Molino fault) are not occupied by wide veins (Fig. 5f–h). The Arco Iris trend consists of narrow, sub-parallel hybrid extension-shear quartz veins and stockwork zones hosting erratic precious metal mineralization (Au ± As) contained in andesitic pyroclastic rocks (Grant et al., 2012). Vein textures are dominated by two types of breccias, either consisting of: (i)

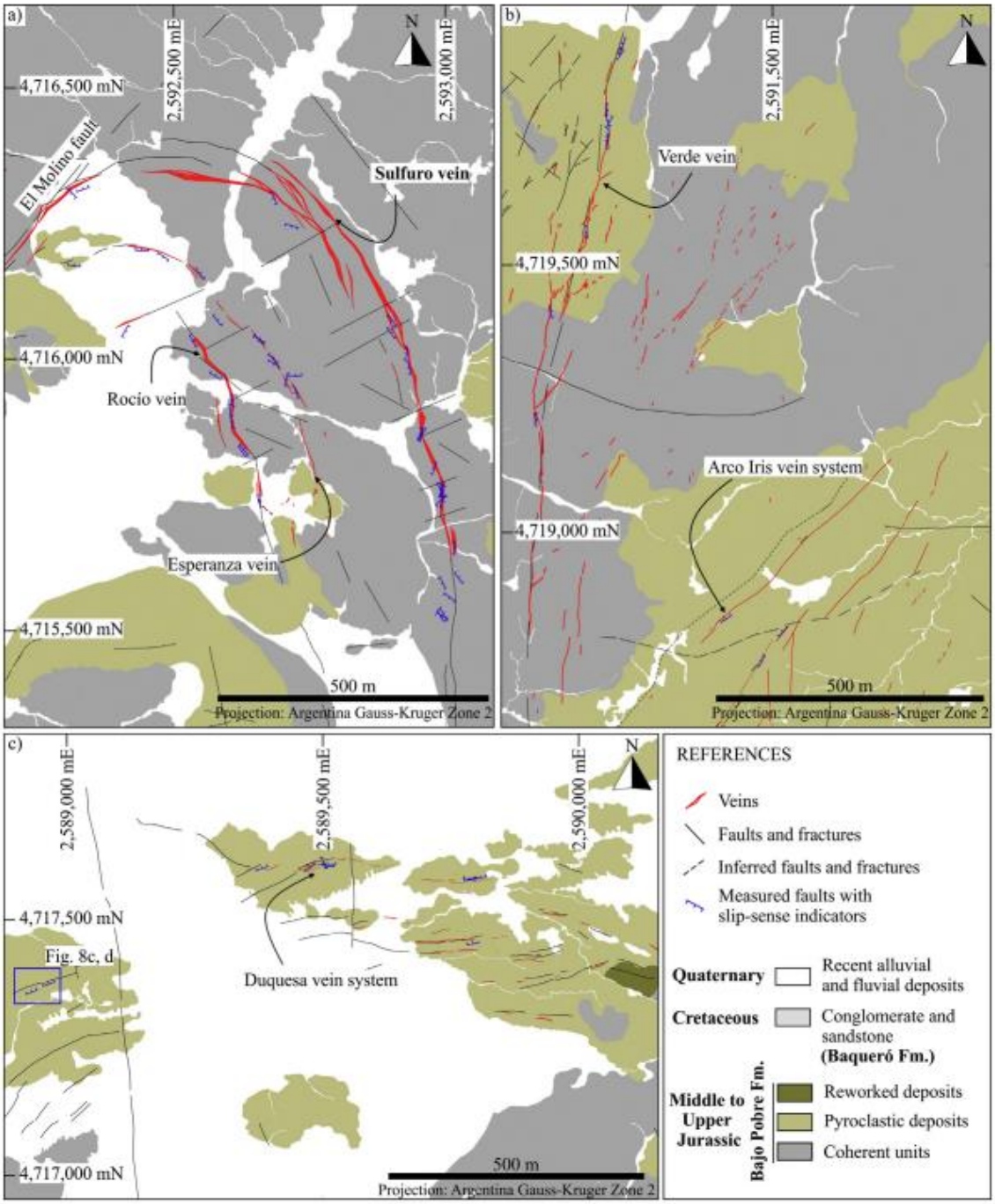

Fig. 4. Close up views of the geological map of Fig. 3, showing measured faults with reliable kinematics indicators (red lines width is proportional to outcrop vein thickness) for: (a) Sulfuro, (b) Verde and Arco Iris, and (c) Duquesa vein systems. (For interpretation of the references to colour in this figure legend, the reader is referred to the web version of this article.)

variable sized wall rock fragments in a grey silica cement (up to 25 vol %) (Fig. 5f), locally with iron oxides; and (ii) brecciated epithermal vein clasts within a fault gouge matrix including iron oxides (Fig. 5g). Microscopy studies carried out by Yamana Resources S.A. found native gold particles between 5 and 40 μm in diameter disseminated within silica cement and narrow quartz veinlets with iron oxides. In the Arco Iris vein, high gold contents extend to the base of the oxidation level, suggesting that the vein systems have been affected by oxidation and secondary enrichment.

The El Molino fault is characterized by a clay-rich fault rock (gouge) with poorly developed veining (typically < 10 vol%) and no gold anomalies (Fig. 5h).

6. Structural analysis

6.1. Methods

Structural data were obtained from field measurement sites mostly located within the numerous trenches carried out for mining exploration along the fracture-fault system exposed in the study area (Fig. 3). The structural analysis was particularly focused on – but not restricted to – fault and fracture sets controlling the mineralization, which generally consist of m-thick veins commonly showing evidence of shear along the walls (i.e. they are hybrid extension-shear fractures). Joints and veins (tensional, or mode I fractures), hybrid extension-shear

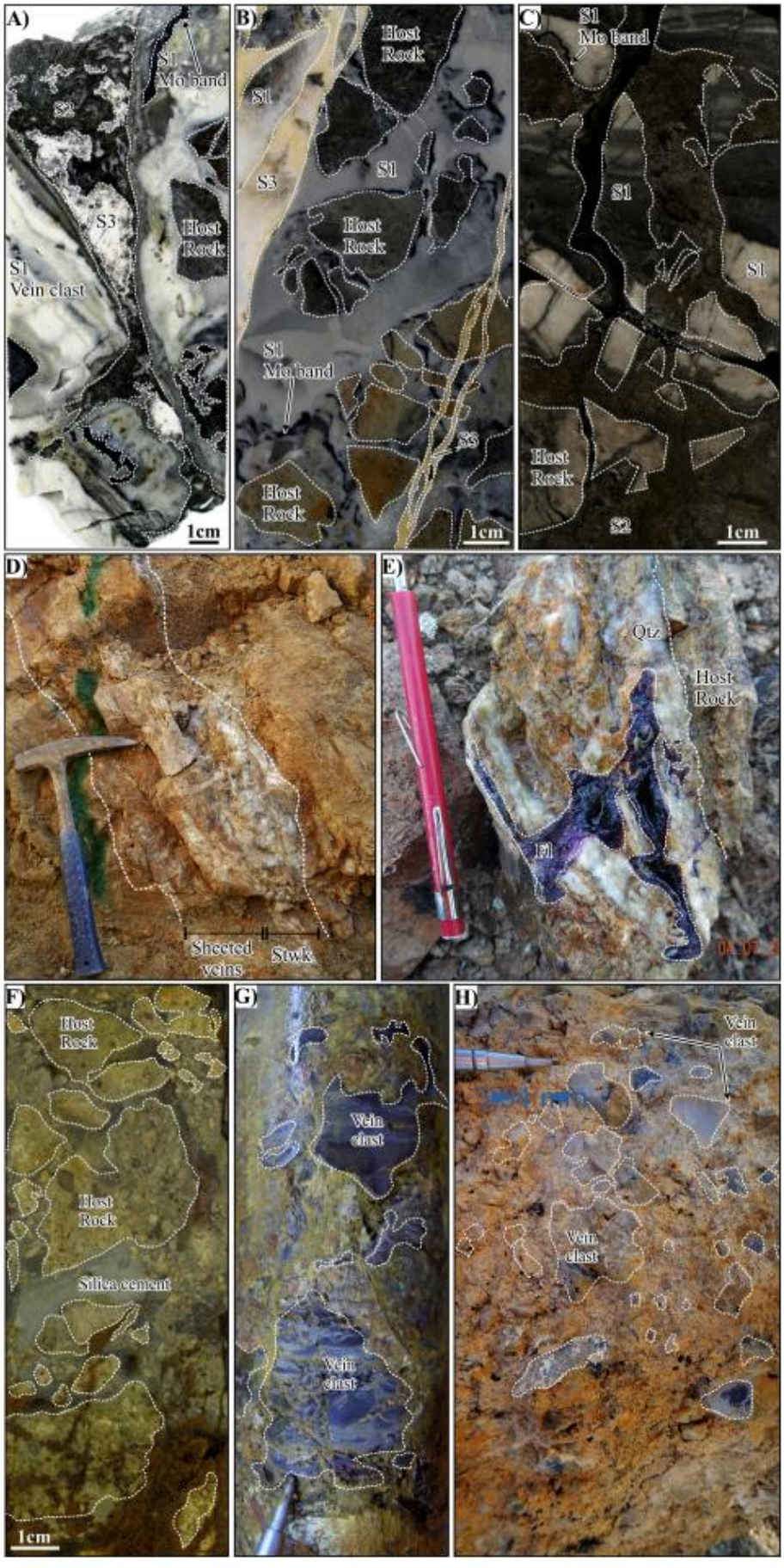

Fig. 5. Textures and crosscutting relationships in NNW to NW, ENE to E-W, and NE striking structures at La Paloma district. (a) Textures and crosscutting relationships between stages 1, 2 and 3 (see text) at Sulfuro vein (Sample Id: DD-14077; Drill-hole: S-D10-87 at 74.5 m; Au grade: 16.75 ppm; Cu: 1050 ppm; Mo: 590 ppm). (b) Drill-hole sample of the Sulfuro vein, showing crosscutting relations between stages 1 and 3 (Sample Id: DD-16225; Drill-hole: S-D10-152 at 204 m; Au grade: 0.21 ppm; Mo: 281 ppm); late stage (S3) veinlets are composed of dolomite and gypsum. (c) Brecciated texture with sub-angular clasts of S1 fine-grained, colloform-banded quartz including molybdenite bands in a massive sulfide-bearing matrix (Sample Id: DD-14072; Drill-hole S-D10-87 at 72 m; Au grade: 33.2 ppm; Cu: 2420 ppm; Mo: 4020 ppm; Pb: 1220 ppm; Zn: 6260 ppm). (d) Vein exposure within trench LP-T14–021 across the Duquesa vein, showing sheeted vein and vein stockwork facies (sample Id: ET-11021; Au grade: 0.21 ppm). (e) Detail of Duquesa vein filling, showing crosscutting relationship between massive milky quartz and fluorite. (f) Brecciated vein texture of Arco Iris vein (Sample Id: DD-0812; Drill-hole: A-D06-04 at 81.5 m; Au grade: 25.2 ppm); the brownish colour of the cement is due to the presence of high amounts of iron oxides. (g) Drill-hole sample of gouge-rich fault breccia from the Arco Iris vein (Sample Id: DD-21322; Drill-hole: A-D10-17 at 29.4 m; Au grade: 0.07 ppm). (h) Hand specimen from the El Molino fault, showing cataclastic texture made at the expenses of a precursor quartz vein (brecciated and preserved as clasts). (For interpretation of the references to colour in this figure legend, the reader is referred to the web version of this article.)

fractures, and faults were measured. Fault-slip data were obtained from mesoscale fault surfaces and sheared vein walls displaying prominent slickenlines and/or slickenfibres of quartz and/or calcite and/or iron oxides with steps. Being aware of the caution that should applied in fault-slip analysis (Sperner and Zweigel, 2010) and taking into account the assumptions and critical limitations of this method (e.g. Marrett and Peacock, 1999; Peacock and Marrett, 2000) – particularly concerning the stress vs. strain interpretation of fault slip data (e.g. Twiss and Unruh, 1998) – in this work we follow the majority of papers that refer to stress inversion (e.g. Angelier, 1994; Dunne and Hancock, 1994; Dasgupta and Mukherjee, 2017). Listing the numerous published methods for stress inversion is beyond the scope of this paper, which particularly focuses on separating homogeneous fault-slip subsets from a heterogeneous dataset (e.g. Huang and Charlesworth, 1989; Yamaji, 2000; Delvaux and Sperner, 2003; Shan and Fry, 2005; Sippel et al., 2009; Delvaux, 2011). Within this framework, the Multiple Inversion Method (Yamaji, 2000), improved by Otsubo and Yamaji (2006), was chosen as it represents a widely accepted and validated tool, particularly suitable to provide information on the paleostress field(s) that governed the development of various fault sets controlling the mineralization in the study area. This method, applied in this study by using the MIM software package (Yamaji et al., 2010), allows one to separate different stress fields from heterogeneous fault-slip data by defining the stress tensors having common orientations of the three principal stress axes σ_1, σ_2, and σ_3 (with $\sigma_1 \geq \sigma_2 \geq \sigma_3$), and a common value of the stress difference ratio $\Phi = (\sigma_2 - \sigma_3) / (\sigma_1 - \sigma_3)$ that defines the shape of the stress ellipsoid (oblate for $\Phi > 0.5$, prolate for $\Phi < 0.5$). The MIM uses the classical scheme of stress tensor inversion (Angelier, 1979) that minimizes the sum of misfit angles between observed and calculated slip directions. The unique assumption of the method consists in the Wallace–Bott hypothesis (Wallace, 1951; Bott, 1959) that the slip is parallel to the resolved shear stress. Starting from a fault-slip dataset, orientations of the stress axes are estimated for subsets, obtained considering all the combinations of a given number of fault data. The method allows one to select handily the σ_1 and σ_3 stress solutions on stress plots and verify the quality of the solution by means of the evaluation of the misfit angles, i.e. the angles between the measured slip vector and those theoretically calculated according to the selected stress solution.

Fieldwork was complemented with remote sensing, based on the interpretation of satellite data and aerial photographs, in order to obtain a comprehensive picture of the fracture and fault pattern controlling the mineralization (Figs. 3 and 4). All observations and interpretations of vein textures, crosscutting relationships between the different hydrothermal stages and surrounding geology were examined by logging exploration drill cores at the mine site and from mapping exposures. This was also complemented by metal grade data provided by Minera Don Nicolas S.A. company, and compiled into a GIS database.

6.2. Results

Orientation data for the various deformation structures are shown in the plots of Fig. 6. Joints (mode I, pure dilation fractures) are common throughout the study area (Fig. 7), forming a network including four main sub-vertical sets (Fig. 6a). Faults observed in the study area also include mainly steep to sub-vertical structures (Fig. 6b). These structures consist of variably thick veins dominantly filled by quartz and recording slip along their walls. Therefore these deformation features, displaying both dilation and shear components, represent hybrid extension-shear fractures. Faults include four main sets striking ENE (Set 1), NNW (Set 2), NE (Set 3), and NW (Set 4) (Fig. 6b), which are roughly parallel to the joint sets. Fault kinematics ranges from purely extensional to strike-slip, with a large amount of oblique-slip faults invariably displaying a normal dip-slip component of motion (Fig. 8a, b). Rare reverse components of motion are associated with oblique-slip

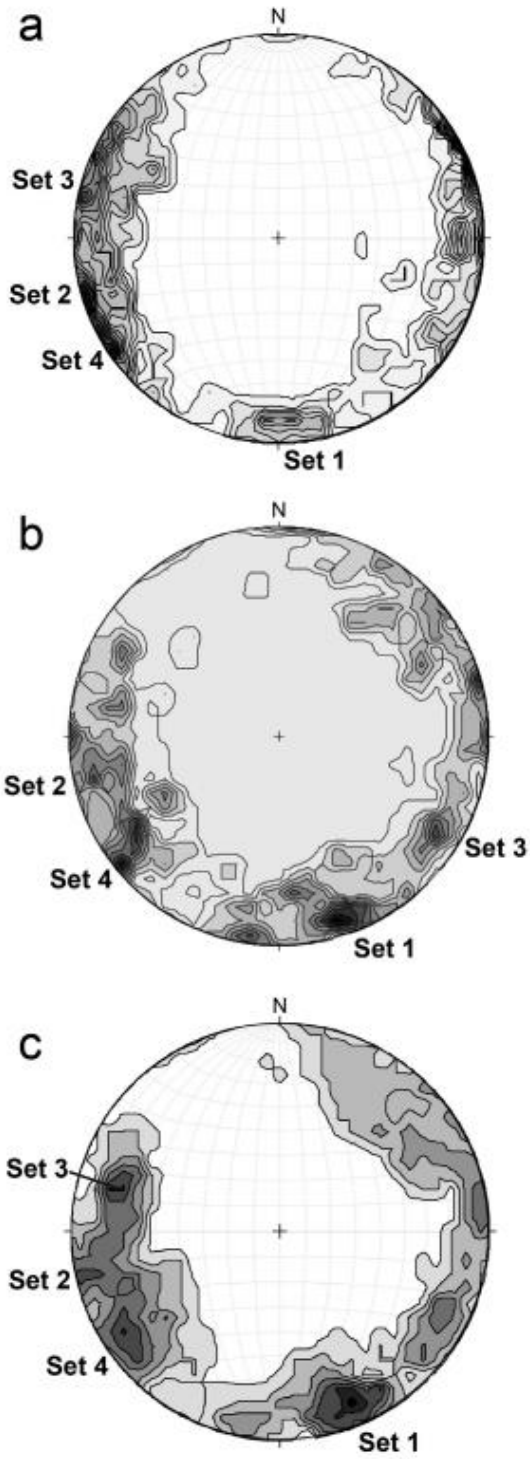

Fig. 6. Orientation data (lower hemisphere, equal area projections showing contours of poles to planes; kamb contours at: 1 interval, 1.5 of significance level, 30 of counting grid spacing). (a) Joints and veins (pure mode I, dilation fractures; 409 data). (b) Faults (slip planes of hybrid extension-shear fractures; 404 data). (c) Subset of previous population, including slip planes (slickensides) to which reliable slip-sense indicators were associated (89 data). These data are used for the paleostress analysis (see text and following figures).

overprinting of pre-existing kinematics (Fig. 8c, d). These reverse components of motion are not included in the first stage of paleostress analysis, which is aimed at unraveling the stress regimes that governed the original development of the hybrid extension-shear fractures controlling the mineralization. However, the reverse components of motion

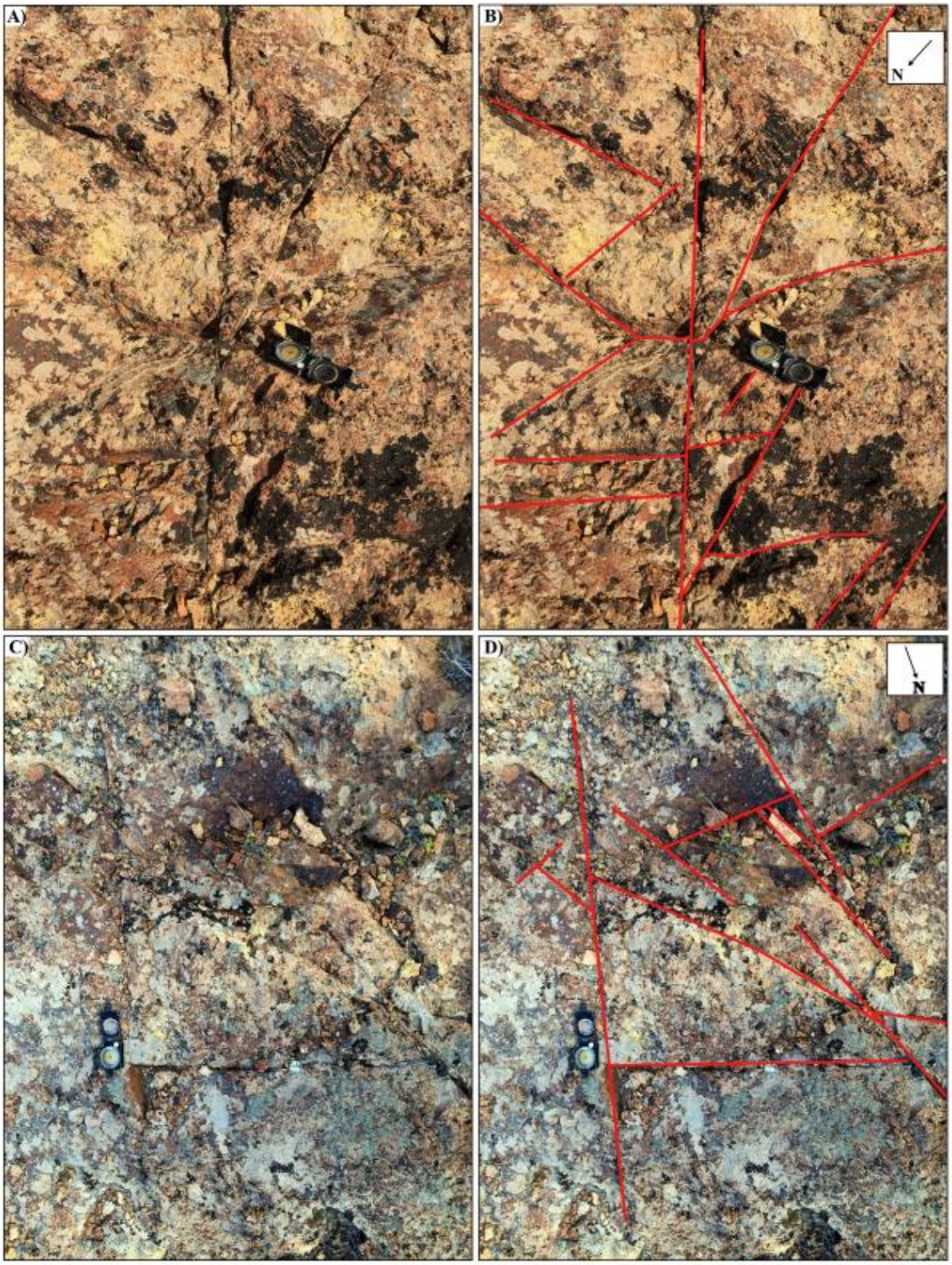

Fig. 7. Joint sets (not reactivated) in volcanic rocks of the Bajo Pobre Formation (top bed surfaces) at locality Princesa. (a) Outcrop pavement, and (b) line drawing of joints. (c) Outcrop pavement, and (d) line drawing of joints. See location in Fig. 3.

characterizing the late reactivation of the studied faults are interesting in terms of far field propagation of Andean stresses into the study area; therefore, they are analysed in a second, separate stage of paleostress analysis.

Paleostress analysis was carried out exclusively from faults displaying reliable kinematic indicators (Fig. 6c). For this subset of structures, fault kinematics has been defined based on well-known brittle shear sense criteria obtained from markers (e.g. slickenlines, abrasion striae, mineral shear fibers, groove marks) exposed on fault surfaces (slickensides). The slip direction is commonly marked by quartz, calcite or iron oxides precipitated on slickenside surfaces (Fig. 8b,d). Inversion of the whole fault-slip dataset (excluding the overprinting reverse components) by means of the MIM furnishes a σ_1 plot characterized by clustering around a vertical direction, and a σ_3 plot with a wide distribution of sub-horizontal axes (Fig. 9). Most Φ values are well below 0.5, thus suggesting the stress field is dominantly

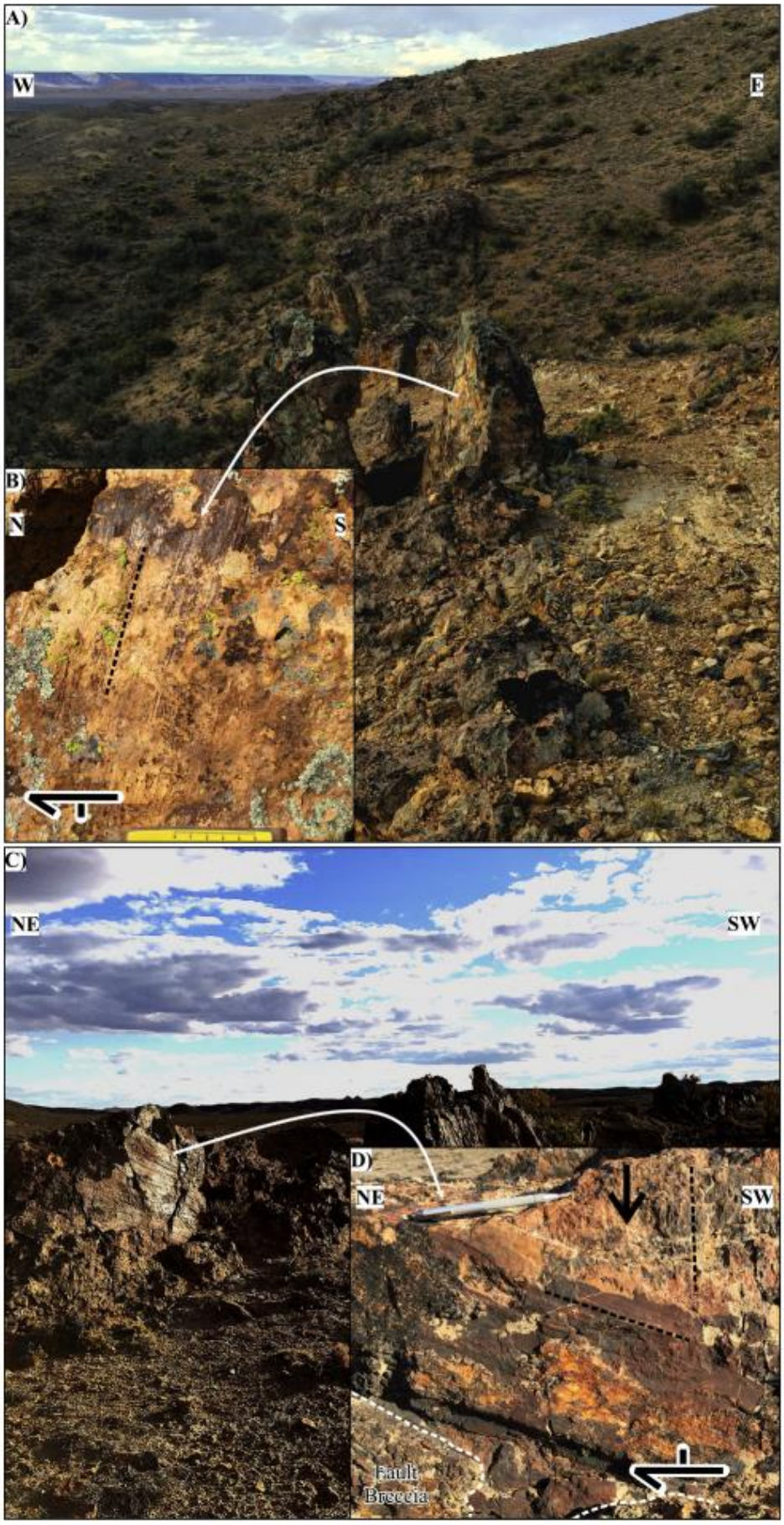

Fig. 8. Fault zone (hybrid extension-shear fracture) in Bajo Pobre Formation at locality Princesa. (a) View normal to fault zone strike and (b) detail showing kinematic indicators (striae marked by dashed line) recording oblique-slip characterized by dominant normal and subordinate dextral strike-slip components of motion. (c) Fault zone (hybrid extension-shear fracture) in Bajo Pobre Formation at locality Duquesa and (d) detail showing kinematic indicators recording normal (vertical dashed line; arrow shows movement direction of the hanging-wall block) and superposed oblique-slip (oblique dashed line) characterized by dominant dextral strike-slip and subordinate reverse components of motion on N-dipping fault plane. See location in Figs. 3 and 4.

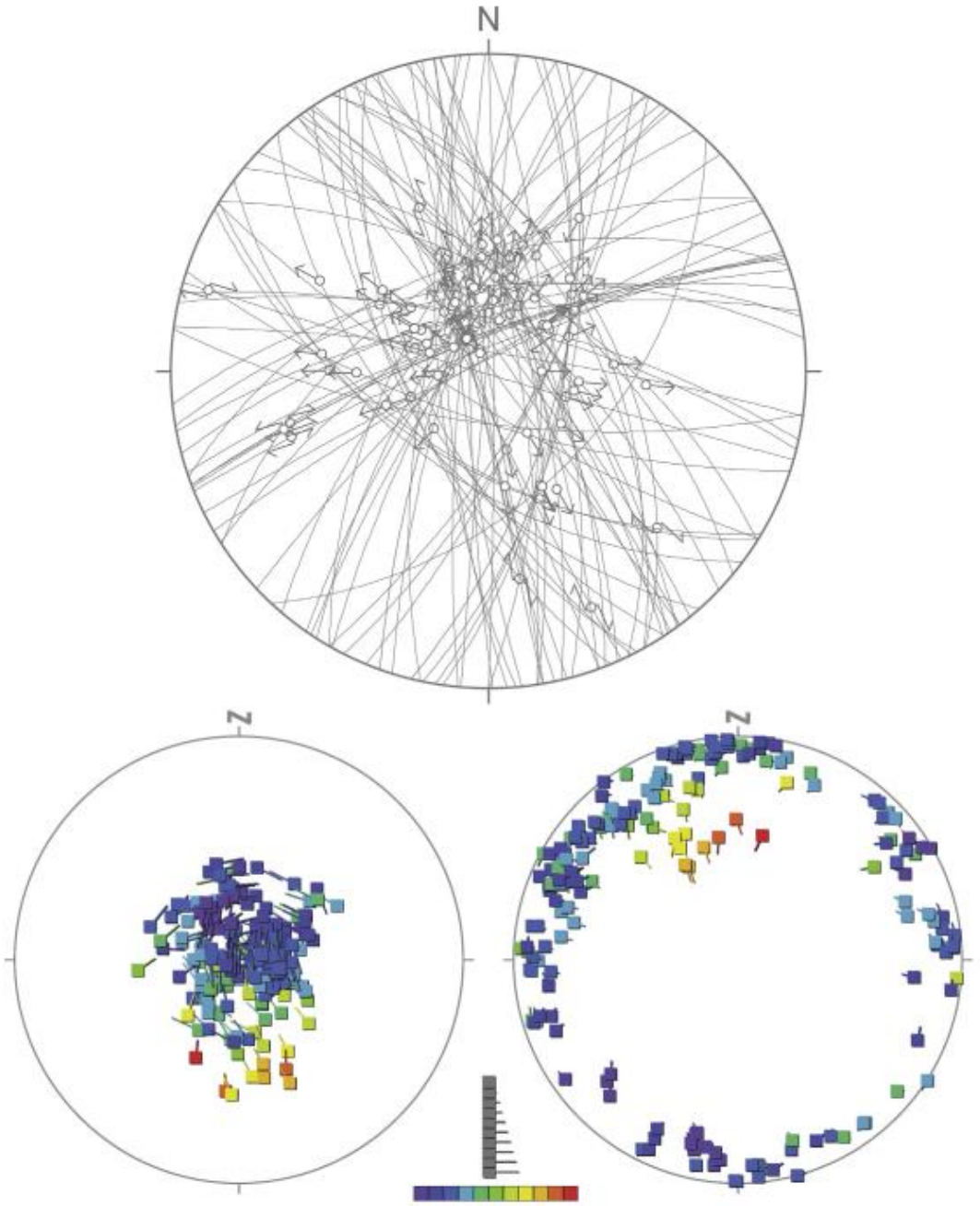

(caption on next page)

Fig. 9. Lower hemisphere, equal area projection of the whole fault population (excluding reverse fault kinematics) with reliable slip-sense indicators. Lower diagrams display the results of the paleostress analysis, showing σ_1 (left) and σ_3 (right) stress axes, performed with the Multiple Inverse Method (MIM). In the legend for paleostress analysis diagrams, the plunge of stress axes is denoted by the length of the tails of tadpole symbols. Φ values are colour-coded with intervals of 0.1. The cold colour of most tadpoles indicates a dominant prolate shape of the stress ellipsoid, which is therefore mostly characterized by similar values of σ_2 and σ_3. (For interpretation of the references to colour in this figure legend, the reader is referred to the web version of this article.)

characterized by similar magnitudes of σ_2 and σ_3. The entire dataset may be split into two fault populations (Fig. 10). For the first one (Group A faults), the frequency histograms of the misfit angles indicate that the best solution, which is that with the maximum number of faults with misfit angles below 30°, is that with a sub-horizontal, NNW trending σ_3, and a sub-vertical σ_1 (Fig. 10). This configuration depicts therefore an extensional tectonic regime controlled by NNW trending stretching. For a second fault population (Group B faults), the frequency histograms of the misfit angles suggest that the best solution is that with a steeply NW plunging σ_1 and a gently ENE plunging σ_3 (Fig. 11). This configuration is that of a dominantly extensional stress regime characterized by ENE trending extension.

The few fault slip indicators recording components of reverse-slip reactivation of pre-existing faults, generally associated with dominant dextral strike-slip (Fig. 8c, d), have been analysed by simple stress inversion performed with the software FaultKin (Fig. 12). The results of this analysis furnish a sub-horizontal, roughly E-W trending maximum compression axis, and a steeply S plunging minimum compression axis.

7. Low-temperature thermochronometry

7.1. Methods

AFT thermochronology is a well-established tool to constrain the cooling path of rocks towards the surface. Typically, data are composed of an age, which is related to cooling below ca. 100 °C, and track length distribution, forming a pattern that reflects the thermal history of rock below 120 °C (Hurford and Green, 1983; Hurford, 1990). These data can be modelled in order to depict the thermal evolution of the rock. Apatites from collected samples have been separated using standard magnetic and heavy liquid techniques. Mounts of apatite in epoxy were ground and polished to expose planar surfaces within the grains and then etched with 5 N HNO_3 at 20 °C for 20 s to reveal spontaneous fission tracks. Samples then were irradiated with thermal neutrons in the reactor at the Radiation Center of Oregon State University with a nominal neutron fluence of 9×10^{15} n cm^{-2}. The CN-5 dosimeter was used to measure neutron fluence. After irradiation, induced fission tracks in the low-U muscovite that covered apatite grain mounts and glass dosimeter were revealed by etching in 40% HF at 20 °C for 40 min. Apatite FT dates were calculated using the external-detector and the zeta-calibration methods (Hurford and Green, 1983) with IUGS age standards (Durango, Fish Canyon and Mount Dromedary apatites) (Hurford, 1990) and a value of 0.5 for the $4\pi/2\pi$ geometry correction factor. The analyses were subjected to the χ^2 test (Galbraith, 1981) to detect whether the data sets contained any extra-Poissonian error.

Quantitative evaluation of the thermal history can be carried out through modelling procedures, which find a range of cooling paths compatible with the AFT data. In this work, inverse modelling of track length data was performed using the HeFTy program (Ketcham, 2005), which generates the possible T–t paths by a Monte Carlo algorithm. Predicted AFT data were calculated according to the Ketcham et al. (2007) annealing model. Dpar values (i.e. the etch pit length) have been used as kinetic parameter.

7.2. Sampled units

Samples G24, G25 and G26 are Lower Jurassic granitoids of the La Leona Fm. (Pankhurst et al., 1993) that crop out approximately 30 km northeast and east of La Paloma (refer to Fig. 1 for sample location). They consist of medium to fine-grained hornblende-biotite monzodiorite to aphyric inequigranular aplite, the last composed mainly by quartz and alkali feldspar, with subordinate plagioclase and rare, small, biotite crystals. Sample G28 belongs to an outcrop from the Bajo Pobre Formation (Middle to Upper Jurassic) located 35 km southeast of La Paloma, in a broad area dominated by flow-banded rhyolitic lavas. It consists of andesitic lava with fresh augite, plagioclase and smectite-altered hypersthene phenocrysts in a holocrystalline groundmass. Many phenocrysts occur in multi-crystal clots giving the appearance of coarse-grained equigranular rock.

7.3. Results

The obtained data show a rather large span of ages, ranging from 53 to 118 Ma. Samples G24 and G25, collected a few kilometers from each other, yield nearly the same age. The χ^2 test indicates clearly the presence of a single age population for each sample, as expected given the lithologies (magmatic rocks). Unfortunately, track lengths could be measured only from two samples. Both of them are characterized by a track length distribution in which many short tracks (i.e. shorter than 13 μm) are present. The presence of short tracks unambiguously indicates a long permanence inside the so-called Partial Annealing Zone (PAZ, between about 120° and 60 °C; Hurford and Green, 1983; Hurford, 1990), i.e. a slow-to-moderate cooling. A more precise definition of thermal paths has been obtained through thermal modelling of sample G24, the only one with a sufficient number of measured lengths. The modelling program HeFTy is usually working with a preliminary input of time-temperature constraints. In this particular case, we only forced the program to start from the intrusion of the granitoids during the Early Jurassic, therefore assuming temperatures higher than 160 °C at about 190 Ma. The results are shown in Fig. 13 as a range of thermal paths with statistically acceptable fit between experimental and model data (shaded area) and the most probable path (thick line). The thermal history between 210 and 90 Ma is not really confined, as shown by the large shaded area that point to a variety of possible thermal paths. The lack of strong constraints is due to the temperatures that are still high, i.e. close to the bottom of the PAZ, and the slow cooling. The last 90 Ma are much better constrained and are characterized by slow (about 1 °C/Ma), steady-state cooling.

The age of sample G28 is apparently discordant with the thermal path inferred by the model. However, we have to take into account that this sample has been collected from a volcanic rock and therefore its thermal history is characterized by an initial fast cooling stage down to very low temperatures. In order to obtain a final AFT age of 118 Ma initial cooling must have been followed by some heating up to temperatures just inside the PAZ (70–80 °C). A plausible explanation for this temperature increase is given by the occurrence in the region of further Upper Jurassic volcanic rocks and of Lower Cretaceous deposits (Bajo Grande and Baquerò formations) that could have provided the burial necessary to reach the inferred temperatures. However, given the lack of track lengths, we cannot define precisely the thermal path, especially related to the last cooling phase.

As a general view, these data demonstrate that the Deseado massif was not affected by a particular exhumation event; rather, it cooled at nearly steady state and low rate in the last ca. 90 Ma. However, the lack of further constraints at lower temperatures (i.e. U-Th/He data) hampers the recognition of possible exhumation events in the very last part of the cooling history.

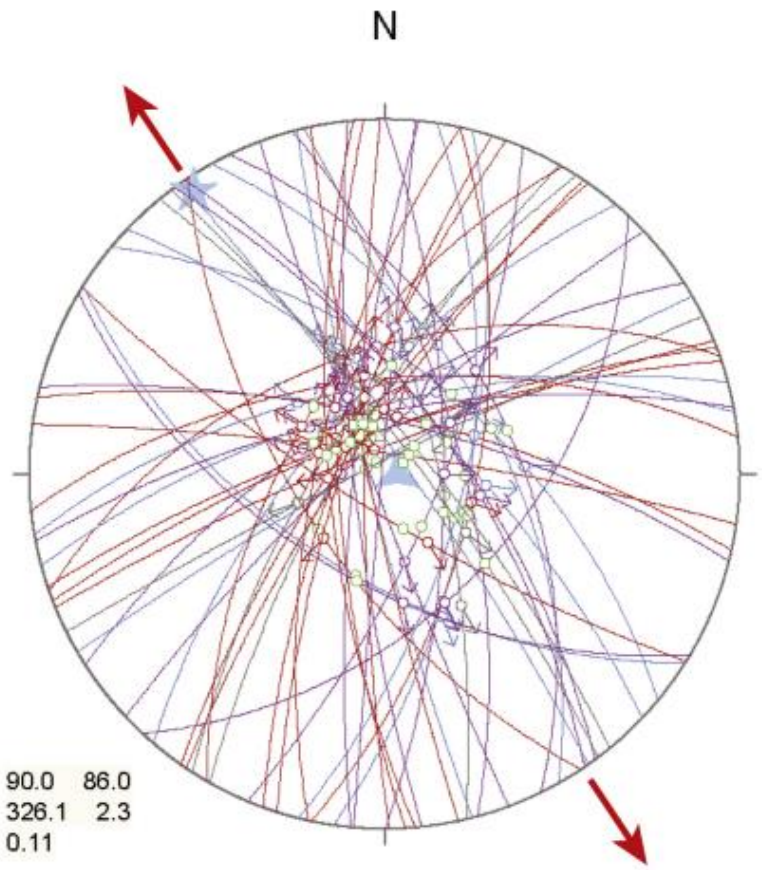

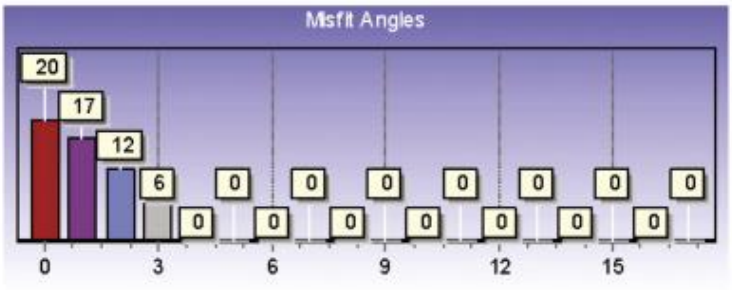

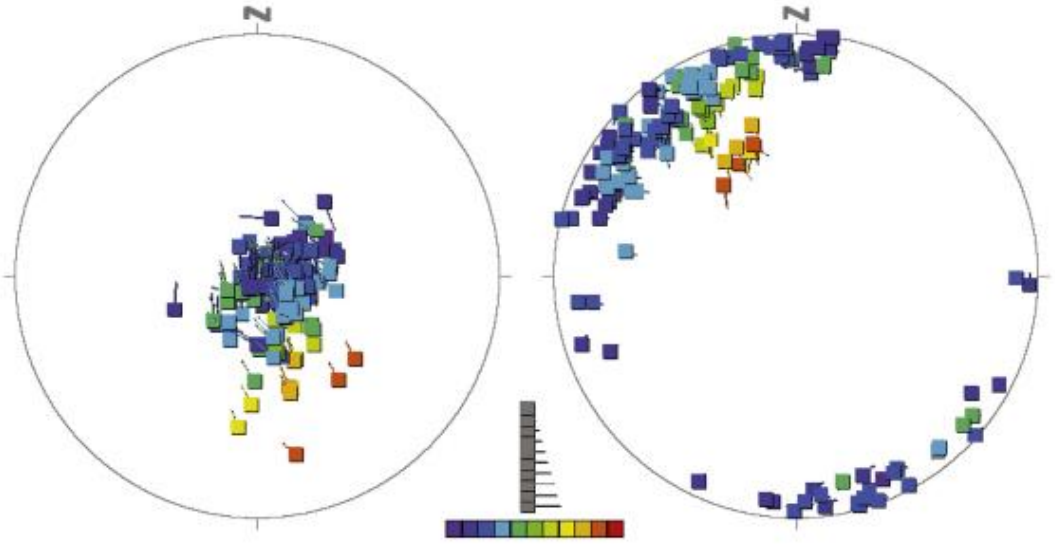

(caption on next page)

Fig. 10. Results of paleostress analysis for Group A faults (in the upper diagram, three-armed star is σ_1, plunging 86° towards 090 N; five-armed star is σ_3, plunging 2° towards 326 N; red arrows show extension direction in the horizontal plane). Misfit angles (see text) are shown in the centre diagram. Legend for the lower diagrams, displaying σ_1 (left) and σ_3 (right) stress axes, as in Fig. 9. (For interpretation of the references to colour in this figure legend, the reader is referred to the web version of this article.)

8. Discussion

The fault systems that host wide, continuous and economic veins throughout the Deseado Massif are NNW to NW striking (e.g., Cerro Moro, Cerro Vanguardia, Manantial Espejo, Martha Mine, San Jose, Monserrat), whereas NE to ENE striking fault systems host discontinuous thin veins, with associated minor mineralization (Echavarría et al., 2005). Magmatic activity provided a renewable fluid supply that has presumably risen continuously into the brittle crust during the Mesozoic extensional phase, producing widespread mineral precipitation within hybrid extension-shear fractures. The occurrence of four sets of hybrid extension-shear fractures implies very low values of differential stress during the development of these structures.

8.1. Hybrid extension-shear fractures origin and kinematics

The inversion of fault slip data carried out in the previous section indicates that stretching was bimodal, the maximum horizontal extension switching between an ENE and a NNW orientation. It is worth noting that Japas et al. (2013) related the Jurassic volcanism of the Chon Aike province to two coeval regimes of horizontal stretching, which match with the bimodal extension documented in the present study. These authors documented a main ENE directed stretching and a secondary NNW trending extension for the eastern domain of the Deseado Massif, relating the emplacement of effusive volcanic rocks (rhyolitic domes, lava flows and dikes) to the second. This is consistent with the fact that ENE trending structures control the emplacement of volcanic rocks in our study area, despite the fact that these structures are subordinate at the map scale (refer to Fig. 3).

Repeated stress permutations are interpreted to have produced the apparently complex fault pattern shown in Fig. 3. In fact, it is widely documented that horizontal extension along the main stretching direction is often accompanied by horizontal extension in the perpendicular direction (e.g. Ramsay and Huber, 1983; Engelder and Gross, 1993; Tavani et al., 2015a, 2015b), i.e. along the regional σ_2. Stretching along the regional σ_2 may occur in the hanging wall of laterally-terminating extensional faults oriented perpendicular to the regional σ_3. This is due to the along-strike extension imposed by the arc-shaped downthrow of the hanging wall, pinned at fault terminations (e.g. Destro, 1995; Medwedeff and Krantz, 2002; Tavani and Muñoz, 2012; Fig. 14a). As the amount of stretching depends on fault length/displacement ratio, which is generally high in nature, secondary faults tend to develop sub-perpendicular to the main fault inducing the along-strike hanging-wall extension (e.g. Tavani and Muñoz, 2012). However, some deviation from the perpendicularity of secondary structures may occur close to the main fault tip and/or at relay ramps among overlapping fault segments, thus resulting in a more fan shape network of minor faults (Fig. 14a). This could have further enhanced the heterogeneity of fault orientation and kinematics, which is anyway likely to be largely controlled by the original distribution of inherited fractures (cooling joints; Figs. 6a and 7).

In our instance, larger normal faults are interpreted to have developed by the shear reactivation of pre-existing joints (Fig. 14b), accompanied by the propagation of their tips and related segment linkage, as commonly observed during fault growth (e.g. Crider and Peacock, 2004; Healy et al., 2006; Mazzoli et al., 2009). Within this framework, pre-existing joint sets are interpreted to have been reactivated as normal faults – or oblique-slip faults with extensional dip-slip components – in response to both the regional stress field (for Group B faults) and the local stress field (for Group A faults) in the hanging wall of laterally-terminating, larger normal faults (Fig. 14c). In agreement, we consider the NNW and ENE striking sets of hybrid extension-shear fractures as belonging to a single structural assemblage. This developed by multiple coaxial extensional pulses, during which the maximum extension direction was oriented either ENE-WSW or NNW-SSE. During these multiple extensional pulses, NE and NW striking joints were variably reactivated as oblique-slip, hybrid extension-shear fractures with normal dip-slip components. Such an oblique-slip reactivation of NE and NW striking joint sets was also governed by either ENE-WSW or NNW-SSE trending, sub-horizontal σ_3, as indicated by their kinematic compatibility with the stress regime controlling either Group B or Group A structures (refer to Figs. 10 and 11). The apparently complex pattern of faults and joints is thus the result of a single extensional phase, characterized by repeated events of permutation between σ_2 and σ_3. Such permutations were facilitated by the prolate nature of the stress field, which was characterized by similar magnitudes of σ_2 and σ_3 (as indicated by the Φ values obtained by stress inversion; refer to Figs. 9, 10 and 11). In addition, we infer that a certain variability of the fault and joint strike, as observed in map view (Figs. 3 and 4) and stereographic projections (Fig. 6), is attributable to the progressively densifying network of faults and joints. Indeed, such variability typically results from local stress perturbation in the vicinity of earlier structures (e.g. Bourne and Willemse, 2001; Maerten et al., 2002). This is outstandingly imaged for the Sulfuro vein corridor, which changes its strike of nearly 90° approaching the El Molino fault (Figs. 3 and 4).

Both Group A and Group B faults developed with a vertical σ_1. However, Group A faults were controlled by a NNW trending, sub-horizontal σ_3, whereas Group B faults formed with σ_3 trending ENE. The latter stress field conditions led to the reactivation of NNW trending joints as normal faults (e.g. Sulfuro Vein Corridor), while NE trending joints were locally reactivated as oblique-slip faults with normal dip-slip and left-lateral strike-slip components of motion (e.g. El Molino fault). Following the local release of the tensional stress in the σ_3 direction and the permutation between the σ_2 and the σ_3 axes according to the processes described above (Fig. 14a), the establishment of stress field conditions characterized by a NNW trending σ_3 led to the reactivation of ENE trending joints as normal faults (e.g. Duchesa Trend), while NE trending joints were reactivated as oblique-slip faults with normal dip-slip and dextral strike-slip components of motion (e.g. Arco Iris trend) (refer to Fig. 3). Repeated cycles of hybrid extension-shear fracturing caused multiple stress permutations and joint reactivation, leading to the development of the vein-fault network characterizing the study area.

8.2. Structural controls on ore distribution

The magmatic rocks hosting the mineralization consist of volcanic/volcaniclastic units and felsic intrusions emplaced during Jurassic rifting. These units are characterized by a dense network of joints (Figs. 3–4) that are best interpreted as having developed early after the emplacement of these units (probably during cooling). The joints are organized into four main sets showing similar orientations to the fault sets (hybrid extension-shear fractures) controlling the mineralization (refer to Fig. 6). This feature, together with the mutually overprinting relationships characterizing the different fault sets, suggest that the faults developed from the reactivation of pre-existing joints, probably as a result of continued extension coeval with the emplacement of the volcanic succession forming the Bajo Pobre Formation. The significant dilation component recorded by thick veins developed along hybrid extension-shear fractures suggests that fluid pressure played a major

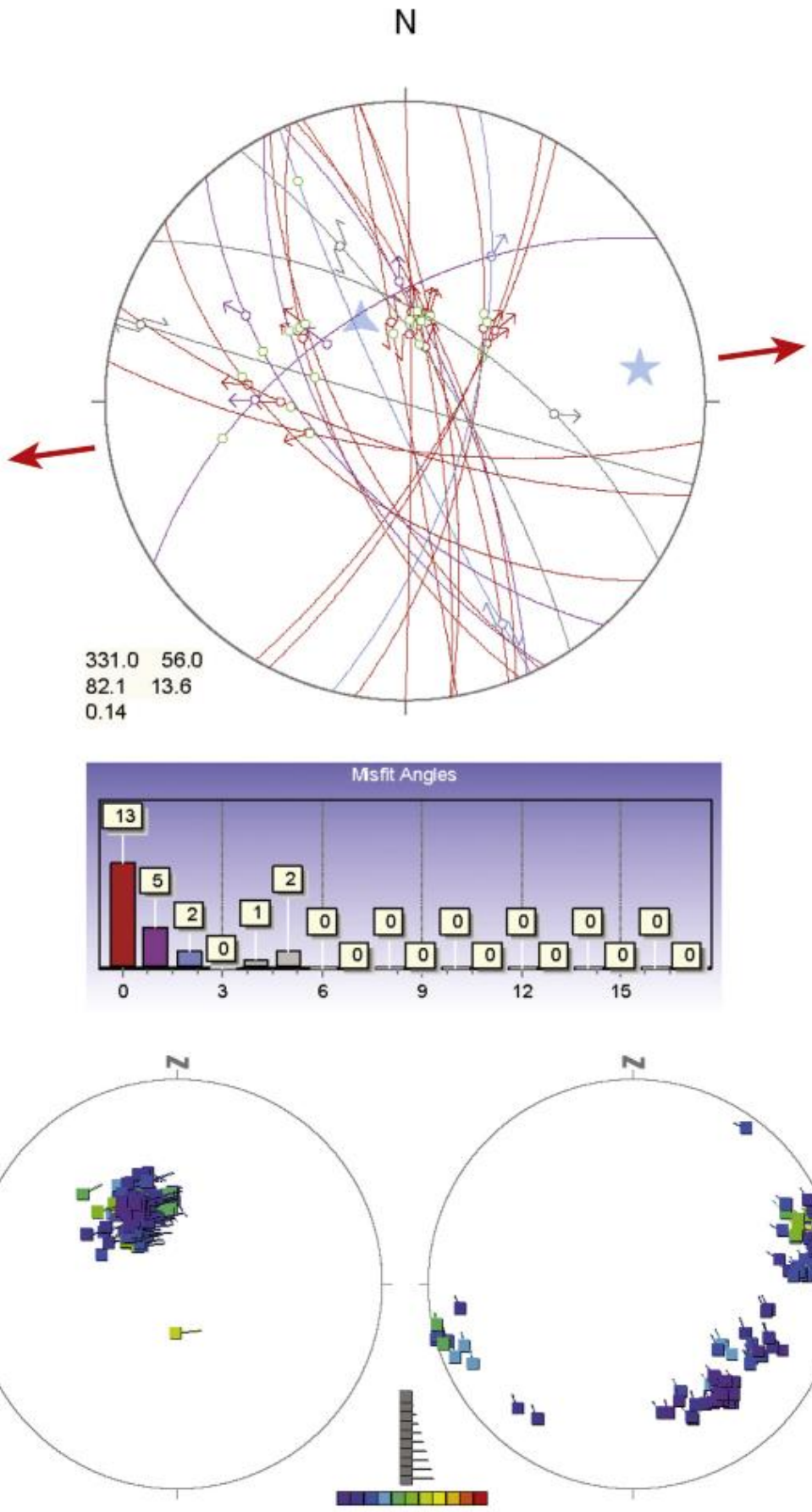

(caption on next page)

Fig. 11. Results of paleostress analysis for Group B faults (in the upper diagram, three-armed star is σ_1, plunging 56° towards 331N; five-armed star is σ_3, plunging 13° towards 082 N; red arrows show extension direction in the horizontal plane). Misfit angles (see text) are shown in the centre diagram. Legend for the lower diagrams, showing σ_1 (left) and σ_3 (right) stress axes, as in Fig. 9. (For interpretation of the references to colour in this figure legend, the reader is referred to the web version of this article.)

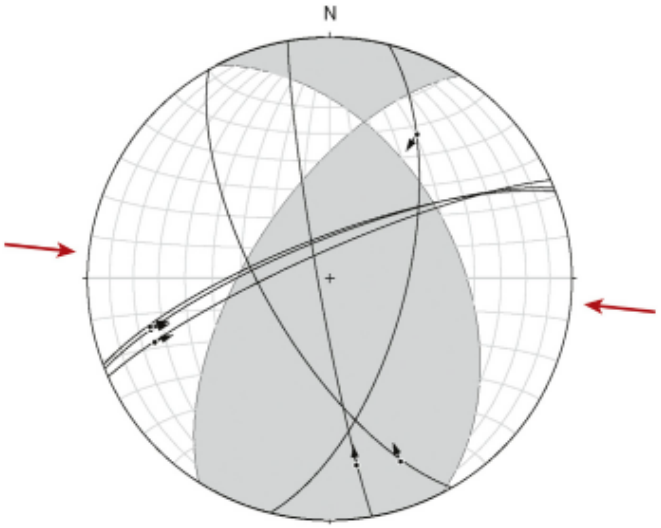

Fig. 12. Fault plot (great circles) with associated slickenlines (black arrow shows hanging-wall motion), and results of paleostress analysis for late-stage fault reactivations. Stress inversion performed with the software FaultKin furnished a maximum compression axis (σ_1) plunging 9° towards 276°N and a minimum compression axis (σ_3) plunging 54° towards 172°N (red arrows show compression direction in the horizontal plane). (For interpretation of the references to colour in this figure legend, the reader is referred to the web version of this article.)

role in the development of the mineralized extensional features. Although the tensile strength of a rock mass already presenting a dense network of early-formed joints is obviously substantially lower than that of the intact rock, it has to be taken into account that tensile strength is likely to be regained as a result of mineralization and cementation processes following each fracturing/fracture reactivation event. The distribution of gold and base metal mineralization along the fracture systems at La Paloma is related to epithermal silica veins, stockworks and breccias that developed during multiple, mutually overprinting extensional events described above. Reactivation of pre-existing joints as hybrid extensional-shear fractures focused large volumes of hydrothermal mineralizing fluids, leading to ore deposit formation. Veins at La Paloma occupy major NNW to NW (with N-S to NNE local variations), ENE to E-W and NE striking normal faults with variable amounts of strike-slip displacement. Thicknesses, textures and ore-shoot geometries within epithermal veins show strong relationships with paleostress conditions during their formation, as discussed below.

The El Molino NE trending structures, which were reactivated by sinistral oblique-slip during regional ENE stretching (therefore belonging to Group B structures), do not show significant dilation and vein opening as shown in Fig. 5h. On the other hand, Group B structures consisting of NNW to NW striking joints reactivated by regional ENE stretching include the major vein systems of the Sulfuro, Princesa & Reyna and Verde trends. They constitute the dominant features in terms of vein strike continuity, thickness and ore grades. The ore-shoots at Sulfuro are characterized by complex, multiphase hydrothermal breccia textures (e.g., Figs. 5a–c) produced by repeated steps of opening and subsequent vein filling. According to the mechanism of brecciation defined by Jébrak (1997), these textures suggest repeated hydraulic fracturing and pressure release during vein formation. The main ore shoot is characterized by a broad area dominated by medium to high gold and base metal content (Mo-Zn-Pb-Cu) with anomalous concentrations of As and Sb, that extends along the vein strike for almost 500 m with a gentle plunge (of approximately 10° towards the S) (Fig. 15a). The sub-horizontal geometry of ore-shoots at the Sulfuro vein (Fig. 15a) is consistent with dominant extensional faulting during mineralization and is characterized by a gentle plunge (of approximately 10° towards the S) and by large vein thicknesses (Fig. 15b). Ore grade distribution shows a structural compartmentalization (Fig. 15a) controlled by ENE to NE striking faults (Fig. 15c). In the southern part of the study area, a ENE- to NE-striking fault is interpreted to constitute the boundary of the Sulfuro vein. Surface recognition of this fault is

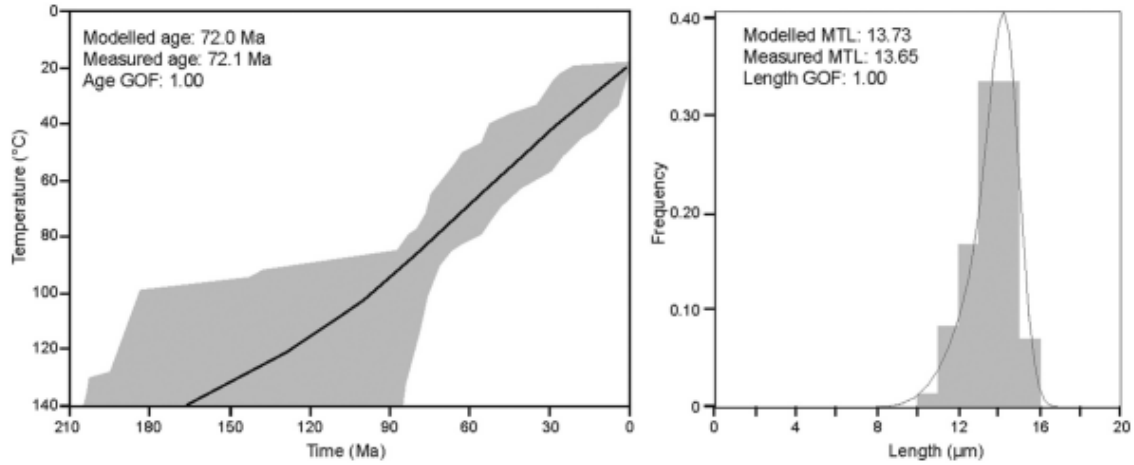

Fig. 13. Time–temperature paths obtained for sample G24 from inverse modelling using the HeFTy program (Ketcham, 2005), which generates possible T–t paths using a Monte Carlo algorithm. Predicted apatite fission-track data were calculated according to the Ketcham et al. (2007) annealing model and Dpars as kinetic parameter. Shaded areas mark envelopes of statistically good fit (goodness-of-fit [GOF] > 0.5) and thick lines correspond to the thermal history with best fit (= maximum GOF). Thermal paths outside the partial annealing zone are largely inferential as fission-track data provide reliable information only in the temperature range 60–120 °C (the exact temperatures depending on resistance to annealing and cooling rate). GOF gives an indication of the fit between observed and predicted data (values close to 1 are best). Mean track lengths (right diagram) are reported after c-axis projection and therefore differ from those listed in Table 1. Intrusion of the rock body containing the sample and present-day mean surface temperature converted into time–temperature boxes have been used as constraints.

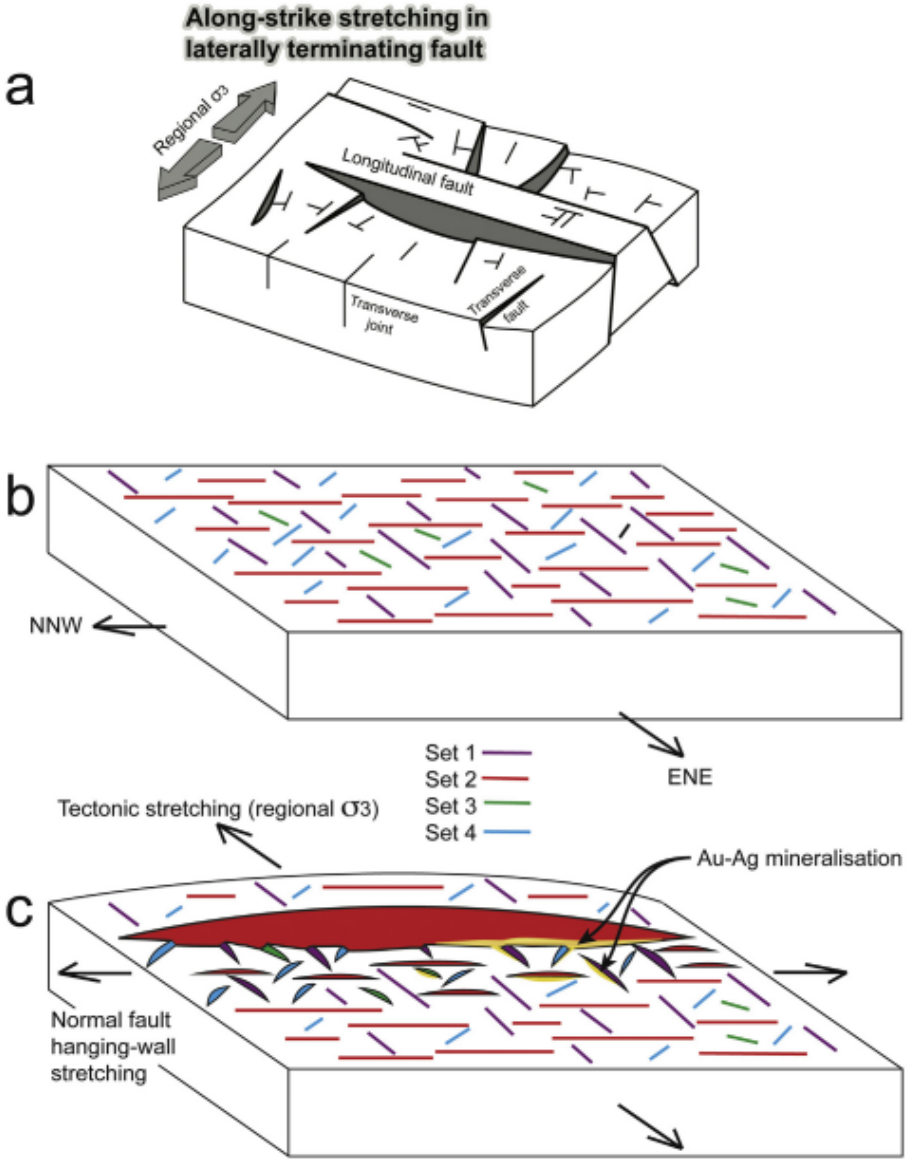

Fig. 14. (a) Cartoon showing along-strike stretching in the hanging wall of a normal fault (e.g. Destro, 1995; Medwedeff and Krantz, 2002; Tavani and Muñoz, 2012; Tavani et al., 2015a, 2015b; see text for details). (b) Interpretative block diagram showing early joint sets of the study area. (c) Schematic representation of joint reactivation as a result of both regional ENE stretching and orthogonal stretching in the hanging wall of a normal fault.

difficult, but it can be inferred from lineaments on satellite imagery and available geophysical data. The steep plunge of the main ore shoot towards the S with increasing depth suggests a significant component of strike-slip motion controlling ore deposition and/or efficient upward fluid flow along the intersection of the Sulfuro vein with both ENE- and NW- striking faults (Fig. 15c), which is also reflected in more intense argillitic alteration at the surface. This sector of steep ore shoot plunge (4,715,700 in Fig. 15a) probably represents the original up-flow zone of the hydrothermal system. Here, upward fluid flow may have been enhanced by the dilation associated with oblique-slip along the almost N-S striking segment of the markedly arcuate, steeply dipping Sulfuro vein. Northward, where the structure has a subtle NW strike swing (4,716,050 in Fig. 15c), ore shoots are smaller and irregularly distributed. They show gentle to moderate plunges (dominantly around 35° towards the south; Fig. 15a), probably associated with variable kinematics of the shear component during vein formation.

ENE to E-W striking structures, reactivated as a result of NNW stretching (Group A structures), include the Duquesa trend which consists of thin disconnected vein segments with minor opening and filling events than thicker NNW to NW striking ones. NE striking joints reactivated as normal and dextral oblique-slip faults controlled by NNW stretching (therefore also belonging to Group A structures) are represented by the Arco Iris trend. This latter is characterized by hybrid extension-shear quartz veins displaying single-phase breccia textures with volumetrically minor vein fill and/or vein clasts within a fault gouge matrix containing iron oxides (e.g., Fig. 5f, g). This feature is consistent with the substantial strike-slip component of motion characterizing the oblique-slip reactivation of these inherited joints.

The fundamental role played by inherited structures in the development of ore deposits of economic interest is thus emphasized by this study. The oblique-slip reactivation of precursor joints resulted in an articulated geometry of ore shoots. These range from gently to steeply plunging for dominant dip-slip and strike-slip joint reactivation, respectively (Nelson, 2006). As ore shoots tend to be parallel to the intermediate (σ_2) stress axis (Nelson, 2006), the permutations between σ_2 and σ_3 stress axes outlined in this study render the system even more complex. However, this complexity is not the result of distinct deformation stages controlled by major changes in the regional stress field

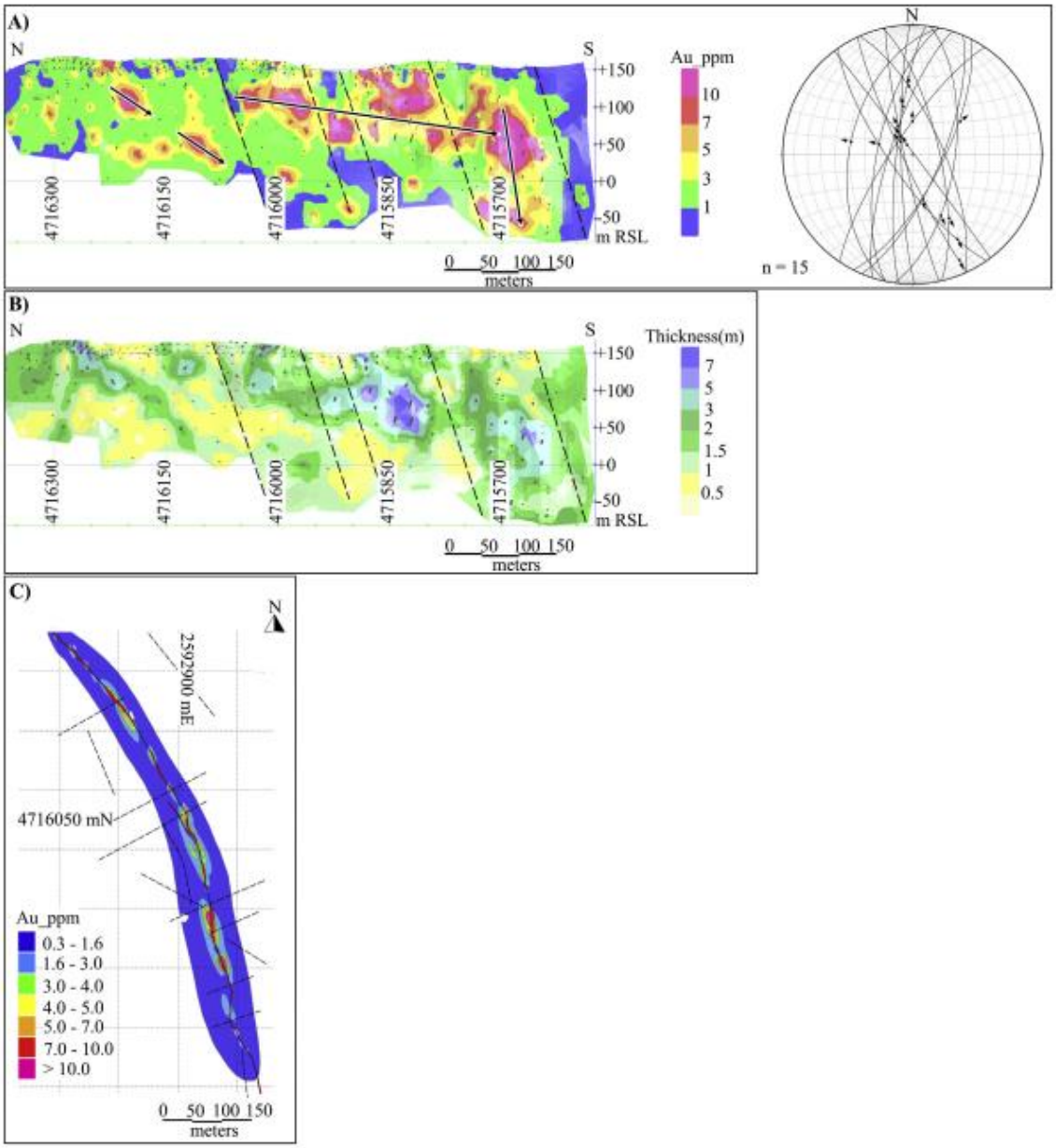

Fig. 15. Ore-shoot characteristics of the Sulfuro vein (dashed lines are faults). (a) Gold content in strike section (black arrows show main ore-shoot gentle plunge in the central part, steep plunge of the mineralization towards the southern part of the vein and gentle to moderate plunges northward. The stereographic projection shows faults (great circles) and associated slickenlines (arrow shows hanging-wall motion). (b) Vein thickness in strike section. (c) Ore grade distribution in map view. (For details on the color codes the reader is referred to the web version of this article.)

and/or tectonic setting, commonly invoked in similar instances. Rather, it is the result of the reactivation pattern of a network of variably oriented, pre-existing joints within the framework of a stress field dominated by a roughly vertical σ_1. This may have major implications for a deeper understanding of processes governing the formation of structurally controlled ore deposits, also allowing for a better definition of their three-dimensional architecture and relative chronology of ore shoots and vein development.

8.3. Late fault reactivation and final exhumation

Subsequent, localized oblique-slip kinematic overprinting was characterized by reverse components of motion accompanying dextral strike-slip (refer to Figs. 8c–d and 12). This late stage fault reactivation occurred without any evidence of reworking of gold mineralization due to fluid circulation. Fault reactivation was associated with a sub-horizontal, roughly E-W trending maximum compressive stress (σ_1) best interpreted as a result of far field propagation of Andean stresses into the Deseado Massif. In fact, it is well known that stages of substantial coupling between the fold-thrust belt and its foreland characterized the geodynamic evolution of Patagonia, producing significant deformation in the interior of the South American plate (e.g. Ramos and Folguera, 2009). The documented late fault reactivation cannot be directly dated in the study area. However, a correlation with the late Early Cretaceous deformation marked by the unconformity at the base of the Baqueró Fm. (Homovc and Constantini, 2001; Giacosa et al., 2010) may be proposed based on the kinematics of fault reactivation and the reconstructed paleostress field. It is worth noting that the AFT cooling ages obtained in this study do not allow the detection of a particular exhumation event, as they indicate nearly steady-state cooling in the last 90 Ma (Fig. 13). Similar cooling ages were obtained by Savignano et al. (2016) based on thermal modelling of U-Th/He data from samples

collected in an equivalent tectonic setting of the Andean foreland at northern latitudes (41°–43°S). Therefore, thermochronometric data suggest that late fault reactivation associated with E-W shortening in the study area was not accompanied by focused erosion of uplifted fault blocks, as the cooling paths seem not to be affected by any particular acceleration. Thermochronometric data neither record enhanced Neogene uplift produced by the Chile ridge subduction and the related development of an asthenospheric window beneath Patagonia (e.g. Guillaume et al., 2009), thus indicating that the dynamic topography associated with these processes was not sufficient to trigger significant exhumation by fast erosional unroofing. The detrital material produced by slow erosional unroofing of the Deseado Massif during the last 90 Ma is most probably preserved in adjacent sedimentary basins, including the Magallanes-Austral Basin to the south and the Golfo San Jorge Basin to the north (refer to Fig. 1).

9. Conclusions

The clear geometric consistency between hybrid extension-shear fracture sets and widespread joint sets in the study area suggest that the former developed by late-stage reactivation of precursor joints. The normal to oblique- to strike-slip reactivation of pre-existing joints led to the hybrid extension-shear fractures hosting a mineralization of economic interest. The observed four sets of hybrid extension-shear fractures form two groups of structures that are kinematically compatible with either ENE or NNW trending σ_3, within the framework of an extensional stress field characterized by multiple permutations between the σ_3 and the σ_2 axes. Such permutations are interpreted to have resulted from the reactivation of some of the NNW striking joints as normal faults in response to regional ENE stretching, and by orthogonal (i.e. NNW) extension in the hanging wall of such laterally-terminating normal faults associated with along-strike stretching produced by the differential downthrow of the hanging-wall block. Within this framework, further (i.e. NE and NW striking) joint sets were variably reactivated as oblique-slip dilational faults invariably showing extensional dip-slip components of motion accompanying strike-slip ones.

The NNW to NW trending hybrid extension-shear fractures controlled by regional ENE stretching were the most effective for hydrothermal fluid circulation. They are characterized by the development of lodes with exceptional width, lateral and vertical extent, and the subsequent ore deposition. Ore shoot formation appears to have been favoured by the early joint sets preferentially developed in the more competent, coherent andesite host rock. Probably several reactivations of the fracture systems favoured metal deposition, as evidenced by dominant hydrothermal breccia textures and by the ore-shoot geometry recorded within the Sulfuro vein trend. Vein textures characterizing the NE striking Arco Iris and El Molino fracture systems record no major dilation and vein opening history. These fracture systems remained almost barren compared with the NNW to NW and ENE to E-W striking veins.

The results of this study provide new insights into the complex interactions between inherited joint sets and stress permutations. In particular, fractures belonging to four sets of precursor joints were locally reactivated as hybrid extension-shear fractures displaying variable components of normal and strike-slip motion. Paleostress analysis by the Multiple Inversion Method (Yamaji, 2000; Otsubo and Yamaji, 2006) indicates that all the resulting faults may be reconciled within an extensional stress field characterized by relatively simple, well-explained permutations between the σ_3 and the σ_2 axes. As multiple stress permutations are common in most extensional settings, the results of this study may allow geologists to gain a better understanding of the structural architecture, modes and relative timing of ore deposit formation controlled by fracture-fault networks.

A record of localized, late fault reactivation associated with a far field propagation of Andean stresses into the Deseado Massif has also been unravelled in the study area. Oblique-slip kinematic overprinting of pre-existing faults was characterized by dominant dextral strike-slip and subordinate reverse components of motion. Paleostress analysis applied to these structures point out a dominant sub-horizontal, roughly E-W trending maximum compressive stress (σ_1). This deformation could be related with the late Early Cretaceous shortening event documented in the area (Homovc and Constantini, 2001; Giacosa et al., 2010). The subsequent tectonic evolution of the study area, as recorded by our new apatite fission track data, was characterized by nearly steady-state exhumation at a rate of c. 1 °C/Ma during the last 90 Ma.

Acknowledgements

This work forms part of a Project financed by Agencia Nacional de Ciencia y Tecnología (PICT n° 2017-4577, préstamo BID), Consejo Nacional de Investigaciones Científicas y Técnicas Argentino (PIP n° 105) and Universidad Nacional del Comahue (PIN 04-I209), and by the University of Padua, Italy (Progetto di Ateneo 2015, CPDA158355). We express our appreciation to the exploration staff of Minera Don Nicolas S.A. mining company for provision of site access, logistic support, and help during the field work. We are especially grateful to the Exploration Manager, Lic. Silvio Franco, for his support that allowed us to conduct the structural analysis at La Paloma. Original datasets are available by contacting the authors (SM for structural data; MLF for ore deposits data; MZ for thermochronological data). The paper greatly benefitted from thorough and constructive reviews by Antonio Benedicto and Vincent Roche, and by the comments of the Editor Philippe Agard.

Author contribution

María Lis Fernández, Stefano Mazzoli and Elisa Savignano carried out the field structural analysis. María Lis Fernández and Alejandro Garrone carried out background geological mining investigations. Marta Franchini integrated and supervised the ore geology part of the study. Stefano Tavani integrated the structural part of the study, also with diagrams. Massimiliano Zattin, Elisa Savignano and Marie Catherine Genge carried out the thermochronological work. María Lis Fernández and Stefano Mazzoli wrote the paper, with the contribution of Massimiliano Zattin for the thermochronological study.

Declaration of competing interest

The authors declare that they have no known competing financial interests or personal relationships that could have appeared to influence the work reported in this paper.

References

Angelier, J., 1979. Determination of the mean principal directions of stresses for a given fault population. Tectonophysics 56, T17–T26.
Angelier, J., 1994. Fault-slip analysis and paleostress reconstruction. In: Hancock, P.L. (Ed.), Continental Deformation. Pergamon, Oxford, pp. 101–120.
Archangelsky, S., 1967. Estudio de la Formación Baqueró, Cretácico inferior de Santa Cruz, Argentina. Rev. Museo de La Plata. Paleontología 5, 63–171.
Archangelsky, S., Cuneo, R., 1984. Zonación del Pérmico continental Argentino sobre la base de sus plantas fósiles. III Congreso Latinoamericano de Paleontología, pp. 143–153.
Arrondo, O., 1972. Estudio geológico y paleontológico de la zona de la Estancia La Juanita y alrededores, provincia de Santa Cruz, Argentina. Rev. Museo de La Plata, Paleontología 7, 1–194.
Begbie, M.J., Spörli, K.B., Mau, J.L., 2007. Structural evolution of the golden cross epithermal Au-Ag deposit, New Zealand. Econ. Geol. 102, 873–892.
Berger, B.R., Tingley, J.V., Drew, L.J., 2003. Structural localization and origin of compartmentalized fluid flow, Comstock lode, Virginia City, Nevada. Econ. Geol. 98, 387–408.
Bott, M.H.P., 1959. The mechanics of oblique slip faulting. Geol. Mag. 96, 109–117.
Bourne, S.J., Willemse, E.J., 2001. Elastic stress control on the pattern of tensile fracturing around a small fault network at Nash Point, UK. J. Struct. Geol. 23, 1753–1770.
Cladera, G., Andreis, R., Archangelsky, S., 1999. Baqueró group: A new stratigraphic proposal for the lower cretaceous of Santa Cruz Province, Argentina. In: VII

International Symposioum on Mesozoic Terrestrial Ecosystems, Buenos Aires, Argentina, Abstracts 17. Museo Argentino de Ciencias Naturales, Buenos Aires.
Cox, S.F., 2005. Coupling between deformation, fluid pressures, and fluid flow in ore-producing hydrotermal systems al depth in the crust. Economic Geology 100th Anniversary 39–75.
Cox, S.F., Knackstedt, M.A., Braun, J., 2001. Principles of structural control on permeability and fluid flow in hydrothermal systems. In: Richards, J.P., Tosdal, R.M. (Eds.), Structural Controls on Ore Genesis. Rev. in Economic Geol, vol. 14. pp. 1–24.
Crider, J.G., Peacock, D.C.P., 2004. Initiation of brittle faults in the upper crust: a review of field observations. J. Struct. Geol. 26, 691–707.
Dasgupta, S., Mukherjee, S., 2017. Brittle shear tectonics in a narrow continental rift: asymmetric non-volcanic Barmer basin (Rajasthan, India). J. Geol. 125, 561–591.
De Barrio, R.E., 1993. El vulcanismo ácido jurásico en el noroeste de Santa Cruz, Argentina. In: XII Congreso Geológico Argentino, Buenos Aires, pp. 189–198.
De Barrio, R.E., Panza, J.L., Nullo, F.E., 1999. Jurásico y Cretácico del Macizo del Deseado, provincia de Santa Cruz. In: Caminos, R. (Ed.), Geología Argentina, Servicio Geológico Minero Argentino, pp. 511–527.
Delvaux, D., 2011. Win-Tensor, an interactive computer program for fracture analysis and crustal stress reconstruction. In: EGU Generai Assembly, Vienna, 2011. Geophys. Res. Abstr. 13, EGU2011–4018.
Delvaux, D., Sperner, B., 2003. New aspects of tectonic stress inversion with reference to the TENSOR program. In: Nieuwland, D.A. (Ed.), New Insights into Structural Interpretation and Modeling. vol. 212. Geological Society of London, Special Publication, pp. 75–100.
Destro, N., 1995. Release fault: a variety of cross fault in linked extensional fault systems, in the Sergipe-Alagoas Basin, NE Brazil. J. Struct. Geol. 17, 615–629. https://doi.org/10.1016/0191-8141(94)00088-H.
Di Persia, C., 1962. Acerca del descubrimiento del Precámbrico en la Patagonia Extrandina (provincia de Santa Cruz). In: Primeras Jornadas Geológicas Argentinas, Anales II, pp. 65–68.
Dunne, W.M., Hancock, P.L., 1994. Paleostress analysis of small-scale brittle structures. In: Hancock, P.L. (Ed.), Continental Deformation. Pergamon, Oxford, pp. 101–120.
Echavarría, L.E., Schalamuk, I.B., Etcheverry, R.O., 2005. Geologic and tectonic setting of Deseado Massif epithermal deposits, Argentina, based on El Dorado-Monserrat. J. S. Am. Earth Sci. 19 (4), 415–432.
Echeveste, H., 2005. Metalogénesis del Distrito Argento-Aurífero Manantial Espejo, Macizo del Deseado, Provincia de Santa Cruz. Ph.D. thesis. Universidad Nacional de La Plata, La Plata, Argentina, pp. 272.
Echeveste, H., Fernández, R., Bellieni, G., Tessone, M., Llambias, E., Schalamuk, I., Piccirillo, E., De Min, A., 2001. Relaciones entre las Formaciones Bajo Pobre y Chon Aike (Jurásico medio a superior) en el área de Estancia El Fénix-Cerro Huemul, zona centro-occidental del Macizo del Deseado, provincia de Santa Cruz. Rev. Asoc. Geol. Argentina 56, 548–558.
Engelder, T., Gross, M.R., 1993. Curving cross joints and the lithospheric stress field in eastern North America. Geology 21, 817. https://doi.org/10.1130/0091-7613(1993)021<0817:CCJATL>2.3.CO;2.
Feraud, G., Alric, V., Fornari, M., Bertrand, H., Haller, M., 1999. $^{40}Ar/^{39}Ar$ dating of the Jurassic volcanic province of Patagonia: migrating magmatism related to Gondwana break-up and subduction. Earth Planet. Sci. Lett. 172 (1), 83–96.
Fernández, R.R., Blesa, A., Moreira, P., Echeveste, H., Mykietiuk, K., Andrada De Palomera, P., Tessone, M., 2008. Los depósitos de oro y plata vinculados al magmatismo Jurásico de la Patagonia: Revisión y perspectivas para la exploración. Rev. Asoc. Geol. Argentina 63 (4), 665–681.
Feruglio, E., 1949. Descripción geológica de la Patagonia. In: Yacimientos Petrolíferos Fiscales, Tomo I, Buenos Aires.
Galbraith, R., 1981. On statistical models for fission track counts. Math. Geol. 13, 471–478.
Garrone, A., 2018Garrone, Unpublished. Reporte de Recursos – Sistema Sulfuro, MDN Internal Reports. pp. 33.
Giacosa, R., Zubia, M., Sánchez, M., Allard, J., 2010. Meso-Cenozoic tectonics of the southern Patagonian foreland: structural evolution and implications for Au–Ag veins in the eastern Deseado Region (Santa Cruz, Argentina). J. S. Am. Earth Sci. 30, 134–150.
González Guillot, M., de Barrio, R., Ganem, F., 2004. Mina Martha, un yacimiento epitermal argentífero en el Macizo del Deseado, provincia de Santa Cruz. In: VII Congreso de Mineralogía y Metalogenia, pp. 119–204.
Gorring, M., Kay, S., Zeitler, P., Ramos, V., Rubiolo, D., Fernández, M., Panza, J., 1997. Neogene Patagonian plateau lavas. Continental magmas associated with ridge collision at the Chile triple junction. Tectonics 16 (1), 1–17.
Grant, C., Ghaffari, H., De Ruijter, A., Corley, D., Guzmán, C., Cadden, A., Sanford, A., Osterberg, S., 2012. Minera IRL Patagonia S.A., Santa Cruz, Argentina. Don Nicolás Gold Project NI 43-101 Technical Report, 207. Available at. http://www.sedar.com.
Guido, D., Schalamuk, I., 2003. Genesis and exploration potential for low sulfidation epithermal deposits in the Deseado Massif, Argentinean Patagonia. In: Eliopoulos, D.G. (Ed.), Mineral Exploration and Sustainable Development. Society for Geology Applied to Mineral Deposits, Balkema-Rotterdam, Athens, Greece, pp. 493–496.
Guido, D., Escayola, M.P., Schalamuk, I., 2004. The basement of the Deseado Massif at Bahía Laura, Patagonia, Argentina: a proposal for its evolution. J. S. Am. Earth Sci. 16, 567–577.
Guido, D.M., Jovic, S.M., Schalamuk, I.B., 2005. A new metallogenic association (Sn–Cd–In–Zn–Ag–Au) in the Deseado Auroargentiferous province, Deseado Massif, Patagonia, Argentina. Meeting the Global Challenge — 8th SGA Meeting, Beijing, China. Mineral Deposit Research 2, 965–968.
Guido, D.M., 2004. Subdivisión litofacial e interpretación del volcanismo jurásico (Grupo Bahía Laura) en eleste del Macizo del Deseado, provincia de Santa Cruz. Rev. Asoc. Geol. Argentina 59 (4), 727–742.
Guido, D., Escayola, M., de Barrio, R., Schalamuk, I., Franz, G., 2006. La Formación Bajo Pobre (Jurásico) en el este del Macizo del Deseado, Patagonia Argentina: Vinculación con el Grupo Bahía Laura. Rev. Asoc. Geol. Argentina 61 (2), 187–196.
Guillaume, B., Martinod, J., Husson, L., Roddaz, M., Riquelme, R., 2009. Neogene up- lift of central eastern Patagonia: dynamic response to active spreading ridge subduction? Tectonics 28, TC2009. https://doi.org/10.1029/2008tc002324.
Healy, D., Jones, R.R., Holdsworth, R.E., 2006. Three-dimensional brittle shear fracturing by tensile crack interaction. Nature 439, 64–67. https://doi.org/10.1038/nature04346.
Hechem, J., Homovc, J.F., 1988. Facies y paleoambientes volcaniclásticos en el Nesocratón del Deseado. Boletín de Informaciones Petroleras 16, 2–23.
Henley, R.W., 1985. The geothermal framework for epithermal deposits. Rev. in Economic Geology 2, 1–24.
Henley, R.W., Berger, B.R., 2000. Self-ordering and complexity in epizonal mineral deposits. Annu. Rev. Earth Planet. Sci. 28, 669–719.
Henley, R.W., Etheridge, M.A., 1995. The structural and hydrodynamic framework for epithermal exploration. Australasian Institute of Mining and Metallurgy, Publication Series 9, 269–277.
Homovc, J.F., Constantini, L., 2001. Hydrocarbon exploration potential within intraplate shear-related depocenters: Deseado and San Julian basins, southern Argentina. Am. Assoc. Pet. Geol. Bull. 85 (10), 1795–1816.
Huang, G., Charlesworth, H., 1989. A FORTRAN-77 program to separate a heterogeneous set of orientations into subsets. Comput. Geosci. 15, 1–7.
Hurford, A.J., 1990. Standardization of fission track dating calibration: recommendation by the Fission Track Working Group of the I.U.G.S. Subcommission on Geochronology. Chem. Geol. 80, 171–178.
Hurford, A.J., Green, P.F., 1983. The zeta age calibration of fission-track dating. Chem. Geol. 41, 285–317.
Japas, M.S., Sruoga, P., Kleiman, L., Gayone, M.R., Maloberti, A., Comito, A., 2013. Cinemática de la extensión jurásica vinculada a la provincia silícea Chon Aike, Santa Cruz. Argentina. Rev. Asoc. Geol. Argentina 70 (1), 16–30.
Jébrak, M., 1997. Hydrothermal breccias in vein-type ore deposits: a review of mechanisms, morphology and size distribution. Ore Geology Review 12, 111–134.
Jovic, S.M., 2010. Geología y Metalogénesis de las mineralizaciones polimetálicas del área El Tranquilo (Cerro León), sector central del Macizo del Deseado, Provincia de Santa Cruz. Ph.D. thesis. 1ra ed. Editorial de la Universidad de La Plata (EDULP), La Plata, Argentina (278 pp).
Jovic, S.M., Jovic, N.R., Guido, D.M., Schalamuk, I.B., 2008. Caracterización de cuerpos intrusivos de la formación Cerro León en el área del Anticlinal el Tranquilo, Macizo del Deseado, Santa Cruz. XVII Congreso Geológico Argentino, Jujuy, pp. 851–852.
Jovic, S.M., Guido, D.M., Schalamuk, I.B., Ríos, F.J., Tassinari, C.C.G., Recio, C., 2011. Pingüino bearing polymetallic vein deposit, Deseado Massif, Patagonia, Argentina: characteristics of mineralization and ore-forming fluids. Mineral. Deposita 46, 257–271.
Ketcham, R.A., 2005. Forward and inverse modeling of low-temperature thermochronometry data. Rev. Mineral. Geochem. 58, 275–314.
Ketcham, R.A., Carter, A., Donelick, R.A., Barbarand, J., Hurford, A.J., 2007. Improved modeling of fission track annealing in apatite. Am. Mineral. 92, 799–810.
Lesta, P., Ferello, R., 1972. Región Extraandina de Chubut y Norte de Santa Cruz. In: Leanza, A. (Ed.), Geología Regional Argentina. Academia Nacional de Ciencias, Córdoba, pp. 602–687.
López, L., Jovic, S.M., Guido, D.M., Permuy Vidal, C., Páez, G.N., Ruiz, R., 2015. Geochemical distribution and supergene behavior of indium at the Pingüino epithermal polymetallic vein system, Patagonia, Argentina. Ore Geol. Rev. 64, 747–755.
Maerten, L., Gillespie, P., Pollard, D.D., 2002. Effects of local stress perturbation on secondary fault development. J. Struct. Geol. 24, 145–153.
Marrett, R., Peacock, D.C.P., 1999. Strain and stress. J. Struct. Geol. 21, 1057–1063.
Mazzoli, S., Vitale, S., Delmonaco, G., Guerriero, V., Margottini, C., Spizzichino, D., 2009. 'Diffuse faulting' in the Macchu Picchu granitoid pluton, Eastern Cordillera, Peru. J. Struct. Geol. 31, 1395–1408.
Medwedeff, D.A., Krantz, R.W., 2002. Kinematic and analog modeling of 3-D extensional ramps: observations and a new 3-D deformation model. J. Struct. Geol. 24, 763–772. https://doi.org/10.1016/S0191-8141(01)00121-3.
Moreira, P., Fernandez, R.R., 2015. La Josefina Au–Ag deposit (Patagonia, Argentina): a Jurassic epithermal deposit formed in a hot spring environment. Ore Geol. Rev. 67, 297–313.
Nelson, E.P., 2006. Drill-hole design for dilational ore shoot targets in fault-fill veins. Econ. Geol. 101, 1079–1085.
Otsubo, M., Yamaji, A., 2006. Improved resolution of the multiple inverse method by eliminating erroneous solutions. Comput. Geosci. 32, 1221–1227.
Páez, G.N., 2012. Génesis del yacimiento de metales preciosos Mina Martha, sector sudoccidental del Macizo del Deseado, provincia de Santa Cruz. Ph.D. thesis. Universidad Nacional de La Plata, La Plata, Argentina 241 pp. Available at. http://sedici.unlp.edu.ar/handle/10915/25765.
Páez, G.N., Ruiz, R., Guido, D.M., Ríos, F.J., Subias, I., Recio, C., Schalamuk, I.B., 2016. Highgrade ore shoots at the Martha epithermal vein system, Deseado Massif, Argentina: the interplay of tectonic, hydrothermal and supergene processes in ore genesis. Ore Geol. Rev. 72, 546–561.
Pankhurst, R.J., Rapela, C.W., Marquez, M., 1993. Geocronología y petrogénesis de los granitoides jurásicos del noreste del Macizo del Deseado. In: XII Congreso Geológico Argentino, Mendoza, pp. 134–141.
Pankhurst, R.J., Caminos, R., Rapela, C.W., 1993a. Problemas geocronológicos de los granitoides Gondwánicos de Nahuel Niyeu, Macizo Norpatagónico. XII Congreso Geológico Argentino, Mendoza, pp. 99–104.
Pankhurst, R.J., Leat, P.T., Sruoga, P., Rapela, C.W., Márquez, M., Storey, B.C., Rilley, T.R., 1998. The Chon Aike province of Patagonia and related rocks in West

Antarctica: a silicic large igneous province. J. Volcanol. Geotherm. Res. 81, 113–136.
Panza, J.L., 1982. Descripción geológica de las Hojas 53e, Gobernador Moyano y 54e Cerro Vanguardia, provincia de Santa Cruz. In: Servicio Geológico Nacional (1982), Buenos Aires, pp. 197.
Panza, J., 1998. Hoja Geológica 4769-IV, Monumento Nacional Bosque Petrificado, Provincia de Santa Cruz, escala 1:250000. Servicio Geológico Minero Argentino, Buenos Aires.
Panza, J., Franchi, M., 2002. Magmatismo Basáltico Cenozoico Extraandino. In: Haller, M.J. (Ed.), Geología y Recursos Naturales de Santa Cruz. XV Congreso Geológico Argentino, Buenos Aires, pp. 259–284.
Peacock, D.C.P., Marrett, R., 2000. Strain and stress: reply. J. Struct. Geol. 22, 1369–1378.
Permuy Vidal, C., 2014. Caracterización detallada de la mineralización en veta Eureka, y su comparación con otras mineralizaciones del Distrito Cerro Negro, Macizo del Deseado, Santa Cruz, Argentina. Ph.D. thesis. Facultad de Ciencias Naturales y Museo, La Plata, Argentina 275 pp. Available at. http://sedici.unlp.edu.ar/handle/10915/36121.
Permuy Vidal, C., Guido, D.M., Jovic, S.M., Bodnar, R.J., Moncada, D., Melgarejo, J.C., Hames, W., 2016. The Marianas-San Marcos vein system: characteristics of a shallow low sulfidation epithermal Au–Ag deposit in the Cerro Negro district, Deseado Massif, Patagonia, Argentina. Mineral. Deposita 51 (6), 725–748.
Ramos, V.A., 2002. Evolución Tectónica. In: Haller, M.J. (Ed.), Recursos Naturales de Santa Cruz, Relatorio XV Congreso Geológico Argentino. Asociación Geológica Argentina, Buenos Aires, pp. 365–387.
Ramos, V.A., Folguera, A., 2009. Andean flat-slab subduction through time. Geol. Soc. London Spec. Publ. 327 (1), 31–54.
Ramsay, J.G., Huber, M.I., 1983. The Techniques of Modern Structural Geology, Volume I: Strain Analysis. Academic Press, London.
Rapela, C.W., Pankhurst, R.J., 1996. Monzonite suites: the innermost Cordilleran plutonism of Patagonia. Trans. R. Soc. Edinburgh: Earth Sci. 87, 193–203.
Rapela, C.W., Pankhurst, R.J., Fanning, C.M., Hervé, F., 2005. Pacific subduction coeval with the Karoo mantle plume: the Early Jurassic Subcordilleran belt of northwestern Patagonia. Geol.Soc. Lond., Spec. Publ. 246, 217–239.
Savignano, E., Mazzoli, S., Arce, M., Franchini, M., Gautheron, C., Paolini, M., Zattin, M., 2016. (Un) coupled thrust belt-foreland deformation in the northern Patagonian Andes: new insights from the Esquel-Gastre sector (41°30′–43° S). Tectonics 35 (11), 2636–2656.
Schalamuk, I.B., Zubia, M., Genini, A., Fernandez, R.R., 1997. Jurassic epithermal Au–Ag deposits of Patagonia, Argentina. Ore Geol. Rev. 12 (3), 173–186.
Schalamuk, I., de Barrio, R., Zubia, M., Genini, A., Echeveste, H., 1999. Provincia Auroargentífera del Deseado, Santa Cruz. In: Zappettini, E. (Ed.), Recursos Minerales de la República Argentina. Instituto de Geología y Recursos Minerales SEGEMAR, pp. 1177–1188.
Shan, Y., Fry, N., 2005. A hierarchical cluster approach for forward separation of heterogeneous fault/slip data into subsets. J. Struct. Geol. 27, 929–936.
Sibson, R.H., 1987. Earthquake rupturing as a mineralizing agent in hydrothermal Systems. Geology 15, 701–704.
Sibson, R.H., 1996. Structural permeability of fluid-driven fault-fracture meshes. J. Struct. Geol. 18, 1031–1042.
Sibson, R.H., 2000. Fluid involvement in normal faulting. J. Geodyn. 29, 469–499.
Sippel, J., Scheck-Wenderoth, M., Reicherter, K., Mazur, S., 2009. Paleostress states at the south-western margin of the central European Basin System - application of fault-slip analysis to unravel a polyphase deformation pattern. Tectonophysics 470, 129–146.
Spalletti, L., Iñíguez Rodríguez, M., Mazzoni, M., 1982. Edades radimétricas de piroclastitas y vulcanitas del Grupo Bahía Laura, Gran Bajo de San Julián, Santa Cruz. Rev. Asoc. Geol. Argentina 37 (4), 483–485.
Sperner, B., Zweigel, P., 2010. A plea for more caution in fault-slip analysis. Tectonophysics 482, 29–41.
Sruoga, P., Palma, M.A., 1984. La Formación Chon-Aike en su área clásica de aflor-amientos. IX Congreso Geológico Argentino, San Carlos de Bariloche, pp. 171–184.
Sruoga, P., Busteros, A., Giacosa, R., Kleiman, L., Japas, S., Maloberti, A., Martínez, H., 2008. Análisis litofacial y estructural del Complejo Bahía Laura en el área El Dorado - Monserrat, provincia de Santa Cruz, Argentina. Rev. Asoc. Geol. Argentina 63 (4), 653–664.
Tavani, S., Muñoz, J.A., 2012. Mesozoic rifting in the Basque-Cantabrian Basin (Spain): Inherited faults, transversal structures and stress perturbation. Terra Nova 24, 70–76. https://doi.org/10.1111/j.1365-3121.2011.01040.x.
Tavani, S., López-Mir, B., Muñoz, J.A., 2015a. Extensional fold-related fracturing in the Armeña rollover (Cotiella Massif, Southern Pyrenees). Ital. J. Geosci. 134, 458–473. https://doi.org/10.3301/IJG.2014.17.
Tavani, S., Storti, F., Lacombe, O., Corradetti, A., Muñoz, J.A., Mazzoli, S., 2015b. A review of deformation pattern templates in foreland basin systems and fold-and-thrust belts: Implications for the state of stress in the frontal regions of thrust wedges. Earth Sci. Rev. 141, 82–104.
Tessone, M., Del Blanco, M., Macambira, M., Rolando, A., 1999. New Radimetric Ages of the Chon Aike and Bajo Pobre Formations in the Central Zone of the Deseado Massif, Argentina. In: II South American Symposium on Isotope Geology, Villa Carlos Paz, Argentina, pp. 132–135.
Twiss, R.J., Unruh, J.R., 1998. Analysis of fault slip inversions: do they constrain stress or strain rate? J. Geophys. Res. 103 (86), 12205–12222.
Viera, R., Pezzuchi, H., 1976. Presencia de sedimentitas pérmicas en contacto con rocas del Complejo metamórfico de la Patagonia extrandina, Ea. Dos Hermanos, provincia de Santa Cruz. Rev. Asoc. Geol. Argentina 31 (4), 281–283.
Wallace, R.E., 1951. Geometry of shearing stress and relationship to faulting. J. Geol. 59, 111–130.
Wallier, S., 2009. The Geology and Evolution of the Manantial Espejo Epithermal Silver (-Gold) Deposit, Deseado Massif, Argentina. Ph.D. thesis. University of British Columbia, Vancouver, Canada.
Yamaji, A., 2000. The multiple inverse method: a new technique to separate stresses from heterogeneous fault-slip data. J. Struct. Geol. 22, 441–452.
Yamaji, A., Sato, K., Otsubo, M., 2010. Multiple Inversion Method Software, Version 6.02. Division of Earth and Planetary Sciences, Kyoto University.

APPENDIX F

JURASSIC TO EARLY CRETACEOUS GEODYNAMIC EVOLUTION OF THE PATAGONIAN DESEADO MASSIF (47° S): INSIGHT FROM LOW TEMPERATURE THERMOCHRONOLOGICAL DATA AND MODELING

Alexis Derycke[*1], Cécile Gautheron[1], **Marie C. Genge**[2,3], Massimiliano Zattin[2], Stefano Mazzoli[4], César Witt[3], Hermann Zeyen[1], Rosella Pinna-Jamme[1], Frederic Haurine[1], Marcelo Marquez[5]

[1] Université Paris-Saclay, CNRS, GEOPS, 91405, Orsay, France

[2] Dipartimento di Geoscienze, Università degli Studi di Padova, via G. Gradenigo 6, 35131 Padova, Italy

[3] Univ. Lille, CNRS, Univ. Littoral Côte d'Opale, UMR 8187, LOG, Laboratoire d'Océanologie et de Géosciences, F 59000 Lille, France

[4] School of Science and Technology, Geology Division, University of Camerino, Italy

[5] Servicio Geológico Minero-Argentino, Delegación Patagonia, Barrio Don Bosco km 8, Comodoro Rivadavia, Argentina

This chapter describes the results obtained from low-temperature thermochronology data on apatites in the Deseado Massif (~47°S). It represents a part of the work carried out during the PhD of Alexis Derycke. This work aims to understand the Mesozoic evolution of the Deseado Massif. Apatite fission tracks have been counted and measured in six samples (one detrital, five in-situ) at the University of Padova and then used for thermal modeling. AD, CG, MCG, MZ, SM, CW and MM carried out the fieldwork, including sampling for thermochronology dating methods. AD and CG realized apatite (U-Th-Sm)/He analysis, with the contribution of RPJ and FH, thermal modeling, thermic models, with the support of HZ. AD and CG are writing the paper and preparing the figures. MCG carried out apatite fission tracks analysis on in-situ and detrital samples, and contribute to write parts of the draft related to apatite fission tracks analysis and results. This manuscript is in preparation for submission to the peer-review scientific *Journal of South American Earth Sciences*.

Abstract

The Deseado Massif (46 – 49 °S) is a large province into the Patagonian Broken Foreland where mainly Paleozoic and Mesozoic rocks are exposed. In this study, we explore a low-temperature thermochronological dataset to infer the thermal history of this intraplate relief. For the first time, a thermochronological study is carried out regionally in the Deseado Massif. Despite the morphological differences in this area, a roughly similar history is recognized. Data allowed to establish that a significant exhumation affected the Deseado Massif at ca. 200 Ma which is roughly coeval with a flat-slab event. Significant heating is then recorded associated to local substantial burial or cooking processes related to a significant magmatism. Then, a slow cooling event is recognized linked to the last exhumation phase which started from ~130 Ma and continued through the entire Cretaceous. Thermal modeling most likely indicate that more than 3 km of rocks has been removed from the Cretaceous to the present. Any younger cooling event during the Cenozoic has been detected, even the sensitive apatite (U-Th-Sm)/He thermochronometer. This study provides new evidence about the tectono-thermal history of the Deseado Massif and the impact of magmatic processes. It evidences also the link between deep geodynamic processes and deformation of the overriding plate.

Introduction

The Deseado Massif is a large geological province belonging to the southern Patagonian Broken Foreland. The Deseado Massif represents the southernmost intraplate relief of the Patagonian Broken Foreland between 46°30' and 49°S delimited by the Patagonian Andes to the west while limits remained unclear to the east. It is surrounded by the Cretaceous San Jorge and Austral Basins to the north and to the south, respectively. The large topographic high is often divided morphologically between its eastern and western domain (Giacosa et al., 2010a). Indeed, the eastern part is characterized by a flat surface dipping gently eastward from 400 to 100 m whereas the western areas are much more incised and related to higher elevations of 800 – 1200 m. The Deseado Massif is characterized by extensive magmatic rocks (mainly the Chon Aike Formation) and Mesozoic sandstones locally covered by Cenozoic lava flows. The Deseado Massif was subjected to several tectonic and magmatic events that may affect the thermal history of this area (Figure 1), especially the Chon Aike event which induced deformation through the foreland (C. Navarrete et al., 2019). Indeed, the area is usually associated to the accretions of three terranes during a Gondwana orogenic phase which started at ca. 400 Ma. Related structures defined the northern and southern limit of the Deseado Massif, developed coevally with an orogenic (and post-orogenic) plutons called the Rio Deseado Complex. The latter is directly overlied unconformably by the Permian continental series of the Tres Cerros and El Tranquilo Formations (Giacosa et al., 2010, and references therein). An angular unconformity is recognized between these deposits and the Triassic –

Early Jurassic Roca Blanca Formation. All these series were folded during a phase, still highly debated, of slab flattening below the Deseado Massif which induce a noticeable deformation toward the surface

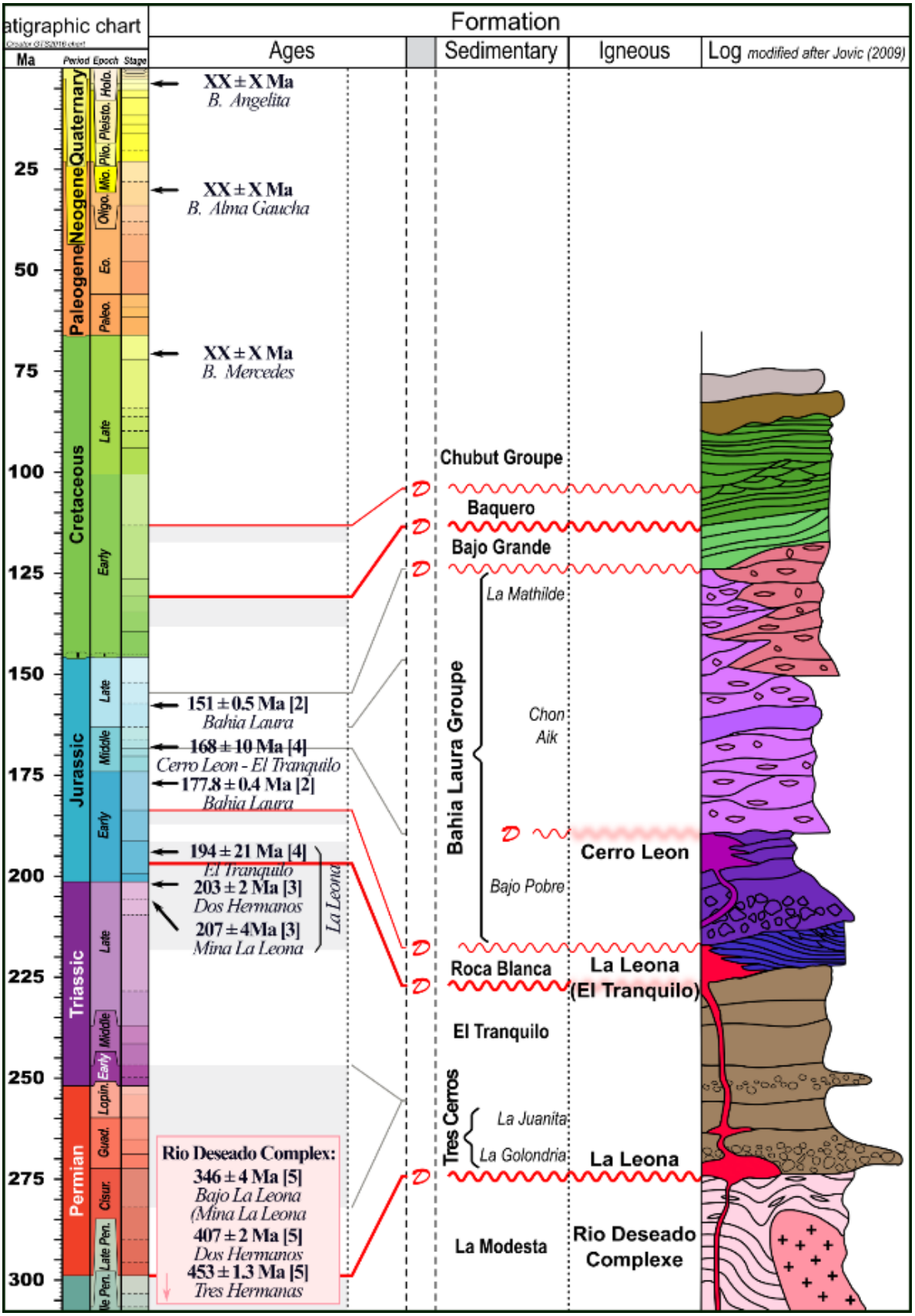

Figure 1. Stratigraphic log of the Deseado Massif (modified after Jovic, 2009).

(Navarrete et al., 2019). These authors proposed that these former rocks were intruded by a serie of plutons named La Leona Formation (~210 – 200 Ma), which presents a mantellic signature linked with the horizontalization of the slab and morphology that mayy be linked to a subsurface emplacement (< 5 km) (Navarrete et al., 2019). La Leona Formation rocks are poorly deformed compared to the former rocks, which is coherent with their emplacement during the deformation of the (e.g.) Roca Blanca Formation due to the flat-slab episode (Jovic et al., 2009; Navarrete et al., 2019; César Navarrete et al., 2019). Then, these formations were buried below the volcaniclastic deposits of the Bahia Laura Complex (~185-150 Ma) which covered approximately 80% of the Deseado Massif with maybe 1 km of thickness locally. These large volcanic deposits can be related i) to the fusion of a hydrated lower crust and upper mantle triggered by the flat-slab, ii) to the fusion of the mantle induced by the westward of the Karoo-Ferrar Mantle Plume, or iii) interaction between the flat-slab and the mantle plume. The Bahia Laura series didn't evidence any syn-deformation features so the unconformity recognized between these strata and former formations is more likely corresponding to the answer at the surface of complex mantle setup. The Bahia Laura Complex encompass the Cerro Leon and the andesitic Bajo Pobre Formations which are intercalated with the Chon Aike silicic volcanics and La Matilde strata constitute reworked Chon Aike volcaniclastic materials (Echeveste et al., 2001; Guido et al., 2006). The two latter formations were formed during a mature phase of volcanism during the Late Jurassic which marked the onset of supercontinent break-up of Gondwana and the activity of a mantle plume during Jurassic (Pankhurst et al., 2000; Riley and Knight, 2001). Tuffaceous Cretaceous strata of the Bajo Grande, Baquero and Chubut are mostly deposited in the central part of the Deseado Massif.

The Bajo Grande Formation, interpreted as Upper Kimmeridgian to Hauterivian age, is a 20 to 420 m thick unit limited westward by NNE oriented faults acting as the active edge of a basin before the Upper Kimmeridgian (Giacosa et al., 2010a). The deposits suggested that the main depositional process for this formation was the reworking of pyroclastic material (Smith and Lowe, 1991). This unit is typically continental characterized by a fast accumulation of fluvial deposits on an irregular relief represented by small local basins of variable extent more or less interconnected (De Giusto et al., 1980). Contemporaneous and intense volcanic activity has been evidenced by the uninterrupted pyroclastic material find across the whole unit (Panza et al., 2001a). The Bajo Grande Formation displays angular unconformity with the Bahía Laura Group at the base and with the Baqueró Formation on top, known as the Bajo Grande Unconformity (Figure 2; Giacosa et al., 2010). Based on the Aptian age of the Baqueró Formation (Homovc and Constantini, 2001), the Bajo Grande Unconformity can be inferred to be a Barremian age. This unconformity has been related with a compressional event responsible of tectonic inversion and the development of regional unconformity as well as the closure of the northernmost Austral Basin and the uplift of the Aysen basin to the north (Giacosa et al., 2010a; Suarez et al., 2009). This Barremian inversion is also recognized in the San Jorge Gulf Basin where a cessation of the subsidence is recorded at that time to the west. A maximal differential uplift of ~ 1 km is finally recognized over the last 25 Ma as demonstrated by geomorphological studies (Bétard et al., 2014). The south-tilted of the Deseado Massif detected from morphology of fluvial terraces indicated that the uplift

is developed in response to dynamic topography based on mantle-lithosphere interaction enhanced by the opening of slab window below the austral Patagonia (Guillaume et al., 2009). Finally, the thin Cenozoic cover, recognized locally, is interbedded with effusive Neogene lava flows linked with the inception of a slab window below the austral Patagonia.

Therefore, we analyzed low-temperature thermochronology from basement and Mesozoic rocks to provide new constraints on the thermal history of this area as few studies have been published in this area (Fernandez et al, 2020). This study aims to reconstruct the thermal history before the Chon Aike event and to quantify a potential Meso-Cenozoic event. This study, based on apatite (U-Th-Sm)/He and fission tracks dating, demonstrate that this area was quite stable during the Cenozoic. The impact of magmatism on low-temperature thermochronometers is also explored.

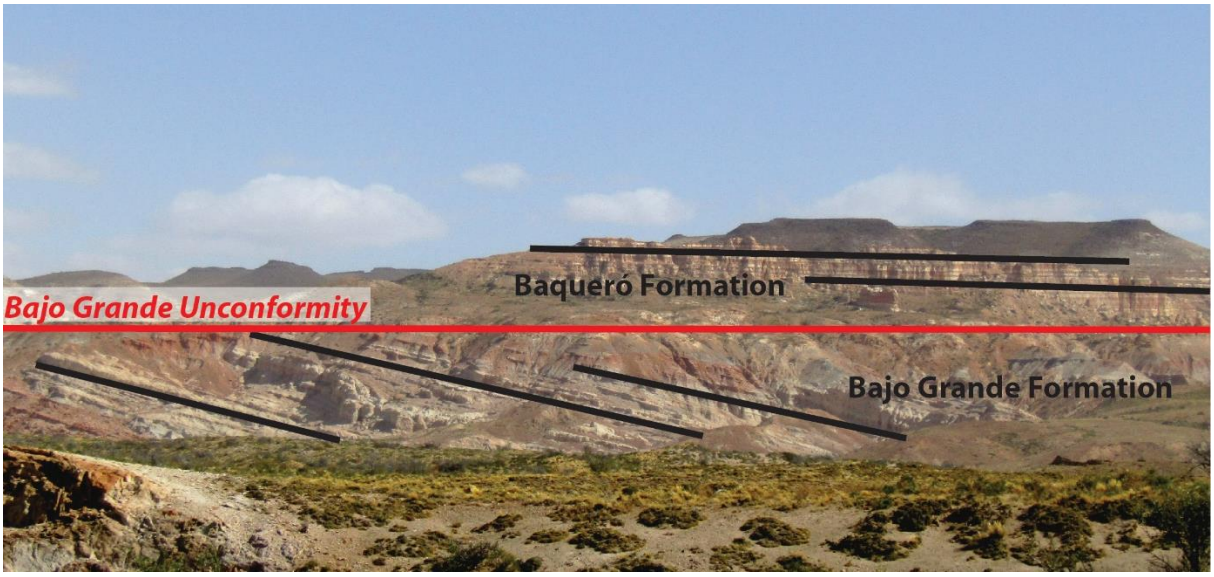

Figure 2. The Bajo Grande unconformity at the Bajo Grande area.

Material and methods

In this study, we present 52 (U-Th)/He (AHe) and six apatite fission-track (AFT) new ages from samples collected from the Deseado Massif between 46° and 49°S (Figure 3). 12 of the new AHe ages were obtained from the same samples that yielded further four AFT ages and track lengths published by Fernández et al. (2020), thus achieving an extensive dataset through this area. Geographic coordinates, elevation, formation (mainly igneous basement, Mesozoic plutons and Mesozoic sandstones), stratigraphic age and rock lithology of all samples are included in Table 1.

Apatite (U-Th-Sm)/He (AHe)

The (U-Th-Sm)/He thermochronology method is based on the diffusion in crystal of ^{4}He gas produced by the decay of radioactive elements (^{238}U, ^{235}U, ^{232}Th, ^{147}Sm) which is controlled by

temperature changes. The Partial Retention Zone (PRZ) is the interval above which He diffusivity is sufficiently low to retain He within the crystal. For apatites, the PRZ ranges approximately from 40 to

Table 1. Samples information including location, stratigraphic ages and rock information

Samples	Field (WGS84)			Geology		
	Longitude	Latitude	Elev. (m)	Formation	Stratigr. age	Rock Type
G24	-67.3292	-47.6439	141	La Leona	Lower Jurassic	granite
G25	-67.3464	-47.6183	143	La Leona	Lower Jurassic	granite
G26	-67.4267	-47.7358	179	La Leona	Lower Jurassic	granite
G28	-67.4794	-47.9556	137	Bajo Pobre	Mid-Up. Jurassic	granite
DES19#01	-67.3447	-47.6188	114	La Leona	Lower Jurassic	granite
DES19#02	-67.0877	-47.7106	138	Rio Deseado Cp.	Paleozoic	granitoid
DES19#05	-67.1791	-47.2927	69	Rio Deseado Cp.	Paleozoic	granitoid
DES19#08	-66.5758	-47.8281	32	Bahia Laura	Mid-Up. Jurassic	rhyolite
DES19#11	-67.3875	-48.1371	106	La Leona	Lower Jurassic	granitoid
DES19#15	-68.7195	-47.9741	432	Bahia Laura	Mid-Up. Jurassic	granitoid
DES19#29	-69.3843	-47.9161	758	Bahia Laura	Mid-Up. Jurassic	ignimbrite
MG52	-68.6409	-47.6752	555	Bajo Grande Fm.	Kimm - Hauterivian	sandstone

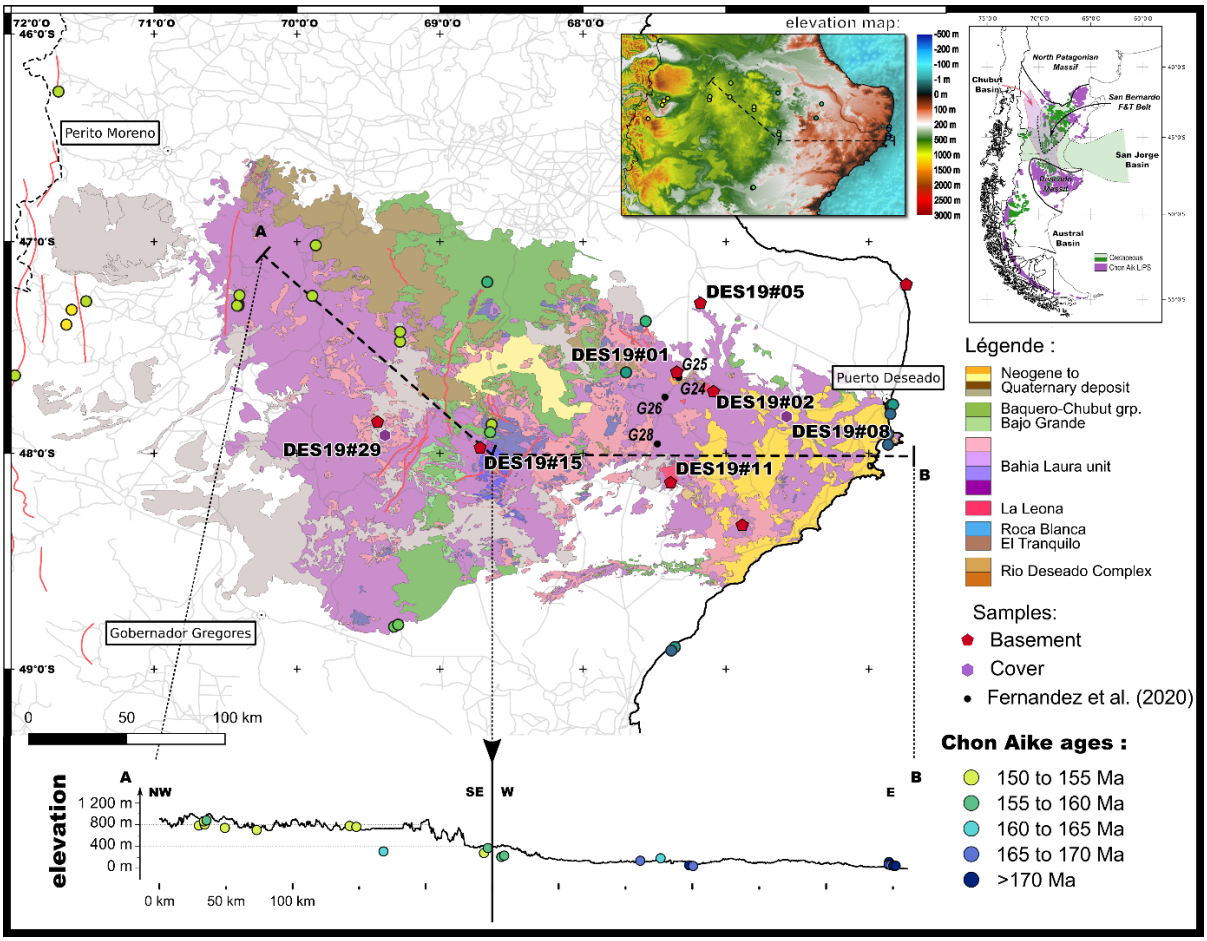

Figure 3. Geological map of the Deseado Massif with Chon Aike ages from Creer et al. (1972) and samples location. Topographic profile below with Chon Aike ages plotted.

100°C (e.g. Farley, 2000; Gautheron et al., 2009; Shuster and Farley, 2009; Wolf et al., 1996). We performed (U-Th-Sm)/He analysis at the University of Paris-Saclay (Orsay, France) on 52 single grains from all the samples except MG52. Apatite grains were selected carefully according to their morphology, size (minimum width of 60 μm) and lack of visible inclusions or grain boundary phases (Murray et al., 2014), and then placed into a platinum basket for He-extraction. From 1 to 3 grains were dated per sample, depending on sample apatite quality. The Niobium baskets were heated twice using a diode laser at 1030 ± 50°C for 5 min, allowing for total He degassing and to check the presence of He trapped in small inclusions (Fillon et al., 2013). The ^{4}He content was determined by comparison with a known amount of ^{3}He spike added during analysis. After He extraction, Nb baskets were placed into single-used polypropylene vials. Apatite grains were dissolved for 3 hours at 70°C in a 50 μL HNO_3 5N-solution containing a known content of 235U, 230Th, and ^{149}Sm, and additional 50 μL HNO_3 5N- and then filled with 0.9 mL of ultrapure MQ water. The final solution was measured for U, Th, and Sm concentrations by quadrupole inductively coupled plasma (ICP-quadrupole) mass spectrometry (Element XR from Thermo Scientific, GEOPS laboratory, Orsay, France). The analysis was calibrated using external age standard, including Durango apatites (i.e., 31.0 ± 1.0 Ma; Kraml et al., 2006; McDowell et al., 2005). Single ages were corrected using the calculated ejection factor FT, determined using the Monte Carlo simulation technique of Ketcham et al. (2011); the equivalent-sphere radius was calculated using the procedure of Gautheron and Tassan-Got (2010). Single-grain apatite He ages and supporting data are presented in Table 2. The 1σ error on single-grain AHe ages should be considered as 9%, reflecting the sum of errors in the ejection-factor correction and age dispersion of the standards.

Apatite fission tracks (AFT)

Spontaneous fission decay of ^{238}U in apatite lead to the accumulation of linear damage trails in the crystal lattice (e.g. Hurford and Green, 1982; Gleadow et al., 1986; Reiners and Brandon, 2006). These trails are erased above ~120 °C and retained below ~60 °C, defining the range of temperature for the Partial Annealing Zone (PAZ; Green et al., 1989). We performed AFT analysis at the University of Padua (Italy). Apatite grains were mounted in epoxy resin, polished and etched at 5.5M HNO_3 during 20 seconds at 20°C to reveal spontaneous tracks. The samples were analyzed by applying the external detector method (Gleadow, 1981) using low-uranium muscovite foils, as external detector, to cover apatite mounts then irradiated at the Radiation Center of Oregon State University with a nominal fluence of 9×10^{15} neutrons/cm². After irradiation, we etched mica detectors for 40 minutes in 40% HF at 20°C to reveal induced tracks. We counted tracks and measured track length distribution using an Olympus optical microscope at a magnification of ×1250. We carried out age calculation and statistics with Trackkey software (Dunkl, 2002). We report AFT ages as central age with 1σ errors (Galbraith and Laslett, 1993), using a zeta calibration approach (Hurford and Green, 1983) with a zeta value of 346 ± 12 for the CN5 dosimeter glass. Dpar measurements were used to characterize the chemical kinetic

properties of the apatite crystals (Burtner et al., 1994). Both track density ratio and average track etch pit diameter (Dpar) is recorded for up to 15 grains per sample (Table 3).

Results

In-situ analysis

New AFT analysis on plutons yield consistent Cretaceous ages from 85.8 ± 5.6 Ma to 129.3 ±7.1 Ma despite the variety of rock types. This indicates that these samples were completely reset. They all passed the χ^2 test indicating a single population. The AHe ages from the basement rocks are partially reset and are spanning from 95.1 ± 6.3 Ma to 201.3 ± 10.5 Ma, which is consistent with the ages of the basement rocks (Table 2). Significantly older ages ae observed for samples collected in La Leona Formation and high effective Uranium eU content (13-65 ppm). A particular high eU content (28-230 ppm) has been recognized for samples from the Rio Deseado Complex. No particular relationships occur between AHe age and eU content (Figure 4), while a clear AHe age – Calcium content correlation has been evidenced (Figure 5) and corresponds to increasing ages with grain size.

The AFT display a central age of 198.60 ± 12.20 Ma (from Trackkey software; Dunkl, 2002) which is older than the deposition age (~ Lower Cretaceous) and is related with the source rock. The χ^2 test (Galbraith, 1981), used to detect any extra-Poissonian error in the sample, suggests the presence of a single age population and consequently a single source rock. Track lengths measured give an average

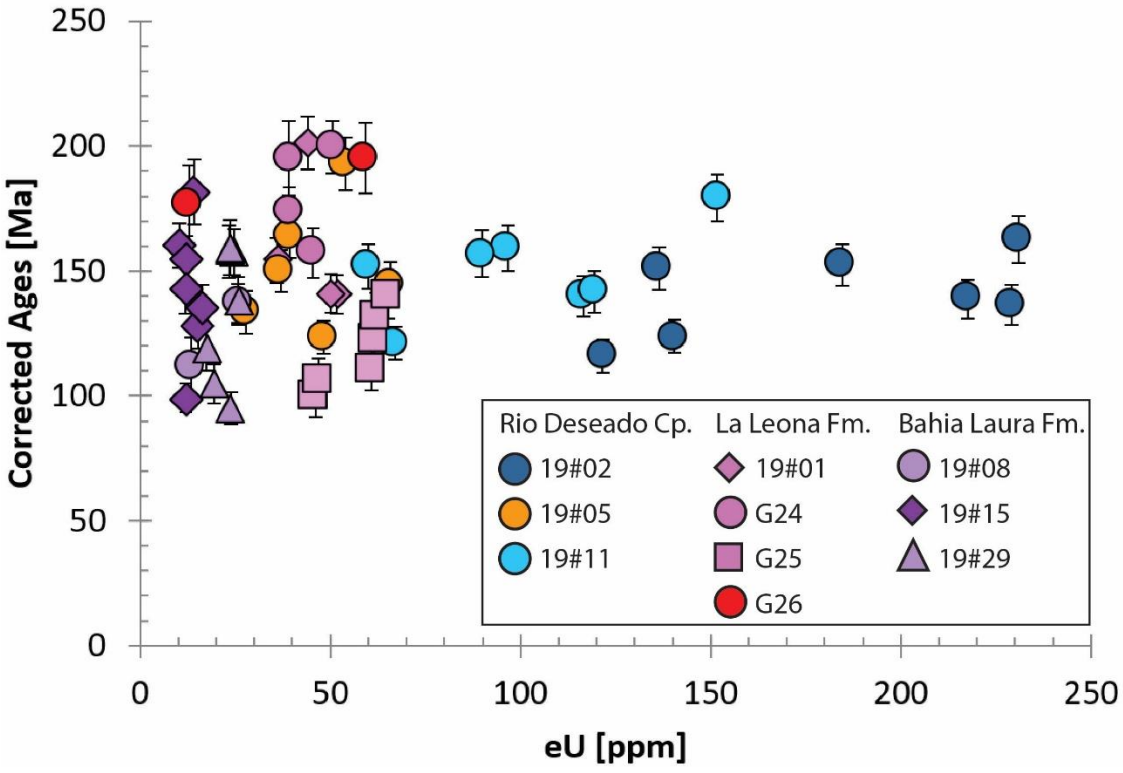

Figure 4. AHe corrected ages for all the samples over eU content.

Tableau 2. Apatite (U-Th-Sm)/He data

Sample		weight (µg)	Rs (µm)	FT	U (ppm)	Th (ppm)	Sm (ppm)	eU (ppm)	Th/U	Sm/Th	AHe age (Ma)	**Corrected AHe age**	**± 1σ (Ma)**
DES19#01	A	2.2	50	0.70	22.8	119.9	17.9	51.7	5.3	1.0	99.1	140.7	*7.8*
	D	2.2	53	0.73	20.3	65.2	16.5	36.0	3.2	1.7	112.0	154.2	*8.8*
	F	7.1	74	0.80	19.4	102.1	28.1	44.1	5.3	1.8	160.9	201.3	*10.5*
	G	1.6	44	0.67	18.8	130.4	20.8	50.2	7.0	1.1	94.5	141.0	*7.9*
G24	A	1.7	46	0.69	44.1	68.0	44.6	60.8	1.5	4.4	77.0	111.0	*8.8*
	B	1.4	44	0.68	30.1	65.6	41.7	46.2	2.2	4.2	68.0	100.0	*8.3*
	C	1.0	44	0.68	41.6	81.8	39.8	61.5	2.0	3.2	82.9	122.2	*9.9*
	D	1.2	47	0.69	28.2	76.2	45.5	46.8	2.7	4.0	73.2	105.7	*9.2*
	E	1.4	37	0.63	40.6	88.4	43.5	62.1	2.2	3.3	83.2	132.0	*9.3*
	G	1.5	45	0.68	44.7	84.5	43.0	65.2	1.9	3.4	95.3	139.9	*8.9*
G25	A	2.5	54	0.73	20.4	103.3	37.5	45.5	5.1	2.4	114.5	157.2	*9.8*
	B	2.5	48	0.69	17.7	88.7	26.1	39.2	5.0	2.0	120.3	173.5	*9.9*
	C	1.3	45	0.68	22.5	67.9	35.9	39.0	3.0	3.5	132.8	195.3	*15.0*
	E	20.7	85	0.82	25.7	102.7	32.5	50.5	4.0	2.1	164.2	199.6	*10.6*
G26E	B	8.0	76	0.82	57.0	8.1	36.8	59.2	0.1	30.3	160.0	195.2	*14.2*
	E	2.5	44	0.68	7.4	22.0	14.6	12.8	3.0	4.4	120.8	176.6	*15.4*
DES19#02	A	1.6	49	0.72	123.4	70.2	32.9	140.5	0.6	3.1	89.6	123.9	*6.6*
	B	1.7	61	0.77	191.2	108.7	25.2	217.5	0.6	1.5	106.6	138.8	*7.7*
	C	3.1	51	0.73	162.2	92.2	26.9	184.5	0.6	1.9	111.4	152.4	*8.4*
	D	3.1	48	0.73	122.5	58.2	13.4	136.5	0.5	1.5	109.7	151.1	*8.5*
	F	3.9	58	0.77	110.3	46.9	15.1	121.6	0.4	2.1	89.0	116.1	*6.6*
	H	1.0	43	0.68	198.1	128.2	35.1	229.2	0.6	1.8	93.0	136.4	*8.0*
	I	3.3	59	0.76	196.1	143.9	35.8	230.8	0.7	1.7	123.7	162.5	*9.3*
DES19#05	A	2.6	53	0.75	34.6	9.6	25.7	37.1	0.3	17.8	112.3	150.0	*8.5*
	B	1.2	44	0.69	61.1	18.8	29.1	65.8	0.3	10.3	100.1	144.9	*8.6*
	C	1.4	49	0.72	25.7	8.7	11.8	27.9	0.3	9.1	96.2	133.4	*8.5*
	D	2.5	58	0.77	49.9	15.5	38.2	53.9	0.3	16.5	148.5	193.0	*10.5*
	E	5.7	71	0.81	45.6	10.5	16.6	48.2	0.2	10.6	99.7	123.5	*6.6*
	G	19.6	105	0.87	37.7	6.4	20.1	39.4	0.2	21.0	142.1	163.8	*8.5*
DES19#11	A	2.2	50	0.72	44.0	65.6	27.7	59.9	1.5	2.8	108.9	151.7	*9.0*
	B	3.7	60	0.76	72.7	99.5	34.4	96.8	1.4	2.3	121.8	159.2	*9.3*
	C	2.5	45	0.69	72.9	70.0	19.0	89.8	1.0	1.8	108.8	156.9	*9.3*
	D	5.7	83	0.83	93.6	94.8	21.3	116.5	1.0	1.5	115.8	139.9	*8.3*
	F	2.4	61	0.76	80.6	160.5	30.3	119.3	2.0	1.3	107.9	141.5	*8.4*
	G	2.6	43	0.67	42.9	100.4	23.0	67.1	2.3	1.5	81.6	121.0	*6.6*
	H	4.1	48	0.71	119.8	131.8	45.9	151.7	1.1	2.3	127.9	179.3	*9.3*
DES19#15	A	2.3	56	0.72	4.8	38.3	35.8	14.2	8.0	6.2	131.2	181.7	*13.1*
	B	3.8	59	0.75	4.8	28.9	36.7	12.0	6.1	8.5	74.2	99.2	*5.8*
	C	1.9	46	0.67	5.8	37.8	42.0	15.2	6.5	7.4	86.0	127.6	*8.5*
	D	1.7	41	0.63	5.8	43.0	46.5	16.4	7.4	7.2	85.8	135.2	*9.1*
	E	6.1	66	0.77	4.7	21.8	37.1	10.2	4.6	11.3	123.9	160.1	*8.9*
	F	2.5	50	0.70	5.1	28.1	42.1	12.2	5.5	10.0	108.8	154.3	*9.8*

	G	3.5	54	0.73	5.0	27.8	38.4	11.9	5.6	9.2	103.4	142.4	*9.6*
	A	2.6	50	0.71	11.4	54.0	49.9	24.7	4.7	6.2	111.4	157.7	*9.1*
	B	1.9	47	0.69	10.0	56.3	39.7	23.8	5.6	4.7	65.9	95.1	*6.3*
	C	3.0	51	0.71	11.4	48.0	53.4	23.3	4.2	7.4	112.0	157.9	*10.6*
DES19#29	D	3.5	60	0.75	11.0	59.7	50.5	25.7	5.4	5.6	103.4	138.0	*9.4*
	E	2.8	64	0.77	10.3	54.5	39.4	23.6	5.3	4.8	122.3	159.5	*10.9*
	F	2.3	46	0.68	7.5	48.4	36.4	19.3	6.5	5.0	71.3	104.7	*7.7*
	G	1.9	50	0.70	7.3	40.7	38.2	17.4	5.5	6.3	83.8	119.1	*9.0*
DES19#08	A	1.0	42	0.65	6.4	28.6	32.5	13.5	4.5	7.6	72.7	112.0	*11.4*
	D	2.4	49	0.72	21.0	18.8	34.6	25.8	0.9	12.2	98.4	137.1	*7.9*

Note: Rs: sphere equivalent radius of hexagonal crystal with the same surface/volume ratio; FT: geometric correction factor for age calculation; eU: effective uranium concentration.

Table 3. Apatite fission tracks data.

Samples	Geology	Fission tracks data†												
	Formation	n	C. age	σ	Ns	ρs	Ni	ρi	Nd	ρD	P(χ²)	Mean Dpar	Length	σ	n
G24	La Leona	26	72.1	4.9	425	9	1076	2	5367	10.6	100		12.27	0.18	
G25	La Leona	20	70.1	4.6	468	6	1207	2	5328	10.5	100		10.69	0.35	
G26	La Leona	20	53.4	3.4	466	6	1578	2	5290	10.5	100				
G28	Bajo Pobre	25	118.4	12.6	168	3	253	4	5251	10.4	91				
DES19#01	La Leona	20	85.8	5.6	482	8	1130	20	7929	13.7	93	1.71	11.87	0.17	52
DES19#02	Rio Deseado Cp.	17	110.8	6.5	705	48	1485	100	7929	13.6	98	1.75			
DES19#05	Rio Deseado Cp.	18	129.3	7.1	954	19	1719	34	7929	13.6	66	1.78	12.06	0.16	74
DES19#11	La Leona	18	109.5	6.6	673	19	1423	40	7929	13.5	71	2.59	12.77	0.17	62
DES19#29	Bahia Laura	20	107.3	8.5	298	6	634	13	7929	13.3	100	2.13			
MG52	Bajo Grande Fm.	45	198.6	12.4	849	9	743	8	5242	10.2	100		13.95	0.14	57

† Zeta= 346 ± 12

N: number of apatite crystal counted; and ρ: track density (x 10^5 tracks/cm²); subscripts s, I and d denote spontaneous, induced and dosimeter, respectively; P(χ²): probability of obtaining a Chi-square value for n degrees of freedom; Dpar: mean diameter of fission-track etch pit parallel to the c-axis.

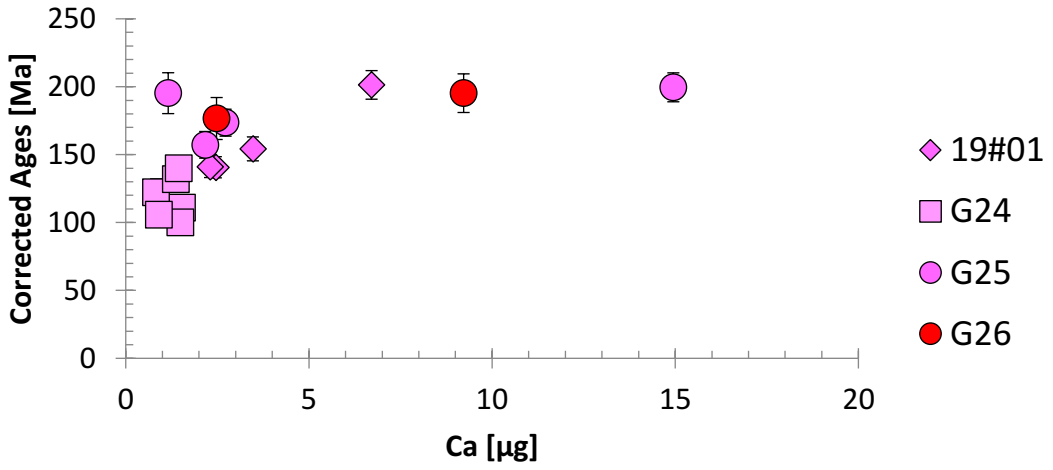

Figure 5. Corrected AHe ages for samples collected in La Leona Formation over Ca content.

Detrital thermochronology

length of 13,946 ± 1,07 μm. It indicates a mostly short permanence into the Partial Annealing Zone (PAZ, ~120° – 60°C after Hurford and Green, 1983) associated with a fast to modest exhumation from Late Permian to Early Jurassic. Thermal path obtained by a Monte Carlo algorithm from the QTQt software (version 5.7.1, Gallagher, 2012) is the result of 100 000 iterations. Dpar values have been used as kinetic parameter. The modeling was only constrained by the depositional age of the Bajo Grande Formation (25° ± 25°C at 141 ± 11 Ma) and the present-day temperature (10° ± 10°C at 0 Ma). About the pre-depositional path, only a very large box (200° ± 200°C at 275 ± 125 Ma) was used to take into consideration any kind of provenance. Therefore, thermal history is not well confined for these high temperatures. The old ages obtained are not, even partially, reset. These results mean that burial was not significant enough to reach the PAZ since the deposition of the Bajo Grande Formation.

Thermal modeling

We used the QTQt software (version 5.7.0) to model 11 samples including those from Fernández et al. (2020). The program allows inverting AFT annealing and AHe diffusion parameters with the Markov chain Monte Carlo method (Gallagher, 2012). The inversion code incorporates kinetic models of He diffusion in apatite (Flowers et al., 2009; Gautheron et al., 2009) and AFT annealing multi-kinetic model (Ketcham et al., 2007). The input parameters used to model each profile are, when available: (i) central AFT ages, (ii) track length distribution, and (iii) single-grain AHe ages, with grain size and chemical characteristics. Chemical composition ranges of the analyzed apatites were taken into consideration during both AFT and AHe modeling, by imposing the mean measured Dpar values for the sample, following Gautheron et al. (2013). Thermal history simulation results were obtained taking into account the influence of α-recoil damage, grain size and apatite kinetic properties.

Discussion

Triassic – Jurassic exhumation

Considering the detrital AFT age obtained, the source of Bajo Grande sandstone is definitely one of the basement rocks that are cropping out in the area. The closest exposed unit is the low-grade metamorphic basement known as La Modesta Formation with a maximum age of sedimentation (U-Pb SHRIMP) about 446 ± 6 Ma (Moreira et al., 2013). Two abnormal K/Ar ages obtained from micaceous shales and given ~ 210 Ma and 205 ± 10 Ma (De Giusto et al., 1980; de Barrio, 1984) have been interpreted as characteristic of tardive rejuvenation (Giacosa et al., 2002). Further, a second source identifiable corresponds to the Lower Jurassic plutonic rocks included in La Leona Formation which has been fastly exhumated at ca. 200 Ma as evidenced by the thermal modeling. Modelling demonstrated

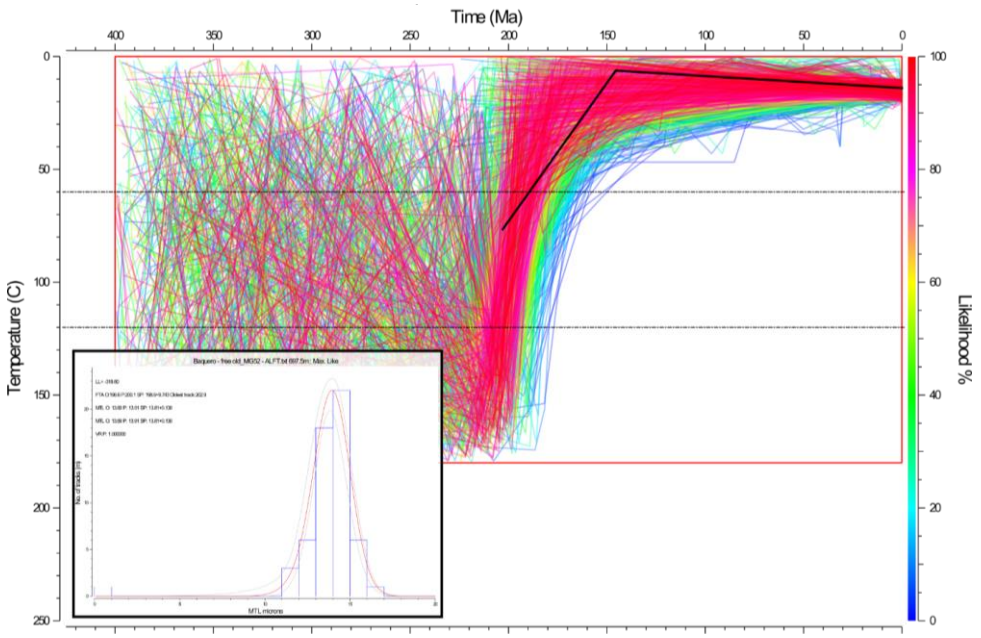

Figure 6. Thermal model for the detrital sample MG52 (Bajo Grande Formation).

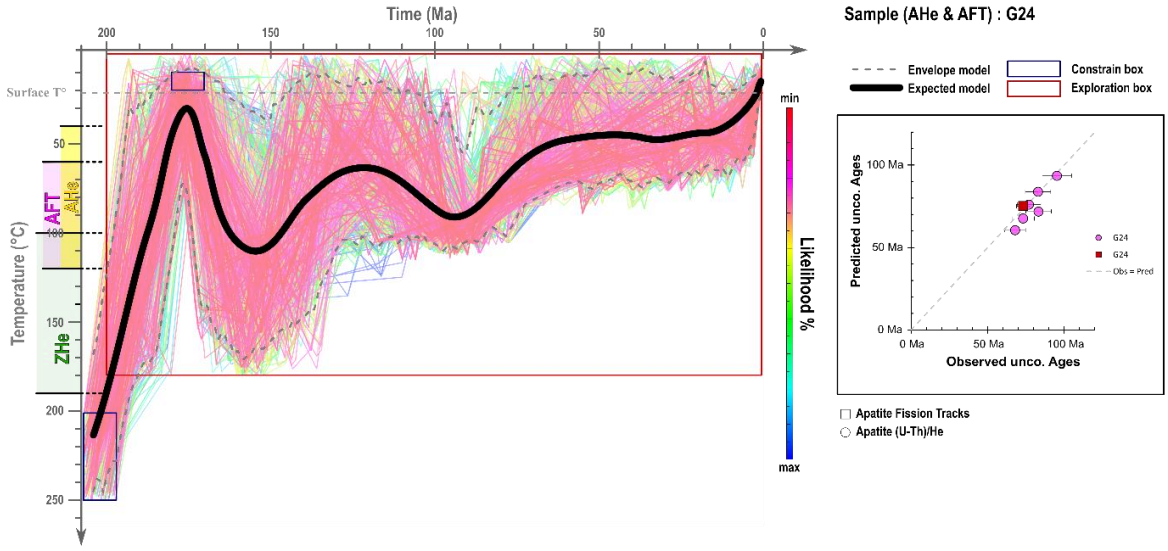

Figure 7. Thermal model and prediction plot for the sample G24 taking in account both AFT and AHe ages.

then that 2-3 km of burial was necessary around ~150 Ma and seems coeval with the Chon Aike event. Thus, significant burial may have been triggered by the SLIP emplacement. However, existing data for this formation (Fernández et al., 2020) show a reset of the AFT during Early – Middle Jurassic while this data demonstrate that this particular area of the Deseado Massif was not buried significantly since the Late Triassic – Early Jurassic (Figure 6). To better constrain the provenance of this sample, the Uranium content can be used as it represents a main difference between La Leona Formation and the Paleozoic metamorphic basement. Looking at AHe data (Table 2), the Uranium content is much higher for samples from the Paleozoic basement, which is consistent with the high spontaneous fission tracks

density observed in all the grains counted. Surrounding Paleozoic metamorphic rocks constituting the basement seem to be the most likely source for the sandstone layers of the Bajo Grande Formation.

The age recorded a moderately fast cooling at 198.60 ± 12.20 Ma. Significant exhumation is recorded for La Leona Formation, directly after emplacement, and may be related to a flat-slab episode extended from Late Triassic to Early Jurassic (Navarrete et al., 2019). The AFT age and measured lengths may correspond to the exhumation of the source rock at that time. Grains were then deposited with the Bajo Grande Formation during Early Cretaceous. As thermal modeling evidences a significant burial for samples of La Leona Formation, detrital AFT results show that burial was not regional and affected some particular areas. Reworking of adjacent Jurassic volcano-sedimentary successions as Roca Blanca (Lower Jurassic) or La Matilde Formations (Upper Jurassic) prior to final deposition can not be disregarded considering the time interval between the AFT age recorded and the deposition age which is about 50 m.y.

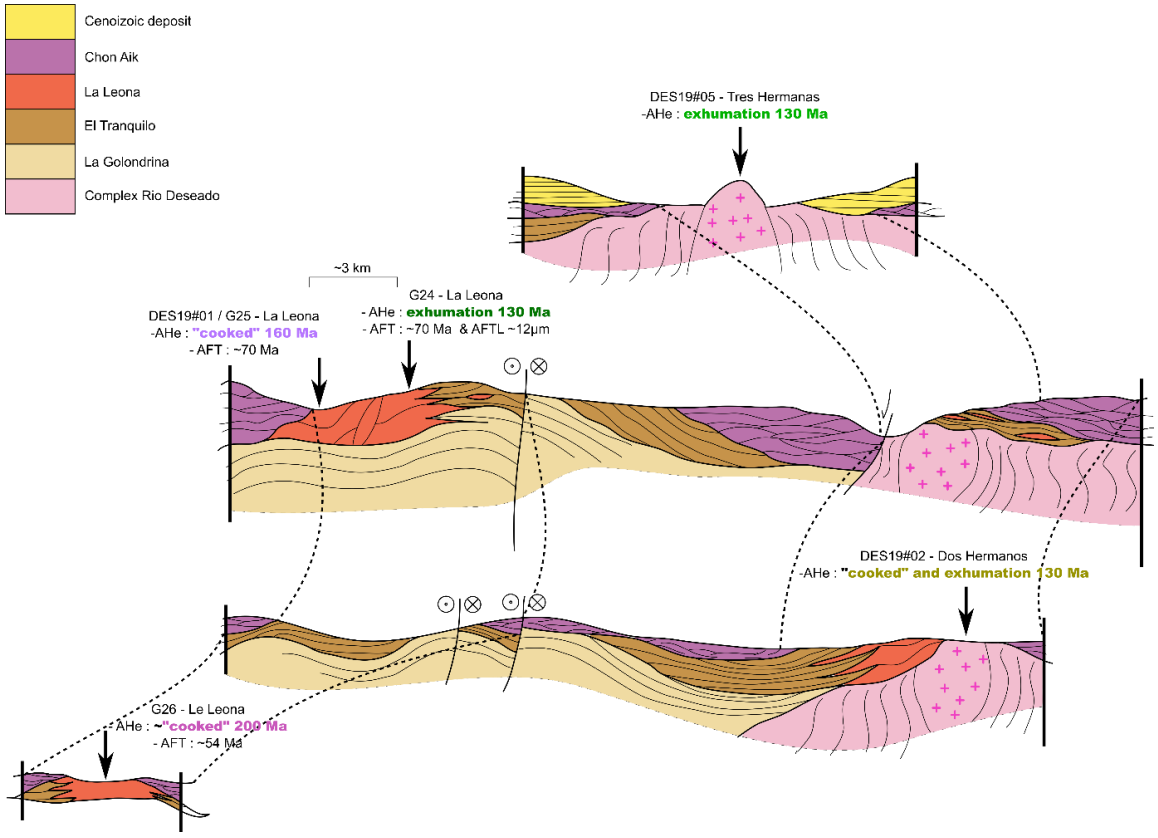

Figure 8. Simplified cross-sections showing the position of samples collected into La Leona Formation and the Rio Deseado Complex as well as their relation with the Chon Aike deposits.

Jurassic – Cretaceous tectono-thermal history

The rocks of the Rio Deseado Complex present a high temperature sensitivity (> 100 °C) and AHe ages partially reset. They record a heating phase followed by a fast cooling stage around 130 Ma that may be related to volcanic activity during the Chon Aike episode, whereas the Chon Aike deposits look quite far to affect significantly this area in a thermal point of view. Heating event are basically

associated to magmatic activity or sedimentary burial. The latter process requires material income and a sink, often associated to subsidence and increase to accommodation space. We expect that burial occurred during the Chon Aike event as extension processes were recorded during this phase and the significant volcaniclastic units offered substantial material input toward the foreland. Nevertheless, it is hard to image a regional burial through the Deseado Massif as detrital data in this study evidences quite old ages. In this case, burial may affect locally the samples and a second process related to coeval magmatism must be considered to explain all the ages obtained. Therefore, we relate these results to a "cooking" phenomenon toward the edges of the pluton or a significant burial, potentially asymmetric, below the Chon Aike deposits.

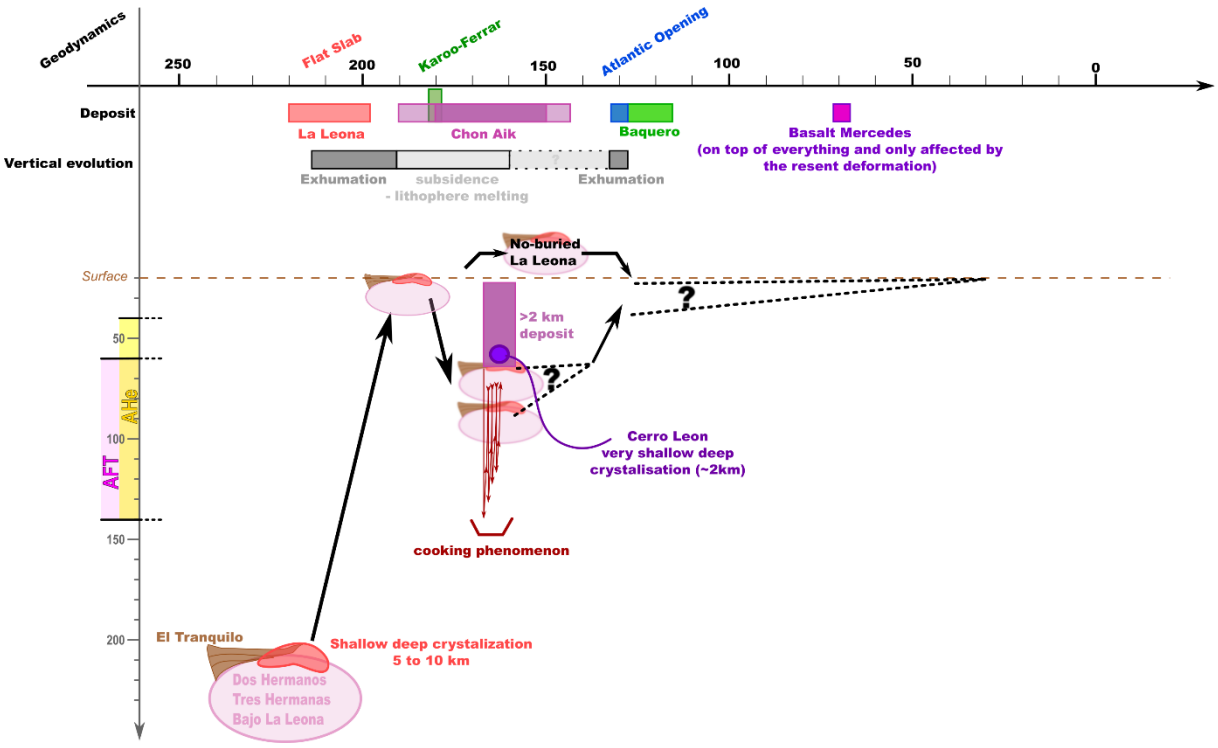

Figure 9. Synthetic thermal model with summary of magmatic and tectonic events.

The samples collected in other formations present an average temperature sensibility (< 100 °C). The data for the latter samples, which present clearly younger ages, indicate that a slow cooling event started as soon as Early Cretaceous. This cooling phase is associated with a regional exhumation phase which started probably at ca. 130 Ma as evidenced by our entire dataset (both AHe and AFT data; Figures F – 7 and F – 8). This cooling phase is consistent with the numerous angular unconformities between the diverse formations, especially the Early Cretaceous Bajo Grande Unconformity. This exhumation event may have been related to the Atlantic opening changes that affected the kinematics of the South American Plate triggering deformation of the Andean fold and thrust belt. Exhumation continues through the entire Cretaceous as demonstrated by the younger AFT records (~70 Ma) in some sites. If AFT data are reliable, it means that AHe data present a significantly higher closure temperature

than the AFT system. In this case, at least 3 km of rocks were exhumed in the foreland since the Cretaceous that may be related to the thick deposits related to the Chon Aike events (e.g. Bahia Laura Group). If AFT are not so reliable, it means that maximum exhumation occurred at ~130 Ma and thermal histories may change slightly. For both cases, we consider that at least 3 km of rocks were exhumed since the Cretaceous (Figure 9).

Conclusions

AFT and AHe data, as well as temperature-time history modeling obtained regionally in the Deseado Massif, suggest two regional exhumation events: i) at ~200 Ma associated with a flat-slab episode; ii) from ~130 Ma related with Andean tectonics. For the latter, our results unravel a significant exhumation of minimum 3 km. Intermediary heating phase may have been induced by local burial below substantial volcaniclastic deposits and by magmatic processes as evidenced by the partial reset of the AHe data. Neogene deformation recognized along the Deseado Massif is not detected by our thermochronology data, meaning that exhumation was moderate.

References

Bétard, F., Peulvast, J.-P., Rabassa, J., and Aguilera, E.Y., 2014, Meso-Cenozoic Paleotopographies and Paleolandscapes in the Deseado Massif (Santa Cruz Province, Argentina), *in* Gondwana Landscapes in Southern South America, Springer, p. 477–501.

De Giusto, J.M., Di Persia, C.A., and Pezzi, E., 1980, Nesocratón del Deseado: Geología Regional Argentina, v. 2, p. 1389–1430.

Dunkl, I., 2002, TRACKKEY: a Windows program for calculation and graphical presentation of fission track data: Computers & Geosciences, v. 28, p. 3–12.

Echeveste, H., Fernández, R.R., Bellieni, G., Tessone, M.O.R., Llambías, E.J., Schalamuk, I.B.A., Piccirillo, E.M., and De Min, A., 2001, Relaciones entre las Formaciones Bajo Pobre y Chon Aike [Jurásico Medio a Superior] en el área Estancia El Fénix-Cerro Huemul, zona centro-occidental del Macizo del Deseado, provincia de Santa Cruz: Revista de la Asociación Geológica Argentina, v. 56.

Farley, K.A., 2000, Helium diffusion from apatite: General behavior as illustrated by Durango fluorapatite: Journal of Geophysical Research: Solid Earth, v. 105, p. 2903–2914.

Fillon, C., Gautheron, C., and van der Beek, P., 2013, Oligocene–Miocene burial and exhumation of the Southern Pyrenean foreland quantified by low-temperature thermochronology: Journal of the Geological Society, v. 170, p. 67–77.

Galbraith, R.F., and Laslett, G.M., 1993, Statistical models for mixed fission track ages: Nuclear tracks and radiation measurements, v. 21, p. 459–470.

Gautheron, C., and Tassan-Got, L., 2010, A Monte Carlo approach to diffusion applied to noble gas/helium thermochronology: Chemical Geology, v. 273, p. 212–224.

Gautheron, C., Tassan-Got, L., Barbarand, J., and Pagel, M., 2009, Effect of alpha-damage annealing on apatite (U–Th)/He thermochronology: Chemical Geology, v. 266, p. 157–170.

Giacosa, R., Zubia, M., Sánchez, M., and Allard, J., 2010, Meso-Cenozoic tectonics of the southern Patagonian foreland: Structural evolution and implications for Au–Ag veins in the eastern Deseado Region (Santa Cruz, Argentina): Journal of South American Earth Sciences, v. 30, p. 134–150.

Gleadow, A.J.W., 1981, Fission-track dating methods: what are the real alternatives? Nuclear Tracks, v. 5, p. 3–14.
Guido, D.M., Escayola, M.P., de Barrio, R.E., Schalamuk, B.I., and Franz, G., 2006, La Formación Bajo Pobre (Jurásico) en el este del Macizo del Deseado, Patagonia: vinculación con el Grupo Bahía Laura:
Guillaume, B., Martinod, J., Husson, L., Roddaz, M., and Riquelme, R., 2009, Neogene uplift of central eastern Patagonia: Dynamic response to active spreading ridge subduction? Tectonics, v. 28.
Homovc, J.F., and Constantini, L., 2001, Hydrocarbon exploration potential within intraplate shear-related depocenters: Deseado and San Julian basins, southern Argentina: AAPG bulletin, v. 85, p. 1795–1816.
Hurford, A.J., and Green, P.F., 1983, The zeta age calibration of fission-track dating: Chemical Geology, v. 41, p. 285–317.
Jovic, S.M., Liñan, P., Guido, D.M., Paéz, G.N., Ruiz, R., and Schalamuk, I.B., 2009, Metals distribution and correlations in polymetallic veins from Pingüino Indium-bearing deposit, Deseado Massif, Patagonia, Argentina, *in* 24th International Applied Geochemistry Symposium, Fredericton, New Brunswick, Canadá, v. 1, p. 501–504.
Ketcham, R.A., Gautheron, C., and Tassan-Got, L., 2011, Accounting for long alpha-particle stopping distances in (U–Th–Sm)/He geochronology: Refinement of the baseline case: Geochimica et Cosmochimica Acta, v. 75, p. 7779–7791.
Kraml, M., Pik, R., Rahn, M., Selbekk, R., Carignan, J., and Keller, J., 2006, A new multi-mineral age reference material for 40Ar/39Ar,(U-Th)/He and fission track dating methods: The Limberg t3 tuff: Geostandards and Geoanalytical Research, v. 30, p. 73–86.
McDowell, F.W., McIntosh, W.C., and Farley, K.A., 2005, A precise 40Ar–39Ar reference age for the Durango apatite (U–Th)/He and fission-track dating standard: Chemical Geology, v. 214, p. 249–263.
Murray, K.E., Orme, D.A., and Reiners, P.W., 2014, Effects of U–Th-rich grain boundary phases on apatite helium ages: Chemical Geology, v. 390, p. 135–151.
Navarrete, C., Gianni, G., Christiansen, R., Kamerbeek, Y., Periale, S., and Folguera, A., 2019a, Jurassic intraplate contraction of southern Patagonia: the El Tranquilo anticline area, Deseado Massif: Journal of South American Earth Sciences, v. 94, p. 102224.
Navarrete, C., Gianni, G., Encinas, A., Márquez, M., Kamerbeek, Y., Valle, M., and Folguera, A., 2019b, Triassic to Middle Jurassic geodynamic evolution of southwestern Gondwana: From a large flat-slab to mantle plume suction in a rollback subduction setting: Earth-science reviews, v. 194, p. 125–159.
Pankhurst, R.J., Riley, T.R., Fanning, C.M., and Kelley, S.P., 2000, Episodic silicic volcanism in Patagonia and the Antarctic Peninsula: chronology of magmatism associated with the break-up of Gondwana: Journal of Petrology, v. 41, p. 605–625.
Panza, J.L.A., Cobos, J.C., Zubía, M.A., and Franchi, M., 2001, Hoja Geológica 4769-III Destacamento La María: Servicio Geológico Minero Argentino. Instituto de Geología y Recursos Minerales.
Riley, T.R., and Knight, K.B., 2001, Age of pre-break-up Gondwana magmatism: Antarctic Science, v. 13, p. 99–110.
Shuster, D.L., and Farley, K.A., 2009, The influence of artificial radiation damage and thermal annealing on helium diffusion kinetics in apatite: Geochimica et cosmochimica acta, v. 73, p. 183–196.
Smith, G.A., and Lowe, D.R., 1991, Lahars: Volcano hydrologic-events and deposition in the debris flow—hyperconcentrated flow continuum:
Suarez, M., De La Cruz, R., Aguirre-Urreta, B., and Fanning, M., 2009, Relationship between volcanism and marine sedimentation in northern Austral (Aisén) Basin, central Patagonia: Stratigraphic, U–Pb SHRIMP and paleontologic evidence: Journal of South American Earth Sciences, v. 27, p. 309–325.
Wolf, R.A., Farley, K.A., and Silver, L.T., 1996, Helium diffusion and low-temperature thermochronometry of apatite: Geochimica et Cosmochimica Acta, v. 60, p. 4231–4240.

APPENDIX G

OUTER FOREARC HIGH CONTROL IN AN EROSIONAL SUBDUCTION REGIME: THE CASE OF THE CENTRAL PERUVIAN FOREARC (6-10°S)

Marie Catherine Genge[1,2], César Witt[1], Frank Chanier[1], Jean-Yves Reynaud[1], Ysabel Calderon[3]

[1] Univ. Lille, CNRS, Univ. Littoral Côte d'Opale, UMR 8187, LOG, Laboratoire d'Océanologie et de Géosciences, F 59000 Lille, France

[2] Dipartimento di Geoscienze, Università degli Studi di Padova, via G. Gradenigo 6, 35131 Padova PD, Italy

[3] Perupetro, Av. Luis Aldana 320, San Borja, Lima, Peru

This chapter describes the tectonic calendar of the central Peruvian forearc (6-10°S) identified by seismic profiles analysis. The complex and segmented geometry of the forearc has been explained by the involvement of former and uneven structures (Cretaceous-Paleogene) during the episodic deformation of a trench-parallel corridor through the Neogene. This study corresponds to my Master thesis on which I continued to work during my PhD to write this paper. Other seismic lines from this area (not included in the following chapter) have been interpreted during my PhD with the aim to start soon the writing of a second paper about tectono-sedimentary evolution of the central Peruvian forearc. This chapter has been published as Genge, M. C., Witt, C., Chanier, F., Reynaud, J. Y., & Calderon, Y. (2020). Outer forearc high control in an erosional subduction regime: The case of the central Peruvian forearc (6–10° S). Tectonophysics, 228546.

Tectonophysics 789 (2020) 228546

Contents lists available at ScienceDirect

Tectonophysics

journal homepage: www.elsevier.com/locate/tecto

Outer forearc high control in an erosional subduction regime: The case of the central Peruvian forearc (6–10°S)

Marie Catherine Genge[a,b,*], César Witt[a], Frank Chanier[a], Jean-Yves Reynaud[a], Ysabel Calderon[c]

[a] Univ. Lille, CNRS, Univ. Littoral Côte d'Opale, UMR 8187, LOG, Laboratoire d'Océanologie et de Géosciences, F 59000 Lille, France
[b] Dipartimento di Geoscienze, Università degli Studi di Padova, via G. Gradenigo 6, 35131 Padova, PD, Italy
[c] Perupetro, Av. Luis Aldana 320, San Borja, Lima, Peru

ARTICLE INFO

Keywords:
Forearc
Subduction
Andes
Outer Forearc High

ABSTRACT

The forearc of the North-Central Peruvian Andes (FNCPA, 6–10°S) provides an exceptional opportunity to study the long-term processes that affect a convergent plate boundary. First, it shows long-term subsidence, depocenter superimposition and individualization. Second, although being mostly extensional and characterized as a typical erosive margin, the FNCPA shows complex uplifted regions. Older deformation is expressed by basement horst and grabens disposed in a complex geometry which onset may have resulted from strike-slip tectonics. A long-lived episode of regional subsidence affected the forearc and led to the relatively thick and regional deposition of the lower Miocene series coeval with a significant increase of the convergence velocity. This period was followed by an episodic uplift of trench-parallel corridors along the so-called Main Deformation Zone. Uplift ceased through the late Miocene and restarted during Pliocene and Quaternary, generating accommodation space by basin flank uplift for a forearc depocenter characterized by landward tilted strata. Significant along-strike differences in the degree of uplift resulted in either uplifting series producing sharp seaward dipping erosional surfaces or less uplifted areas covered by seawards prograding clinoforms. As a consequence of the shallow-water marine setting, the seismic strata geometry, lateral extent and thickness of the deposits for the Neogene successions in the FNCPA have been also tightly controlled by accommodation changes. Uplift is uneven along-strike independently of fault direction and closely followed the increase of the subsidence of the continental slope produced by subduction-erosion. Therefore, sediment underplating seems the most appropriate mechanism at the origin of uplift; as observed in other parts of the Peruvian and Chilean margins. Although the erosive character of the margin, the effects on basin geometry of the raised zone resemble that of typical outer forearc highs in accretionary margins such as in the Kumano basin in Japan.

1. Introduction

The forearc basins reflect the history of plate subduction. However, subsidence history in forearc basins is more complex and less predictable than in rifted continental margins and foreland basins (Moxon and Graham, 1992; Xie and Heller, 2009). The main parameters controlling basin evolution (sediment supply and accommodation, e.g. Takano et al., 2013), are intimately controlled at the local and regional scale by a variety of factors such as the age and geometry of the subducting slab (Clift et al., 2003; Taylor et al., 2005), the friction of the down-going plate (Larroque et al., 1995), the thermal regime and the dynamic topography (Gerbault et al., 2009; Kimbrough et al., 2001), the plate kinematics and the accretional or erosional character of the subduction regime (Clift and Vannucchi, 2004; Martinod et al., 2010), among other aspects (e.g. Allmendinger and González, 2010; Gutscher and Westbrook, 2009; Strasser et al., 2009). Vertical motion of the forearc and the sedimentary response on the trench slope at the short-term reflects the seismogenic cycle and therefore the subduction-fault activity (Bilek, 2010; Bilek et al., 2003; Melnick, 2016; Paquet et al., 2011; Pouderoux et al., 2014; Wells et al., 2003). However, the tectonic and topographic record of forearc regions at the long-term are still poorly documented.

The formation of a structural high between the trench and the volcanic arc is relatively common in margins related to a subduction-accretion regime (those related to accretionary prisms). This structural high forms the so-called 'Outer-Forearc High' (OFH; Moore et al., 2007; Noda, 2016) or the 'trench-slope break' (Dickinson, 1995; Takano et al., 2013), which often represents an out-of-sequence thrust fault rooted at the plate interface. The OFH of the Nankai margin in Japan (Moore et al., 2007; Park et al., 2002; Strasser et al., 2009; Moore et al., 2015)

* Corresponding author at: Univ. Lille, CNRS, Univ. Littoral Côte d'Opale, UMR 8187, LOG, Laboratoire d'Océanologie et de Géosciences, F 59000 Lille, France.
E-mail address: mariecatherine.genge@phd.unipd.it (M.C. Genge).

https://doi.org/10.1016/j.tecto.2020.228546
Received 7 April 2020; Received in revised form 10 June 2020; Accepted 17 June 2020
Available online 21 June 2020
0040-1951/

may represent the most studied example worldwide; although other examples in Cascadia (Pazzaglia and Brandon, 2001), Sumatra (Fisher et al., 2007), New Zealand (Buret et al., 1997; Chanier et al., 1999; Bailleul et al., 2013) and Ecuador (Witt et al., 2019), have been documented. Among other aspects, the OFH controls the formation of the forearc basin (sensu-*strictu*) and the landward tilting of its sedimentary series, which are accompanied by basin expansion (a landward expansion of 20 km has been calculated for the Kumano basin in the Nankai forearc domain; Moore et al., 2015). This configuration restricts the forearc depocenter landward from the OFH in accretionary margins whereas, in non-accretionary (erosional) margins, the depocenter may extend trenchward up to the lower continental slope (Clift and Vannucchi, 2004; Noda, 2016). In erosional margins, such as the Peruvian segment of the South America trench, the absence of an accretionary prism intuitively prevents the definition of a typical OFH. Nevertheless, although not defined as typical OFHs, similar structures can be found in erosional margins near the slope-break (see Noda, 2016) with near slope-break uplift being related to plate interface processes such as underplating as proposed for the Chilean margin (Clift and Hartley, 2007).

The Peruvian forearc, as most of Andean forearcs, shows widespread evidence of extensional deformation only sporadically interrupted by uplift (e.g. Aizprua et al., 2019; Hernández et al., 2020; Hessler and Fildani, 2015; Clift et al., 2003; Clift and Hartley, 2007; Noda, 2016). Indeed, it is believed that subsidence has been active in the Peruvian margin since at least 50 m.y., locally and temporally interrupted by relatively local uplift highly asynchronous at the scale of the margin (e.g. Von Huene and Suess, 1988; Von Huene and Lallemand, 1990; Clift et al., 2003; Bourgois et al., 2007; Viveen and Schlunegger, 2018). These last authors suggest that in general, the evidences of extension are related to transgressive sedimentary units spanning from Eocene to Miocene, which are often faulted by normal and transtensional faults. At the scale of the entire Peruvian margin, extensional events have been mainly related to the subduction of the Nazca ridge and from the erosive regime of subduction (Von Huene and Suess, 1988; Bourgois et al., 2007; Viveen and Schlunegger, 2018). The Forearc of the North-Central Peruvian Andes (FNCPA; 6°-10°S, Fig. 1) was not affected by the subduction of the Nazca ridge (Hampel, 2002), thus providing an exceptional opportunity to study the controls and the evolution of the long-term vertical movements that affect a convergent plate boundary.

The present study focuses on the tectono-sedimentary evolution of the FNCPA during the Cenozoic. Reprocessed industrial time-migrated seismic profiles provided by Perupetro (Fig. 1) have been used to show the evolution of a complex fault system controlling several forearc depocenters and a structural high which is similar to an OFH as defined in accretionary settings. The seismic profiles have been interpreted to create a line-to-line mapping of structures and sedimentary bodies to constrain the tectonic forcing and the construction of the margin. Seismic interpretation shows that the FNCPA has underwent subsidence for most of its Cenozoic history and that it exemplifies a more complex scenario than either an ideally accretionary or erosional margin, likewise highlighting the significant role of basement fabrics in controlling the Neogene structural development of the margin.

2. Geodynamic and geological setting

In-situ observations and rock dating in off-shore areas demonstrate that the basement of the FNCPA consist of a complex amalgamation of metamorphic, intrusive and volcanic rocks (Bellido et al., 2007; Winter et al., 2010). The Paleozoic basement crops out to the north of the study area (around the Illescas and the Paita Massifs at −6°S; IM, Fig. 1) and is mainly composed of metasediments and quartzites intruded by Triassic granites and andesite-type intrusive bodies corresponding to the southern continuation of the Amotapes Massif (AM, Fig. 1; Romero et al., 2013; Witt et al., 2017). Two samples that could be dated at the San Martin 1X well and at the Macabi Island (SM and MI, Fig. 1) strongly suggest that the basement in these areas is a prolongation of the basement outcropping in the North in the Illescas and Amotapes Massifs (Romero et al., 2013). In the study area the basement was reached by the Morsa Norte 1X, the Ballena 1X and the Delfin 1X wells, where it has been mostly interpreted as a Paleozoic granitic basement (PARSEP, 2001 and references therein). South of the study zone, at the Lima Basin latitude (10–12°S), the offshore basement dated in the Lobera and Hormigas de Afuera islands represents an extension of the Grenville-age basement observed in the Arequipa Massif (Romero et al., 2013). Alternatively, a lack of Precambrian basement in the emerged part of the forearc and regional gravimetric models (Mamani et al., 2009) have been related to the presence of a continuous block of dense mafic material (no presence of continental basement) inherited from a possible late Paleozoic rifting (Polliand et al., 2005). However, as supported in the work of Romero et al. (2013) in the offshore regions of the FNCPA: 1) there is no evidence of mafic basement and 2) crystalline rocks have a significant continental signature as old as Precambrian.

Several documented features observed in the Peruvian margin are diagnostic of a subduction-erosion regime. These aspects include: a landward retreat of the trench, a forearc subsidence, a high rate of forearc basal erosion, normal faults and finally the presence of a small frontal prism (Bourgois et al., 2007; Clift and Vannucchi, 2004; Kukowski and Oncken, 2006; Von Huene et al., 2004; Von Huene and Lallemand, 1990). Alternatively, a recent model derived from similar seismic records as the ones used here, suggest that the basin architecture may be controlled by the presence of thrust faults deeply rooted in the basement (Prudhomme et al., 2019).

Near the study zone, drilling in ODP site 683 (3082 m water depth) found middle Eocene shallow water nannofossils (at ~500 m bsl) and benthic foraminifera from the upper and middle bathyal zones. The Eocene section is overlaid by a 40 to 25 Ma sedimentary hiatus. Sedimentation resumed with middle Miocene sediments showing lower bathyal paleontological assemblages (Von Huene and Suess, 1988; Resig, 1990), thus, defining subsidence of the outer margin of about 1500 m during 15 m.y. This is in agreement with the subsidence resulting from subduction erosion in the Lima basin (sites 682 and 688; Von Huene and Suess, 1988; Resig, 1990; Clift et al., 2003) which found similar Eocene and Miocene paleontological assemblages.

In the FNCPA the Nazca plate plunges beneath the South American plate with an angle of −17°-35°; although landwards, it may become almost horizontal at ~100 km from the trench to be again inclined −30° below the Eastern Andes (Antonijevic et al., 2015; Boyd et al., 1984; Gutscher et al., 2000; Hasegawa and Sacks, 1981; James and Snoke, 1994). It has been proposed that this flat slab was initiated by the subduction of two oceanic buoyant crustal features: the Inca plateau and the Nazca ridge (Soler et al., 1989; Gutscher et al., 1999). The subduction of the Nazca ridge started between 16 Ma and 11 Ma at ~10°S and migrated progressively southward to its current position (at ~15°S) whereas the Inca plateau subduction may have begun at ~13 Ma at ~5°S and supposedly being entirely consumed by subsequent subduction (Gutscher et al., 1999; Hampel, 2002; Rosenbaum et al., 2005; Hu et al., 2016).

The FNCPA is segmented in the study area into three basins (Sechura, Salaverry and Trujillo Basins) with no clear structural limits (Azalgara, 1994; Marty, 1989; Romero et al., 2013; Thornburg and Kulm, 1981; Travis et al., 1976; Fig. 1). Indeed, these basins are bounded by diffuse structural highs, extending onshore in the Coastal Massifs of Illescas and Paita to the north (Romero et al., 2013; Witt et al., 2017), or buried in the outer shelf to the south where it corresponds to the Salaverry-Trujillo High (Azalgara, 1994), or to the 'Outer-Shelf High' (Romero et al., 2013).

The free-air gravity anomalies show a patchy distribution of positive and negative values with a main trend roughly parallel to the trench (Fig. 2). Correlation of gravity anomalies with our seismic data confirms the close correspondence between positive anomalies and basement highs, and of negative anomalies with main depocenters. The

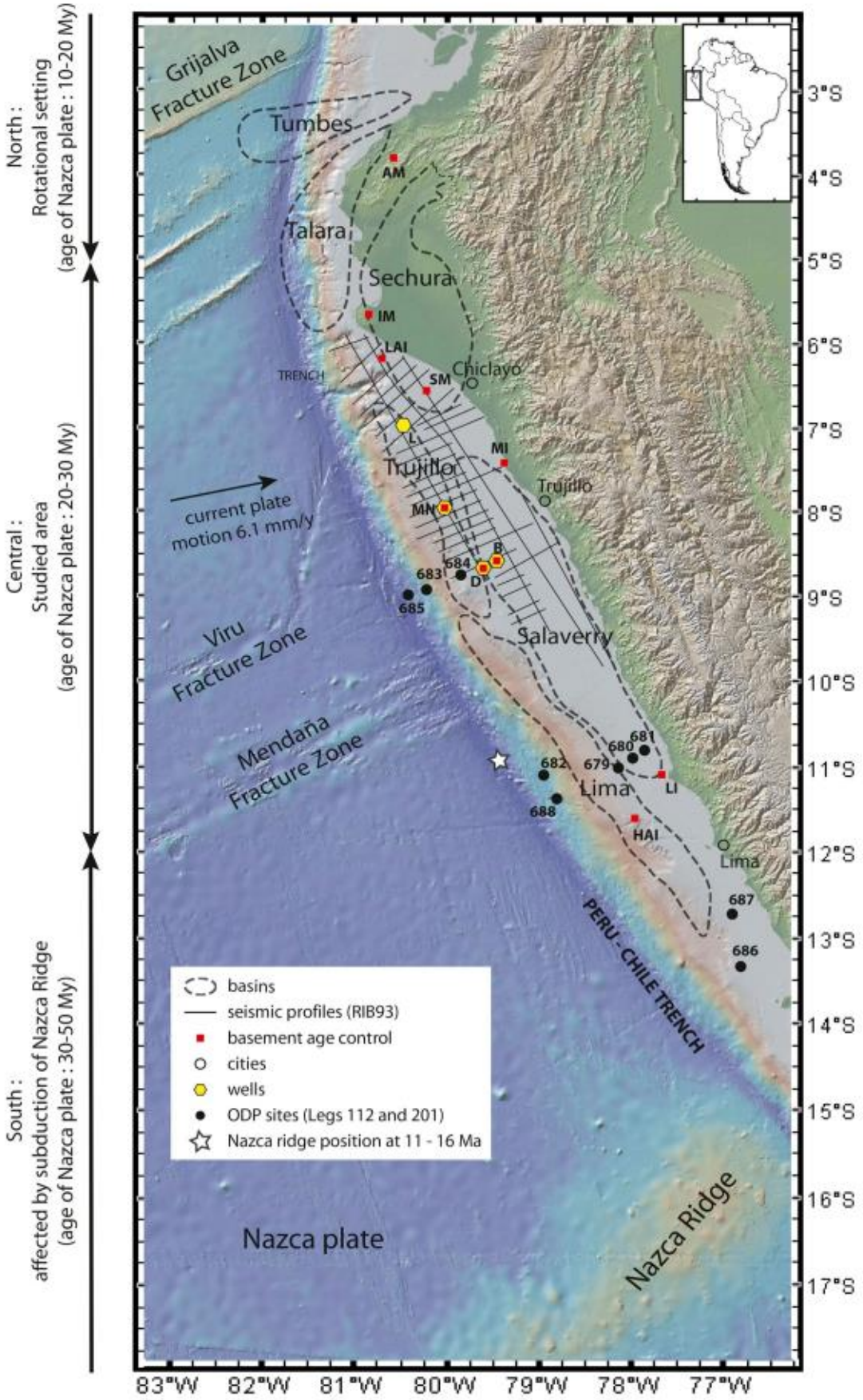

(caption on next page)

Fig. 1. Geodynamic sketch of North and Central Peru showing the location of seismic lines used in this study. Black circles show ODP sites from Leg 112 and 201 (sites' number indicated on the map). Yellow hexagons show industrial well sites (B: Ballena 1X, D: Delfin 1X, L: Lobos 1X, MN: Morsa Norte 1X). Red rectangles refer to obtained basement ages discussed in the text (AM: Amotapes Massif, HAI: Homigas de Afuera Island, IM: Illescas Massif, LAI: Lobos de Afuera Island, LI: Lobera Island, MI: Macabi Island, SM: San Martin 1X). Basins boundaries were obtained from Perupetro. Plate ages obtained from Müller et al. (1997). Current plate motion estimated from the Nazca-South America convergence pole of the NUVEL-1 global plate of motion model (DeMets et al., 1994). Topography and bathymetry from GeoMapApp. (For interpretation of the references to colour in this figure legend, the reader is referred to the web version of this article.)

structural corridor represented in land by the highs of Paita and Illescas extend seawards and is coincident with high positive anomalies (Fig. 2); also coincident with the Lobos de Afuera Island (LAI, Fig. 1). The trench-parallel depocenters are bounded by basement highs and are dissected along-strike. On land, the uplift of the Paita and Illescas structural highs is diachronous along the margin. In the Paita Massif, a single bedrock sample yielded a 63 ± 7 Ma age from apatite fission tracks and a 52.1 ± 1.6 Ma age from apatite (U−Th)/He (Wipf, 2006). Thermal modelling suggests that exhumation took place in two periods, the first one at ~65 ± 5 Ma and the most recent one at about 5 Ma (Eude et al., 2015; Garver et al., 2005; Wipf, 2006). Further south and along the west piedmont of the Andes, apatite fission-track and

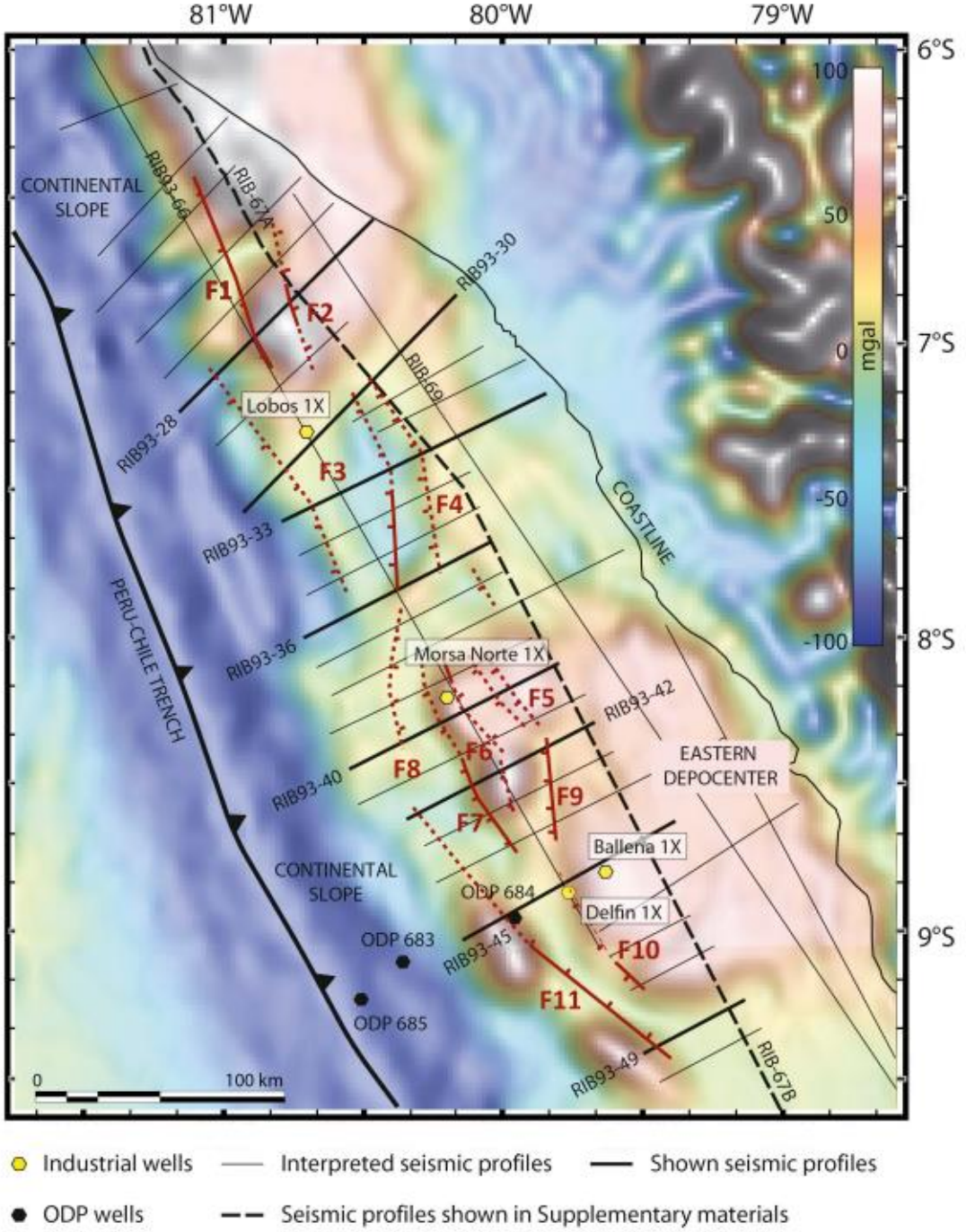

Fig. 2. Gravity map (Sandwell and Smith, 1997) from GeoMapApp (resolution: 1,75 km^2) with the position of seismic lines interpreted in this study and wells used for chronology purposes (PARSEP, 2001). Faults are located after seismic interpretation.

(U−Th)/He ages combined with thermal modelling suggest a regional exhumation at ~15 Ma (Eude et al., 2015; Margirier et al., 2015; Michalak et al., 2016).

3. Material and methods

The seismic profiles presented in this work were acquired by a joint venture between Ribiana and Perupetro S.A. in 1993. The seismic data from this survey has been migrated in the time domain and has been recently reprocessed (Perupetro) to improve the quality of the shallow reflections. Seismic profiles are mainly oriented NE-SW (e.g. perpendicular to the trench axis) with the exception of five trench-parallel profiles (Figs. 1 and 2). The survey was carried out by the vessel M/V Digicon Explorer, equipped with a DSS-240 digital streamer, 4500 m length, 180 channels, 25 m group interval with the acquisition system resulting in a 60-fold coverage. Thirty-five profiles were analyzed in this study, over an average total length of ~4100 km. Line penetration is 6 s (TWTT, two-way travel time) with clear reflections down to ~4 s (TWTT); because of high uncertainties no interpretation has been performed beneath this depth. Seismic Profiles were interpreted using conventional techniques in the Kingdom Suite® software. For the sake of simplicity lines are called here only by their number without the RIB93 prefix.

The top of basement has been difficult to identify only from interpretations of seismic lines, because of 1) inhomogeneous quality of reflectors at the top of the basement; 2) the absence of extensive core control of the top of the basement; 3) layered reflections near the top of the basement (metasediments?) and 4) a lack of clear seismic reflections in the deepest part of the depocenters. Consequently, we conducted a paired analysis of reflection seismic geometries and of free-air gravity anomalies via forward modelling on GM-SYS Geosoft®, in order to propose a reliable location of the top of the basement in areas where the use of only seismic data was not satisfactory (see Supplementary materials).

In this study, sedimentary rock description and chronology was obtained from published paleontological records from four exploratory wells and ODP data (PARSEP, 2001; mostly based on former REPSOL internal reports; Von Huene and Suess, 1988; Suess et al., 1988). The Ballena 1X well (maximum depth 744 m) and Delfin 1X well (maximum depth 2459 m) drilled by Occidental in 1971, and several sites drilled during the 1986 ODP Leg 112 campaign (mostly site 684) offer stratigraphical and chronological constraints for the seismic profile 45 (Figs. 2 and 3). Similarly, the Morsa Norte 1X (maximum depth 989 m) and Lobos 1X (maximum depth 2028 m) wells, drilled by Repsol in 1999, offer stratigraphical and chronological constraints for the seismic profiles 40 and 30, respectively (Figs. 2 and 3).

4. Stratigraphic framework

The basement was reached in three of the wells shown here (Delfin 1X, Ballena 1X and Morsa Norte 1X). In these wells, the basement is overlain by a poorly studied Cenozoic succession starting generally in the middle Eocene (Fig. 3; PARSEP, 2001). The sedimentary succession from late Mesozoic to early Cenozoic strata is only observed in the Lobos 1X well (PARSEP, 2001; Sternbach et al., 2010). In this latter, Campanian and Maastrichtian series indicate depositional settings ranging from continental shelf to upper slope, while Paleocene and early Eocene units bear debris flows and turbidites indicative of a deeper setting or a steeper slope.

The Paleogene sediments found in the four industrial wells are mostly defined as fine-grained hemipelagic sediments with fauna typical of deep marine environments, locally interstratified with coarse-grained clastic facies (Lobos 1X, Morsa Norte 1X). The Oligocene is found only in Lobos 1X and Delfin 1X wells, topped by a regional unconformity that truncates the Paleogene. The definition of the sedimentary hiatus associated to this unconformity was one of the main results of the ODP Leg 112 (the IQ unconformity of Von Huene and Suess, 1988), which in site 683 ranges from 40 to 25 Ma (Von Huene and Suess, 1988). Its duration reaches a maximum where the early Miocene sediments rest on the middle Eocene, supposedly on horsts (e.g. Ballena 1X and Morsa 1X wells), whereas Oligocene sediments are preserved in grabens (e.g. Delfin 1X) and it is most likely correlatable with the IQ unconformity (Suess et al., 1988) related with sea level eustatic fall during upper Oligocene (Haq et al., 1987; PARSEP, 2001)..

The lower, middle and upper Miocene units are present and have been differentiated in all industrial exploratory wells. They correspond to dominant shallow-water, fine-grained carbonate facies sometimes dolomitized (PARSEP, 2001; Von Huene and Suess, 1988), contrasting with the coeval deep-water facies recorded in the Lima basin. In all wells, the uppermost part of the lower Miocene corresponds to an erosional surface (PARSEP, 2001), truncating sediments aged between 17.8 and 16.4 Ma in the Ballena 1X well (Schrader and Castaneda, 1990). In the latter Ballena 1X well the lower Miocene shows a deepening upward sequence, whereas the middle and upper Miocene successions show a shallowing upward sequence (PARSEP, 2001). Trenchwards, a hardground layer is observed in the ODP Site 684 through the topmost layers of the upper Miocene defining the base of a sedimentary hiatus at 4.3 Ma (Von Huene and Suess, 1988). Pliocene sediments present in the Delfin 1X well and in the ODP Site 684 suggest a deposition in a water depth of ~100 m (PARSEP, 2001). At the top of the Pliocene section, there is a ~ 2 Ma hiatus encompassing the upper Pliocene and the Pleistocene (Resig, 1990; Suess et al., 1990).

5. Results from seismic interpretation and well data analysis

The seismic lines interpreted here show that the continental margin of the FNCPA is highly segmented. The eastern part of the margin is a large and flat floored platform with an average slope less than 1° and water depth of less than 375 m. To the west, the trench-slope break is clearly (Fig. 4A) or poorly (Fig. 4B) defined and delimits a deeper western domain (the upper continental slope) generally marked by chaotic reflections. The current trench-slope break develops independently of the deformed area (called here the Main Deformation Zone, MDZ) as it is located nearby the border (e.g. line 28, Fig. 4A) or in the core of the MDZ (e.g. line 33, Fig. 5A). Overall, in the study area, the FNCPA can be divided into three main longitudinal zones (Fig. 2): 1) an 'eastern depocenter' with sediment thickness up to about 2 s TWTT mostly unaffected by basement faults; 2) a central deformed zone (MDZ), defined by local basement emersion or shallow-water basement, raised reflectors and main faults deep-rooted in the basement forming grabens and half-grabens and 3) a westward continental slope, partially imaged from seismic records, and with unclear limits with the MDZ. Zones 1 and 2 have been ascribed in some previous works (e.g. Romero et al., 2013) to the Salaverry and Trujillo basins, respectively; whereas zone 3 has been ascribed in several works to the Yaquina basin or graben (e.g. Krabbenhöft et al., 2004). The MDZ defined in zone 2 is trench parallel and coincides, in the northern part of the study area, with the southern prolongation of the structural high outlined by the Illescas Massif and the Lobos de Afuera Island (Lines 28 and 30; Figs. 1, 4A and B).

The architecture of the margin is complex and defined by uplifted and subsided areas disposed in a complex patchy distribution in the MDZ. Main faults on the seismic profiles are difficult to correlate ubiquitously in a line-to-line basis considering the ~15 km spacing between profiles. However, it is clear that the basement structure is controlled by numerous large faults that delimitate half-grabens (e.g. F3 and F4 in line 36, Fig. 5B), grabens (e.g. F5/F6 in line 40, Fig. 6A; F6/F9 in line 42, Fig. 6B), and horsts (e.g. F6/F7 in line 40) coinciding with negative (for half-grabens and grabens) and positive (for horsts) free-air gravimetric anomalies (Fig. 2). Indeed, the gravimetric anomaly map mimics the basement structural position, especially east of the slope break where the sea-floor is flat and hence, where free-air anomalies are

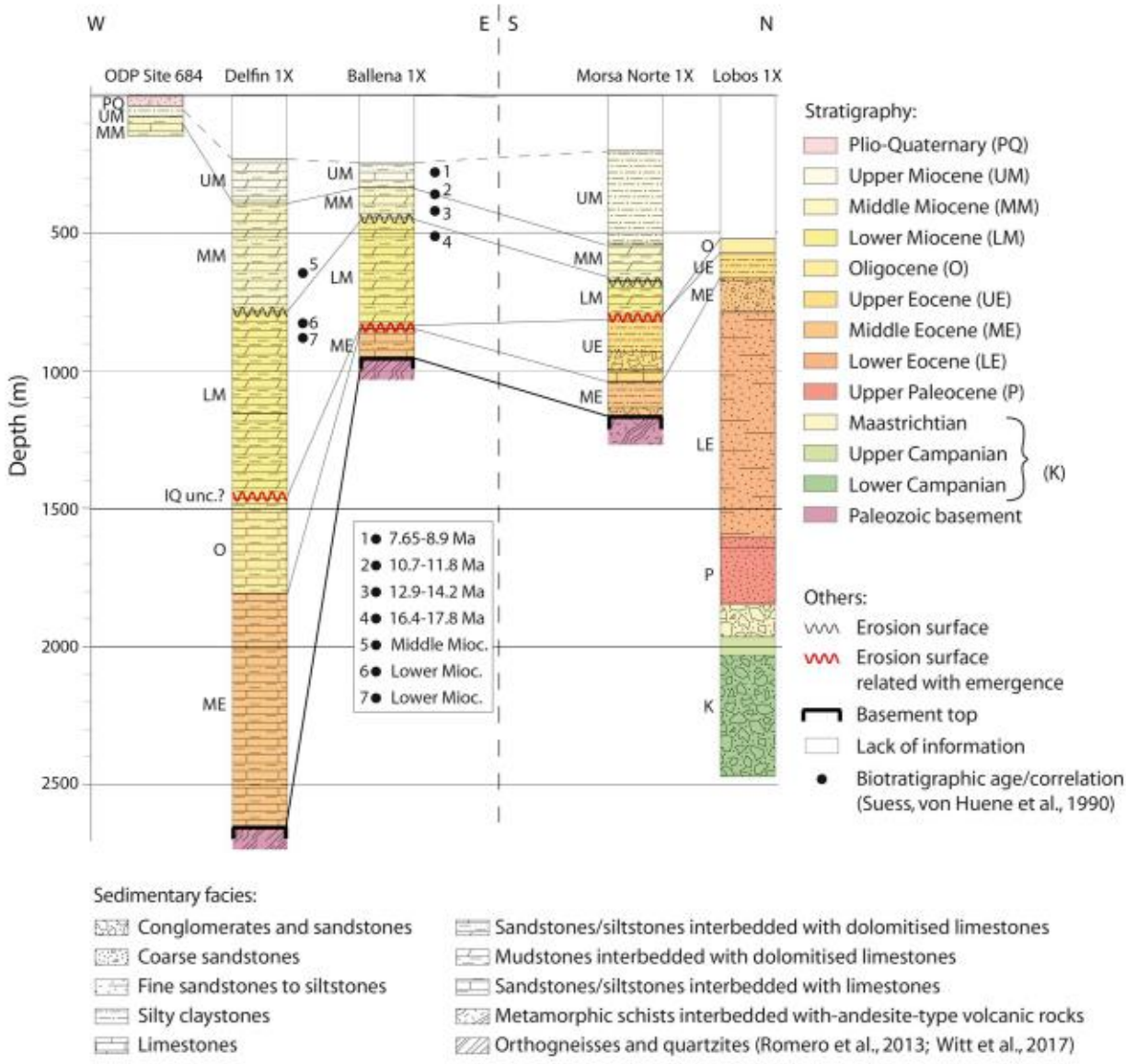

Fig. 3. Log of wells used for stratigraphic correlation and basement top location (Suess et al., 1990; Suess and Von Huene, 1988; PARSEP, 2001).

intrinsically related to lithological variations at depth.

In places where the top of the basement is clearly imaged from seismic lines, it is defined by a high-amplitude short wave-length irregular reflector outlining erosional structures possibly related to subaerial erosion processes (Fig. 5A). This erosive surface can be observed to the east and beneath the main depocenters of the MDZ suggesting that this major erosional episode could be as old as pre-Campanian (line 30 with chronology defined by the Lobos 1X well; Figs. 3 and 4B). Grabens and half-grabens in the MDZ show a complex distribution and may locally contain thick strata, reaching about 4 km-thick on line 45 (Fig. 7A) with chaotic to parallel reflections most likely reflecting *syn*-sedimentary deformation. Furthermore, Paleogene series are almost entirely restricted to these grabens (Figs. 4B and 7A), with the exception of the wedge that pinches-out above the basement of the eastern depocenter where no fault activity could be observed (Figs. 4B, 5A, 7A and B).

Well data (see also Delfin 1X well in Fig. 7A) and line-to-line correlations suggest that younger sedimentary rocks sealing main depocenters in the MDZ are late Eocene in age north of ~8°S (e.g. line 40, Fig. 6A) and late Oligocene south of ~8°S (e.g. line 42, Fig. 6B). Indeed, the Oligocene series observed in wells pinch-out to the north and are only observed in the southern part of the studied zone. The erosional hiatuses that have been identified on top of Paleogene deposits in the wells are prominent in the MDZ, forming angular unconformities (better imaged on its corresponding zoom in the supplementary materials). The clearer of the Paleogene deformed depocenters was drilled at the Lobos 1X well (line 30; Fig. 4B) and reached Cretaceous sedimentary rocks (see former section). Paleogene depocenters in the MDZ show few unconformities, difficult to correlate because of space between lines. One of these unconformities is observed in line 33 (better imaged on its corresponding zoom in the supplementary materials; Fig. 5A) and may represent the seawards expression of the erosional surface observed at the top of the basement, thus attesting for active subsidence after basement incision. Other minor unconformities may be also observed in line 40 (Fig. 6A).

Above the Oligocene unconformity, a relatively thick lower Miocene unit is observed over the entire study zone, except in uplifted areas. It overlies Eocene sediments (Fig. 6A), Oligocene sediments (Fig. 7A) and in the eastern depocenter, it onlaps onto the eroded basement (Fig. 7B). The onlapping character of the lower Miocene unit above the basement in the eastern depocenter suggests that these onlaps may be originated by a transgression; an aspect supported by the upward deepening character of the early Miocene series observed in the Ballena 1X well (PARSEP, 2001). In most of the seismic lines, the top of the lower

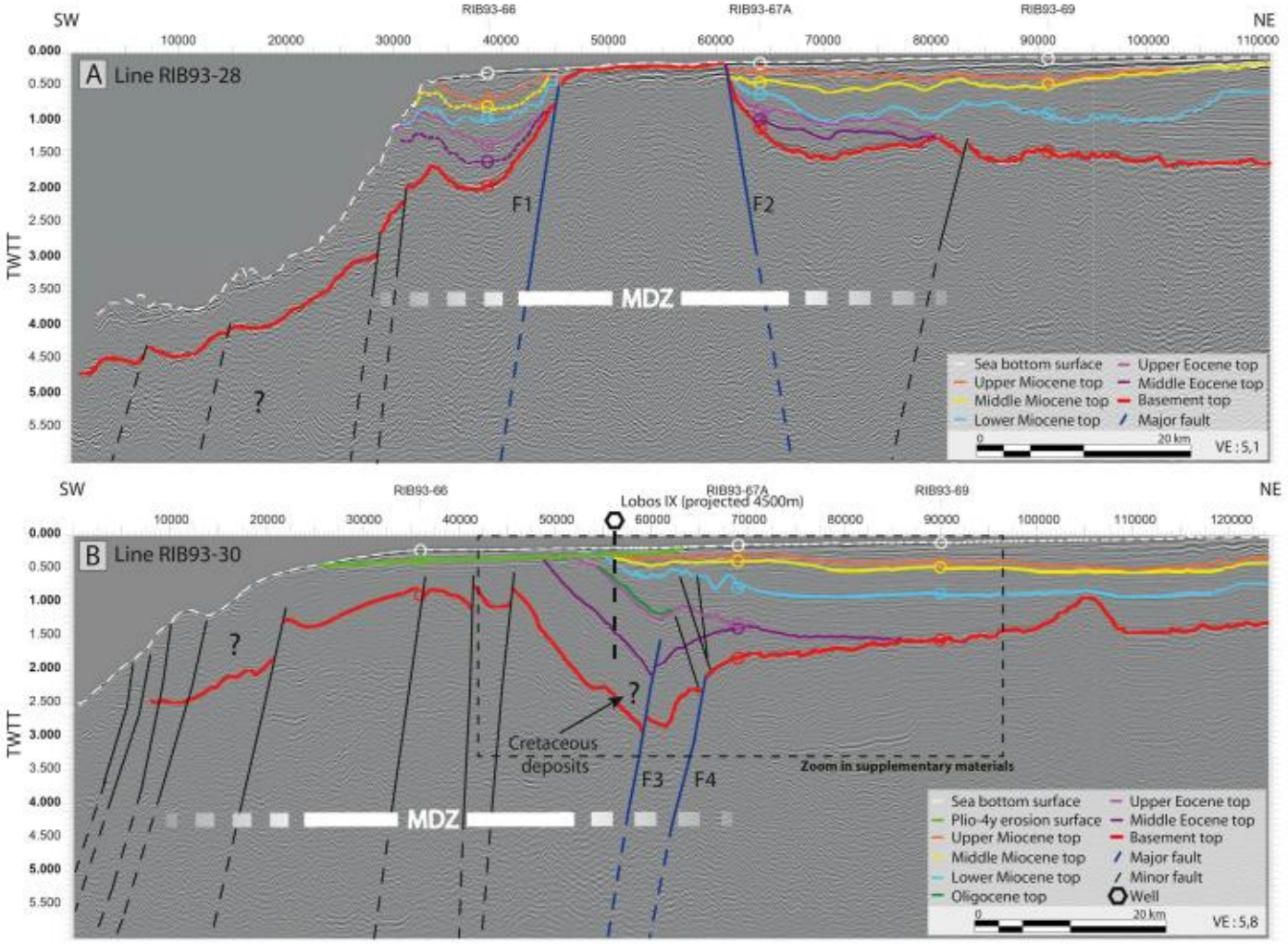

Fig. 4. A. Seismic profile RIB93–28. Note the erosional slope and the near-edge basement horst. The units are folded against the faults, with an upward decreasing dip. **B.** Seismic profile RIB93–30. The basement high is buried below tilted Paleogene units covered unconformably by Plio-Quaternary deposits near the surface. Dotted square indicates the area zoomed in the supplementary materials (DR4A). See location in Fig. 2. Corresponding non-interpreted seismic profiles in supplementary materials (DR6).

Miocene is defined as a clear erosional surface (dated at circa 15 ± 2 Ma in the well Ballena 1X; see previous section) and observed on the flanks (e.g. line 30, Fig. 4B, offset −65,000) or above the core of the MDZ (line 42, Fig. 6B, offset ~45,000). In the eastern depocenter this erosion surface is locally associated with strata tilted landward and responsible for the formation of apparent downlaps (tilted onlaps) above the gently dipping basement south of 8°S (e.g. line 45, Fig. 7A, offset ~60,000). This tilting process is likely due to the pre-Pliocene uplift in the eastern part of the MDZ toward the west. Therefore, we consider that uplift along the MDZ coincides directly with the maximum of erosion on top of lower Miocene unit. Alternatively, the coeval erosion surfaces not related with uplift at the MDZ are most likely incision led by canyons (e.g. lines 30 and 40; Figs. 4A and 6A).

As for the top of the lower Miocene, the tops of the middle and upper Miocene series could also be identified over the whole margin except for some highly deformed areas within the core of the MDZ, where they are locally truncated. The middle and upper Miocene strata are unconformable over the lower Miocene series. The thickness and seismic facies of the middle and upper Miocene units rapidly change along and across strike, possibly linked to the presence of submarine canyons (e.g. Fig. 6A, offset ~45,000). The increasing thickness of the units toward the MDZ emphasizes a cessation (or at least the decrease) of uplift in the MDZ during middle and upper Miocene, which is also clearly appearing in the south of the study area from line 49 (Fig. 7B). It is more debatable for the lines located to the north (lines 28 and 30) as middle and upper Miocene units are tilted and truncated over the MDZ. Some paleo trench slope breaks, middle and upper Miocene in age, can be observed from line 40 (Fig. 6A) at offset 42,500, 0.7 twtt (middle Miocene) and at offset 40,000, 0.6 twtt (upper Miocene). The position of these slope breaks, with the upper Miocene slope break located at shallower depth, suggests subsidence of the margin without any resumption of the uplift of the MDZ in this area (Fig. 6A). Restricted subsidence to the east is also observed in thin sedimentary growth strata as the one observed in the hanging-wall of F9 on line 42 (Fig. 6B). Nevertheless, the interval between the top of the lower Miocene and the top of the upper Miocene shows no major fault-related thickness variations and defines a period of tectonic quiescence in the FNCPA (e.g. F9 in line 42, Fig. 6B). However, the late tilting of middle and upper Miocene series and the eroded top of upper Miocene deposits over the flanks and the core of the MDZ (e.g. lines 36 and 45; Figs. 5B and 7A) evidence a local renewal of the uplift of the MDZ during latest Miocene to Pliocene times.

The Plio-Quaternary reflectors form a relatively thick unit mostly observed in the eastern depocenter mainly south of 8°S (see along-strike profile in Supplementary Materials, DR2B). The Plio-Quaternary section shows a decreasing thickness over the MDZ (e.g. line 49, Fig. 7B) and is locally truncated by the present sea bottom surface as can be seen on lines 40 and 45 (Figs. 6A and 7A). The thickness of the unit attests for a

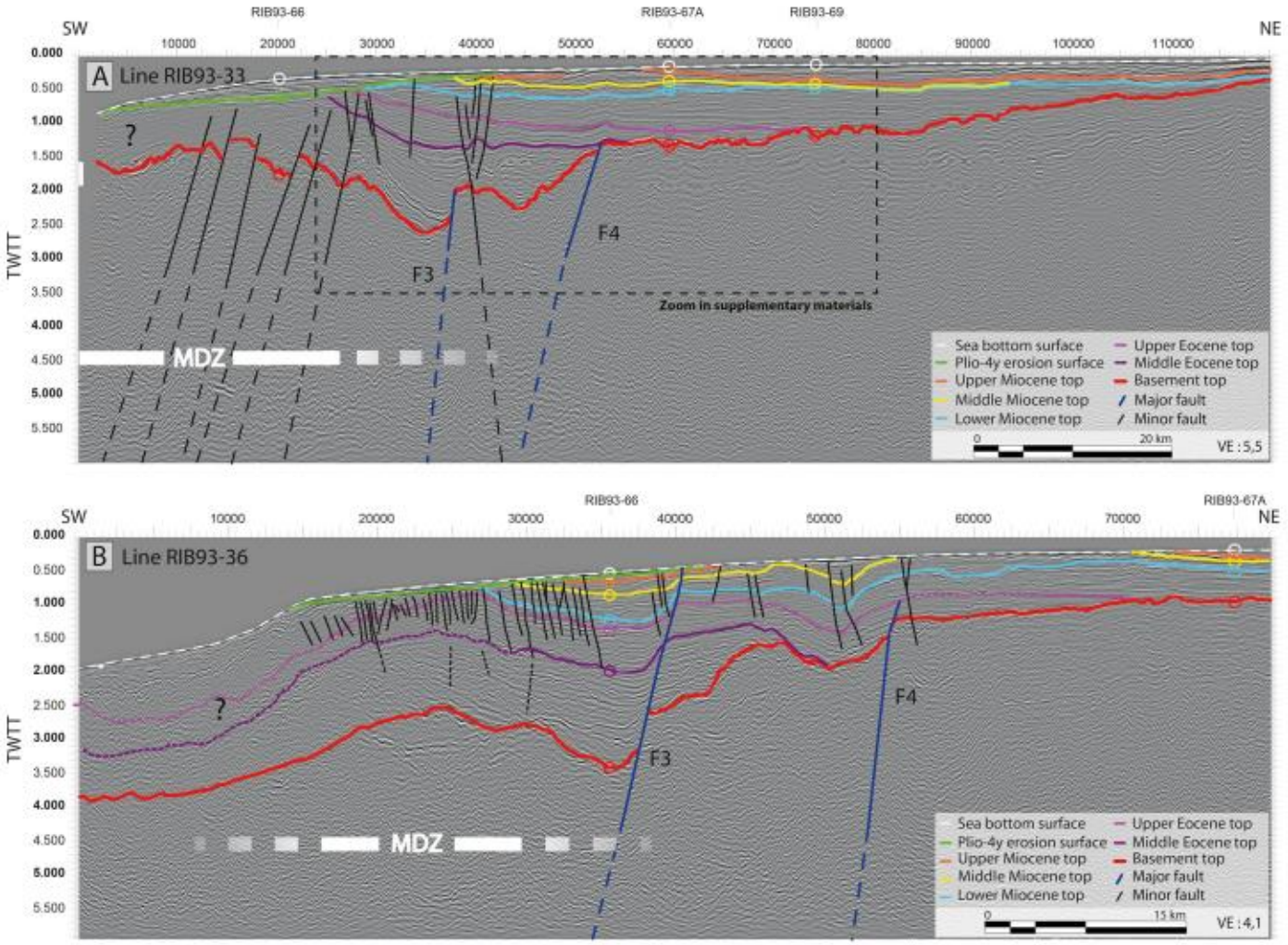

Fig. 5. A. Seismic profile RIB93–33. The basement high is buried by Paleogene units below a major unconformity. Neogene deposits related with a transgression onlap the basement landward. Dotted square indicates the area zoomed in the supplementary materials (DR4B). **B.** Seismic profile RIB93–36. The basement high has a lower amplitude and is buried under Cenozoic deposits. See location in Fig. 2. Corresponding non-interpreted seismic profiles in supplementary materials (DR7).

main subsiding area localized in the eastern depocenter during Plio-Quaternary times. Toward the slope-break, older units have been tilted and either covered unconformably by Plio-Quaternary deposits on the continental slope (Fig. 6A), or literally truncated by a Plio-Quaternary erosion surface (Fig. 5A). This recent period is also remarkable for widespread tectonic activity evidenced by the development of numerous normal faults noticeable across the entire margin, to the slope break (e.g. line 28, Fig. 4A) as well as the eastern depocenter (e.g. F9 line 42, Fig. 6B).

6. Discussion

The margin of the FNCPA exemplifies a predominantly extensional margin in which local uplift along the MDZ produces the individualization of a depocenter (i.e. formation of the eastern depocenter) with architecture similar to that observed in accretionary settings. Seismic records show that the Neogene evolution of the offshore part of the FNCPA can be divided into four main tectonic episodes: 1) a pre-Miocene episode resulting in graben and half-graben structures in the MDZ; 2) a regional subsidence episode during the lower Miocene; 3) a late early Miocene-Quaternary episode resulting in localized and episodic uplift which promoted the onset of basin individualization and 4) renewal of regional subsidence during Plio-Quaternary times accompanied by widespread normal faulting localized in the MDZ.

6.1. Pre-Miocene extension: strike-slip related depocenters?

Tectonic models in the Peruvian margin suggest that deformation resulting from oblique convergence may have started during the Late Cretaceous, coeval with the formation of intra-arc volcanosedimentary basins on the western flank of the Andes (Jaillard et al., 2000; Polliand et al., 2005). Dextral shear resulting from a Caribbean plate interaction has been also invoked as a deformation mechanism for the area north of 8°S (Kennan and Pindell, 2009). How the plate convergence obliquity is accommodated at the plate boundary is related to several parameters including interplate coupling, the length of the oblique subduction zone and the degree of obliquity (e.g. Jarrard, 1986; Jaillard et al., 2000; Chemenda et al., 2000; Philippon and Corti, 2016). Oblique convergence is well known to create partitioned systems across the forearc and/or backarc domains, with the development of roughly trench-parallel strike-slip faults typically segmented along hundreds of kilometers as observed in Japan (Median Tectonic Line, Otsuki, 1992, Tsutsumi and Okada, 1996), Sumatra (McCaffrey, 1991; McCarthy and Elders, 1997), Ecuador (Alvarado et al., 2016; Witt and Bourgois, 2010; Yepes et al., 2016), among other systems.

Based on field observations, geomorphologic analysis, geophysical and borehole data, Viveen and Schlunegger (2018) suggested that pre-existing margin-parallel lineaments (which forms a margin-parallel strip from the piedmont to the coastline) were operating as right-lateral transfer faults between 47 and 28 Ma, the chronology of deformation

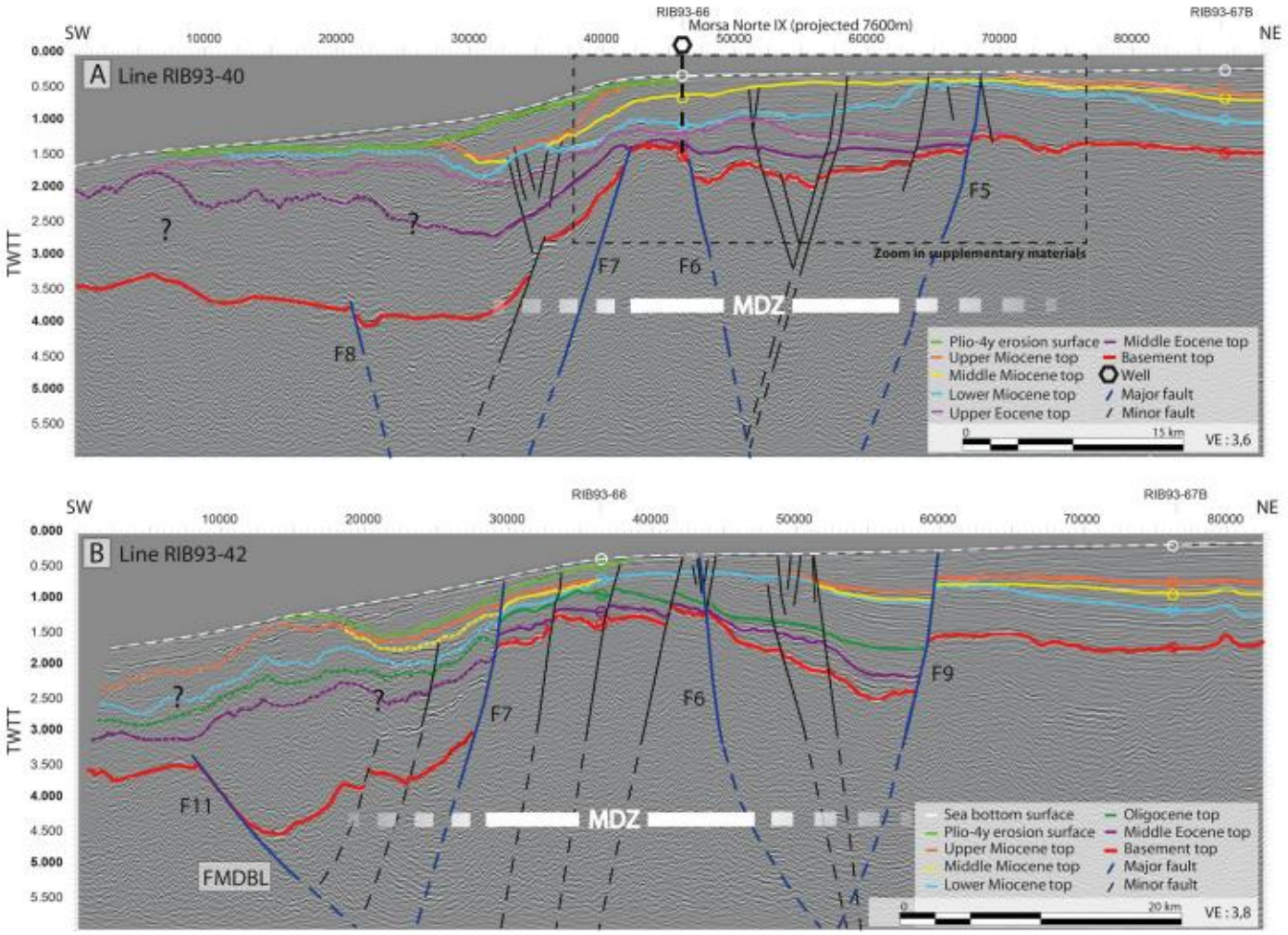

Fig. 6. A. Seismic profile RIB93–40. Lower Miocene top is eroded and filled by middle and upper Miocene prograding deposits. Lower Miocene strata form apparent downlaps along the basement landward. Dotted square indicates the area zoomed in the supplementary materials (DR5A). **B.** Seismic profile RIB93–42. The fault F9 was active recently as evidence by the different thickness of Plio-Quaternary deposits on both side of the faults. FMDBL: Forward Modelling Inverse-Derived Basement Location (see Supplementary materials DR1). See location in Fig. 2. Corresponding non-interpreted seismic profiles in supplementary materials (DR8).

being in accordance with the regional plate tectonic models of Somoza and Ghidella (2012). Viveen and Schlunegger (2018) proposed that former Jurassic to Cretaceous margin-parallel faults could have been reactivated in this context. In the FNCPA, the grabens formed are mostly parallel to the MDZ and are, at least partly, coeval with the deformation strip defined onshore by Viveen and Schlunegger (2018). Therefore, although it is not clear in seismic records whether graben and half-graben systems observed in the MDZ resulted from strike-slip tectonics, we consider that their depth, their complex geometry, their patchy distribution and their local extent most likely suggest a strike-slip origin, as observed in their onland counterparts. A strike-slip regime resulting from subduction partitioning may be difficult to conceal with the plate motion estimates obtained by Somoza and Ghidella (2012), which suggest that convergence was almost orthogonal in central and north Peru between 47 and 28 Ma, and hence that no partition of the subduction movement was occurring at that time. However, other models such as the one by Müller et al. (2008); see Fig. 1 of Quinteros and Sobolev, 2013) or Müller et al. (2016); see Fig. 1 of Fennell et al., 2018) propose a very high oblique convergence since the Late Cretaceous to Oligocene; thus better supporting the deformation style observed in onshore and offshore parts of the FNCPA.

Near trench margin parallel extensional structures may also be explained by a subduction erosion regime and by slab roll back. Slab roll back estimates exist only for the southernmost Peruvian margin (Oncken et al., 2006) whereas, although the resolution of the timing of subduction erosion processes in the margin is poor (see next section); the depocenters of the MDZ were formed before the onset of major subduction erosion of the margin. Although major strike-slip faults, those that controls the tectonic escape of the forearc-arc sliver, are located in a roughly arc position in modern systems, it cannot be ruled-out that some strike slip systems, participating in the partitioning, may have formed near the trench. Furthermore, the present-day observed distance between the strike-slip systems and the trench (roughly 100 km) may have been reduced through time because of frontal erosion at the toe of the margin. Such trench retreat have been estimated to about 30 to 40 km at the latitude of the Lima Basin without taking in consideration the frontal erosion produced by the subduction of the Nazca ridge (Von Huene and Lallemand, 1990; Clift et al., 2003) and about 25–35 km at 23°S (Von Huene and Ranero, 2003) but has not been constrained for the FNCPA. We consider likely that a similar length of the margin (*c.* 25–40 km) has also been eroded in the FNCPA. According to the literature and worldwide examples, we assume that the pre-Miocene depocenters in the FNCPA were most likely linked to strain partitioning occurring during the Late Cretaceous due to oblique convergence (Fig. 8A). Strike-slip motion was sustained through the Paleogene as pre-existing lineaments operated as transfer faults in an oblique convergence setting as supported by plate tectonic models (Müller et al., 2008).

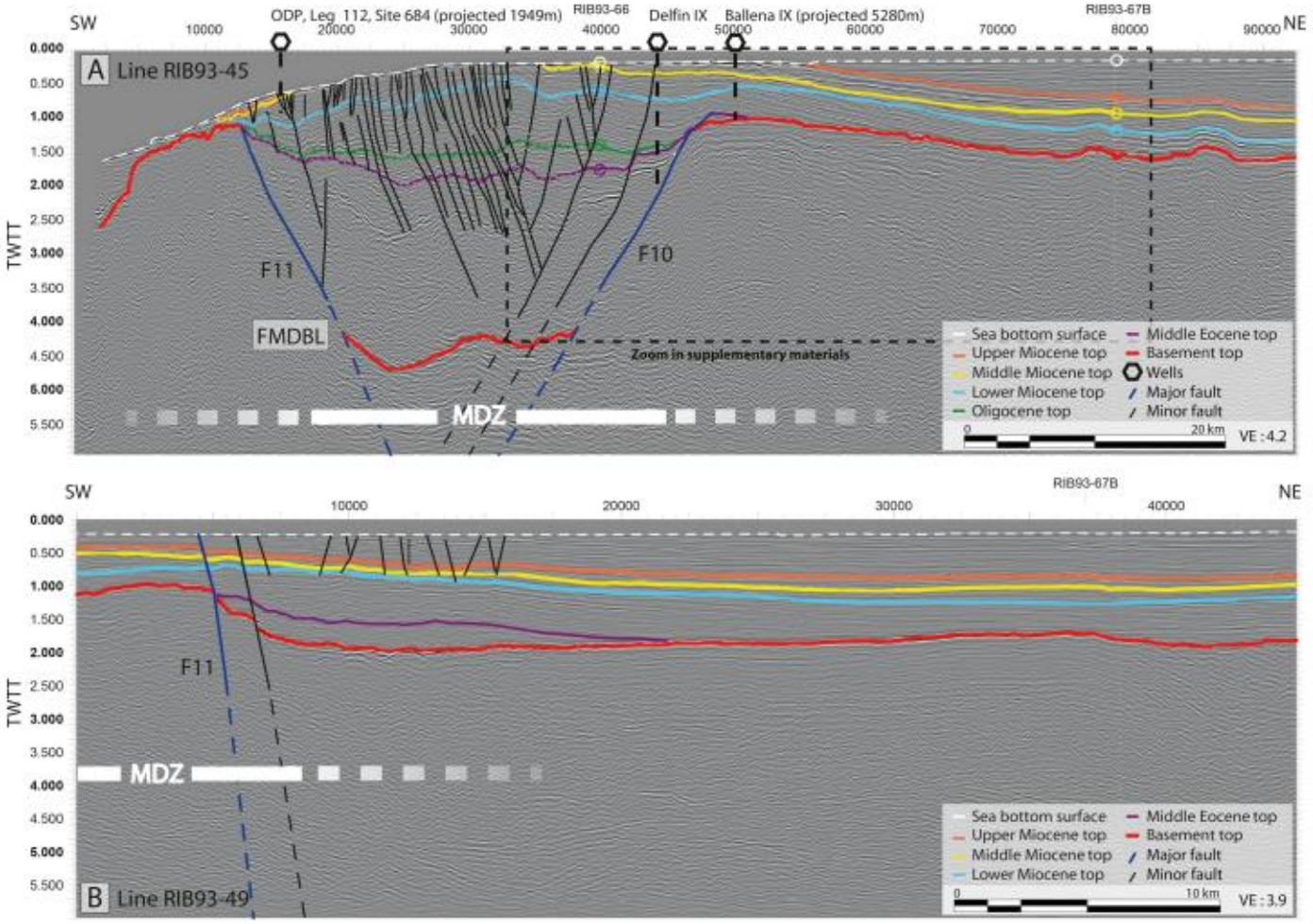

Fig. 7. A. Seismic profile RIB93–45. Graben inverted during the Neogene. Landward Plio-Quaternary reflectors are tilted close to the MDZ and truncated by the current seafloor. FMDBL: Forward Modelling Inverse-Derived Basement Location (see Supplementary materials). Dotted square indicates the area zoomed in the supplementary materials (DR5B). **B.** Seismic profile RIB93–49. Lower Miocene reflectors still downlap the basement landward. See location in Fig. 2. Corresponding non-interpreted seismic profiles in supplementary materials (DR9).

6.2. Early miocene regional subsidence

A major unconformity, related with an emersion period, truncated the Paleogene sediments mostly restricted to the MDZ. It affected middle Oligocene sediments in depocenters and middle to upper Eocene sediments in structural highs. Afterwards, the onset of Miocene sedimentation also reflects a change to a shallower sedimentation in platform settings, which is similar to that observed in several segments of the margin (north Chile, northern Peru, South and Central Ecuador) that also attest for a major change in sedimentation environment between Paleogene and Miocene times, passing mostly from slope to platform environments (PARSEP, 2001; Suess et al., 1988; Viveen and Schlunegger, 2018; Von Huene and Suess, 1988; Witt et al., 2019). Undoubtedly, more regional work is needed to compare the sedimentation patterns along the margin, nonetheless, the transition from deeper Paleogene to shallower lower Miocene series seems related to a regional plate-scale episode that resulted in uplift of the margin.

This major unconformity is overlain by a thick sedimentary unit (0.5 s TWTT in average) deposited along the entire study area. This large-scale deposition attests for a major change from localized pre-Oligocene strike-slip related subsidence to a regional subsidence during the early Miocene, and mainly ascribed to the transgressive nature of the unit above the basement. Widespread sedimentation during the early Miocene is in good agreement with a regional subsidence of the entire forearc domain, which may be related to the best-defined subduction erosion period observed from 15°S to 30°S, starting at least 20 m.y. ago (Clift and Hartley, 2007). Indeed, a direct relationship between large-scale and long-term forearc subsidence and the erosive regime of subduction has been proposed by several authors as a consequence of important basal erosion corresponding to a period of high convergence velocity (Clift and Vannucchi, 2004; Hussong, 1981; Jaillard and Soler, 1996; Kulm et al., 1982; Somoza, 1998; Somoza and Ghidella, 2012; Von Huene et al., 2004; Von Huene and Scholl, 1991; Von Huene and Lallemand, 1990). Indeed, the formation of the major unconformity at the base of the shallow water sedimentation roughly coincides with a major change in the convergence velocity (from −10 to −15 cm/yr) between the juvenile Nazca and South American Plates (Pardo-Casas and Molnar, 1987; Somoza, 1998; Somoza and Ghidella, 2012) and a modest change of obliquity toward nearly orthogonal convergence (Müller et al., 2008; Müller et al., 2016).

6.3. Rise of the MDZ and forearc basin individualization from Neogene to Quaternary

The evidence for uplift along the MDZ is related to basin flank uplift and comes from: 1) erosion (e.g. line 42, Fig. 6B) or thickness reduction (e.g. line 49, Fig. 7B) of sedimentary units above uplifted basement; 2) differential erosion with uplifted areas being more eroded than surrounding areas (e.g. line 30, Fig. 4B); 3) raised reflectors in both sides of outcropping basement (e.g. line 28, Fig. 4A) or shallow water depth

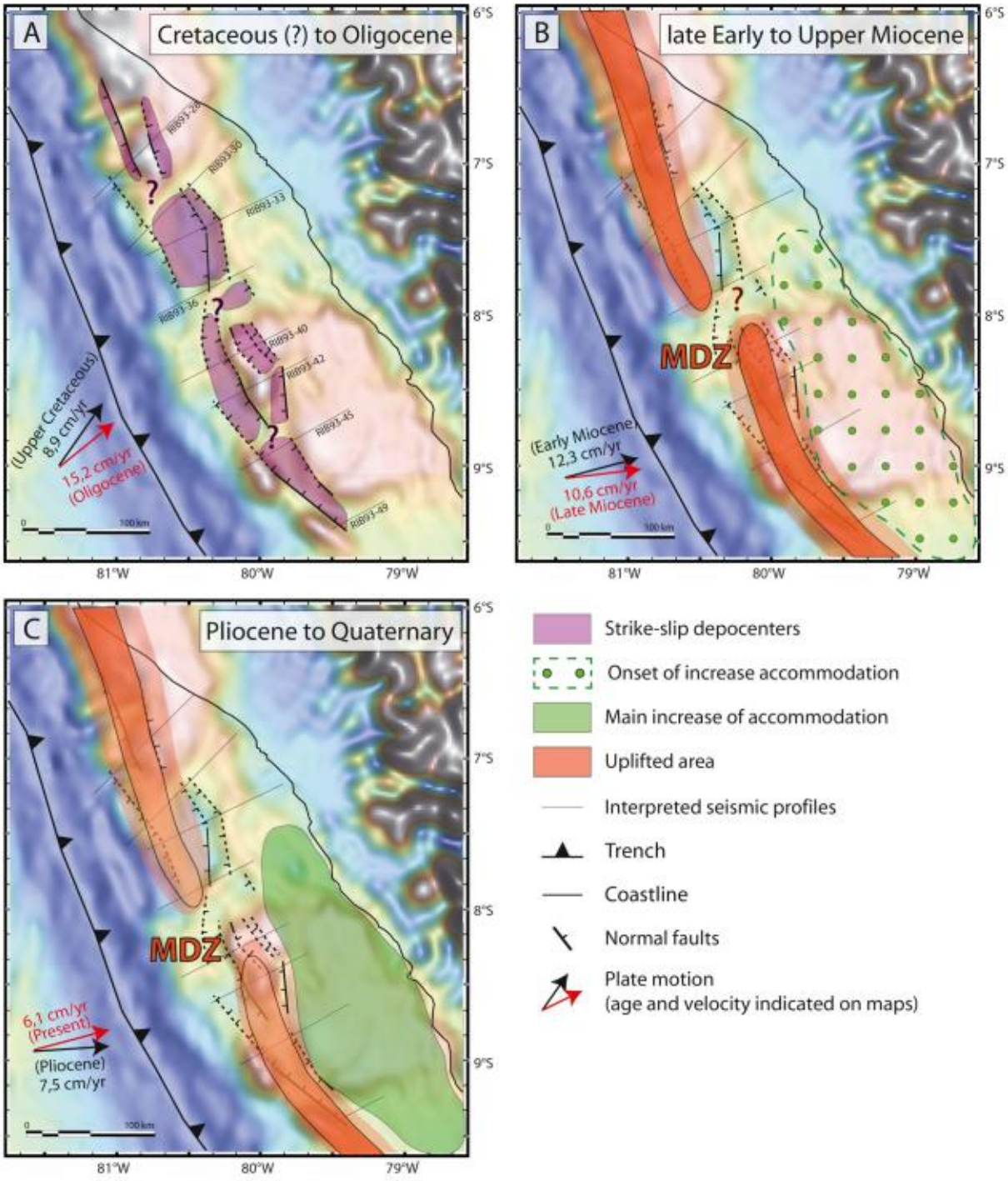

Fig. 8. Gravity maps (Sandwell and Smith, 1997) representing main vertical motions at different periods along the FNCPA. **A.** Approximate location of subsiding pull-apart basins through the Paleogene. Transtension across the margin was ended during the Oligocene due to the change of convergence obliquity (estimated from Quinteros and Sobolev, 2013; based on Müller et al., 2008). **B.** Regional subsidence affected the entire margin during early Miocene. Compressional event allowed the uplift of the OFH as soon as the end of early Miocene. **C.** Due to basal erosion and uplift of the MDZ, a localized basin appeared between the MDZ and the continent (here called the eastern depocenter). Uplift ceased around Pleistocene between 8 and 10°S and continued to recently north of 8°S.

basement (e.g. lines 30 and 33, Figs. 4B and 5A) and 4) apparent downlapping of lower Miocene reflectors on top of the basement of the eastern depocenter (e.g. lines 30, 45 and 49, Figs. 4B, 7A and B). Similar tilted geometries (apparent downlaps) have been described in the Kumano basin in Japan (Moore et al., 2007; Park et al., 2002; Strasser et al., 2009a, 2009b) and from the Hikurangi trench slope-basins in New-Zealand (Bailleul et al., 2013) and are also related to basin flank uplift. Although less obvious in the FNCPA, uplift is also highlighted by long wavelength diffuse deformation resulting in an antiform-like structure probably linked to small-displacement inversion of normal faults (e.g. line 36 and 45, Figs. 5B and 7A). The MDZ geometry is therefore controlled by the pre-existing strike-slip faults and related basins.

The erosional surface that topped the lower Miocene strata is observed regionally, not only in the vicinity of faulted areas. Furthermore, shallow-water shelf environments are recorded from the wells in the entire Miocene series (PARSEP, 2001). This character indicates a model in which eustatic falls maybe associated with emergence periods that

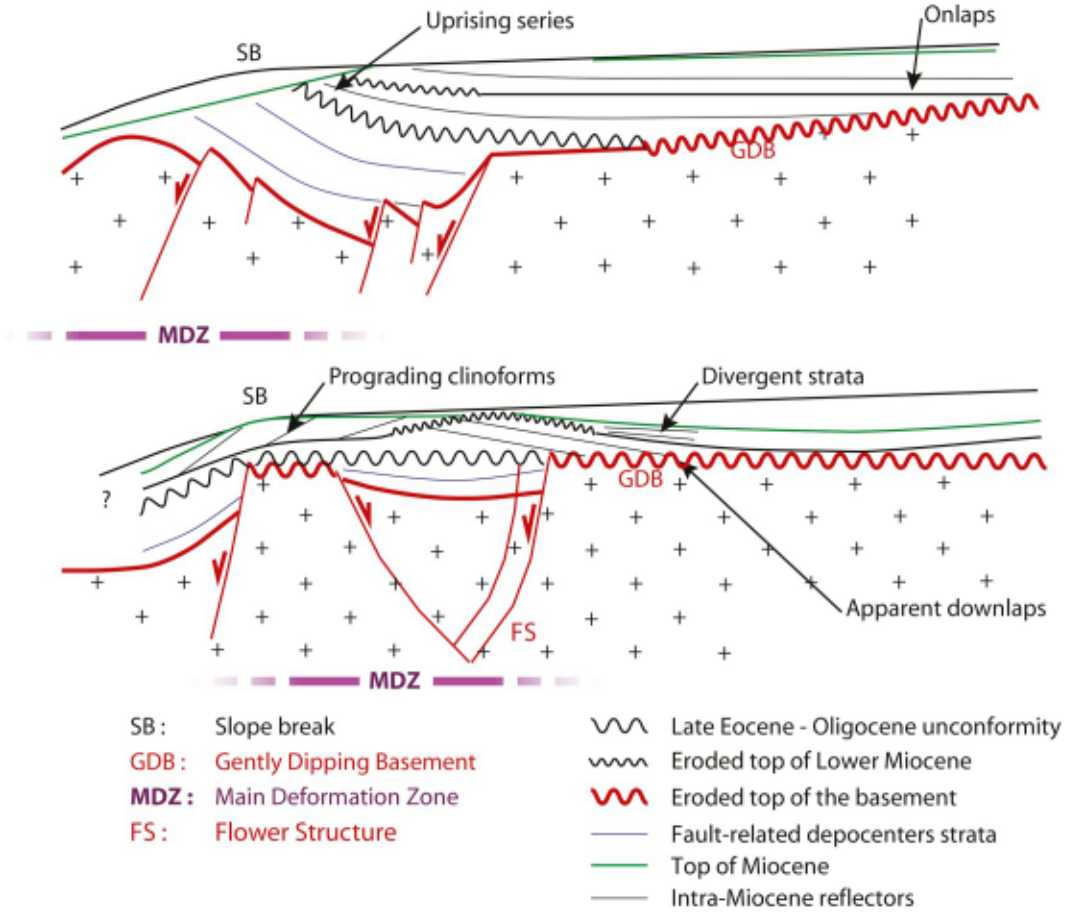

Fig. 9. Cartoons of the architecture of the FNCPA showing the main aspects discussed in this study. **A.** Significant uplift at the MDZ. **B.** Weak uplift at the MDZ.

could explain the appearance of the main lower-middle Miocene erosional surface and other subsequent minor unconformities. As a consequence of the shallow-water marine setting, the seismic strata geometry, lateral extent and thickness of the Neogene deposits in the FNCPA have been tightly controlled by accommodation changes. The main erosional surface on top of lower Miocene deposits is nearly coincident with the samples dated by Schrader and Castaneda (1990) between 17.8 and 16.4 to 14.2–12.9 Ma and matches one of the two well-known global eustatic sea-level falls occurring between ~16 and ~ 15 Ma (e.g. Haq et al., 1987; Kominz et al., 1998; Miller et al., 2005). The erosional processes were enhanced by eustatic fall affecting more the eastern flank of the MDZ as the localized uplift produced more significant incisions. A major erosional surface at *c.* 16 Ma has been also identified in north Peru in the offshore Tumbes basin and has been related to one of the two eustatic falls mentioned above (Aizprua et al., 2019) suggesting that the erosional surface observed in the FNCPA is a significant regional surface.

All the aspects mentioned above unable us to propose an age for the onset of the uplift to the late early Miocene – early middle Miocene (Fig. 8B). Deformation timing in the MDZ is in relatively good agreement with former seismic analysis (Kulm et al., 1982; Prudhomme et al., 2019), and with onland thermochronological records north of 8°S; which suggests a recent post late Miocene cooling in the Illescas Massif (Wipf, 2006). South of 8°S, temperature-time models in the western Andean piedmont constrain onset of exhumation at *c.* 15 Ma (Margirier et al., 2015; Michalak et al., 2016). High shortening rates are also underlined between 17 and 8 Ma by the sequential restoration calibrated with low-thermochronological data (Eude et al., 2015).

The younger reflectors on the little deformed line 40 (Fig. 6A) and the thickening character of the middle Miocene unit toward the MDZ (e.g. line 45, Fig. 7A) clearly define a decrease or an interruption of the uplift in the studied area from the middle Miocene to the upper Miocene. However, middle and upper Miocene units appear tilted, more or less eroded in the core of the MDZ (e.g. line 40, Fig. 6A) and covered unconformably by Plio-Quaternary deposits. These observations suggest a resumption of the uplift after the deposition of the upper Miocene unit (Fig. 8C). This is in agreement with other studies suggesting that upper Miocene to Pleistocene sedimentary hiatuses observed in the well ODP 684 may be related to uplift episodes (Resig, 1990; Suess et al., 1990).

To the east, middle Miocene, upper Miocene and Plio-Quaternary units are deposited in the so-called eastern depocenter. The individualization of this depocenter (south of 8°S, Fig. 8B and C) resulted from diffuse basin flank uplift at the MDZ. The lack of evidences of normal faults in the basin and the relative stable position of the eastern depocenter through time support the assumption that the development of accommodation space in this depocenter is controlled by the uplift of the MDZ. Maximum thickness in the depocenter may have reached ~800 m (considering a 0.8 s TWTT depth and an average 2000 m/s velocity) for deposits younger than the late middle Miocene marker. A moderate tectonic subsidence may have thus accompanied the filling of this depocenter, taking into consideration that long-term eustatic variations since middle Miocene may not have exceeded 50 m, accordingly to recent, oxygen isotope-based eustatic charts (e.g. Miller et al., 2005). Similar forearc basin individualization following regional subsidence has been also observed and described in New-Zealand (Buret et al., 1997). These authors associated the forearc subsidence to subduction-erosion and the individualization of the basin to the uplift of a structural high across the forearc domain, which is closely similar to that we observe along the FNCPA. The uplift of the MDZ seems to have

continued to recent time (especially north of 8°S) as most of the Plio-Quaternary reflectors of the eastern margin are truncated by the seafloor. The seafloor is almost flat on the shelf, and dominantly draped with conformable strata down to the slope margin, except where the latter is crossed by active canyons (Fig. 4A). At the seismic scale however, it corresponds to a surficial erosion observed along the entire Peruvian margin (Calvès et al., 2017). This indicates that the shelf is overfilled, with significant bypass to the trench slope, suggesting a sediment supply greater than the accommodation space created. Considering the dominantly flat parallel or offlap-dominated seismic layering of most units, this situation prevailed over the Neogene. The unit-bounding unconformities may have been formed during short tectonic episodes.

Overall, two main architectural styles have been synthetized after our observations in order to summarize the diverse structural geometries extended along the FNCPA (Fig. 9). The first architecture (Fig. 9A) represents mostly the structures observed north of 8°S, where the MDZ is characterized by an overall uprising of the entire sedimentary successions showing near the slope-break a sharp Plio-Quaternary erosion surface. On the contrary, south of 8°S, the series above the MDZ have been characterized by the tilting and erosion of the lower Miocene unit and more locally the presence of westward shelf regradational middle Miocene clinoforms which extend seawards from the slope-break (Fig. 9B). Nevertheless, the MDZ shows significant along-strike variations in the amount of deformation (with a minimum deformation at 8°S) resulting in either highly uplifting basement producing sharp seaward dipping erosional surfaces (weak trenchward bypass, e.g. line 30, Fig. 4B) or less uplifted areas covered by seawards prograding clinoforms (strong trenchward bypass, e.g. line 40, Fig. 6A). In both cases the MDZ has a trench-parallel axis and separates the forearc basin from the trench slope.

In subduction-accretion regimes, the OFH represents a structural high parallel to the trench, most likely related to the activity of an out-of-sequence thrust (mega splay fault for Strasser et al., 2009b) with periodical rather than constant activity (e.g. Conin et al., 2012). Its development controls the forearc configuration preventing (at least partially) the bypass of sediments to the trench, restricting the forearc basin depocenter and tilting the sedimentary series in a landward direction (e.g. Moore et al., 2007; Moore et al., 2015; Noda, 2016). The evidences presented here attest for the development of a linear domain uplifted during the late early Miocene – early middle Miocene. This domain is similar to those observed on accretionary prisms, but characterized by a longer wavelength and more diffuse geometries. The processes responsible for uplift of the trench-parallel MDZ remain unclear, but the age of the first uplift event (mainly end of early Miocene - middle Miocene) and the location of the deformation over an inherited weakness zone, may suggest a mechanism associating seaward upper plate basal erosion and accretion with underplating beneath the MDZ, a mechanism suggested for other parts of the margin (e.g. Seely, 1979; Clift and Hartley, 2007) sharing more or less similar characteristics than the FNCPA.

7. Conclusions

The detailed study of seismic data allows reconstruction of the tectono-sedimentary evolution of the forearc of the North Central Peruvian Andes (FNCPA). The interpretation led us to propose that strike-slip depocenters were developed during the Late Cretaceous due to high convergence obliquity and subsequent partitioning along the margin. The strike-slip system developed throughout the Paleogene, forming a trench-parallel corridor of transtensional structures, called here the Main Deformation Zone (MDZ). A major unconformity, affecting middle Eocene series north of −8°S and Oligocene series south of it, seal these deposits and may represent the landward extension of the main IQ unconformity previously described from ODP drilling records. Sedimentation resumed with the widespread early Miocene series. It is plausible that the erosive subduction regime favored basal erosion generating a long-term and regional subsidence of the forearc as evidenced by the important thickness of the lower Miocene unit.

The MDZ was affected by episodic uplift during the end of the early Miocene and during the Pliocene. Uplift along the MDZ produced a tectonic setting very similar to an outer forearc high, typical of many accretionary settings. Uplift produced the landward tilting of lower Miocene strata enhancing local erosion, generally in the axis or on the eastern flank of the MDZ as localized uplift coeval with eustatic falls in a shelf environment produce more significant erosion. The local thickening of the middle and upper Miocene units in the core of the deformed area (MDZ) indicates uplift interruption. Resumption of the uplift is noticed after the deposition of upper Miocene sediments which induced the development of a depocenter to the east. The individualization of such a forearc basin (i.e. the eastern depocenter) resulting from the formation of a seaward structural high is generally typical from accretionary margins. Our study shows that this particular type of basin can also develop along active margins that are characterized by an erosional tectonic regime.

The patchy distribution and complex geometry of depocenters and structural highs observed along the FNCPA can result from the interaction between pre-existing strike-slip faults and related basins and subsequent basin flank uplift. Uplift activity seems to closely follow the onset of the erosional subduction regime in the margin. Therefore, the spatial distribution and timing of uplift, as well as the tectonic evolution of the margin, bring us to propose that basal underplating is the most likely process to account for the episodic uplift episodes observed in the FNCPA.

Credit author statement

Marie C. Genge: Conceptualization, Investigation, Writing – Original Draft, Visualization.

Cesar Witt: Conceptualization, Writing – Review & Editing, Supervision, Funding acquisition.

Frank Chanier: Writing – Review & Editing, Validation.

Jean-Yves Reynaud: Writing – Review & Editing, Validation.

Ysabel Calderon: Resources, Conceptualization, Review & Editing.

Declaration of Competing Interest

The authors declare that they have no known competing financial interests or personal relationships that could have appeared to influence the work reported in this paper.

Acknowledgements

We kindly thank Perupetro for helping us to get access to the data used in this work. This study was financed by the INSU (Institut National des Sciences de l'Univers, France) through a Telus-Syster scholarship accorded to CW. We thank Jacky Ferrière, Kiko Valencia and Darwin Romero for helpful discussions that helped to construct this manuscript. We thank E. Jaillard for his constructive review that helped us to improve the quality of the paper. We would also like to thank IHS for the academic license of the Kingdom suite software.

Appendix A. Supplementary data

Supplementary data to this article can be found online at https://doi.org/10.1016/j.tecto.2020.228546.

References

Aizprua, C., Witt, C., Johansen, S.E., Barba, D., 2019. Cenozoic Stages of Forearc Evolution following the Accretion of a Sliver from the late Cretaceous-Caribbean large Igneous Province: SW Ecuador-NW Peru. Tectonics 38 (4), 1441–1465.

Allmendinger, R.W., González, G., 2010. Invited review paper: Neogene to Quaternary tectonics of the coastal Cordillera, northern Chile. Tectonophysics 495, 93–110.
Alvarado, A., Audin, L., Nocquet, J.M., Jaillard, E., Mothes, P., Jarrín, P., Segovia, M., Rolandone, F., Cisneros, D., 2016. Partitioning of oblique convergence in the Northern Andes subduction zone: Migration history and the present-day boundary of the North Andean Sliver in Ecuador. Tectonics 35, 1048–1065. https://doi.org/10.1002/2016TC004117.
Antonijevic, S.K., Wagner, L.S., Kumar, A., Beck, S.L., Long, M.D., Zandt, G., Tavera, H., Condori, C., 2015. The role of ridges in the formation and longevity of flat slabs. Nature 524, 212–215.
Azalgara, C., 1994. Structural Evolution of the Offshore Forearc Basins of Peru, Including the Salaverry, Trujillo, Lima, West Pisco and East Pisco Basins. Rice University.
Bailleul, J., Chanier, F., Ferrière, J., Robin, C., Nicol, A., Mahieux, G., Gorini, C., Caron, V., 2013. Neogene evolution of lower trench-slope basins and wedge development in the Central Hikurangi subduction margin, New Zealand. Tectonophysics 591, 152–174.
Bellido, F., Valverde, P., Jaimes, F., Carlotto, V., Díaz-Martinez, E., 2007. Datación y caracterización geoquímica de los granitoides peralumínicos de los cerros de Amotape y de los Macizos de Illescas y Paita (Noroeste de Perú). 103. Boletín Sociedad Geológica del Perú, pp. 197–213.
Bilek, S.L., 2010. Invited review paper: Seismicity along the south American subduction zone: Review of large earthquakes, tsunamis, and subduction zone complexity. Tectonophysics 495, 2–14.
Bilek, S.L., Schwartz, S.Y., DeShon, H.R., 2003. Control of seafloor roughness on earthquake rupture behavior. Geology 31, 455–458.
Bourgois, J., Bigot Cormier, F., Bourles, D., Braucher, R., Dauteuil, O., Witt, C., Michaud, F., 2007. Tectonic record of strain buildup and abrupt coseismic stress release across the northwestern Peru coastal plain, shelf, and continental slope during the past 200 kyr-art. No. B04104. J. Geophys. Res. Solid Earth 112, NIL_46–NIL_67.
Boyd, T.M., Snoke, J.A., Sacks, I.S., Rodriguez B, A., 1984. High-resolution determination of the Benioff zone geometry beneath southern Peru. Bull. Seismol. Soc. Am. 74, 559–568.
Buret, C., Chanier, F., Ferrière, J., Proust, J.-N., 1997. Individualization of a forearc basin during the active margin evolution: Hikurangi subduction margin, New Zealand. C. R. Acad. Sci. Ser. IIA Earth Planet. Sci. 8, 615–621.
Calvès, G., Auguy, C., De Lavaissière, L., Brusset, S., Calderon, Y., Baby, P., 2017. Fore-arc seafloor unconformities and geology: Insight from 3-D seismic geomorphology analysis, Peru. Geochem. Geophys. Geosyst. 18 (8), 3062–3077.
Chanier, F., Ferrière, J., Angelier, J., 1999. Extensional deformation across an active margin, relations with subsidence, uplift and rotations: the Hikurangi subduction, New Zealand. Tectonics 18, 862–876.
Chemenda, A., Lallemand, S., Bokun, A., 2000. Strain partitioning and interplate friction in oblique subduction zones: Constraints provided by experimental modeling. J. Geophys. Res. Solid Earth 105 (B3), 5567–5581.
Clift, P.D., Hartley, A.J., 2007. Slow rates of subduction erosion and coastal underplating along the Andean margin of Chile and Peru. Geology 35, 503–506.
Clift, P., Vannucchi, P., 2004. Controls on tectonic accretion versus erosion in subduction zones: Implications for the origin and recycling of the continental crust. Rev. Geophys. 42.
Clift, P.D., Pecher, I., Kukowski, N., Hampel, A., 2003. Tectonic erosion of the Peruvian forearc, Lima Basin, by subduction and Nazca Ridge collision. Tectonics 22.
Conin, M., Henry, P., Godard, V., Bourlange, S., 2012. Splay fault slip in a subduction margin, a new model of evolution. Earth Planet. Sci. Lett. 341–344, 170–175. https://doi.org/10.1016/j.epsl.2012.06.003.
DeMets, C., Gordon, R.G., Argus, D.F., Stein, S., 1994. Effect of recent revisions to the geomagnetic reversal time scale on estimates of current plate motions. Geophys. Res. Lett. 21, 2191–2194.
Dickinson, W.R., 1995. Forearc basins. In: Busby, C.J., Ingersoll, R.V. (Eds.), Tectonics of Sedimentary Basins. Blackwell Science, Cambridge, Massachusetts, pp. 221–261.
Eude, A., Roddaz, M., Brichau, S., Brusset, S., Calderon, Y., Baby, P., Soula, J.C., 2015. Controls on timing of exhumation and deformation in the northern Peruvian eastern Andean wedge as inferred from low-temperature thermochronology and balanced cross section. Tectonics 34 (4), 715–730.
Fennell, L.M., Quinteros, J., Iannelli, S.B., Litvak, V.D., Folguera, A., 2018. The role of the slab pull force in the late Oligocene to early Miocene extension in the Southern Central Andes (27-46 S): Insights from numerical modeling. J. S. Am. Earth Sci. 87, 174–187.
Fisher, D., Mosher, D., Austin, J.A., Gulick, S.P.S., Masterlark, T., Moran, K., 2007. Active deformation across the Sumatran forearc over the December 2004 Mw9.2 rupture. Geology 35, 99–102. https://doi.org/10.1130/G22993A.1.
Garver, J.I., Reiners, P.W., Walker, L.J., Ramage, J.M., Perry, S.E., 2005. Implications for timing of Andean uplift from thermal resetting of radiation-damaged zircon in the Cordillera Huayhuash, northern Peru. J. Geol. 113 (2), 117–138.
Gerbault, M., Cembrano, J., Mpodozis, C., Farias, M., Pardo, M., 2009. Continental margin deformation along the Andean subduction zone: Thermo-mechanical models. Phys. Earth Planet. Inter. 177, 180–205.
Gutscher, M.-A., Westbrook, G.K., 2009. Great earthquakes in slow-subduction, low-taper margins. In: Subduction Zone Geodynamics. Springer, pp. 119–133.
Gutscher, M.-A., Olivet, J.-L., Aslanian, D., Eissen, J.-P., Maury, R., 1999. The "lost Inca Plateau": cause of flat subduction beneath Peru? Earth Planet. Sci. Lett. 171, 335–341.
Gutscher, M.-A., Spakman, W., Bijwaard, H., Engdahl, E.R., 2000. Geodynamics of flat subduction: Seismicity and tomographic constraints from the Andean margin. Tectonics 19, 814–833.
Hampel, A., 2002. The migration history of the Nazca Ridge along the Peruvian active margin: a re-evaluation. Earth Planet. Sci. Lett. 203, 665–679.
Haq, B.U., Hardenbol, J.A.N., Vail, P.R., 1987. Chronology of fluctuating sea levels since the Triassic. Science 235 (4793), 1156–1167.
Hasegawa, A., Sacks, I.S., 1981. Subduction of the Nazca plate beneath Peru as determined from seismic observations. J. Geophys. Res. Solid Earth 86, 4971–4980.
Hernández, M.J., Michaud, F., Collot, J.Y., Proust, J.N., d'Acremont, E., 2020. Evolution of the Ecuador offshore nonaccretionary forearc basin and margin segmentation. Tectonophysics 781https://doi.org/10.1016/j.tecto.2020.228374. 228374.
Hessler, A.M., Fildani, A., 2015. Andean forearc dynamics, as recorded by detrital zircon from the Eocene Talara Basin, Northwest Peru. J. Sediment. Res. 85 (6), 646–659.
Hu, J., Liu, L., Hermosillo, A., Zhou, Q., 2016. Simulation of late Cenozoic South American flat-slab subduction using geodynamic models with data assimilation. Earth Planet. Sci. Lett. 438, 1–13.
Hussong, D.M., 1981. Tectonic processes and the history of the Mariana arc: a synthesis of the results of Deep Sea Drilling Project Leg 60. Initial Rep. Deep Sea Drill. Proj. 60, 909–929.
Jaillard, E., Soler, P., 1996. Cretaceous to early Paleogene tectonic evolution of the northern Central Andes (0–18 S) and its relations to geodynamics. Tectonophysics 259 (1–3), 41–53.
Jaillard, E., Hérail, G., Monfret, T., Díaz-Martínez, E., Baby, P., Lavenu, A., Dumont, J.F., 2000. Tectonic evolution of the Andes of Ecuador, Peru, Bolivia and northernmost Chile. Tectonic Evolution of South America 31, 481–559.
James, D.E., Snoke, J.A., 1994. Structure and tectonics in the region of flat subduction beneath Central Peru: Crust and uppermost mantle. J. Geophys. Res. Solid Earth 99, 6899–6912.
Jarrard, R.D., 1986. Relations among subduction parameters. Rev. Geophys. 24 (2), 217–284.
Kennan, L., Pindell, J.L., 2009. Dextral shear, terrane accretion and basin formation in the Northern Andes: best explained by interaction with a Pacific-derived Caribbean Plate? Geol. Soc. Lond., Spec. Publ. 328 (1), 487–531.
Kimbrough, D.L., Smith, D.P., Mahoney, J.B., Moore, T.E., Grove, M., Gastil, R.G., Ortega-Rivera, A., Fanning, C.M., 2001. Forearc-basin sedimentary response to rapid late cretaceous batholith emplacement in the Peninsular Ranges of southern and Baja California. Geology 29, 491–494.
Kominz, M.A., Miller, K.G., Browning, J.V., 1998. Long-term and short-term global Cenozoic Sea-level estimates. Geology 26 (4), 311–314.
Krabbenhöft, A., Bialas, J., Kopp, H., Kukowski, N., Hübscher, C., 2004. Crustal structure of the Peruvian continental margin from wide-angle seismic studies. Geophys. J. Int. 159, 749–764.
Kukowski, N., Oncken, O., 2006. Subduction Erosion—the "Normal" Mode of Fore-Arc Material transfer along the Chilean margin? In: The Andes. Springer, pp. 217–236.
Kulm, L.D., Thornburg, T.M., Schrader, H.J., Resig, J.M., 1982. Cenozoic structure, stratigraphy and tectonics of the Central Peru forearc. Geol. Soc. Lond., Spec. Publ. 10 (1), 151–169.
Larroque, C., Calassou, S., Malavieille, J., Chanier, F., 1995. Experimental modelling of forearc basin development during accretionary wedge growth. Basin Res. 7 (3), 255–268.
Mamani, M., Carlotto, V., Santos, A., Acosta, H., Rodríguez, R., Martiarena, R., Rodriguez, J., Navarro, J., Cacya, L., Alvan, A., Cornejo, T., Peña, D., Aguilar, R., 2009. Resultados de la interpolación regional de las anomalías de Bouguer y su correlación con los dominios geotectónicos del Perú Bol. Soc. Geol. Perú 103, 255–263.
Margirier, A., Robert, X., Audin, L., Gautheron, C., Bernet, M., Hall, S., Simon-Labric, T., 2015. Slab flattening, magmatism, and surface uplift in the Cordillera Occidental (northern Peru). Geology 43, 1031–1034.
Martinod, J., Husson, L., Roperch, P., Guillaume, B., Espurt, N., 2010. Horizontal subduction zones, convergence velocity and the building of the Andes. Earth Planet. Sci. Lett. 299, 299–309.
Marty, R.C., 1989. Stratigraphy and Chemical Sedimentology of Cenozoic Biogenic Sediments from the Pisco and Sechura Basins. Rice University, Peru PhD Thesis.
McCaffrey, R., 1991. Slip vectors and stretching of the Sumatran fore arc. Geology 19 (9), 881–884.
McCarthy, A.J., Elders, C.F., 1997. Cenozoic deformation in Sumatra: oblique subduction and the development of the Sumatran Fault System. Geol. Soc. Lond., Spec. Publ. 126 (1), 355–363.
Melnick, D., 2016. Rise of the central Andean coast by earthquakes straddling the Moho. Nat. Geosci. 9 (5), 401.
Michalak, M.J., Hall, S.R., Farber, D.L., Audin, L., Hourigan, J.K., 2016. (U-Th)/he thermochronology records late Miocene accelerated cooling in the north-central Peruvian Andes. Lithosphere 8 (2), 103–115.
Miller, K.G., Kominz, M.A., Browning, J.V., Wright, J.D., Mountain, G.S., Katz, M.E., Sugarman, P.J., Cramer, B.S., Christie-Blick, N., Pekar, S.F., 2005. The Phanerozoic record of global sea-level change. science 310 (5752), 1293–1298.
Moore, G.F., Bangs, N.L., Taira, A., Kuramoto, S., Pangborn, E., Tobin, H.J., 2007. Three-dimensional splay fault geometry and implications for tsunami generation. Science 318, 1128–1131.
Moore, G.F., Boston, B.B., Strasser, M., Underwood, M.B., Ratliff, R.A., 2015. Evolution of tectono-sedimentary systems in the Kumano Basin, Nankai Trough forearc. Mar. Pet. Geol. 67, 604–616. https://doi.org/10.1016/j.marpetgeo.2015.05.032.
Moxon, I.W., Graham, S.A., 1992. History and controls of subsidence in the Late Cretaceous-Tertiary Great Valley forearc basin, California. pp. 1–4.
Müller, R.D., Roest, W.R., Royer, J.Y., Gahagan, L.M., Sclater, J.G., 1997. Digital isochrons of the world's ocean floor. J. Geophys. Res. 102 (B2), 3211–3214.
Müller, R.D., Sdrolias, M., Gaina, C., Roest, W.R., 2008. Age, spreading rates, and spreading asymmetry of the world's ocean crust. Geochem. Geophys. Geosyst. 9 (4).
Müller, R.D., Seton, M., Zahirovic, S., Williams, S.E., Matthews, K.J., Wright, N.M., Shepard, G.E., Maloney, K.T., Barnett-Moore, N., Hosseinpour, M., Bower, D.J., Cannon, J., 2016. Ocean basin evolution and global-scale plate reorganization events

since Pangea breakup. Annu. Rev. Earth Planet. Sci. 44, 107–138.
Noda, A., 2016. Forearc basins: Types, geometries, and relationships to subduction zone dynamics. Geol. Soc. Am. Bull. 128, 879–895.
Oncken, O., Hindle, D., Kley, J., Elger, K., Victor, P., Schemmann, K., 2006. Deformation of the central Andean upper plate system—Facts, fiction, and constraints for plateau models. In: The Andes. Springer, Berlin, Heidelberg, pp. 3–27.
Otsuki, K., 1992. Oblique subduction, collision of microcontinents and subduction of oceanic ridge: their implications on the cretaceous tectonics of Japan. Island Arc 1 (1), 51–63.
Paquet, F., Proust, J.-N., Barnes, P.M., Pettinga, J.R., 2011. Controls on active forearc basin stratigraphy and sediment fluxes: the Pleistocene of Hawke Bay, New Zealand. GSA Bull. 123, 1074–1096.
Pardo-Casas, F., Molnar, P., 1987. Relative motion of the Nazca (Farallon) and South American plates since late cretaceous time. Tectonics 6 (3), 233–248.
Park, J.-O., Tsuru, T., Kodaira, S., Cummins, P.R., Kaneda, Y., 2002. Splay fault branching along the Nankai subduction zone. Science 297, 1157–1160.
PARSEP, Torres, J., Fontecha, B., 2001. Stratigraphy and sedimentology of wells Morsa Norte Z29M-37-1X and Lobos Z29M-9-1X.
Pazzaglia, F.J., Brandon, M.T., 2001. A Fluvial Record of Long-term Steady-state Uplift and Erosion across the Cascadia Forearc High, Western Washington State. Am. J. Sci. 301, 385–431. https://doi.org/10.2475/ajs.301.4-5.385.
Philippon, M., Corti, G., 2016. Obliquity along plate boundaries. Tectonophysics 693, 171–182.
Polliand, M., Schaltegger, U., Frank, M., Fontbote, L., 2005. Formation of intra-arc volcanosedimentary basins in the western flank of the central Peruvian Andes during late cretaceous oblique subduction: field evidence and constraints from U–Pb ages and Hf isotopes. Int. J. Earth Sci. 94, 231–242.
Pouderoux, H., Proust, J.-N., Lamarche, G., 2014. Submarine paleoseismology of the northern Hikurangi subduction margin of New Zealand as deduced from turbidite record since 16 ka. Quat. Sci. Rev. 84, 116–131.
Prudhomme, A., Baby, P., Robert, A., Brichau, S., Cuipa, E., Eude, A., Calderon, Y., O'Sullivan, P., 2019. Western thrusting and uplift in northern Central Andes (western Peruvian margin). In: Andean Tectonics. Elsevier, pp. 299–331.
Quinteros, J., Sobolev, S.V., 2013. Why has the Nazca plate slowed since the Neogene? Geology 41 (1), 31–34.
Resig, J.M., 1990. Benthic foraminiferal stratigraphy and paleoenvironments off Peru, Leg 112. In: Proceedings of the Ocean Drilling Program, Scientific Results, pp. 263–296.
Romero, D., Valencia, K., Alarcón, P., Peña, D., Ramos, V.A., 2013. The offshore basement of Perú: evidence for different igneous and metamorphic domains in the forearc. J. S. Am. Earth Sci. 42, 47–60.
Rosenbaum, G., Giles, D., Saxon, M., Betts, P.G., Weinberg, R.F., Duboz, C., 2005. Subduction of the Nazca Ridge and the Inca Plateau: Insights into the formation of ore deposits in Peru. Earth Planet. Sci. Lett. 239, 18–32.
Sandwell, D.T., Smith, W.H.F., 1997. Marine gravity anomaly from Geosat and ERS 1 satellite altimetry. J. Geophys. Res. Solid Earth 102, 10039–10054. https://doi.org/10.1029/96JB03223.
Schrader, H., Castaneda, J.C., 1990. 13. The BALLENA and DELFIN wells off Central Peru: Revised AGES1. In: Proceedings of the Ocean Drilling Program: Scientific Results, pp. 209 (The Program).
Seely, D.R., 1979. The Evolution of Structural Highs Bordering Major Forearc Basins: Convergent Margins.
Soler, P., Carlier, G., Marocco, R., 1989. Evidence for the subduction and underplating of an oceanic plateau beneath the south Peruvian margin during the late cretaceous: structural implications. Tectonophysics 163 (1–2), 13–24.
Somoza, R., 1998. Updated Nazca (Farallon)—South America relative motions during the last 40 my: implications for mountain building in the central Andean region. J. S. Am. Earth Sci. 11, 211–215.
Somoza, R., Ghidella, M.E., 2012. Late cretaceous to recent plate motions in western South America revisited. Earth Planet. Sci. Lett. 331, 152–163.
Sternbach, L. R., Bang, S., Bianchi, C., Cespedes, J., Han, Y., & Choi, D. S., 2010. PS Offshore Peru, Trujillo Basin, Block Z-46: 2D PSTM Seismic Processing Reveals Deep Basins, Normal and Trans-Tensional Faulting, and Thick Eocene/Oligocene Stratigraphically Complex Submarine Fans Linked to Evidence of Hydrocarbons/DHIs.
Strasser, M., Moore, G.F., Kimura, G., Kitamura, Y., Kopf, A.J., Lallemant, S., Park, J.-O., Screaton, E.J., Su, X., Underwood, M.B., et al., 2009a. Origin and evolution of a splay fault in the Nankai accretionary wedge. Nat. Geosci. 2, 648–652.
Strasser, M., Moore, G.F., Kimura, G., Kitamura, Y., Kopf, A.J., Lallemant, S., Park, J.-O., Screaton, E.J., Su, X., Underwood, M.B., Zhao, X., 2009b. Origin and evolution of a splay fault in the Nankai accretionary wedge. Nat. Geosci. 2, 648–652. https://doi.org/10.1038/ngeo609.
Suess, E., Von Huene, R., 1988. Ocean Drilling Program Leg 112, Peru continental margin: part 2, Sedimentary history and diagenesis in a coastal upwelling environment. Geology 16, 939–943.
Suess, E., Von Huene, R., et al., 1988. Shipboard Scientific Party, 1988. Site 684. In: Proceedings of Ocean Drilling Program, Leg. 112. College Station, TX (Ocean Drilling Program), Initial Reports, Part A, pp. 525–595.
Suess, E., Von Huene, R., et al., 1990. Proceedings of the Ocean Drilling Program. Vol. 112 Scientific Results, Peru Continental Margin. Ocean Drilling Program.
Takano, O., Itoh, Y., Kusumoto, S., 2013. Variation in forearc basin configuration and basin-filling depositional systems as a function of trench slope break development and strike-slip movement: Examples from the Cenozoic Ishikari-Sanriku-Oki and Tokai-Oki-Kumano-Nada forearc basins, Japan. In: Mechanism of Sedimentary Basin Formation: Multidisciplinary Approach on Active Plate Margins, pp. 3–25.
Taylor, F.W., Mann, P., Bevis, M.G., Edwards, R.L., Cheng, H., Cutler, K.B., Gray, S.C., Burr, G.S., Beck, J.W., Phillips, D.A., others, 2005. Rapid forearc uplift and subsidence caused by impinging bathymetric features: Examples from the New Hebrides and Solomon arcs. Tectonics 24(6).
Thornburg, T.M., Kulm, L.D., 1981. Sedimentary basins of the Peru continental margin: Structure, stratigraphy, and Cenozoic tectonics from 6 S to 16 S latitude. Geological Society of America Memoir 154, 393–422.
Travis, R.B., Gonzales, G., Pardo, A., 1976. Hydrocarbon Potential of Coastal Basins of Peru: Hydrocarbons. pp. 331–338.
Tsutsumi, H., Okada, A., 1996. Segmentation and Holocene surface faulting on the median Tectonic Line, Southwest Japan. J. Geophys. Res. Solid Earth 101 (B3), 5855–5871.
Viveen, W., Schlunegger, F., 2018. Prolonged extension and subsidence of the Peruvian forearc during the Cenozoic. Tectonophysics 730, 48–62. https://doi.org/10.1016/j.tecto.2018.02.018.
Von Huene, R., Lallemand, S., 1990. Tectonic erosion along the Japan and Peru convergent margins. Geol. Soc. Am. Bull. 102, 704–720.
Von Huene, R., Ranero, C.R., 2003. Subduction erosion and basal friction along the sediment-starved convergent margin off Antofagasta, Chile. J. Geophys. Res. Solid Earth 108. https://doi.org/10.1029/2001JB001569.
Von Huene, R., Scholl, D.W., 1991. Observations at convergent margins concerning sediment subduction, subduction erosion, and the growth of continental crust. Rev. Geophys. 29 (3), 279–316.
Von Huene, R., Suess, E., 1988. Ocean Drilling Program Leg 112, Peru continental margin: part 1, tectonic history. Geology 16, 934–938.
Von Huene, R., Ranero, C.R., Vannucchi, P., 2004. Generic model of subduction erosion. Geology 32, 913–916.
Wells, R.E., Blakely, R.J., Sugiyama, Y., Scholl, D.W., Dinterman, P.A., 2003. Basin-centered asperities in great subduction zone earthquakes: a link between slip, subsidence, and subduction erosion? J. Geophys. Res. Solid Earth 108, 10.
Winter, L.S., Tosdal, R.M., Mortensen, J.K., Franklin, J.M., 2010. Volcanic stratigraphy and geochronology of the cretaceous Lancones Basin, northwestern Peru: Position and timing of giant VMS deposits. Econ. Geol. 105 (4), 713–742.
Wipf, M.A., 2006. Evolution of the Western Cordillera and coastal margin of Peru: evidence from low-temperature thermochronology and geomorphology.
Witt, C., Bourgois, J., 2010. Forearc basin formation in the tectonic wake of a collision-driven, coastwise migrating crustal block: the example of the North Andean block and the extensional Gulf of Guayaquil-Tumbes Basin (Ecuador-Peru border area). Geol. Soc. Am. Bull. 122, 89–108. https://doi.org/10.1130/b26386.1.
Witt, C., Rivadeneira, M., Poujol, M., Barba, D., Beida, D., Beseme, G., Montenegro, G., 2017. Tracking ancient magmatism and Cenozoic topographic growth within the Northern Andes forearc: Constraints from detrital U-Pb zircon ages. Geol. Soc. Am. Bull. 129 (3–4), 415–428.
Witt, C., Reynaud, J.Y., Barba, D., Poujol, M., Aizprua, C., Rivadeneira, M., Amberg, C., 2019. From accretion to forearc basin initiation: the case of SW Ecuador, Northern Andes. Sediment. Geol. https://doi.org/10.1016/j.sedgeo.2018.11.009.
Xie, X., Heller, P.L., 2009. Plate tectonics and basin subsidence history. Geol. Soc. Am. Bull. 121, 55–64.
Yepes, H., Audin, L., Alvarado, A., Beauval, C., Aguilar, J., Font, Y., Cotton, F., 2016. A new view for the geodynamics of Ecuador: Implication in seismogenic source definition and seismic hazard assessment. Tectonics 35, 1249–1279. https://doi.org/10.1002/2015TC003941.